Expanding the Scope of Bioactive Natural Products from Myxobacteria through Alteration of Cultivation Conditions

Dissertation

zur Erlangung des Grades

des Doktors der Naturwissenschaften

der Naturwissenschaftlich-Technischen Fakultät

der Universität des Saarlandes

von

Sebastian Walesch

Saarbrücken

2023

Tag des Kolloquiums:	20.11.2023
Dekan:	Prof. Dr. Ludger Santen
Berichterstatter:	Prof. Dr. Rolf Müller
	Prof. Dr. Anna Hirsch
Vorsitz:	Prof. Dr. Christine Beemelmanns
Akad. Mitarbeiter:	Dr. Nikolas Eckert

Diese Arbeit entstand unter der Anleitung von Prof. Dr. Rolf Müller am Institut für Pharmazeutische Biotechnologie der Naturwissenschaftlich-Technischen Fakultät der Universität des Saarlandes von Oktober 2018 bis September 2023.

„Wichtig ist, dass man nicht aufhört zu fragen. Neugier hat ihren eigenen Seinsgrund.“

Albert Einstein

Danksagung

Zuerst möchte ich mich bei meinem Doktorvater Prof. Dr. Rolf Müller für die Möglichkeit bedanken, meine Doktorarbeit in seiner Arbeitsgruppe durchführen zu dürfen. Die mir gelassene Freiheit bei der Projektauswahl und – gestaltung in Kombination mit guten Ratschlägen und kritischen Nachfragen haben mir die Möglichkeit gegeben, mich als Wissenschaftler weiterzuentwickeln und nach kreativen Lösungen zu suchen. Zudem möchte ich mich bei Prof. Dr. Anna Hirsch dafür bedanken, dass sie meine Doktorarbeit als wissenschaftliche Begleiterin unterstützt hat und mir in den Thesis Commitee Meetings mit guten Anmerkungen und ihrer unterstützenden Art geholfen hat.

Ein großer Dank geht an meinen Betreuer Dr. Daniel Krug für seine durchgängige Unterstützung meiner Arbeit, sein offenes Ohr für Fragen, Sorgen und Ideen und für seine Motivation und Optimismus in schwierigen Phasen. Die zahlreichen wissenschaftlichen Gespräche und Ratschläge haben mir sehr geholfen, als Wissenschaftler zu wachsen, über den Tellerrand hinaus zu schauen und verschiedenste Probleme aus unterschiedlichen Blickwinkeln zu betrachten.

Bei meinen ehemaligen und aktuellen Kollegen Joachim, Chantal, Jake und vor allem Fabian möchte ich mich für die Betreuung im Labor, dem Beibringen zahlreicher Methoden, viele wissenschaftliche Gespräche und Ratschläge bedanken, die für meine Projekte sehr hilfreich waren. Weiterhin möchte ich mich bei Anna-Lena, Christine, Nico, Markus und Clemens für die guten Gespräche, ihre Unterstützung und Freundschaft bedanken.

Allen ehemaligen und aktuellen Mitgliedern von MINS möchte ich für die gute Zusammenarbeit, die interessanten Gespräche und den vielen Spaß auf der Arbeit und bei Freizeit-Aktivitäten danken, durch solch tolle Kollegen kann man die guten Zeiten besser genießen und die schlechten Zeiten besser ertragen.

Bei meiner Familie möchte ich mich für die Unterstützung während der Doktorarbeit, aber auch in meiner gesamten Ausbildungszeit bedanken.

Mein größter Dank gilt Joy, durch dich bin und werde ich ein besserer Wissenschaftler und Mensch. Vielen Dank für deine Hilfe, Unterstützung und Ermutigungen beim Verfassen dieser Doktorarbeit und alle schönen Momente, die wir gemeinsam erleben.

Veröffentlichungen, die nicht Teil dieser Arbeit sind

Alexander Popoff†, Joachim J. Hug†, **Sebastian Walesch**, Ronald Garcia, Lena Keller and Rolf Müller*: Structure and Biosynthesis of Myxofacyclines: Unique Myxobacterial Polyketides Featuring Varying and Rare Heterocycles. *Chemistry*, 10.1002/chem.202103095 (2021).

Sebastian Walesch†, Joy Birkelbach†, Gwenaëlle Jézéquel, F P Jake Haeckl, Julian D Hegemann, Thomas Hesterkamp, Anna K H Hirsch, Peter Hammann and Rolf Müller*: Fighting antibiotic resistance—strategies and (pre)clinical developments to find new antibacterials. *EMBO reports*, 10.15252/embr.202256033 (2023).

Julian D Hegemann, Joy Birkelbach, **Sebastian Walesch** and Rolf Müller*: Current developments in antibiotic discovery. *EMBO reports*, 10.15252/embr.202256184 (2023).

†These authors contributed equally to this work

Tagungsbeiträge

Sebastian Walesch, Ronald Garcia, Daniel Krug and Rolf Müller **(2019)** Intriguing antibacterial activities of MSr12523 (Oral Communication). **VIII. Symposium of the Interdisciplinary Graduate School of Natural Product Research, Saarbrucken, Germany.**

Sebastian Walesch, Ronald Garcia, Daniel Krug and Rolf Müller **(2019)** Investigation of MSr12523 – a myxobacterium with intriguing biosynthetic potential for anti-Gram-negative secondary metabolite production (Poster). **Vereinigung für Allgemeine und Angewandte Mikrobiologie (VAAM) Workshop, Jena, Germany.**

Sebastian Walesch, Sophie Hönig, Fabian Panter, Ronald Garcia, Daniel Krug and Rolf Müller **(2021)** The Revival of Angiolam as an Example of Chemical Diversity in a Regional Sampling Project (Poster). **HIPS Symposium, Saarbrücken, Germany.**

Joy Birkelbach†, **Sebastian Walesch†** and Daniel Krug† **(2022)** Myxobacterial Biodiversity – the Basis for Natural Product Discovery by Screening and Genome/Metabolome-Mining (Oral communication). **A Natural Product Workshop to cover best practice in isolation, separation and characterisation, virtual meeting, Ghana.**

Sebastian Walesch, Janetta Coetzee, Ronald Garcia, Sophie Hönig, Fabian Panter, Daniel Krug and Rolf Müller **(2022)** Revisiting Angiolams, a Class of Neglected Antibiotics From Myxobacteria (Poster). **Bayreuth Natural Products & Drugs Symposium (BNPDS), Bayreuth, Germany.**

Sebastian Walesch, Janetta Coetzee, Ronald Garcia, Sophie Hönig, Fabian Panter, Daniel Krug and Rolf Müller **(2022)** Revisiting Angiolams, a Class of Neglected Antibiotics From Myxobacteria (Oral communication). **Vereinigung für Allgemeine und Angewandte Mikrobiologie (VAAM) Workshop, Dortmund, Germany.**

Markus Neuber†, **Sebastian Walesch†**, Chantal Bader, Daniel Krug and Rolf Müller **(2023)** Co-cultivation of unusual myxobacteria stimulates the production of antitubercular compounds (Poster). **Vereinigung für Allgemeine und Angewandte Mikrobiologie (VAAM) Workshop, Saarbrücken, Germany.**

Zusammenfassung

Myxobakterien haben sich als ergiebige Quelle für neuartige Naturstoffe mit vielfältigen chemischen Gerüsten und faszinierenden Bioaktivitäten erwiesen. Die meisten Biosynthesewege in den Genomen von Myxobakterien können jedoch in Standard-Laborkulturen nicht mit den jeweiligen Naturstoffen in Verbindung gebracht werden. Ziel dieser Arbeit war es, dieses kryptische biosynthetische Potenzial durch Veränderung der Kultivierungsbedingungen auszunutzen. Durch Veränderungen in der Zusammensetzung der Kultivierungsmedien konnte die Produktion des Antibiotikums Angiolam gesteigert werden, wodurch die Aufreinigung von vier neuen Strukturvarianten möglich wurde. Darüber hinaus führte die Kultivierung des neuartigen Myxobakteriums MSr12523 in verschiedenen Kultivierungsmedien zur Entdeckung und Isolierung des Antibiotikums Sorangicin P als Ergänzung der Sorangicin-Klasse. Die Co-Kultivierung von MSr12523 mit mykolsäurehaltigen Bakterien löste die Produktion der neuen antimykobakteriellen Antibiotika Myxenolon und Thuggacin P aus beziehungsweise erhöhte sie. Alle Molekülfamilien wurden bezüglich ihrer chemischen Strukturen, Biosynthesewege und biologischen Aktivitäten untersucht. Schließlich wurde eine Hochdurchsatz-Screening-Plattform für Myxobakterien entwickelt, die einen neuen und schnelleren Zugang zum kryptischen Biosynthesepotenzial dieser Mikroorganismen bietet.

Abstract

Myxobacteria have turned out to be a prolific source of novel natural products with diverse chemical scaffolds and intriguing bioactivities. However, the majority of biosynthetic pathways in myxobacterial genomes cannot be linked to the matching natural products in standard laboratory cultivation settings. This thesis aimed to exploit this cryptic biosynthetic potential by altering cultivation conditions. Variations in the composition of cultivation media, increased the production levels of the antibiotic angiolam, enabling the purification of four novel congeners. Furthermore, cultivation of the novel myxobacterium MSr12523 in several cultivation media led to the discovery and purification of the sorangicin P antibiotic as an addition to the sorangicin scaffold. Co-cultivation of MSr12523 with mycolic acid containing bacteria triggered and increased the production of the novel anti-mycobacterial myxenolone and thuggacin P antibiotics, respectively. All compound families were investigated for their chemical structures, biosynthetic pathways, and biological activities. Finally, a high-throughput elicitor screening platform for myxobacteria was developed as a novel and faster way to access the cryptic biosynthetic potential of these microorganisms.

Table of Contents

1 Introduction

1.1 Bacterial infections in the 21st century

For the longest time of human history bacterial infectious diseases were among the common dangers to life, as humankind had very limited options to fight the disease-causing pathogens[1,2]. However, these infections lost their imminent life-threatening characteristic with the discovery and application of small-molecule antibiotics in the past century[1,3]. Antibiotics have become one of the pillars of modern medicine[3] after the discovery and deployment of prontosil, the first synthetic sulfonamide antibiotic, in the 1930s[4].

The purification and use of the natural products penicillin[5,6] and streptomycin[7] in the 1940s were the kick-off for a very productive era in the discovery of novel antibiotics. This era between the 1940s and 1960s, also referred to as the "golden age of antibiotics", saw the introduction of almost three quarters of the currently used antibiotic scaffolds[1]. However, decreasing discoveries of novel antibiotics from the extensively screened bacterial phylum of Actinobacteria[3,8,9] and failed attempts to find novel antibiotics by high-throughput screens of synthetic molecule libraries[10,11] drained the antibiotic discovery pipeline in the past five decades. Furthermore, the constant rise of bacteria that are resistant against several or most antibiotic classes threatens to limit the treatment of bacterial infections and consequently set humanity back into a pre-antibiotic era[12,13]. Therefore, the search for new antibiotics or other options to treat bacterial infections is still relevant today, as attested by approximately 4.95 million deaths worldwide associated with antibiotic-resistant bacteria in 2019[14] or about 1.6 million deaths caused by tuberculosis alone in 2021[15]. We recently reviewed the current (pre)clinical pipeline of antibacterial agents, the challenges associated with the development of such drugs and the opportunities to find new antibacterial agents in the future[1].

1.2 Natural products as promising source for novel drugs

Humanity has used nature as a source for the treatment of a wide range of diseases for thousands of years. The earliest records of plant-based remedies were dated around 2600 BC and the first described use of moulds and medicinal soils as medicines dates back to about 1500 BC[3,16].

Even in the 21st century, nature remains one of the most important sources for the discovery or as inspiration for new medicines. About one third of the small molecule

drugs that were approved within the past four decades are natural products or derivatives thereof[17]. If defined plant extracts and synthetic molecules whose pharmacophores are derived from a natural product are taken into account, the share of small-molecule drugs discovered from or inspired by nature rises to 51%[17] (Figure 1.1A).

Natural products are a particularly fruitful source for antibiotics, more than two thirds of the antibiotics approved between 1981 and 2019 are natural products or derivatives thereof[17]. When considering antibiotics for the systemic treatment of bacterial infections (excluding Mycobacteria), 79% of the antibiotics, currently marketed in the USA are natural products or their derivatives[1] (Figure 1.1B).

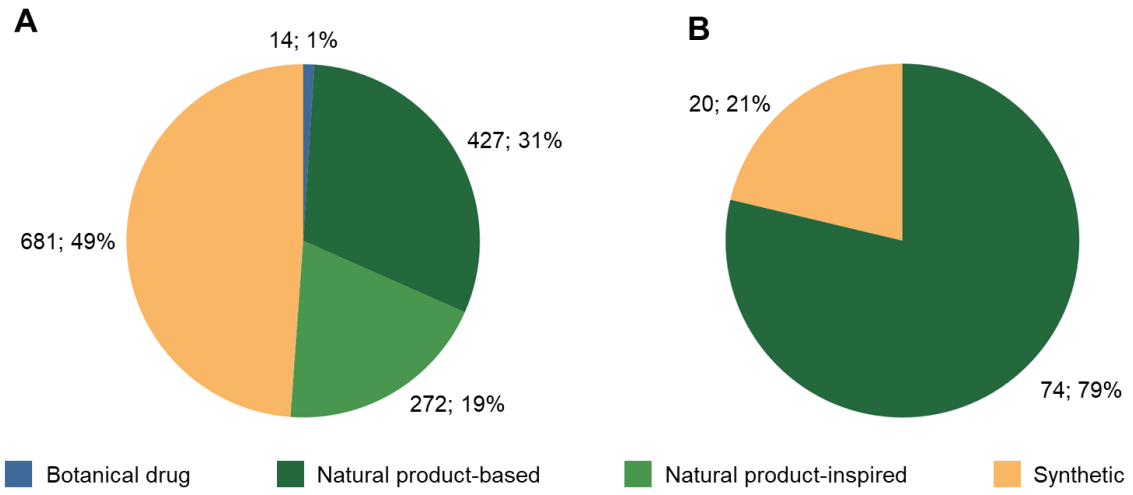

Figure 1.1: The impact of natural products as drugs: (**A**) All small-molecule drugs that were approved between 01/1981 and 09/2019. (**B**) Systemic antibiotics currently approved and marketed in the United States without antitubercular treatment. Natural product-based drugs include unaltered natural products and natural product derivatives. Natural product-inspired drugs are synthetic drugs with a natural product pharmacophore. Adapted from Newman *et al.*[17] and Walesch, Birkelbach *et al*.[1].

Moreover, natural products are great sources for the treatment of other infectious diseases, as exemplified by the antifungal amphotericin B[18], the antiprotozoal artemisinin[19] or the anthelminthic ivermectin[20]. Natural products are also used outside the realm of infectious diseases to treat a variety of illnesses, as displayed by the anticancer daunorubicin[21], the immunosuppressant rapamycin[22–24], the cholesterol biosynthesis-inhibitor lovastatin[25] or the analgesic morphine[26] (Figure 1.2).

The exceptional success of natural products as drugs against infectious diseases and cancer is obvious, as their activity might be related to the function these molecules carry out for the producing (micro)organism[27]. In order to defend themselves against their enemies or to gain an advantage over competitors, plants and microorganisms rely on

chemical warfare with small molecules, which were perfected by evolution in terms of physico-chemical properties to penetrate cell walls, cellular activity and selectivity[3,9,27,28]. Furthermore, natural products display extraordinary structural diversity with unique molecular frameworks[29], which makes them a great source and inspiration for drug discovery[16,27,29].

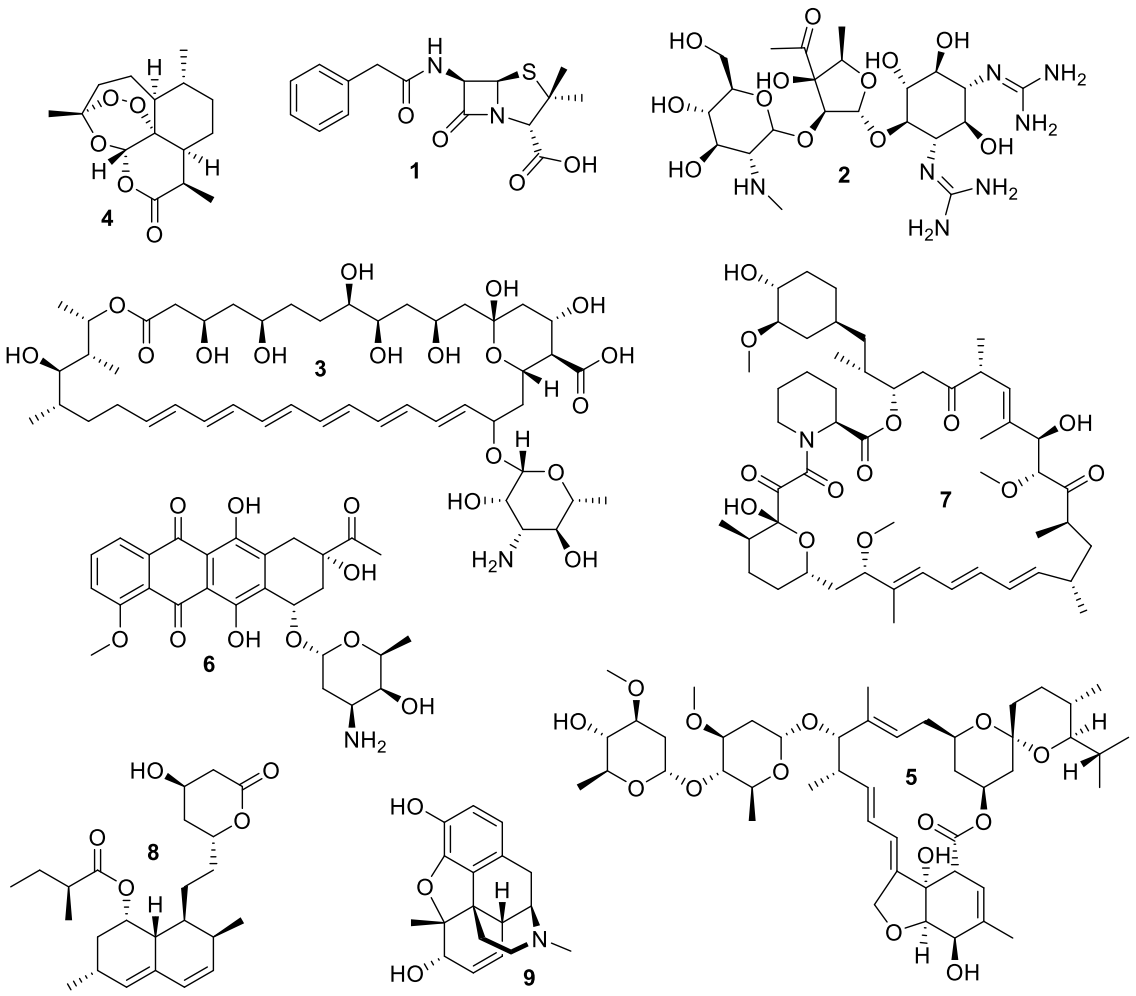

Figure 1.2: Examples of natural products with various biological activities: (**1**) Penicillin G, antibacterial; (**2**) streptomycin, antibacterial; (**3**) amphotericin B, antifungal; (**4**) artemisinin, anti-protozoal; (**5**) ivermectin, anthelminthic; (**6**) daunorubicin, cytotoxic; (**7**) rapamycin, immunosuppressing; (**8**) lovastatin, cholesterol biosynthesis-inhibiting and (**9**) morphine, analgesic.

1.2.1 **Microorganisms as prolific producers of natural products**

Historically, plants have been the main source of human medicine, although only 5-15% of plant species have been investigated for their natural products[16]. However, microorganisms might hold an even greater promise for drug discovery and development, as they display a much greater, less investigated taxonomic diversity[30],

and can be fermented in the laboratory and in large scales[31]. Furthermore, investigation and manipulation of the biosynthesis of potentially interesting natural products is much simpler in microorganisms[31].

According to the “Natural Product Atlas”, a database for microbial natural products[32], more than 20000 fungal and 13000 bacterial natural products are known as of July 2023. While fungi display a promising potential for the discovery of natural products[33,34], analysis and alteration of the underlying biosynthetic pathways can be complicated due to complex genomic architectures and limited tools for genetic manipulation[31,33]. Consequently, less than 500 biosynthetic gene clusters (BGCs) were characterised from fungi, while the number of characterised BGCs from bacteria exceeds 2000[35].

Following the findings of Waksman and colleagues in the 1940s that Gram-positive actinobacteria display an exceptional capability to produce natural products with antimicrobial and cytotoxic activities[36], they were extensively screened for antibiotics and further biologically active metabolites[1,9]. As a consequence of those screening efforts, more than half of the reported bacterial natural products and investigated BGCs belong to this phylum[32,35]. However, other less-investigated bacterial phyla like Firmicutes, Cyanobacteria and Proteobacteria have displayed their capability to produce biologically active natural products[9,32,35,37]. A recent study about the genome-encoded capability of different bacterial taxa to produce diverse arrays of natural products also counts several genera of Gram-negative myxobacteria among the potentially useful sources of new secondary metabolites[37].

1.3 **Myxobacteria**

Rod-shaped myxobacteria are a bacterial order that is ubiquitously distributed around the globe. Mostly known as soil-dwellers, the majority of described myxobacteria was isolated from soil samples in temperate climates or tropical rain forests[38]. Furthermore, they were found to grow in a variety of other environments like arctic tundra, alpine mountain regions, deserts[38], acidic soils[39], caves[40] and marine or saline settings[41–43].

As of May 2018, the reported myxobacterial strains were classified into three suborders, ten families, 29 genera and 58 species, based on 16S rRNA analysis[44]. However, the phylogenetic diversity of myxobacteria is far from covered by those taxa, as several cultivation independent analyses identified many unknown myxobacterial taxa in a variety of environmental samples[39,45,46].

Myxobacteria display an intriguing social behaviour, such as coordinated moving in multicellular swarms[47]. Upon starvation, swarms of many myxobacterial taxa form

characteristic macroscopic fruiting bodies that contain spherical dormant myxo-spores and persister-like rods[44,47,48]. With the exception of some cellulose-decomposing genera, myxobacteria are predators that feed on other microorganisms in their habitats[47]. Their cooperative behaviour also becomes obvious during predation with coordinated swarming to or around their prey and the potentially shared use of a variety of lytic enzymes and secondary metabolites[49]. Although the ability of myxobacteria to inhibit and lyse a wide range of bacteria was investigated since the late 1940s[44,50,51], it took another 30 years until the antifungal ambruticin was purified as the first secondary metabolite from myxobacteria[52].

1.3.1 Myxobacterial natural products and their biosynthesis

In the past 45 years, more than 600 different natural products belonging to a variety of chemical scaffolds were reported from myxobacteria[44] (Figure 1.3). Many of the reported natural products from myxobacteria display antibacterial, antifungal or cytotoxic activities[53,54]. This is probably due to the fact that historically most screening efforts for myxobacteria mainly focused on those activities[55,56]. Examples for myxobacterial antibiotics are the myxovirescins, mainly active against Gram-negative bacteria[57,58], the sorangicins with activities against Gram-positive bacteria[59,60] and the cystobactamids with activities against both[61]. In addition to the aforementioned ambruticin, the icumazols are examples of myxobacterial antifungals[62]. The hitherto only approved drug of myxobacterial origin is ixabepilone[63], a semisynthetic representative of the epothilone scaffold[64–67]. Other examples for cytotoxic natural products from myxobacteria are the disorazols[68] and the tubulysins[69,70]. Furthermore, screening efforts against other pathogens displayed the antiviral activities of sandacrabins[71] and thiamyxins[72] or the anti-protozoal activities of macyranone A[73]. Intriguingly, several natural product scaffolds display more than one promising biological activity, as displayed by the antibiotic or immunosuppressing properties of argyrins[74,75] and the antibiotic and anti-plasmodial activity of chlorotonil A[76,77].

Although myxobacterial natural products are chemically diverse, they seem to be mostly polyketides, non-ribosomal peptides or hybrids thereof[78,79]. However, the biosynthetic potential of myxobacteria also includes many other pathways, as exemplified by the terpenoid-based sandacrabins[71], ribosomally-synthesised and post-translationally modified peptides (RiPPs) like crocagins[80] or others like the recently reported deoxyenhygrolides[81] that might be synthesised by a few enzymes. Considering their relevance for myxobacterial natural product discovery and the natural products that were

studied in the course of this thesis, polyketide synthases (PKS) and non-ribosomal peptide synthetases (NRPS) will be shortly introduced in the following section.

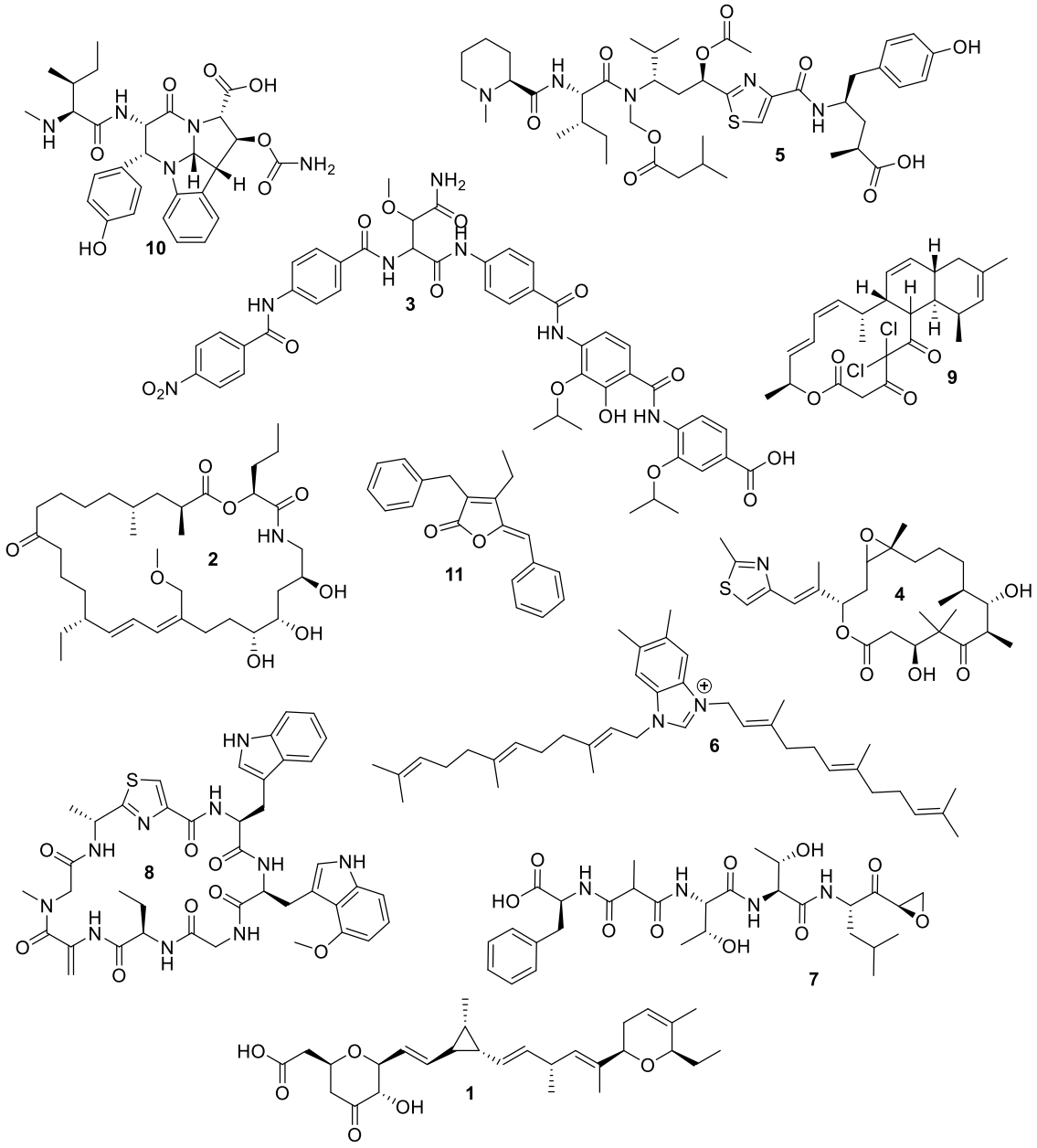

Figure 1.3: Selected examples of natural products from myxobacteria. (**1**) Ambruticin; (**2**) myxovirescin A1; (**3**) cystobactamid 919-2; (**4**) epotilone B; (**5**) tubulysin A; (**6**) sandacrabin B; (**7**) macyranone A; (**8**) argyrin B; (**9**) chlorotonil; (**10**) crocagin and (**11**) deoxyenhygrolide C.

1.3.1.1 **Modular polyketide and non-ribosomal peptide biosynthesis**

The structural diversity of polyketides and non-ribosomal peptides is especially noteworthy as they are generated out of short-chain carboxylic acid and amino acid monomers that are condensed and subsequently modified by a limited number of enzymatic reactions. Although the respective biosynthetic pathways differ in origin,

activation, condensation and subsequent modification of the incorporated building blocks, they share the modular assembly line organisation of the responsible megaenzmyes[79]. Modular PKS and NRPS assembly lines contain several modules that catalyse one elongation step of the growing polyketide or peptide, respectively. Every module includes several domains, which perform different tasks in the condensation and potential tailoring reactions of the nascent natural product[82,83]. The modular structure of PKS and NRPS facilitates a combination of these two biosynthetic pathways[84] and particularly myxobacteria feature many PKS-NRPS hybrid BGCs. Furthermore, increasing knowledge about the different domains in PKS and NRPS allow predictions about the incorporated monomers, the subsequent tailoring reactions of the growing natural product and the resulting stereochemistry[85–87].

Similar to fatty acid biosynthesis, polyketides are built by repetitive decarboxylative Claisen condensations of activated short-chain carboxylic acids[88]. In addition to modular non-iterative type I PKS megasynthases that are frequently found in myxobacteria, they sometimes also possess the biosynthetic machineries of type II and type III PKS[89,90]. These iteratively acting PKS systems are aggregates of monofunctional enzymes[83] and will not be discussed here.

The biosynthesis in a modular PKS is initiated in the loading module, where the acyltransferase (AT) domain selectively recruits a starter unit and catalyses its condensation to the acyl carrier protein (ACP; Figure 1.4A). Afterwards, the starter unit is transferred to the ketosynthase (KS) domain of the first elongation module. Each elongation module consists of at least these three domains. As described for the loading module, the AT domain recruits an extender unit that is then bound to the ACP. Afterwards, the KS domain catalyses a carbon-carbon bond formation between the nascent chain and the new extender unit attached to the ACP domain (Figure 1.4B). The resulting *β*-keto residue can be subsequently modified to an alcohol by a ketoreductase (KR) domain, converted to a double-bond by an additional dehydratase (DH) domain or fully reduced to a saturated C_2 unit by an additional enoylreductase (ER) domain (Figure 1.4C). The final module typically contains a thioesterase (TE) domain that catalyses hydrolysis or macrocyclisation of the full-length linear ketide[83,91]. Next to the varying oxidation states in the polyketide backbone, the structural diversity is greatly influenced by the incorporated starter and extender units. In addition to the typical acetyl-CoA and propionyl-CoA, CoA-thioesters of e.g. branched, aromatic or cyclic carboxylic acids can be used as starter units[83,92]. The typical extender units are malonyl-CoA and methylmalonyl-CoA, but in some biosynthetic pathways alternative extender units like ethylmalonyl-CoA, hydroxymalonyl-CoA or methoxymalonyl-CoA are incorporated[83,93].

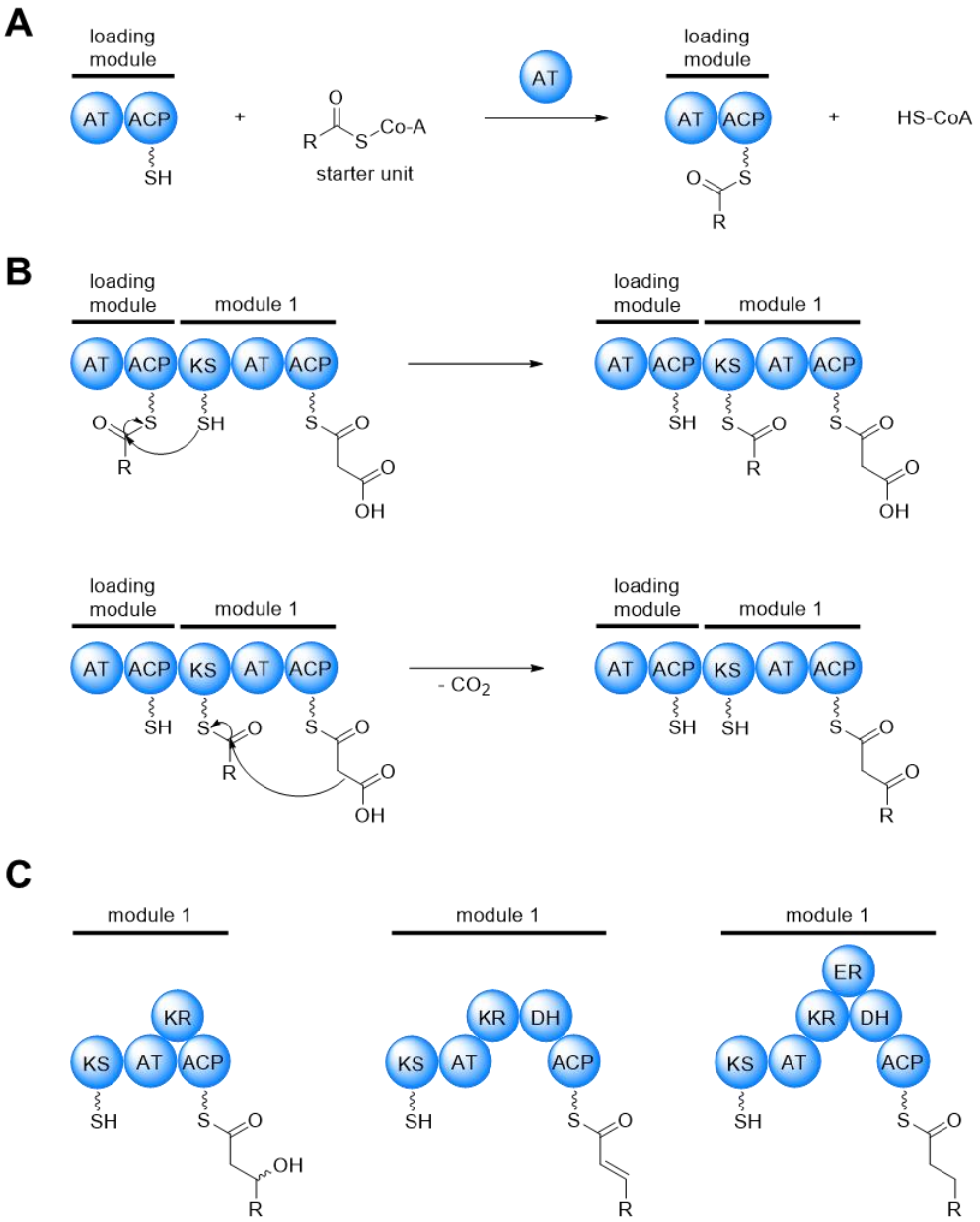

Figure 1.4: Schematic illustration of a PKS assembly line. (**A**) Loading of an acyl-CoA starter unit, catalysed by an AT domain. (**B**) Chain elongation by decarboxylative Claisen condensation. (**C**) Reductive modifications of the formed ketide by further domains in extender modules. Abbreviations are explained in the main text.

Some myxobacterial natural products like sorangicins[94] or disorazols[95] are produced by less common *trans*-AT PKS pathways. In contrast to the described type I PKS systems, *trans*-AT PKS do not contain AT domains. Instead, they possess stand-alone AT domains that are recognised by so-called docking-domains in all modules. Furthermore, they can contain additional biosynthetic features like pyran synthase (PS) domains, the ability to incorporate *β*-branches, dehydrating bi-modules or modules that incorporate *β*,*γ*-double bonds, all leading to the biosynthesis of very diverse natural products[96].

As deducible from their name, NRPS biosynthesise peptides independently of ribosomes. Similar to the modular PKS systems, NRPS are megasynthetases with a modular organisation and each module catalyses one elongation step[97]. Biosynthesis of non-ribosomal peptides is usually initiated in the loading module with the selective activation of an amino acid building block with adenosine-triphosphate (ATP) by the adenylation (A) domain (Figure 1.5). The resulting amino acyl adenylate is then condensed with the phosphopantheinyl thiol group of a peptidyl carrier protein (PCP) to form an amino acyl thioester. Next, the condensation (C) domain of the next elongation module catalyses the peptide bond formation between the amino-group of the activated extender unit bound to the PCP domain in this module and thioester of the starter unit or the growing peptide in the previous module. Finally, the biosynthesis is ended by a thioesterase (TE) domain in the last module that hydrolyses the linear peptide from the NRPS or catalyses the formation of a macrolactone or macrolactam with a hydroxyl-or amino-residue in the peptide[79,82,87]. Moreover, the nascent peptide can be modified within each module by additional domains catalysing e.g. the methylation, epimerisation, oxidation, heterocyclisation or formylation of the growing natural product[98]. Non-ribosomal peptides comprise a great diversity of chemical scaffolds, as NRPS systems are not restricted to proteinogenic amino acids as monomers for peptide synthesis, in addition to the possible modifications of amino acids within the assembly line[99,100].

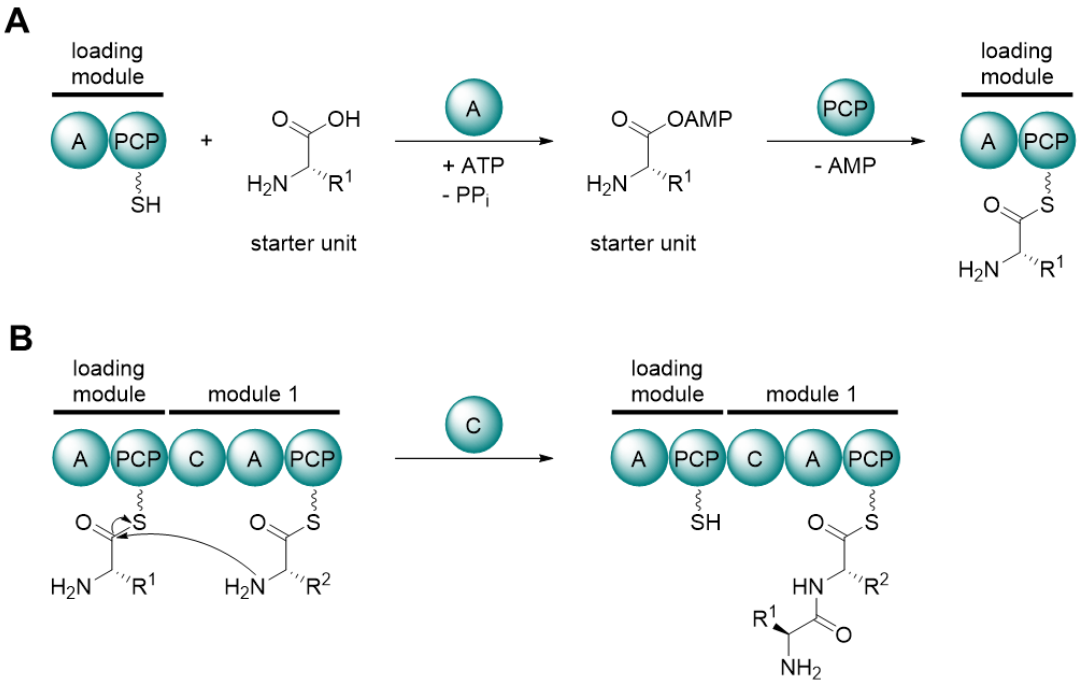

Figure 1.5: Schematic illustration of a NRPS assembly line. (**A**) Activation of an amino acid and loading on a PCP catalysed by an A domain. (**B**) Chain elongation by peptide bond formation catalysed by a C domain. Abbreviations are explained in the main text.

1.3.2 The biosynthetic potential of myxobacteria

Possibly owing to their complex life cycle and social behaviour, myxobacteria have large genomes with chromosome sizes up to 16 MBp[101,102]. Many myxobacteria dedicate at least 10% of their genomic capacity to secondary metabolism[103,104], which results in approximately 20 to 40 BGCs per strain[105]. However, several myxobacterial isolates or taxa seem to be particularly promising for natural product discovery, as exemplified by almost 50 putative BGCs in the genome of *Cystobacter* sp. SBCb004[106] or around 60 putative BGCs in several representatives of the family *Pendulisporaceae*[107].

These numbers display the vast biosynthetic potential of myxobacteria, which goes foreseeable beyond the natural product classes described from this group of bacteria to date. While different representatives of all myxobacterial suborders have displayed the capability to produce more than one chemical scaffold, the number of BGCs in their genomes is much higher[108,109]. Even in well-studied myxobacteria like *Chondromyces crocatus* Cm c5 or the "model organism" *Myxococcus xanthus* DK1622 about two thirds of the predicted BGCs could not be linked to a natural product class so far[105,108]. Therefore, comprehensive evaluation of the genomes, metabolomes and bioactivities of known and novel myxobacterial taxa holds promise to discover hitherto unknown natural products.

1.4 Assessing and accessing the biosynthetic potential of microorganisms

The ability of many microorganisms to produce more than one class of natural products and the potential effect of nutrient alterations on their metabolome has been known for several decades[110,111]. However, the actual discrepancy between the number of isolated or observed natural product scaffolds and the number of potential biosynthetic pathways was first demonstrated at the beginning of the millennium with the analysis of the complete genome sequence of the model actinomycete *Streptomyces coelicolor*[112]. With significant progress in sequencing technologies in the past two decades, providing the opportunity for rapid and cheap whole-genome sequencing, the number of publicly available genomes of microorganisms has strongly increased[113].

Evaluation of the genomes of natural product producing microorganisms displayed that only a small fraction of the observed BGCs in prolific and promising producers like Actinomycetes[114], fungi[115] or myxobacteria[108,116] could be linked to a secondary metabolite in standard laboratory cultivation settings. The cryptic biosynthetic potential

of microorganisms can be assessed with bioinformatic tools like antiSMASH that identifies putative BGCs in (genome) sequences and gives information about their location, type and predicted substructures of the potential natural products[117,118]. Further tools like PRISM or ARTS can be used to predict structures and biological activities of the products of identified BGCs[119,120], or to screen for antibiotic resistance target genes to prioritise BGCs for further evaluation[121,122].

Over the past two decades, a variety of cultivation-based and molecular-biological strategies has been introduced to access the cryptic biosynthetic potential of microorganisms.

1.4.1 Cultivation-based strategies

Cultivation-based strategies to access the unrealised biosynthetic potential of microorganisms have the advantage that they do not require genetic amenability of the organism of interest. Therefore, they can be applied to every cultivated microorganism[123].

Observations about the effects of different media components on the production of antibiotics in fungi[124] and bacteria[125] were already reported in the middle of the last century. Moreover, the antibiotic Jadomycin B was discovered in the 1990s, after its production was induced by applying stress factors to the producer strain *S. venezuelae,* such as heat shocks or addition of ethanol [126]. The enormous effects of easily accessible parameters on the metabolomes of several fungal and *Streptomyces* strains, like cultivation medium, cultivation vessel, temperature, pH or aeration, were demonstrated by Zeeck and co-workers. By comprehensive variation of these parameters, they were able to identify and purify a multitude of novel natural products and termed this approach OSMAC (One Strain MAny Compounds)[110]. Due to the simplicity and success of the method, the variation of cultivation parameters has been applied over the last two decades to find novel natural products from a variety of terrestrial and marine microorganisms[127,128]. Even in well-studied taxa like *Streptomyces*, media screening experiments can lead to the discovery of novel biologically active natural products, as exemplified by the discovery of polyether ionophores terrosamycins[129]. The identification of a fitting cultivation condition can enable the secondary metabolism of a microorganism that has not been known for its capability to produce natural products. Addition of an aqueous soil extract to cultivations of the anaerobic model organism *Clostridium cellulolyticum* enabled the production of the antibiotic closthioamide[130].

In their natural habitats, microorganisms are usually part of diverse microbial communities and employ small molecule metabolites for communication or cooperation,

but also to gain an advantage over other microorganisms. Given the significance of natural products in microbial communities, co-cultivation of two or more microorganisms presents a promising way to trigger the expression of BGCs that are cryptic in standard laboratory cultivation settings[123,131,132]. However, natural product discovery from co-cultivation of microorganisms can be complicated by the search for a promising combination of microorganisms, reproducibility issues and the complexity of resulting extracts[123,132].

Although the discovery of penicillin was the result of an unplanned co-cultivation[5], the research of microbial co-cultivation for natural products discovery has gained increasing attention since the 2000s with the availability of better analytical and chemoinformatic methods, which allow evaluation at the molecular level[132]. The capability of microbial co-cultivation to increase or trigger the production of known toxins was already shown in the last century[132,133]. However, the discoveries of the antibiotics alchivemycin A[134], keyicin[135] and amycomicin[136] from different co-cultivation settings demonstrate the opportunities of this approach for the discovery of novel biologically active natural products. Among the many microorganisms that have been investigated for their ability to induce the production of secondary metabolites in other microbes, mycolic acid containing bacteria (MACB) like *Tsukamurella*, *Rhodococcus* or *Corynebacterium* stood out for their high success rates in activating cryptic BGCs in *Streptomyces* and other actionbacteria[134,137].

While some co-cultivation settings depend on cell-cell contacts of the microbes[134,138,139], studies with different *Streptomyces* strains traced the induction of biosynthesis back to single natural products, such as the siderophore desferrioxamine E[140] or the toxins goadsporin[141] and promomycin[142]. Furthermore, signalling molecules like *γ*-butyrolactones[111], cell wall components like *N*-acetylglucosamine[143] or synthetic enzyme inhibitors[144] displayed the ability to trigger the production of secondary metabolites.

The observed ability of some small molecules to influence the production of microbial metabolites opened the possibility of screening chemical elicitors in a high-throughput manner to induce secondary metabolism of microorganisms[131,145]. In a first high throughput elicitor screening, a compound library of more than 30000 small molecules was screened for their ability to increase the production of the antibiotic pigment actinorhodin in *S. coelicolor*. The thus identified series of slightly antibiotic compounds with structural similarities to the antibiotic triclosan displayed the ability to increase or trigger the production of known and novel natural products in several *Streptomyces* and other actinobacterial strains[145]. In the past decade, Seyedsayamdost and co-workers have demonstrated the applicability of high throughput elicitor screening (HiTES) to a

wide range of microorganisms like *Burkholderia*[146], *Pseudomonas*[147], rare actinobacteria[148] or fungi[149]. Depending on the detection method, HiTES can be used to screen for elicitors based on their effect on single BGCs with genetic reporter constructs[146], the production of natural products with different bioactivities[148,150] or changes in the metabolome[147,151,152]. The capacity of HiTES to enable the discovery of novel natural products with interesting biological activities is demonstrated by the antibiotic taylorflavins[148], the antifungal acyl-suguramide A[153] or the antiproliferative momomycin[154].

At the moment, there are only few reports yet about the effects of altered cultivation conditions, co-cultivation or small molecule elicitors on the metabolome of myxobacteria. However, these studies demonstrate the opportunities of cultivation-based strategies to discover novel and bioactive natural products from different myxobacteria[155–158].

1.4.2 **Molecular-biological strategies**

In contrast to the untargeted cultivation-based strategies to trigger the production of cryptic metabolites, molecular-biological strategies enable researchers to prioritise specific BGCs for investigation, for instance based on a biosynthetic pathway or the presence of self-resistance genes within or nearby the cluster[1,159,160]. These strategies can be divided into methods to activate or enhance the expression of biosynthetic genes in the natural host or methods to heterologously express the BGC in another microorganism.

The advantage of using the original host for biosynthetic pathway activations is that it should also possess the pathways for precursor supply, cofactors and additional enzymes that might be encoded outside the BGC[123]. A successful strategy for the activation of cryptic BGCs in many different bacteria is the introduction of constitutively active or inducible promoters to control the expression of crucial biosynthetic genes[123,159,160]. In myxobacteria this strategy has recently led to the discovery of the antibiotic pyxidicycline[89] or the plasmid encoded sandarazols[161]. In many prokaryotic and eukaryotic producers of natural products pathway specific regulators were identified within or near the respective BGCs[123,160]. These regulators can be used to realise the production of otherwise cryptic natural products as exemplified by the discovery of the cytotoxic stambomycin[162]. Moreover, in well-studied microorganisms such as *Aspergillus* or *Streptomyces*, the discovery and manipulation of pleiotropic regulators could be used to control the expression of several biosynthetic pathways[160,163,164].

The investigation of BGCs of interest in the native host can be complicated by slow growth or the lack of tools for genetic manipulation. In these cases, heterologous expression of those BGCs in genetically tractable and fast-growing host strains can enable the production of the respective natural product[123,159,160]. Over the past decade, the heterologous expression of unknown BGCs has become a viable strategy for the discovery of new antibiotics as demonstrated by the purification of taromycin[165] or thiotetronic acid[166]. Also in myxobacteria, the heterologous expression of interesting BGCs can lead to the discovery of new natural products as displayed by the discoveries of the type lll PKS derived alkylpyrones[90] or the NRPS-derived siderophore sorangibactin[167].

1.5 Outline of this thesis

Myxobacteria have demonstrated their value as source for biologically active natural products in the past decades. As the majority of observed BGCs cannot be linked to a natural product in standard laboratory cultivation settings, the hitherto discovered natural products present only a small fraction of the actual biosynthetic potential of myxobacteria. Inspired by the successful application of different strategies to harness the cryptic biosynthetic potential of a variety of microorganisms, the work described in this thesis was aimed at using cultivation based strategies to enable the discovery of novel bioactive natural products from myxobacteria. The thus purified compounds were then investigated for their structures, biological activities and biosyntheses.

Evaluation of two novel myxobacterial isolates from a regional sampling campaign revived the interest in the weak antibiotic angiolam A, which was originally reported almost 40 years ago[168,169]. In chapter 2, the production of angiolam A and its previously unknown congeners could be improved by the use of a different cultivation medium. Moreover, the addition of biosynthetic precursors channelled the production towards novel angiolam derivatives D and F. In the course of this study, the angiolam BGC could be verified by single crossover gene disruption. Furthermore, the previously unknown anti-protozoal bioactivity of the angiolam scaffold was demonstrated.

Chapter 3 describes an OSMAC-style media screening with the new and promising myxobacterium *Pendulispora* sp. MSr12523. In one of the screened media, crude extracts of MSr12523 displayed a good activity against several bacteria. Follow-up and larger scale cultivation in bioreactors led to the purification of a novel subclass of the antibiotic sorangicin scaffold. The evaluated sorangicin P-796 displays moderate

activities against *Escherichia coli* and *Acinetobacter baumannii* and good activities against a range of Gram-positive bacteria.

Based on its immense biosynthetic potential, MSr12523 was also chosen for co-cultivation studies with several mycolic acid containing bacteria (Chapter 4). Co-cultivation extracts of MSr12523 with *Tsukamurella pseudospuame* stood out because of a strongly increased antibiotic activity against *Mycobacterium smegmatis* and obvious changes in the LC-MS chromatogram, compared to crude extracts of axenic cultures. The capability of co-cultivation to trigger the production of novel natural products with promising biological activities was demonstrated with the discovery and investigation of the myxenolone compound family.

In order to establish a quicker way to access the cryptic biosynthetic potential of myxobacteria, a higher throughput elicitor screening was developed in chapter 5. Screening events in a 24 deep-well plate scale displayed the effects of ten rationally chosen elicitors on the metabolome of several myxobacterial strains from all three suborders. A comprehensive statistical evaluation of cultivations of *M. xanthus* DK1622 with several elicitor conditions pointed towards the transferability of results from the screening scale to standard flask cultivations. Furthermore, two of the tested elicitors demonstrated their capabilities to trigger the production of previously undetected molecular networks in three myxobacteria.

Altogether, the work presented within this thesis demonstrates the impact and successful application of different cultivation-based strategies to trigger the production of novel and biologically active natural products from myxobacteria.

1.6 References

1. Walesch, S. *et al.* Fighting antibiotic resistance-strategies and (pre)clinical developments to find new antibacterials. *EMBO Rep.,* e56033; 10.15252/embr.202256033 (2022).
2. Harrison, F. *et al.* A 1,000-Year-Old Antimicrobial Remedy with Antistaphylococcal Activity. *mBio* **6,** e01129; 10.1128/mBio.01129-15 (2015).
3. Hutchings, M. I., Truman, A. W. & Wilkinson, B. Antibiotics: past, present and future. *Curr. Opin. Microbiol.* **51,** 72–80; 10.1016/j.mib.2019.10.008 (2019).
4. Otten, H. Domagk and the development of the sulphonamides. *J Antimicrob Chemother* **17,** 689–696; 10.1093/jac/17.6.689 (1986).
5. A Fleming. On the antibacterial action of cultures of a penicillium, with special reference to their use in the isolation of B. influenzæ. Br. J. Exp. Pathol. 10, 226–236 (1929). *Br. J. Exp. Pathol.* **10,** 226 (1929).
6. Abraham, E. P. *et al.* FURTHER OBSERVATIONS ON PENICILLIN. *The Lancet* **238,** 177–189; 10.1016/S0140-6736(00)72122-2 (1941).
7. Waksman, S. A. & Schatz, A. Streptomycin–Origin, Nature, and Properties*††Journal Series Paper of the Department of Microbiology of the New Jersey Agricultural Experiment Station, Rutgers University. *Journal of the American Pharmaceutical Association (Scientific ed.)* **34,** 273–291; 10.1002/jps.3030341102 (1945).
8. Ribeiro, M. & Simões, M. Advances in the antimicrobial and therapeutic potential of siderophores. *Environ Chem Lett* **17,** 1485–1494; 10.1007/s10311-019-00887-9 (2019).
9. Wright, G. D. Opportunities for natural products in 21st century antibiotic discovery. *Nat. Prod. Rep.* **34,** 694–701; 10.1039/c7np00019g (2017).
10. Payne, D. J., Gwynn, M. N., Holmes, D. J. & Pompliano, D. L. Drugs for bad bugs: confronting the challenges of antibacterial discovery. *Nat. Rev. Drug Discov.* **6,** 29–40; 10.1038/nrd2201 (2007).
11. Tommasi, R., Brown, D. G., Walkup, G. K., Manchester, J. I., & Miller, A. A. ESKAPEing the labyrinth of antibacterial discovery, 529–542 (2015).
12. Ventola, C. L. The Antibiotic Resistance Crisis: Part 1: Causes and Threats. *Pharmacy and Therapeutics* **40,** 277–283 (2015).

13. Lewis, K. The Science of Antibiotic Discovery. *Cell* **181,** 29–45; 10.1016/j.cell.2020.02.056 (2020).

14. Murray, C. J. L. *et al.* Global burden of bacterial antimicrobial resistance in 2019: a systematic analysis. *Lancet* **399,** 629–655; 10.1016/S0140-6736(21)02724-0 (2022).

15. World Health Orgaization (WHO). Global tuberculosis report 2022. *World Health Organization* (2022).

16. Cragg, G. M. & Newman, D. J. Natural products: a continuing source of novel drug leads. *Biochim. Biophys. Acta* **1830,** 3670–3695; 10.1016/j.bbagen.2013.02.008 (2013).

17. Newman, D. J. & Cragg, G. M. Natural Products as Sources of New Drugs over the Nearly Four Decades from 01/1981 to 09/2019. *Journal of natural products* **83,** 770–803; 10.1021/acs.jnatprod.9b01285 (2020).

18. Dutcher, J. D. The Discovery and Development of Amphotericin B. *Diseases of the Chest* **54,** 296–298; 10.1378/chest.54.Supplement_1.296 (1968).

19. Klayman, D. L. *et al.* Isolation of artemisinin (qinghaosu) from Artemisia annua growing in the United States. *J. Nat. Prod.* **47,** 715–717; 10.1021/np50034a027 (1984).

20. Chabala, J. C. *et al.* Ivermectin, a new broad-spectrum antiparasitic agent. *J. Med. Chem.* **23,** 1134–1136; 10.1021/jm00184a014 (1980).

21. Tan, C., Tasaka, H., Yu, K.-P., Murphy, M. L. & Karnofsky, D. A. Daunomycin, an antitumor antibiotic, in the treatment of neoplastic disease.Clinical evaluation with special reference to childhood leukemia. *Cancer* **20,** 333–353; 10.1002/1097-0142(1967)20:3<333::AID-CNCR2820200302>3.0.CO;2-K (1967).

22. Sehgal, S. N., Baker H. & Vézina, C. Rapamycin (AY-22,989), a new antifungal antibiotic. II. Fermentation, isolation and characterization. *J. Antibiot.* **28,** 727–732; 10.7164/antibiotics.28.727 (1975).

23. Vézina, C., Kudelski, A. & Sehgal, S. N. Rapamycin (AY-22,989), a new antifungal antibiotic. I. Taxonomy of the producing streptomycete and isolation of the active principle. *J. Antibiot.* **28,** 721–726; 10.7164/antibiotics.28.721 (1975).

24. Swindells, D. N., White, P. S. & Findlay, J. A. The X-ray crystal structure of rapamycin, $C_{51}H_{79}NO_{13}$. *Can. J. Chem.* **56,** 2491–2492; 10.1139/v78-407 (1978).

25. Alberts, A. W. Discovery, biochemistry and biology of lovastatin. *Am. J. Cardiol.* **62,** 10J-15J; 10.1016/0002-9149(88)90002-1 (1988).

26. Schmitz, R. Friedrich Wilhelm Sertürner and the discovery of morphine. *Pharmacy in history* **27,** 61–74 (1985).

27. Laraia, L. & Waldmann, H. Natural product inspired compound collections: evolutionary principle, chemical synthesis, phenotypic screening, and target identification. *Drug discovery today. Technologies* **23,** 75–82; 10.1016/j.ddtec.2017.03.003 (2017).

28. Lakemeyer, M., Zhao, W., Mandl, F. A., Hammann, P. & Sieber, S. A. Thinking Outside the Box-Novel Antibacterials To Tackle the Resistance Crisis. *Angewandte Chemie (International ed. in English)* **57,** 14440–14475; 10.1002/anie.201804971 (2018).

29. Grabowski, K. & Schneider, G. Properties and Architecture of Drugs and Natural Products Revisited. *Current Chemical Biology* **1,** 115–127; 10.2174/187231307779814066 (2007).

30. Locey, K. J. & Lennon, J. T. Scaling laws predict global microbial diversity. *Proc. Natl. Acad. Sci. USA* **113,** 5970–5975; 10.1073/pnas.1521291113 (2016).

31. Bode, H. B. & Müller, R. The impact of bacterial genomics on natural product research. *Angew. Chem. Int. Ed. Engl.* **44,** 6828–6846; 10.1002/anie.200501080 (2005).

32. van Santen, J. A. *et al.* The Natural Products Atlas 2.0: a database of microbially-derived natural products. *Nucleic Acids Res.* **50,** D1317-D1323; 10.1093/nar/gkab941 (2022).

33. van der Lee, Theo A J & Medema, M. H. Computational strategies for genome-based natural product discovery and engineering in fungi. *Fungal Genet. Biol.* **89,** 29–36; 10.1016/j.fgb.2016.01.006 (2016).

34. Hyde, K. D. *et al.* The amazing potential of fungi: 50 ways we can exploit fungi industrially. *Fungal Diversity* **97,** 1–136; 10.1007/s13225-019-00430-9 (2019).

35. Terlouw, B. R. *et al.* MIBiG 3.0: a community-driven effort to annotate experimentally validated biosynthetic gene clusters. *Nucleic Acids Res.* **51,** D603-D610; 10.1093/nar/gkac1049 (2023).

36. Waksman, S. A., Schatz, A. & Reynolds, D. M. Production of antibiotic substances by actinomycetes. *Annals of the New York Academy of Sciences* **1213,** 112–124; 10.1111/j.1749-6632.2010.05861.x (2010).

37. Gavriilidou, A. *et al.* Compendium of specialized metabolite biosynthetic diversity encoded in bacterial genomes. *Nat. Microbiol.* **7,** 726–735; 10.1038/s41564-022-01110-2 (2022).

38. Dawid, W. Biology and global distribution of myxobacteria in soils. *FEMS Microbiol. Rev.* **24,** 403–427; 10.1111/j.1574-6976.2000.tb00548.x (2000).

39. Mohr, K. I., Zindler, T., Wink, J., Wilharm, E. & Stadler, M. Myxobacteria in high moor and fen: An astonishing diversity in a neglected extreme habitat. *MicrobiologyOpen* **6,** e00464; 10.1002/mbo3.464 (2017).

40. Menne, B. Myxobacteria in cave sediments of the French Jura Mountains. *Microbiol. Res.* **154,** 1–8; 10.1016/S0944-5013(99)80027-5 (1999).

41. Albataineh, H. & Stevens, D. C. Marine Myxobacteria. A Few Good Halophiles. *Mar. Drugs* **16**; 10.3390/md16060209 (2018).

42. Iizuka, T. *et al.* Enhygromyxa salina gen. nov., sp. nov., a slightly halophilic myxobacterium isolated from the coastal areas of Japan. *Syst. Appl. Microbiol.* **26,** 189–196; 10.1078/072320203322346038 (2003).

43. Iizuka, T. *et al. Pseudenhygromyxa salsuginis* gen. nov., sp. nov., a myxobacterium isolated from an estuarine marsh. *Int. J. Syst. Evol. Microbiol.* **63,** 1360–1369; 10.1099/ijs.0.040501-0 (2013).

44. Mohr, K. I. Diversity of Myxobacteria-We Only See the Tip of the Iceberg. *Microorganisms* **6**; 10.3390/microorganisms6030084 (2018).

45. Mohr, K. I., Stechling, M., Wink, J., Wilharm, E. & Stadler, M. Comparison of myxobacterial diversity and evaluation of isolation success in two niches: Kiritimati Island and German compost. *MicrobiologyOpen* **5,** 268–278; 10.1002/mbo3.325 (2016).

46. Petters, S. *et al.* The soil microbial food web revisited: Predatory myxobacteria as keystone taxa? *ISME J.*; 10.1038/s41396-021-00958-2 (2021).

47. Reichenbach, H. The ecology of the myxobacteria. *Environ. Microbiol.* **1,** 15–21; 10.1046/j.1462-2920.1999.00016.x (1999).

48. Cao, P., Dey, A., Vassallo, C. N. & Wall, D. How Myxobacteria Cooperate. *J. Mol. Biol.*; 10.1016/j.jmb.2015.07.022 (2015).

49. Munoz-Dorado, J., Marcos-Torres, F. J., Garcia-Bravo, E., Moraleda-Munoz, A. & Perez, J. Myxobacteria: Moving, Killing, Feeding, and Surviving Together. *Front. Microbiol.* **7,** 781; 10.3389/fmicb.2016.00781 (2016).

50. Singh, B. N. Myxobacteria in soils and composts; their distribution, number and lytic action on bacteria. *J. Gen. Microbiol.* **1,** 1–10; 10.1099/00221287-1-1-1 (1947).

51. Oxford, A. Observations concerning the growth and metabolic activities of myxococci in a simple protein-free liquid medium. *J. Bacteriol.* **53,** 129–138 (1947).

52. Ringel, S. M. *et al.* Ambruticin (W7783), a new antifungal antibiotic. *J. Antibiot.* **30,** 371–375; 10.7164/antibiotics.30.371 (1977).

53. Schäberle, T. F., Lohr, F., Schmitz, A. & König, G. M. Antibiotics from myxobacteria. *Nat. Prod. Rep.* **31,** 953–972; 10.1039/c4np00011k (2014).

54. Herrmann, J., Fayad, A. A. & Müller, R. Natural products from myxobacteria: novel metabolites and bioactivities. *Nat. Prod. Rep.* **34,** 135–160; 10.1039/C6NP00106H (2017).

55. Landwehr, W., Wolf, C. & Wink, J. Actinobacteria and Myxobacteria-Two of the Most Important Bacterial Resources for Novel Antibiotics. *Curr. Top. Microbiol. Immunol.*; 10.1007/82_2016_503 (2016).

56. Reichenbach, H. & Höfle, G. Biologically active secondary metabolites from myxobacteria. *Biotechnol Adv* **11,** 219–277 (1993).

57. Gerth, K., Irschik, H., Reichenbach, H. & Trowitzsch, W. The myxovirescins, a family of antibiotics from *Myxococcus virescens* (Myxobacterales). *J Antibiot (Tokyo)* **35,** 1454–1459; 10.7164/antibiotics.35.1454 (1982).

58. Trowitzsch, W., Wray, V., Gerth, K. & Höfle, G. Structure of myxovirescin A, a new macrocylic antibiotic from gliding bacteria. *J. Chem. Soc., Chem. Commun.,* 1340; 10.1039/c39820001340 (1982).

59. Jansen, R., Wray, V., Irschik, H., Reichenbach, H. & Höfle, G. Isolation and spectroscopic structure elucidation of sorangicin A, a new type of macrolide-polyether antibiotic from gliding bacteria - XXX. *Tetrahedron Lett.* **26** (1985).

60. Irschik, H., Jansen, R., Gerth, K., Hofle, G. & Reichenbach, H. The sorangicins, novel and powerful inhibitors of eubacterial RNA polymerase isolated from myxobacteria. *J. Antibiot.* **40,** 7–13 (1987).

61. Baumann, S. *et al.* Cystobactamids: myxobacterial topoisomerase inhibitors exhibiting potent antibacterial activity. *Angew. Chem. Int. Ed.* **53,** 14605–14609; 10.1002/anie.201409964 (2014).

62. Barbier, J. *et al.* Isolation and total synthesis of icumazoles and noricumazoles—antifungal antibiotics and cation-channel blockers from *Sorangium cellulosum*. *Angew. Chem. Int. Ed. Engl.* **51,** 1256–1260; 10.1002/anie.201106435 (2012).

63. Conlin, A., Fornier, M., Hudis, C., Kar, S. & Kirkpatrick, P. Ixabepilone. *Nat Rev Drug Discov* **6,** 953–954; 10.1038/nrd2469 (2007).

64. Flörsheimer, A. & Altmann, K. H. Epothilones and their analogues - a new class of promising microtubule inhibitors. *Expert Opin Ther Pat Expert Opin Ther Pat* **11,** 951–968 (2001).

65. Bollag, D. M. *et al.* Epothilones, a new class of microtubule-stabilizing agents with a taxol-like mechanism of action. *Cancer Res.* **55,** 2325–2333 (1995).

66. Gerth, K., Bedorf, N., Hofle, G., Irschik, H. & Reichenbach, H. Epothilons A and B: antifungal and cytotoxic compounds from Sorangium cellulosum (Myxobacteria). Production, physico-chemical and biological properties. *J. Antibiot.* **49,** 560–563 (1996).

67. Höfle, G. *et al.* Epothilone A and B—Novel 16-Membered macrolides with cytotoxic activity: Isolation, crystal structure, and conformation in solution. *Angew. Chem. Int. Ed. Engl.* **35,** 1567–1569; 10.1002/anie.199615671 (1996).

68. Jansen, R., Irschik, H., Reichenbach, H., Wray, V. & Höfle, G. Disorazoles, highly cytotoxic metabolites from the Sorangicin-producing bacterium *Sorangium cellulosum,* strain So ce12. *Liebigs Ann. Chem.* **1994,** 759–773 (1994).

69. Sasse, F., Steinmetz, H., Heil, J., Höfle, G. & Reichenbach, H. Tubulysins, new cytostatic peptides from myxobacteria acting on microtubuli. Production, isolation, physico-chemical and biological properties. *J. Antibiot.* **53,** 879–885; 10.7164/antibiotics.53.879 (2000).

70. Steinmetz, H. *et al.* Isolation, Crystal and Solution Structure Determination, and Biosynthesis of Tubulysins—Powerful Inhibitors of Tubulin Polymerization from Myxobacteria. *Angew. Chem.* **116,** 4996–5000; 10.1002/ange.200460147 (2004).

71. Bader, C. D. *et al.* Sandacrabins - Structurally Unique Antiviral RNA Polymerase Inhibitors from a Rare Myxobacterium. *Chemistry – A European Journal* **28,** e202104484; 10.1002/chem.202104484 (2022).

72. Haack, P. A. *et al.* Thiamyxins: Structure and Biosynthesis of Myxobacterial RNA-Virus Inhibitors. *Angew. Chem. Int. Ed.* **61,** e202212946; 10.1002/anie.202212946 (2022).

73. Keller, L. *et al.* Macyranones: Structure, Biosynthesis, and Binding Mode of an Unprecedented Epoxyketone that Targets the 20S Proteasome. *J. Am. Chem. Soc.* **137,** 8121–8130; 10.1021/jacs.5b03833 (2015).

74. Sasse, F. *et al.* Argyrins, immunosuppressive cyclic peptides from myxobacteria. I. Production, isolation, physico-chemical and biological properties. *J. Antibiot.* **55,** 543–551 (2002).

75. Vollbrecht, L. *et al.* Argyrins, immunosuppressive cyclic peptides from myxobacteria. II. Structure elucidation and stereochemistry. *J. Antibiot.* **55,** 715–721; 10.7164/antibiotics.55.715 (2002).

76. Jungmann, K. *et al.* Two of a kind-The biosynthetic pathways of chlorotonil and anthracimycin. *ACS Chem. Biol.* **10,** 2480–2490; 10.1021/acschembio.5b00523 (2015).

77. Held, J. *et al.* Antimalarial activity of the myxobacterial macrolide chlorotonil A. *Antimicrob. Agents Chemother.* **58,** 6378–6384; 10.1128/AAC.03326-14 (2014).

78. Wenzel, S. C. & Müller, R. The biosynthetic potential of myxobacteria and their impact on drug discovery. *Curr. Opin. Drug Discov. Devel.* **12,** 220–230 (2009).

79. Hug, J. J. & Müller, R. Host Development for Heterologous Expression and Biosynthetic Studies of Myxobacterial Natural Products. 6.09. In *Comprehensive Natural Products III,* edited by H.-W. (. Liu & T. P. Begley (Elsevier, Oxford, 2020), Vol. 6, pp. 149–216.

80. Viehrig, K. *et al.* Structure and biosynthesis of crocagins: polycyclic postranslationally modified ribosomal peptides from *Chondromyces crocatus*. *Angew. Chem.,* 1–5; 10.1002/anie.201612640 (2017).

81. Hug, J. J., Kjaerulff, L., Garcia, R. & Müller, R. New Deoxyenhygrolides from *Plesiocystis pacifica* Provide Insights into Butenolide Core Biosynthesis. *Mar. Drugs* **20,** 72; 10.3390/md20010072 (2022).

82. Sieber, S. A. & Marahiel, M. A. Molecular mechanisms underlying nonribosomal peptide synthesis: approaches to new antibiotics. *Chem Rev* **105,** 715–738; 10.1021/cr0301191 (2005).

83. Hertweck, C. The Biosynthetic Logic of Polyketide Diversity. *Angew. Chem. Int. Ed. Engl.* **48,** 4688–4716; 10.1002/anie.200806121 (2009).

84. Du, L. & Shen, B. Biosynthesis of hybrid peptide-polyketide natural products. *Curr. Opin. Drug Discov. Devel.* **4,** 215–228 (2001).

85. Keatinge-Clay, A. T. The structures of type I polyketide synthases. *Nat. Prod. Rep.* **29,** 1050–1073; 10.1039/c2np20019h (2012).

86. Stachelhaus, T., Mootz, H. D. & Marahiel, M. A. The specificity-conferring code of adenylation domains in nonribosomal peptide synthetases. *Chem. Biol.* **6,** 493–505; 10.1016/S1074-5521(99)80082-9 (1999).

87. Miller, B. R. & Gulick, A. M. Structural Biology of Nonribosomal Peptide Synthetases. *Methods Mol. Biol.* **1401,** 3–29; 10.1007/978-1-4939-3375-4_1 (2016).

88. Staunton, J. & Weissman, K. J. Polyketide biosynthesis: a millennium review. *Natural product reports* **18,** 380–416 (2001).

89. Panter, F., Krug, D., Baumann, S. & Müller, R. Self-resistance guided genome mining uncovers new topoisomerase inhibitors from myxobacteria. *Chem. Sci.* **9,** 4898–4908; 10.1039/C8SC01325J (2018).

90. Hug, J. J., Panter, F., Krug, D. & Müller, R. Genome mining reveals uncommon alkylpyrones as type III PKS products from myxobacteria. *J. Ind. Microbiol. Biotechnol.* **46,** 319–334; 10.1007/s10295-018-2105-6 (2019).

91. Dutta, S. *et al.* Structure of a modular polyketide synthase. *Nature* **510,** 512–517; 10.1038/nature13423 (2014).

92. Moore, B. S. & Hertweck, C. Biosynthesis and attachment of novel bacterial polyketide synthase starter units. *Nat. Prod. Rep.* **19,** 70–99; 10.1039/b003939j (2002).

93. Chan, Y. A., Podevels, A. M., Kevany, B. M. & Thomas, M. G. Biosynthesis of Polyketide Synthase Extender Units. *Nat. Prod. Rep.* **26,** 90–114; 10.1039/b801658p (2009).

94. Irschik, H. *et al.* Analysis of the sorangicin gene cluster reinforces the utility of a combined phylogenetic/retrobiosynthetic analysis for deciphering natural product assembly by trans-AT PKS. *ChemBioChem* **11,** 1840–1849; 10.1002/cbic.201000313 (2010).

95. Carvalho, R., Reid, R., Viswanathan, N., Gramajo, H. & Julien, B. The biosynthetic genes for disorazoles, potent cytotoxic compounds that disrupt microtubule formation. *Gene* **359,** 91–98; 10.1016/j.gene.2005.06.003 (2005).

96. Helfrich, E. J. N. & Piel, J. Biosynthesis of polyketides by *trans*-AT polyketide synthases. *Nat. Prod. Rep.* **33,** 231–316; 10.1039/c5np00125k (2016).

97. Marahiel, M. A. A structural model for multimodular NRPS assembly lines. *Nat. Prod. Rep.* **33,** 136–140; 10.1039/c5np00082c (2016).

98. Walsh, C. T. *et al.* Tailoring enzymes that modify nonribosomal peptides during and after chain elongation on NRPS assembly lines. *Curr. Opin. Chem. Biol.* **5,** 525–534 (2001).

99. Walsh, C. T., O'Brien, R. V. & Khosla, C. Nonproteinogenic amino acid building blocks for nonribosomal peptide and hybrid polyketide scaffolds. *Angew. Chem. Int. Ed. Engl.* **52,** 7098–7124; 10.1002/anie.201208344 (2013).

100. Caboche, S. *et al.* Norine: a database of nonribosomal peptides. *Nucleic Acids Res.* **36,** D326-D331; 10.1093/nar/gkm792 (2008).

101. Pal, S., Sharma, G. & Subramanian, S. Complete genome sequence and identification of polyunsaturated fatty acid biosynthesis genes of the myxobacterium *Minicystis rosea* DSM 24000T. *BMC Gen.* **22,** 655; 10.1186/s12864-021-07955-x (2021).

102. Han, K. *et al.* Extraordinary expansion of a Sorangium cellulosum genome from an alkaline milieu. *Scientific Reports* **3,** 2101; 10.1038/srep02101 (2013).

103. Bode, H. B. & Müller, R. Secondary metabolism in myxobacteria. In *Myxobacteria: Multicellularity and differentiation,* edited by D. Whitworth (ASM Press, Chicago, 2007), pp. 259–282.

104. Baltz, R. H. Gifted microbes for genome mining and natural product discovery. *J. Ind. Microbiol. Biotechnol.*; 10.1007/s10295-016-1815-x (2016).

105. Zaburannyi, N., Bunk, B., Maier, J., Overmann, J. & Müller, R. Genome analysis of the fruiting body forming myxobacterium *Chondromyces crocatus r*eveals high potential for natural product Biosynthesis. *Appl. Environ. Microbiol.* **82,** 1945–1957; 10.1128/AEM.03011-15 (2016).

106. Zeng, H. *et al.* Expanding the Ajudazol Cytotoxin Scaffold: Insights from Genome Mining, Biosynthetic Investigations, and Novel Derivatives. *Journal of natural products*; 10.1021/acs.jnatprod.2c00637 (2022).

107. Garcia, R. *et al.* Pendulisporaceae – a unique myxobacterial family with distinct sporulation behaviour and high potential for natural product discovery **Manuscript in preparation** (2023).

108. Bader, C. D., Panter, F. & Müller, R. In depth natural product discovery - Myxobacterial strains that provided multiple secondary metabolites. *Biotechnol. Adv.* **39,** 107480; 10.1016/j.biotechadv.2019.107480 (2020).

109. Amiri Moghaddam, J. *et al.* Analysis of the Genome and Metabolome of Marine Myxobacteria Reveals High Potential for Biosynthesis of Novel Specialized Metabolites. *Sci. Rep.* **8,** 16600; 10.1038/s41598-018-34954-y (2018).

110. Bode, H. B., Bethe, B., Höfs, R. & Zeeck, A. Big effects from Small Changes: Possible Ways to Explore Nature's Chemical Diversity. *ChemBioChem* **3,** 619–627 (2002).

111. Scherlach, K. & Hertweck, C. Triggering cryptic natural product biosynthesis in microorganisms. *Org. Biomol. Chem.* **7,** 1753–1760; 10.1039/b821578b (2009).

112. Bentley, S. D. *et al.* Complete genome sequence of the model actinomycete *Streptomyces coelicolor* A3(2). *Nature* **417,** 141–147; 10.1038/417141a (2002).

113. Land, M. *et al.* Insights from 20 years of bacterial genome sequencing. *Funct. Integr. Genomics* **15,** 141–161; 10.1007/s10142-015-0433-4 (2015).

114. Nett, M., Ikeda, H. & Moore, B. S. Genomic basis for natural product biosynthetic diversity in the actinomycetes. *Nat. Prod. Rep.* **26,** 1362–1384; 10.1039/b817069j (2009).

115. Robey, M. T., Caesar, L. K., Drott, M. T., Keller, N. P. & Kelleher, N. L. An interpreted atlas of biosynthetic gene clusters from 1,000 fungal genomes. *Proceedings of the National Academy of Sciences of the United States of America* **118,** 1–9; 10.1073/pnas.2020230118 (2021).

116. Weissman, K. J. & Müller, R. Myxobacterial secondary metabolites: bioactivities and modes-of-action. *Nat. Prod. Rep.* **27,** 1276–1295; 10.1039/c001260m (2010).

117. Medema, M. H. *et al.* antiSMASH: rapid identification, annotation and analysis of secondary metabolite biosynthesis gene clusters in bacterial and fungal genome sequences. *Nucleic Acids Res.* **39,** W339-46; 10.1093/nar/gkr466 (2011).

118. Blin, K. *et al.* antiSMASH 7.0: new and improved predictions for detection, regulation, chemical structures and visualisation. *Nucleic Acids Res.*; 10.1093/nar/gkad344 (2023).

119. Skinnider, M. A. *et al.* Genomes to natural products PRediction Informatics for Secondary Metabolomes (PRISM). *Nucleic Acids Res.* **43,** 9645–9662; 10.1093/nar/gkv1012 (2015).

120. Skinnider, M. A. *et al.* Comprehensive prediction of secondary metabolite structure and biological activity from microbial genome sequences. *Nature communications* **11,** 6058; 10.1038/s41467-020-19986-1 (2020).

121. Alanjary, M. *et al.* The Antibiotic Resistant Target Seeker (ARTS), an exploration engine for antibiotic cluster prioritization and novel drug target discovery. *Nucleic Acids Res.* **45,** W42-W48; 10.1093/nar/gkx360 (2017).

122. Mungan, M. D. *et al.* ARTS 2.0: feature updates and expansion of the Antibiotic Resistant Target Seeker for comparative genome mining. *Nucleic Acids Res.*; 10.1093/nar/gkaa374 (2020).

123. Covington, B. C., Xu, F. & Seyedsayamdost, M. R. A Natural Product Chemist's Guide to Unlocking Silent Biosynthetic Gene Clusters. *Annu. Rev. Biochem.* **90,** 763–788; 10.1146/annurev-biochem-081420-102432 (2021).

124. DAVEY, V. F. & JOHNSON, M. J. Penicillin production in corn steep media with continuous carbohydrate addition. *Appl. Microbiol.* **1,** 208–211; 10.1128/am.1.4.208-211.1953 (1953).

125. Masuma, R., Tanaka, Y., Tanaka, H. & Omura, S. Production of nanaomycin and other antibiotics by phosphate-depressed fermentation using phosphate-trapping agents. *J Antibiot* **39,** 1557–1564; 10.7164/antibiotics.39.1557 (1986).

126. Doull, J. L., Singh, A. K., Hoare, M. & Ayer, S. W. Conditions for the production of jadomycin B by Streptomyces venezuelae ISP5230: effects of heat shock, ethanol treatment and phage infection. *J. Ind. Microbiol.* **13,** 120–125; 10.1007/BF01584109 (1994).

127. Romano, S., Jackson, S. A., Patry, S. & Dobson, A. D. W. Extending the "One Strain Many Compounds" (OSMAC) Principle to Marine Microorganisms. *Mar. Drugs* **16**; 10.3390/md16070244 (2018).

128. Pan, R., Bai, X., Chen, J., Zhang, H. & Wang, H. Exploring Structural Diversity of Microbe Secondary Metabolites Using OSMAC Strategy: A Literature Review. *Front. Microbiol.* **10,** 294; 10.3389/fmicb.2019.00294 (2019).

129. Sproule, A. *et al.* Terrosamycins A and B, Bioactive Polyether Ionophores from Streptomyces sp. RKND004 from Prince Edward Island Sediment. *Marine drugs* **17**; 10.3390/md17060347 (2019).

130. Lincke, T., Behnken, S., Ishida, K., Roth, M. & Hertweck, C. Closthioamide: an unprecedented polythioamide antibiotic from the strictly anaerobic bacterium *Clostridium cellulolyticum*. *Angew. Chem. Int. Ed.* **49,** 2011–2013; 10.1002/anie.200906114 (2010).

131. Okada, B. K. & Seyedsayamdost, M. R. Antibiotic dialogues: induction of silent biosynthetic gene clusters by exogenous small molecules. *FEMS Microbiol. Rev.* **41,** 19–33; 10.1093/femsre/fuw035 (2017).

132. Bertrand, S. *et al.* Metabolite induction via microorganism co-culture: a potential way to enhance chemical diversity for drug discovery. *Biotechnol. Adv.* **32,** 1180–1204; 10.1016/j.biotechadv.2014.03.001 (2014).

133. Sonnenbichler, J., Dietrich, J. & Peipp, H. Secondary Fungal Metabolites and Their Biological Activities, V. Investigations Concerning the Induction of the Biosynthesis of Toxic Secondary Metabolites in Basidiomycetes. *Biol. Chem. Hoppe. Seyler* **375,** 71–80; 10.1515/bchm3.1994.375.1.71 (1994).

134. Onaka, H., Mori, Y., Igarashi, Y. & Furumai, T. Mycolic acid-containing bacteria induce natural-product biosynthesis in *Streptomyces* species. *Appl. Environ. Microbiol.* **77,** 400–406; 10.1128/AEM.01337-10 (2011).

135. Adnani, N. *et al.* Co-culture of Marine Invertebrate-Associated Bacteria and Interdisciplinary Technologies Enable Biosynthesis and Discovery of a New Antibiotic, Keyicin. *ACS Chem. Biol.* **12,** 3093–3102; 10.1021/acschembio.7b00688 (2017).

136. Pishchany, G. *et al.* Amycomicin is a potent and specific antibiotic discovered with a targeted interaction screen. *Proceedings of the National Academy of Sciences of the United States of America* **115,** 10124–10129; 10.1073/pnas.1807613115 (2018).

137. Hoshino, S., Onaka, H. & Abe, I. Activation of silent biosynthetic pathways and discovery of novel secondary metabolites in actinomycetes by co-culture with mycolic acid-containing bacteria. *Journal of Industrial Microbiology & Biotechnology* **46,** 363–374; 10.1007/s10295-018-2100-y (2019).

138. Cueto, M. *et al.* Pestalone, a new antibiotic produced by a marine fungus in response to bacterial challenge. *J. Nat. Prod.* **64,** 1444–1446; 10.1021/np0102713 (2001).

139. Schroeckh, V. *et al.* Intimate bacterial-fungal interaction triggers biosynthesis of archetypal polyketides in *Aspergillus nidulans*. *PNAS* **106,** 14558–14563; 10.1073/pnas.0901870106 (2009).

140. Yamanaka, K. *et al.* Desferrioxamine E produced by *Streptomyces griseus* stimulates growth and development of *Streptomyces tanashiensis*. *Microbiology* **151,** 2899–2905; 10.1099/mic.0.28139-0 (2005).

141. Onaka, H., TABATA, H., Igarashi, Y., SATO, Y. & Furumai, T. Goadsporin, a Chemical Substance which Promotes Secondary Metabolism and Morphogenesis in Streptomycetes. I. Purification and Characterization. *J. Antibiot.* **54,** 1036–1044; 10.7164/antibiotics.54.1036 (2001).

142. Sho-ichi Amano *et al.* Promomycin, a polyether promoting antibiotic production in Streptomyces spp. *J Antibiot* **63,** 486–491; 10.1038/ja.2010.68 (2010).

143. Rigali, S. *et al.* Feast or famine: the global regulator DasR links nutrient stress to antibiotic production by Streptomyces. *EMBO Rep.* **9,** 670–675; 10.1038/embor.2008.83 (2008).

144. Foley, T. L., Young, B. S. & Burkart, M. D. Phosphopantetheinyl transferase inhibition and secondary metabolism. *FEBS J* **276,** 7134–7145; 10.1111/j.1742-4658.2009.07425.x (2009).

145. Craney, A., Ozimok, C., Pimentel-Elardo, S. M., Capretta, A. & Nodwell, J. R. Chemical perturbation of secondary metabolism demonstrates important links to primary metabolism. *Chem. Biol.* **19,** 1020–1027; 10.1016/j.chembiol.2012.06.013 (2012).

146. Seyedsayamdost, M. R. High-throughput platform for the discovery of elicitors of silent bacterial gene clusters. *Proc. Natl. Acad. Sci. USA* **111,** 7266–7271; 10.1073/pnas.1400019111 (2014).

147. Xu, F. *et al.* A genetics-free method for high-throughput discovery of cryptic microbial metabolites. *Nat. Chem. Biol.*; 10.1038/s41589-018-0193-2 (2019).

148. Moon, K., Xu, F., Zhang, C. & Seyedsayamdost, M. R. Bioactivity-HiTES Unveils Cryptic Antibiotics Encoded in Actinomycete Bacteria. *ACS Chem. Biol.* **14,** 767–774; 10.1021/acschembio.9b00049 (2019).

149. Lee, S. R. & Seyedsayamdost, M. R. Induction of Diverse Cryptic Fungal Metabolites by Steroids and Channel Blockers. *Angewandte Chemie (International ed. in English)* **61,** e202204519; 10.1002/anie.202204519 (2022).

150. Han, E. J., Lee, S. R., Hoshino, S. & Seyedsayamdost, M. R. Targeted Discovery of Cryptic Metabolites with Antiproliferative Activity. *ACS Chem. Biol.* **17,** 3121–3130; 10.1021/acschembio.2c00588 (2022).

151. Zhang, C. & Seyedsayamdost, M. R. Discovery of a Cryptic Depsipeptide from Streptomyces ghanaensis via MALDI-MS-Guided High-Throughput Elicitor Screening. *Angewandte Chemie (International ed. in English)* **59,** 23005–23009; 10.1002/anie.202009611 (2020).

152. Covington, B. C. & Seyedsayamdost, M. R. MetEx, a Metabolomics Explorer Application for Natural Product Discovery. *ACS Chem. Biol.* **16,** 2825–2833; 10.1021/acschembio.1c00737 (2021).

153. Xu, F., Nazari, B., Moon, K., Bushin, L. B. & Seyedsayamdost, M. R. Discovery of a Cryptic Antifungal Compound from Streptomyces albus J1074 Using High-Throughput Elicitor Screens. *J. Am. Chem. Soc.* **139,** 9203–9212; 10.1021/jacs.7b02716 (2017).

154. Li, Y., Lee, S. R., Han, E. J. & Seyedsayamdost, M. R. Momomycin, an Antiproliferative Cryptic Metabolite from the Oxytetracycline Producer Streptomyces rimosus. *Angewandte Chemie (International ed. in English)*; 10.1002/anie.202208573 (2022).

155. Neuber, M. Alteration of the metabolite spectrum of myxobacteria through alternative cultivation and extraction techniques. Doctoral Thesis. Saarland University, 2022.

156. Walt, C., Bader, C. D., Krug, D. & Müller, R. Aggravated Cultivation of Myxobacteria Stimulates Secondary Metabolism. *(Manuscript in preparation)*.

157. Jenny Schwarz, Georg Hubmann, Ayla Schwarz, Katrin Rosenthal & Stephan Lütz. Bivariate OSMAC Designs Expand the Secondary Metabolite Production Space in Corallococcus Coralloides; 10.20944/preprints202203.0118.v1 (2022).

158. Mccurdy, H. D. & MacRae, T. H. Xanthacin. A bacteriocin of Myxococcus xanthus fb. *Can. J. Microbiol.* **20,** 131–135; 10.1139/m74-021 (1974).

159. Panter, F., Bader, C. D. & Müller, R. Synergizing the potential of bacterial genomics and metabolomics to find novel antibiotics. *Chem. Sci.,* 5994–6010; 10.1039/D0SC06919A (2021).

160. Rutledge, P. J. & Challis, G. L. Discovery of microbial natural products by activation of silent biosynthetic gene clusters. *Nat. Rev. Microbiol.* **13,** 509–523; 10.1038/nrmicro3496 (2015).

161. Panter, F., Bader, C. D. & Müller, R. The Sandarazols are Cryptic and Structurally Unique Plasmid-Encoded Toxins from a Rare Myxobacterium*. *Angewandte Chemie (International ed. in English)* **60,** 8081–8088; 10.1002/anie.202014671 (2021).

162. Laureti, L. *et al.* Identification of a bioactive 51-membered macrolide complex by activation of a silent polyketide synthase in *Streptomyces ambofaciens*. *Proc. Natl. Acad. Sci. USA* **108,** 6258–6263; 10.1073/pnas.1019077108 (2011).

163. Bayram, O. *et al.* VelB/VeA/LaeA complex coordinates light signal with fungal development and secondary metabolism. *Science* **320,** 1504–1506; 10.1126/science.1155888 (2008).

164. McKenzie, N. L. *et al.* Induction of antimicrobial activities in heterologous streptomycetes using alleles of the *Streptomyces coelicolor* gene *absA1*. *J. Antibiot.* **63,** 177–182; 10.1038/ja.2010.13 (2010).

165. Yamanaka, K. *et al.* Direct cloning and refactoring of a silent lipopeptide biosynthetic gene cluster yields the antibiotic taromycin A. *Proc. Natl. Acad. Sci. USA* **111,** 1957–1962; 10.1073/pnas.1319584111 (2014).

166. Tang, X. *et al.* Identification of Thiotetronic Acid Antibiotic Biosynthetic Pathways by Target-directed Genome Mining. *ACS Chem. Biol.* **10,** 2841–2849; 10.1021/acschembio.5b00658 (2015).

167. Gao, Y., Walt, C., Bader, C. D. & Müller, R. Genome-Guided Discovery of the Myxobacterial Thiolactone-Containing Sorangibactins. *ACS Chem. Biol.* **18,** 924–932; 10.1021/acschembio.3c00063 (2023).

168. Werner Kohl, Barbara Witte, Brigitte Kunze, Victor Wray, Dietmar Schomburg, Hans Reichenbach und Gerhard Höfle. Angiolam A - ein neues Antibiotikum aus Angiococcus. *Liebigs Ann. Chem.,* 2088–2097 (1985).

169. Kunze, B., Kohl, W., Höfle, G. & Reichenbach, H. Production, isolation, physico-chemical and biological properties of angiolam A, a new antibiotic from *Angiococcus disciformis* (Myxobacterales). *J. Antibiot.* **38,** 1649–1654 (1985).

2 Chapter: Angiolams

New Myxobacteria of the *Myxococcaceae* Clade Produce Angiolams with Antiparasitic Activities

Sebastian Walesch, Ronald Garcia, Abelhalim B. M. Mahmoud, Fabian Panter, Sophie Hönig, Pascal Mäser, Marcel Kaiser, Daniel Krug and Rolf Müller

Manuscript submitted

Contributions to the presented work

Author's effort

The author contributed to the concept of this study, planned and executed experiments, evaluated and interpreted resulting data. The author performed cultivations of MCy12716 and MCy12733 in different media and did statistical analysis of the resulting extracts to identify the novel angiolam derivatives by feature-based molecular networking. Furthermore, he purified angiolams A, B, C, D and F and conducted structure elucidation. The author also verified the angiolam biosynthetic gene cluster by single crossover gene inactivation and did the *in silico* description of the biosynthetic gene cluster as well as the resulting biosynthetic model. Moreover, the author contributed to the conception and writing of this manuscript.

Contributions by others

Ronald Garcia contributed to the project by isolating MCy12716 and MCy12733, scientific discussions and by writing of the manuscript. Abelhalim B. M. Mahmoud contributed by evaluation of bioactivity data and by writing of the manuscript. Fabian Panter contributed to the concept of this study, mentoring and conceiving, editing and proofreading of this manuscript. Sophie Hönig contributed by assisting in cultivations of MCy12716 and MCy12733 and purification of angiolam A, B and C. Marcel Kaiser performed biological assays. Daniel Krug and Rolf Müller contributed by supervision of the project and conceiving, editing and proofreading of this manuscript. The authors thank Joy Birkelbach for the verification and proofreading of the structure elucidation and scientific discussions and Clemens Schumm for his assistance in the verification of the gene inactivation. Furthermore, we wish to thank Monica Cal, Romina Rocchetti and Sonja Keller-Märki for their assistance with the parasite and cytotoxicity assays.

2.1 Abstract

Over the past century, microbial natural products have proven themselves as a substantial and fruitful source of anti-infectives. In addition to the well-studied Actinobacteria, understudied bacterial taxa like the Gram-negative myxobacteria increasingly gain attention in the ongoing search for novel and biologically active natural products. In the course of a regional sampling campaign to source novel myxobacteria we recently uncovered new myxobacterial strains MCy12716 and MCy12733 belonging to the *Myxococcaceae* clade. Early bioactivity screens of the bacterial extracts revealed the presence of bioactive natural products that were identified as angiolam A including several novel derivatives. Sequencing of the corresponding producer strains made possible the identification of the angiolam biosynthetic gene cluster which was verified by targeted gene inactivation. Based on bioinformatic analysis of the biosynthetic gene cluster a concise biosynthesis model was devised to explain angiolam biosynthesis. Importantly, novel angiolam derivatives named angiolam B, C, and D were found to display promising antiparasitic activities against *Plasmodium falciparum* in the 0.3-0.8 µM range.

Importance

The COVID-19 pandemic as well as continuously emerging antimicrobial resistance (AMR) have recently raised the awareness about limited treatment options against some infectious diseases. However, the shortage of treatment options against protozoal parasitic infections, like malaria, is much more severe, especially for the treatment of so-called neglected tropical diseases. The observation of anti-parasitic bioactivities of angiolams from MCy12716 and MCy12733 displays the hidden potential of scarcely studied natural products to have promising biological activities in understudied indications. Furthermore, the improved biological activities of novel angiolam derivatives against *P. falciparum* and the evaluation of its biosynthesis display the opportunities of the angiolam scaffold on route to treat protozoal parasitic infections as well as possible ways to increase the production of derivatives with improved bioactivities.

2.2 Introduction

Many infectious diseases have lost their status as life-threatening conditions due to the discovery, development, and application of - often natural products-based - drugs. However, protozoal parasitic infections remain among the most devastating causes of

mortality and morbidity, particularly in low- and middle-income countries. These diseases affect more than a billion people world-wide and are contributing to poverty and under-development[1–3]. Examples from the WHO list of neglected tropical diseases (NTDs) are Human African Trypanosomiasis (HAT) caused by *Trypanosoma rhodesiense* spp., Leishmaniasis caused by *Leishmania* spp., and Chagas disease (American trypanosomiasis) caused by *Trypanosoma cruzi*[4]. The three pathogens belong to the trypanosomatidae, a large family of flagellated protozoa. Although malaria, caused by *Plasmodium falciparum*, is no longer considered an NTD since 2000, the disease still remains a major challenge due to the heavy death toll and high mortality levels among pregnant women and children in malaria endemic African countries[5].

The currently available drugs to treat these diseases are problematic given their serious adverse effects, limited efficacy, and the emergence of drug resistance. Thus, there is an urgent need for the development of new, efficacious, safe, and cost-effective drugs for the fight against protozoal tropical diseases[6–8].

Natural products remain a successful source of inspiration for the discovery of new drugs. About two thirds of the drugs launched over the last twenty years derive directly or indirectly from natural resources. Moreover, of the 20 approved antiparasitic drugs, 9 were natural products or derivatives thereof[9]. So far, all approved natural products-based drugs for the treatment of protozoal infections are plant derived[9], but also microbial natural products can have promising bioactivities against protozoa, as displayed by fungal leucinostatins[10] or myxobacterial macyranone A[11] or chlorotonil A[12]. As demonstrated by the over 32,500 reported natural products, microorganisms are a prolific source of diverse and putatively biologically active metabolites[13]. This plethora of natural products holds the promise of hidden bioactivities against often under-screened pathogens. Considering myxobacterial natural products, this is displayed by the recent findings of chondramides active against SARS-CoV-2[14], the antitubercular properties of myxovalargin[15] or the potent anti-filarial activity of corallopyronin A through inhibition of its *Wolbachia* endosymbionts[16]. Moreover, evaluation of the biosynthesis can be used to enable improved production titers in the heterologous expression of a natural product as displayed for corallopyronin A[17] or to heterologously produce improved derivatives of a natural product family as displayed for the disorazoles[18].

Following the initial purification of the antifungal ambruticin from a *Sorangium* sp. strain[19], myxobacteria as a group have increasingly gained attention as prolific producers of natural products. Their immense potential to produce compounds with novel chemical scaffolds and a wide range of biological activities is displayed by their large genomes with many biosynthetic gene clusters (BGCs) as well as the over 600 known

myxobacterial natural products[20,21]. Taking into account that the majority of myxobacterial taxa has not been isolated yet[22] and that increasing phylogenetic diversity in myxobacteria entails increasing chances to find new chemical scaffolds[23], sampling campaigns to find, isolate and cultivate novel myxobacteria are a promising undertaking.

In this study, we describe the isolation of new myxobacterial producers of natural products leading to the discovery of four novel derivatives of the known natural product angiolam A. Whole genome sequencing of the new strains allowed identification of the angiolam biosynthetic gene cluster that was verified by gene disruption in the genetically amenable producer *Pyxidicoccus fallax* An d48[24,25]. Furthermore, we report the sub-micromolar bioactivities of several novel angiolam derivatives against the malaria pathogen *Plasmodium falciparum*.

2.3 Results and discussion

2.3.1 New producers of angiolam

As part of our ongoing efforts to isolate, investigate and cultivate new myxobacteria as producers of novel and bioactive natural products, we launched a regional citizen science campaign named “Sample das Saarland”. Thereby, soil samples were taken by members of the general public and channelled into the institute’s strain isolation and characterisation workflow. Among the isolates from this sampling campaign, strain MCy12716 caught our attention because its crude extract displayed anti-parasitic activities in an initial screening. HPLC-MS analysis of the bacterial extract followed by dereplication of the secondary metabolite profile of MCy12716 revealed decent production of the myxobacterial antibiotic angiolam A (**1**), previously described from *Pyxidicoccus fallax* An d30 (formerly classified as *Angiococcus disciformis* strain An d30, Figure 2.1)[26]. In addition, a number of compounds with similar fragmentation patterns suggestive of similar chemical scaffolds were observed (Figure 2.2 A, B). However, MCy12716 showed strong variations in angiolam production within subsequent cultivations, hence we searched for an alternative strain showing more stable production patterns. Thus, strain MCy12733 was eventually chosen for further analysis of the extended angiolam compound family. Based on phylogenetic analysis, strains MCy12716 and MCy12733 represent two novel producers of angiolams which are located in a phylogenetically divergent clade compared to the original producer strains An d30 and An d48 (Figure 2.1). The two novel isolates clustered within the *P. trucidator-P. caerfyrddinensis-P. xibeiensis* clade while the previously known angiolam producers

branched with *P. fallax*, displaying the contribution of the biosynthetic ability to produce angiolam in the genus *Pyxidicoccus*.

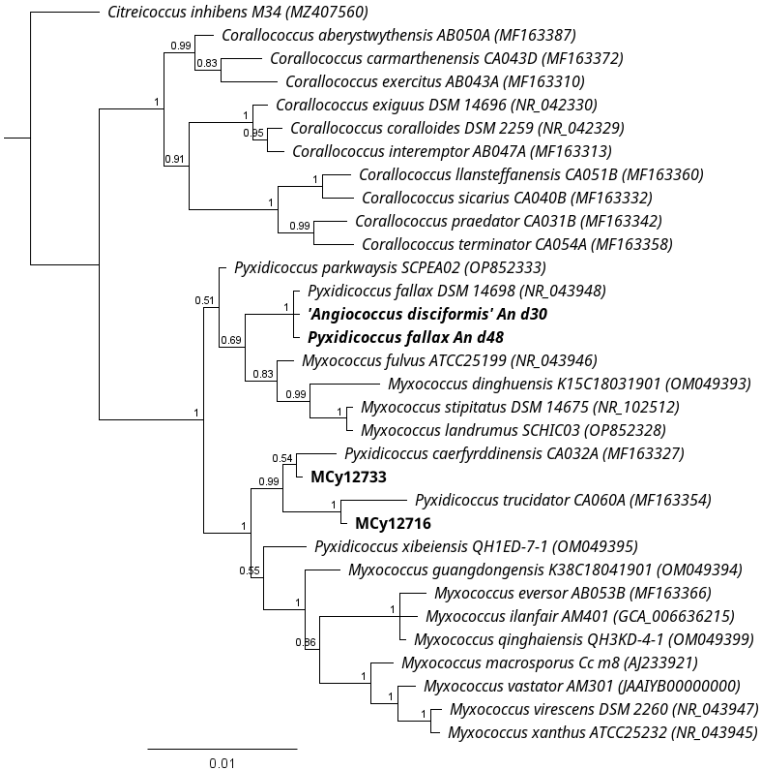

Figure 2.1: Phylogenetic cladogram inferred from 16S rRNA gene sequence showing the position of novel angiolam producer strains MCy12716 and MCy12733 in the *Myxococcaceae* clade.

2.3.2 Observation, production and structure elucidation of novel angiolam derivatives

In order to obtain a better overview of the natural product repertoire of MCy12733, the strain was cultivated in standard Cy/H medium and the resulting extracts were subjected to an untargeted metabolome mining workflow, using feature detection with subsequent MS/MS-based molecular networking according to the GNPS method[27–29]. Evaluation of these data showed that the MS/MS spectra of known angiolam A (**1**) cluster with MS/MS fragmentation spectra of five additional, to date unknown angiolam congeners (Figure 2.2 B).

As several of these observed angiolam-like compounds were produced in very low levels, a cultivation media screening was performed to improve their production. Cultivation of MCy12733 in RG5 medium improved the production of most observed angiolam derivatives two- to three-fold (Figure 2.2 C, Tables S 2.8 – S 2.9). Analysis of

the new extracts by MS/MS feature-based molecular networking showed the production of seven additional angiolam derivatives, although mostly in trace amounts only (Figure S 2.1).

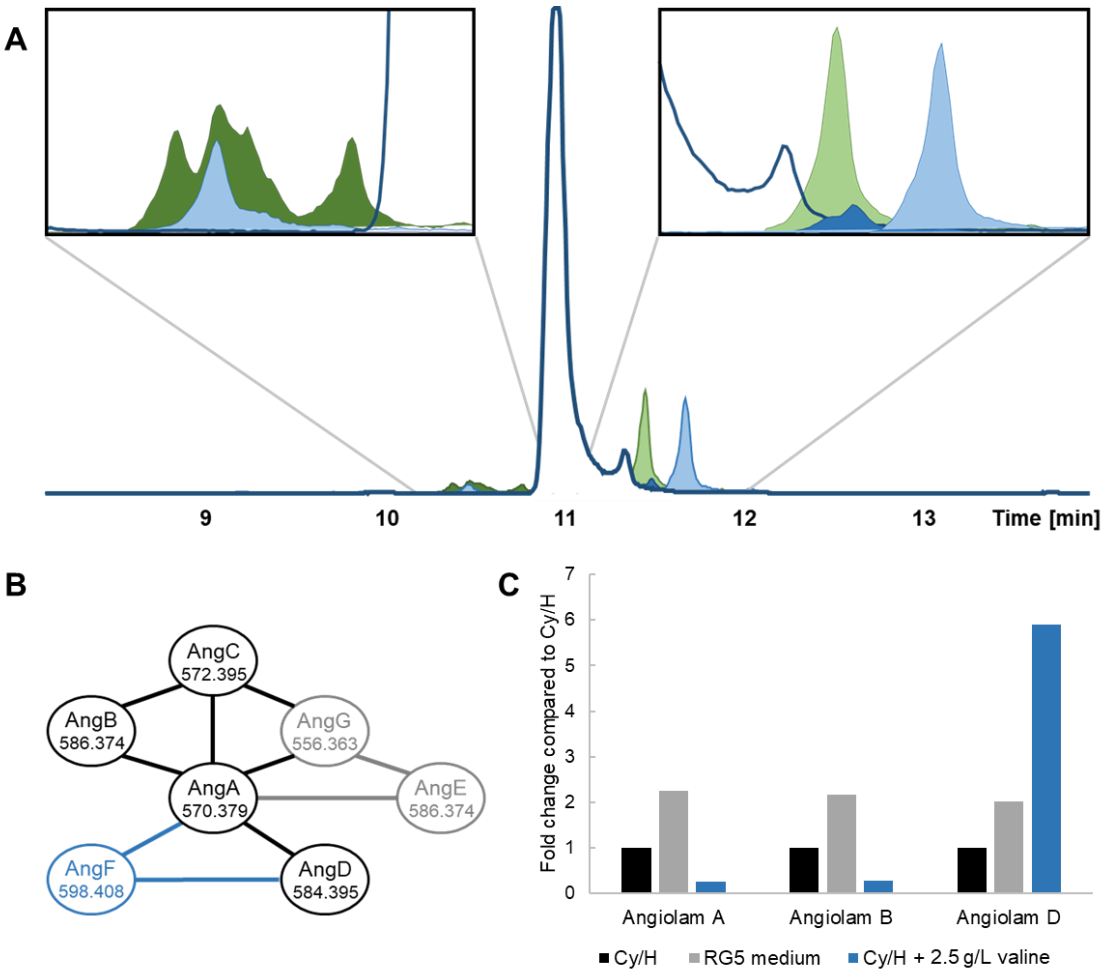

Figure 2.2: The angiolam compound family and their production. (**A**) Extracted ion chromatograms (EIC) of angiolam A (**1**, middle, dark blue/white) and its derivatives. Right box: angiolam B (**2**, light blue), C (**3**, light green) and D (**4a**/**4b**, blue). Left box: angiolam E (light blue) and G (dark green). (**B**) Feature-based molecular network, constructed by GNPS, of the angiolam compound family. Derivatives that were observed in Cy/H medium and subsequently purified are marked black. Angiolam F (**5**, blue) was observed and purified from Cy/H with additional 2.5 g/L L-valine. Angiolam derivatives that could not be purified due to low production yields are marked grey. The m/z ratios of the main ion in HPLC-MS measurements are indicated with the respective angiolam derivatives. Main ions, retention times and sum formulae for the observed angiolam derivatives can be found in the supporting information, Table S 2.7. (**C**) Relative production of angiolam A (**1**), B (**2**) and D (**4a**/**4b**) of MCy12733, when cultivated in different media. Data for all angiolam derivatives can be found in tables S 2.8 and S 2.9.

Furthermore, the effect of added amino acids and polyketide precursors on the production of angiolam derivatives was tested. Addition of 2.5 g/L L-valine to Cy/H medium improved the production of novel angiolam D (**4a/4b**) about six-fold (Figure 2.2B, Tables S 2.7 – S 2.8). Production of all other angiolam derivatives was reduced about

four-fold under these conditions making this a good example of precursor guided steering of the angiolam biosynthesis. Further analysis of the extract with MS/MS feature-based molecular networking also led to the observation of novel angiolam F (**5**) that was only produced in cultivations with L-valine added to the production medium (Figure 2.2 A).

In order to allow compound isolation angiolams were produced in large scale cultivations of MCy12733 using different media and subsequently purified by preparative HPLC and, in case of angiolam derivatives C (**3**) and D (**4a/4b**), further separated by supercritical fluid chromatography.

As part of compound purification efforts angiolam A was also isolated and its known structure verified. High-resolution electrospray-ionisation mass spectrometry (HRESI-MS) of angiolam A (**1**) shows a $[M\text{-}H_2O+H]^+$ signal at *m/z* 570.3785 (calc. 570.37889 Δ = 0.68 ppm) that corresponds to a molecular sum formula of $C_{34}H_{53}NO_7$ for [M]. The sum formula as well as the resulting nine double bond equivalents (DBEs) match the reported structure of angiolam A[30,31]. Comparison of ^1H, ^{13}C and HSQC NMR spectra of **1** with authentic angiolam A confirmed the purified compound as angiolam A. Following the biosynthetic logic of angiolam A, we propose and employ a numeration for this family of natural products (Figure 2.3).

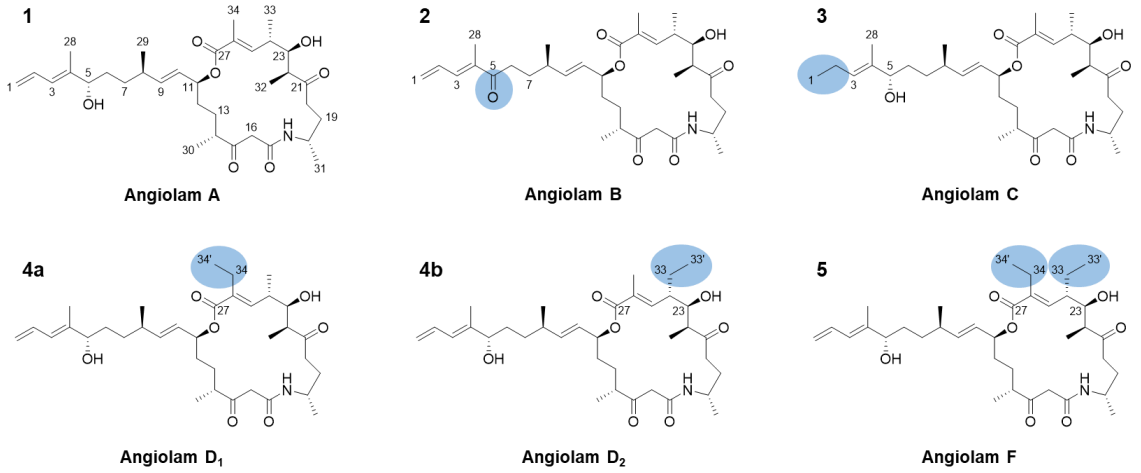

Figure 2.3: Structures of known angiolam A and novel derivatives A, B, C, D_1, D_2 and F. Differences between angiolam A and novel derivatives are highlighted in the respective structures.

Angiolam B (**2**) shows a HRESI-MS $[M+H]^+$ signal at *m/z* 586.3748 (calc. 586.37385 Δ = 1.62 ppm), corresponding to the molecular sum formula of $C_{34}H_{51}NO_7$ that has an unsaturation degree of ten DBEs. With respect to the respective spectra of angiolam A, the ^{13}C NMR spectrum of **2** displays a further carbonyl signal at $\delta_{C\text{-}5}$ 210.2 and the HSQC NMR spectrum lacks the signal corresponding to the hydroxylated methine 5 in the side

chain of **1**. HMBC NMR correlations of the surrounding H-3, H-6a, H-6b, H-7a, H-7b and H-28 to this carbonyl signal demonstrate its location as C-5.

The HRESI-MS signal of the Angiolam C (**3**) ion $[M\text{-}H_2O+H]^+$ at *m/z* 572.3955 (calc. 572.39455 Δ = 1.66 ppm) points to the molecular sum formula $C_{34}H_{55}NO_7$ for [M] with eight DBEs. Similar to angiolam B, angiolam C differs from angiolam A in the side chain. The HSQC NMR spectrum of **3** lacks the signals belonging to the terminal alkene of **1** but displays a new methyl group ($\delta_{C\text{-}1}$ 14.1, $\delta_{H\text{-}1}$ 0.97) and a new methylene group ($\delta_{C\text{-}2}$ 20.8, $\delta_{H\text{-}2}$ 2.03). COSY NMR correlations between this methylene group with the methyl group as well as with H-3 show that angiolam C is fully saturated at the end of the side chain.

Evidence from the HRESI-MS $[M\text{-}H_2O+H]^+$ signal at *m/z* 584.3953 (calc. 584.39455 Δ = 1.28 ppm) suggested that angiolam D (**4a**/**4b**) possesses a molecular sum formula of $C_{35}H_{55}NO_7$ for [M] and nine DBEs. In contrast to the angiolam derivatives described above, angiolam D seems to be a mixture of one main and several minor components with very similar retention times (Figure S 2.2). Consequently, the purification workflow yielded the mixture of angiolam D_1 (**4a**) as major and angiolam D_2 (**4b**) as minor component. However, it was possible to elucidate the structures of **4a** and **4b** out of the same data set of 1D and 2D NMR spectra.

The difference between angiolam A and D is located within the macrocycle. While **1** holds methyl-residues at C-24 and C-26, they are exchanged by an ethyl-residue at C-26 in **4a** and at C-24 in **4b**. In **4a** this is demonstrated by the HSQC NMR signals of a methyl group ($\delta_{C\text{-}34'}$ 14.0, $\delta_{H\text{-}34'}$ 1.01) and a diastereotopic methylene ($\delta_{C\text{-}34}$ 20.6, $\delta_{H\text{-}34a}$ 2.35, $\delta_{H\text{-}34b}$ 2.29). The methyl-protons H-34' show COSY-NMR correlations to the methylene protons H-34a and H-34b and HMBC-NMR correlations to the olefinic C-26 ($\delta_{C\text{-}26}$ 135.1). Furthermore, the HMBC correlations of the methylene protons H-34a and H-34b to C-25 ($\delta_{C\text{-}25}$ 141.3), C-26 ($\delta_{C\text{-}26}$ 135.1) and C-27 ($\delta_{C\text{-}27}$ 167.4) as well as the HMBC correlation between H-25 ($\delta_{H\text{-}25}$ 6.39) and C-34 demonstrate the structure of angiolam D_1. The ethyl-residue in **4b** is indicated by the HSQC NMR signals of a diastereotopic methylene ($\delta_{C\text{-}33}$ 24.2, $\delta_{H\text{-}33a}$ 2.00, $\delta_{H\text{-}33b}$ 1.33) and a methyl group ($\delta_{C\text{-}33'}$ 11.2, $\delta_{H\text{-}33'}$ 0.86). COSY NMR correlations of methylene-protons H-33a and H-33b to H-24 ($\delta_{H\text{-}24}$ 2.46) as well as to the methyl-group H-33' ($\delta_{H\text{-}33'}$ 0.86) show that these signals belong to an ethyl-residue that is bound to C-24. This is further evidenced by HMBC-NMR correlations of H-23 ($\delta_{H\text{-}23}$ 3.84) and H-25 ($\delta_{H\text{-}25}$ 6.41) to C-33 ($\delta_{C\text{-}33}$ 24.2) and reciprocal HMBC correlations between the methine H-24 ($\delta_{C\text{-}24}$ 43.2, $\delta_{H\text{-}24}$ 2.46) and the methyl-group H-33' ($\delta_{C\text{-}33'}$ 11.2, $\delta_{H\text{-}33'}$ 0.86).

Angiolam F (**5**) shows a HRESI-MS $[M\text{-}H_2O+H]^+$ signal at *m/z* 598.4121 (calc. 598.41025 Δ = 3.09 ppm), corresponding to the molecular sum formula of $C_{36}H_{57}NO_7$ for [M] and nine DBEs. Similar to angiolam D, a mixture of one major and several minor components can be seen in the crude extracts (Figure S 2.2). However, the purification workflow resulted in one pure natural product. Compared to **1**, the HSQC NMR spectrum of **5** lacks the methyl-groups 33 and 34. Instead, it displays two slightly different methyl groups at $\delta_{C\text{-}33'}$ 11.2, $\delta_{H\text{-}33'}$ 0.86 and $\delta_{C\text{-}34'}$ 13.6, $\delta_{H\text{-}34'}$ 0.99 as well as two methylene groups at $\delta_{C\text{-}33}$ 24.2, $\delta_{H\text{-}33}$ 1.98 and $\delta_{C\text{-}34}$ 20.7, $\delta_{H\text{-}34}$ 2.34, similar to the signals belonging to the ethyl-residues in **4a** and **4b**. As described above, COSY NMR correlations of methylene H-33 ($\delta_{H\text{-}33}$ 1.98) to H-24 ($\delta_{H\text{-}24}$ 2.45) and the methyl-group H-33' ($\delta_{H\text{-}33'}$ 0.86) identify an ethyl-residue bound to C-24. Furthermore, methyl-group H-34' ($\delta_{H\text{-}34'}$ 0.99) shows COSY correlations to methylene H-34 ($\delta_{H\text{-}34}$ 2.34) and HMBC-NMR correlations to olefinic C-26 ($\delta_{C\text{-}26}$ 136.6), pointing towards an ethyl-residue, bound to C-26. The identity and location of both ethyl-residues within the macrocycle are further evidenced by HMBC-NMR correlations, as elaborated for **4a** and **4b**.

Due to their low production yields, angiolam derivatives E and G could not be purified in amounts sufficient for NMR-based structure elucidation.

Considering a common biosynthetic route for angiolam A and its derivatives, it was deemed likely that they are produced by a set of enzymatic domains involved in PKS-type biosynthesis. Within the biosynthetic assembly line, these domains control the incorporation of single building blocks into the growing scaffold and determine the stereochemistry of the emerging natural product. Therefore, we propose that the reported stereochemistry of angiolam A should be found also in all newly described derivatives (Figure 2.3).

2.3.3 *In silico* analysis of the angiolam BGC and biosynthesis hypothesis

The discovery and understanding of the biosynthetic pathway for a given natural product class provides valuable insights that can be used to improve the production of these natural products or to alter its biosynthesis towards the production of novel derivatives.

In order to find the biosynthetic origin of the angiolam compound family, genome sequences of both novel producers MCy12716 and MCy12733 were obtained by Illumina sequencing. Analysis of both sequences with antiSMASH[32] together with retro-biosynthetic considerations pinpointed a candidate polyketide synthase-nonribosomal peptide synthetase (PKS-NRPS) hybrid cluster with twelve modules spanning five

genes. Alignment of the core BGC and its flanking regions was used to determine the likely cluster borders of the Angiolam BGC. According to the similarities of both sequences the *ang* BGC comprises a total of 14 genes spanning a 78.5 kb region. Detailed analysis of the genes in the *ang* BGC in MCy12733 was carried out by BLAST searches against the NCBI database (see below and supporting information, Tables S 2.18 - S 2.19). Interestingly, the genome of *P. caerfyrddinensis* CA032A, the closest described relative of MCy12733, harbours genes coding for proteins highly similar to the ones of the putative ang BGC. While these genes are present in the same order in both strains, *P. caerfyrddinensis* lacks the PKS-NRPS core as well as *angF*, encoding an acyl-CoA/acyl-ACP dehydrogenase. Therefore, it remains speculative whether the *ang* BGC only consists of the biosynthetic core *angA-angE* and *angF* or also includes the flanking genes *ang1-ang6* upstream and *ang7-ang9* downstream the core region that might also perform relevant functions for angiolam biosynthesis.

BLAST searches of *angA-angE* against draft genomes (unpublished data) of the known angiolam producing strains *Pyxidicoccus fallax* An d30[26,30] and *P. fallax* An d48[24] indicated the presence of the BGC, but divided into several contigs due to poor DNA sequence quality. Furthermore, parts of the biosynthetic machinery, divided into at least two contigs could be observed in the deposited genomes of *P. fallax* An d47 (GCA_012933655.1) and *P. fallax* CA059B (GCA_013155555.1).

In order to unambiguously verify the compound-to-BGC assignment, the angiolam biosynthetic gene cluster was inactivated via single crossover plasmid insertion. As genetic manipulation of both new angiolam producing strains MCy12716 and MCy12733 could not be achieved, the inactivation was performed in the genetically amenable producer *P. fallax* An d48[24,25]. A pCR2.1-TOPO derived vector carrying a 1 kb homology fragment of the *angB* gene was integrated into the *angB* gene on the *P. fallax* An d48 chromosome. A mutant strain was selected on YM agar, supplemented with 50 µg/mL kanamycin. It was then cultivated for gDNA extraction and subsequent verification via PCR (Figure S 2.8) as well as to generate crude extracts to monitor angiolam production.

The single cross-over inactivation abolished production of angiolam A (**1**, Figure 2.4). Furthermore, no other angiolam derivative could be detected. This finding confirmed the *ang* BGC as the locus responsible for production of the angiolam compound family.

Our biosynthetic findings agree with previous feeding experiments, revealing the biogenesis of angiolam A to comprise seven propionate equivalents, five acetate equivalents and L-alanine[30]. According to predictions by antiSMASH[32] and domain fingerprints[33], the acyltransferases (ATs) of the loading module and modules 1, 3, 6, 10, 11 and 12 selectively incorporate methylmalonyl-CoA and the ATs of modules 2, 4, 5, 7

and 9 are selective for malonyl-CoA (Table S 2.20, Figure S 2.3). The adenylation (A) domain of module 8 incorporates glycine or alanine, according to antiSMASH (Table S 2.20). Analysis of the ketoreductase (KR), dehydratase (DH), enoylreductase (ER) domains was done by antiSMASH, according to fingerprints[34,35] or based on a hidden markov model[36] (Table S 2.21, Figures S 2.4 – S 2.6). Deviations from the "colinearity rule" can be explained by inactive ER domains in modules 2 and 12, an inactive KR domain in module 10 and a missing KR domain as well as an inactive DH domain in module 7. Moreover, the *in-silico* predictions of the stereochemistry based on KR, DH and ER domains matched the actual stereochemistry of angiolam A.

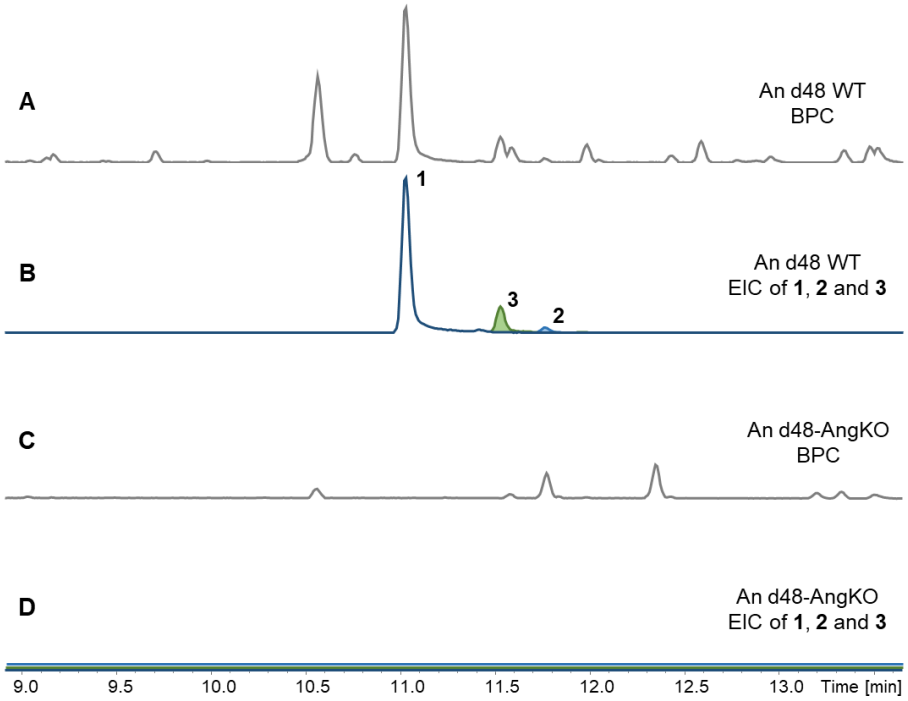

Figure 2.4: Analytical verification of the angiolam BGC assignment. UHPLC MS extracted ion chromatogram (EIC) traces of angiolam A, B, and C (B, D; blue, red, green) as $[M\text{-}H_2O+H]^+$ ions (**1**: 570.379 Da and **3**: 572.395 Da) and as $[M+H]^+$ ions (**2**: 586.374 Da) in the wild type (A, B) and in the angB single crossover inactivation mutant (C, D) crude extracts. Gray traces represent the corresponding base peak chromatograms (BPC). Intensity scale in D is magnified 100 fold. EIC traces in D are stacked for a better overview.

An unusual feature of angiolam A is the distal alkene moiety, an altogether rare structural feature in natural products[37]. The terminal alkenes in curacin A and tautomycetin are formed while or after they are released from the respective megasynthase[38,39]. Similar to angiolam A, the alkene starter in haliangicin A is part of its starter unit and is formed by the acyl-CoA dehydrogenase HliR through a γ,δ-dehydrogenation of 2-methylpent-2-enoyl-CoA[40]. Based on this finding, a possible explanation for the distal alkene moiety of angiolam A could be a dehydrogenation of the methylmalonyl-CoA derived starter unit to

prop-2-enoyl-ACP by the acyl-CoA/acyl-ACP dehydrogenase AngF in the loading module (Figure 2.5 B). However, dehydrogenation to form the distal alkene is also possible later during or after the assembly line biosynthesis.

Following incorporation of the starter unit, angiolam A undergoes seven PKS-derived elongation steps including the incorporation of four malonyl-CoA and three methylmalonyl-CoA extender units with varying oxidation states, based on the respective reductive loops. Next, L-valine is incorporated by the NRPS module 8. This is followed by four further PKS-derived elongation steps of one malonyl-CoA and three methylmalonyl-CoA extender units to form the angiolam A backbone. Finally, the fully elongated intermediate is cyclised and released from the PKS-NRPS machinery by the thioesterase (TE) domain in module 12 (Figure 2.5 A).

The likely explanations for the structural differences observed in angiolams B and C are incomplete reduction by the KR domain in module 2 and dehydrogenation reactions at the end of the angiolam side chain, respectively. The observation of the ethyl-residues in modules 11 and 12 in angiolams D and F is more surprising. As feeding experiments with L-methionine-(methyl ^{13}C) did not result in mass shifts (Figure S 2.7), a SAM dependent methylation of the respective methyl residues seemed unlikely. Therefore, we concluded that these ethyl residues originate from ethylmalonyl-CoA extender units and are incorporated by AT domains with broader substrate specificities. A prominent example for an AT domain that incorporates methylmalonyl-CoA and ethylmalonyl-CoA is the AT domain of module 5 of the monensin biosynthesic gene cluster[41]. Screening of the ang AT domains for the reported signature sequence RiDVV[41] revealed that not only modules 11 and 12, but also modules 3, 6 and 10 might have the capacity to accept ethylmalonyl-CoA as extender unit (Figure S 2.3), leading to the observed natural diversity of angiolams. We reason that this explains also the finding of angiolams D and F as mixture of several components. However, the reasons for the increased incorporation of ethylmalonyl-CoA by modules 11 and 12 in comparison to the others remains elusive. Interestingly, AT domains in modules 2, 5, 6, 7, and 8 in the epothilone BGC in *Sorangium cellulosum* So ce90[42] also display the signature sequence RiDVV. So far, there is only one report about an epothilone derivative with an ethyl-residue, putatively incorporated by one of these AT domains[43], indicating that this signature sequence might point towards AT domains that accept either methyl- or ethylmalonyl CoA as their substrate. However, the prioritisation of the substrate seems to depend on other parameters like other sequence motifs within the AT domains, KS domain substrate specificities or precursor supply.

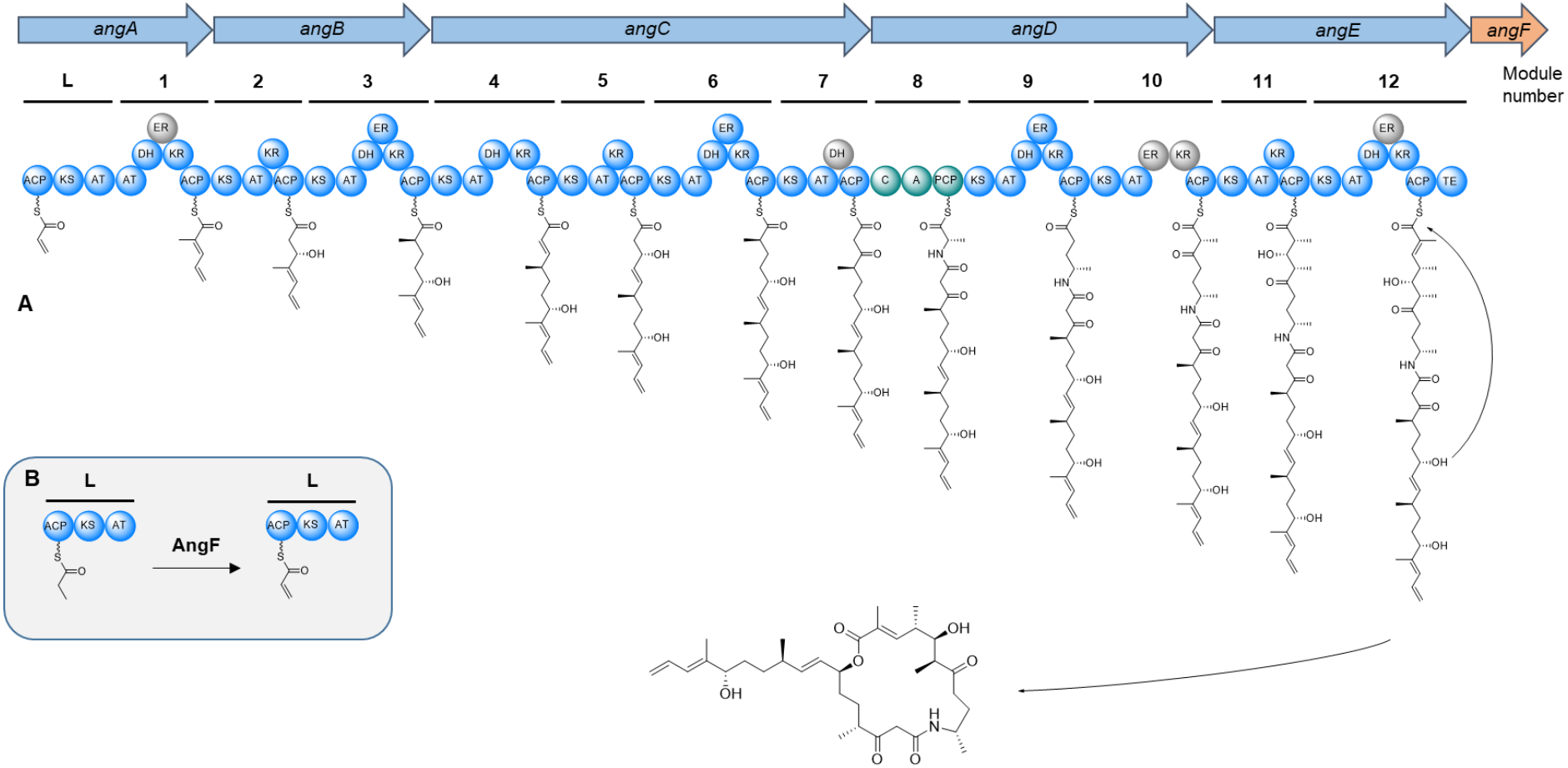

Figure 2.5: *in silico* biosynthesis of angiolam A. (**A**) Scheme of the proposed angiolam BGC and the angiolam biosynthesis model by its megasynthase. (**B**) Potential biosynthesis of the prop-2-enoyl-ACP starter unit via dehydrogenation of propanoyl-ACP by AngF. (Arrows: genes; circles: domains; A: adenylation; ACP/PCP: acyl-/peptidyl-carrier protein; AT: acyl transferase; C: condensation; DH: dehydratase; ER: enoylreductase; KR: ketoreductase; KS: ketosynthase; TE: thioesterase)

The importance of precursor supply for the incorporation of ethylmalonyl-CoA is demonstrated by the increased production of angiolams D and F in cultivations with added L-valine, as it can be a precursor for ethylmalonyl-CoA[44]. As L-valine can also be a precursor of methylmalonyl-CoA[44], feeding experiments with L-valine $^{13}C_5$ resulted in inconclusive results (data not shown). However, the role of L-valine as precursor for the ethylmalonyl-CoA supply in MCy12733 is further evidenced by the presence of a gene encoding a fused isobutyryl-CoA mutase elsewhere within its genome (Tables S 2.19 – S 2.20). Furthermore, addition of butyrate, a possible intermediate in the pathway from L-valine to ethylmalonyl-CoA also increased the production of angiolams D and F (Table S 2.22) reinforcing this hypothesis.

2.3.4 **Antiparasitic activities**

Based on the antiparasitic bioactivity of the crude extract of MCy12716, angiolams A (**1**), B (**2**), C (**3**), D (**4**), and F (**5**) were tested for their *in vitro* activities against the following protozoan parasites: *Trypanosoma brucei rhodesiense* (STIB 900) bloodstream forms, *Trypanosoma cruzi* (Tulahuen C4) amastigotes, *Leishmania donovani* (MHOM/ET/67/L82) axenic amastigotes, and *Plasmodium falciparum* (NF54) proliferative erythrocytic stages. In parallel, cytotoxicity of these compounds in rat skeletal myoblasts (L-6 cells) was determined in order to obtain an initial assessment of their selectivity. The results are reported in Table 2.1.

Activity against Trypansomatids: Comparing the activity of different angiolam congeners against *Trypanosoma brucei rhodesiense*, there is a clear matching between the antitrypanosomal activity and selectivity (A>C>D1>B>F). Angiolam A showed the highest activity (IC_{50} of 1.5 µM) towards *T. brucei* as well as preferential selectivity across all the three trypansomatids. Its trypanocidal activity is comparable to that previously described for Macyranone A, a peptide-epoxyketone isolated from another myxobacterial strain *Cystobacter fuscus* MCy9118[11]. Angiolams B, C and D showed similar activity and toxicity profiles against *T.b. rhodesiense* (IC_{50} range 4.5-6.3 µM, SI 4.4-6.8), while angiolam F was the least active and most cytotoxic.

Trypanosoma cruzi was the least sensitive parasite (IC_{50} 6.6-34.0 µM) with unfavorable selectivities displayed by most of the tested compounds (angiolams B, C, and F) due to their relatively high cytotoxicity (SI ≤ 2.1). Although both *T. brucei* and *T. cruzi* are trypansomatids, however, the lack of overlapping activity is not unusual[45]. This could be partially explained by the intracellular nature of the parasite[46]. Nevertheless, angiolam D

was found to be the most active (IC_{50} 6.5 µM), with two folds higher activity compared to angiolam A. This could be attributed to the CH_3 extension at C-33 or C-34, which on the other hand diminished the selectivity.

Angiolams exhibited moderate to low activity (IC_{50} 6.6-17.6 µM), and unsatisfactory selectivity (selectivity indices (SI) of 2–6) toward *L. donovani* axenic amastigotes. Angiolam B has shown the highest activity (IC_{50} 6.6 µM), though 20 fold less than its displayed activity against *P. falciparum*, followed by angiolam D (IC_{50} 8.2 µM). Angiolams A, C, and F showed comparable activities (IC_{50} 15.4-17.6 µM) while angiolam C being the most cytotoxic.

Activity against *Plasmodium falciparum*: The *in vitro* activity of angiolams against the erythrocytic stages of the *P. falciparum* strain NF54 was the most promising compared to the other parasites tested. Angiolams B, C and D showed activity in submicromolar concentrations (IC_{50} 0.3-0.8 µM) with high selectivities (SI ≥ 30). The most promising compound of this series was angiolam B exhibiting submicromolar activity (IC_{50} 0.3 µM) and highest selectivity (SI 91.6). We assume this could be due to the oxidation of C-5 that has an augmenting effect on both activity and selectivity. Angiolams D and F showed IC_{50} values of 0.8 and 1.3 µM, respectively. The presence of two ethyl groups in angiolam F may have contributed to the reduced activity, however, this substitution didn't show an effect on the selectivity (SI 37 for both D and F). Unlike its antitrypanosomal activity, angiolam A showed the least antiplasmodial activity and selectivity among the tested angiolam derivatives.

Table 2.1: *In vitro* Activity of compounds 1−5 against *L. donovani* (MHOM-ET-67/L82) axenic amastigotes, *P. falciparum* (NF54), *T. b. rhodesiense* (STIB 900), *T. cruzi* (Tulahuen C4) and cytotoxicity in L6 Cells.

	T. b. rhodesiense		*T. cruzi*		*L. donovani*		*P. falciparum*		Cytotox L6 Cells
ID No	IC_{50} [a] (µM)	SI [b]	IC_{50} [a] (µM)	SI [b]	IC_{50} [a] (µM)	SI [b]	IC_{50} [a] (µM)	SI [b]	IC_{50} [a] (µM)
Angiolam A (**1**)	1.5 ± 0.6	63.2	12.9 ± 5.3	7.3	16.7 ± 7.3	5.62	2.7 ± 0.5	34.9	94.0 ± 23.7
Angiolam B (**2**)	6.3 ± 1.0	4.4	30.4 ± 10.0	0.9	6.6 ± 1.9	4.22	0.3 ± 0.1	91.6	27.8 ± 2.0
Angiolam C (**3**)	4.5 ± 0.4	6.8	34.0 ± 11.6	0.9	15.4 ± 2.3	1.99	0.6 ± 0.4	53.7	30.6 ± 2.3
Angiolam D (**4**)	4.7 ± 1.9	6.0	6.5 ± 2.2	4.3	8.2 ± 4.5	3.38	0.8 ± 0.6	37.1	27.8 ± 3.7
Angiolam F (**5**)	25.0 ± 1.4	2.0	24.4 ± 5.0	2.1	17.6 ± 2.1	2.83	1.3 ± 0.6	37.4	49.9 ± 21.6
Positive control	0.02 [c]		2.47 [d]		0.53 [e]		0.004 [f]		0.02 [g]

[a] The IC_{50}s are mean values from at least three independent replicates ± standard deviation. [b] Selectivity index (SI): IC_{50} in L6 cells divided by IC_{50} in the titled parasitic strain; [c] Melarsoprol; [d] Benznidazole; [e] Miltefosine; [f] Chloroquine; [g] Podophyllotoxin.

2.4 Conclusion and outlook

This study demonstrates the opportunities of a regional sampling campaign to bring forward new myxobacterial producers of natural products, in combination with screening efforts that go beyond antibacterial or cytotoxic activities. The finding of new producing strains with unexpected bioactivities reinvigorated the interest in angiolam almost 40 years after it was first reported as an antibiotic[26,30]. This interest subsequently led to the characterisation of several novel angiolam derivatives with improved bioactivities against *P. falciparum.* It also initiated the elucidation of the underlying biosynthesis, including a potentially rare enzymatic dehydrogenation of the starter unit. Moreover, our present data highlight the potential of the angiolam scaffold as a starting point for the development of novel drugs with anti-parasitic bioactivities. This view is supported by the promising selectivity index of most angiolam derivatives against *P. falciparum* in combination with the reported tolerability of angiolam A in mice as well as the availability of a total synthesis route[26,31].

Taken together, this study illustrates the opportunities of reinvestigating “old” natural products with improved analytical and computational resources at hand. Given the energetic effort that microorganisms put into the biosynthesis of these compounds, it is likely that the competitive advantage conveyed by these natural products comes with additional biological activities awaiting their future discovery through suitable bioassays.

2.5 References

1. World Health Orgaization (WHO). Neglected tropical diseases—GLOBAL. Available at https://www.who.int/health-topics/neglected-tropical-diseases (2023).
2. Mahmoud, A. B. *et al.* Lignans, Amides, and Saponins from Haplophyllum tuberculatum and Their Antiprotozoal Activity. *Molecules (Basel, Switzerland)* **25**; 10.3390/molecules25122825 (2020).
3. Mahmoud, A. B., Mäser, P., Kaiser, M., Hamburger, M. & Khalid, S. Mining Sudanese Medicinal Plants for Antiprotozoal Agents. *Front. Pharmacol.* **11,** 865; 10.3389/fphar.2020.00865 (2020).
4. Stuart, K. *et al.* Kinetoplastids: related protozoan pathogens, different diseases. *J Clin Invest* **118,** 1301–1310; 10.1172/JCI33945 (2008).
5. World Health Orgaization (WHO). World malaria report 2022. *World Health Organization* (2022).

6. Rycker, M. de, Wyllie, S., Horn, D., Read, K. D. & Gilbert, I. H. Anti-trypanosomatid drug discovery: progress and challenges. *Nat Rev Microbiol* **21,** 35–50; 10.1038/s41579-022-00777-y (2023).

7. Rao, S. P. S. *et al.* Drug Discovery for Kinetoplastid Diseases: Future Directions. *ACS Infect. Dis.* **5,** 152–157; 10.1021/acsinfecdis.8b00298 (2019).

8. Wicht, K. J., Mok, S. & Fidock, D. A. Molecular Mechanisms of Drug Resistance in Plasmodium falciparum Malaria. *Annu. Rev. Microbiol.* **74,** 431–454; 10.1146/annurev-micro-020518-115546 (2020).

9. Newman, D. J. & Cragg, G. M. Natural Products as Sources of New Drugs over the Nearly Four Decades from 01/1981 to 09/2019. *Journal of natural products* **83,** 770–803; 10.1021/acs.jnatprod.9b01285 (2020).

10. Ishiyama, A. *et al.* In vitro and in vivo antitrypanosomal activities of three peptide antibiotics: leucinostatin A and B, alamethicin I and tsushimycin. *J Antibiot (Tokyo)* **62,** 303–308; 10.1038/ja.2009.32 (2009).

11. Keller, L. *et al.* Macyranones: Structure, Biosynthesis, and Binding Mode of an Unprecedented Epoxyketone that Targets the 20S Proteasome. *J. Am. Chem. Soc.* **137,** 8121–8130; 10.1021/jacs.5b03833 (2015).

12. Held, J. *et al.* Antimalarial activity of the myxobacterial macrolide chlorotonil A. *Antimicrob. Agents Chemother.* **58,** 6378–6384; 10.1128/AAC.03326-14 (2014).

13. van Santen, J. A. *et al.* The Natural Products Atlas 2.0: a database of microbially-derived natural products. *Nucleic Acids Res.* **50,** D1317-D1323; 10.1093/nar/gkab941 (2022).

14. Fernandez, R. A. *et al.* Myxobacterial depsipeptide chondramides interrupt SARS-CoV-2 entry by targeting its broad, cell tropic spike protein. *J. Biomol. Struct. Dyn.,* 1–12; 10.1080/07391102.2021.1969281 (2021).

15. Koller, T. O. *et al.* The Myxobacterial Antibiotic Myxovalargin: Biosynthesis, Structural Revision, Total Synthesis, and Molecular Characterization of Ribosomal Inhibition. *J. Am. Chem. Soc.* **accepted**; 10.1021/jacs.2c08816 (2023).

16. Schiefer, A. *et al.* Corallopyronin A Specifically Targets and Depletes Essential Obligate Wolbachia Endobacteria From Filarial Nematodes In Vivo. *J. Infect. Dis.* **206,** 249–257; 10.1093/infdis/jis341 (2012).

17. Pogorevc, D. *et al.* Production optimization and biosynthesis revision of corallopyronin A, a potent anti-filarial antibiotic. *Metab. Eng.* **55,** 201–211; 10.1016/j.ymben.2019.07.010 (2019).

18. Wang, Z.-J. *et al.* Engineered Biosynthesis of Complex Disorazol Polyketides in a Streamlined Burkholderia thailandensis. *ACS Synth. Biol.*; 10.1021/acssynbio.2c00610 (2023).

19. Ringel, S. M. *et al.* Ambruticin (W7783), a new antifungal antibiotic. *J. Antibiot.* **30,** 371–375; 10.7164/antibiotics.30.371 (1977).

20. Mohr, K. I. Diversity of Myxobacteria-We Only See the Tip of the Iceberg. *Microorganisms* **6**; 10.3390/microorganisms6030084 (2018).

21. Herrmann, J., Fayad, A. A. & Müller, R. Natural products from myxobacteria: novel metabolites and bioactivities. *Nat. Prod. Rep.* **34,** 135–160; 10.1039/c6np00106h (2017).

22. Petters, S. *et al.* The soil microbial food web revisited: Predatory myxobacteria as keystone taxa? *ISME J.*; 10.1038/s41396-021-00958-2 (2021).

23. Hoffmann, T. *et al.* Correlating chemical diversity with taxonomic distance for discovery of natural products in myxobacteria. *Nat. Commun.* **9,** 803; 10.1038/s41467-018-03184-1 (2018).

24. Sandmann, A., Sasse, F. & Müller, R. Identification and analysis of the core biosynthetic machinery of tubulysin, a potent cytotoxin with potential anticancer activity. *Chem. Biol.* **11,** 1071–1079; 10.1016/j.chembiol.2004.05.014 (2004).

25. Panter, F., Krug, D., Baumann, S. & Müller, R. Self-resistance guided genome mining uncovers new topoisomerase inhibitors from myxobacteria. *Chem. Sci.* **9,** 4898–4908; 10.1039/C8SC01325J (2018).

26. Kunze, B., Kohl, W., Höfle, G. & Reichenbach, H. Production, isolation, physico-chemical and biological properties of angiolam A, a new antibiotic from *Angiococcus disciformis* (Myxobacterales). *J. Antibiot.* **38,** 1649–1654 (1985).

27. Hoffmann, T., Krug, D., Hüttel, S. & Müller, R. Improving natural products identification through targeted LC-MS/MS in an untargeted secondary metabolomics workflow. *Anal. Chem.* **86,** 10780–10788; 10.1021/ac502805w (2014).

28. Wang, M. *et al.* Sharing and community curation of mass spectrometry data with Global Natural Products Social Molecular Networking. *Nat. Biotechnol.* **34,** 828–837; 10.1038/nbt.3597 (2016).

29. Nothias, L.-F. *et al.* Feature-based molecular networking in the GNPS analysis environment. *Nat Methods* **17,** 905–908; 10.1038/s41592-020-0933-6 (2020).

30. Werner Kohl, Barbara Witte, Brigitte Kunze, Victor Wray, Dietmar Schomburg, Hans Reichenbach und Gerhard Höfle. Angiolam A - ein neues Antibiotikum aus Angiococcus. *Liebigs Ann. Chem.,* 2088–2097 (1985).

31. Gieseler, M. T. & Kalesse, M. Synthesis of Angiolam A. *Org. Lett.* **16,** 548–551; 10.1021/ol403423r (2014).

32. Blin, K. *et al.* antiSMASH 6.0: improving cluster detection and comparison capabilities. *Nucleic Acids Res.* **49,** W29-W35; 10.1093/nar/gkab335 (2021).

33. Keatinge-Clay, A. T. The structures of type I polyketide synthases. *Nat. Prod. Rep.* **29,** 1050–1073; 10.1039/c2np20019h (2012).

34. Keatinge-Clay, A. T. A Tylosin Ketoreductase Reveals How Chirality is Determined in Polyketides. *Chem. Biol.* **14,** 898–908; 10.1016/j.chembiol.2007.07.009 (2007).

35. Kwan, D. H. *et al.* Prediction and manipulation of the stereochemistry of enoylreduction in modular polyketide synthases. *Chem. Biol.* **15,** 1231–1240; 10.1016/j.chembiol.2008.09.012 (2008).

36. Kitsche, A. & Kalesse, M. Configurational assignment of secondary hydroxyl groups and methyl branches in polyketide natural products through bioinformatic analysis of the ketoreductase domain. *ChemBioChem* **14,** 851–861; 10.1002/cbic.201300063 (2013).

37. Blake-Hedges, J. M. *et al.* Structural Mechanism of Regioselectivity in an Unusual Bacterial Acyl-CoA Dehydrogenase. *J. Am. Chem. Soc.* **142,** 835–846; 10.1021/jacs.9b09187 (2020).

38. Gu, L. *et al.* Polyketide decarboxylative chain termination preceded by o-sulfonation in curacin a biosynthesis. *J. Am. Chem. Soc.* **131,** 16033–16035; 10.1021/ja9071578 (2009).

39. Li, W. *et al.* Characterization of the Tautomycetin Biosynthetic Gene Cluster from Streptomyces griseochromogenes Provides New Insight into Dialkylmaleic Anhydride Biosynthesis (#). *J. Nat. Prod.*; 10.1021/np8007478 (2009).

40. Sun, Y. *et al.* Heterologous Production of the Marine Myxobacterial Antibiotic Haliangicin and Its Unnatural Analogues Generated by Engineering of the Biochemical Pathway. *Sci. Rep.* **6,** 22091; 10.1038/srep22091 (2016).

41. Oliynyk, M. *et al.* Analysis of the biosynthetic gene cluster for the polyether antibiotic monensin in Streptomyces cinnamonensis and evidence for the role of monB and monC genes in oxidative cyclization. *Mol. Microbiol.* **49,** 1179–1190; 10.1046/j.1365-2958.2003.03571.x (2003).

42. Molnár, I. *et al.* The biosynthetic gene cluster for the microtubule-stabilizing agents epothilones A and B from *Sorangium cellulosum* So ce90. *Chem. Biol.* **7,** 97–109; 10.1016/S1074-5521(00)00075-2 (2000).

43. Wang, J.-D. *et al.* New epothilone congeners from Sorangium cellulosum strain So0157-2. *Nat. Prod. Res.* **25,** 1707–1712; 10.1080/14786419.2011.553719 (2011).

44. Chan, Y. A., Podevels, A. M., Kevany, B. M. & Thomas, M. G. Biosynthesis of Polyketide Synthase Extender Units. *Nat. Prod. Rep.* **26,** 90–114; 10.1039/b801658p (2009).

45. Witschel, M., Rottmann, M., Kaiser, M. & Brun, R. Agrochemicals against malaria, sleeping sickness, leishmaniasis and Chagas disease. *PLoS Negl. Trop. Dis.* **6,** e1805; 10.1371/journal.pntd.0001805 (2012).

46. Field, M. C. *et al.* Anti-trypanosomatid drug discovery: an ongoing challenge and a continuing need. *Nat Rev Microbiol* **15,** 217–231; 10.1038/nrmicro.2016.193 (2017).

Supporting information

New Myxobacteria of the *Myxococcaceae* Clade Produce Angiolams with Antiparasitic Activities

Sebastian Walesch, Ronald Garcia, Abdelhalim B. M. Mahmoud, Fabian Panter, Sophie Hönig, Pascal Mäser, Marcel Kaiser, Daniel Krug, and Rolf Müller

Materials and methods

Bacterial strains, oligonucleotides, plasmids and cultivation media

Table S 2.1: List of strains used in this study

Strain	Function	Source
E. coli HS996	Standard cloning host	Invitrogen
Pyxidicoccus fallax An d48	Genetically amenable producer of angiolam, used for genetic proof of the angBGC	MINS-Lab, GBF[1]
P. fallax An d48-AngKO	Transformant of *P. fallax* An d48 with gene disruption in the angBGC by single cross-over	This study
MCy12716	Producer of angiolam, isolated in "Sample das Saarland" project	This study
MCy12733	Producer of angiolam, isolated in "Sample das Saarland" project	This study

Table S2.2: List of primers

Primer name	Primer sequence 5'-3'
48_Ang_Fw	TATAGAATTCGCAGTCCTATCAGGTCCACC
48_Ang_Rv	TATAGAATTCACACGTCGAGGAAGTTGAGG
M13-24F	CCAGGGTTTTCCCAGTCACG
M13-24R	CGGATAACAATTTCACACAGG
48_Test_Fw	GCTATCTGGAGATGGCGCTC
48_Test_Rv	AGCTGGTTGTTGGCGTAGTA

Table S2.3: List of plasmids

Name	Function	Origin
pCR2.1-TOPO	Cloning vector for single cross-over gene disruptions	Thermo Fisher Scientific
pTOPO-AngKO	pCR2.1-TOPO derivative for the gene disruption of the *angB* gene	This study

Cultivation media

Each medium used in this study was prepared with deionised water. To create a solid medium of any of those listed below, agar (BD) was added to a final concentration of 15 g/L, for soft agar to a final concentration of 7.5 g/L. All media were sterilised by autoclaving at 121 °C, 2 bar for 20 min. For cloning purposes, to select transformants with integrated vector and all further cultivations of these transformants, 50 µg/mL kanamycin was added to the respective media.

LB-medium was used for cultivation of *E. coli*, all other media for myxobacteria.

Table S2.4: List of culture medium recipes

LB medium		
Amount	**Ingredient**	**Supplier**
10 g/L	Tryptone	Roth
5 g/L	Yeast extract	Roth
5 g/L	NaCl	Grüssing
PH adjusted to 7.2 with 1 N KOH.		
Cy/H medium		
Amount	**Ingredient**	**Supplier**
1.5 g/L	Casitone	BD
1.5 g/L	Yeast extract	BD

4.0 g/L	Soluble starch	Roth
1.0 g/L	Soy flour	Hensel
1.0 g/L	Glucose	Roth
1.0 g/L	$CaCl_2$ x 2 H_2O	Sigma Aldrich
0.5 g/L	$MgSO_4$ x 7 H_2O	Grüssing
11.9 g/L	HEPES	Roth
8.0 mg/L	EDTA-iron*	Sigma Aldrich
0.5 mg/L	Vitamin B_{12}**	Roth
PH adjusted to 7.4 with 10 N KOH.		
RG5 medium		
Amount	**Ingredient**	**Supplier**
0.5 g/L	Soy peptone	Roth
0.5 g/L	Soytone	BD
2.0 g/L	Soy flour	Hensel
1.0 g/L	Corn steep solids	Sigma Aldrich
0.5 g/L	Yeast extract	BD
8.0 g/L	Soluble starch	Roth
5.0 g/L	Baker's yeast	Wonnemeyer
2.0 g/L	Gluten from wheat	Sigma Aldrich
1.0 g/L	$MgSO_4$ x 7 H_2O	Grüssing
1.0 g/L	$CaCl_2$ x 2 H_2O	Sigma Aldrich
5.95 g/L	HEPES	Roth
PH adjusted to 7.0 with 10 N KOH.		
VY/2 medium		
Amount	**Ingredient**	**Supplier**
5.0 g/L	Baker's yeast	Wonnemeyer
1.0 g/L	$CaCl_2$ x 2 H_2O	Sigma Aldrich

0.1 mg/L	Vitamin B_{12}**	Roth
PH adjusted to 7.2 with 1 N KOH.		
YM medium		
Amount	**Ingredient**	**Supplier**
5.0 g/L	Pepton phyton	BD
10.0 g/L	Glucose	Roth
3.0 g/L	Malt extract	BD
3.0 g/L	Yeast extract	BD
1.0 g/L	$MgSO_4$ x 7 H_2O	Grüssing
1.0 g/L	$CaCl_2$ x 2 H_2O	Sigma Aldrich
1 mL/L	0.1 M $K_xH_yPO_4$ solution	Sigma Aldrich
10 mM	Tris x HCl, pH 8.0	Sigma Aldrich
PH adjusted to 7.5 with 10 N KOH.		

* Prepared as stock solution of 8.0 g/L EDTA-iron in deionised water and autoclaved individually. Stock solution is added to medium prior cultivation.

** Prepared as stock solution of 0.5 g/L Vitamin B12 in deionised water, filter sterilised using a 0.22 µm filter and stored at 4 °C. Stock solution is added to medium prior cultivation.

Microbiological methods

Isolation of myxobacteria

Myxobacterial strains MCy12716 and MCy12733 were both originated from a citizen-science campaign “Sample das Saarland”, a regional project initiated in 2017 that aims to discover novel antibiotics and new anti-infectives from local samples. The first strain MCy12716 was isolated in March 2019 based on standard bacterial predation method using *Escherichia coli.* This strain came from pond soil sediments collected in summer 2018 (June 03) in an area between Karlsbrunn and Ludweiler, Germany (coordinates: 49.20153847434484,6.800456559291888). On the other hand, the second myxobacterium MCy12733 was isolated after a month (April 2019) but from a soil sample with decaying leaves collected in August 09, 2018 at Aßweiler, Germany (GPS coordinates: 49.2189122,7.192166499999985). Its discovery was also based on *E. coli lysis*, formation of swarming colony and development of fruiting bodies on Stan-21 mineral salt agar medium. Axenic cultures were achieved by repeated transferring of the swarm cells taken from colony margin and by maintaining in VY/2 agar, which

supports growth developmental stages including swarming and fruiting body formation. These two myxobacterial isolates were identified by 16S rRNA gene amplification using universal 27F and 1492R primers. Their closest related type strains were determined by BLAST search and phylogenetic analysis.

Fermentation of myxobacteria for analytical purposes

Cultures for analytical purposes were grown in 300 mL shaking flasks containing 50 or 100 mL of the respective fermentation medium inoculated with 2% (v/v) pre-culture. The medium was supplemented with 4% (v/v) of a sterile aqueous solution of XAD-16 adsorber resin (Sigma Aldrich) to bind secondary metabolites in the culture medium. After 7-10 d cultivation, the culture is pelleted in 50 mL falcon tubes in an Eppendorf centrifuge 5804R at 8288 x g and 4 °C for 10 min. The pellet is then stored at -20 °C until further use.

Feeding experiments with stable isotope-labelled precursors

Feeding experiments were performed in 100 mL shaking flasks containing 20 mL of the respective fermentation medium inoculated with 2.5% (v/v) SBCy413 pre-culture. At 12, 24, 36, 48, and 60 h post inoculation, 200 µL of an aqueous solution of 50 mM L-alanine ^{15}N (Sigma Aldrich) or L-methionine-(methyl ^{13}C) (Cambridge Isotope Laboratories) was added to the cultures. After another 12 h of cultivation, 5% (v/v) sterile aqueous solution of XAD-16 adsorber resin was added to the cultures. After approximately 4 d cultivation, the culture is pelleted in 50 mL falcon tubes in an Eppendorf centrifuge 5804R at 8288 x g and 4 °C for 10 min. The pellet is then stored at -20 °C until further use.

Large scale fermentation for compound purification

Pre-cultures of MCy12733 were cultivated in 300 mL shaking flasks containing 100 mL of the respective fermentation medium at 30 °C and 180 rpm for 5 d. These pre-cultures are used to inoculate (5% (v/v) inoculum) 6 x 2 L of the respective fermentation medium, supplemented with 5% (v/v) of a sterile aqueous solution of XAD-16 adsorber resin, in 5 L shaking flasks. Fermentation was performed at 30 °C and 170 rpm for 21 d. Afterwards the combined cultures were pelleted with an Avanti J-26 XP centrifuge, equipped with a JLA-8.1 rotor (Beckman Coulter) at 11978 x g and 4 °C for 15 min. The pellet was then frozen, freeze-dried and stored at -20 °C until further use.

Molecular biological methods

Preparation of gDNA

Genomic DNA of *P. fallax* An d48 for cloning purposes and *P. fallax* An d48-AngKO to verify integration of pTOPO-AngKO within angB was isolated using the Puregene Core Kit A (Qiagen) or the DNeasy UltraClean Microbial Kit (Qiagen), according to manufacturer's instructions.

To isolate gDNA of MCy12716 and MCy12733 for Illumina sequencing, phenol-chloroform extraction was used.

50–100 mL of a myxobacterial culture, grown to an appropriate density, was centrifuged at 8288 x g and 4 °C (Eppendorf Centrifuge 5804R) for 10 min. Pelleted cells were washed once with 15 mL SET buffer and afterwards resuspended in 5 mL SET buffer. After addition of 50 µL RNase stock solution, cells were incubated for 30–60 min at 37 °C. 300 µL Proteinase K stock solution were added, the falcon was inverted several time and 600 µL 10% SDS solution were added. The mixture was incubated at 55 °C for approx. 2 h until it turned viscous. After addition of 1 volume (= 6 mL) Phenol:Chloroform:Isoamylalcohol (25:24:1, Roth) the tube was swung at 5 rpm for 1 h. Afterwards, the mixture was centrifuged at 8288 x g for 5 min and the upper phase was transferred into a new tube with an Eppendorf pipette with an end-cut 1 mL tip. Washing step of the (upper) aqueous phase was repeated one more time.

The cleaned upper phase was moved to a new Falcon tube, mixed with 5 mL Chloroform:Isoamylalcohol (24:1, Roth) and swung at 5 rpm for 1 h. The mixture was swung at 8288 x g for 10 min and ~ 4 mL of the upper phase were carefully transferred to a new falcon. After addition of 440 µL of 3 M sodium acetate (pH 5.2) and 11 mL of ice-cold pure EtOH, Falcon tube was inverted several times, until cotton-like DNA appeared. The DNA was collected with a Pasteur pipette and washed several times with 70% EtOH in a 2 mL Eppendorf tube. Washed DNA was air-dried and carefully suspended in 0.5–1.0 mL sterile MQ-water. DNA-solution was stored at -20 °C.

PCR and cycler protocols

Amplification of a genetic region in *angB* for gene disruption by single cross-over and PCRs to verify the integration of the plasmid into the angiolam BGC in *P. fallax* An d48 were done with the Phusion High-Fidelity polymerase (Thermo scientific). All PCR amplifications were performed in a MasterCycler Pro S (Eppendorf). Success of PCR amplifications was checked by agarose gel electrophoresis. Bands of PCR products for

cloning purposes were cut out and purified using the Nucleospin Gel and PCR Clean-Up Kit (Macherey-Nagel).

PCR mix for amplification of KO region

4 µL 5 x GC buffer
1 µL DMSO
1 µL Forward primer (10 µM)
1 µL Reverse primer primer (10 µM)
0.4 µL dNTP-mix (10 mM)
0.4 µL gDNA template (~50 ng/ µL)
0.2 µL Phusion DNA Polymerase
12 µL Milli-Q. water

PCR mix to verify integration in ang BGC

4 µL 5 x HF buffer
4 µL DMSO
1 µL gDNA template (~50 ng/ µL)
0.5 µL Forward primer (10 µM)
0.5 µL Reverse primer primer (10 µM)
0.5 µL dNTP-mix (10 mM)
0.2 µL Phusion DNA Polymerase
9.3 µL Milli-Q. water

Table S2.5: PCR cycler protocol for amplification of KO region

Step	**Time [min:s]**	**Temperature [°C]**
Initial denaturation	3:00	98
Cycle, repeat 30 x	0:20 0:30 0:30 per kbp to amplify	98 68 72
Final elongation	10:00	72

Table S2.6: PCR mix to verify integration in ang BGC

Step	Time [min:s]	Temperature [°C]
Initial denaturation	3:00	98
Cycle, repeat 30 x	0:20 0:30 0:30 per kbp to amplify	98 64 72
Final elongation	10:00	72

Restriction enzyme digestion protocols

Restriction enzyme digestions for cloning purposes were performed in volumes of 20 µL with 350 ng PCR product or 1.2 µg cyclised pCR2.1-TOPO vector, respectively. Aqueous solutions of the PCR product or the cyclised pCR2.1-TOPO vector were mixed with 2 µL 10 x EcoRI buffer and 1 µL EcoRI (10 U/µL, Thermo scientific) and incubated at 37 °C. After 2 h, 1 µL FastAP (1 U/µL, Thermo scientific) was added to the reaction mixture of the vector to dephosphorylate its ends. All digestion reactions were stopped after 3 h of incubation and the resulting products were subsequently purified, using the Nucleospin Gel and PCR Clean-Up Kit (Macherey-Nagel).

Control digestions to verify the success of cloning were performed in volumes of 10 µL with approximately 1 µg plasmid. Aqueous solutions of cloned plasmid were mixed with 1 µL Tango buffer (Thermo scientific) and 0.5 µL NcoI (10 U/ µL, Thermo scientific) or 0.5 µL NaeI (10 U/ µL, Thermo scientific) and incubated at 37 °C for 2 h. Successful cloning was verified by agarose gel electrophoresis and sequencing of the obtained plasmid.

Ligation protocol

Ligation of DNA was carried out with ~ 50 ng vector and a five fold molar excess of insert. Vector and insert were mixed with 2 µL 10x T4 buffer, 1 µL T4 ligase (5 U/ µL; Thermo Fisher Scientific) and autoclaved Milli-Q. water to a final volume of 20 µL. Reactions were incubated at 25 °C for 4 h or at 16 °C overnight and subsequently electroporated into *E. coli* HS996.

Transformation of *E. coli* HS996

1 mL of an overnight culture of *E. coli* cells in LB was inoculated into 20 mL of LB medium and grown at 37 °C until it reached an OD_{600} of 0.6. The cells were centrifuged at 11467 x g and 4 °C (HIMAC CT15RE, Koki Holdings Co.) for 90 s in 2 mL Eppendorf tubes. The cell pellet was washed twice with ice-cold sterile MQ water, first with 1000 µL, then with 800 µL. After the washing procedure, *E. coli* cells were resuspended in 50 µL ice-cold sterile MQ water, kept on ice and subsequently used for electroporation.

E. coli cells were mixed with 3–5 µL ligation product or 100 ng plasmid and transferred to an electroporation cuvette. Electroporation was carried out at 25 µF, 200 Ω and 1250 V. The electroporation product was immediately mixed with 1 mL LB medium and incubated in a 2 mL Eppendorf tubes at 37 °C and 750 rpm for 45 min. Incubated cells were spread on LB-agar plates containing 50 µg/mL kanamycin and incubated at 37 °C overnight. Around 10 clones were picked and cultivated in 5 mL LB containing 50 µg/mL kanamycin for subsequent plasmid isolation.

Plasmid isolation

Plasmid isolation for cloning purposes or for transformation into *P. fallax* An d48 was performed with the GeneJET Miniprep Kit (Thermo scientific). Plasmid isolation for control digestions to verify successful cloning was done with standard alkaline lysis[2].

Transformation into *P. fallax* An d48

Electroporation of *P. fallax* An d48 was adapted from Panter et al[3]. 2 mL of an An d48 culture in YM medium at OD_{600} of approximately 0.7 were centrifuged at 11467 x g (HIMAC CT15RE, Koki Holdings Co.) for 2 min. The pelleted cells were washed twice with sterile MQ water, first with 1000 µL, then with 800 µL. After the washing procedure, the cells were resuspended in 50 µL sterile MQ water, mixed with 5 µL of plasmid solution at a concentration of 0.3-0.4 µg/µL and moved to an electroporation cuvette. Electroporation was performed at 675 V, 400 Ω, 25 µF and 1 mm cuvette width. Afterwards, the cells were flushed out with 1 mL YM medium and moved to a 2 mL eppendorf tube with a small hole in the lid. After incubation at 30 °C and 1000 rpm for 5 h, the cell suspension was mixed with 3 mL YM soft agar, containing 50 µg/mL kanamycin, and the mixture distributed on a YM agar plate, containing 50 µg/mL kanamycin. Slightly red, sperical transformants could be observed after 10-14 d cultivation at 30 °C.

Analytical methods

Crude extract generation for analytical purposes

Frozen or freeze-dried pellets from small scale cultivations were suspended in 40 or 80 mL methanol and stirred at 250 rpm at room temperature for 2 h. The supernatant was decanted into a round flask through a 125 micron folded filter. The solvent and potential residual water were removed on a rotary evaporator with a water bath temperature of 40 °C at appropriate pressures. The dried extract was dissolved/resuspended in 1100 µL MeOH/100 mL cultivation volume. The crude extract was stored at -20 °C until further analysis. For the purpose of UHPLC-*hr*MS analysis, the crude extract was diluted 1:5 with methanol and centrifuged at 21500 x g and 4 °C (HIMAC CT15RE, Koki Holdings Co.) for 5 min to remove residual insolubilities such as salts, cell debris and XAD fragments.

Standardised UHPLC-MS conditions

UPLC-hrMS analysis was performed on a Dionex (Germering, Germany) Ultimate 3000 RSLC system using a Waters (Eschborn, Germany) BEH C18 column (50 x 2.1 mm, 1.7 µm) equipped with a Waters VanGuard BEH C18 1.7 µm guard column. Separation of 1 µL sample was achieved by a linear gradient from (A) H2O + 0.1 % formic acid (FA) to (B) ACN + 0.1 % FA at a flow rate of 600 µL/min and a column temperature of 45 °C. Gradient conditions for crude extract analysis were as follows: 0 – 0.5 min, 5% B; 0.5 – 18.5 min, 5 – 95% B; 18.5 – 20.5 min, 95% B; 20.5 – 21 min, 95 – 5% B; 21-22.5 min, 5% B. Following gradient conditions were applied to monitor angiolams during purification: 0 – 0.5 min, 5% B; 0.5 – 9.5 min, 5 – 95% B; 9.5 – 10.5 min, 95% B; 10.5 – 11 min, 95 – 5% B; 11-12.5 min, 5% B. UV spectra were recorded by a DAD in the range from 200 to 600 nm. The LC flow was split to 75 µL/min before entering the Bruker Daltonics maXis 4G *hr*ToF mass spectrometer (Bremen, Germany) equipped with an Apollo II ESI source. Mass spectra were acquired in centroid mode ranging from 150 – 2500 m/z at a 2 Hz full scan rate. Mass spectrometry source parameters were set to 500 V as end plate offset; 4000 V as capillary voltage; nebuliser gas pressure 1 bar; dry gas flow of 5 L/min and a dry temperature of 200 °C. Ion transfer and quadrupole settings were set to funnel RF 350 Vpp.; multipole RF 400 Vpp as transfer settings and ion energy of 5 eV as well as a low mass cut of 300 m/z. Collision cell was set to 5.0 eV and pre-pulse storage time was set to 5 µs. Spectra acquisition rate was set to 2 Hz. Calibration was done automatically before every LC-MS run by injection of a sodium formate solution and calibration on the respective clusters formed in the ESI source. All MS analyses

were acquired in the presence of the lock masses ($C_{12}H_{19}F_{12}N_3O_6P_3$, $C_{18}H_{19}O_6N_3P_3F_2$ and $C_{24}H_{19}F_{36}N_3O_6P_3$) which generate the [M+H]+ ions of 622.0289; 922.0098 and 1221.9906.

Statistics based metabolome filtering

For statistical metabolomics analysis, both the myxobacterial culture and medium blanks were incubated and extracted in triplicates as described above. Each extract was measured as technical duplicate, giving a total number of six replicates each for the bacterial culture and medium blank extracts. T-ReX-3D molecular feature finder of MetaboScape 2022b (Bruker Daltonics, Billerica, MA, USA) was used to obtain molecular features. Detection parameters were set to intensity threshold 5×10^3 and minimum peak length of five spectra to ensure a precursor selection that has a sufficient intensity to generate tandem MS data. Identification of bacterial features was performed with the built-in ANOVA/t-test routine and filtered to appearance in all six bacterial extracts and in none of the medium blank extracts. The t-test table was used to create a scheduled precursor list (SPL) for tandem MS fragmentation[4].

Acquisition parameters for high-resolution tandem MS data

LC and MS conditions for SPL guided MS/MS data acquisitions were kept constant according to section standardised UHPLC-*hr*MS conditions. MS/MS data acquisition parameters were set to exclusively fragment scheduled precursor list entries. SPL tolerance parameters for precursor ion selection were set to 0.2 minutes and 0.05 m/z in the SPL MS/MS method. The method picked up to 2 precursors per cycle, applied smart exclusion after 5 spectra and performed CID and MS/MS spectra acquisition time ramping. CID Energy was ramped from 35 eV for 500 m/z to 45 eV for 1000 m/z and 60 eV for 2000 m/z. MS full scan acquisition rate was set to 2 Hz and MS/MS spectra acquisition rates were ramped from 1 to 4 Hz for precursor ion intensities of 10 kcts. to 1000 kcts..

Parameters for feature based molecular networking

All supporting feature based molecular networking data presented here was created based on the UHPLC-*hr*MS² chromatograms using the parameters specified in the previous section. All molecular features were obtained by Metaboscape 2022b, with the same parameters as in the section statistics based metabolome filtering and the

respective MS/MS spectra were detected by the built-in “extract MS/MS data” function. The resulting output files were exported with the built-in “Export for GNPS/Sirius” function and uploaded to the GNPS server at University of California San Diego via FileZilla FTP upload to ftp:// ccms-ftp01.ucsd.edu and all acquired SPL MS/MS spectra were used for feature-based network creation.[5] A molecular network was created using the online workflow at GNPS. The data was filtered by removing all MS/MS peaks within +/- 17 Da of the precursor m/z. MS/MS spectra were window filtered by choosing only the top 6 peaks in the +/- 50 Da window throughout the spectrum. The data was then clustered with a parent mass tolerance of 0.02 Da and a MS/MS fragment ion tolerance of 0.02 Da to create consensus spectra. No further filtering of consensus spectra was done before spectral network creation. A network was then created where edges are filtered to have a cosine score above 0.7 and more than 6 matched peaks. Further edges between two nodes were kept in the network if and only if each of the nodes appeared in each other's respective top 10 most similar nodes.[5] Furthermore, library search parameters were set to a cosine of 0.7 and a minimum of 6 matched peaks. Library searches included analogs with mass differences up to 200 Da.The dataset was downloaded from the server and subsequently visualised using Cytoscape 3.9.1.

Compound purification and structure elucidation

Extraction and liquid/liquid partitioning

Extraction and liquid/liquid partitioning of cultures of MCy12733 in different production media were done with 100 mL of the respective solvents per 10 g freeze-dried pellet.

Freeze-dried pellets were extracted four times with a 1:1 mixture of methanol and acetone. For each extraction step, the suspension was stirred at 250 rpm for 30 min and decanted through glass wool and a 125 micron folded filter. The combined extracts were dried using a rotary evaporator at 40 °C water bath temperature and appropriate pressures. The dried extract was then dissolved/resuspended in a 95:5 mixture of methanol and water and defatted three times with hexane. Finally, the defatted extract was partitioned three times between water and chloroform. The angiolam derivatives were retained in the chloroform phase. The chloroform phase was concentrated, moved to glass vials, dried and stored at -20 °C.

Pre-purification by reverse phase flash chromatography

Reverse phase flash chromatography was carried out using the Isolera One (Biotage). Versa Flash Spherical C18 silica 45-75 µm 70 Å in a 25 g SNAP column (Biotage) was used as stationary phase and H_2O (A) and MeOH (B) were used as mobile phase. Flow rate was 25 mL/min, fractions of 45 mL were collected in glass tubes and solvent volume was measured in column volumes (CV); 1 CV = 33 mL. After equilibration of the system with 3 CV of 50% B, ~ 300 µg sample were loaded on the column using vacuum dried iSolute beads (Biotage). The conditions were kept at 50% B for 2 CV, followed by an increase to 80% B over 30 CV, a ramp to 100% B over 5 CV and a flushing step at 100% B for 5 CV. Fractions were pooled according to the abundance of angiolam derivatives, dried and stored in glass vials at -20 °C.

Purification of angiolams A, B, and F

Purification of angiolams A (**1**), B (**2**) and F (**5**) as well as a mixture of angiolam C (**3**) and D (**4a/4b**) from the respective pooled flash chromatography fractions was carried out on the Waters Autopurifier (Eschborn, Germany) high pressure gradient system. Separation was carried out on a Waters X-Bridge prep C-18 5 µm, 150 x 19 mm column using H_2O +0.1% FA (A) and ACN + 0.1% FA (B) as mobile phase at a flow rate of 25 mL/min. Separation was started with 5% B for 1 min, followed by a ramp to 40% B over 2 min and an increase to 70% B over 22 min. The column was then flushed with a ramp to 95% B over 2 min, brought back to 5% B within 1 min and was re-equilibrated at 5% for 2 min. Purified angiolams A (**1**), B (**2**) and F (**5**) were dried with a rotary evaporator, moved to glass vials, freeze-dried and stored at -20 °C.

Purification of angiolams C and D

The mixture of angiolams C (**3**) and D (**4a/4b**) was separated on a Waters Prep 15 SFC System equipped with a 5 µm Torus Diol 130 Å OBD Prep Column 250 x 19 mm (Waters) thermostated at 50°C. Separation was achieved with following multistep-gradient of methanol as co-solvent to the supercritical CO_2. A ramp of 5-11% co-solvent within 1 min was followed by an increase to 17% over 18 min to separate angiolams C (**3**) and D (**4a/4b**). Afterwards the column was flushed with an increase of 20% co-solvent for 1 min, the co-solvent was decreased to 5% within 0.5 min and the system re-equilibrated at 5% co-solvent for 2.5 min. Flow rate was set to 15 mL/min, make-up flow to 3 mL/min and backpressure to 120 bar.

NMR-based structure elucidation

The chemical structures of angiolam derivatives were determined via multidimensional NMR analysis. 1D and 2D NMR spectra were recorded at 500 MHz (^{1}H) and 125 MHz (^{13}C) or 700 MHz (^{1}H) and 175 MHz (^{13}C) conduction using an Avance III (Ultrashield) 500 MHz spectrometer or an Avance III (Ascend) 700 MHz spectrometer, respectively, both equipped with a cryogenically cooled triple resonance probe (Bruker Biospin Rheinstetten, Germany). All observed chemical shift values (δ) are given in ppm and coupling constant values (J) in Hz. Standard pulse programs were used for HMBC, HSQC, and gCOSY experiments. HMBC experiments were optimized for $^{2,3}J_{C\text{-}H}$ = 6 Hz. The spectra were recorded in chloroform-*d* and chemical shifts of the solvent signals at δ_H 7.27 ppm and δ_C 77.0 ppm were used as reference signals for spectra calibration. To increase sensitivity, the measurements were conducted in a 5 mm Shigemi tube (Shigemi Inc., Allison Park, PA 15101, USA). The NMR signals are grouped in the tables below and correspond to the numbering in the schemes corresponding to every table.

Biological assays

In vitro antiparasitic activity assays:

In vitro activity assays against a panel of protozoal parasites, namely; *Trypanosoma brucei rhodesiense* (STIB 900), *Trypanosoma cruzi* (Tulahuen C4), *Leishmania donovani* (MHOM/ET/67/L82), and *Plasmodium falciparum* (NF54), and cytotoxicity tests against mammalian cells (L6-cell line from rat-skeletal myoblasts) were performed according to previously described methods[6,7]. All assays were performed in at least three independent replicates.

Results

Observation and production of novel angiolam derivatives

Table S 2.7: Further information on observed angiolam derivatives

Name	Rt [min]	Observed Ion and *m/z* ratio	Sum formula
Angiolam A (**1**)	11.06	$[M\text{-}H_2O+H]^+$: 570.379 u	$C_{34}H_{53}NO_7$
Angiolam B (**2**)	11.80	$[M+H]^+$: 586.374 u	$C_{34}H_{51}NO_7$
Angiolam C (**3**)	11.57	$[M\text{-}H_2O+H]^+$: 572.395 u	$C_{34}H_{55}NO_7$
Angiolam D_1 (**4a**)	11.61	$[M\text{-}H_2O+H]^+$: 584.395 u	$C_{35}H_{55}NO_7$
Angiolam D_2 (**4b**)	11.81	$[M\text{-}H_2O+H]^+$: 584.395 u	$C_{35}H_{55}NO_7$

Angiolam E	10.58	$[M+H]^+$: 586.374 u	$C_{34}H_{51}NO_7$
Angiolam F (**5**)	12.14	$[M-H_2O+H]^+$: 598.408 u	$C_{36}H_{57}NO_7$
Angiolam G	10.59	$[M-H_2O+H]^+$: 556.363 u	$C_{33}H_{51}NO_7$

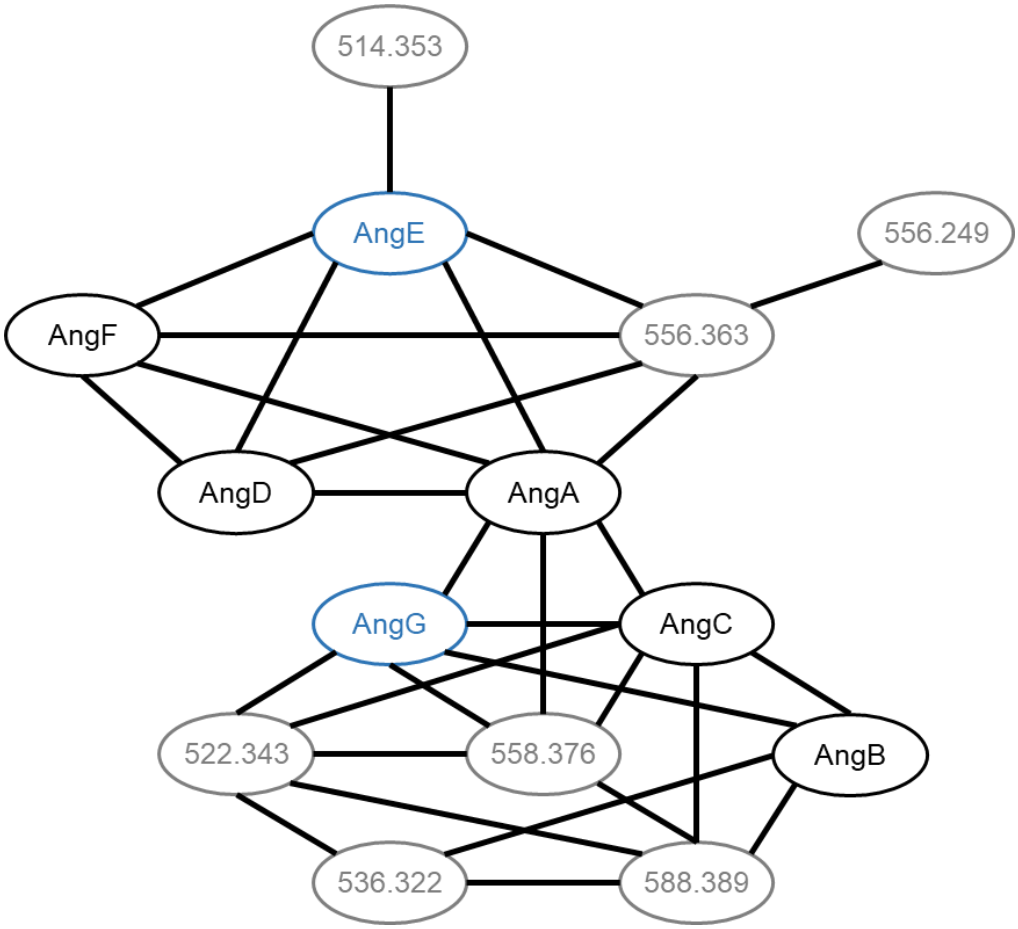

Figure S 2.1: Feature based molecular network of angiolam derivatives, observed in crude extracts of Mcy12733 in CyH with and without 2.5 g/L L-valine or RG5. All purified angiolam derivatives are marked black, derivatives observed in CyH and RG5 cultivations are marked blue and derivatives only observed in RG5 cultivations are marked grey.

Table S 2.8: Production of angiolam derivatives in different media

	Cy/H		Cy/H-Val[c]		RG5	
	Area	Average area	Area	Average area	Area	Average area
A[a]	6087406	6186722	1497941	1309585	15847265	13895320
	6026506		1210982		14044722	
	6446253		1219833		11793973	
B[b]	1654065	1547731	426438	378231	4251220	3357829
	1450610		429611		2444472	
	1538517		278645		3377795	
C[b]	4212455	4084209	1139368	1144831	6846988	5584982
	4133524		1349834		4413185	
	3906647		945291		5494772	
D[b]	572186	569492	3241019	3365068	1276269	1146982
	598411		3977963		982698	
	537879		2876223		1181980	
E[b]	153573	147199	32198	32914	515338	446892
	134020		39869		361496	
	154004		26674		463841	
F[b]	0	0	871836	927082	0	0
	0		1074687		0	
	0		834723		0	
G[b]	1060346	1056732	351480	402603	1242016	1013780
	1091466		502060		793880	
	1018383		354269		1005443	

[a] Areas were calculated from a 1:40 diluted crude extract.
[b] Areas were calculated from a 1:10 diluted crude extract.
[c] Cy/H medium with added 2.5 g/L L-valine.

Table S 2.9: Relative production of angiolam derivatives in different media

	Cy/H [%]	Cy/H-Val[a] [%]	RG5 [%]
A	100	21	225
B	100	24	217
C	100	28	137
D	100	591	201
E	100	22	304
F	0	100	0
G	100	38	96

[a] Cy/H medium with added 2.5 g/L L-valine.

Relative production levels of angiolam derivatives were normalised to their respective production in Cy/H medium.

Purification and structure elucidation

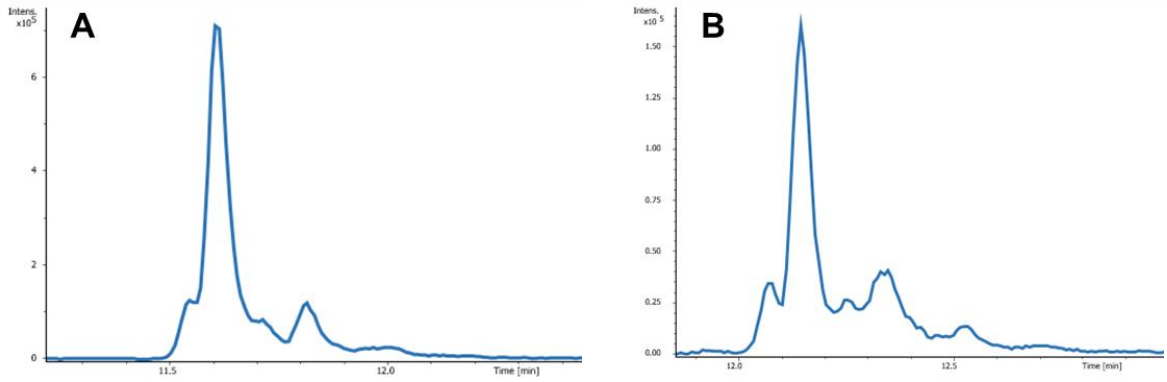

Figure S 2.2: Multicomponent mixtures of angiolams D (A) and F (B) in crude extracts of MCy12733 in Cy/H with 2.5 g/L L-valine. Extracted ion chromatograms (EICs) of *m/z* 584.395 (A) and 598.408 (B).

NMR-based comparison of purified angiolam A with authentic angiolam A

As previous structure elucidation of angiolam A (**1**) was performed based on mass-spectrometry, 1D and (selective) NOE-based NMR experiments and X-ray analysis[8], authentic angiolam A was acquired from the Helmholtz Centre for infection research (HZI) for comparison. Evaluation of ^{1}H, ^{13}C and HSQC NMR spectra of authentic and newly purified angiolam A (**1**) verified that the newly purified natural product was indeed angiolam A (see spectra overlay in Figures S 2.9 & S 2.10 and Table S 2.10 & S 2.11). Due to organic synthesis of angiolam A, the stereochemistry was verified previously[9]. Furthermore, a new numbering of carbon atoms was introduced, following the biosynthesis of angiolam A (See Figure 2.3).

Table S 2.10: ^{1}H-NMR spectroscopic data of authentic angiolam A vs angiolam A (1) from MCy12733

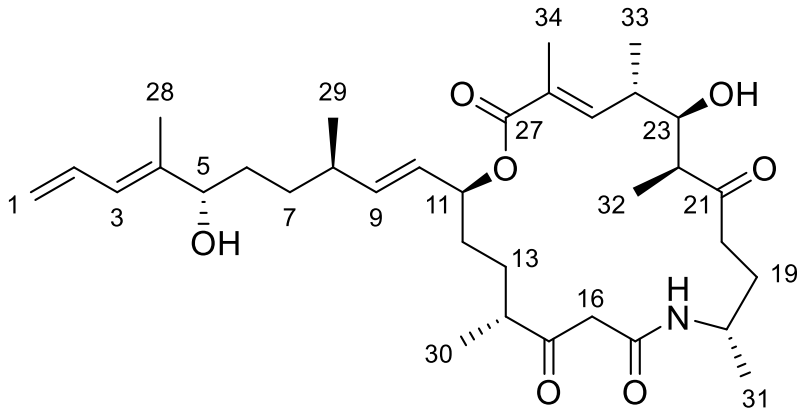

Position	δ_H[a] [ppm] of angiolam A from Mcy12733	δ_H[a] [ppm] of authentic angiolam A	Δ ($\delta_{H\ angiolam\ A\ from\ Mcy12733} - \delta_{H\ authentic\ angiolam\ A}$)
1a	5.20	5.20	0.00
1b	5.11	5.11	0.00
2	6.59	6.59	0.00
3	6.04	6.04	0.00
4	-	-	-
5	4.00	4.00	0.00
6	1.53	1.53	0.00
7a	1.36	1.37	-0.01
7b	1.25	1.25	0.00
8	2.13	2.13	0.00
9	5.53	5.53	0.00
10	5.41	5.41	0.00
11	5.14	5.15	-0.01
12a	1.70	1.71	-0.01
12b	1.50	1.50	0.00
13a	1.83	1.82	0.01
13b	1.32	1.32	0.00
14	2.65	2.65	0.00
15	-	-	-
16a	3.57	3.57	0.00
16b	3.26	3.26	0.00
17	-	-	-
18	4.02	4.02	0.00
19a	1.86	1.85	0.01
19b	1.54	1.53	0.01
20a	2.67	2.67	0.00
20b	2.53	2.53	0.00
21	-	-	-
22	2.64	2.64	0.00
23	3.76	3.76	0.00

24	2.59	2.58	0.01
25	6.49	6.49	0.00
26	-	-	-
27	-	-	-
28	1.74	1.74	0.00
29	0.98	0.99	-0.01
30	1.11	1.11	0.00
31	1.19	1.20	-0.01
32	1.05	1.05	0.00
33	1.14	1.14	0.00
34	1.85	1.85	0.00

[a] Acquired in chloroform-*d* at 500 MHz and calibrated to solvent signal at 7.27 ppm.

Table S 2.11: ^{13}C-NMR spectroscopic data of authentic angiolam A vs angiolam A (1) from MCy12733

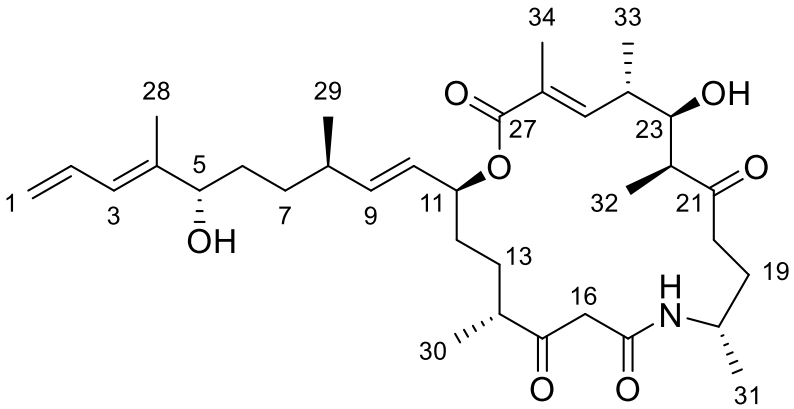

Position	δ_C[a] [ppm] of angiolam A from Mcy12733	δ_C[a] [ppm] of authentic angiolam A	Δ ($\delta_{C\ angiolam\ A\ from\ Mcy12733} - \delta_{C\ authentic\ angiolam\ A}$)
1	117.0	117.0	0.0
2	132.7	132.7	0.0
3	125.8	125.8	0.0
4	140.5	140.5	0.0
5	77.2	77.3	-0.1
6	32.8	32.8	0.0
7	32.7	32.7	0.0
8	36.5	36.5	0.0
9	139.3	139.3	0.0
10	126.7	126.7	0.0
11	74.5	74.6	-0.1
12	33.0	33.0	0.0
13	27.7	27.7	0.0
14	47.6	47.6	0.0
15	209.8	209.8	0.0
16	49.2	49.2	0.0
17	165.0	165.0	0.0
18	44.9	44.9	0.0
19	30.5	30.5	0.0

20	38.8	38.8	0.0
21	215.8	215.9	-0.1
22	47.8	47.7	0.1
23	74.0	74.0	0.0
24	36.3	36.3	0.0
25	142.4	142.4	0.0
26	128.7	128.7	0.0
27	167.6	167.7	-0.1
28	12.1	12.1	0.0
29	20.4	20.4	0.0
30	16.0	16.0	0.0
31	21.8	21.8	0.0
32	8.7	8.7	0.0
33	16.7	16.7	0.0
34	12.6	12.6	0.0

[a] Acquired in chloroform-*d* at 125 MHz and calibrated to solvent signal at 77.0 ppm.

Although the identity of newly purified angiolam A (**1**) was verified by NMR comparisons with authentic angiolam A, a full set of ^{1}H, ^{13}C, COSY, HSQC, and HMBC-NMR spectra was recorded for a NMR-based structure elucidation of angiolam A (**1**), purified from MCy12733. COSY-correlations are indicated in bold, relevant HMBC correlations as arrows (Table S 2.12).

Table S 2.12: NMR Spectroscopic data for angiolam A (1)

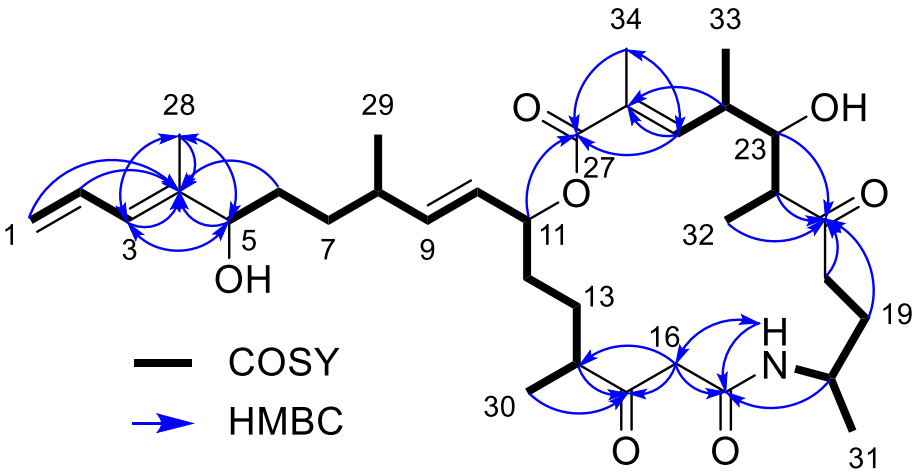

Position	δ_C[a] [ppm]	Type	δ_H[b] [ppm]	H Multiplicity (*J* [Hz])	COSY[c]	HMBC[d]
1a	117.0	CH_2	5.20	m	1b, 2, 3, 28	2, 3
1b			5.11	m	1a, 2, 3, 28	2, 3, 4
2	132.7	CH	6.59	m	1a, 1b 3	1, 3, 4, 5
3	125.8	CH	6.04	m	1a, 1b, 2, 5, 28	1, 2, 4, 5, 6, 28

4	140.5	C	-	-	-	-
5	77.2	CH	4.00	m	3, 6, 28	3, 4, 7, 28
6	32.8	CH_2	1.53	m	5, 7a, 7b	4, 5, 7, 8
7a	32.7	CH_2	1.36	m	6, 7b, 8	5, 6, 8, 9, 29
7b			1.25	m	6, 7a, 8	5, 6, 8, 9, 29
8	36.5	CH	2.13	m	7a, 7b, 9, 10, 29	6, 7, 9, 10, 29
9	139.3	CH	5.53	dd (15.5, 7.9)	8, 10, 11, 29	7, 8, 10, 11, 29
10	126.7	CH	5.41	m	8, 9, 11	8, 9, 11, 12, 29
11	74.5	CH	5.14	m	9, 10, 12a, 12b	9, 10, 12, 13, 27
12a	33.0	CH_2	1.70	m	11, 12b, 13a, 13b	10, 11, 13, 14
12b			1.50	m	11, 12a, 13a, 13b	10, 11, 13, 14
13a	27.7	CH_2	1.83	m	12a, 12b, 13b, 14	11, 12, 14, 15, 30
13b			1.32	m	12a, 12b, 13a, 14	11, 12, 15, 30
14	47.6	CH	2.65	m	13a, 13b, 30	12, 13, 15, 30
15	209.8	C	-	-	-	-
16a	49.2	CH_2	3.57	br s	16b	14, 15, 17, 18
16b			3.26	m	16a	15, 17
17	165.0	C	-	-	-	-
18	44.9	CH	4.02	m	19a, 19b, 31, NH	17, 19, 20, 31
19a	30.5	CH_2	1.86	m	18, 19b, 20a, 20b	18, 20, 21, 31
19b			1.54	m	18, 19a, 20a, 20b	18, 20, 21, 31
20a	38.8	CH_2	2.67	m	19a, 19b, 20b	18, 19, 21
20b			2.53	m	19a, 19b, 20a	18, 19, 21
21	215.8	C	-	-	-	-
22	47.8	CH	2.64	m	23, 32	21, 23, 24, 32
23	74.0	CH	3.76	m	22, 24, 33	21, 24, 25, 32, 33
24	36.3	CH	2.59	m	23, 25, 33	22, 23, 25, 26, 33
25	142.4	CH	6.49	dd (10.1, 1.4)	24, 34	23, 24, 26, 27, 33, 34
26	128.7	C	-	-	-	-
27	167.6	C	-	-	-	-
28	12.1	CH_3	1.74	d (0.8)	1a, 1b, 3, 5	1, 2, 3, 4, 5
29	20.4	CH_3	0.98	m	8, 9	7, 8, 9
30	16.0	CH_3	1.11	d (7.0)	14	13, 14, 15
31	21.8	CH_3	1.19	d (6.6)	18	18, 19, 20
32	8.7	CH_3	1.05	d (7.1)	22	21, 22, 23
33	16.7	CH_3	1.14	d (6.6)	23, 24	23, 24, 25
34	12.6	CH_3	1.85	M	25	23, 24, 25, 26, 27
NH	-	NH	6.25	br d (9.2)	18	16, 17, 18, 19, 31

[a] Acquired in chloroform-*d* at 125 MHz and calibrated to solvent signal at 77.0 ppm.
[b] Acquired in chloroform-*d* at 500 MHz and calibrated to solvent signal at 7.27 ppm.
[c] Proton showing COSY correlations to indicated proton.
[d] Proton showing HMBC correlations to indicated carbon.

NMR-based structure elucidation of novel angiolam derivatives

The structures of the novel angiolam derivatives B (**2**), C (**3**), D (**4a/b**), and F (**5**) were elucidated based on ^{1}H, ^{13}C, COSY, HSQC, and HMBC NMR spectra. As all angiolam derivatives are produced by the same biosynthetic machinery, they display the same stereochemistry. Correlations that were used to display the changes of the novel angiolam derivatives compared to angiolam A (**1**) are shown in a bold line for COSY and as arrows for HMBC.

Table S 2.13: NMR Spectroscopic data for angiolam B (2)

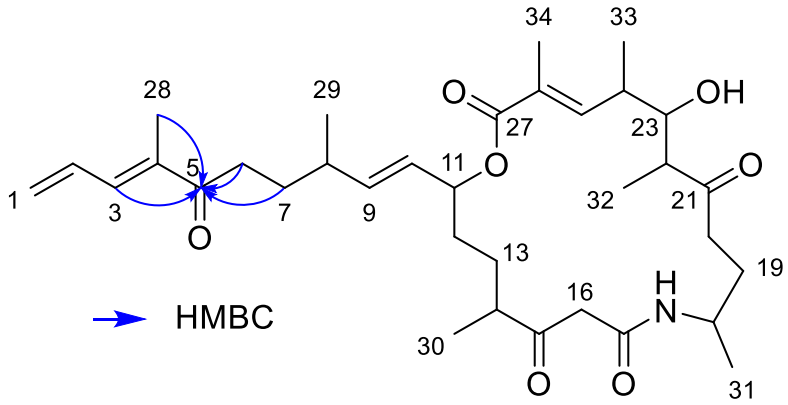

Position	δ_C[a] [ppm]	Type	δ_H[b] [ppm]	H Multiplicity (*J* [Hz])	COSY[c]	HMBC[d]
1a	124.5	CH_2	5.63	br d (18.3)	1b, 2, 3, 28	2, 3, 4
1b	124.5	CH_2	5.50	d (10.1)	1a, 2, 3, 28	3, 5
2	132.9	CH	6.74	dt (16.8, 10.5, 10.5)	1a, 1b, 3	3, 4
3	138.0	CH	7.02	br d (11.0)	1a, 1b, 2, 28	1, 2, 4, 5, 28
4	136.6	C	-	-	-	-
5	202.2	C	-	-	-	-
6a	35.1	CH_2	2.72	m	6b, 7a	5, 7, 8
6b			2.62	m	6a, 7a	5, 7, 8
7a	31.4	CH_2	1.68	m	6a, 6b, 7b, 8	5, 6, 8, 9, 29
7b			1.57	m	7a, 8	5, 6, 8, 9, 29
8	36.2	CH	2.16	m	7a, 7b, 9, 29	6, 7, 9, 10, 29
9	139.4	CH	5.58	m	8, 10	7, 8, 10 ,11, 29
10	127.5	CH	5.44	m	9, 11	8, 9, 11, 29
11	75.1	CH	5.10	m	10, 12a, 12b	9, 10, 27
12a	33.2	CH_2	1.67	m	11, 12b, 13a, 13b	10, 11, 13, 14
12b			1.51	m	11, 12a, 13a, 13b	10, 11, 13, 14
13a	28.0	CH_2	1.81	m	12a, 12b, 13b, 14	11, 12, 14, 15, 30
13b			1.33	m	12a, 12b, 13a, 14	11, 12, 14, 15, 30
14	47.5	CH	2.66	m	13a, 13b, 30	12, 13, 15, 30
15	209.7	C	-	-	-	-
16a	49.3	CH_2	3.56	d (15.9)	16b	14, 15, 17, 18
16b			3.27	d (15.9)	16a	15, 17

17	165.0	C	-	-	-	-
18	45.0	CH	4.02	m	19a, 19b, 31, NH	17, 19, 20, 31
19a	30.5	CH_2	1.85	m	18, 20a, 20b	18, 20, 21, 31
19b			1.54	m	18, 20a, 20b	18, 20, 21, 31
20a	38.7	CH_2	2.73	m	19a, 19b, 20b	18, 19, 21
20b			2.54	m	19a, 19b, 20a	18, 19, 21
21	215.9	C	-	-	-	-
22	47.8	CH	2.66	m	23, 32	20, 21, 23, 32
23	73.9	CH	3.78	br d (10.0)	22, 24	21, 24, 25, 32, 33
24	36.3	CH	2.59	m	23, 25, 33	22, 23, 25, 26, 33
25	142.5	CH	6.52	dd (10.2, 1.3)	24, 34	23, 24, 26, 27, 33, 34
26	128.6	C	-	-	-	-
27	167.8	C	-	-	-	-
28	11.7	CH_3	1.89	s	1a, 1b, 3	1, 2, 3, 4, 5
29	20.4	CH_3	1.02	d (6.7)	8	7, 8, 9
30	16.3	CH_3	1.12	d (7.1)	14	13, 14, 15
31	21.8	CH_3	1.20	d (6.6)	18	18, 19, 20
32	8.8	CH_3	1.06	d (7.2)	22	21, 22, 23
33	16.7	CH_3	1.14	d (6.6)	24	23, 24, 25
34	12.7	CH_3	1.84	d (1.1)	25	23, 24, 25, 26, 27, 33
NH	-	NH	6.17	br d (9.0)	18	17, 18, 19, 31

[a] Acquired in chloroform-*d* at 125 MHz and calibrated to solvent signal at 77.0 ppm.
[b] Acquired in chloroform-*d* at 500 MHz and calibrated to solvent signal at 7.27 ppm.
[c] Proton showing COSY correlations to indicated proton.
[d] Proton showing HMBC correlations to indicated carbon.

Table S 2.14: NMR Spectroscopic data for angiolam C (3)

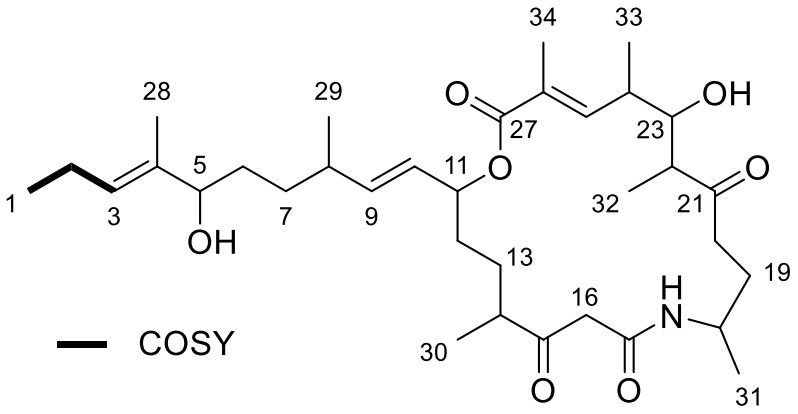

Position	δ_C[a] [ppm]	Type	δ_H[b] [ppm]	H Multiplicity (*J* [Hz])	COSY[c]	HMBC[d]
1	14.1	CH_3	0.97	t (7.5, 7.5)	2, 3	2, 3
2	20.8	CH_2	2.03	m	1, 3	1, 4
3	128.4	CH	5.37	m	1, 2, 5, 28	1, 2, 5, 28
4	136.4	C	-	-	-	-
5	77.9	CH	3.93	br t (6.7, 6.7)	3, 6	3, 4, 7
6	32.9	CH_2	1.52	m	5, 7a, 7b	4, 5, 7, 8
7a	32.7	CH_2	1.35	m	6, 7b, 8	5, 6, 8, 9, 29

7b			1.22	m	6, 7a, 8	5, 9, 29
8	36.5	CH	2.13	dt (13.8, 6.9, 6.9)	7a, 7b, 9, 29	6, 9, 10, 29
9	139.5	CH	5.55	dd (15.4, 7.7)	8, 10, 29	6, 8, 10, 11, 29
10	126.6	CH	5.41	dd (15.4, 6.9)	9, 11	8, 11, 12
11	74.6	CH	5.16	m	10, 12a, 12b	9, 10, 12, 13, 27
12a	33.1	CH_2	1.72	m	11, 12b, 13a, 13b	13, 14
12b			1.51	m	11, 12a, 13a, 13b	11, 13, 14
13a	27.8	CH_2	1.81	m	12a, 12b, 13b, 14	12, 14, 30
13b			1.33	m	12a, 12b, 13a, 14	11, 12, 14, 15, 30
14	47.8	CH	2.67	m	13a, 13b, 30	12, 13, 15, 30
15	209.8	C	-	-	-	-
16a	49.2	CH_2	3.57	d (15.8)	16b	15, 17, 18
16b			3.26	d (15.8)	16a	15, 17
17	165.0	C	-	-	-	-
18	45.0	CH	4.02	m	19a, 19b, 31, NH	17, 19, 31
19a	30.6	CH_2	1.84	m	18, 19b, 20a, 20b	20
19b			1.54	m	18, 19a, 20a, 20b	18, 20
20a	38.8	CH_2	2.68	m	19a, 19b, 20b	18, 19, 21
20b			2.54	m	19a, 19b, 20a	18, 19, 21
21	215.8	C	-	-	-	-
22	47.6	CH	2.64	m	32	20, 21, 23, 24, 32
23	74.1	CH	3.76	br d (9.8)	24	21, 24, 25, 32, 33
24	36.3	CH	2.59	m	23, 25, 33	22, 23, 25, 26, 33
25	142.4	CH	6.49	br d (10.1)	24, 34	23, 24, 26, 27, 33, 34
26	128.7	C	-	-	-	-
27	167.7	C	-	-	-	-
28	11.1	CH_3	1.59	s	3	1, 2, 3, 4, 5
29	20.4	CH_3	0.99	d (6.5)	8, 9	6, 8, 9
30	16.0	CH_3	1.12	br d (7.0)	14	13, 14, 15
31	21.8	CH_3	1.20	br d (6.5)	18, NH	18, 19
32	8.8	CH_3	1.06	d (7.0)	22	21, 22, 23
33	16.7	CH_3	1.15	br d (6.7)	24	23, 24, 25
34	12.6	CH_3	1.86	m	25	24, 25, 26, 27
NH	-	NH	6.25	br d (9.1)	18, 31	17, 18

[a] Acquired in chloroform-*d* at 125 MHz and calibrated to solvent signal at 77.0 ppm.
[b] Acquired in chloroform-*d* at 500 MHz and calibrated to solvent signal at 7.27 ppm.
[c] Proton showing COSY correlations to indicated proton.
[d] Proton showing HMBC correlations to indicated carbon.

Table S 2.15: NMR Spectroscopic data for angiolam D_1 (4a)

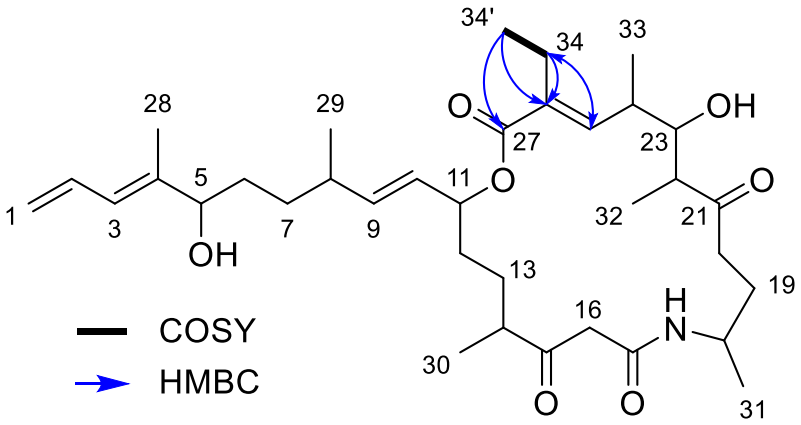

Position	δ_C[a] [ppm]	Type	δ_H[b] [ppm]	H Multiplicity (*J* [Hz])	COSY[c]	HMBC[d]
1a	116.9	CH_2	5.20	m	1b, 2	2, 3, 4
1b			5.11	m	1a, 2	3
2	132.7	CH	6.59	dt (16.8, 10.5, 10.5)	1a, 1b, 3	3, 4
3	125.8	CH	6.04	ddd (11.3, 1.8, 0.8)	2, 28	1, 2, 4, 5, 28
4	140.5	C	-	-	-	-
5	77.3	CH	4.00	m	6	3, 4, 6, 28
6	32.8	CH_2	1.54	m	5, 7a, 7b	4, 5, 7, 8
7a	32.7	CH_2	1.38	m	6, 7b, 8	5, 6, 8, 9, 29
7b			1.27	m	6, 7a, 8	5, 6, 8, 9, 29
8	36.5	CH	2.14	m	7a, 7b, 9, 29	6, 9, 10, 29
9	139.3	CH	5.53	m	8, 10	7, 8, 10, 11, 29
10	126.7	CH	5.42	m	9, 11	8, 9, 11, 12
11	74.5	CH	5.17	m	10, 12a, 12b	9, 10, 13, 27
12a	33.0	CH_2	1.71	u	11, 12b, 13a, 13b	10, 11, 13, 14
12b			1.49	m	11, 12a, 13a, 13b	10, 13, 14
13a	27.7	CH_2	1.83	m	12a, 12b, 13b, 14	
13b			1.33	m	12a, 12b, 13a, 14	11, 14,15, 30
14	47.7	CH	2.66	m	13a, 13b, 30	12, 13, 15, 30
15	209.9	C	-	-	-	-
16a	49.2	CH_2	3.58	m	16b	15, 17, 18
16b			3.25	m	16a	15, 17
17	165.0	C	-	-	-	-
18	44.9	CH	4.03	m	19b, 31, NH	17, 19, 31
19a	30.5	CH_2	1.83	m	20a, 20b	18, 20, 21, 31
19b			1.55	m	18, 20a, 20b	18, 20, 21, 31
20a	38.8	CH_2	2.63	m	19a, 19b, 20b	18, 19, 21
20b			2.53	m	19a, 19b, 20a	18, 19, 21
21	215.8	C	-	-	-	-
22	47.6	CH	2.65	m	23, 32	20, 21, 32
23	74.2	CH	3.76	m	22, 24	21, 25, 32, 33
24	36.0	CH	2.60	m	23, 25, 33	22, 23, 25, 26, 33
25	141.3	CH	6.39	br d (10.2)	24	23, 24, 26, 27, 33, 34
26	135.1	C	-	-	-	-

27	167.4	C	-	-	-	-
28	12.1	CH_3	1.75	d (1.2)	3	2, 3, 4, 5
29	20.4	CH_3	0.98	d (6.7)	8	7, 8, 9
30	15.8	CH_3	1.11	dd (7.0, 1.6)	14	13, 14, 15
31	21.8	CH_3	1.20	dd (6.6, 3.1)	18	18, 19
32	8.8	CH_3	1.05	dd (7.2, 1.8)	22	21, 22, 23
33	17.4	CH_3	1.16	d (6.6)	24	23, 24, 25
34a	20.6	CH_2	2.35	m	34b, 34'	25, 26, 27, 34'
34b			2.29	m	34a, 34'	25, 26, 27, 34'
34'	14.0	CH_3	1.01	m	34a, 34b	26, 34
NH	-	NH	6.29	br d (9.2)	18	17, 18

[a] Acquired in chloroform-*d* at 175 MHz and calibrated to solvent signal at 77.0 ppm.
[b] Acquired in chloroform-*d* at 700 MHz and calibrated to solvent signal at 7.27 ppm.
[c] Proton showing COSY correlations to indicated proton.
[d] Proton showing HMBC correlations to indicated carbon.

Table S 2.16: NMR Spectroscopic data for angiolam D_2 (4b)

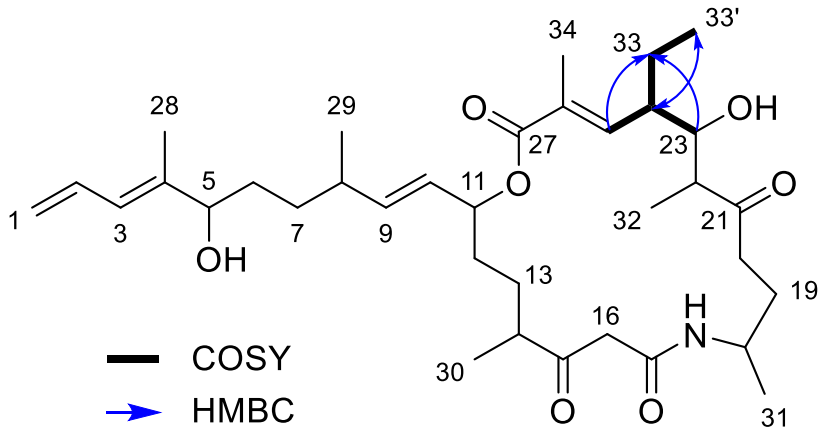

Position	δ_C[a] [ppm]	Type	δ_H[b] [ppm]	H Multiplicity (*J* [Hz])	COSY[c]	HMBC[d]
1a	116.9	CH_2	5.20	m	1b, 2	2, 3, 4
1b			5.11	m	1a, 2	3
2	132.7	CH	6.59	dt (16.8, 10.5, 10.5)	1a, 1b, 3	3, 4
3	125.8	CH	6.04	ddd (11.3, 1.8, 0.8)	2, 28	1, 2, 4, 5, 28
4	140.5	C	-	-	-	-
5	77.3	CH	4.00	m	6	3, 4, 6, 28
6	32.8	CH_2	1.54	m	5, 7a, 7b	4, 5, 7, 8
7a	32.7	CH_2	1.38	m	6, 7b, 8	5, 6, 8, 9, 29
7b			1.27	m	6, 7a, 8	5, 6, 8, 9, 29
8	36.5	CH	2.14	m	7a, 7b, 9, 29	6, 9, 10, 29
9	139.3	CH	5.53	m	8, 10	7, 8, 10, 11, 29
10	126.7	CH	5.42	m	9, 11	8, 9, 11, 12
11	74.5	CH	5.17	m	10, 12a, 12b	9, 10, 13, 27
12a	33.0	CH_2	1.71	m	11, 12b, 13a, 13b	10, 11, 13, 14
12b			1.49	m	11, 12a, 13a, 13b	10, 13, 14
13a	27.7	CH_2	1.83	m	12a, 12b, 13b, 14	
13b			1.33	m	12a, 12b, 13a, 14	11, 14,15, 30

14	47.7	CH	2.66	m	13a, 13b, 30	12, 13, 15, 30
15	209.9	C	-	-	-	-
16a	49.2	CH_2	3.58	m	16b	15, 17, 18
16b			3.25	m	16a	15, 17
17	165.0	C	-	-	-	-
18	44.9	CH	4.03	m	19b, 31, NH	17, 19, 31
19a	30.5	CH_2	1.83	m	20a, 20b	18, 20, 21, 31
19b			1.55	m	18, 20a, 20b	18, 20, 21, 31
20a	38.8	CH_2	2.63	m	19a, 19b, 20b	18, 19, 21
20b			2.53	m	19a, 19b, 20a	18, 19, 21
21	215.8	C	-	-	-	-
22	48.0	CH	2.57	m	23, 32	21
23	72.4	CH	3.84	dd (9.8, 1.3)	22, 24	21, 24, 25, 33
24	43.2	CH	2.46	m	23, 25, 33a, 33b	23, 25, 26, 33, 33'
25	141.4	CH	6.41	dd (10.8, 1.4)	24, 34	23, 24, 26, 27, 33, 34
26	130.1	C	-	-	-	-
27	167.5	C	-	-	-	-
28	12.1	CH_3	1.75	d (1.2)	3	2, 3, 4, 5
29	20.4	CH_3	0.98	d (6.7)	8	7, 8, 9
30	15.8	CH_3	1.11	dd (7.0, 1.6)	14	13, 14, 15
31	21.8	CH_3	1.20	dd (6.6, 3.1)	18	18, 19
32	8.9	CH_3	1.05	m	22	21, 22, 23
33a	24.2	CH_2	2.00	m	24, 33b, 33'	33'
33b			1.33	m	24, 33a, 33'	24, 33'
33'	11.2	CH_3	0.86	t (7.5, 7.5)	33a, 33b	24, 33
34	13.2	CH_3	1.87	d (1.4)	25	23, 24, 25, 26, 27, 33
NH		NH	6.29	br d (9.2)	18	17, 18

[a] Acquired in chloroform-*d* at 175 MHz and calibrated to solvent signal at 77.0 ppm.
[b] Acquired in chloroform-*d* at 700 MHz and calibrated to solvent signal at 7.27 ppm.
[c] Proton showing COSY correlations to indicated proton.
[d] Proton showing HMBC correlations to indicated carbon.

Table S 2.17: NMR Spectroscopic data for angiolam F (5)

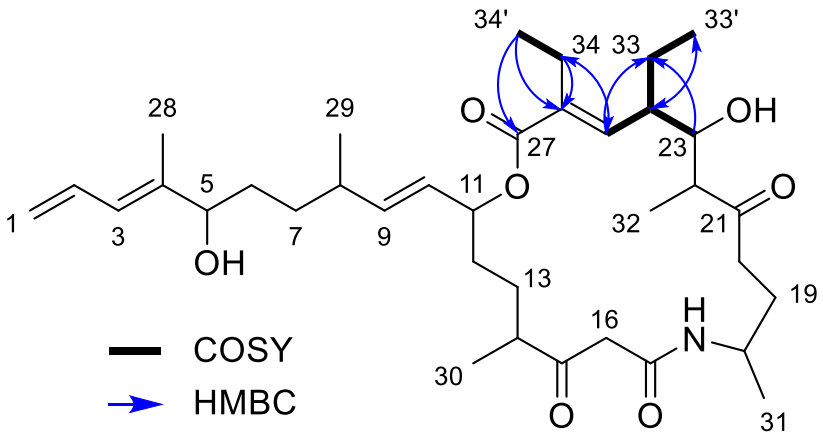

Position	δ_C[a] [ppm]	Type	δ_H[b] [ppm]	H Multiplicity (*J* [Hz])	COSY[c]	HMBC[d]
1a	117.0	CH_2	5.20	m	1b, 2, 3	2, 3
1b			5.11	br d (10.0)	1a, 2, 3	3
2	132.7	CH	6.59	dt (16.8, 10.6, 10.6)	1a, 1b, 3	3, 4
3	125.8	CH	6.04	br d (11.1)	1a, 1b, 2, 5, 28	1, 2, 5, 28
4	140.5	C	-	-	-	-
5	77.3	CH	4.00	m	3, 6	3, 4, 7, 28
6	32.9	CH_2	1.53	m	5, 7a, 7b	4, 5, 7, 8
7a	32.8	CH_2	1.37	m	6, 8	5, 8, 9
7b			1.24	m	6, 8	8, 9
8	36.7	CH	2.14	dt (13.5, 6.9, 6.9)	7a, 7b, 9, 29	6, 9, 10, 29
9	139.2	CH	5.52	m	8, 10	7, 8, 10, 11, 29
10	126.7	CH	5.43	dd (15.5, 6.4)	9, 11	8, 9, 11, 12, 29
11	74.1	CH	5.22	m	10, 12a, 12b	9, 13, 27
12a	32.9	CH_2	1.74	m	11, 12b, 13a, 13b	10, 11, 14
12b			1.50	m	11, 12a, 13a, 13b	
13a	27.6	CH_2	1.84	m	12a, 12b, 14	
13b			1.32	m	12a, 12b, 14	14, 15, 30
14	47.7	CH	2.65	m	13a, 13b, 30	12, 13, 15, 30
15	209.9	C	-	-	-	-
16a	49.0	CH_2	3.59	br d (15.7)	16b	15, 17
16b			3.24	d (15.7)	16a	15, 17
17	164.9	C	-	-	-	-
18	44.9	CH	4.03	m	19a, 19b, 31	17, 31
19a	30.5	CH_2	1.85	m	18, 19b, 20a, 20b	18, 20, 21, 31
19b			1.52	m	18, 19a, 20a, 20b	18, 20, 21, 31
20a	38.8	CH_2	2.67	m	19a, 19b	18, 19, 21
20b			2.55	m	19a, 19b	18, 19, 21
21	216.0	C	-	-	-	-
22	47.7	CH	2.60	m	23, 32	21, 32
23	72.4	CH	3.82	br d (9.8)	22, 24	21, 24, 25, 32, 33
24	42.8	CH	2.45	ddd (19.7, 9.6, 2.9)	23, 25, 33	23, 25, 26, 33, 33'
25	139.9	CH	6.26	d (10.8)	24	23, 24, 26, 27, 33, 34, 34'
26	136.6	C	-	-	-	-
27	167.3	C	-	-	-	-
28	12.1	CH_3	1.75	m	3	3, 4, 5
29	20.6	CH_3	0.98	m	8	7, 8, 9
30	15.7	CH_3	1.11	d (6.9)	14	12, 13, 14, 15
31	21.9	CH_3	1.20	d (6.6)	18	18, 19
32	8.8	CH_3	1.06	br d (7.1)	22	21, 23
33	24.2	CH_2	1.98	m	24, 33'	23, 24, 25
33'	11.2	CH_3	0.86	m	33	24, 33
34	20.7	CH_2	2.34	m	34'	25, 26, 27, 34'
34'	13.6	CH3	0.99	m	34	26, 34
NH	-	NH	6.32	br d (9.3)	-	17, 18

[a] Acquired in chloroform-*d* at 125 MHz and calibrated to solvent signal at 77.0 ppm.

[b] Acquired in chloroform-*d* at 500 MHz and calibrated to solvent signal at 7.27 ppm.
[c] Proton showing COSY correlations to indicated proton.
[d] Proton showing HMBC correlations to indicated carbon.

Analysis of angiolam BGC

Based on *in silico* analyses of the genomes of MCy12716 and MCy12733 with antiSMASH[10], the ang BGC could be observed. All coding sequences surrounding the angiolam biosynthetic machinery in both strains were extracted from the MCy12733 (ctg39_13-ctg39_27) genome sequence, translated and searched with the blastp algorithm against the RefSeq non-redundant protein sequence database at NCBI. Furthermore, the gene putatively encoding a fused isobutyryl-CoA mutase (ctg31_31) was treated accordingly.

Table S 2.18: Blastp results of the CDS regions in the ang BGC

CDS Name	Length [AA]	Closest homologue [Organism of origin]	Identity [%] and query coverage [%]	Accession Nr.
ang1	393	acetyl-CoA C-acetyltransferase [Pyxidicoccus caerfyrddinensis]	98.2; 100	WP_163996527.1
ang2	232	CoA transferase subunit A [Pyxidicoccus caerfyrddinensis]	98.7; 100	WP_163996526.1
ang3	218	CoA transferase subunit B [Pyxidicoccus caerfyrddinensis]	100,0; 100	WP_163996525.1
ang4	131	TIGR02266 family protein [Pyxidicoccus caerfyrddinensis]	98.5; 100	WP_163996524.1
ang5	431	class I SAM-dependent RNA methyltransferase [Pyxidicoccus caerfyrddinensis]	97.9; 100	WP_163996523.1
ang6	465	VWA domain-containing protein [Pyxidicoccus caerfyrddinensis]	100.0; 100	WP_163996522.1
angA	2672	SDR family NAD(P)-dependent oxidoreductase [Pyxidicoccus fallax]	82.1; 99	NMO18055.1
angB	3652	type I polyketide synthase [Pyxidicoccus fallax]	85.4; 99	WP_169347329.1
angC	6523	type I polyketide synthase [Pyxidicoccus fallax]	84.1; 96	WP_169345687.1
angD	5062	amino acid adenylation domain-containing protein [Pyxidicoccus fallax]	85.3; 100	NMO16395.1
angE	3855	type I polyketide synthase [Pyxidicoccus fallax]	83.4; 99	WP_169345685.1
angF	386	acyl-CoA dehydrogenase family protein [Pyxidicoccus fallax]	89.4; 99	WP_169345684.1

ang8	397	efflux RND transporter periplasmic adaptor subunit [Pyxidicoccus caerfyrddinensis]	97.7; 100	WP_163996521.1
ang9	1043	efflux RND transporter permease subunit [Pyxidicoccus caerfyrddinensis]	98.6; 100	WP_163996520.1
ctg31_31	1155	methylmalonyl-CoA mutase family protein [Pyxidicoccus caerfyrddinensis]	98.9; 100	WP_163996481.1

As all observed CDS regions belong to the genus of *Pyxidicoccus* and share high similarities with the query sequences, the first non-*Pyxidicoccus* hits were also retrieved.

Table S 2.19: Blastp results of the CDS regions in the *ang* BGC without the genus *Pyxidicoccus*

CDS Name	Length [AA]	Closest homologue without *Pyxidicoccus* strains [Organism of origin]	Identity [%] and query coverage [%]	Accession Nr.
ang1	393	acetyl-CoA C-acetyltransferase [Myxococcus sp. RHSTA-1-4]	93.4; 100	WP_223754820.1
ang2	232	CoA transferase subunit A [Myxococcus sp. RHSTA-1-4]	97.0; 100	WP_223754821.1
ang3	218	CoA transferase subunit B [Myxococcus sp. RHSTA-1-4]	95.9; 100	WP_223754822.1
ang4	131	TIGR02266 family protein [Myxococcus sp. RHSTA-1-4]	88.6; 100	WP_223754823.1
ang5	431	class I SAM-dependent RNA methyltransferase [Myxococcus sp. RHSTA-1-4]	94.9; 100	WP_223754824.1
ang6	465	VWA domain-containing protein [Myxococcus sp. XM-1-1-1]	92.7; 100	WP_223748567.1
angA	2672	type I polyketide synthase [Polyangium spumosum DSM14734]	42.7; 97	WP_153821595.1
angB	3652	epoD [Sorangium cellulosum SMP44]	52.1; 99	AAF62883.1
angC	6523	epoD [Sorangium cellulosum SMP44]	46.8; 99	AAF62883.1
angD	5062	epoD [Sorangium cellulosum SMP44]	61.9; 79	AAF62883.1
angE	3855	polyketide synthase [Sorangium cellulosum So0157-2]	69.1; 84	ACB46196.1
angF	386	acyl-CoA/acyl-ACP dehydrogenase [Enhygromyxa salina]	63.7; 99	WP_052559235.1
ang8	397	efflux RND transporter periplasmic adaptor subunit [Myxococcus sp. RHSTA-1-4]	77.6; 100	WP_223755293.1
ang9	1043	efflux RND transporter permease subunit [Myxococcus sp. RHSTA-1-4]	88.3; 100	WP_223755292.1

ctg31_31	1155	methylmalonyl-CoA mutase family protein [Corallococcus sp. CA053C]	93.3; 100	WP_120611036.1

Table S 2.20: Substrate specificity of angiolam BGC AT domains

	Main substrate	**AntiSMASH[10]**	**Fingerprint[11]**	**RIDVV-motif[12]**
L	Methylmanonyl-CoA	Methylmanonyl-CoA[a]	Methylmanonyl-CoA	No
M1	Methylmanonyl-CoA	Methylmanonyl-CoA[a]	Methylmanonyl-CoA	No
M2	Malonyl-CoA	Malonyl-CoA	Malonyl-CoA	
M3	Methylmanonyl-CoA	Methylmanonyl-CoA[a]	Methylmanonyl-CoA	Yes
M4	Malonyl-CoA	Malonyl-CoA	Malonyl-CoA	
M5	Malonyl-CoA	Malonyl-CoA	Malonyl-CoA	
M6	Methylmanonyl-CoA	Methylmanonyl-CoA[a]	Methylmanonyl-CoA	Yes
M7	Malonyl-CoA	Malonyl-CoA	Malonyl-CoA	
M8-A	Alanine	Glycine/Alanine	-	
M9	Malonyl-CoA	Malonyl-CoA	Malonyl-CoA	
M10	Methylmanonyl-CoA	Methylmanonyl-CoA[a]	Methylmanonyl-CoA	Yes
M11	Methylmanonyl-CoA	Methylmanonyl-CoA[a]	Methylmanonyl-CoA	Yes
M12	Methylmanonyl-CoA	Methylmanonyl-CoA[a]	Methylmanonyl-CoA	Yes

[a] Monomer specificity predictions in antiSMASH are methylmalonyl-CoA, but according to active site details in antiSMASH these AT domains are unspecific.

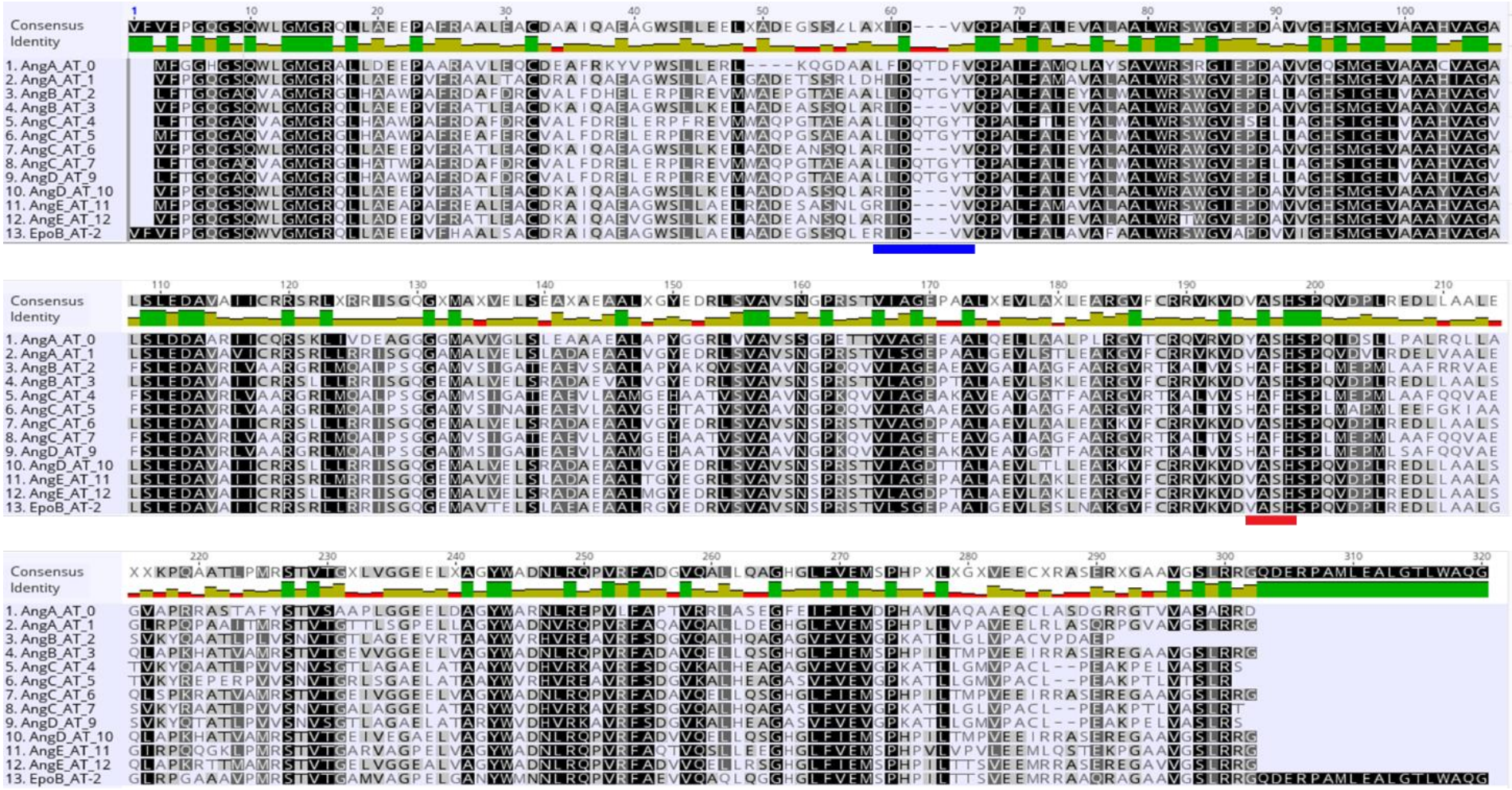

Figure S 2.3: Alignment of the AT domains in the *ang* BGC and the AT domain in module 2 of the *epo* BGC in *Sorangium cellulosum* So ce90. The fingerprint region for the distinction of the substrate specificity between malonyl-CoA (HAFH) and methylmalonyl-CoA (Y/VASH) is highlighted with a red bar, the putative region indicating a substrate specificity of methylmalonyl-CoA and ethylmalonyl-CoA (RiDVV) is highlighted with a blue bar.

Table S 2.21: Reductive loops in angiolam BGC and *in silico* predictions of the stereochemistry of angiolam A

Module	Position	Final stereochemistry	Relative stereochemistry in module	AntiSMASH[10]	KR type[13]	KR HMM[14]	DH fingerprint[11]	ER fingerprint[15]
1	C3	double bond: *E*	double bond: *E*	D (KR)	B1: *R*	D	*E* (B1 KR)	Inactive[a]
	C4	double bond: *E*	double bond: *E*	*R* (ER)	B1: *R*	L	*E* (B1 KR)	Inactive[a]
2	C5	*S*	*S*/D	D (KR)	A1: *S*	L	No DH	No ER
	C6	-	-	-	-	-	No DH	No ER
3	C7	-	-	D (KR)	B1: *R*	D	*E* (B1 KR)	-
	C8	*R*	*R*/D	*R* (ER)	B1: *R*	D	*E* (B1 KR)	*R*
4	C9	double bond: *E*	double bond: *E*	D (KR)	B1: *R*	D	*E* (B1 KR)	No ER
	C10	double bond: *E*	double bond: *E*	-	-	-	*E* (B1 KR)	No ER
5	C11	*S*	*S*/D	D (KR)	B1: *R*	D	No DH	No ER
	C12	-	-	-	-	-	No DH	No ER
6	C13	-		D (KR)	B1: *R*	D	*E* (B1 KR)	-
	C14	*R*	*R*/D	R (ER)	B1: *R*	D	*E* (B1 KR)	*R*
7	C15	-	-	-	No KR	No KR	Inactive[b]	No ER
	C16	-	-	-	No KR	No KR	Inactive[b]	No ER
8	C17	-	-	-	NRPS module	NRPS module	NRPS module	NRPS module
	C18	*S*	*S*	-				
9	C19	-	-	D (KR)	B1: *R*	D	*E* (B1 KR)	-
	C20	-	-	S (ER)	-	-	*E* (B1 KR)	S
10	C21	-		L (KR)	C, unspecified[c]	D	No DH	-
	C22	*S*	*R*/D	*R* (ER)	C, unspecified[c]	D	No DH	Unclear[d]
11	C23	*R*	*S*/L	L (KR)	A1: *S*	L	No DH	No ER
	C24	*S*	*R*/D	-	A1: *R*	D	No DH	No ER
12	C25	double bond: *E*	double bond: *E*	D (KR)	B1: *R*	D	*E* (B1 KR)	Inactive[a]
	C26	double bond: *E*	double bond: *E*	inconclusive (ER)	B1: *R*	D	*E* (B1 KR)	Inactive[a]

In-silico predictions of modules 1-12 and the positions the respective KR, DH and ER domains effect. Domains that determine the stereochemistry of the respective positions are marked in green, when they are fitting. In modules 2 and 5 the stereochemistry predictions of the KR domains differed between prediction tools and in 10 only the predicted stereochemistries of antiSMASH were correct. This might be explained by the limited number of domains that were available when the rules for the manually applied classification systems for KR[13,14] and ER[15] domains were formulated.

[a] ER domains in modules 1 and 12 are lacking the NADPH binding site needed for their reductive activities.

[b] The DH domain in module 7 does not possess the catalytic triad H, P, G.
[c] The KR domain in module 10 does not belong to type A or type B KRs, as it possesses neither a W residue in the catalytic region nor a LDD motif in the loop. As the catalytic region features an intact YAAAN motif, it belongs neither to the C1 nor the C2 type KRs[13].
[d] The ER domain in module 10 does not possess the typical fingerprins leading to neither a (2*S*)- nor a (2*R*)-configuration.

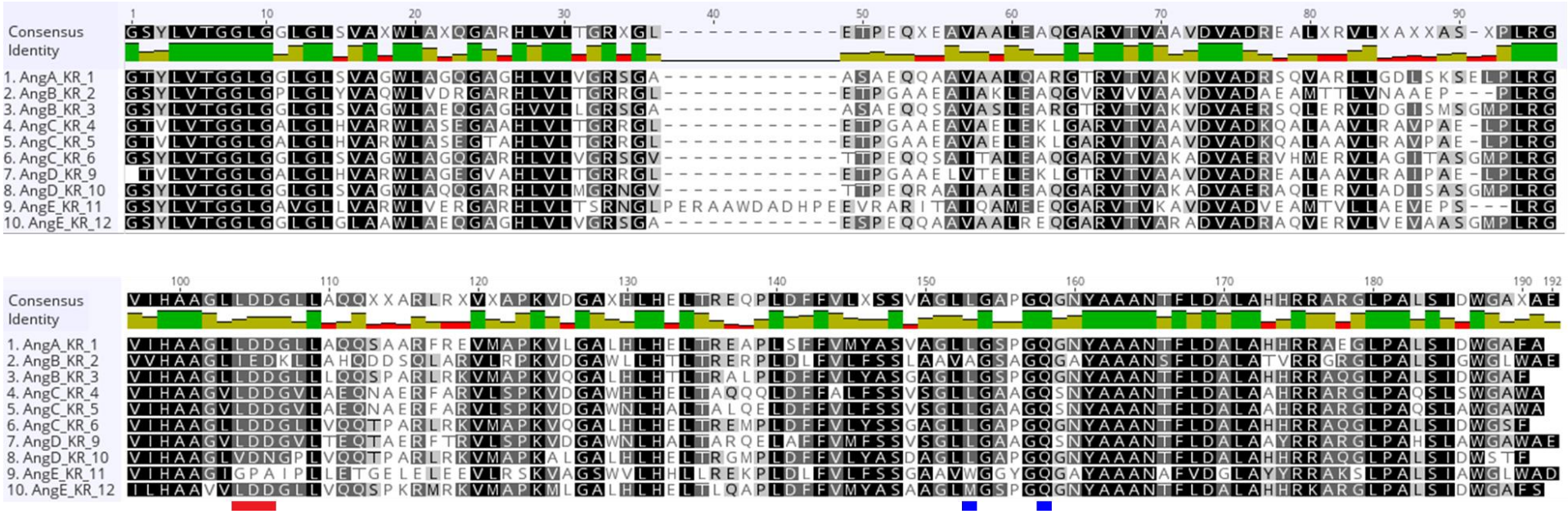

Figure S 2.4: Alignment of the KR domains in the *ang* BGC. The fingerprint region indicative for B-type KR domains (LDD) is highlighted with a red bar, regions that distinguish A1 and A2 type KR domains are highlighted with a blue bar.

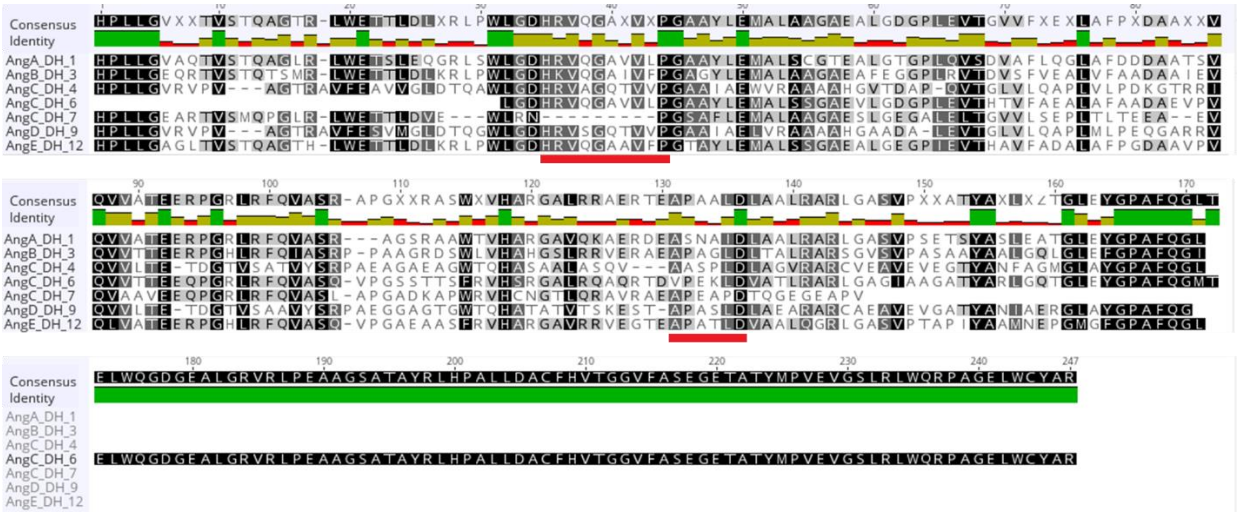

Figure S 2.5: Alignment of the DH domains in the *ang* BGC. The catalytic regions (HxxxGxxxxP and HPALLD) needed for the elimination of water, are highlighted with red bars.

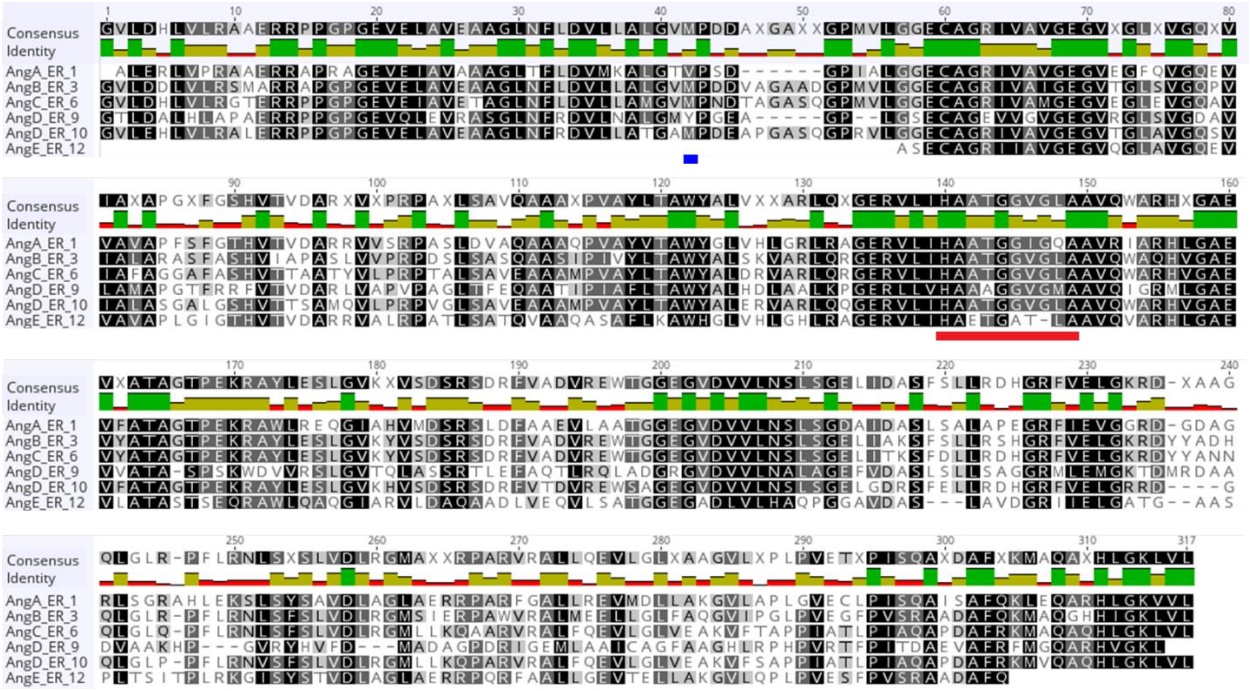

Figure S 2.6: Alignment of the ER domains in the *ang* BGC. The NADPH binding site (HaAtGGVGxA) is highlighted with a red bar. The tyrosine residue, catalysing the *S*-conformation of residues bound to position two in a given module is indicated with a blue bar.

Origin of ethyl-residues in angiolams D (4a/4b) and F (5)

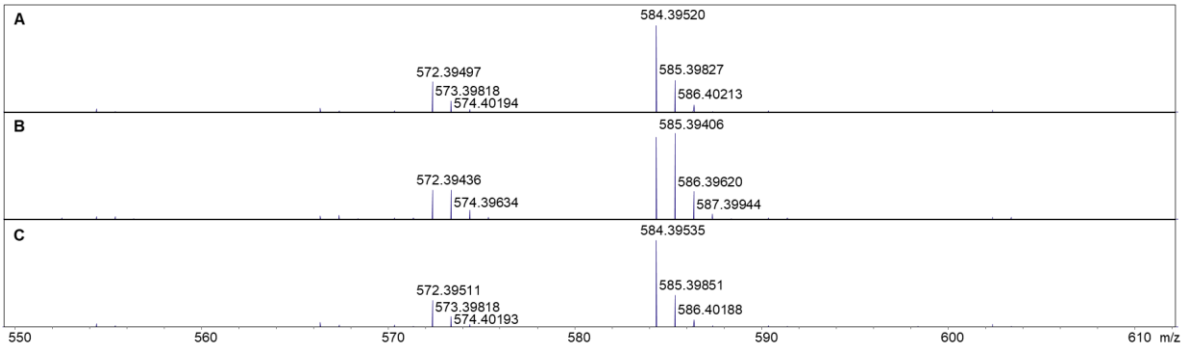

Figure S 2.7: Mass spectra of angiolam D from cultivations with labelled precursors. Isotope patterns of angiolams C (*m/z* 572.39) and D (*m/z* 584.39) cultivations of MCy12733 in Cy/H medium as control (A), with L-alanine ^{15}N (B) and L-methionine-(methyl ^{13}C) (C).

Table S 2.22: Production of angiolams A, D and F in Cy/H medium and with additional acetate, propionate, butyrate or L-valine

	Cy/H		Cy/H-Acetate[a]		Cy/H-Propionate[b]		Cy/H-Butyrate[c]		Cy/H-Valine[d]	
	Area	Average area	Area	Average area	Area	Average area	Area	Average area	Area	Average area
A	25655576	25355307	19816828	17255239	11008598	8350200	9136835	8042633	7678847	7753207
	25483662		15746595		4027166		7346901		9128582	
	24926684		16202293		10014836		7644162		6452191	
D	572186	569492	357620	316774	58126	148363	892692	794822	3241019	3365068
	598411		286440		332349		734559		3977963	
	537879		306263		54615		757215		2876223	
F	0	0	0	0	0	0	82104	71727	871836	927082
	0		0		0		66037		1074687	
	0		0		0		67040		834723	

[a] Addition of 20 mM Na acetate to Cy/H medium.
[b] Addition of 20 mM Na propionate to Cy/H medium.
[c] Addition of 20 mM Na butyrate to Cy/H medium.
[d] Addition of 2.5 g/L L-valine to Cy/H medium.

Disruption of angiolam BGC by single cross-over inactivation

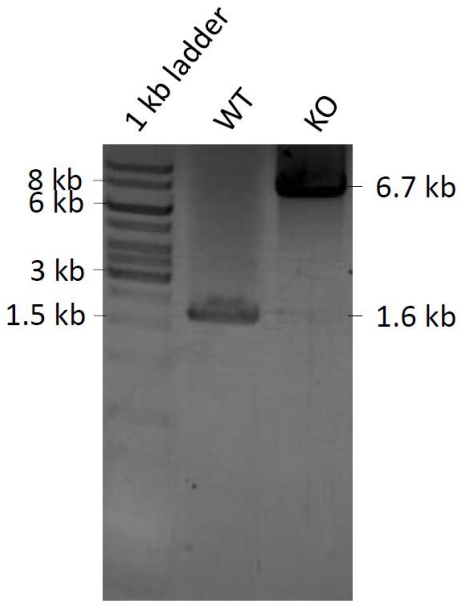

Figure S 2.8: Verification PCRs of integration of pTOPO-AngKO in the genome of *P. fallax* An d48. Verification PCRs for integration of pTOPO-AngKO into the genome of *P. fallax* An d48 were done with primers 48_Test_Fw and 48_Test_Rv, that bind ~ 300 bp up- and downstream the homologous region in *angB*. As shown in Figure S 4, the amplified region in the wild type strain covers 1.6 kb, while the integration mutant shows an amplified fragment of the size of ~ 6.7 kb that additionally accounts for pTOPO-AngKO with a size of 5067 bp.

NMR spectra employed in structure elucidation

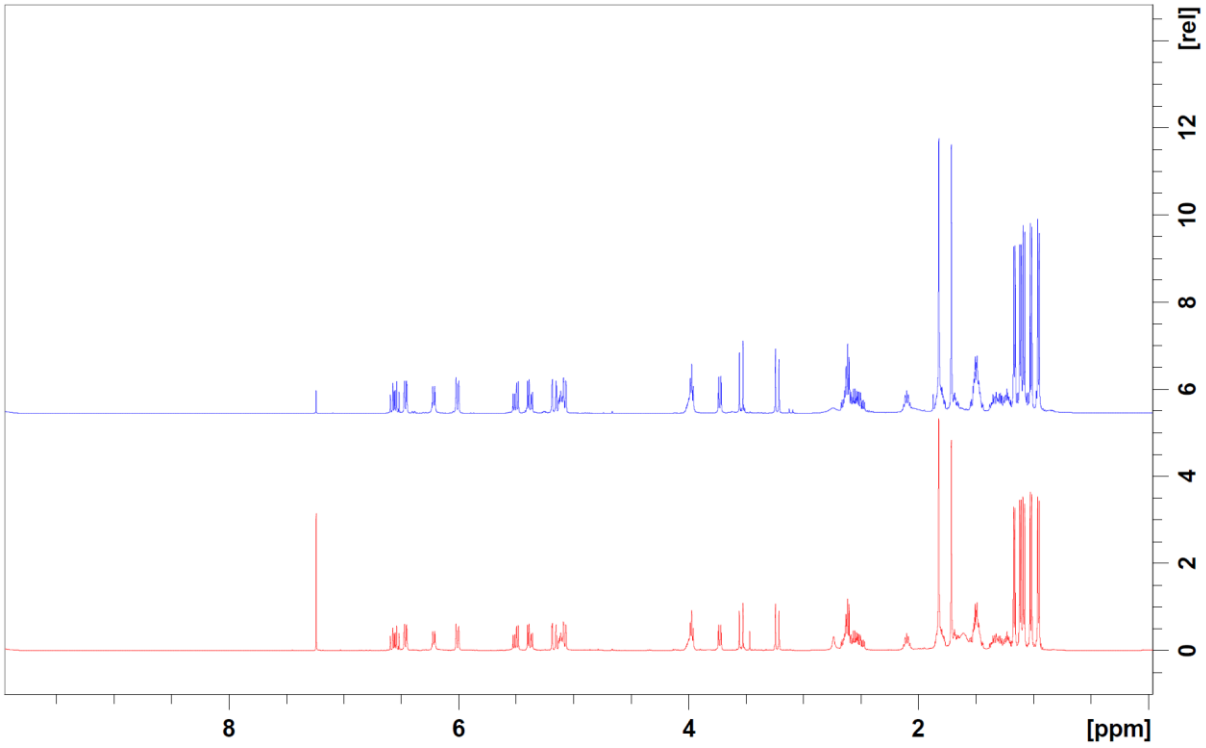

Figure S 2.9: Comparison of ^{1}H NMR spectra of purified angiolam A (1, blue) and authentic angiolam A (red) in chloroform-*d* at 500 MHz.

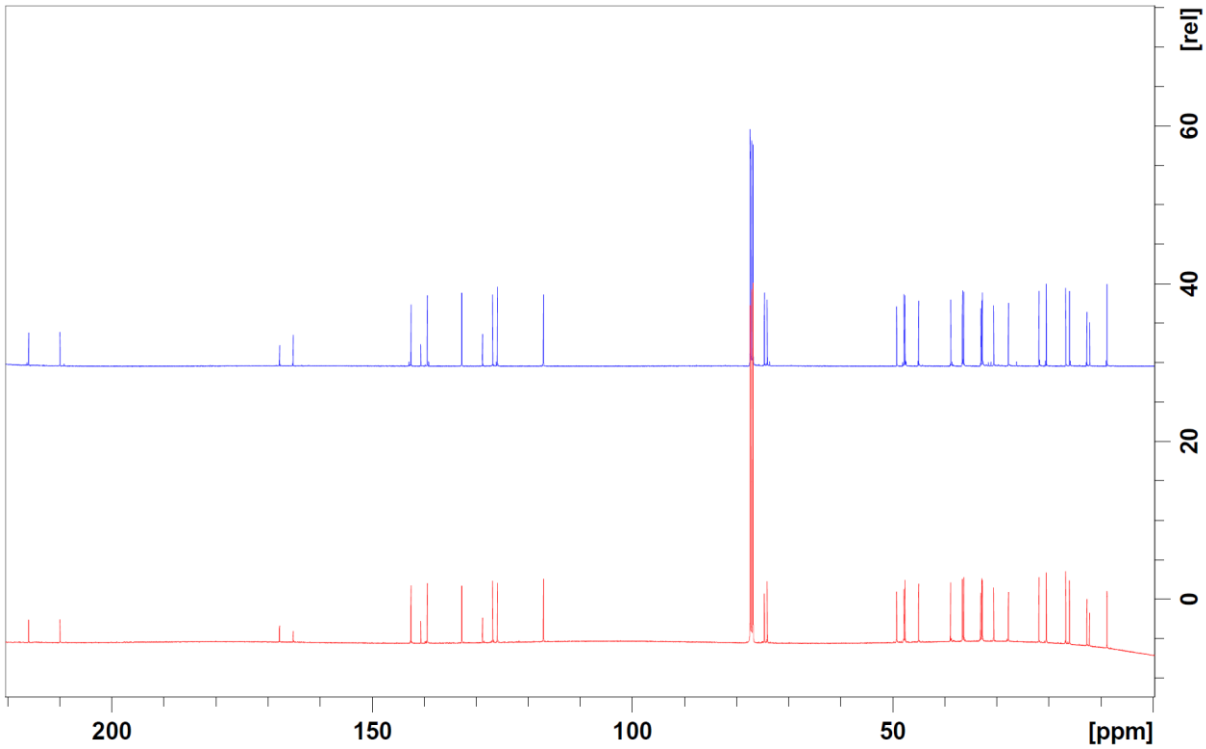

Figure S 2.10: Comparison of ^{13}C NMR spectra of purified angiolam A (1, blue) and authentic angiolam A (red) in chloroform-*d* at 125 MHz.

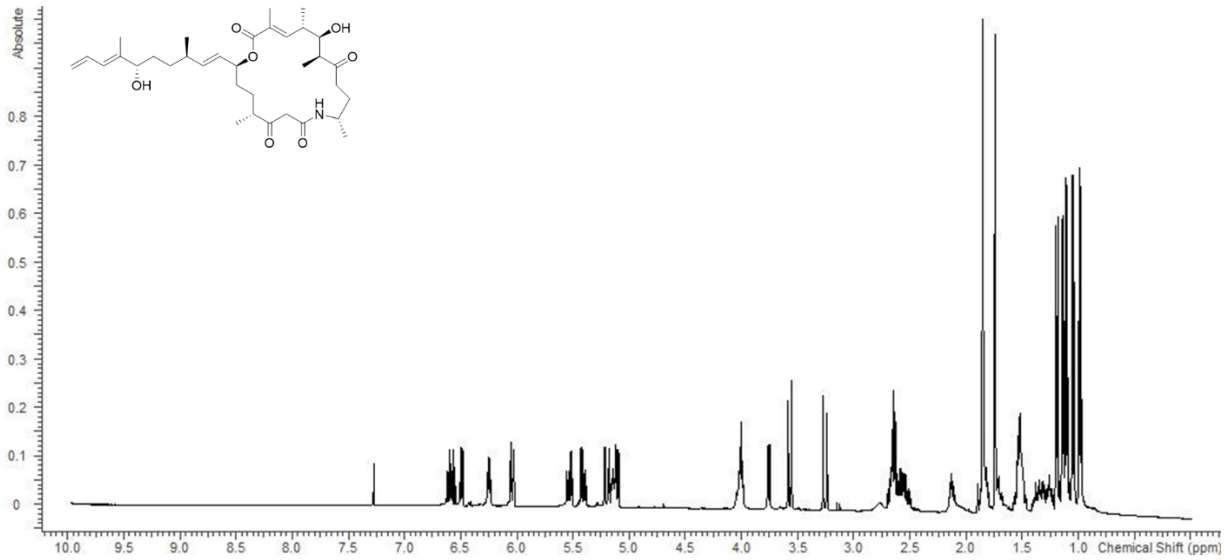

Figure S 2.11: ^{1}H spectrum of angiolam A (1) in chloroform-*d* at 500 MHz.

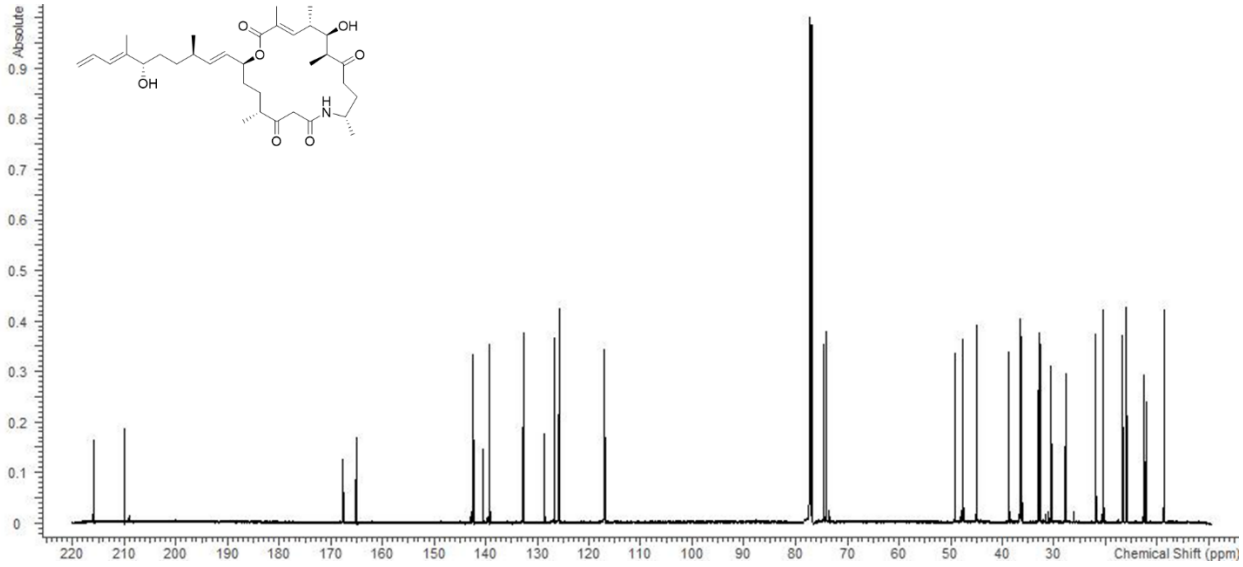

Figure S 2.12: ^{13}C spectrum of angiolam A (1) in chloroform-*d* at 125 MHz.

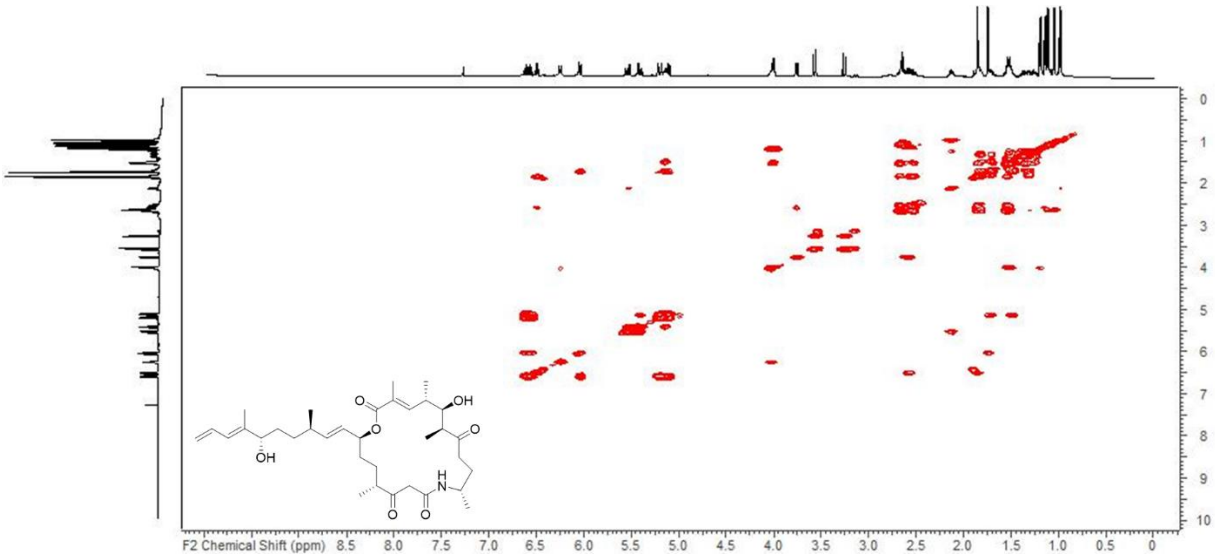

Figure S 2.13: COSY spectrum of angiolam A (1) in chloroform-*d* at 500 MHz.

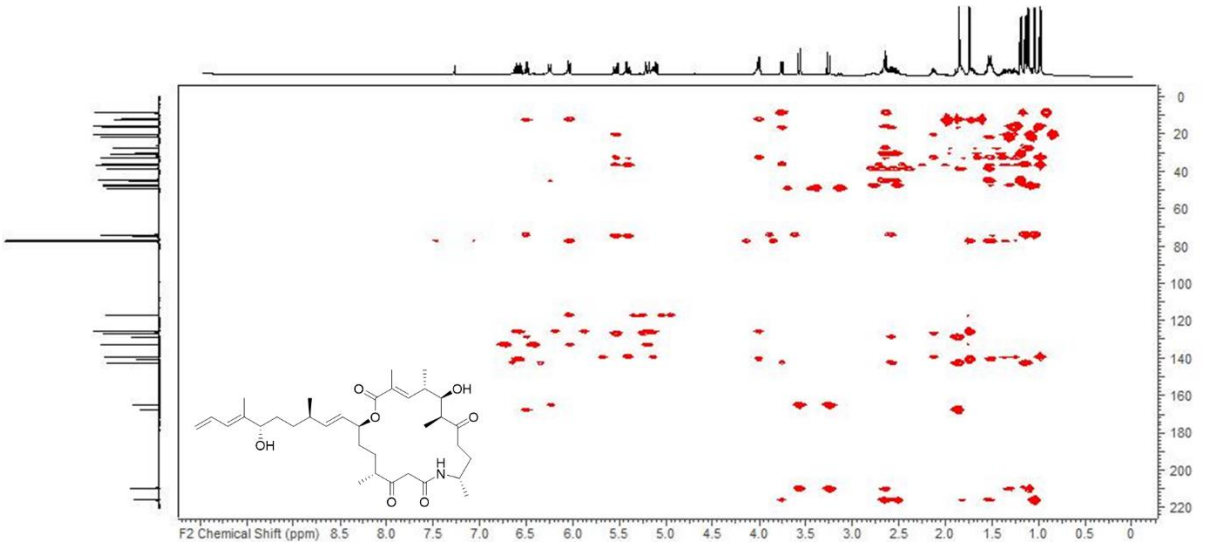

Figure S 2.14: HMBC spectrum of angiolam A (1) in chloroform-*d* at 125/500 (F1/F2) MHz.

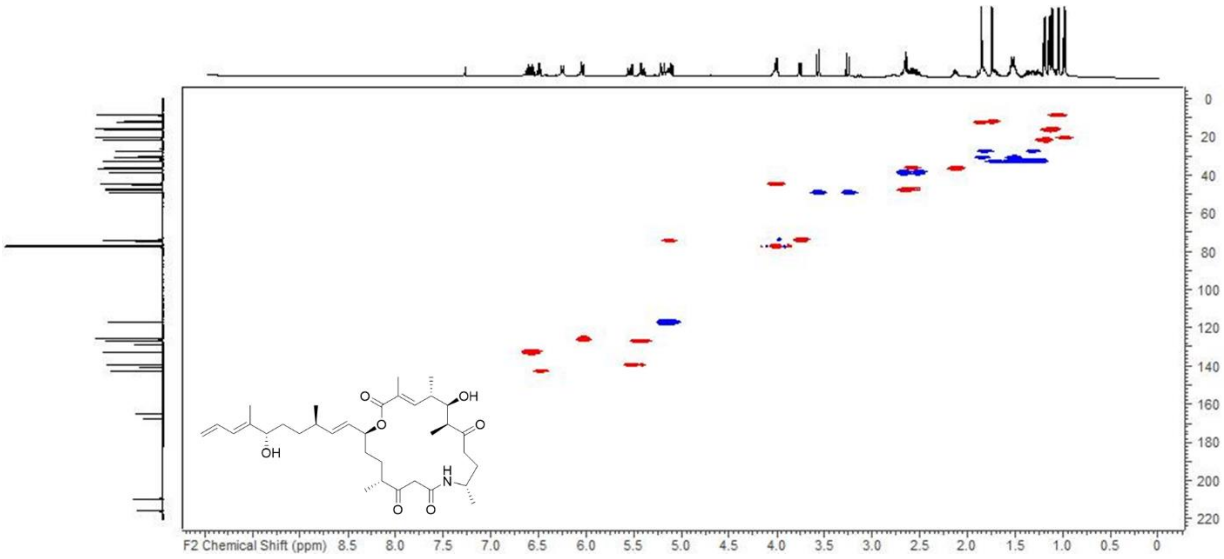

Figure S 2.15: HSQC spectrum of angiolam A (1) in chloroform-*d* at 125/500 (F1/F2) MHz.

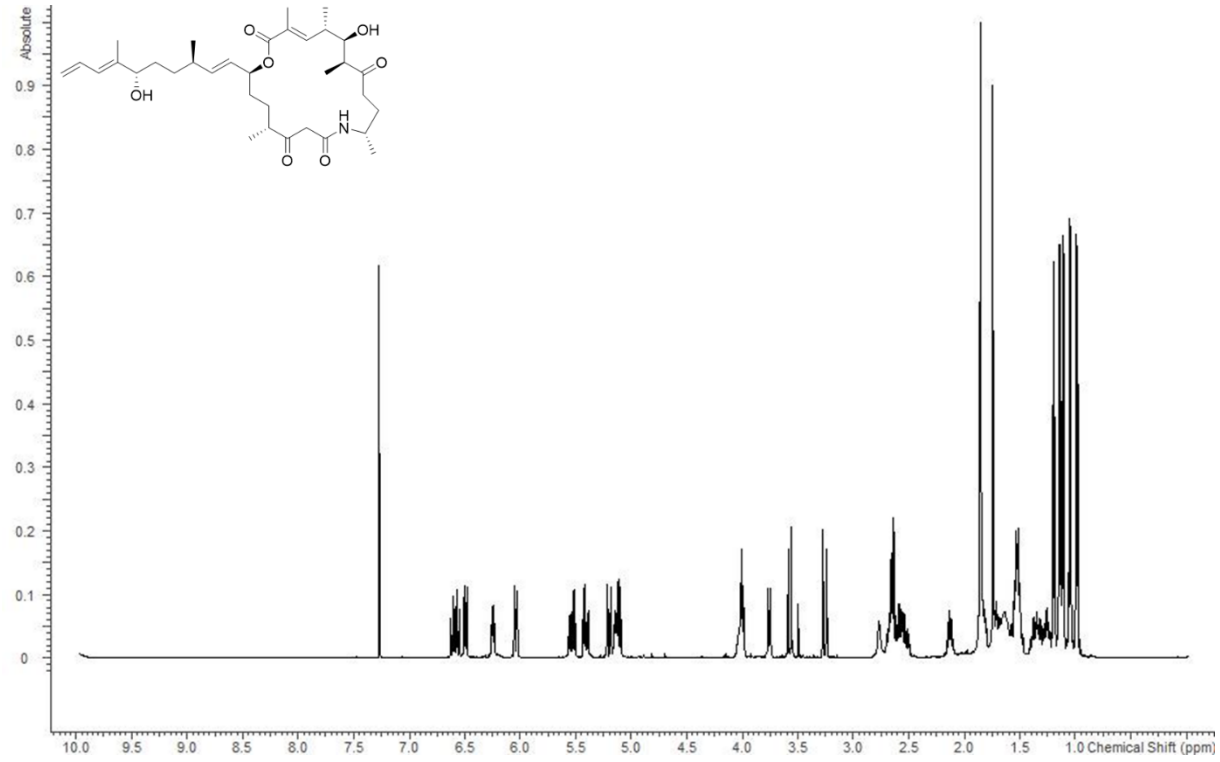

Figure S 2.16: ^{1}H spectrum of authentic angiolam A in chloroform-*d* at 500 MHz.

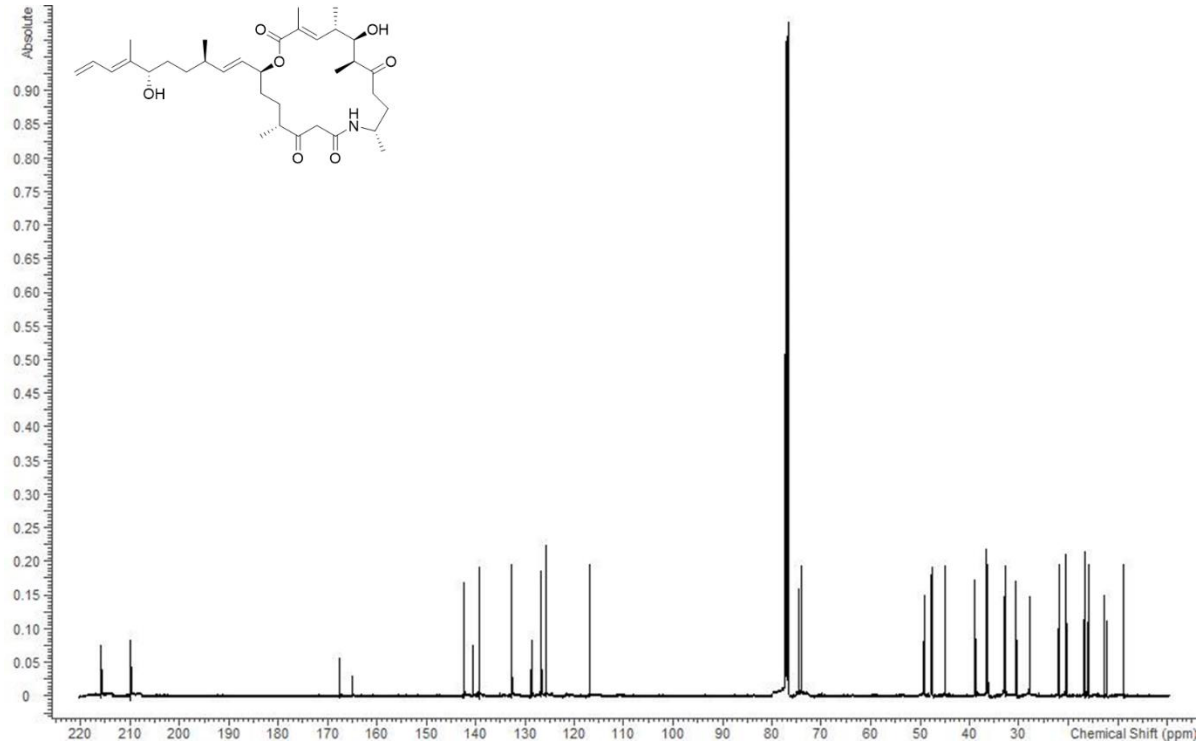

Figure S 2.17: ^{13}C spectrum of authentic angiolam A in chloroform-*d* at 125 MHz.

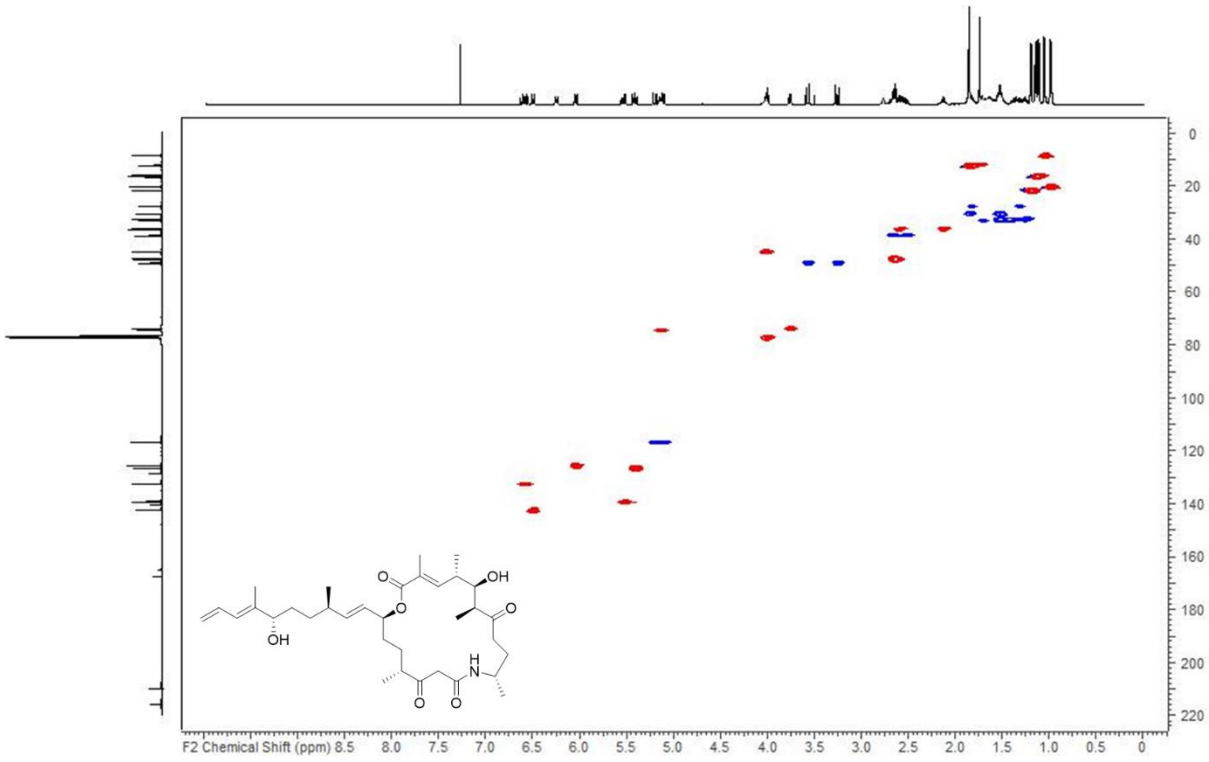

Figure S 2.18: HSQC spectrum of authentic angiolam A in chloroform-*d* at 125/500 (F1/F2) MHz.

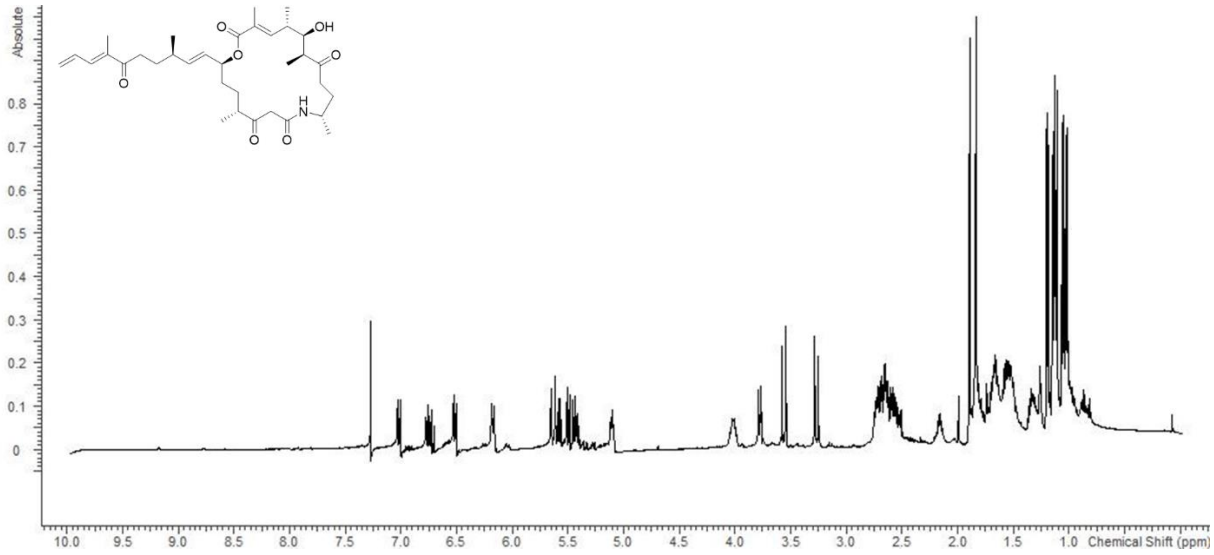

Figure S 2.19: ^{1}H spectrum of angiolam B (2) in chloroform-*d* at 500 MHz.

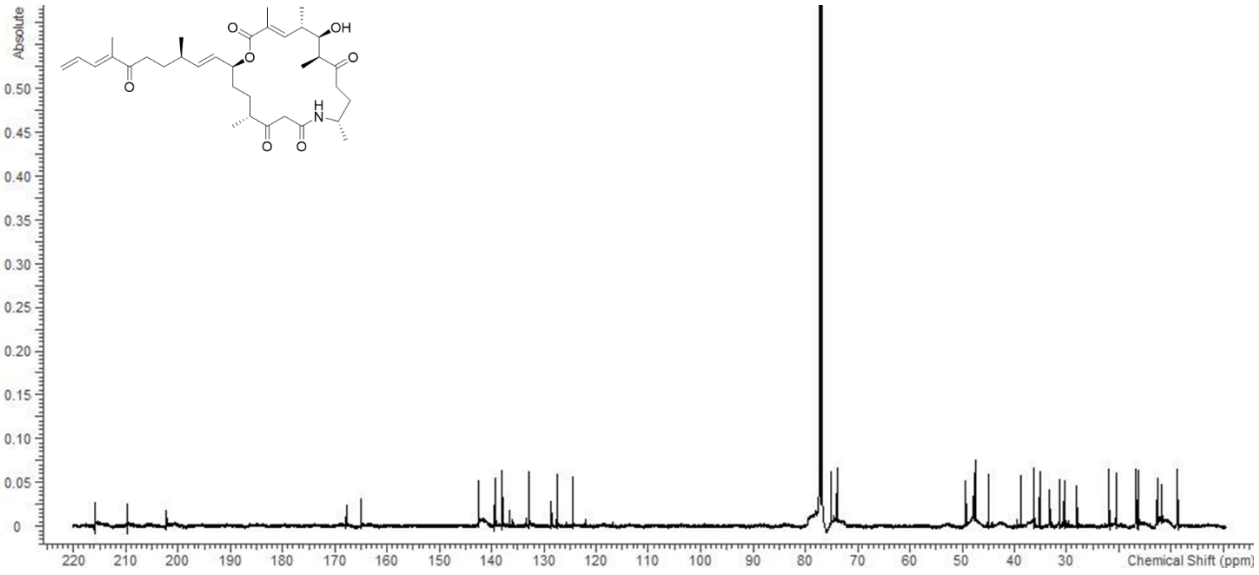

Figure S 2.20: ^{13}C spectrum of angiolam B (2) in chloroform-*d* at 125 MHz.

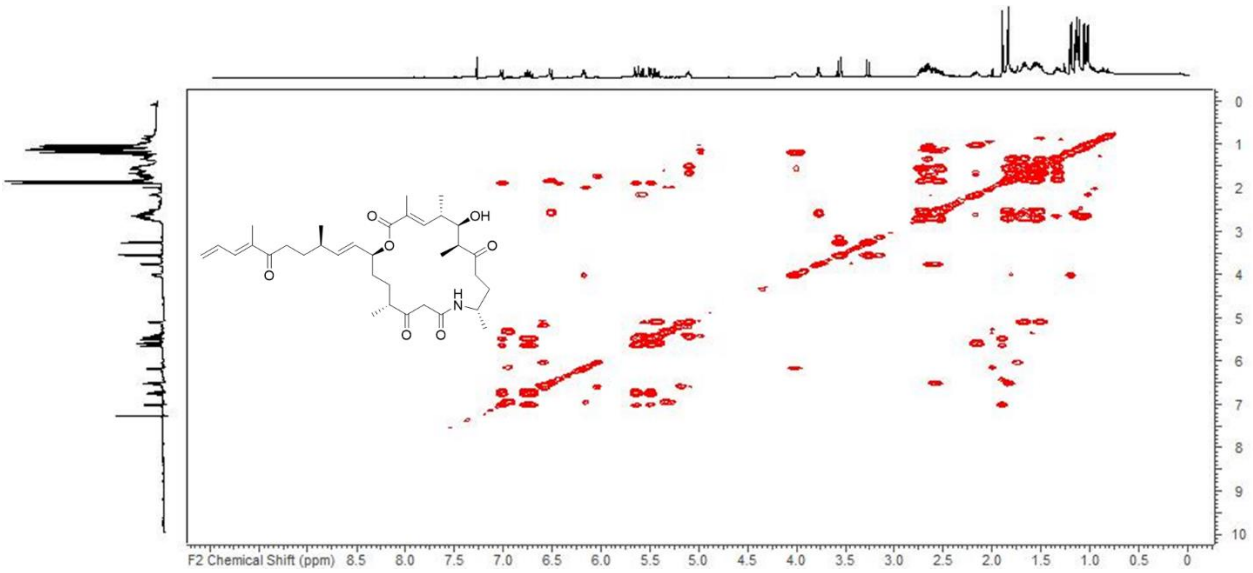

Figure S 2.21: COSY spectrum of angiolam B (2) in chloroform-*d* at 500 MHz.

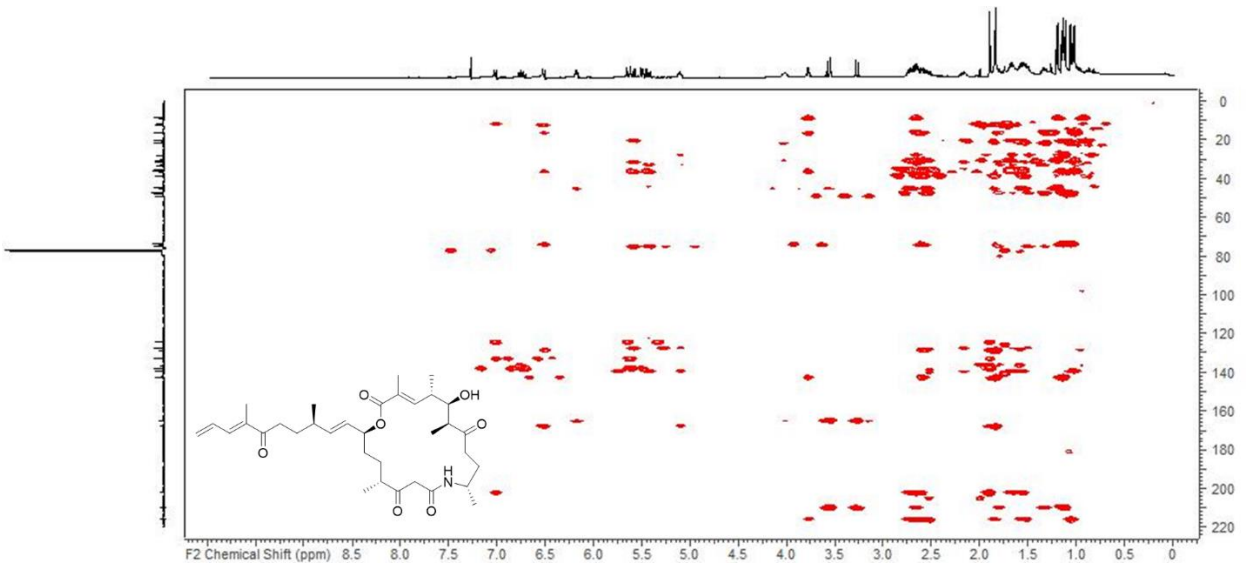

Figure S 2.22: HMBC spectrum of angiolam B (2) in chloroform-*d* at 125/500 (F1/F2) MHz.

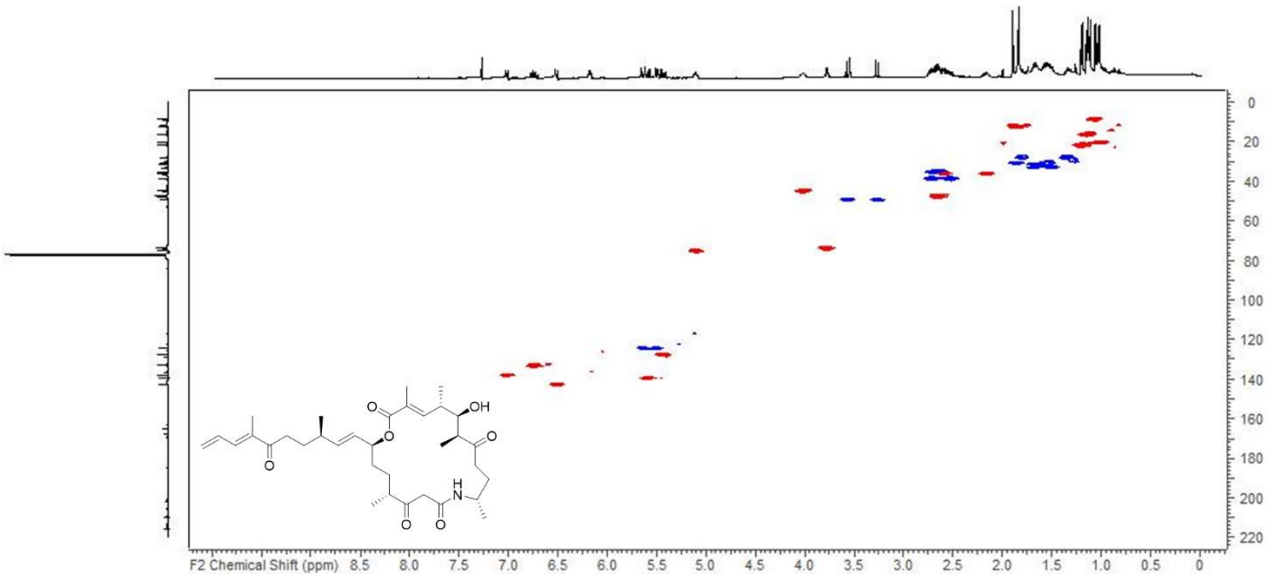

Figure S 2.23: HSQC spectrum of angiolam B (2) in chloroform-*d* at 125/500 (F1/F2) MHz.

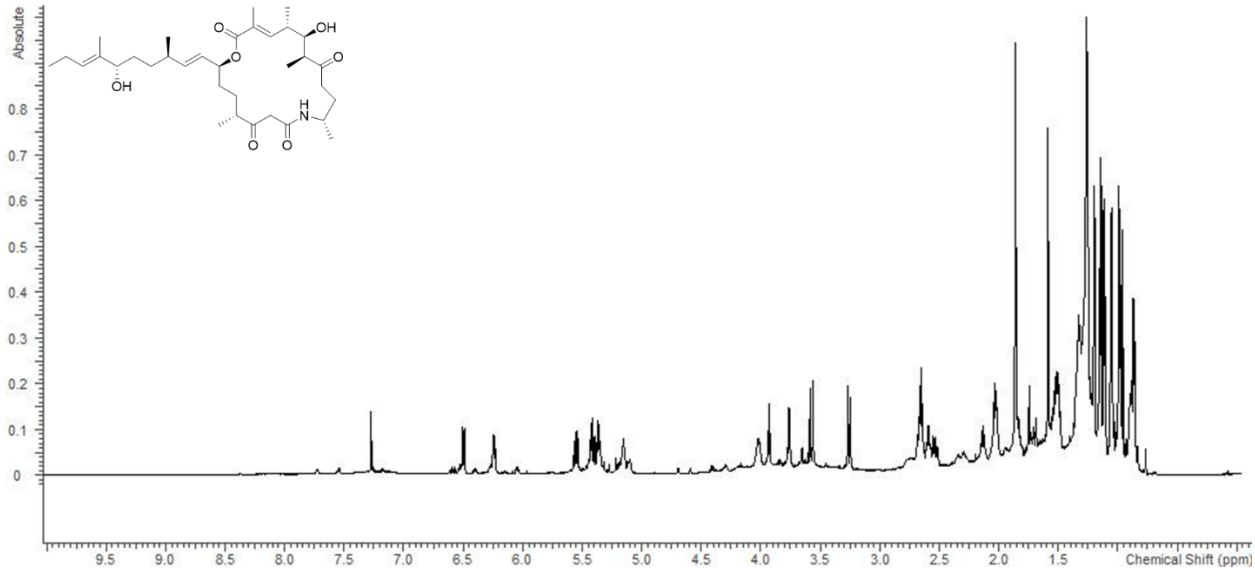

Figure S 2.24: ^{1}H spectrum of angiolam C (3) in chloroform-*d* at 500 MHz.

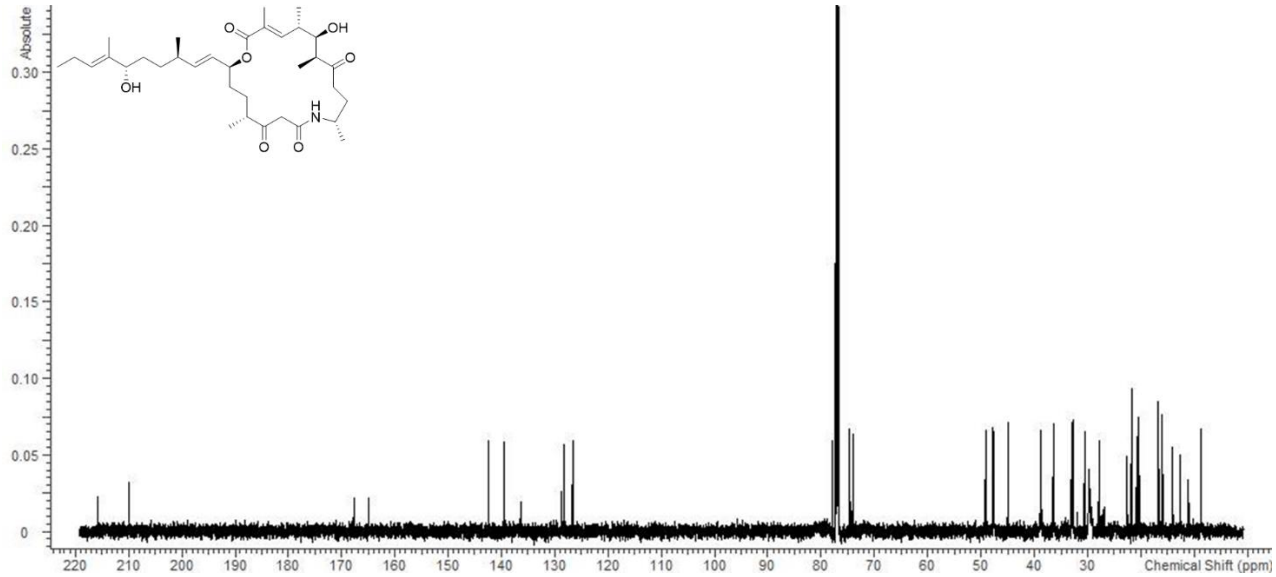

Figure S 2.25: ^{13}C spectrum of angiolam C (3) in chloroform-*d* at 125 MHz.

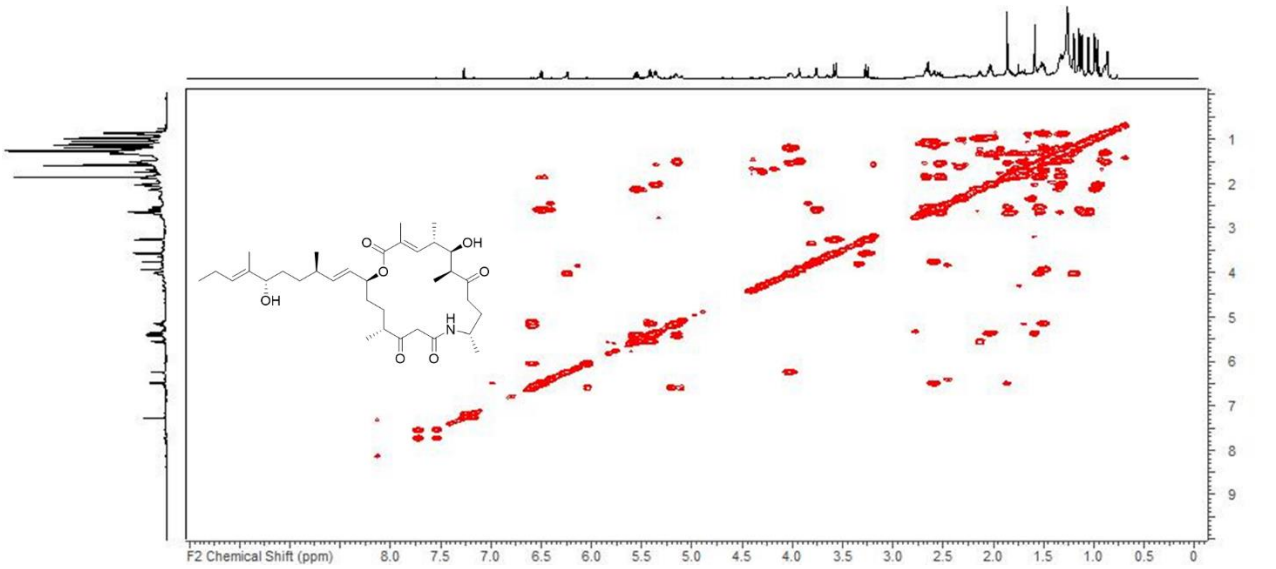

Figure S 2.26: COSY spectrum of angiolam C (3) in chloroform-*d* at 500 MHz.

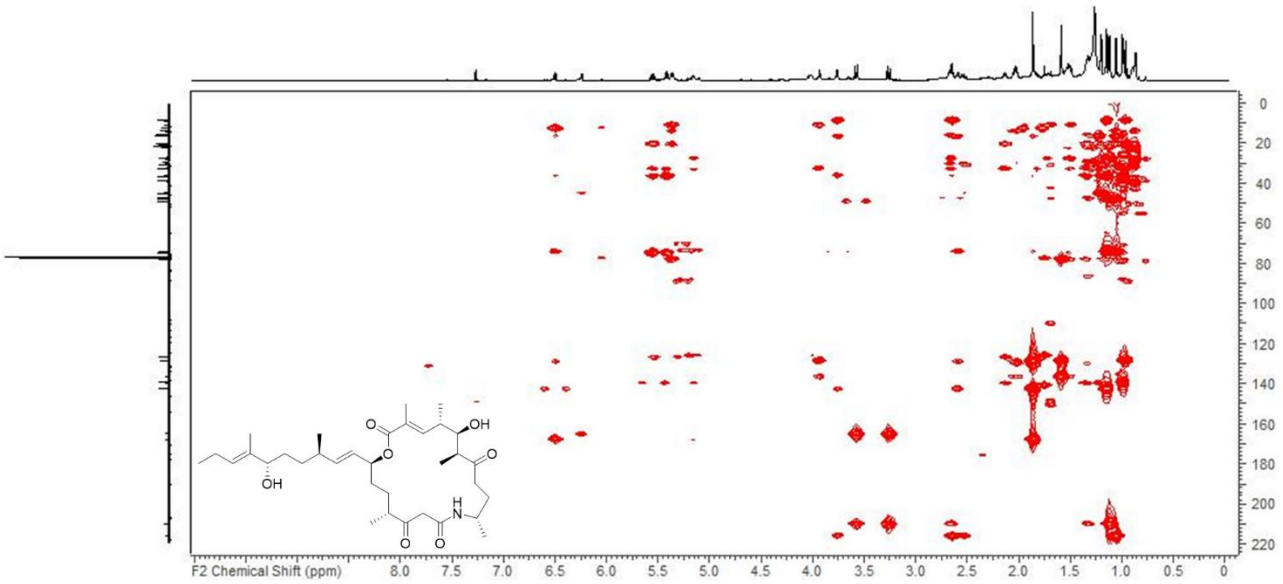

Figure S 2.27: HMBC spectrum of angiolam C (3) in chloroform-*d* at 125/500 (F1/F2) MHz.

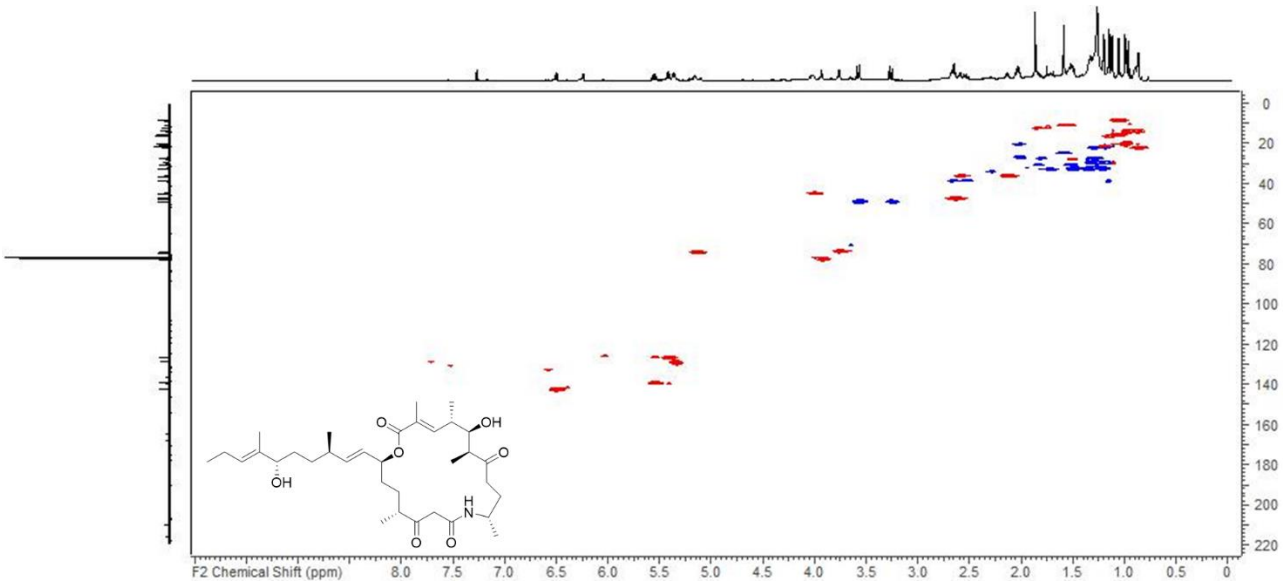

Figure S 2.28: HSQC spectrum of angiolam C (3) in chloroform-*d* at 125/500 (F1/F2) MHz.

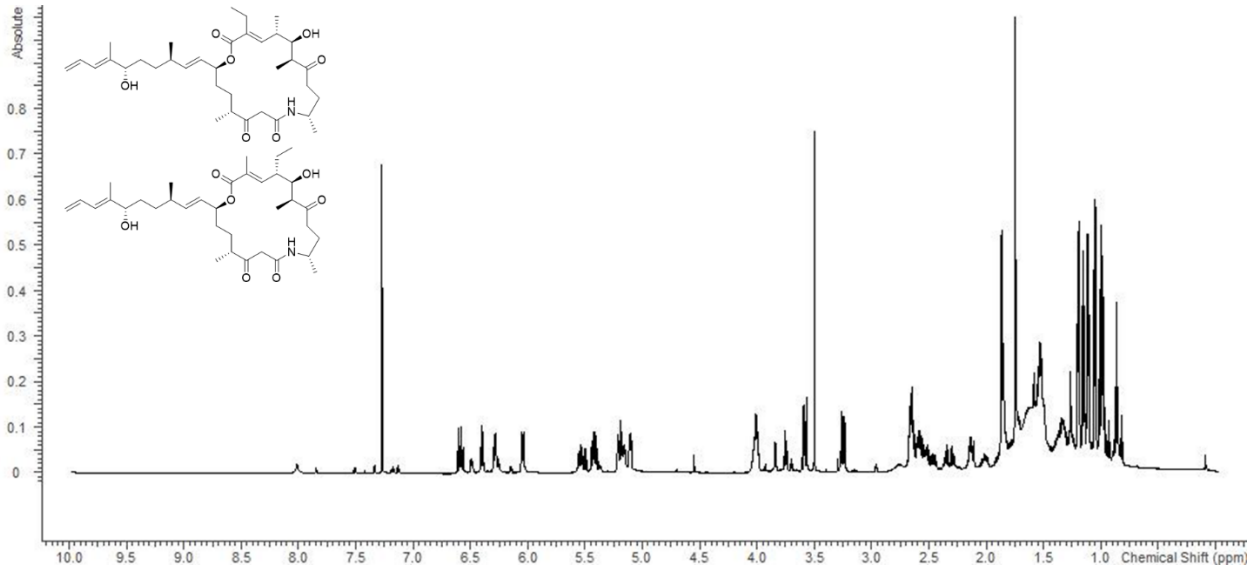

Figure S 2.29: ^{1}H spectrum of angiolam D_1 (4a) and D_2 (4b) in chloroform-*d* at 700 MHz.

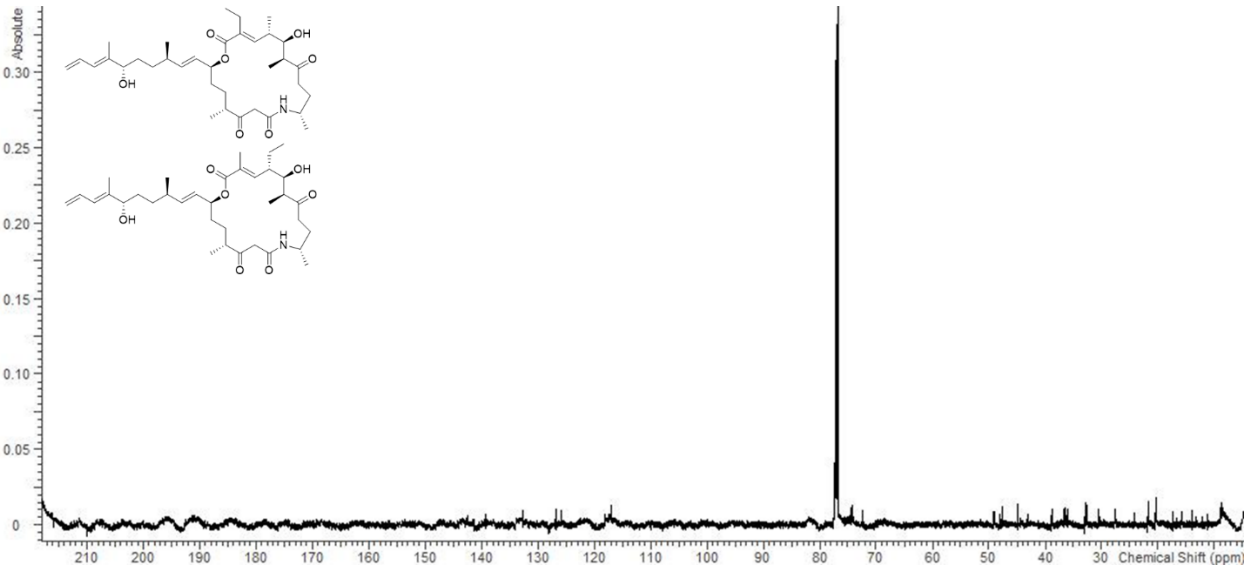

Figure S 2.30: ^{13}C spectrum of angiolam D_1 (4a) and D_2 (4b) in chloroform-*d* at 175 MHz.

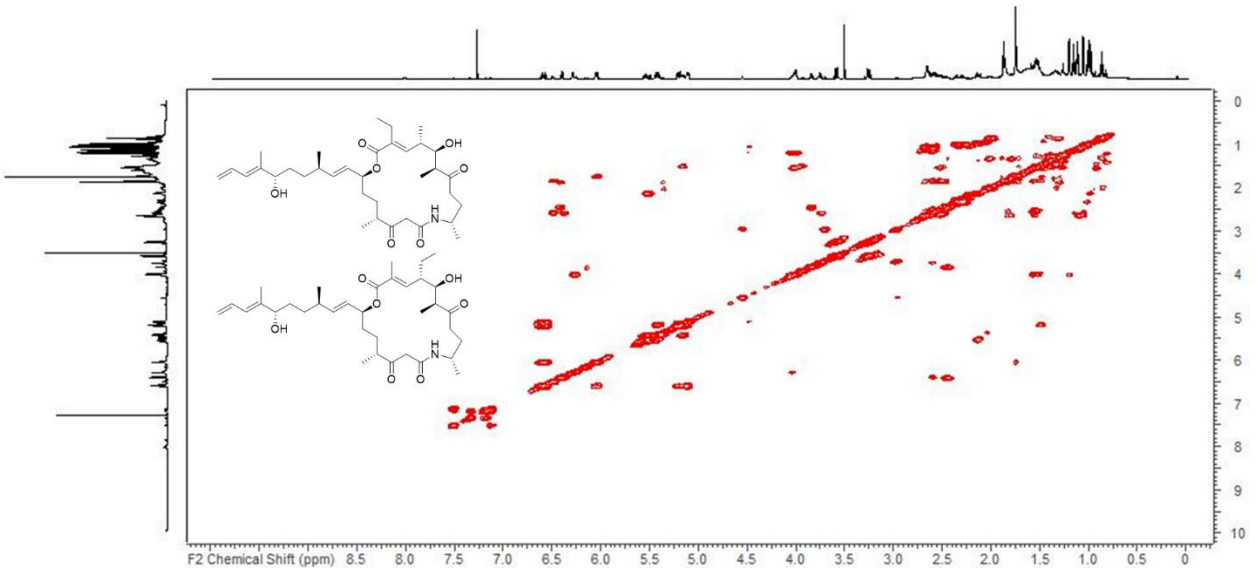

Figure S 2.31: COSY spectrum of angiolam D_1 (4a) and D_2 (4b) in chloroform-*d* at 700 MHz.

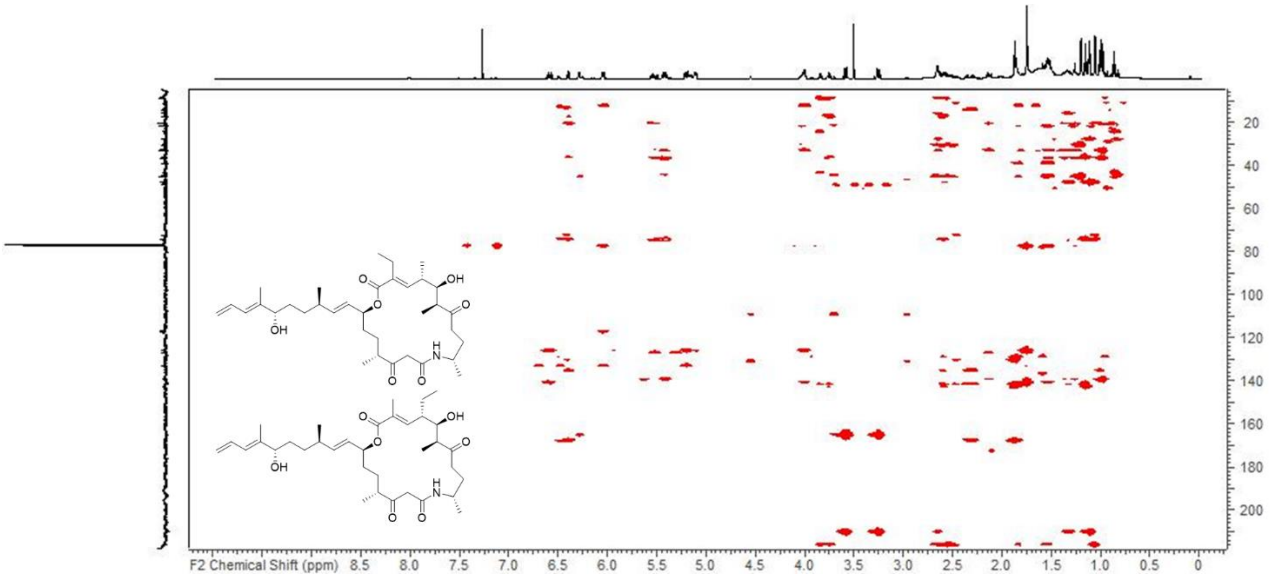

Figure S 2.32: HMBC spectrum of angiolam D_1 (4a) and D_2 (4b) in chloroform-*d* at 175/700 (F1/F2) MHz.

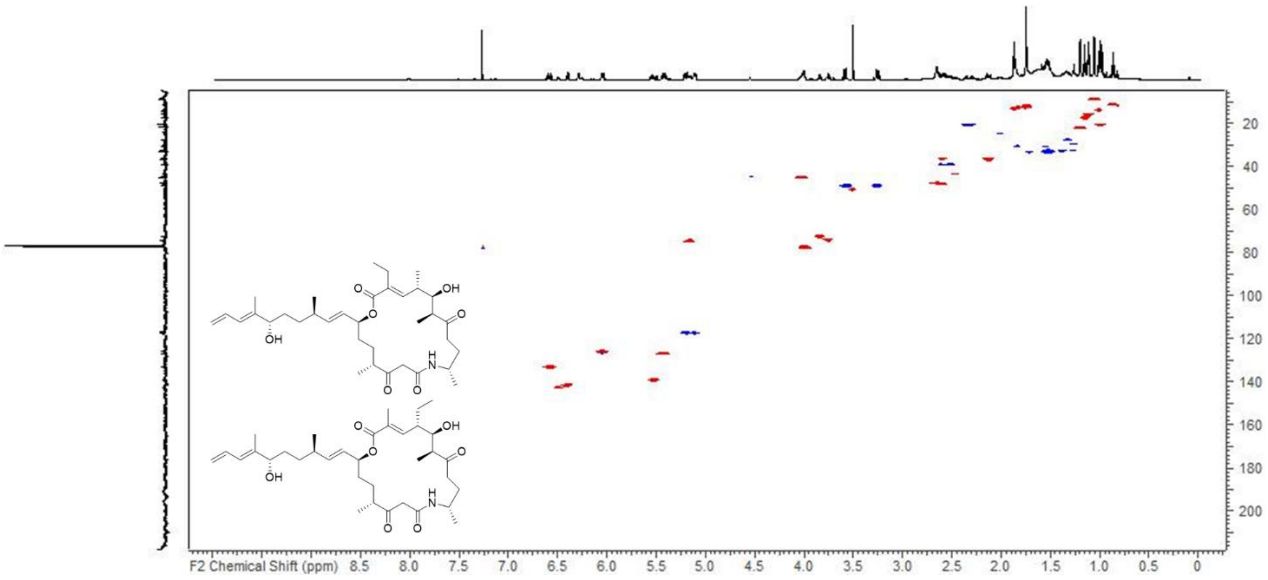

Figure S 2.33: HSQC spectrum of angiolam D_1 (4a) and D_2 (4b) in chloroform-*d* at 175/700 (F1/F2) MHz.

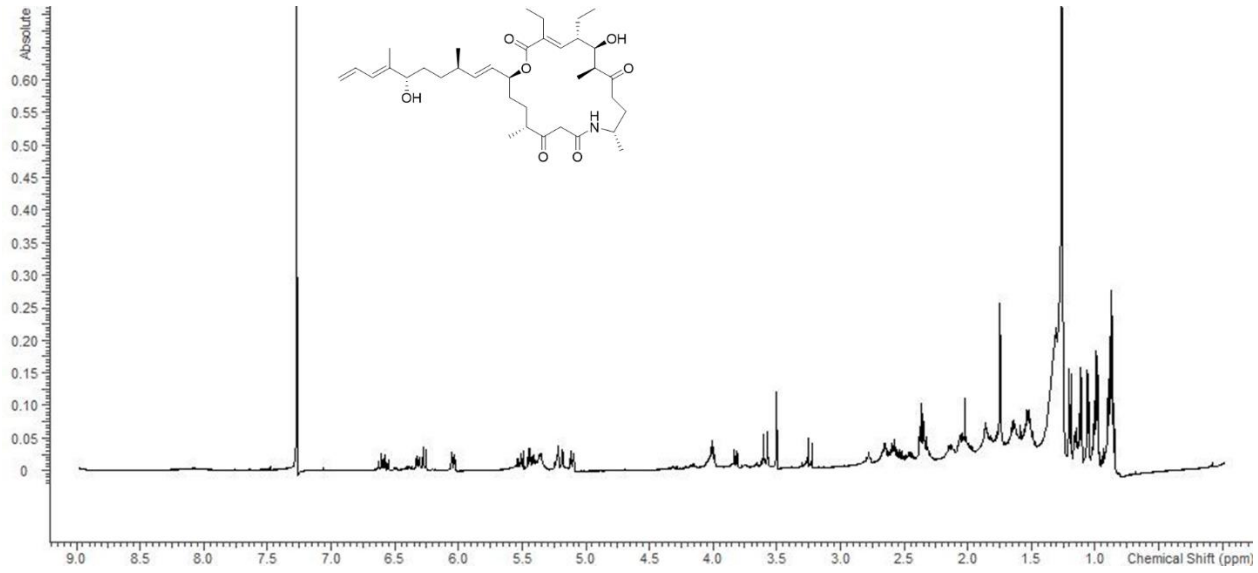

Figure S 2.34: ^{1}H spectrum of angiolam F (5) in chloroform-*d* at 500 MHz.

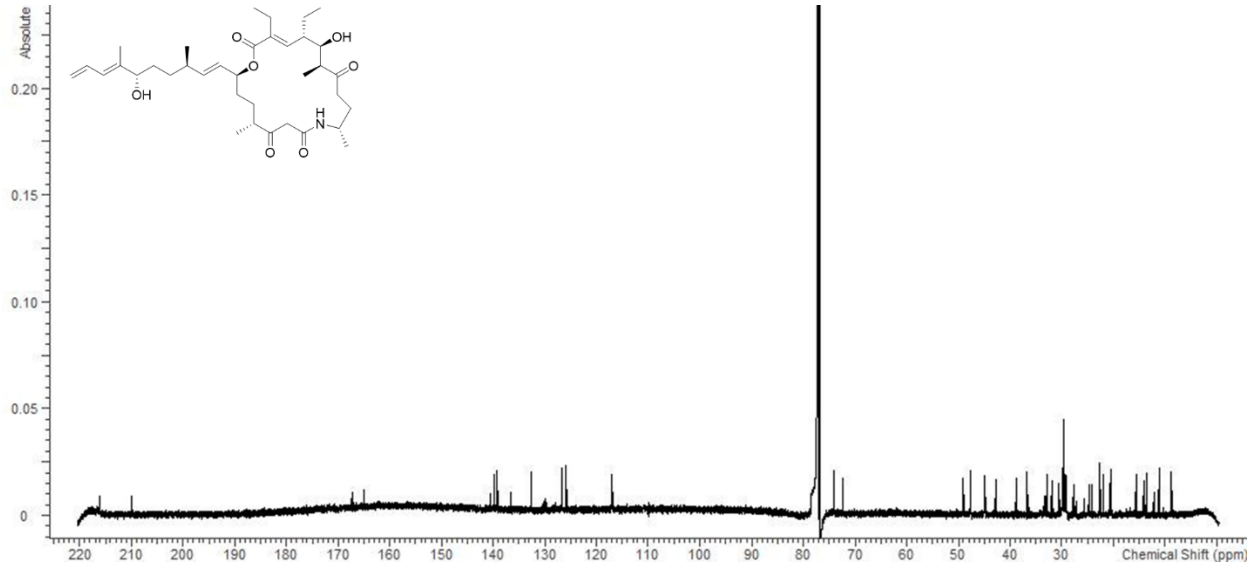

Figure S 2.35: ^{13}C spectrum of angiolam F (5) in chloroform-*d* at 125 MHz.

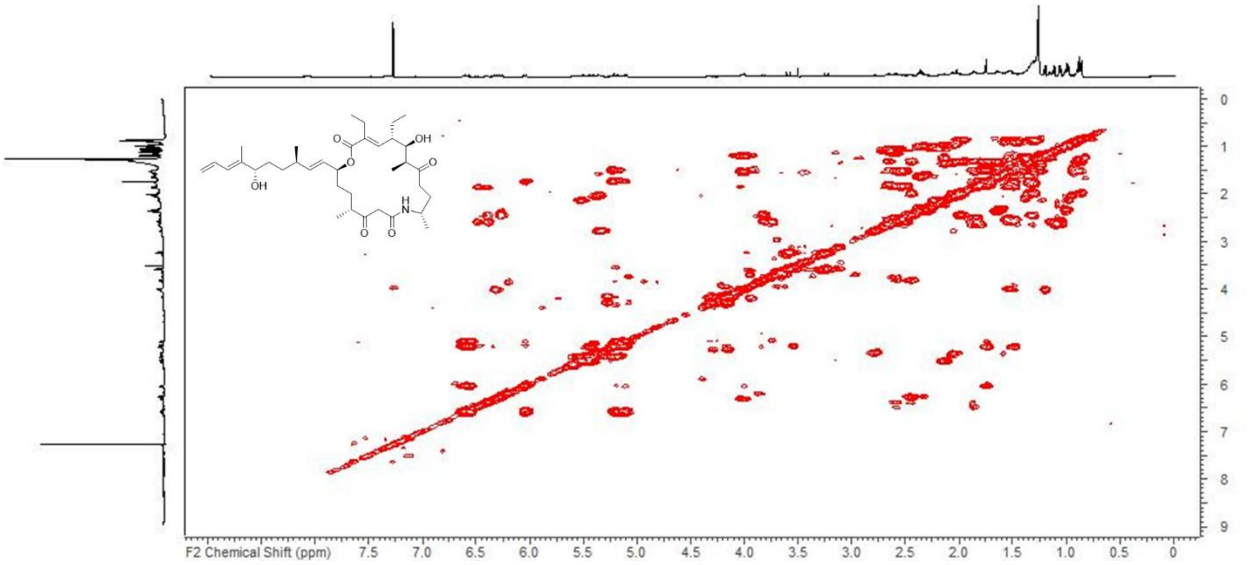

Figure S 2.36: COSY spectrum of angiolam F (5) in chloroform-*d* at 500 MHz.

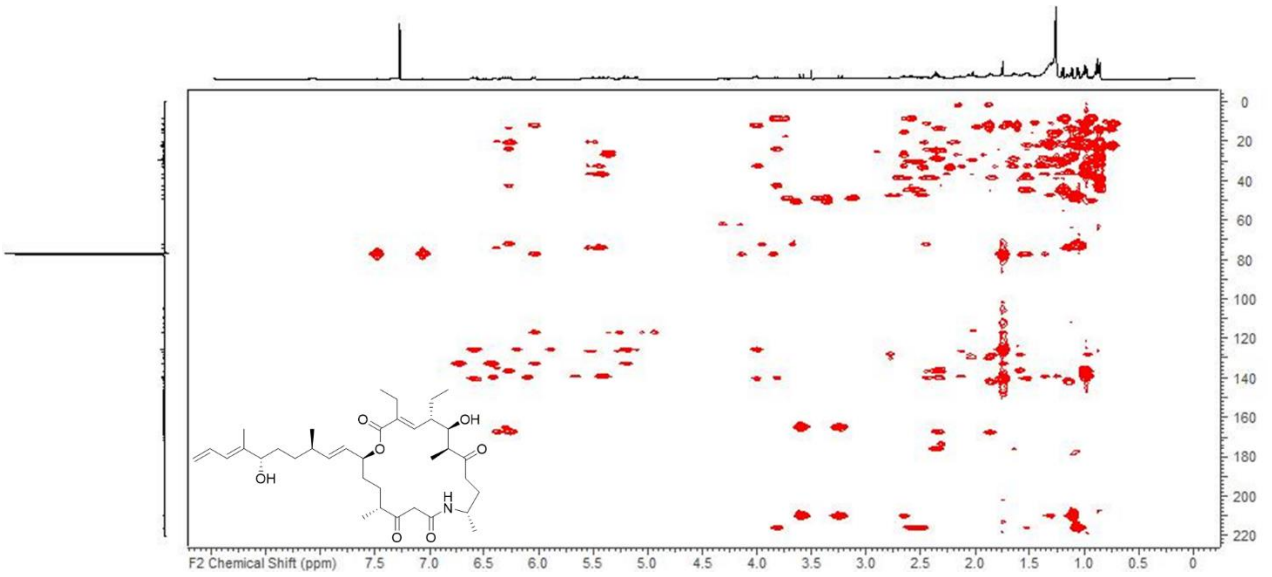

Figure S 2.37: HMBC spectrum of angiolam F (5) in chloroform-*d* at 125/500 (F1/F2) MHz.

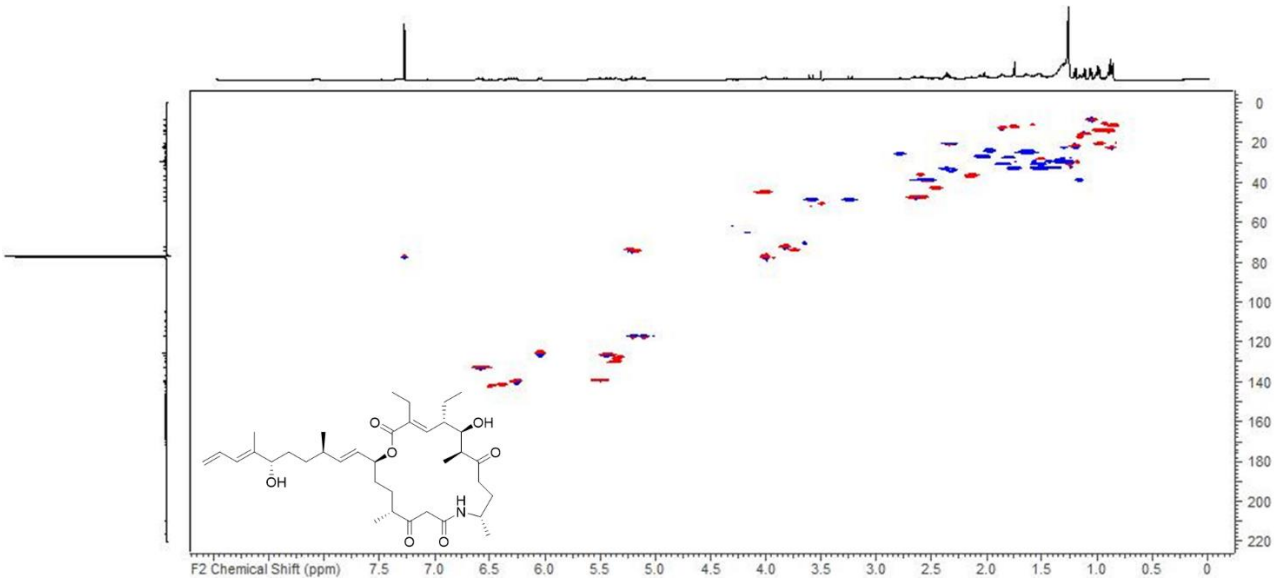

Figure S 2.38: HSQC spectrum of angiolam F (5) in chloroform-*d* at 125/500 (F1/F2) MHz.

References

1. Sandmann, A., Sasse, F. & Müller, R. Identification and analysis of the core biosynthetic machinery of tubulysin, a potent cytotoxin with potential anticancer activity. *Chem. Biol.* **11,** 1071–1079; 10.1016/j.chembiol.2004.05.014 (2004).
2. Green, M. R. & Sambrook, J. *Molecular cloning. A laboratory manual.* 4th ed. (Cold Spring Harbor Laboratory Press, Cold Spring Harbor, N.Y., 2012).
3. Panter, F., Krug, D., Baumann, S. & Müller, R. Self-resistance guided genome mining uncovers new topoisomerase inhibitors from myxobacteria. *Chem. Sci.* **9,** 4898–4908; 10.1039/C8SC01325J (2018).
4. Hoffmann, T., Krug, D., Hüttel, S. & Müller, R. Improving natural products identification through targeted LC-MS/MS in an untargeted secondary metabolomics workflow. *Anal. Chem.* **86,** 10780–10788; 10.1021/ac502805w (2014).
5. Wang, M. *et al.* Sharing and community curation of mass spectrometry data with Global Natural Products Social Molecular Networking. *Nat. Biotechnol.* **34,** 828–837; 10.1038/nbt.3597 (2016).
6. Mahmoud, A. B., Mäser, P., Kaiser, M., Hamburger, M. & Khalid, S. Mining Sudanese Medicinal Plants for Antiprotozoal Agents. *Front. Pharmacol.* **11,** 865; 10.3389/fphar.2020.00865 (2020).
7. Mahmoud, A. B. *et al.* Lignans, Amides, and Saponins from Haplophyllum tuberculatum and Their Antiprotozoal Activity. *Molecules (Basel, Switzerland)* **25**; 10.3390/molecules25122825 (2020).
8. Werner Kohl, Barbara Witte, Brigitte Kunze, Victor Wray, Dietmar Schomburg, Hans Reichenbach und Gerhard Höfle. Angiolam A - ein neues Antibiotikum aus Angiococcus. *Liebigs Ann. Chem.,* 2088–2097 (1985).
9. Gieseler, M. T. & Kalesse, M. Synthesis of Angiolam A. *Org. Lett.* **16,** 548–551; 10.1021/ol403423r (2014).
10. Blin, K. *et al.* antiSMASH 6.0: improving cluster detection and comparison capabilities. *Nucleic Acids Res.* **49,** W29-W35; 10.1093/nar/gkab335 (2021).
11. Keatinge-Clay, A. T. The structures of type I polyketide synthases. *Nat. Prod. Rep.* **29,** 1050–1073; 10.1039/c2np20019h (2012).
12. Oliynyk, M. *et al.* Analysis of the biosynthetic gene cluster for the polyether antibiotic monensin in Streptomyces cinnamonensis and evidence for the role of

monB and monC genes in oxidative cyclization. *Mol. Microbiol.* **49,** 1179–1190; 10.1046/j.1365-2958.2003.03571.x (2003).

13. Keatinge-Clay, A. T. A Tylosin Ketoreductase Reveals How Chirality is Determined in Polyketides. *Chem. Biol.* **14,** 898–908; 10.1016/j.chembiol.2007.07.009 (2007).
14. Kitsche, A. & Kalesse, M. Configurational assignment of secondary hydroxyl groups and methyl branches in polyketide natural products through bioinformatic analysis of the ketoreductase domain. *ChemBioChem* **14,** 851–861; 10.1002/cbic.201300063 (2013).
15. Kwan, D. H. *et al.* Prediction and manipulation of the stereochemistry of enoylreduction in modular polyketide synthases. *Chem. Biol.* **15,** 1231–1240; 10.1016/j.chembiol.2008.09.012 (2008).

3 Chapter: Sorangicin P

Bioactivity-guided Discovery of Sorangicin P-796 from the rare Myxobacterium *Pendulispora* spp. MSr12523

Sebastian Walesch, Chantal D Bader, Daniel Krug and Rolf Müller

Manuscript in preparation

Contributions to the presented work

Author's effort

The author contributed to the concept of this study, planned and executed experiments, evaluated and interpreted resulting data. The author performed comparative cultivations of MSr12523 in different media, did statistical analysis of the bioactive extract and identified the new sorangicin P derivatives as antibiotic ingredients by bioactivity-guided fractionation. Furthermore, he purified the bioactive sorangicin P derivatives and conducted structure elucidation. The author also did the *in silico* description of the biosynthetic gene cluster as well as the resulting biosynthetic model. Moreover, the author contributed to the conception and writing of this manuscript.

Contributions by others

Chantal Bader contributed to the project by conducting structure elucidation, scientific discussions and by editing and proofreading the structure elucidation section. Daniel Krug and Rolf Müller contributed by supervision of the project and conceiving, editing and proofreading of this manuscript. The authors thank Jake Haeckl for scientific discussions and proof-reading of the manuscript.

3.1 Abstract

Microbial natural products have shown their value as drug leads in the past, particularly as anti-infectives. With the rise of antibiotic resistant bacteria, understudied bacterial taxa gain increasing attention as promising producers of novel antibiotics. In the course of our ongoing efforts to find new biologically active natural products, media experiments with the rare and biosynthetically gifted myxobacterium *Pendulispora* spp. MSr12523 yielded promising antibacterial activity. Bioactivity-guided compound purification led to the discovery of a new subclass of the myxobacterial sorangicin antibiotics. The structure of novel sorangicin P-796 was elucidated based on comprehensive NMR spectroscopy. Based on the putative *sra*BGC in the genome of MSr12523 a biosynthetic model was devised to explain the biosynthesis of sorangicin P-796. Furthermore, sorangicin P-796 displayed moderate antibiotic activities against several Gram-negative and improved antibiotic activities against several Gram-positive pathogens.

3.2 Introduction

Over the past century, the discovery, development and market-deployment of antibiotics have significantly improved global health by giving humanity the ability to effectively treat bacterial infections[1,2]. However, emerging antimicrobial resistance (AMR) and stagnating development of novel antibiotic scaffolds threaten this progress and have led to approximately 4.95 million deaths world-wide in 2019 that were associated with AMR[2,3]. Due to limited treatment options against antibiotic-resistant Gram-negative *Acinetobacter baumannii*, *Pseudomonas aeruginosa* and *Enterobacteriaceae*, novel antibiotics targeting these pathogens are sought after in particular[4,5].

About two thirds of approved antibiotics are microbial natural products or their congeners, displaying the prominent capability of microorganisms to produce antibiotic scaffolds[2,6]. The majority of the approved antibiotic scaffolds originate from the well-studied phylum of Actinomycetes, but over the past decade, further phyla have shown their potential to produce bioactive natural products[7,8]. One promising example are the myxobacteria, Gram-negative rod-shaped delta-proteobacteria, having large genomes with many biosynthetic gene clusters (BGCs)[9–11]. The large biosynthetic potential of myxobacteria is evidenced by the discovery of several hundred natural products with diverse chemical scaffolds and biological activities[10,12,13]. Moreover, myxobacteria are a prolific source of new antibiotic scaffolds, as displayed by the discovery of antibiotics like the corallopyronins[14], sorangicins[15], cystobactamids[16] and corramycins[17] over the past 40 years. According to a recent study with 2300 myxobacteria, investigation of new or

understudied taxa increases the possibility to discover natural products with novel chemical scaffolds[18]. This finding is supported by the recent discoveries of the toxic sandarazols[19] and the antiviral sandacrabins[20] from an understudied myxobacterial family.

However, similar to other established natural product producers[21–23], the majority of BGCs in myxobacteria seems to be cryptic in routine laboratory cultivation settings, as their potential products cannot be detected using standard protocols[9–11]. In order to access the untapped biosynthetic potential of microorganisms, a plethora of molecular biological and cultivation-based approaches were developed and successfully applied over the past decades[23]. The well-established 'One Strain - Many Compounds' (OSMAC) approach describes the effect of variations of cultivation conditions like media composition, pH value, cultivation vessel, aeration, temperature, or illumination on the secondary metabolomes of microorganisms[24]. By way of example, changes in media composition led to changes in the metabolomes of different fungi, *Streptomyces* strains and myxobacteria[25–27].

Herein, we describe the effect of different cultivation media on the antibacterial activities of resulting crude extracts of the phylogenetically distinct myxobacterium *Pendulispora* spp. MSr12523. Bioactivity-guided fractionation of a crude extract with antibacterial activity against several Gram-negative pathogens led to the observation of a new subclass of the sorangicin scaffold. *De novo* and comparative structure elucidation of the purified sorangicin P-796 revealed some characteristic differences compared to previously described sorangicin derivatives. Furthermore, the putative sorangicin P BGC in the genome of MSr12523 is compared with the *sor*BGC in *Sorangium cellulosum* So ce12 and a detailed biosynthetic model for the formation of sorangicin P-796 is created. Finally, this study covers the antibiotic activities of sorangicin P-796 against a panel of Gram-negative and Gram-positive bacteria.

3.3 Results and discussion

3.3.1 Producer, media experiments, fractionation

The rare myxobacterium *Pendulispora* spp. MSr12523 was isolated during our continuous efforts to find novel or understudied taxa of myxobacteria. On VY/2 agar plates, its colonies display an unusual morphology that is reminiscent of many actionbacteria (Figure 3.1 A). MSr12523 is part of the *Sorangiineae* suborder and forms a new genus or even family with three other recently discovered isolates (Figure S 3.1)[28].

In addition to its unusual morphology and its phylogenetically distinct position, MSr12523 has a large genome of ~ 13.4 Mbp that harbours 60 putative BGCs according to an analysis with antiSMASH[29], indicating an exceptional biosynthetic potential. More than two thirds of these predicted BGCs are polyketide synthases (PKSs), nonribosomal peptide synthetases (NRPSs) or hybrids thereof, but also several putative RiPP (ribosomally synthesised and post-translationally modiefied peptide) BGCs can be observed (Figure 3.1 B). Furthermore, more than 40% of the observed BGCs do not share any similarity with reported biosynthetic pathways and in only six cases the similarity is at least 50%, based on the observation of similar genes (Table S 3.2). These cases include the myxobacterial BGCs of gulmirecin[30], thuggacin A[31] and ajudazol A[32] as well as the BGCs of geldanamycin[33], alpiniamide[34] and bisucaberin B[35] from different taxa. The BGC architecture and homology aligns well for those similar to thuggacin A, gulmirecin, and alpiniamide, while in the cases of ajudazol A, geldanamycin, and bisucaberin B, the arrangement and number of homologous genes is more different (Figure S 3.2).

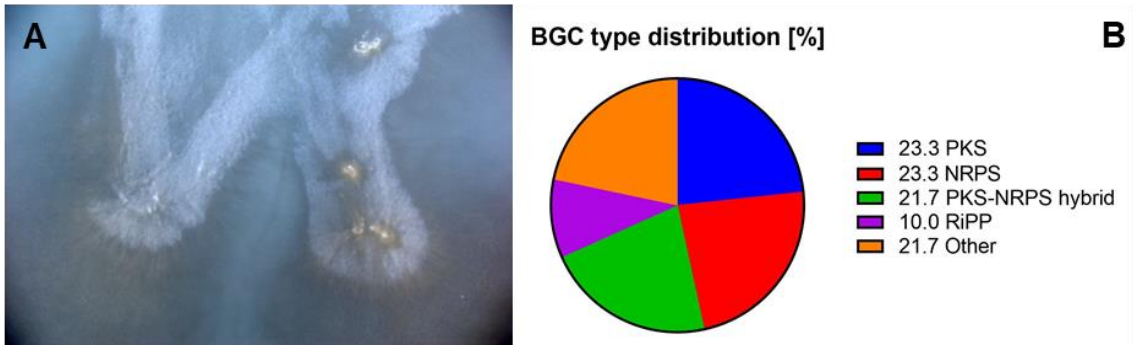

Figure 3.1: Morphology of MSr12523 on VY/2 agar (A) and predicted BGC types in the genome of MSr12523 (B).

To assess the possibility to genetically manipulate MSr12523, its susceptibility against a total of 15 antibiotics was evaluated. However, the strain displayed resistance to almost all antibiotics and only chloramphenicol was able to inhibit the growth of MSr12523 on VY/2 agar at the high concentration of 100 µg/mL (Table S 3.3). As the extensive antibiotic resistance of MSr12523 complicates potential genetic manipulations, heterologous expression of putatively interesting BGCs and untargeted cultivation-based approaches seemed to be more fruitful to access the biosynthetic potential of MSr12523.

Based on the promising biosynthetic potential, MSr12523 was cultivated in six different fermentation media and the resulting crude extracts were tested for their antimicrobial activities. Of these six different conditions, crude extracts of MSr12523 in 2SWT and

RGSR media stood out, as they resulted in reproducible antibiotic activities. While cultivations in 2SWT medium resulted in low activities against *Escherichia coli* JW0451-2 (Δ*acrB*) and good activities against *Bacillus subtilis* DSM10, crude extracts of MSr12523 in RGSR displayed good bioactivities against these two strains as well as wild-type *E. coli* BW25113 (Table S 3.4). Furthermore, these crude extracts of MSr12523 displayed good antibiotic activity against *Staphylococcus aureus* Newman, *Mycobacterium smegmatis* mc^2155 and *Acinetobacter baumannii* DSM30008 and low antibiotic activity against *Citrobacter freundii* DSM30039 and *Pseudomonas aeruginosa* PA14.

Using bioactivity-guided fractionation, the antibiotic activity against the Gram-negative bacteria was linked to three compounds that were later identified as novel sorangicins P-796, P-814A and P-814B. Evaluation of crude extracts of MSr12523 in different media verified that these compounds are exclusively produced in cultivations in RGSR and further, minor, components observed in active fractions can be also found in cultivations of MSr12523 in other media (Figure S 3.3).

The novelty of all components observed in fractions with activity against Gram-negative bacteria was verified by dereplication against the in-house database "Myxobase"[18], the "Natural Products Atlas 2.0"[8] and the "Dictionary of Natural Products"[36]. Furthermore, dereplication of all LC-MS features (exact *m/z* and retention time) against the "Myxobase" by MetaboScape 2022b only yielded the siderophore nocardamine[37] as reported natural product. A statistical evaluation of metabolites produced by MSr12523 in RGSR medium with subsequent SPL-based MS/MS fragmentation[38] and GNPS-based molecular networking[39] displayed similar fragmentation pattern of the novel sorangicin P derivatives but did not show a fragment-based clustering with published natural products. Subsequent attempts to cluster these compounds with the known compound sorangicin A also yielded no confirmation, as there was no reference spectrum deposited in the public repositories and in-house data generated after purification of these new derivatives only provides a loose association with the known compounds, if any.

Upscaling experiments of MSr12523 in RGSR medium displayed a strongly reduced production of the novel sorangicin P derivatives when cultivated in 5 L shaking flasks but a good and stable production in bioreactors.

3.3.2 **Purification and structure elucidation**

Based on the stable and good production of the sorangicin P derivatives, MSr12523 was fermented in RGSR medium in bioreactors for compound production. However, sorangicins P-814A and P-814B isomerised during semi-preparative HPLC purification (Figure S 3.4), strongly impeding structure elucidation. As sorangicin P-796 could be purified without these complications, it was prioritised for structure elucidation and further evaluation.

High-resolution electrospray-ionisation mass spectrometry data of sorangicin P-796 showed an [M+H] signal at m/z 797.4255, corresponding to an elemental formula of $C_{48}H_{60}O_{10}$ (calc. 797.4260; Δ 0.56 ppm), which contains 19 double-bond equivalents (DBEs).

As displayed in Figure 3.2, sorangicin P-796 (**1**) differs from the reported sorangicin A[40,41] (**2**) in several parts of the molecule. The first difference is adjacent to the free carboxylic acid
($\delta_{C\text{-}1}$ 170.4) which is bound to an olefin ($\delta_{C\text{-}2}$ 123.4, $\delta_{H\text{-}2}$ 5.71, $\delta_{C\text{-}3}$ 151.5, $\delta_{H\text{-}3}$ 6.83), as evidenced by HMBC correlations of the respective protons to C-1. Consecutive COSY and HMBC correlations as well as highly similar ^{1}H and ^{13}C shifts (Tables S8 and S9) demonstrated that the rest of the chain between the methylenes C-4 ($\delta_{C\text{-}4}$ 31.4, $\delta_{H\text{-}4}$ 2.06) and C-14 ($\delta_{C\text{-}14}$ 36.1, $\delta_{H\text{-}14a}$ 2.51, $\delta_{H\text{-}14b}$ 2.30) resembles the one in sorangicin A (**2**).

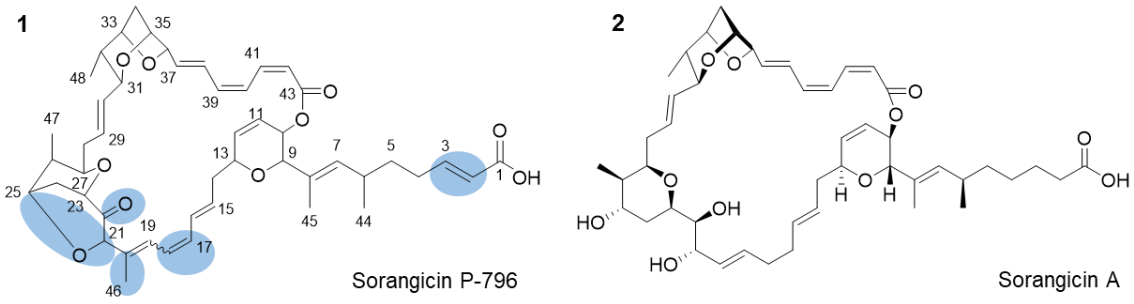

Figure 3.2: Structures of novel sorangicin P-796 (1) and sorangicin A (2). Differences of (**1**) compared to (**2**) are highlighted in blue.

Differing from **2**, the methylene C-14 is connected to the triene C-15 to C-20. Clear COSY correlations between the first four olefinic protons ($\delta_{H\text{-}15}$ 5.90, $\delta_{H\text{-}16}$ 6.16, $\delta_{H\text{-}17}$ 6.37, $\delta_{H\text{-}18}$ 6.30) demonstrated the constitution of the first two double bonds. Due to overlapping proton signals, the position of C-19 at 133.1 ppm had to be established by HMBC correlations from adjacent protons. Based on chemical shift and HMBC correlation

analysis, C-20 was found to be a quaternary carbon ($\delta_{C\text{-}20}$ 134.4) substituted with the methyl-group C-46 ($\delta_{C\text{-}46}$ 11.7, $\delta_{H\text{-}46}$ 1.51).

Furthermore, HMBC correlations from H-19 ($\delta_{H\text{-}19}$ 6.29) and H-46 ($\delta_{H\text{-}46}$ 1.51) to a deshielded hydroxylated methine ($\delta_{C\text{-}21}$ 81.4, $\delta_{H\text{-}21}$ 5.12) and a ketone ($\delta_{C\text{-}22}$ 210.3), unlike in **2**, indicate their close vicinity and connection to C-20. The position of C-21 was verified by ^{1}H,^{1}H TOCSY NMR experiments, which showed that the singlet H-21 ($\delta_{H\text{-}21}$ 5.12) is not part of any spin system. Furthermore, the connection of the carbonyl C-22 to a hydroxylated methine ($\delta_{C\text{-}23}$ 76.6, $\delta_{H\text{-}23}$ 4.20) is displayed by a HMBC correlation from H-23 to C-22. According to COSY and HMBC correlations as well as similar ^{1}H and ^{13}C shifts (Tables S 3.8 and S 3.9), **1** shows a high resemblance of the oxane, the propylene linkage, the dioxabicyclooctane moiety, and the heptatrienoic acid to **2** (C-23 – C-43). Finally, in accordance to **2**, the HMBC correlation from H-10 ($\delta_{H\text{-}10}$ 5.43) to C-43 ($\delta_{C\text{-}43}$ 168.1) provides the structure of the macrolactone.

However, the thus described molecule has a molecular formula of $C_{48}H_{62}O_{11}$, which corresponds to one less DBE and the addition of H_2O in comparison to the calculated molecular formula of **1**. Therefore, based on the determined molecular formula, and the characteristic chemical shift of C-21 that indicates participation in an ether or ester functionality, an intramolecular ether bridge was established between C-21 and C-25, even though the chemical shift of C-25 and H-25 resemble the free methine bearing a free hydroxy and it could not be confirmed by any additional HMBC correlations. However, the detection of a broad singlet at 12.2 ppm in DMSO-d_6 (Figure S 3.14) corresponding to the free acid function and the detection of HMBC correlations unambiguously assigning the other four intramolecular ether bridges only left the hydroxylated C-25 for building a fifth ether bridge.

The configuration of *Z* and *E* double bonds was determined by their vicinal coupling constants of < 12 Hz and 14-15 Hz, respectively. In previously published sorangicin derivatives, the ROESY data does not agree with the *J*-coupling data for the configuration of the olefin C-7 – C-8. However, crystallography data resolves this discrepancy, indicating the E configuration proposed from the ROESY data[41,42]. We therefore assigned the same configuration for **1**.

Furthermore, the configuration of double-bonds C-17 to C-18 and C-19 to C-20 could not be solved by coupling constant analysis, due to overlapping proton signals. The configuration of the double-bond C-17 to C-18 remains elusive, as no unambiguous ROESY correlations of H-17 to either H-18, or H-19 could be observed. Moreover, the attempted determination of coupling constants of H-17 or H-18 by selective TOCSY experiments did not produce clear results. On the other hand, a clear ROESY correlation

between H-19 ($\delta_{H\text{-}19}$ 6.28) and H-21 ($\delta_{H\text{-}21}$ 5.11) could be used to determine the configuration of the double-bond C-19 – C-20 as *E*.

Following the reasoning of the structure elucidation of sorangicin A, the triene C37-C42 should be connected *endo* to the dioxabicyclooctane system, because of apparent ROESY correlations between H-31 and H-37[41]. Comparing the δ_C and δ_H of sorangicin P-796 (**1**) to the ones of sorangicin A (**2**), most differences were ≤ 1.0 ppm and ≤ 0.2 ppm, respectively, indicating a similar stereochemistry (Tables S 3.8 and S 3.9, Figure S 3.5). The only greater differences were observed at the connection of the ring system with the triene and could be caused by changes in ring tension of the macro-lactone. Similar effects could be the reason for the surprisingly high differences of δ_C of C-10 and C-11 with 0.9 and 0.7 ppm, respectively. Most other differences in carbon shifts are logical consequences of the additional double-bonds at C-2 – C-3 and C-17 – C18, the different oxidation state of C-22 and the ring formation between C-21 and C-25. However, to unambiguously elucidate the absolute configuration of sorangicin P-796 (**1**), crystallography should be conducted, as done for sorangicin A (**2**)[41].

Taken together, sorangicin P-796 (**1**) and sorangicin A (**2**) belong to the same chemical scaffold. However, **1** differs from **2** by an olefin in the side chain and one additional olefin, methyl residue, oxo-group and six-membered ether ring in the macrolactone (Figure 3.2).

3.3.3 BGC and *in silico* biosynthesis

The putative sorangicin P biosynthetic gene cluster (*sra* BGC) in the genome of MSr12523 was identified based on antiSMASH[29] results and manual analysis in Geneious prime 2022.2.2 due to its similarity to the *sor* BGC in *Sorangium cellulosum* So ce12[43]. Genes up- and downstream of the biosynthetic machinery were compared to the genome sequences of phylogenetically related strains MSr11367 and MSr11368, which do not have the *sra* BGC, in order to determine cluster boundaries (Table S 3.10). Based on this analysis, the *sra* BGC consists of 18 genes and spans 114.5 kBp (Figure 3.3). Its biosynthetic machinery consists of six large PKS genes *sraG* – *sraJ* and *sraL* – *sraM*, *sraC* coding for the two trans-AT (acyl transferase) domains and *sraB* possibly encoding a trans-acting enoyl reductase (ER) domain. Similar to the *sor* BGC in So ce12, the *sra* BGC consists of the putative glycosyl-transferase SraK and the putative glucosidase SraQ, possibly involved in self-resistance. Furthermore, it contains *sraN* – *sraP*, which encode amidohydrolases and *sraF*, coding for a putative asparagine synthase. These four enzymes are homologs of SorK, SorQ, SorR and SorS, which are putatively involved in the chain release and macro-lactone formation during the biosynthesis of sorangicin A[43]. Finally, the *sra* BGC contains the putative

methyltransferase SraA, a putative acyl carrier protein (ACP) SraE and the putative protein kinase SraR (Figure 3.3 and Table S 3.11).

Similar to the *sor* BGC in So ce12, the biosynthetic machinery in the *sra* BGC in MSr12523 consists of two trans-acting AT domains, a putatively trans-acting ER domain and 23 elongation modules. However, the biosynthetic machinery in MSr12523 is encoded in six instead of eight genes. Here, SraI covers the modules of SorC and SorD, while SraL covers the modules of SorG and SorH. Moreover, modules 2 (dehydrogenase: DH), 5 (DH & ketoreductase: KR), 11 (KR & methyl transferase: MT), and 23 (2nd, but inactive DH) in the *sra* BGC contain additional domains and module 12 lacks a MT domain, compared to the *sor* BGC[43]. An analysis of the keto synthase (KS) domains in the *sra* and *sor* BGCs with the "TransATor" tool[44] furthermore showed different substrate predictions for the KS domains in modules 6 and 13 pointing towards possible structural differences incorporated in modules 5 and 12. A comprehensive analysis of all domains can be found in Table S 3.12.

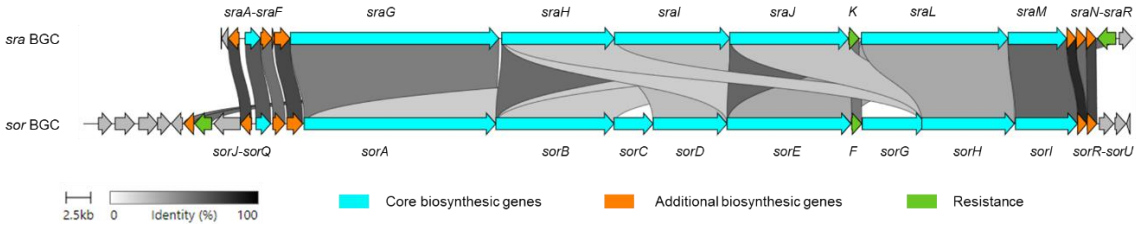

Figure 3.3: Comparison of the genes in the different sorangicin BGCs in *Pendulispora* sp. MSr12523 (*sra* BGC) and *S. cellulosum* So ce12. Alignment and graphic was done with the CAGECAT application[45].

A biosynthesis model for sorangicin P-796 (**1**) is formulated in the following based on retro-biosynthesis of the molecule, predicted substrate specificities of all KS domains and based on the occurrence and analysis of all further domains in the *sra*BGC (Figure 3.4).

Based on feeding experiments for the biosynthesis of sorangicin A (**2**) and the shared organisation and predicted substrate specificity of modules 1 in the *sra*BGC and *sor*BGC[43,46], it seems likely that the biosynthesis of sorangicin P-796 (**1**) starts with malonate, which is elongated with malonyl-CoA. Although the organisation of module 1 and the predicted substrate specificity of KS-2 in the *sra*BGC is similar to the respective module and domain in the *sor*BGC, sorangicin P-796 (**1**) differs from sorangicin A (**2**) by a double-bond next to the carboxylic acid residue. According to the substrate specificity prediction of KS-2 with the 2nd highest score (shifted double-bond, table S 3.12), this double-bond is incorporated in module 1. Considering the incorporation of β, γ double-

bonds by bioinformatically unremarkable DH domains in the biosyntheses of bacillaene[47] and rhizoxin[48], a dehydration with a concomitant double-bond shift by the DH domain in module 1 seems plausible. Nevertheless, following the highest scored substrate specificity prediction of KS-2 (completely reduced, table S 3.12), a possible explanation for this discrepancy could also be a complete saturation of the growing natural product by an in-trans acting ER domain, as described in the biosynthesis of sorangicin A[43], and a dehydrogenation at this position post-assembly line. However, the *sra*BGC does not contain any gene encoding an enzyme that could perform this dehydrogenation reaction.

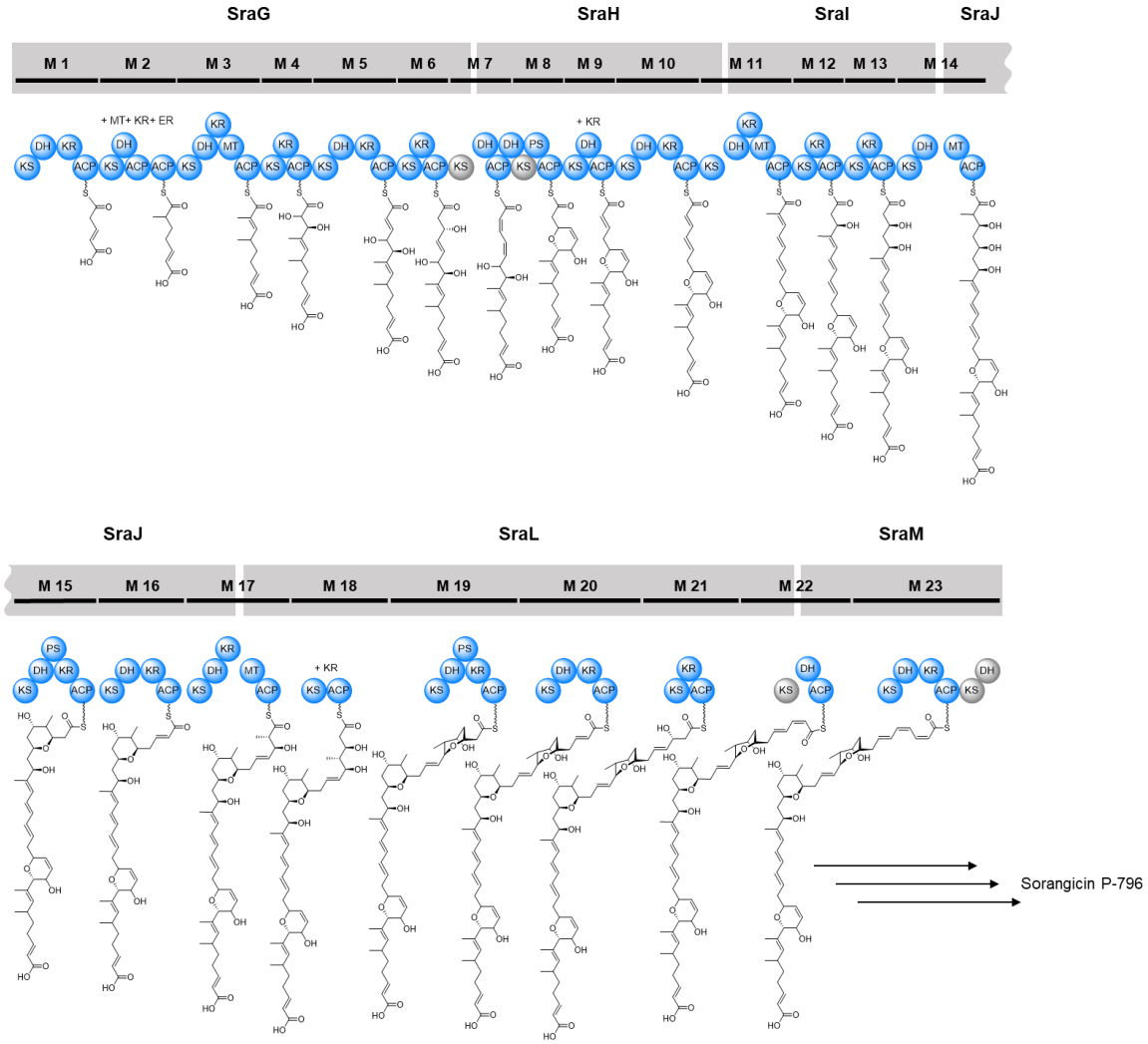

Figure 3.4: *in silico* biosynthesis of sorangicin P-796. Biosynthetic model for sorangicin P-796, based on retro-biosynthesis, phylogenetic analysis of KS domains and occurrence of further domains within the respective modules. Active modules are marked in blue, inactive models in grey. Putatively in trans-acting domains, needed to explain the observed structures are indicated above each module. (ACP: acyl-carrier protein; DH: dehydratase; ER; enoylreductase; KR: ketoreductase; KS: ketosynthase; MT: methyltransferase; PS: pyran synthase)

Similar to the biosynthesis of sorangicin A (**2**)[43], in trans-acting KR, MT, and ER domains are needed in module 2 in order to yield the observed α-methylated reduced polyketide backbone. The elongation and subsequent modification steps of sorangicin P-796 (**1**) in modules 3-6 are in accordance with the domains in these modules. The following, non-elongating modules 7 and 8, which form the tri-hydro-pyran moiety between C-9 and C-13 are in accordance with the respective modules in the sorangicin A (**2**) biosynthesis[43]. However, according to the predicted stereochemistry of the KR domain in module 5[49] and substrate specificity of the KS domain in module 6, the double-bond C-11 – C-12 should have an *E* – configuration instead of the observed *Z* – configuration. Similar to the observations in the *sor*BGC, the DH domains in module 7 lack one (DH-7_a) or two (DH-7_b) of the characteristic active site motif HxxxGxxxxP. Following the speculations in the biosynthesis of sorangicin A (**2**), the similarity of DH-7_a to DH-22 in the dehydrating bimodule 21-22, the examples of similar DH domains that form *Z* configured double-bonds in the biosynthesis of bacillaene[50] and the predicted substrate specificity of the KS-domain in module 8, it seems likely that DH-7_a causes a *Z* configured double-bond. Moreover, it might be possible that DH-7_a or DH-7_b changes the configuration of the double-bond C-11 – C-12 from the predicted *E* to the observed *Z* configuration in a so far unknown mechanism. It is noteworthy that sorangicin P-796 (**1**) and sorangicin A (**2**) share this structural motif, although they differ in module 5 and the substrate prediction of the KS domain in module 6.

Comparable to the biosynthesis of sorangicin A (**2**), an in-trans acting KR domain is needed to explain the generation of a double-bond in module 9[43]. Interestingly, the BGC of both sorangicin congeners display a similar set of domains in module 10 and a similar substrate specificity prediction for the KS domain in module 11, but differ at positions C-17 and C-18, which are generated by this module. Based on the shared predicted substrate specificity of the KS domain in module 11, the growing sorangicin P-796 (**1**) chain should be completely reduced by an in trans-acting ER domain, as predicted for sorangicin A (**2**)[43]. In order to yield the double-bond at this position, it should be dehydrogenated at a later stage of the biosynthesis or post-assembly line, but as the *sra*BGC does not contain any gene encoding an enzyme that could perform this dehydrogenation reaction, it would have to be encoded somewhere else in the genome of MSr12523. However, as the set of domains in module 10 should generate a double-bond, another possible explanation would be that, in contrast to the prediction, the KS in module 11 also accepts substrates with a double-bond at the α, β position.

The additional KR and MT domains in module 11 and lacking MT domain in module 12 of the *sra*BGC, compared to the *sor*BGC, are in accordance with the observed structure of sorangicin P-796 (**1**) and the substrate specificity predictions of the KS domains in

modules 12 and 13. Furthermore, they explain the origin of the additional methyl-group bound to C-20 in sorangicin P-796 (**1**) compared to sorangicin A (**2**).

Based on the accordance of the structures of both sorangicin congeners between C-23 and C-43 as well as of the organisation of all domains in modules 13 to 23, it seems likely that the remaining 10 elongation steps in the biosynthesis of sorangicin P-796 (**1**) resemble the ones described for sorangicin A (**2**)[43]. Similar to the biosynthesis of sorangicin A (**2**)[43], these elongation steps include the formation of oxanes in modules 15 and 19 and the non-elongating module 22 that is responsible for the formation of the *Z*-configured olefin C-39 – C-40. While most of these modules are in accordance with the co-linearity rule, the action of an in trans-acting KR domain is needed in module 18 in order to comply with the retro-biosynthesis.

As observed in the *sor*BGC[43], the *sra*BGC does not contain a TE domain to catalyse the chain release and macrocyclisation of sorangicin P-796 (**1**). However, the *sra*BGC contains the putative amidohydrolases SraN, SraO, and SraP, the putative aspartate synthase SraF and the putative amidase SraD, which are homologs of SorK and SorP to SorS in the *sor*BGC. Therefore, following the reasoning of the biosynthesic model of sorangicin A (**2**), a possible explanation could be a chain release from the biosynthetic machinery by one of the amidohydrolases SraN, SraO or SraP, an amide formation by the aspartate synthase SraF with a subsequent lactonisation by the amidase SraD[43]. Nevertheless, as discussed for sorangicin A (**2**), other possibilites for the macro-cyclisation of sorangicin P-796 (**1**) include a direct chain release and lactonisation by one of the amidohydrolases or the involvement of a TE domain or another enzyme or domain encoded elsewhere in the genome of MSr12523[43,51].

Similar to the biosynthesis of sorangicin A (**B**)[43], the biosynthetic machinery in the *sra*BGC does not explain the existence of the second ether formations between C-33 and C-36 and C-21 and C-25 in both bicyclic ether moieties in sorangicin P-796 (**1**). As discussed for the biosynthesis of sorangicin A (**B**), a possible explanation of the formation of the C-33 – C-36 ether could be the involvement of a cytochrome P450 monooxygenase, encoded elsewhere in the genome of MSr12523[43]. Comparable with the proposed mechanisms of AurH in the furan formation in the aureothin biosynthesis[43,52–54] and PtmU in the penitrem biosynthesis[55], the ether could be either formed through a radical mechanism or a hydroxylation with subsequent elimination of water at C-36[56].

However, the ether between C-21 and C-25 in the second bicyclic ether moiety in sorangicin P-796 (**1**) might have a different origin, as it may derive from two hydroxyl-groups, incorporated by modules 12 and 14. A possible explanation for the formation of

this tetrahydropyran may be iterative functions of the DH and PS domains in module 17, comparable to the discussed formation of the tetrahydropyran ring A in the last step of the salinomycin biosynthesis[57]. Nevertheless, a post-assembly line dehydration at C-25 and a subsequent formation of an intramolecular ether bridge is another possibility. Another possible formation of this bicyclic ether moiety via a cytochrome P450 monooxygenase may furthermore explain the origin of the keto-group at C-22, which, based on the predicted substrate specificity of the KS domain in module 13, is saturated in the assembly line. This putative mechanism entails the enzymatic formation of a radical at C-22 and a subsequent formation of an epoxide ring with the hydroxyl-group bound to C-21. Due to steric hindrance of C-22 or potential differences in ring strain or stability, the hydroxyl-group bound to C-25 forms the tetrahydropyran through a nucleophilic attack on C-21. The keto-group at C-22 is either formed through formation of an alcohol and subsequent oxidation or by a direct loss of the remaining hydrogen. However, the incorporation of hydroxymalonate, as hypothesised for the biosynthesis of sorangicin A (**2**)[43], and subsequent oxidation of the resulting hydroxy-group at C-22 by an oxidase or monooxygenase, encoded elsewhere in the genome, is another possible origin of the keto-group at C-22.

The observation of the putative glycosyltransferase SraK and the putative glucosidase SraQ, indicate a mechanism of self-resistance that involves the inactivation of the antibiotic by glycosylation within the cell and the subsequent hydrolysation to the free antibiotic outside the cell, as hypothesised for sorangicin A and described for oleandomycin[43,58,59]. However, unlike for sorangicin A and derivatives from *S. cellulosum* So ce12[42], no glycosylated counterparts of the sorangicin P congeners could be observed in the respective crude extracts. As sorangicin P-796 (**1**) does not contain a free hydroxy-group for glycosylation, it is possible that no glycosylated sorangicin P derivatives are produced by MSr12523. Further possible explanations include a complete de-glycosylation by SraQ or a weak binding of putative sorangicin P-glycosides to the used XAD-16 adsorber resin.

Considering the obscurities in the formation of the macrolactone and both bicyclic ether moieties as well as the origin of the keto-group at C-22 in sorangicin P-796 (**1**) an in depth *in vivo* or *in vitro* analysis of the *sra*BGC would be needed to fully decipher its biosynthesis. Due to the resistance of MSr1253 against a broad range of antibiotics, a heterologous expression of the *sra*BGC seems to be a more promising approach than to screen for fitting selection markers to genetically alter MSr12523. However, as several crucial biosynthetic enzymes seem to be encoded elsewhere in the genome of MSr12523, an attempted heterologous expression of the herein described *sra*BGC might not result in the production of sorangicin P-796 and its congeners. As a matter of fact,

no heterologous expression of the *sor*BGC was reported after its description in 2010, which might be explained by the absence of several important biosynthetic genes within the described BGC.

Therefore, a possible road to the heterologous expression of sorangicin P-796 and subsequent analysis of the *sra*BGC might be a comparative transcriptomics and proteomics analysis of cultivation conditions of MSr12523 with and without the production of this natural product. This approach might lead to the discovery of the biosynthetic enzymes encoded elsewhere in the genome, in case that they would be stringently co-regulated. Finally, a complete version of the *sra*BGC could be synthesised, assembled and heterologously expressed in an appropriate host, as described for the cystobactamid BGC[60].

3.3.4 **Bioactivities**

Following the antibiotic activities observed in the crude extract and in the fraction containing sorangicin P-796 as well as the reported bioactivities of the RNA polymerase inhibitor sorangicin A[15], sorangicin P-796 was tested for its effect on a panel of Gram positive and Gram negative bacteria.

Sorangicin P-796 displays a weak antibiotic activity against Gram-negative pathogens *A. baumannii* and *E. coli* and no activity up to 64 µg/mL against both tested *P. aeruginosa* strains. As it does not show a greatly improved activity against both Gram negative bacteria with inactivated efflux-pumps (*E. coli* Δ*acrB*(JW0451-2) and *P. aeruginosa* PA14 Δ*mexAB*), the weak antibiotic activity of sorangicin P-796 cannot be explained by an active efflux out of the respective bacteria. Similar to sorangicin A, the novel sorangicin congener has a moderate to good activity against several Gram positive bacteria, including *Mycobacteria*.

Following the known cross-resistance of sorangicin A with the established antibiotic rifampicin[61–63], sorangicin P-796 was tested for its activity against in-house available rifampicin-resistant *S. aureus* and *A. baumannii*. While it had full cross-resistance with rifampicin in *S. aureus*, the activity of sorangicin P-796 against rifampicin-resistant *A. baumannii* was comparable to the respective wild-type strain. However, previous *in vitro* experiments showed that, depending on the mutated position, sorangicin A still inhibited the activity of rifampicin-resistant RNA polymerases from Gram-negative bacteria[62,63] and *Mycobacterium tuberculosis*[64]. Therefore, the activity of sorangicin P-796 was tested against *A. baumannii* strains that are resistant against neosorangicin, a sorangicin congener with improved antibiotic activities[65]. Against these strains,

sorangicin P-796 did not show an effect up to 64 µg/mL, indicating that it shares the binding site of the sorangicin scaffold on the RNA polymerase in *A. baumannii*.

Table 3.1: Antibiotic activities of sorangicin P-796 against a panel of Gram positive and Gram negative bacteria with rifampicin as control for *A. baumannii* and *S. aureus* strains.

Indicator strain	Sorangicin P-796 [µg/mL]	Rifampicin [µg/mL]
Acinetobacter baumannii DSM-30008	32-64	2
Acinetobacter baumannii DSM-30008 Rif^{R}#1	64	> 64
Acinetobacter baumannii DSM-30008 Neosor^{R}#1	>64	> 64
Acinetobacter baumannii DSM-30008 Neosor^{R}#4	>64	> 64
Citrobacter freundii DSM-30039	> 64	-
Escherichia coli DSM-1116	64	-
Escherichia coli BW25113 (WT)	64	-
Escherichia coli Δ*acrB*(JW0451-2)[a]	32	-
Pseudomonas aeruginosa PA14	> 64	-
Pseudomonas aeruginosa PA14 Δ*mexAB*	> 64	-
Enterococcus faecium DSM-20477	16	-
Enterococcus faecium DSM-17050 (VRE)	1	-
Staphylococcus aureus Newman	2	0.03
Staphylococcus aureus Newman Rif^{R}	> 64	> 64
Staphylococcus aureus N315 (MRSA)	0.03	-
Streptococcus pneumoniae DSM-20566	8	-
Streptococcus pneumoniae DSM-11865 (PRSP)	64	-
Mycobacterium smegmatis mc^{2}155	8	-
Mycobacterium marinum M/mCherry[b]	16	-

[a] Pre-culture + 50 µg/mL kanamycin.
[b] Pre-culture + 20 µg/mL kanamycin.

3.4 Conclusion

The observation and purification of the antibiotic sorangicin P-796 from the rare myxobacterium *Pendulispora* spp. MSr12523 is yet another example that highlights the importance to screen for understudied (myxo)bacterial taxa in order to find novel and biologically active natural products[18–20,66]. Furthermore, this work displays the relevance and opportunities of easily accessible OSMAC-style cultivation experiments with novel (myxo)bacterial isolates as the biologically active sorangicin P congeners were only produced in one of the six tested conditions.

Sorangicin P-796 displays several structural differences to other representatives of the sorangicin scaffold. While the additional methylation and potentially also the two additional olefins compared to sorangicin A can be explained by the trans-AT PKS

biosynthetic machinery, the origin of the second bicyclic ether moiety remains elusive. The determined antibiotic activities of sorangicin P-796 against a panel of Gram-negative and Gram-positive bacteria are comparable with sorangicin A and similar to other representatives of this scaffold, it displays cross-resistance with rifampicin in *S. aureus*[61].

Moreover, this work displays the strengths and weaknesses of genome and metabolome-based dereplication tools. According to manual evaluation, half of the six putative BGCs in the genome of MSr12523 with gene similarities of at least 50% to reported BGCs (according to antiSMASH) do not share the organisation of the biosynthetic machinery with the respective template. The *sra*BGC on the other hand, only displayed similarity to 43% of the genes in the *sor*BGC, according to antiSMASH, although the biosynthetic machineries (and resulting products) in both BGCs are highly similar. This may be interpreted as a hint towards "shared protein sequence identity/similarity" being a too simple metric for assessment of conceptual relatedness of large multimodular BGCs and needs to be amended by e.g. a more architecture-accentuated comparison method in the future. Furthermore, automated annotation with MetaboScape 2022b against the in-house database "Myxobase", as well as GNPS-based molecular networking (data not shown) identified the siderophore nocardamine in the crude extract of MSr12523 in RGSR medium, displaying in principle the power and validity of these dereplication workflows. Yet, despite the structural similarity of sorangicin P-796 to sorangicin A it was not identified by the same procedure as a potential representative of the sorangicin scaffold, pointing at the necessity for ever increasing and more fine-grained collections of reference data when fully automated and highly reliable dereplication is demanded from these tools.

Nevertheless, considering the emerging AMR, every potentially novel antibiotic should be basically investigated and evaluated. As evidenced by the improved antibiotic activity of methyl-griselimycin against *Mycobacterium tuberculosis*[67] or the improved anti-parasitic activities of angiolams B, C and D against *Plasmodium falciparum* (Chapter 2), natural derivatives of known natural products can display improved biological activities. Differences in the biosynthesis of natural product scaffolds in different producers can improve the biological activities as shown for neosorangicin A compared to sorangicin A[15,65], or completely change the spectrum of activity, as displayed by antibiotic and anti-fungal ajudazols A and B from *Chodromyces crocatus* Cm c5[68,69] and cytotoxic ajudazols C-H from *Cystobacter* sp. SBCb004[70]. In addition to the possibility for preliminary structure activity relationship (SAR) assumptions, the analysis of slightly different versions of similar BGCs in different producing organisms might improve the understanding of the biosynthesis and enable subsequent heterologous expression as displayed for the cytotoxic disorazol scaffold[71–73]. Therefore, the discovery of the

sorangicin P subfamily and a description of the underlying biosynthesis might contribute to improve the properties of the sorangicin scaffold.

3.5 References

1. Cook, M. A. & Wright, G. D. The past, present, and future of antibiotics. *Sci. Transl. Med.* **14,** eabo7793; 10.1126/scitranslmed.abo7793 (2022).
2. Walesch, S. *et al.* Fighting antibiotic resistance-strategies and (pre)clinical developments to find new antibacterials. *EMBO Rep.,* e56033; 10.15252/embr.202256033 (2022).
3. Murray, C. J. L. *et al.* Global burden of bacterial antimicrobial resistance in 2019: a systematic analysis. *Lancet* **399,** 629–655; 10.1016/S0140-6736(21)02724-0 (2022).
4. Boucher, H. W. *et al.* Bad bugs, no drugs: no ESKAPE! An update from the Infectious Diseases Society of America. *Clin Infect Dis.* **48,** 1–12; 10.1086/595011 (2009).
5. World Health Organization. Global priority list of antibiotic-resistant bacteria to guide research, discovery, and development of new antibiotics - 2017, 2017.
6. Newman, D. J. & Cragg, G. M. Natural Products as Sources of New Drugs over the Nearly Four Decades from 01/1981 to 09/2019. *Journal of natural products*; 10.1021/acs.jnatprod.9b01285 (2020).
7. Wright, G. D. Opportunities for natural products in 21st century antibiotic discovery. *Nat. Prod. Rep.* **34,** 694–701; 10.1039/c7np00019g (2017).
8. van Santen, J. A. *et al.* The Natural Products Atlas 2.0: a database of microbially-derived natural products. *Nucleic Acids Res.* **50,** D1317-D1323; 10.1093/nar/gkab941 (2022).
9. Wenzel, S. C. & Müller, R. The biosynthetic potential of myxobacteria and their impact on drug discovery. *Curr. Opin. Drug Discov. Devel.* **12,** 220–230 (2009).
10. Bader, C. D., Panter, F. & Müller, R. In depth natural product discovery - Myxobacterial strains that provided multiple secondary metabolites. *Biotechnol. Adv.* **39,** 107480; 10.1016/j.biotechadv.2019.107480 (2020).
11. Zaburannyi, N., Bunk, B., Maier, J., Overmann, J. & Müller, R. Genome analysis of the fruiting body forming myxobacterium *Chondromyces crocatus r*eveals high

potential for natural product Biosynthesis. *Appl. Environ. Microbiol.* **82,** 1945–1957; 10.1128/AEM.03011-15 (2016).

12. Mohr, K. I. Diversity of Myxobacteria-We Only See the Tip of the Iceberg. *Microorganisms* **6**; 10.3390/microorganisms6030084 (2018).
13. Herrmann, J., Fayad, A. A. & Müller, R. Natural products from myxobacteria: novel metabolites and bioactivities. *Natural product reports* **34,** 135–160; 10.1039/c6np00106h (2017).
14. Irschik, H., Jansen, R., Höfle, G., Gerth, K. & Reichenbach, H. The corallopyronins, new inhibitors of bacterial RNA synthesis from Myxobacteria. *J. Antibiot.* **38,** 145–152 (1985).
15. Irschik, H., Jansen, R., Gerth, K., Hofle, G. & Reichenbach, H. The sorangicins, novel and powerful inhibitors of eubacterial RNA polymerase isolated from myxobacteria. *J. Antibiot.* **40,** 7–13 (1987).
16. Baumann, S. *et al.* Cystobactamids: myxobacterial topoisomerase inhibitors exhibiting potent antibacterial activity. *Angew. Chem. Int. Ed.* **53,** 14605–14609; 10.1002/anie.201409964 (2014).
17. Couturier, C. *et al.* Structure Elucidation, Total Synthesis, Antibacterial In Vivo Efficacy and Biosynthesis Proposal of Myxobacterial Corramycin. *Angew. Chem., Int. Ed. Engl.,* 10.1002/anie.202210747; 10.1002/anie.202210747 (2022).
18. Hoffmann, T. *et al.* Correlating chemical diversity with taxonomic distance for discovery of natural products in myxobacteria. *Nat. Commun.* **9,** 803; 10.1038/s41467-018-03184-1 (2018).
19. Panter, F., Bader, C. D. & Müller, R. The Sandarazols are Cryptic and Structurally Unique Plasmid-Encoded Toxins from a Rare Myxobacterium*. *Angewandte Chemie (International ed. in English)* **60,** 8081–8088; 10.1002/anie.202014671 (2021).
20. Bader, C. D. *et al.* Sandacrabins - Structurally Unique Antiviral RNA Polymerase Inhibitors from a Rare Myxobacterium. *Chemistry – A European Journal* **28,** e202104484; 10.1002/chem.202104484 (2022).
21. Scherlach, K. & Hertweck, C. Triggering cryptic natural product biosynthesis in microorganisms. *Org. Biomol. Chem.* **7,** 1753–1760; 10.1039/b821578b (2009).
22. Katz, L. & Baltz, R. H. Natural product discovery: past, present, and future. *J. Ind. Microbiol. Biotechnol.* **43,** 155–176; 10.1007/s10295-015-1723-5 (2016).

23. Covington, B. C., Xu, F. & Seyedsayamdost, M. R. A Natural Product Chemist's Guide to Unlocking Silent Biosynthetic Gene Clusters. *Annu. Rev. Biochem.* **90,** 763–788; 10.1146/annurev-biochem-081420-102432 (2021).

24. Bode, H. B., Bethe, B., Höfs, R. & Zeeck, A. Big effects from Small Changes: Possible Ways to Explore Nature's Chemical Diversity. *ChemBioChem* **3,** 619–627 (2002).

25. Pan, R., Bai, X., Chen, J., Zhang, H. & Wang, H. Exploring Structural Diversity of Microbe Secondary Metabolites Using OSMAC Strategy: A Literature Review. *Front. Microbiol.* **10,** 294; 10.3389/fmicb.2019.00294 (2019).

26. Schwarz, J., Hubmann, G., Rosenthal, K. & Lütz, S. Triaging of Culture Conditions for Enhanced Secondary Metabolite Diversity from Different Bacteria. *Biomolecules* **11**; 10.3390/biom11020193 (2021).

27. Jenny Schwarz, Georg Hubmann, Ayla Schwarz, Katrin Rosenthal & Stephan Lütz. Bivariate OSMAC Designs Expand the Secondary Metabolite Production Space in Corallococcus Coralloides; 10.20944/preprints202203.0118.v1 (2022).

28. Garcia, R. *et al.* Pendulisporaceae – a unique myxobacterial family with distinct sporulation behaviour and high potential for natural product discovery **Manuscript in preparation** (2023).

29. Blin, K. *et al.* antiSMASH 6.0: improving cluster detection and comparison capabilities. *Nucleic Acids Res.* **49,** W29-W35; 10.1093/nar/gkab335 (2021).

30. Schieferdecker, S. *et al.* Structure and biosynthetic assembly of gulmirecins, macrolide antibiotics from the predatory bacterium *Pyxidicoccus fallax*. *Chemistry (Weinheim an der Bergstrasse, Germany)* **20,** 15933–15940; 10.1002/chem.201404291 (2014).

31. Buntin, K. *et al.* Biosynthesis of thuggacins in myxobacteria: comparative cluster analysis reveals basis for natural product structural diversity. *Chem. Biol.* **17,** 342–356; 10.1016/j.chembiol.2010.02.013 (2010).

32. Buntin, K. *et al.* Production of the antifungal isochromanone ajudazols A and B in *Chondromyces crocatus* Cm c5: biosynthetic machinery and cytochrome P450 modifications. *Angew. Chem. Int. Ed. Engl.* **47,** 4595–4599; 10.1002/anie.200705569 (2008).

33. Shin, J.-C. *et al.* Characterization of tailoring genes involved in the modification of geldanamycin polyketide in Streptomyces hygroscopicus JCM4427. *J. Microbiol. Biotechnol.* **18,** 1101–1108 (2008).

34. Zhou, H. *et al.* Alkaloids from an endophytic streptomyces sp. YIM66017. *Nat. Prod. Commun.* **8,** 1393–1396 (2013).

35. Fujita, M. J., Nakano, K. & Sakai, R. Bisucaberin B, a linear hydroxamate class siderophore from the marine bacterium Tenacibaculum mesophilum. *Molecules (Basel, Switzerland)* **18,** 3917–3926; 10.3390/molecules18043917 (2013).

36. Dictionary of Natural Products. Available at http://dnp.chemnetbase.com/faces/chemical/ChemicalSearch.xhtml (2019).

37. Hossain, M. B., van der Helm, D. & Poling, M. The structure of deferriferrioxamine E (nocardamin), a cyclic trihydroxamate. *Acta Crystallogr B Struct Sci* **39,** 258–263; 10.1107/S0108768183002360 (1983).

38. Hoffmann, T., Krug, D., Hüttel, S. & Müller, R. Improving natural products identification through targeted LC-MS/MS in an untargeted secondary metabolomics workflow. *Anal. Chem.* **86,** 10780–10788; 10.1021/ac502805w (2014).

39. Wang, M. *et al.* Sharing and community curation of mass spectrometry data with Global Natural Products Social Molecular Networking. *Nature biotechnology* **34,** 828–837; 10.1038/nbt.3597 (2016).

40. Jansen, R., Wray, V., Irschik, H., Reichenbach, H. & Höfle, G. Isolation and spectroscopic structure elucidation of sorangicin A, a new type of macrolide-polyether antibiotic from gliding bacteria - XXX. *Tetrahedron Lett.* **26** (1985).

41. Jansen, R. *et al.* Antibiotika aus Gleitenden Bakterien, XXXVII. Sorangicin A, ein hochwirksames Antibiotikum mit neuartiger Makrolid-Polyether-Struktur aus *Sorangium cellulosum*, So ce12: Spektroskopische Strukturaufklärung, Kristall- und Lösungsstruktur. *Liebigs Ann. Chem.* **1989,** 111–119; 10.1002/jlac.198919890124 (1989).

42. Jansen, R., Irschik, H., Reichenbach, H., Wray, V. & Höfle, G. Natürliche Strukturvarianten von Sorangicin A aus *Sorangium cellulosum*, So ce12. *Liebigs Ann. Chem.* **3,** 213–222 (1989).

43. Irschik, H. *et al.* Analysis of the sorangicin gene cluster reinforces the utility of a combined phylogenetic/retrobiosynthetic analysis for deciphering natural product assembly by trans-AT PKS. *Chembiochem : a European journal of chemical biology* **11,** 1840–1849; 10.1002/cbic.201000313 (2010).

44. Helfrich, E. J. N. *et al.* Automated structure prediction of *trans*-acyltransferase polyketide synthase products. *Nat. Chem. Biol.* **15,** 813–821; 10.1038/s41589-019-0313-7 (2019).

45. van den Belt, M. *et al.* CAGECAT: The CompArative GEne Cluster Analysis Toolbox for rapid search and visualisation of homologous gene clusters. *Bmc Bioinform.* **24,** 181; 10.1186/s12859-023-05311-2 (2023).

46. Jansen, R., Irschik, H., Reichenbach, H., Wray, V. & Höfle, G. Biosynthese von Sorangicin A in *Sorangium cellulosum*, So ce12. *Liebigs Ann. Chem.,* 309–313 (1989).

47. Moldenhauer, J. *et al.* The Final Steps of Bacillaene Biosynthesis in *Bacillus amyloliquefaciens* FZB42: Direct Evidence for β,γ Dehydration by a *trans*-Acyltransferase Polyketide Synthase. *Angew. Chem. Int. Ed.* **49,** 1465–1467; 10.1002/anie.200905468 (2010).

48. Kusebauch, B., Busch, B., Scherlach, K., Roth, M. & Hertweck, C. Functionally Distinct Modules Operate Two Consecutive α,ß ->ß,γ Double-Bond Shifts in the Rhizoxin Polyketide Assembly Line. *Angew. Chem. Int. Ed. Engl.* **49,** 1460–1464; 10.1002/anie.200905467 (2010).

49. Keatinge-Clay, A. T. The structures of type I polyketide synthases. *Nat. Prod. Rep.* **29,** 1050–1073; 10.1039/c2np20019h (2012).

50. Moldenhauer, J., Chen, X. H., Borriss, R. & Piel, J. Biosynthesis of the antibiotic bacillaene, the product of a giant polyketide synthase complex of the trans-AT family. *Angew. Chem. Int. Ed. Engl.* **46,** 8195–8197 (2007).

51. Little, R. F. & Hertweck, C. Chain release mechanisms in polyketide and non-ribosomal peptide biosynthesis. *Nat. Prod. Rep.* **39,** 163–205; 10.1039/d1np00035g (2022).

52. He, J., Müller, M. & Hertweck, C. Formation of the aureothin tetrahydrofuran ring by a bifunctional cytochrome p450 monooxygenase. *Adv. Ceram. Mater.* **126,** 16742–16743; 10.1021/ja046104h (2004).

53. Richter, M. E., Traitcheva, N., Knupfer, U. & Hertweck, C. Sequential asymmetric polyketide heterocyclization catalyzed by a single cytochrome P450 monooxygenase (AurH). *Angew. Chem. Int. Ed. Engl.* **47,** 8872–8875; 10.1002/anie.200803714 (2008).

54. Zocher, G., Richter, M. E. A., Mueller, U. & Hertweck, C. Structural fine-tuning of a multifunctional cytochrome P450 monooxygenase. *J. Am. Chem. Soc.* **133,** 2292–2302; 10.1021/ja110146z (2011).

55. Liu, C. *et al.* Reconstitution of biosynthetic machinery for the synthesis of the highly elaborated indole diterpene penitrem. *Angewandte Chemie (International ed. in English)* **54,** 5748–5752; 10.1002/anie.201501072 (2015).

56. Tang, M.-C., Zou, Y., Watanabe, K., Walsh, C. T. & Tang, Y. Oxidative Cyclization in Natural Product Biosynthesis. *Chemical reviews* **117,** 5226–5333; 10.1021/acs.chemrev.6b00478 (2017).

57. Yurkovich, M. E. *et al.* A late-stage intermediate in salinomycin biosynthesis is revealed by specific mutation in the biosynthetic gene cluster. *Chembiochem : a European journal of chemical biology* **13,** 66–71; 10.1002/cbic.201100590 (2012).

58. Quirós, L. M., Aguirrezabalaga, I., Olano, C., Méndez, C. & Salas, J. A. Two glycosyltransferases and a glycosidase are involved in oleandomycin modification during its biosynthesis by Streptomyces antibioticus. *Mol. Microbiol.* **28,** 1177–1185 (1998).

59. Olano, C., Rodríguez, A. M., Méndez, C. & Salas, J. A. A second ABC transporter is involved in oleandomycin resistance and its secretion by Streptomyces antibioticus. *Mol Microbiol* **16,** 333–343; 10.1111/j.1365-2958.1995.tb02305.x (1995).

60. Groß, S., Schnell, B., Haack, P. A., Auerbach, D. & Müller, R. In vivo and in vitro reconstitution of unique key steps in cystobactamid antibiotic biosynthesis. *Nat. Commun.* **12,** 1696; 10.1038/s41467-021-21848-3 (2021).

61. O'Neill, A. *et al.* RNA Polymerase Inhibitors with Activity against Rifampin-Resistant Mutants of Staphylococcus aureus. *Antimicrobial agents and chemotherapy* **44,** 3163–3166; 10.1128/AAC.44.11.3163-3166.2000 (2000).

62. Xu, M., Zhou, Y. N., Goldstein, B. P. & Jin, D. J. Cross-resistance of Escherichia coli RNA polymerases conferring rifampin resistance to different antibiotics. *J. Bacteriol.* **187,** 2783–2792; 10.1128/JB.187.8.2783–2792.2005 (2005).

63. Campbell, E. A. *et al.* Structural, functional, and genetic analysis of sorangicin inhibition of bacterial RNA polymerase. *EMBO J.* **24,** 674–682 (2005).

64. Lilic, M. *et al.* The antibiotic sorangicin A inhibits promoter DNA unwinding in a *Mycobacterium tuberculosis* rifampicin-resistant RNA polymerase. *Proc. Natl. Acad. Sci. U.S.A.*; 10.1073/pnas.2013706117 (2020).

65. Zaburannyi, N., Herrmann, J., Jansen, R., Mohr, K. & Karwehl, S. *Novel Sorangicin Antibiotc. EP3498714*. Available at https://data.epo.org/publication-server/document?iDocId=5956084&iFormat=0 (2017).

66. Herrmann, J. *et al.* Strategies for the discovery and development of new antibiotics from natural products: Three case studies. *Curr. Top. Microbiol. Immunol.* **398,** 339–363; 10.1007/82_2016_498 (2016).

67. Kling, A. *et al.* Targeting DnaN for tuberculosis therapy using novel griselimycins. *Science* **348,** 1106–1112; 10.1126/science.aaa4690 (2015).

68. Kunze, B., Jansen, R., Höfle, G. & Reichenbach, H. Ajudazols, new inhibitors of the mitochondrial electron transport from Chondromyces crocatus. Production, antimicrobial activity and mechanism of action. *J Antibiot* **57,** 151–155; 10.7164/antibiotics.57.151 (2004).

69. Essig, S. *et al.* Predictive Bioinformatic Assignment of Methyl-Bearing Stereocenters, Total Synthesis, and an Additional Molecular Target of Ajudazol B. *The Journal of organic chemistry* **81,** 1333–1357; 10.1021/acs.joc.5b02844 (2016).

70. Zeng, H. *et al.* Expanding the Ajudazol Cytotoxin Scaffold: Insights from Genome Mining, Biosynthetic Investigations, and Novel Derivatives. *Journal of natural products*; 10.1021/acs.jnatprod.2c00637 (2022).

71. Tu, Q. *et al.* Genetic engineering and heterologous expression of the disorazol biosynthetic gene cluster via Red/ET recombineering. *Scientific Reports* **6,** 21066; 10.1038/srep21066 (2016).

72. Gao, Y. *et al.* The Disorazole Z Family of Highly Potent Anticancer Natural Products from Sorangium cellulosum: Structure, Bioactivity, Biosynthesis and Heterologous Expression **in preparation** (2023).

73. Wang, Z.-J. *et al.* Engineered Biosynthesis of Complex Disorazol Polyketides in a Streamlined Burkholderia thailandensis. *ACS Synth. Biol.*; 10.1021/acssynbio.2c00610 (2023).

Supporting information

Bioactivity-guided Discovery of Sorangicin P-796 from the rare Myxobacterium *Pendulispora* spp. MSr12523

Sebastian Walesch, Chantal D Bader, Daniel Krug and Rolf Müller

Materials and methods

Cultivation media

Each medium used in this study was prepared with deionised water. To create a solid medium of any of those listed below, agar (BD) was added to a final concentration of 15 g/L. All media were sterilised by autoclaving at 121 °C, 2 bar for 20 min.

Table S3.1: List of culture medium recipes

2SWT medium		
Amount	**Ingredient**	**Supplier**
1.0 g/L	Soytone	BD
2.0 g/L	Soluble starch	Roth
2.0 g/L	Glucose	Roth
1.0 g/L	Maltose monohydrate	Sigma Aldrich
2.0 g/L	Cellobiose	MP Biomedicals
0.5 g/L	$CaCl_2$ x 2 H_2O	Sigma Aldrich
1.0 g/L	$MgSO_4$ x 7 H_2O	Grüssing
2.38 g/L	HEPES	Roth
PH adjusted to 7.0 with 10 N KOH.		
M7/S4 medium		
Amount	**Ingredient**	**Supplier**
5.0 g/L	Soy flour	Hensel
5.0 g/L	Corn starch	Sigma Aldrich
2.0 g/L	Glucose	Roth
1.0 g/L	Yeast extract	BD
1.0 g/L	$CaCl_2$ x 2 H_2O	Sigma Aldrich
1.0 g/L	$MgSO_4$ x 7 H_2O	Grüssing
10.0 g/L	HEPES	Roth
0.1 mg/L	Vitamin B_{12}*	Roth

5.0 mg/L	$FeCl_3$**	Sigma Aldrich
PH adjusted to 7.4 with 10 N NaOH.		
RG5 medium		
Amount	**Ingredient**	**Supplier**
0.5 g/L	Soy peptone	Roth
0.5 g/L	Soytone	BD
2.0 g/L	Soy flour	Hensel
0.1 g/L	Corn steep solids	Sigma Aldrich
0.5 g/L	Yeast extract	BD
8.0 g/L	Soluble starch	Roth
5.0 g/L	Baker's yeast	Wonnemeyer
2.0 g/L	Gluten from wheat	Sigma Aldrich
1.0 g/L	$MgSO_4$ x 7 H_2O	Grüssing
1.0 g/L	$CaCl_2$ x 2 H_2O	Sigma Aldrich
5.95 g/L	HEPES	Roth
PH adjusted to 7.4 with 10 N KOH.		
RGAE2 medium		
Amount	**Ingredient**	**Supplier**
3.5 g/L	Casitone	BD
1.0 g/L	Soytone	BD
0.5 g/L	Yeast extract	BD
2.0 g/L	Glucose	Roth
2.0 g/L	Soluble starch	Roth
1.0 g/L	Sucrose	Roth
1.0 g/L	Maltose monohydrate	Sigma Aldrich
2.0 g/L	Cellobiose	MP Biomedicals
1.0 g/L	$MgSO_4$ x 7 H_2O	Grüssing

0.5 g/L	$CaCl_2$ x 2 H_2O	Sigma Aldrich
2.38 g/L	HEPES	Roth
PH adjusted to 7.0 with 10 N KOH.		
RGSR medium		
Amount	**Ingredient**	**Supplier**
1.0 g/L	Soytone	BD
2.0 g/L	Casitone	BD
2.0 g/L	Glucose	Roth
1.0 g/L	Maltose monohydrate	Sigma Aldrich
2.0 g/L	Cellobiose	MP Biomedicals
2.5 g/L	Baker's yeast	Wonnemeyer
2.5 g/L	Potato starch	Roth
2.0 g/L	Soy flour	Hensel
1.0 g/L	Oatmeal	Holo
0.5 g/L	$MgSO_4$ x 7 H_2O	Grüssing
0.5 g/L	$CaCl_2$ x 2 H_2O	Sigma Aldrich
2.38 g/L	HEPES	Roth
PH adjusted to 7.0 with 10 N KOH.		
S15 medium		
Amount	**Ingredient**	**Supplier**
3.0 g/L	Casitone	BD
1.0 g/L	Yeast extract	BD
3.0 g/L	Soluble starch	Roth
2.5 g/L	Cellobiose	MP Biomedicals
2.5 g/L	Maltose monohydrate	Sigma Aldrich
1.0 g/L	$CaCl_2$ x 2 H_2O	Sigma Aldrich
1.0 g/L	$MgSO_4$ x 7 H_2O	Grüssing

2.38 g/L	HEPES	Roth
PH adjusted to 7.0 with 10 N KOH.		
VY/2 medium		
Amount	**Ingredient**	**Supplier**
5.0 g/L	Baker's yeast	Wonnemeyer
1.0 g/L	$CaCl_2$ x 2 H_2O	Sigma Aldrich
0.1 mg/L	Vitamin B_{12}*	Roth
PH adjusted to 7.2 with 1 N KOH.		

* Prepared as stock solution of 0.5 g/L Vitamin B_{12} in deionised water, filter sterilised using a 0.22 µm filter and stored at 4 °C. Stock solution is added to medium prior cultivation.

** Prepared as stock solution of 5.0 g/L $FeCl_3$ in deionised water, filter sterilised using a 0.22 µm filter and stored at 4 °C. Stock solution is added to medium prior cultivation.

Microbiological methods

Fermentation of MSr12523 for analytical purposes

Cultures for analytical purposes were grown in 300 mL shaking flasks containing 100 mL of the respective fermentation medium inoculated with 2% (v/v) pre-culture. The medium was supplemented with 2% (v/v) of a sterile aqueous solution of XAD-16 adsorber resin (Sigma Aldrich) to bind secondary metabolites in the culture medium. After 7-10 d cultivation, the culture is pelleted in 50 mL falcon tubes in an Eppendorf centrifuge 5804R at 8288 x g and 4 °C for 10 min. The pellet is then stored at -20 °C until further use.

Large scale fermentation for compound purification

Pre-cultures of MSr12523 were cultivated in 300 mL shaking flasks containing 100 mL of the respective fermentation medium at 30 °C and 180 rpm for 5 d. These pre-cultures were used to inoculate (2% (v/v) inoculum) 6 x 1.67 L of the respective fermentation medium, supplemented with 2% (v/v) of a sterile aqueous solution of XAD-16 adsorber resin, in 5 L shaking flasks. Fermentation was performed at 30 °C and 170 rpm for 14 d. Afterwards the combined cultures were pelleted with an Avanti J-26 XP centrifuge, equipped with a JLA-8.1 rotor (Beckman Coulter) at 11978 x g and 4 °C for 15 min. The pellet was then frozen, freeze-dried and stored at -20 °C until further use.

Fermentation of MSr12523 in bioreactors for compound purification

Bioreactors (2 L labfors bioreactor, INFORS HT) were filled with 1 L RGSR medium and additional 2.5% (v/v) XAD-16 adsorber resin, closed and autoclaved at 121 °C and 2 bar for 30 min. Autoclaved fermenters were inoculated with 10% (v/v) of seed culture and run at 300 rpm, 28–32 °C and a O_2-flow of 0.8 L/min for 7 d. Afterwards the cultures were pelleted with an Avanti J-26 XP centrifuge, equipped with a JLA-8.1 rotor (Beckman Coulter) at 11978 x g and 4 °C for 15 min. The pellet was then frozen, freeze-dried and stored at -20 °C until further use.

Evaluation of the antibiotic susceptibility of MSr12523

Plates with VY/2 agar containing 50 and 100 µg/mL of the respective antibiotic were inoculated with one drop of a 7 d culture of MSr12523 in 2SWT. The plates were inoculated at 30 °C for 10 d and evaluated for the growth of MSr12523, compared to a VY/2 agar plate without added antibiotic.

Molecularbiological methods

Preparation of gDNA

Genomic DNA of MSr12523 for Illumina sequencing was isolated via phenol-chloroform extraction.

50–100 mL of a myxobacterial culture, grown to an appropriate density, was centrifuged at 8288 x g and 4 °C (Eppendorf Centrifuge 5804R) for 10 min. Pelleted cells were washed once with 15 mL SET buffer and afterwards resuspended in 5 mL SET buffer. After addition of 50 µL RNase stock solution, cells were incubated for 30–60 min at 37 °C. 300 µL Proteinase K stock solution were added, the falcon was inverted several time and 600 µL 10% SDS solution were added. The mixture was incubated at 55 °C for approx. 2 h until it turned viscous. After addition of 1 volume (= 6 mL) Phenol:Chloroform:Isoamylalcohol (25:24:1, Roth) the tube was swung at 5 rpm for 1 h. Afterwards, the mixture was centrifuged at 8288 x g for 5 min and the upper phase was transferred into a new tube with an Eppendorf pipette with an end-cut 1 mL tip. Washing step of the (upper) aqueous phase was repeated one more time.

The cleaned upper phase was moved to a new Falcon tube, mixed with 5 mL Chloroform:Isoamylalcohol (24:1, Roth) and swung at 5 rpm for 1 h. The mixture was swung at 8288 x g for 10 min and ~ 4 mL of the upper phase were carefully transferred to a new falcon. After addition of 440 µL of 3 M sodium acetate (pH 5.2) and 11 mL of

ice-cold pure EtOH, Falcon tube was inverted several times, until cotton-like DNA appeared. The DNA was collected with a Pasteur pipette and washed several times with 70% EtOH in a 2 mL Eppendorf tube. Washed DNA was air-dried and carefully suspended in 0.5–1.0 mL sterile MQ-water. DNA-solution was stored at -20 °C.

Analytical methods

Crude extract generation for analytical purposes

Frozen or fresh pellets from small scale cultivations were suspended in 80 mL acetone and stirred at 250 rpm at room temperature for 3 h. The supernatant was decanted into a round flask through a 125 micron folded filter. The solvent and potential residual water were removed on a rotary evaporator with a water bath temperature of 40 °C at appropriate pressures. The dried extract was dissolved/resuspended in 1100 µL MeOH. The crude extract was stored at -20 °C until further analysis. For the purpose of UHPLC-*hr*MS analysis, the crude extract was diluted 1:10 with methanol and centrifuged at 21500 x g and 4 °C (HIMAC CT15RE, Koki Holdings Co.) for 5 min to remove residual insolubilities such as salts, cell debris and XAD fragments.

Standardised UHPLC-MS conditions

UPLC-hrMS analysis was performed on a Dionex (Germering, Germany) Ultimate 3000 RSLC system using a Waters (Eschborn, Germany) BEH C18 column (50 x 2.1 mm, 1.7 µm) equipped with a Waters VanGuard BEH C18 1.7 µm guard column. Separation of 1 µL sample was achieved by a linear gradient from (A) H2O + 0.1 % formic acid (FA) to (B) ACN + 0.1 % FA at a flow rate of 600 µL/min and a column temperature of 45 °C. Gradient conditions for crude extract analysis were as follows: 0 – 0.5 min, 5% B; 0.5 – 18.5 min, 5 – 95% B; 18.5 – 20.5 min, 95% B; 20.5 – 21 min, 95 – 5% B; 21-22.5 min, 5% B. Following gradient conditions were applied to monitor compounds of interest during purification: 0 – 0.5 min, 5% B; 0.5 – 9.5 min, 5 – 95% B; 9.5 – 10.5 min, 95% B; 10.5 – 11 min, 95 – 5% B; 11-12.5 min, 5% B. UV spectra were recorded by a DAD in the range from 200 to 600 nm. The LC flow was split to 75 µL/min before entering the Bruker Daltonics maXis 4G hrToF mass spectrometer (Bremen, Germany) equipped with an Apollo II ESI source. Mass spectra were acquired in centroid mode ranging from 150 – 2500 m/z at a 2 Hz full scan rate. Mass spectrometry source parameters were set to 500 V as end plate offset; 4000 V as capillary voltage; nebuliser gas pressure 1 bar; dry gas flow of 5 L/min and a dry temperature of 200 °C. Ion transfer and quadrupole settings were set to funnel RF 350 Vpp.; multipole RF 400 Vpp as transfer settings and ion energy

of 5 eV as well as a low mass cut of 300 m/z. Collision cell was set to 5.0 eV and pre-pulse storage time was set to 5 µs. Spectra acquisition rate was set to 2 Hz. Calibration was done automatically before every LC-MS run by injection of a sodium formate solution and calibration on the respective clusters formed in the ESI source. All MS analyses were acquired in the presence of the lock masses ($C_{12}H_{19}F_{12}N_3O_6P_3$, $C_{18}H_{19}O_6N_3P_3F_2$ and $C_{24}H_{19}F_{36}N_3O_6P_3$) which generate the [M+H]+ ions of 622.0289; 922.0098 and 1221.9906.

Statistics based metabolome filtering

For statistical metabolomics analysis, both the myxobacterial culture and medium blanks were incubated and extracted in triplicates as described above. Each extract was measured as technical duplicate, giving a total number of six replicates each for the bacterial culture and medium blank extracts. T-ReX-3D molecular feature finder of MetaboScape 2022b (Bruker Daltonics, Billerica, MA, USA) was used to obtain molecular features. Detection parameters were set to intensity threshold 5×10^3 and minimum peak length of five spectra to ensure a precursor selection that has a sufficient intensity to generate tandem MS data. Identification of bacterial features was performed with the built-in ANOVA/t-test routine and filtered to appearance in all six bacterial extracts and in none of the medium blank extracts. The t-test table was used to create a scheduled precursor list (SPL) for tandem MS fragmentation[1].

Acquisition parameters for high-resolution tandem MS data

LC and MS conditions for SPL guided MS/MS data acquisitions were kept constant according to section standardised UHPLC-hrMS conditions. MS/MS data acquisition parameters were set to exclusively fragment scheduled precursor list entries. SPL tolerance parameters for precursor ion selection were set to 0.2 minutes and 0.05 m/z in the SPL MS/MS method. The method picked up to 2 precursors per cycle, applied smart exclusion after 5 spectra and performed CID and MS/MS spectra acquisition time ramping. CID Energy was ramped from 35 eV for 500 m/z to 45 eV for 1000 m/z and 60 eV for 2000 m/z. MS full scan acquisition rate was set to 2 Hz and MS/MS spectra acquisition rates were ramped from 1 to 4 Hz for precursor ion intensities of 10 kcts. to 1000 kcts..

Parameters for fragment based molecular networking

All supporting fragment based molecular networking data presented here was created based on the UHPLC-*hr*MS² chromatograms using the parameters specified in the previous section. The MS/MS chromatograms were exported containing all MS/MS data as an .mzML data file and uploaded to the GNPS server at University of California San Diego via FileZilla FTP upload to ftp:// ccms-ftp01.ucsd.edu and all acquired SPL MS/MS spectra were used for spectral network creation.[2] A molecular network was created using the online workflow at GNPS. The data was filtered by removing all MS/MS peaks within +/- 17 Da of the precursor m/z. MS/MS spectra were window filtered by choosing only the top 6 peaks in the +/- 50 Da window throughout the spectrum. The data was then clustered with a parent mass tolerance of 0.05 Da and a MS/MS fragment ion tolerance of 0.1 Da to create consensus spectra. No further filtering of consensus spectra was done before spectral network creation. A network was then created where edges are filtered to have a cosine score above 0.65 and more than 4 matched peaks. Further edges between two nodes were kept in the network if and only if each of the nodes appeared in each other's respective top 10 most similar nodes.[2] Library search parameters were set to a cosine of 0.7 and a minimum of 6 matched peaks. Library searches included analogs with mass differences up to 100 Da. All other settings were left as default values. The dataset was downloaded from the server and subsequently visualised using Cytoscape 3.9.1.

UPLC-MS coupled fractionation of crude extracts for bioactivity testings

All measurements were performed on a Dionex Ultimate 3000 RSLC system using a Waters BEH C18, 100 x 2.1 mm, 1.7 µm dp column by injection of 5 µl sample in MeOH. Separation was achieved by a linear gradient with (A) 5 mM NH4HCOO in H2O and (B) 5 mM NH4HCOO in ACN/H2O 9:1 (v:v) at a flow rate of 550 µL/min and 45 °C. The gradient was initiated by a 0.27 min isocratic step at 5% B, followed by an increase to 100% B in 18 min to end up with a 1.5 min flush step at 100% B before re-equilibration under the initial conditions. Coupling the HPLC to the MS was supported by an Advion Triversa Nanomate nano-ESI system attached to a maXis 2G qTOF. UV spectra were recorded by a DAD in the range from 200 to 600 nm The flow was split to 500 nL/min before entering the ion source. The Nanomate transfers the remaining LC flow into a 96 well plate within the time range from 0.6 to 20.6 min. Each well was filled for approx. 0.22 min (120 µl) yielding 92 wells in summary. The well plate was dried using a Genevac centrifugal evaporator (Genevac Ltd., Suffolk, UK) and used for bioactivity assay

afterwards. Mass spectra were acquired in centroid mode ranging from 150 – 2000 m/z at a 2 Hz scan rate.

Compound purification and structure elucidation

Extraction and liquid/liquid partitioning

Extraction and liquid/liquid partitioning of bioreactor cultures of MSr12523 in RGSR medium was done with 100 mL of the respective solvents per 10 g freeze-dried pellet.

Freeze-dried pellets were extracted four times with a 1:1 mixture of methanol and acetone. For each extraction step, the suspension was stirred at 250 rpm for 30 min and decanted through glass wool and a 125-µm folded filter. The combined extracts were dried using a rotary evaporator at 40 °C water bath temperature and appropriate pressures. The dried extract was then dissolved/resuspended in a 95:5 mixture of methanol and water and defatted three times with hexane. Finally, the defatted extract was partitioned three times between water and dichlormethane (DCM). The sorangicin P derivatives were retained in the DCM phase. The DCM phase was concentrated, moved to glass vials, dried and stored at -20 °C.

Pre-purification by normal phase flash chromatography

Normal phase flash chromatography was carried out using the Isolera One (Biotage). Silica gel (high purity grade, pore size 60 Å, Sigma-Aldrich) in a 25 g SNAP column (Biotage®) was used as stationary phase and Hexane (Solvent A), DCM (B), EA (C) and MeOH (D) were used as mobile phase. Flow rate was 25 mL/min, fractions of 45 mL were collected in glass tubes and solvent volume was measured in column volumes (CV); 1 CV = 33 mL. After equilibration of the system with 3 CV of 50% B, 200-250 mg sample were dissolved in MeOH, dripped on a KP-SIL SNAP: Samplet (Biotage®), air-dried and loaded on the column. The conditions were kept at 50% B for 2 CV, followed by an increase to 100% B over 12 CV and a plateau of 100% B for 4 CV. Afterwards B was replaced by C with a linear gradient over 15 CV, followed by a plateau of 100% C for 5 CV. More polar metabolites were separated by a ramp to 50% D over 20 CV. Finally, the column was flushed with a ramp to 100% D over 5 CV. Fractions were pooled according to the UV-based abundance of different sorangicin P derivatives, dried and stored in glass vials at -20 °C.

Purification of sorangicin P derivatives

Purification of sorangicin P derivatives from the respective pooled flash chromatography fractions was carried out on a Dionex (Germering, Germany) Ultimate 3000 SL system linked to a Bruker Daltonics HCT plus ion trap system (Bremen, Germany) with standard ESI ion source. Separation was carried out on a Waters xSelect Peptide CSH130 C18, 5 µM, 250 x 10 mm column using H_2O +0.1% FA (A) and ACN + 0.1% FA (B) as mobile phase at a flow rate of 5 mL/min. Separation was started with 5% B for 2 min, followed by a ramp to 62% B over 3 min and an increase to 68.9% B over 18 min. The column was then flushed with a ramp to 95% B over 0.5 min, followed by a plateau at 95% B for 3 min brought back to 5% B within 0.5 min and was re-equilibrated at 5% for 5 min. Purified sorangicin P derivatives were dried with a rotary evaporator, moved to glass vials, dried and stored at -20 °C.

NMR-based structure elucidation

The chemical structure of sorangicin P-796 was determined via multidimensional NMR analysis. 1D and 2D NMR spectra were recorded at 500 MHz (^{1}H) and 125 MHz (^{13}C) or 700 MHz (^{1}H) and 175 MHz (^{13}C) conduction using an Avance III (Ultrashield) 500 MHz spectrometer or an Avance III (Ascend) 700 MHz spectrometer, respectively, both equipped with a cryogenically cooled triple resonance probe (Bruker Biospin Rheinstetten, Germany). All observed chemical shift values (δ) are given in ppm and coupling constant values (J) in Hz. Standard pulse programs were used for HMBC, HSQC, TOCSY, ROESY, and gCOSY experiments. HMBC experiments were optimized for $^{2,3}J_{C\text{-}H}$ = 6 Hz. The spectra were recorded in methanol-d_4 and chemical shifts of the solvent signals at δ_H 3.31 ppm and δ_C 49.2 ppm were used as reference signals for spectra calibration. To increase sensitivity, the measurements were conducted in a 5 mm Shigemi tube (Shigemi Inc., Allison Park, PA 15101, USA). The NMR signals are grouped in the tables below and correspond to the numbering in the schemes corresponding to every table.

Biological assays

Antimicrobial assays

All microorganisms used in this study were obtained from the German Collection of Microorganisms and Cell Cultures (DSMZ), the Coli Genetic Stock Center (CGSC) or were part of our internal collection and were handled according to standard sterile microbiological procedures and techniques.

Minimum inhibitory concentrations (MIC) of sorangicin P-796 and bioactivities of crude extracts were determined by microbroth dilution assays. Methanolic stocks (1 mg/mL or undiluted crude extract) were used to prepare serial dilutions (0.125 to 64 µg/mL or 15 (A) to 1920 (H) fold dilution) in sterile 96 well plates and the test strain was added to a final suspension of 10^4 to 10^5 colony forming units (CFU)/mL. Afterwards the plates were incubated for 24 h at 30 °C or 37 °C, depending on the microorganism. The lowest concentration at which no growth was observed by visual observation was considered as the MIC.

The antimicrobial activity of fractions was evaluated without further dilution steps.

Cytotoxicity assay

Cell lines were obtained from the German Collection of Microorganisms and Cell Cultures (Deutsche Sammlung für Mikroorganismen und Zellkulturen, DSMZ) or were part of our internal collection and were cultured under the conditions recommended by the depositor.

Cells were seeded at 6 x 10^3 cells per well of 96-well plates in 120 µL complete medium and treated with purified compounds in serial dilution after 2 h of equilibration. Each compound was tested in duplicate as well as the internal solvent control. After 5 d incubation, 20 µL of 5 mg/mL MTT (thiazolyl blue tetrazolium bromide) in PBS was added per well and it was further incubated for 2 h at 37°C. The medium was then discarded and before adding 100 µL 2-propanol/10 N HCl (250:1) in order to dissolve formazan granules. The absorbance at 570 nm was measured using a microplate reader (Tecan Infinite M200Pro), and cell viability was expressed as percentage relative to the respective methanol control. IC_{50} values were determined by sigmoidal curve fitting.

Results

Producer, media experiments and fractionation

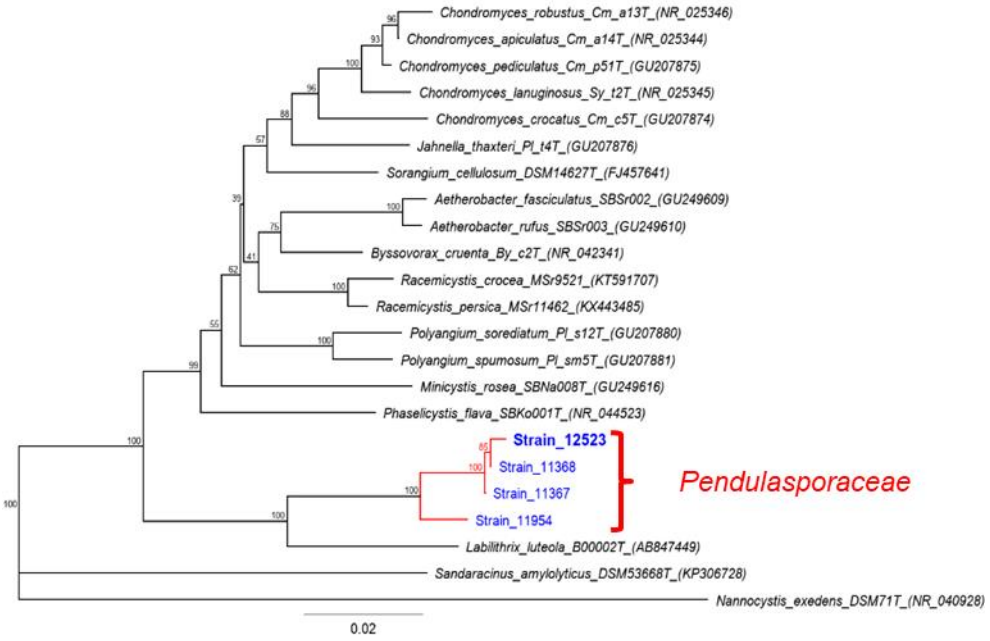

Figure S 3.1: Phylogenetic position of MSr12523. Analysis based on 16S (r)RNA gene sequence. *Nannocystis exedens* was used to root the tree. GenBank accession numbers are shown in parentheses. The numbers at branch points indicate the level of bootstrap support in percent based on 1000 resamplings. Bar 0.02 nucleotide substitution per site.

Table S3.2: Putative BGCs in the genome of MSr12523, according to antiSMASH

BGC region	Type	Most similar known cluster	Similarity [%]
1	Other[a]	-	-
2	RiPP	-	-
3	Terpene	-	-
4	PKS	-	-
5	PKS	Lydicamycin	20
6	PKS-NRPS hybrid	Linearmycin A-C	14
7	NRPS	Catenulisporolides	3
8	PKS-NRPS hybrid	Ajudazol A	30
9	Other[a]	Pyralomicin 1a	14
10	PKS	Chondramide A	15
11	PKS	Disorazol A	14
12	RiPP	-	-
13	RiPP	-	-
14	PKS-NRPS hybrid	Thuggacin A	80
15	PKS-NRPS hybrid	Alpiniamide	55
16	Other[a]	-	-
17	PKS	Sorangicin A	43
18	NRPS	Glycinocin A	6
19	PKS	-	-
20	NRPS	Ralsolamycin	40
21	PKS-NRPS hybrid	ECO-0501	21
22	PKS	Jerangolid A/D	9

23	PKS-NRPS hybrid	Dkxanthene	11
24	NRPS	Bonnevilleamide D/E	13
25	PKS-NRPS hybrid	-	-
26	Other[a]	Malleobactin X	13
27	PKS	Hexacosalactone A	6
28	PKS-NRPS hybrid	Ambruticin	32
29	Other	-	-
30	NRPS	-	-
31	RiPP	-	-
32	NRPS	-	-
33	NRPS	Coprisamide C/D	8
34	PKS	Monensin	20
35	Other[a]	-	-
36	NRPS	Zwittermicin A	7
37	PKS-NRPS hybrid	Hapalosin	40
38	PKS	Puwainaphycin A-D	30
39	PKS	-	-
40	PKS	Ossamycin	19
41	PKS-NRPS hybrid	Azotobactin D	33
42	Other[a]	-	-
43	PKS-NRPS hybrid	Geldanamycin	75
44	PKS	Simocyclinone D8	16
45	RiPP	-	-
46	PKS	Gulmirecin A	85
47	NRPS	Enantio-pyochelin	30
48	NRPS	Bohemamine A-C	12
49	Other[a]	-	-
50	NRPS	-	-
51	NRPS	-	-
52	Other[a]	-	-
53	NRPS	Megapolibactin A-F	15
54	Other[a]	Bisucaberin B	50
55	PKS	Marinopyrrole A-E	16
56	RiPP	-	-
57	Other[a]	-	-
58	PKS-NRPS hybrid	Ajudazol A	76
59	Other[a]	-	-
60	NRPS	-	-

[a] Other includes following predicted BGC types: indole, butyrolactone, amglyccycl, ladderane, arylpolyene, hgIE-KS, NRPS-independent siderophore, RRE-containing and redox-cofactor.

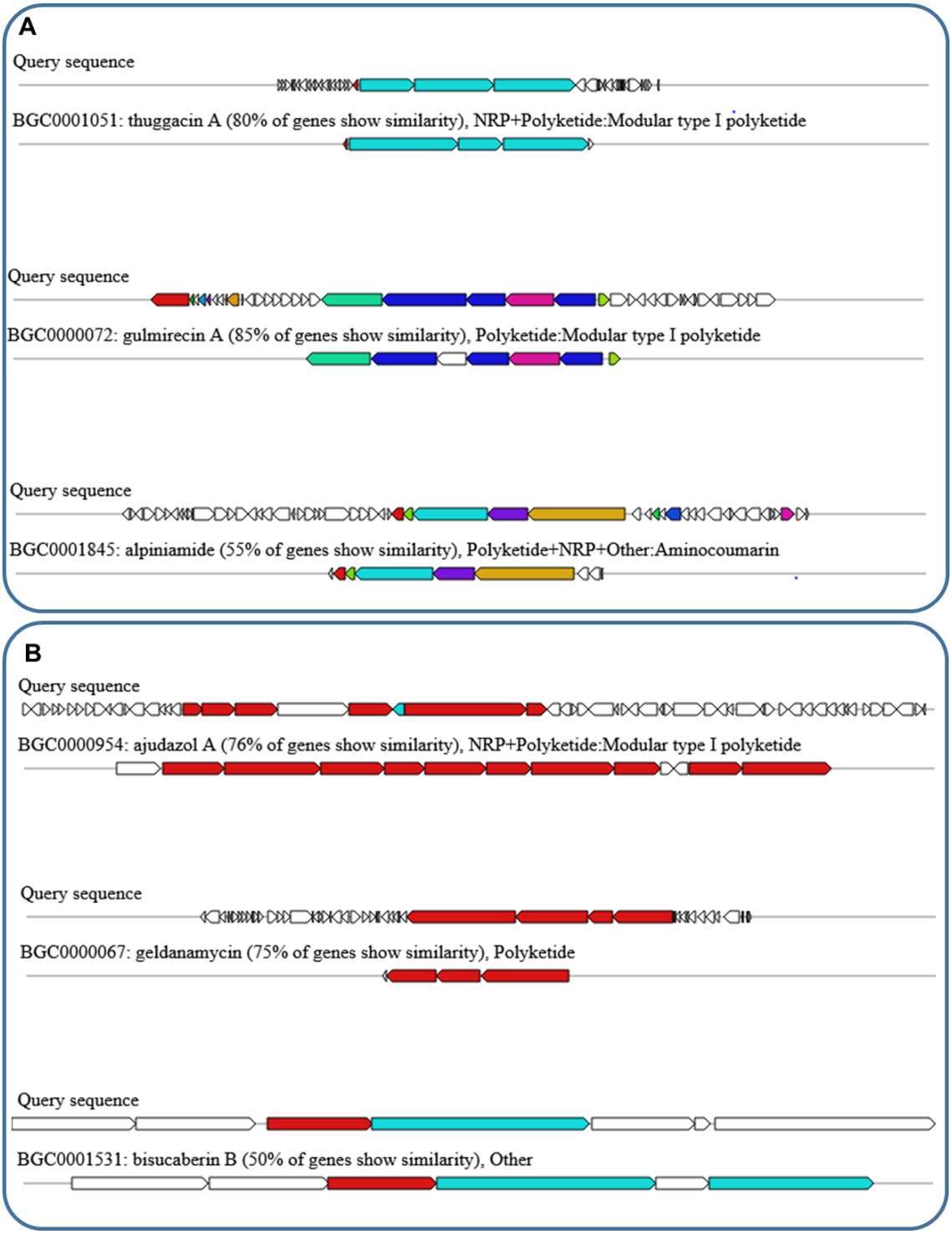

Figure S 3.2: BGCs in the genome of MSr12523 with a gene similarity of ≥ 50%, according to AntiSMASH. (**A**) BGCs with fitting arrangement and number of similar genes. (**B**) BGCs with different arrangement and number of similar genes. Graphics are taken from antiSMASH results, colour coding of different gene types, according to antiSMASH analysis.

Table S3.3: Antibiotic susceptibility of MSr12523. Growth of MSr12523 on VY/2 agar with different antibiotics relativ to VY/2 agar without added antibiotics.

Antibiotics	50 µg/mL	100 µg/mL	150 µg/mL
Hygromycin	n.t.[a]	n.t.[a]	++
Kanamycin	n.t.[a]	++	n.t.[a]
Oxytetracyclin	++	++	n.t.[a]
Ampicillin	++	++	n.t.[a]
Gentamicin	++	+	n.t.[a]
Polymyxin	++	++	n.t.[a]
Kasugamycin	++	++	n.t.[a]
Spectinomycin	++	++	n.t.[a]
Cephalosporin	++	++	n.t.[a]
Chloramphenicol	+	-	-
Bacitracin	++	++	n.t.[a]
Neomycin	++	++	n.t.[a]
Trimethoprim	+	+	n.t.[a]
Fusidic acid	++	++	n.t.[a]
Thiostrepton	++	++	n.t.[a]

- No growth.
+ Reduced growth compared to positive control.
++ Growth comparable to positive control.
[a] not tested.

Table S3.4: Bioactivity scores of crude extracts of MSr12523 in 2SWT and RGSR media

Test organism	MSr12523 in 2SWT medium	MSr12523 in RGSR medium
P. anomala DSM6766	-	-
M. hiemalis DSM2656	B	A
C. albicans DSM1665	n.t.[a]	-
B. subtilis DSM10	F-G	H
S. aureus Newman	n.t.[a]	H
M. smegmatis MC2155	n.t.[a]	H
E. coli BW25113	-	E
E. coli JW0451-2	A-B	E
A. baumanii DSM30008	n.t.[a]	G
C. freundii DSM30039	n.t.[a]	C
P. aeruginosa PA14	n.t.[a]	B

[a] Crude extract of MSr12523 in 2SWT medium was not tested against these microorganisms. Bioactivity scores display the minimal concentration, a tested crude extract showed inhibitory activity against the tested pathogen. The underlying dilutions are A = 1:15, B = 1:30, C = 1:60, D = 1:120, E = 1:240, F = 1:480, G = 1:960, H = 1:1920.

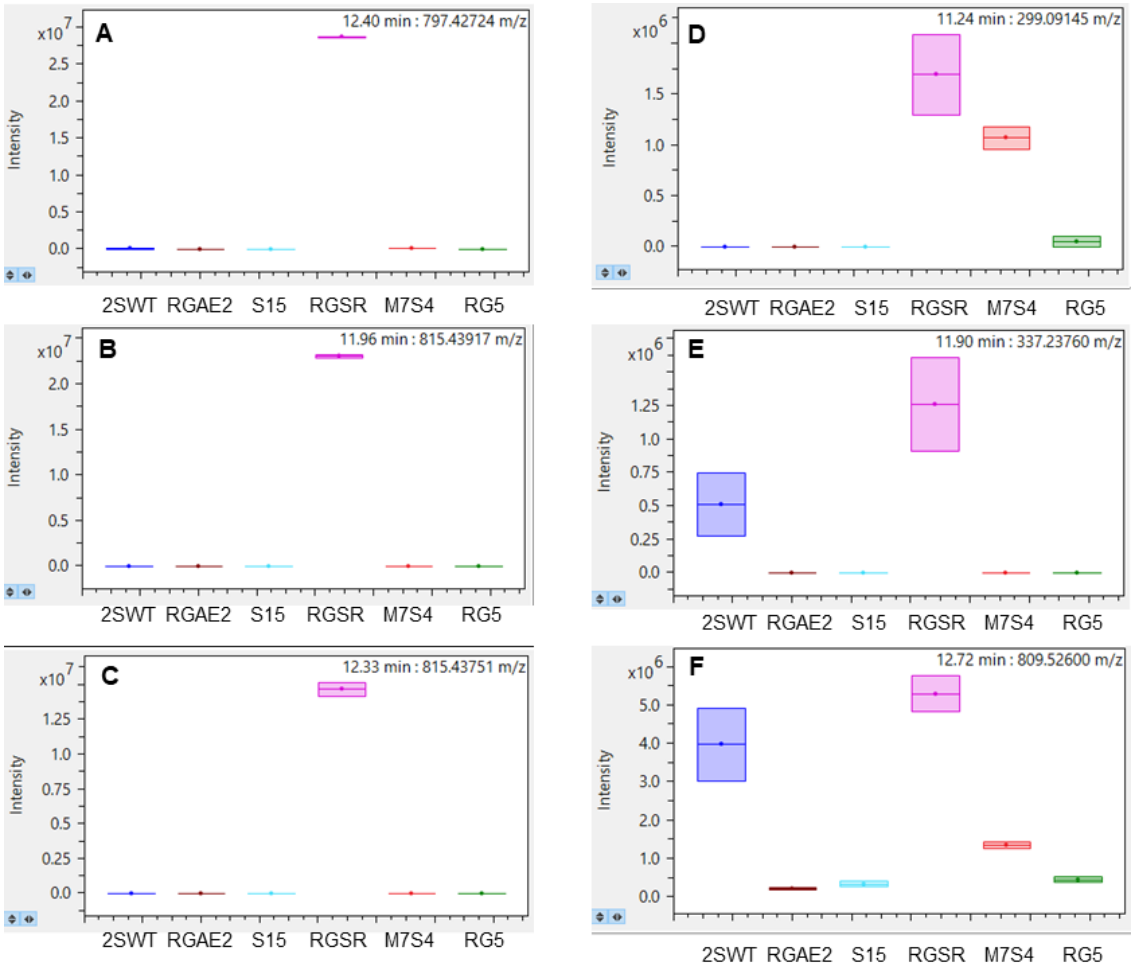

Figure S3.3: Constituents of active fractions in crude extracts of MSr12523 in RGSR. Sorangicin P-796 (**A**), P-814A (**B**) and P-814B (**C**) are only observed in cultivations of MSr12523 in RGSR, while the other, minor constituents (**D**-**F**) can be also found in crude extracts of cultivations in other media.

Purification and NMR-based structure elucidation

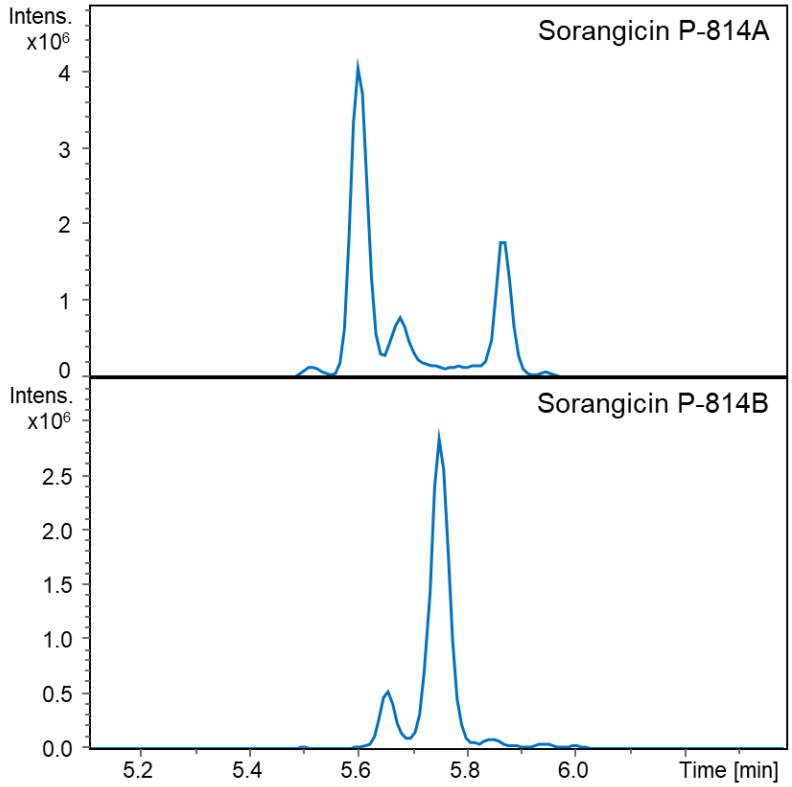

Figure S3.4: Isomerisation of sorangicin P-814A and P-814B during semi-preparative HPLC purification.

NMR-based structure elucidation of sorangicin P-796

The structure of sorangicin P-796 was elucidated based on ^{1}H, ^{13}C, COSY, HSQC, HMBC, TOCSY, and ROESY NMR spectra. As the TOCSY and ROESY NMR spectra were recorded at a later timepoint and with a different instrument ^{1}H shifts of both datasets were compared in Table S 3.6. COSY correlations used for the structure elucidation of sorangicin P-796 are indicated in bold, relevant HMBC correlations as blue arrows and relevant ROESY correlations as violet dashed arrows. Due to the high structural similarity of sorangicin P-796 with the reported sorangicin A, observed ^{1}H and ^{13}C shifts were compared with the published data[3,4] in tables S 3.8 and S 3.9.

Table S3.5: NMR spectroscopic data of sorangicin P-796, acquired at 500/125 MHz

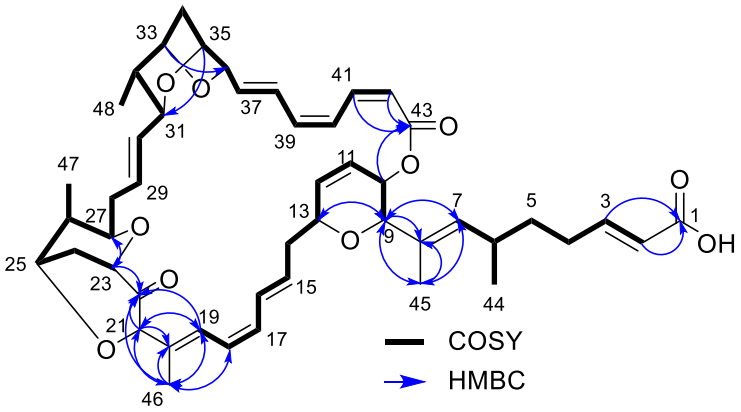

Position	δ_C[a] [ppm]	Type	δ_H[b] [ppm]	H Multiplicity (*J* [Hz])	COSY[c]	HMBC[d]
1	170.4	C	-	-	-	-
2	123.4	CH	5.71	br d (15.6)	3, 4	1, 4, 5
3	151.5	CH	6.83	m	2, 4	1, 2, 4, 5
4	31.4	CH_2	2.06	br d (6.8)	2, 3, 5a, 5b	2, 3, 5, 6
5a	37.5	CH_2	1.54	m	4, 5b	3, 4, 6, 7, 44, 45
5b			1.12	ddt (13.3, 10.6, 5.4, 5.4)	4, 5a, 6	3, 4, 6, 7, 44
6	32.0	CH	2.24	ddt (13.7, 6.9, 3.5, 3.5)	5b, 7, 44	4, 5, 7, 8, 44
7	133.1	CH	5.17	br d (10.2)	6, 9, 45	5, 6, 8, 9, 44, 45
8	130.8	-	-	-	-	-
9	73.8	CH	4.11	s	7, 10, 11, 45	5, 7, 8, 10, 11, 13, 45
10	66.0	CH	5.43	dd (6.1, 1.0)	9, 11	8, 9, 11, 12, 43
11	124.5	CH	6.09	ddd (9.8, 6.1, 2.3)	9, 10, 12, 13	9, 10, 13
12	137.1	CH	6.17	m	11, 13, 14b	10, 14
13	75.0	CH	4.55	dq (11.6, 2.5, 2.5, 2.5)	11, 12, 14a, 14b	9, 11, 12, 14, 15
14a	36.1	CH_2	2.51	dt (13.9, 11.0, 11.0)	13, 14b, 15, 16	12, 13, 16
14b			2.30	m	12, 13, 14a, 15, 16	13, 16
15	134.8	CH	5.90	ddd (14.9, 10.3, 4.3)	14a, 14b, 16	13, 14, 16, 17
16	134.5	CH	6.16	m	14a, 14b, 15, 17	14, 17, 18
17	136.0	CH	6.37	m	16, 18, 46	16, 18, 19, 21, 46
18	127.7	CH	6.30	m	17, 46	16, 19, 21, 46
19	133.1	CH	6.29	m	21, 46	18, 20, 21, 22, 46
20	134.4	C	-	-	-	-
21	81.4	CH	5.12	s	19	19, 20, 22, 46
22	210.3	C	-	-	-	-
23	76.6	CH	4.20	br dd (11.4, 2.9)	24a, 24b	22, 24, 25, 27
24a	30.1	CH_2	1.77	m	23, 24b, 25	25, 26
24b			1.70	m	23, 24a, 25	22, 23
25	70.3	CH	3.87	m	24a, 24b, 26	23, 27
26	37.3	CH	1.58	m	25, 27, 47	24, 25, 47
27	75.5	CH	3.89	m	26, 28	23, 25, 28, 29, 47
28	36.6	CH_2	2.33	m	27, 29, 30	26, 27, 29, 30
29	130.5	CH	5.34	m	28, 30	27, 28, 30, 31
30	134.0	CH	5.38	dd (15.6, 7.7)	28, 29, 31	28, 32

31	81.2	CH	3.84	m	30, 32	29, 30, 32, 33, 48
32	42.1	CH	1.38	br dd (9.4, 7.0)	31, 33, 48	30, 31, 34, 48
33	81.3	CH	4.31	br d (6.4)	32, 34a, 34b	31, 34, 35, 36, 48
34a	39.6	CH_2	2.03	m	33, 34b, 35	32, 34
34b			1.92	br dd (11.6, 1.2)	33, 34a, 35	32, 35, 36
35	77.7	CH	4.40	br d (1.3)	34a, 34b, 36	31, 33
36	81.6	CH	4.61	br d (2.1)	35, 37, 38, 39	38
37	136.0	CH	6.32	m	36, 38, 39, 40	35, 36, 39
38	128.1	CH	7.03	br t (14.0)	36, 37, 39, 40, 41	36, 40
39	138.0	CH	6.48	br t (11.2, 11.2)	36, 37, 38, 40, 41, 42	37, 38, 40, 41
40	127.3	CH	7.24	br t (11.5, 11.5)	37, 38, 39, 41, 42	38, 41, 42
41	139.6	CH	7.11	br t (11.8, 11.8)	38, 39, 40, 42	38, 39, 40, 42, 43
42	120.0	CH	5.54	br d (11.5)	39, 40, 41	40, 41, 43
43	168.1	C	-	-	-	-
44	22.3	CH_3	0.77	d (6.6)	6	5, 6, 7
45	15.0	CH_3	1.53	s	7,9	5, 7, 8, 9
46	11.7	CH_3	1.51	s	17, 18, 19	18, 19, 20, 21, 22
47	10.7	CH_3	0.86	d (7.2)	26	25, 26, 27, 28
48	15.6	CH_3	0.80	d (6.8)	32	31, 32

[a] Acquired in methanol-d_4 at 125 MHz and calibrated to solvent signal at 49.2 ppm.
[b] Acquired in methanol-d_4 at 500 MHz and calibrated to solvent signal at 3.31 ppm.
[c] Proton showing COSY correlations to indicated proton.
[d] Proton showing HMBC correlations to indicated carbon.

Table S3.6: Comparison of ^{1}H NMR signals of sorangicin P-796 at 500 and 700 MHz

Position	δ_H[a] [ppm] at 500 MHz	δ_H[b] [ppm] at 700 MHz	Δ ($\delta_{H \text{ at } 500 \text{ MHz}} - \delta_{H \text{ at } 700 \text{ MHz}}$)
1	-	-	-
2	5.71	5.74	-0.03
3	6.83	6.77	0.06
4	2.06	2.03	0.03
5a	1.54	1.52	0.02
5b	1.12	1.13	0.00
6	2.24	2.27	-0.02
7	5.17	5.18	0.00
8	-	-	-
9	4.11	4.11	0.00
10	5.43	5.42	0.01
11	6.09	6.09	0.00
12	6.17	6.16	0.01
13	4.55	4.55	0.01
14a	2.51	2.50	0.00
14b	2.30	2.29	0.01
15	5.90	5.89	0.01
16	6.16	6.16	-0.01
17	6.37	6.36	0.01
18	6.30	6.32	-0.02
19	6.29	6.28	0.00

20	-	-	-
21	5.12	5.11	0.01
22	-	-	-
23	4.20	4.21	-0.01
24a	1.77	1.77	0.00
24b	1.70	1.71	-0.01
25	3.87	3.87	0.00
26	1.58	1.58	0.00
27	3.89	3.89	0.00
28	2.33	2.33	-0.01
29	5.34	5.35	-0.01
30	5.38	5.38	0.00
31	3.84	3.85	0.00
32	1.38	1.38	0.00
33	4.31	4.31	0.00
34a	2.03	2.02	0.02
34b	1.92	1.92	0.00
35	4.40	4.40	0.00
36	4.61	4.60	0.00
37	6.32	6.33	-0.01
38	7.03	7.03	0.00
39	6.48	6.47	0.01
40	7.24	7.24	0.00
41	7.11	7.11	0.00
42	5.54	5.55	0.00
43	-	-	-
44	0.77	0.76	0.00
45	1.53	1.54	-0.01
46	1.51	1.52	-0.01
47	0.86	0.86	0.00
48	0.80	0.80	0.00

[a] Acquired in methanol-d_4 at 500 MHz and calibrated to solvent signal at 3.31 ppm.
[b] Acquired in methanol-d_4 at 700 MHz and calibrated to solvent signal at 3.31 ppm.

Table S3.7: Additional NMR spectroscopic data of sorangicin P-796, acquired at 700 MHz

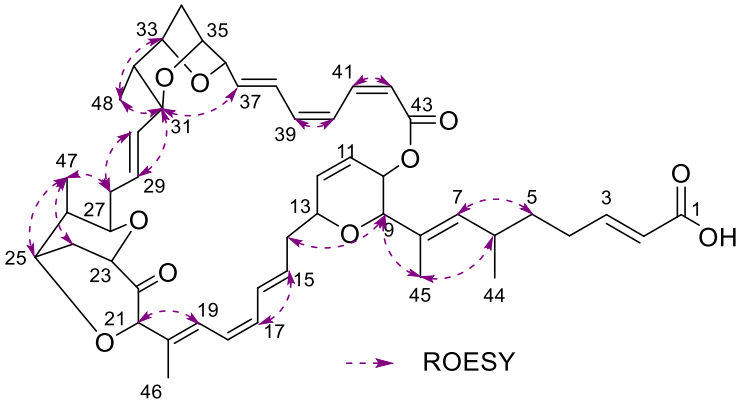

Position	δ_H[a] [ppm]	TOCSY[b]	ROESY[c]
1	-	-	-
2	5.74	3, 4, 5, 6, 7	4
3	6.77	2, 4, 5, 6, 7, 44	
4	2.03	2, 3, 5, 6, 7, 9, 44, 45	2
5a	1.52	2, 3, 4, 6, 7, 44	6
5b	1.13	2, 3, 4, 6, 7, 9, 44, 45	7
6	2.27	2, 3, 4, 5, 7, 9, 44, 45	5, 44, 45
7	5.18	2, 3, 4, 5, 6, 9, 44, 45	5, 44
8	-	-	-
9	4.11	4, 5, 6, 7, 10, 11, 12, 13, 44, 45	10, 14a, 45
10	5.42	9, 11, 12, 13, 14	9, 11, 45
11	6.09	9, 10, 12, 13, 14, 16	10
12	6.16	9, 10, 11, 13, 14, 15	13, 14a, 14b
13	4.55	9, 10, 11, 12, 14, 15, 16, 17, 18, 19	12, 14b, 15
14a	2.50	11, 12, 13, 15, 16, 17, 18, 19	9, 12, 15
14b	2.29	10, 11, 12, 13, 15, 16, 17, 18, 19	13, 16
15	5.89	12, 13, 14, 16, 17, 18, 19, 46	13, 14a, 17
16	6.16	11, 13, 14, 15, 17, 18, 19, 46	14b
17	6.36	13, 14, 15, 16, 18, 19, 46	15
18	6.32	13, 14, 15, 16, 17, 19, 46	-
19	6.28	13, 14, 15, 16, 17, 18, 46	21
20	-	-	-
21	5.11	-	19
22	-	-	-
23	4.21	24, 25, 27, 29	24
24a	1.77	23, 25, 27	23, 25
24b	1.71	23, 25, 27	25, 47
25	3.87	23, 24, 26, 29, 30, 47	24, 26, 47
26	1.58	25, 27, 47	25, 27, 28, 47
27	3.89	23, 24, 26, 28, 29, 30, 31, 47, 48	26, 28
28	2.33	27, 29, 30, 31, 48	26, 27, 30, 47
29	5.37	23, 25, 27, 28, 31, 32, 48	31
30	5.40	25, 27, 28, 31, 32, 48	28
31	3.85	27, 28, 29, 30, 32, 48	29, 37, 48
32	1.38	29, 30, 31, 33, 48	33, 34, 48
33	4.31	32, 34, 35, 36	32, 34, 48
34a	2.02	33, 35, 36	33, 35, 36
34b	1.92	33, 35, 36	32, 33, 35
35	4.40	33, 34, 36, 37, 38, 39	34, 36
36	4.60	33, 34, 35, 37, 38, 39, 40, 41, 42	34, 35, 37
37	6.33	35, 36, 38, 39, 40, 41, 42	31, 36
38	7.03	35, 36, 37, 39, 40, 41, 42	
39	6.47	35, 36, 37, 38, 40, 41, 42	40
40	7.24	36, 37, 38, 39, 41, 42	39
41	7.11	36, 37, 38, 39, 40, 42	42
42	5.55	36, 37, 38, 39, 40, 41	41
43	-	-	-
44	0.76	3, 4, 5, 6, 7, 9, 45	6, 7, 45

45	1.54	4, 5, 6, 7, 9, 44	6, 9, 10, 44
46	1.52	15, 16, 17, 18, 19	-
47	0.86	25, 26, 27	24, 25, 26, 28, 29, 30
48	0.80	27, 28, 29, 30, 31, 32	31, 32, 33

[a] Acquired in methanol-d_4 at 700 MHz and calibrated to solvent signal at 3.31 ppm.
[b] Proton showing TOCSY correlations to indicated proton.
[c] Proton showing ROESY correlations to indicated proton.

Table S3.8: Comparison of ^{13}C NMR signals of sorangicin P-796 and sorangicin A

Position	δ_C[a] [ppm] sorangicin P-796	Position	δ_C[b] [ppm] sorangicin A	Δ ($\delta_{C\ sorangicin\ P\text{-}796}$ - $\delta_{C\ sorangicin\ A}$)
1	170.4	1	177.9	-7.4
2	123.4	2	35.3	88.1
3	151.5	3	26.3	125.3
4	31.4	4	28.2	3.2
5	37.5	5	38.5	-1.0
6	32.0	6	33.0	-1.0
7	133.1	7	134.2	-1.1
8	130.8	8	131.2	-0.5
9	73.8	9	74.4	-0.6
10	66.0	10	66.9	-0.9
11	124.5	11	123.8	0.7
12	137.1	12	136.9	0.2
13	75.0	13	75.3	-0.3
14	36.1	14	35.5	0.6
15	134.8	15	128.3	6.4
16	134.5	16	133.6	0.9
17	136.0	17	33.4	102.6
18	127.7	18	34.0	93.7
19	133.1	19	134.4	-1.2
20	134.4	20	130.2	4.3
21	81.4	21	74.4	7.0
22	210.3	22	77.8	132.5
23	76.6	23	75.1	1.6
24	30.1	24	30.9	-0.7
25	70.3	25	71.1	-0.8
26	37.3	26	38.5	-1.2
27	75.5	27	74.9	0.6
28	36.6	28	37.1	-0.5
29	130.5	29	133.0	-2.5
30	134.0	30	132.8	1.2
31	81.2	31	81.2	0.0
32	42.1	32	42.2	-0.1
33	81.3	33	81.0	0.3
34	39.6	34	39.9	-0.2
35	77.7	35	77.6	0.1
36	81.6	36	82.3	-0.7
37	136.0	37	134.9	1.1

38	128.1	38	127.8	0.2
39	138.0	39	137.6	0.5
40	127.3	40	127.0	0.4
41	139.6	41	139.1	0.5
42	120.0	42	119.7	0.3
43	168.1	43	167.7	0.4
44	22.3	44	21.7	0.7
45	15.0	45	14.3	0.7
46	11.7	-	-	-
47	10.7	46	10.9	-0.2
48	15.6	47	15.4	0.3

[a] Acquired in methanol-d_4 at 125 MHz and calibrated to solvent signal at 49.2 ppm.
[b] Shifts retrieved from Jansen *et al*[3].

Table S3.9: Comparison of ^{1}H NMR signals of sorangicin P-796 and sorangicin A

Position	δ_H[a] [ppm] sorangicin P-796	Position	δ_H[b] [ppm] sorangicin A	Δ ($\delta_{H\ sorangicin\ P\text{-}796}$ – $\delta_{H\ sorangicin\ A}$)
1	-	1	-	-
2	5.71	2	2.3	3.41
3	6.83	3	1.62	5.21
4a	2.06	4a	1.36	0.70
4b	2.06	4b	1.3	0.76
5a	1.54	5a	1.42	0.12
5b	1.12	5b	1.25	-0.13
6	2.24	6	2.43	-0.19
7	5.17	7	5.34	-0.17
8	-	8	-	-
9	4.11	9	4.28	-0.18
10	5.43	10	5.35	0.08
11	6.09	11	6.05	0.04
12	6.17	12	6.17	0.00
13	4.55	13	4.43	0.12
14a	2.51	14a	2.43	0.08
14b	2.30	14b	2.17	0.13
15	5.90	15	5.58	0.32
16	6.16	16	5.58	0.58
17	6.37	-	-	-
18	6.30	-	-	-
-	-	17a	2.24	-
-	-	17b	2.14	-
-	-	18a	2.24	-
-	-	18b	2.17	-
19	6.29	19	5.79	0.50
20	-	20	5.64	-
21	5.12	21	4.19	0.93
22	-	22	3.52	-
23	4.20	23	3.73	0.47

24a	1.77	24a	1.76	0.01
24b	1.70	24b	1.7	0.00
25	3.87	25	3.87	0.00
26	1.58	26	1.59	-0.01
27	3.89	27	3.89	0.00
28a	2.33	28a	2.32	0.01
28b	2.33	28b	2.17	0.16
29	5.34	29	5.54	-0.20
30	5.38	30	5.42	-0.04
31	3.84	31	3.87	-0.03
32	1.38	32	1.46	-0.08
33	4.31	33	4.32	-0.01
34a	2.03	34a	2.09	-0.06
34b	1.92	34b	1.97	-0.05
35	4.40	35	4.45	-0.05
36	4.61	36	4.61	0.00
37	6.32	37	6.26	0.06
38	7.03	38	7.03	0.00
39	6.48	39	6.48	0.00
40	7.24	40	7.24	0.00
41	7.11	41	7.19	-0.08
42	5.54	42	5.66	-0.12
43	-	43	-	-
44	0.77	44	0.93	-0.17
45	1.53	45	1.68	-0.15
46	1.51	-	-	-
47	0.86	46	0.93	-0.07
48	0.80	47	0.86	-0.06

[a] Acquired in methanol-d_4 at 500 MHz and calibrated to solvent signal at 3.31 ppm.
[b] Shifts retrieved from Jansen *et al*[3].

Analysis of the sorangicin P BGC

The first half of the putative *sra* BGC in the genome was identified with antiSMASH[5], the remaining genes were deduced from the sequence, based on the genetic architecture. Genes in the vicinity of the biosynthetic machinery were used as templates for local BLAST searches against the genomes of closely related MSr11367 and Msr11368 in Geneious prime 2022.2.2 to deduce the borders of the putative *sra*BGC. Both genomes have genes with high similarities to the genes *sra*_-3 to *sra*_-1 upstream and *sra*_+1 to *sra*_+4 downstream the putative *sra*BGC in the same succession as in the genome of MSr12523 but do not contain the 18 genes of the putative *sra*BGC (Table S 3.10). The coding sequences of the putative *sra*BGC were extracted from the MSr12523 genome (ctg1_3420-ctg1_37), translated and searched with the blastp algorithm against the RefSeq non-redundant protein sequence database at NCBI (Table S 3.11).

Table S3.10: Flanking genes of the putative *sra*BGC in the genome of MSr12523 and similar genes in the genomes of MSr11367 and MSr11368

	Corresponding gene in MSr 11367: identity [%] and query coverage [%]	Corresponding gene in MSr 11368: identity [%] and query coverage [%]
Sra_-3	95,2; 100	95.2; 100
Sra_-2	87.9; 100	87.9; 100
Sra_-1	92.6; 100	92.6; 100
Sra_+1	74.8; 99	74.8; 99
Sra_+2	83.3; 100	83.3; 100
Sra_+3	86.3; 100	86.3; 100
Sra_+4	87.1; 100	87.1; 100

Table S3.11: Blastp results of the CDS regions in the *sra*BGC

CDS Name	Length [AA]	Closest homologue [Organism of origin]	Identity [%] and query coverage [%]	Accession Nr.
sraA	271	class I SAM-dependent methyltransferase [Amycolatopsis azurea]	46.9; 95	WP_005166209.1
sraB	456	SorN [Sorangium cellulosum]	79.9; 99	ADN68488.1
sraC	642	SorO [Sorangium cellulosum]	72.4; 99	ADN68489.1
sraD	483	SorP [Sorangium cellulosum]	67.2; 97	ADN68490.1
sraE	84	acyl carrier protein [Xenorhabdus sp. PB62.4]	54.6; 91	WP_222942851.1
sraF	656	SorQ [Sorangium cellulosum]	79.2; 98	ADN68491.1
sraG	8747	too big to be analysed		
sraH	4728	SorB [Sorangium cellulosum]	66.0; 99	ADN68477.1
sraI	4836	SorA [Sorangium cellulosum]	55.8; 98	ADN68476.1
sraJ	4975	SorE [Sorangium cellulosum]	68.0; 99	ADN68480.1
sraK	430	SorF [Sorangium cellulosum]	61.8; 97	ADN68481.1
sraL	6155	SorH [Sorangium cellulosum]	69.8; 93	ADN68483.1
sraM	2452	SorI [Sorangium cellulosum]	67.2; 99	ADN68484.1
sraN	382	SorR [Sorangium cellulosum]	87.4; 99	ADN68492.1
sraO	407	SorK [Sorangium cellulosum]	76.5; 100	ADN68486.1
sraP	403	SorS [Sorangium cellulosum]	80.0; 98	ADN68493.1
sraQ	768	glycoside hydrolase family 3 C-terminal domain-containing protein [Paraburkholderia saeva]	67.2; 99	WP_228937976.1
		SorL [Sorangium cellulosum]	72.4; 89	ADN68487.1
sraR	546	protein kinase [Myxococcales bacterium]	47.1: 52	MCA9642025.1

Table S3.12: Analysis of domains in the *sra*BGC in MSr12523. Substrate specificities of acyl-transferase (AT) domains are based on antiSMASH[5] predictions and fingerprint comparison of AT domains in the *sor*BGC[6]. Analysis of the ketosynthase (KS) domains was done based on phylogenie with the transATor tool[7] and clades with the highest score were listed. In case of the KS domains in modules 2 and 15, the prediction with the second highest score was also listed, as it was in line with the observed structure. The stereochemistry predictions for the dehydratase (DH) domains are based on the orientation of the respective hydroxy-group[8]. The listed stereochemistries for the ketoreductase (KR) domains are based on antiSMASH[5] predictions. Activities of all domains were evaluated based on reported fingerprints of active sites[8,9]. Additional modules and different KS types, compared to the ones in the *sor*BGC are marked bold.

Gene	Module	Domain	Characterisation/comment
SraC	Trans-AT	AT_a	Malonyl-CoA; Hydroxy-malonyl-CoA
		AT_b	Malonyl-CoA
SraG	1	KS	Clade 8: unusual starter: AMT/succinate
		DH	E configured double bond
		KR	D configured hydroxy-group
		ACP	
	2	KS	Clade 25: completely reduced (Score 746.2) Clade 108: shifted double bonds (Score 701.1)
		DH	Stereochemistry unclear
		ACP_a	
		ACP_b	
	3	KS	Clade 74: α Me reduced/keto/D-OH
		DH	E configured double bond
		KR	D configured hydroxy-group
		MT	
		ACP	
	4	KS	Clade 113: double bonds (e-configured; (some with α Me)
		KR	L configured hydroxy-group
		ACP	
	5	KS	Clade 66: ß L-OH
		DH	E configured double bond
		KR	D configured hydroxy-group
		ACP	
	6	KS	**Clade 82: double bonds (mostly e-configured)**
		KR	D configured hydroxy-group
		ACP	
	7	KS[a]	Clade 31: non-elongating (bimodule ß D-OH)
SraH		DH_a[b]	Catalytic triad incomplete[c]
		ACP	
		DH_b[b]	Catalytic triad incomplete[c]
	8	KS[a]	Clade 76: non-elongating (double bonds)
		PS	
		ACP	
	9	KS	Clade 26: pyran/furan rings
		DH	Stereochemistry unclear
		ACP	
	10	KS	Clade 82: double bonds (mostly e-configured)
		DH	E configured double bond
		KR	D configured hydroxy-group
		ACP	
SarI	11	KS	Clade 25: completely reduced
		DH	E configured double bond
		KR	D configured hydroxy-group
		MT	
		ACP	
	12	KS	Clade 113: double bonds (e-configured; (some with α Me))
		KR	L configured hydroxy-group
		ACP	
	13	KS	**Clade 66: ß L-OH**
		KR	L configured hydroxy-group

		ACP	
	14	KS	Clade 66: ß L-OH
		KR	L configured hydroxy-group
		MT	
		ACP	
	15	KS	Clade 74: α Me reduced/keto/D-OH (Score 710.6) Clade_68 α L-OH/Me β D-OH (Score 645.4)
		DH	
		PS	
		KR	D configured hydroxy-group
SarJ		ACP	
	16	KS	Clade 26: pyran/furan rings
		DH	E configured double bond
		KR	D configured hydroxy-group
		ACP	
	17	KS	Clade 82: double bonds (mostly e-configured)
		DH	Z configured double bond
		KR	L configured hydroxy-group
		MT	
		ACP	
	18	KS	Clade_68 α L-OH/Me β D-OH
		ACP	
	19	KS	Clade 103: ß OMe
		DH	
		PS	
		KR	D configured hydroxy-group
SarL		ACP	
	20	KS	Clade 26: pyran/furan rings
		DH	E configured double bond
		KR	D configured hydroxy-group
		ACP	
	21	KS	Clade 82: double bonds (mostly e-configured)
		KR	L configured hydroxy-group
		ACP	
	22	KS[a]	Clade 31: non-elongating (bimodule ß D-OH)
		DH	Z configured double bond
		ACP	
	23	KS	Clade 82: double bonds (mostly e-configured)
		DH	Z configured double bond
SarM		KR	L configured hydroxy-group
		ACP	
		KS[a]	Clade 76: non-elongating (double bonds)
		DH	Inactive, catalytic triad missing[c]

[a] KS domains have an incomplete CHH catalytic triad and are therefore inactive.
[b] Both DH domains in module 7 miss the catalytic triad in the characteristic HxxxGxxxxP motif, but are highly similar to the respective DH domains in the *sor*BGC[6].
[c] DH domains miss the catalytic triad in the characteristic HxxxGxxxxP motif.

NMR spectra employed in structure elucidation

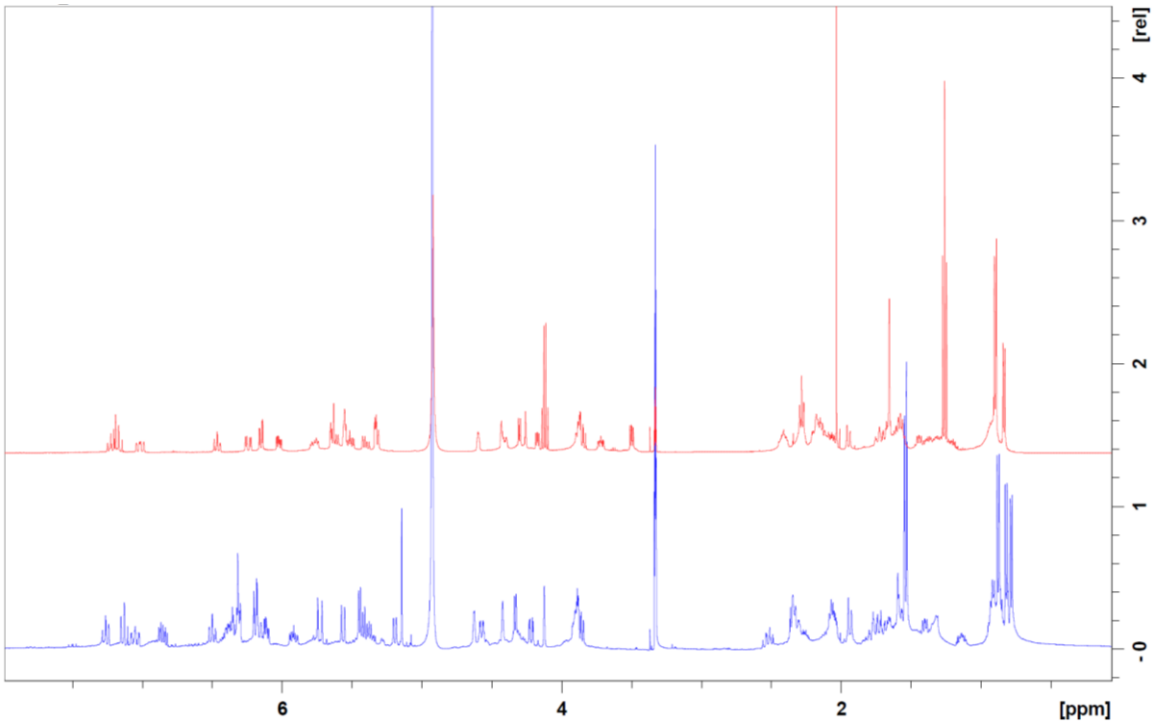

Figure S 3.5: Comparison of ^{1}H NMR spectra of sorangicin A (2, red) and sorangicin P-796 (1, blue) in methanol-d_4 at 500 MHz.

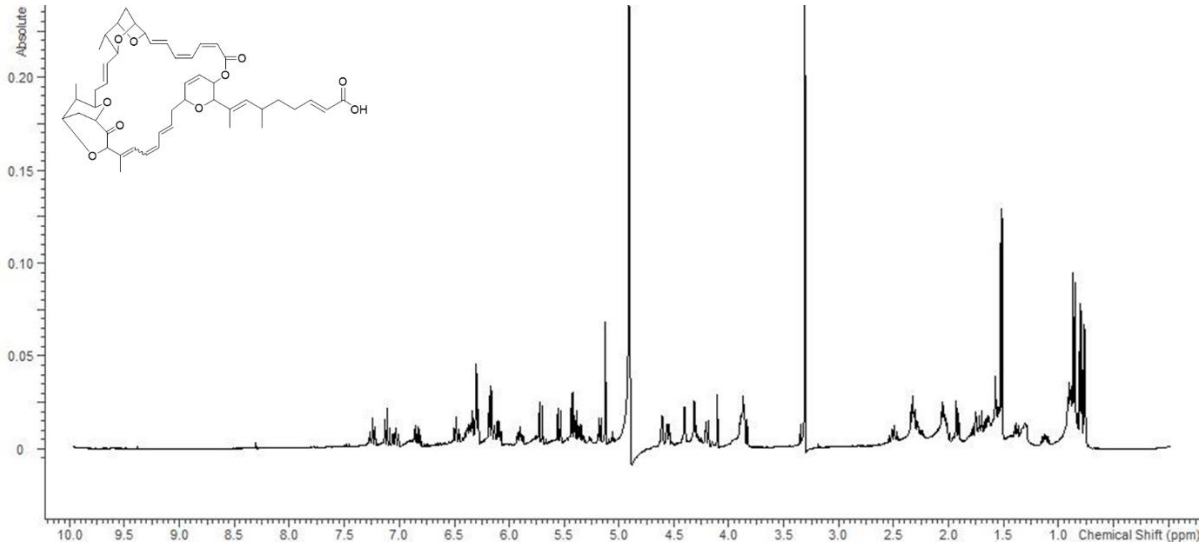

Figure S3.6: ^{1}H spectrum of sorangicin P-796 in methanol-d_4 at 500 MHz.

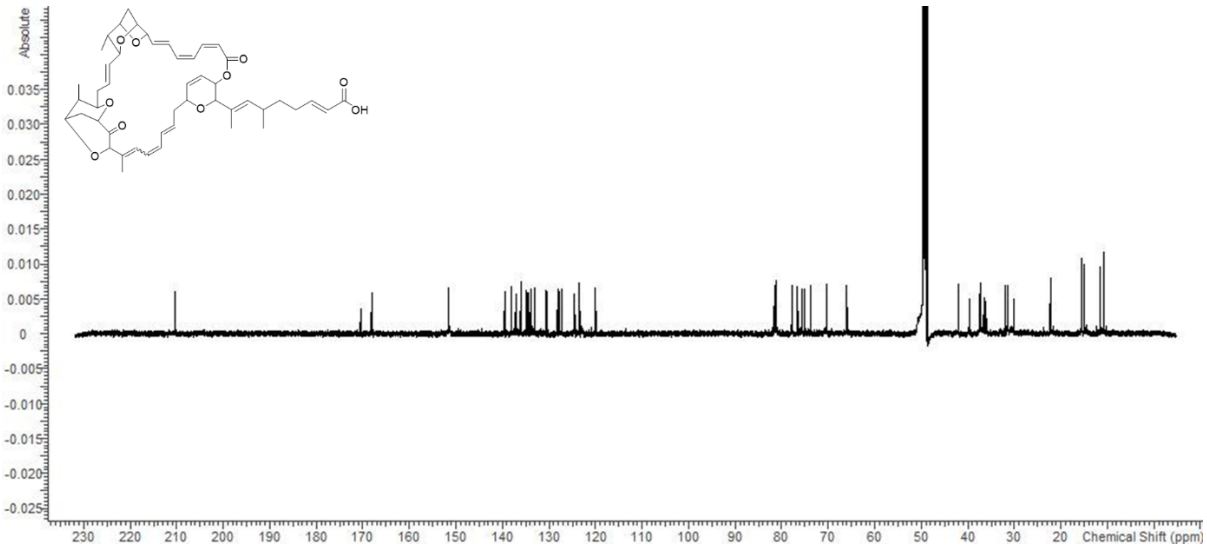

Figure S3.7: ^{13}C spectrum of sorangicin P-796 in methanol-d_4 at 125 MHz.

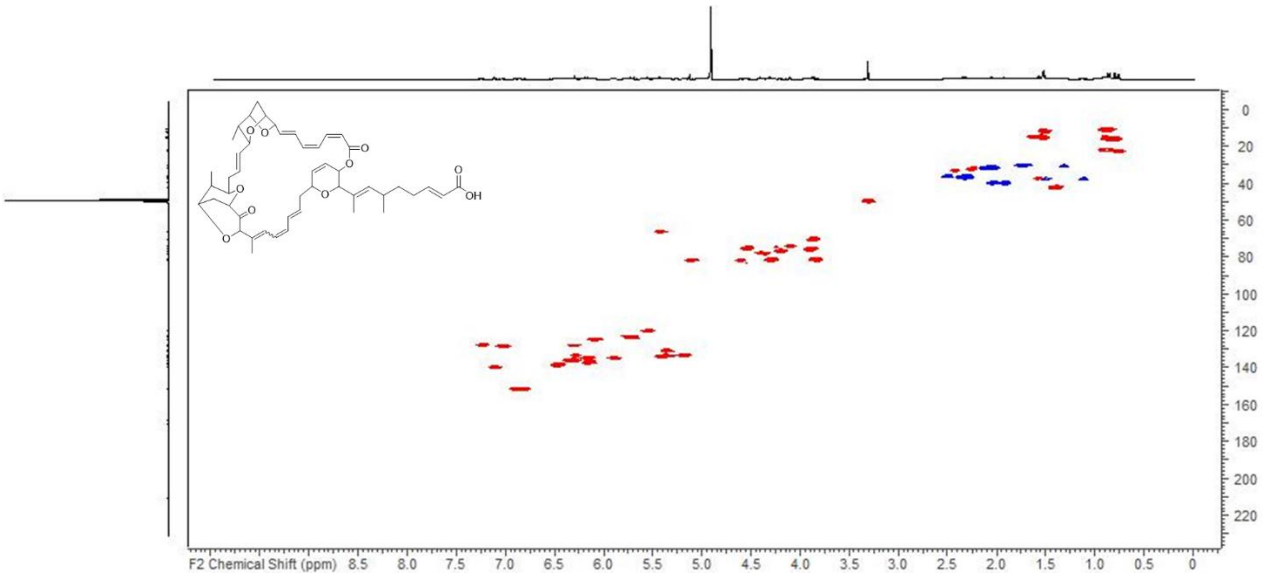

Figure S3.8: HSQC spectrum of sorangicin P-796 in methanol-d_4 at 125/500 (F1/F2) MHz.

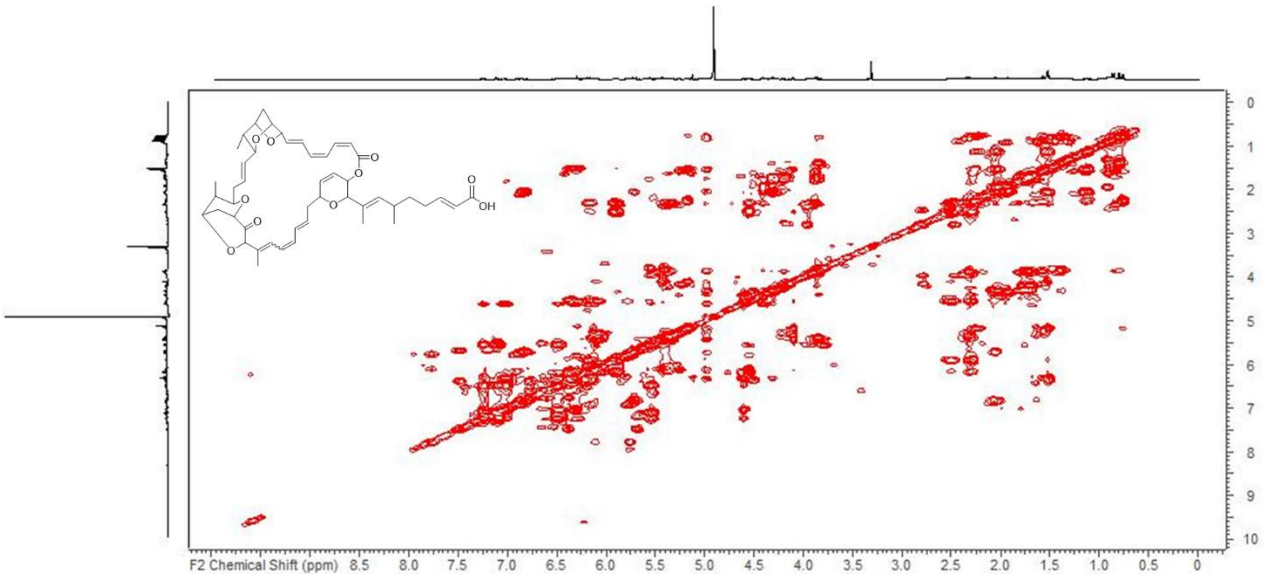

Figure S3.9: COSY spectrum of sorangicin P-796 in methanol-d_4 at 500 MHz.

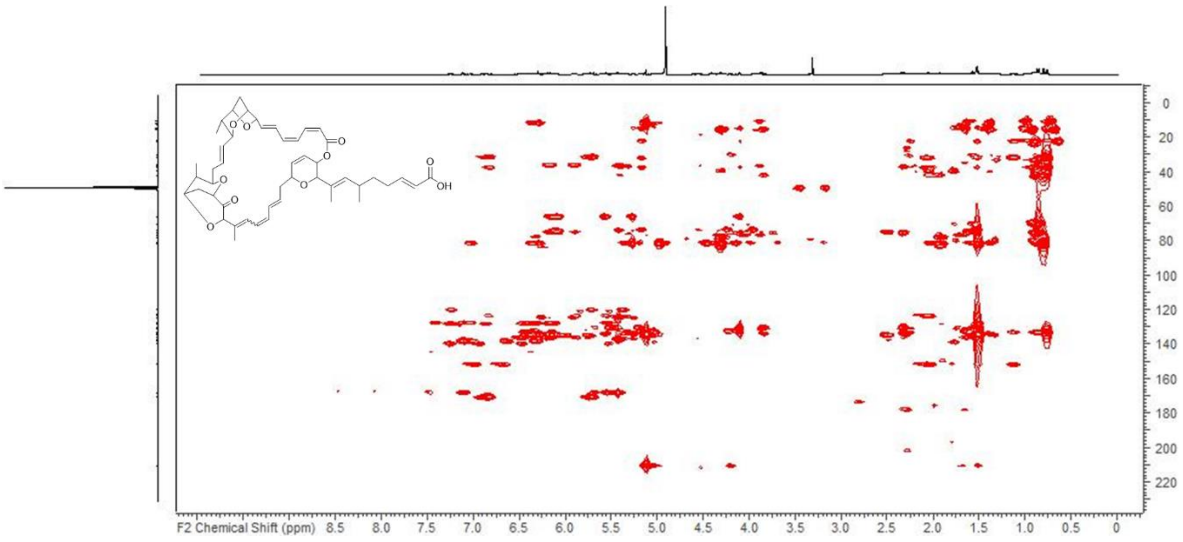

Figure S3.10: HMBC spectrum of sorangicin P-796 in methanol-d_4 at 125/500 (F1/F2) MHz.

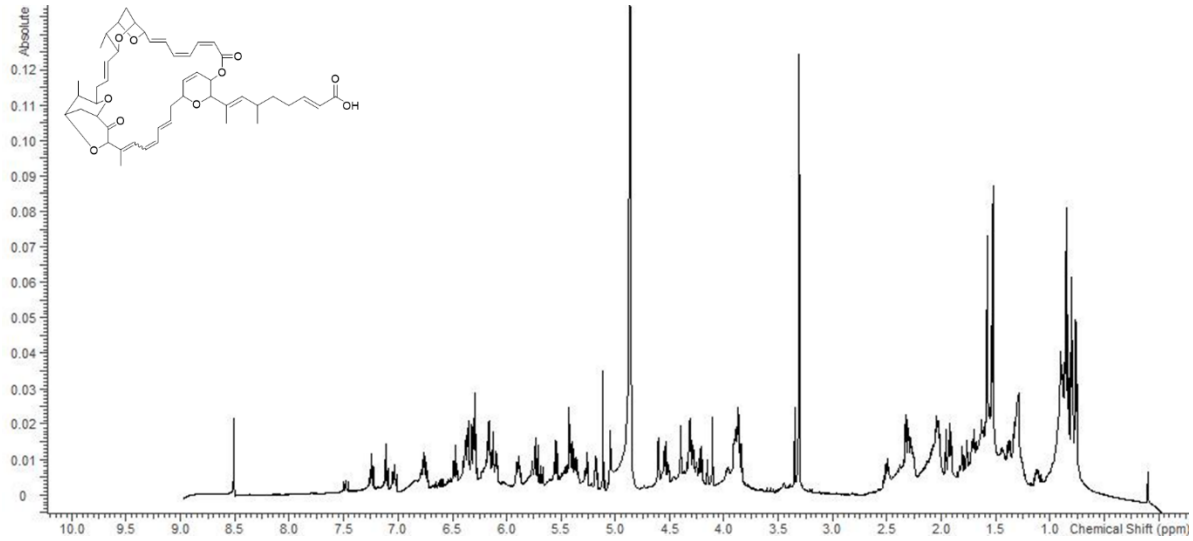

Figure S3.11: ^{1}H spectrum of sorangicin P-796 in methanol-d_4 at 700 MHz.

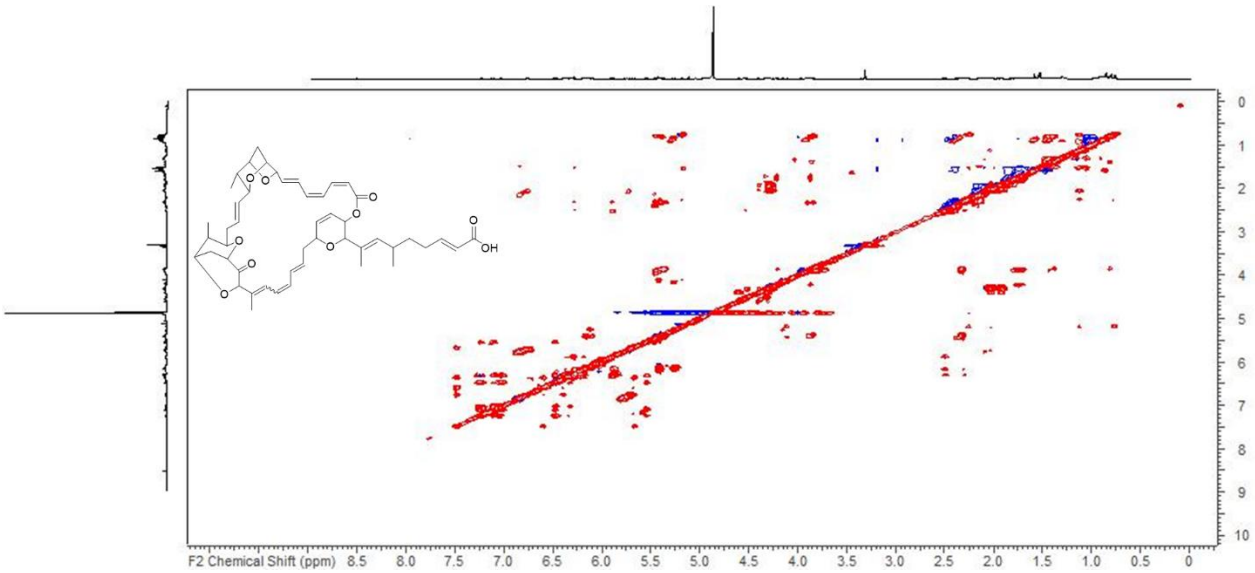

Figure S3.12: TOCSY spectrum of sorangicin P-796 in methanol-d_4 at 700 MHz.

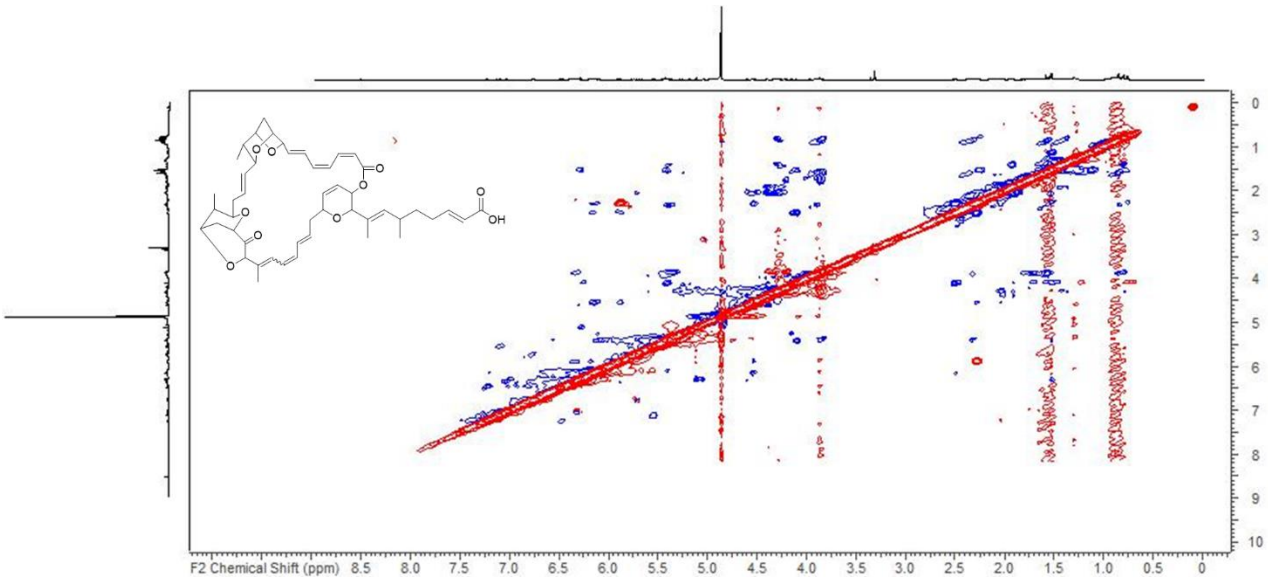

Figure S3.13: ROESY spectrum of sorangicin P-796 in methanol-d_4 at 700 MHz.

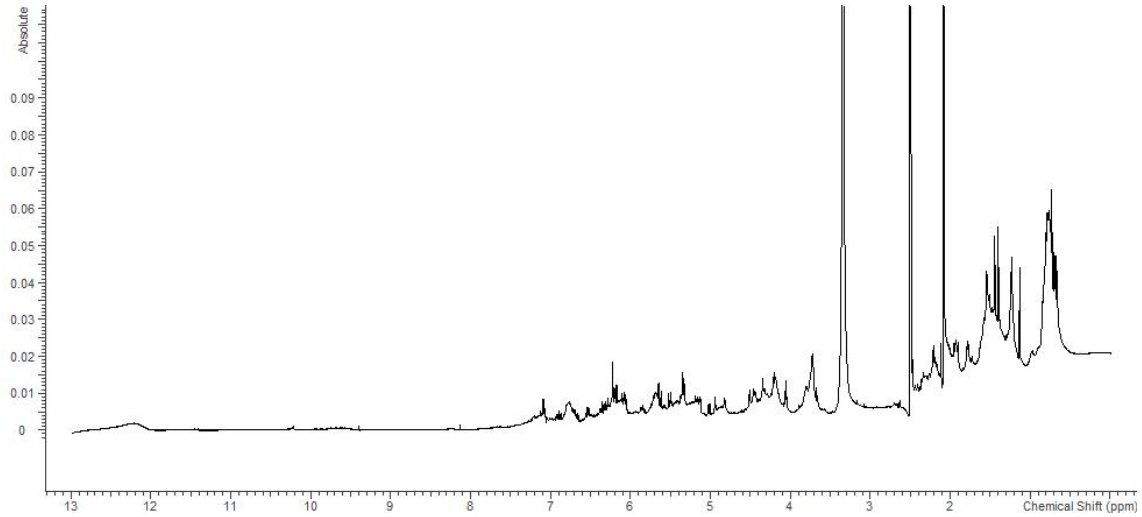

Figure S3.14: ^{1}H spectrum of sorangicin P-796 in DMSO-d_6 at 500 MHz.

References

1. Hoffmann, T., Krug, D., Hüttel, S. & Müller, R. Improving natural products identification through targeted LC-MS/MS in an untargeted secondary metabolomics workflow. *Analytical chemistry* **86,** 10780–10788; 10.1021/ac502805w (2014).
2. Wang, M. *et al.* Sharing and community curation of mass spectrometry data with Global Natural Products Social Molecular Networking. *Nat. Biotechnol.* **34,** 828–837; 10.1038/nbt.3597 (2016).
3. Jansen, R., Wray, V., Irschik, H., Reichenbach, H. & Höfle, G. Isolation and spectroscopic structure elucidation of sorangicin A, a new type of macrolide-polyether antibiotic from gliding bacteria - XXX. *Tetrahedron Lett.* **26** (1985).
4. Jansen, R. *et al.* Antibiotika aus Gleitenden Bakterien, XXXVII. Sorangicin A, ein hochwirksames Antibiotikum mit neuartiger Makrolid-Polyether-Struktur aus *Sorangium cellulosum*, So ce12: Spektroskopische Strukturaufklärung, Kristall- und Lösungsstruktur. *Liebigs Ann. Chem.* **1989,** 111–119; 10.1002/jlac.198919890124 (1989).
5. Blin, K. *et al.* antiSMASH 6.0: improving cluster detection and comparison capabilities. *Nucleic Acids Res.* **49,** W29-W35; 10.1093/nar/gkab335 (2021).
6. Irschik, H. *et al.* Analysis of the sorangicin gene cluster reinforces the utility of a combined phylogenetic/retrobiosynthetic analysis for deciphering natural product assembly by trans-AT PKS. *Chembiochem : a European journal of chemical biology* **11,** 1840–1849; 10.1002/cbic.201000313 (2010).
7. Helfrich, E. J. N. *et al.* Automated structure prediction of *trans*-acyltransferase polyketide synthase products. *Nat. Chem. Biol.* **15,** 813–821; 10.1038/s41589-019-0313-7 (2019).
8. Keatinge-Clay, A. T. The structures of type I polyketide synthases. *Nat. Prod. Rep.* **29,** 1050–1073; 10.1039/c2np20019h (2012).
9. Wagner, D. T. *et al.* Structural and Functional Studies of a Pyran Synthase Domain from a trans-Acyltransferase Assembly Line. *ACS Chem. Biol.* **13,** 975–983; 10.1021/acschembio.8b00049 (2018).

4 Chapter: Co-cultivation

Co-cultivation of MSr12523 with *Tsukamurella* Strains Upregulates Production of Antitubercular Compound Families

Sebastian Walesch*, Markus Neuber*, Chantal D. Bader, Daniel Krug, Rolf Müller

Manuscript in preparation

Contributions to the presented work

Author's effort

The author contributed to the concept of this study, planned and executed experiments, evaluated and interpreted resulting data. The author performed comparative cultivations of MSr12523 in different media and purified all macrocyclic thuggacin P derivatives. Furthermore, he is responsible for the NMR-based structure elucidation of all thuggacin P derivatives as well as most myxenolone derivatives. The author also did the *in silico* descriptions of both biosynthetic gene clusters as well as the resulting biosynthetic models. Moreover, he evaluated the data of detoxification experiments of thuggacin P derivatives with *Tsukamurella pseudospumae*. In addition, the author contributed to the conception and writing of this manuscript.

Contributions by others

Markus Neuber contributed to the concept of this study, planned and executed experiments, evaluated and interpreted resulting data. Furthermore, he developed and performed co-cultivation experiments and analysed the corresponding LC-MS data using statistical methods and molecular networks. In the course of this, Markus Neuber identified and purified the myxenolone compound family as well as the non-cyclised thuggacin P derivatives, which were not present in axenic cultures. Moreover, he performed the detoxification experiments of thuggacin P derivatives with *Tsukamurella pseudospumae*. Chantal Bader performed the NMR-based structure elucidation of myxenolone D1. Daniel Krug and Rolf Müller contributed by supervision of the project and conceiving, editing and proofreading of this manuscript.

4.1 Abstract

Over the past decades, myxobacteria have proven to be a valuable source of novel and biologically active natural product scaffolds. Considering the exceptionally large genomes of myxobacteria, harbouring numerous biosynthetic gene clusters (BGCs), the currently known natural products merely scratch the surface of their vast biosynthetic capabilities. In order to access this potential, the myxobacterium MSr12523 was co-cultivated with several mycolic acid containing bacteria (MACB), leading to the observation and subsequent purification of two natural product families. The resulting myxenolone class and novel thuggacin P subclass were structurally characterised by comprehensive *hr*MS and NMR spectroscopy. Based on detailed *in silico* analyses of both putative BGCs, biosynthetic models were created, explaining the biosyntheses of the myxenolone and thuggacin P natural products. Several myxenolone and thuggacin P derivatives displayed promising antibiotic activity against *Mycobacterium tuberculosis* 7H37Ra. In addition to that, the MACB *Tsukamurella pseudospumae* displayed a remarkable resistance mechanism by hydrolysing the macrolactone ring of thuggacin P derivatives, leading to ring-opened thuggacin P derivatives that did not display anti-mycobacterial activity.

4.2 Introduction

In 2021, tuberculosis alone caused approximately 1.6 million deaths, highlighting the constant need of novel antibiotics against the causing pathogen *Mycobacterium tuberculosis*[1]. Within the past decade, the approval of several new antibiotic scaffolds has broadened the arsenal to treat infections with *M. tuberculosis* and the current clinical pipeline holds the promise of further treatment options in the future. Nevertheless, the progressing resistance development of *M. tuberculosis* strains against applied antibiotics and the lengthy treatment with multiple drugs emphasise the importance of an ongoing discovery and development of novel antibiotic classes[2–4].

Natural products from microorganisms are a promising source for new antibiotic scaffolds; more than two thirds of approved antibiotics are natural products or derivatives thereof[5,6]. Historically, the majority of biologically active compound classes was purified from the bacterial phylum of Actinomycetes, but also Gram-negative proteobacteria displayed great potential for the discovery of novel biologically active scaffolds[6,7]. For example, myxobacteria have shown their capability to produce natural products that cover a wide array of chemical scaffolds as well as biological activities[8–10]. Moreover, their large genomes, harbouring a high number of, often unassigned, biosynthetic gene

clusters (BGCs) make them a promising source for the search of new and bioactive natural products[8,10–13].

A major bottleneck in natural products research is that most microorganisms only seem to produce natural products that account for not more than 10% of their BGCs in routine laboratory cultivation settings[14]. Various approaches to access the other, so-called cryptic, BGCs have been successfully applied in the past years, displaying the untapped potential of new and known microorganisms[6,15,16].

Given the high diversity and abundance that microorganisms encounter in their natural habitat, co-cultivation of two or more microorganisms seems to be the most obvious approach to access their metabolomes[17–19]. Consequently, this approach has led to the discovery of many new and bioactive natural products, as evidenced by the antibiotics rhodostreptomycins[20], keyicin[21] and amycomycin[22]. In previous co-cultivation settings, myxobacteria have shown their ability to enhance the production of bioactive natural products in Actinomycetes[23,24]. Furthermore, a recently reported study displayed the effect of several partner microorganisms on the metabolome of *Myxococcus xanthus* DK1622 and led to the observation of a compound class, previously not associated with myxobacteria[25].

The choice of partner organism is crucial for the success of any co-cultivation approach, but it seems like that some bacterial phyla are better suited for modulating their partners metabolomes. A prominent example are mycolic acid containing bacteria (MACB), belonging to the order *Corynebacteriales*[26]. Several phylogenetically distinct representatives of this phylum were able to alter the metabolomes of almost 90% of *Streptomyces* strains in a co-cultivation screen[27]. Co-cultivations of MACB with different *Streptomyces* strains led to the discoveries of several new antibiotic families[27–29]. Furthermore, their potential value as partner strains might not be restricted to the genus *Streptomyces*, as co-cultivation of a MACB with *Actinosynnema mirum* resulted in the production of several new derivatives of a known antibiotic class[30].

This study describes the successful co-cultivation of the novel myxobacterium MSr12523 with several MACB, leading to increased bioactivities of the resulting extracts against *Mycobacterium smegmatis* mc^{2}155 as well as obvious changes in the metabolome. Subsequent purification of newly detected and upregulated metabolites led to the discovery and description of the new myxenolone compound family and a new subclass of the thuggacin antibiotics. Furthermore, this study covers *in silico* biosynthetic models for both described compound families, their antibiotic activities against *M. tuberculosis,* and provides insights into a putative resistance mechanism of the partner strain *Tsukamurella pseudospumae* against derivatives of the new thuggacin P subclass.

4.3 Results and discussion

4.3.1 Co-cultivation experiments of MSr12523 with MACB awaken interest in two compound families

The myxobacterium MSr12523 is part of a new genus or family within the suborder *Sorangiineae* (Chapter 3). Its distinct phylogenetic position as well as its large genome with approximately 60 (BGCs) make it a promising source for novel and potentially bioactive natural products.

In an effort to find novel antibiotics against *M. tuberculosis*, a direct co-cultivation approach of MSr12523 with MACB *Corynebacterium glutamicum*, *Rhodococcus erythropolis*, *T. pseudospumae* and *T. soli* was established[25]. The resulting crude extracts were evaluated for their antibiotic activity against *M. smegmatis* mc^2155 as surrogate for the tuberculosis-causing pathogen. As co-cultivation extracts of MSr12523 with both *Tsukamurella* strains displayed strongly improved activities against *M. smegmatis* mc^2155, they were analysed for metabolome-wide changes[25]. This analysis displayed the impact of both partner strains on the metabolism of MSr12523, with approximately 25% additionaly detected metabolites in co-cultivation extracts with *T. soli* and even over 36% newly detected metabolites after co-cultivation with *T. pseudospumae*[25].

Among the newly observed metabolites in co-cultivation extracts of MSr12523 with *T. pseudospumae*, representatives of two MS/MS-fragment based molecular networks were prioritised for further analysis, based on their abundance in these extracts. The first molecular network consists of a group of compounds in the mass range of 250-350 Da and was observed only in co-cultivation extracts (Figure 4.1 A). In contrast to that, the second molecular network is a mixture of compounds that are produced in axenic and co-cultivations and of compounds that are exclusive to co-cultivation extracts (Figure 4.1 B)[25]. In a different study, MSr12523 was cultivated in a range of different media to evaluate the changes in its metabolome and bioactivity against *Escherichia coli* BW25113. Cultivation in RGSR medium led to an increased production of the metabolites with the *m/z* of 548.304 and 562.320, but none of the other compounds displayed in Figure 4.1 B were observed. Based on the standard dereplication workflow of all axenic and co-cultivation extracts of MSr12523 including a LC-MS feature-based (exact *m/z* and retention time) search against the in-house database "Myxobase"[31] and a GNPS-based analysis[32] of the respective LC-MS/MS data, those metabolites did not seem to belong to a reported chemical scaffold. However, in a later conducted GNPS analysis of an axenic MSr12523 extract alongside in-house generated LC-MS/MS data

of a number of purified myxobacterial natural products, they were identified as novel thuggacin derivatives, based on their similarity to thuggacin A, previously described from *Sorangium cellulosum* So ce895[33].

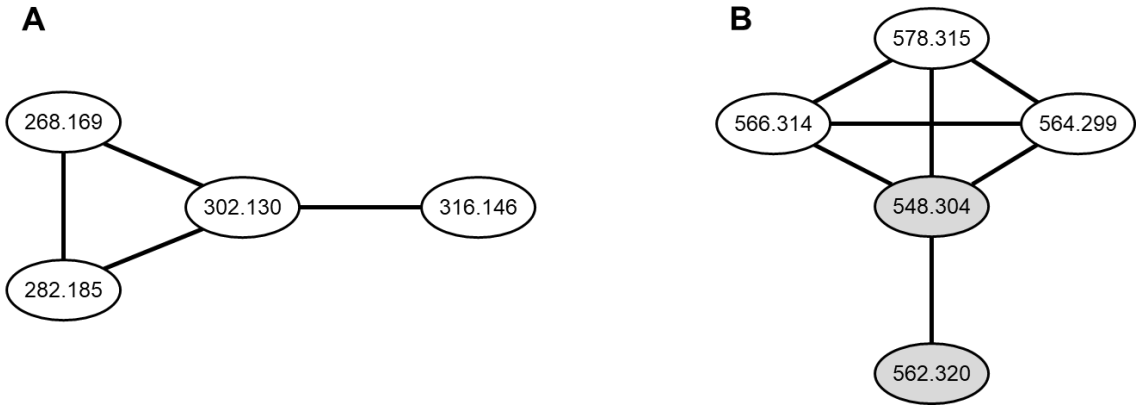

Figure 4.1:Molecular networks of prioritised and purified metabolites of the co-cultivation of MSr12523 with *T. pseudospumae*. (**A**) Molecular network of prioritised compounds, only observed in co-cultivation extracts. (**B**) Molecular network of the novel thuggacin P subclass, produced in axenic and co-cultivations (grey background) and derivatives, only observed in co-cultivation extracts (white background). Numbers indicate the recorded *m/z* values of the respective metabolites. (Adapted from Neuber, 2022).

During the upscaling and extraction process of co-cultures of MSr12523 with *T. pseudospumae*, *M. tuberculosis* 7H37Ra became available for in-house bioactivity screening. Therefore, a supercritical fluid extraction fraction (SFE with 20% MeOH as organic co-solvent), containing the most abundant representatives of both prioritised molecular networks[25], was tested for its activity against *M. tuberculosis* 7H37Ra. This fraction displayed a strong inhibitory effect against the tested pathogen with a MIC of 0.5 µg/mL, reinforcing the assumption that these metabolites display antibiotic activity against *M. tuberculosis*.

4.3.2 Purification and structure elucidation of myxenolones

The purification of the myxenolone compound family from co-cultures of MSr12523 with *T. pseudospumae* was done and described by Markus Neuber[25].

High-resolution electrospray-ionisation mass spectrometry (HRESI-MS) of myxenolone A shows a $[M+H]^+$ signal at *m/z* 268.1694 (calc. 268.1696, Δ = 0.75 ppm) that correspond to a molecular sum formula of $C_{18}H_{21}NO$ with nine double bond equivalents (DBEs). In seeming disagreement with this sum formula, the carbon NMR spectrum of myxenolone A consist of a total of 35 carbon signals. However, about half

of these carbon signals appear in pairs with a difference smaller than 0.2 ppm. Evaluation of the COSY and HMBC spectra revealed a mixture of two highly similar compounds, myxenolones A1 and A2 (**1** and **2**).

Myxenolone A1 (**1**) has a terminal methyl group ($\delta_{C\text{-}19}$ 14.5, $\delta_{H\text{-}19}$ 0.93) which is part of a pentyl-residue that is bound to an olefinic methine ($\delta_{C\text{-}14}$ 143.8, $\delta_{H\text{-}14}$ 6.18), as displayed by consecutive COSY-correlations within the chain between H-14 and H-19. Together with three further olefinic methines ($\delta_{C\text{-}13}$ 130.9, $\delta_{H\text{-}13}$ 6.34, $\delta_{C\text{-}12}$ 139.3, $\delta_{H\text{-}12}$ 7.28, $\delta_{C\text{-}11}$ 123.2, $\delta_{H\text{-}11}$ 6.38), C-14 forms two conjugated double bonds. As evidenced by coupling constants greater 15 Hz between H-11 and H-12 as well as H-13 and H-14 both double bonds display an *E* configuration.

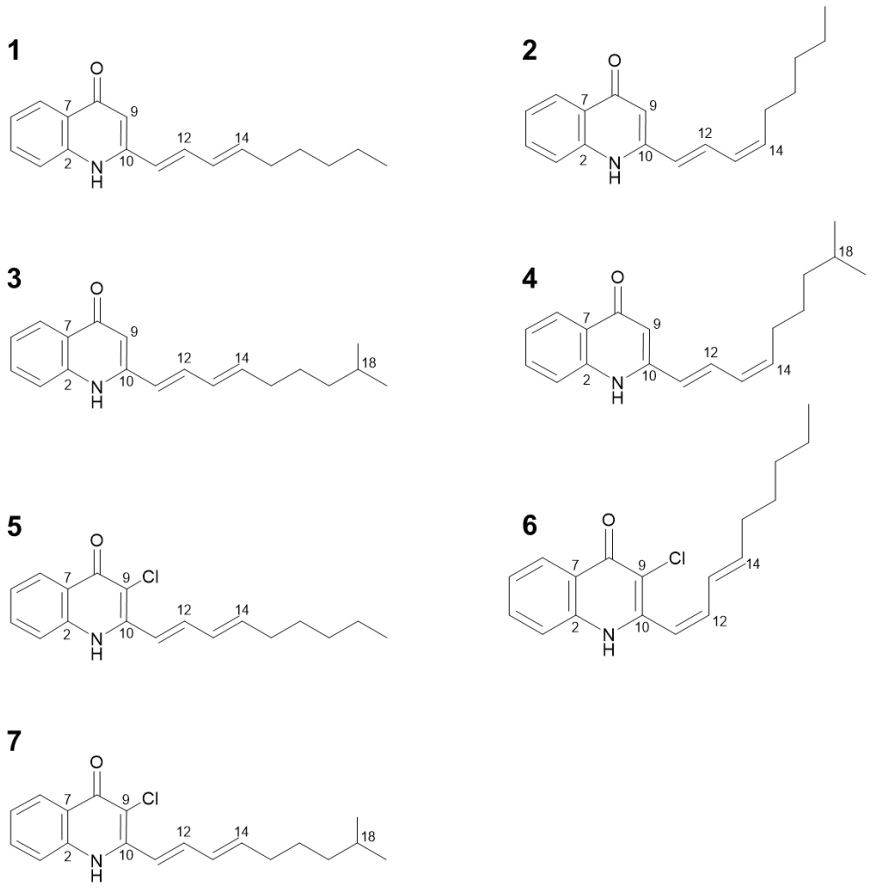

Figure 4.2: Structures of purified myxenolone derivatives A1 (1), A2 (2), B1 (3), B2 (4), C1 (5), C2 (6) and D1 (7).

The other part of **1** therefore distributes seven DBEs over C_9H_6NO, which could be explained by a quinolone-like ring system. The respective ^{1}H and ^{13}C NMR shifts indicate a 4-hydroxy-quinoline with a substitution at position 2[34,35]. The connection of the chain to the quinolone-core is shown through HMBC correlations of H-11 ($\delta_{H\text{-}11}$ 6.38) to the olefinic C-10 ($\delta_{C\text{-}10}$ 150.9) and reciprocal HMBC correlations with the neighbouring

olefinic methine ($\delta_{C\text{-}9}$ 106.9, $\delta_{H\text{-}9}$ 6.45). Further, HMBC correlations of H-9 ($\delta_{H\text{-}9}$ 6.45) to carbonyl C-8 ($\delta_{C\text{-}8}$ 180.5), aromatic C-7 ($\delta_{C\text{-}7}$ 126.1) and aromatic methine CH-6 ($\delta_{C\text{-}6}$ 126.0, $\delta_{H\text{-}6}$ 8.19) evidence its position to be next to the carbonyl.

Myxenolone A2 (**2**) only differs from (**1**) in the configuration of the double bond between olefinic methines CH-13 ($\delta_{C\text{-}13}$ 129.0, $\delta_{H\text{-}13}$ 6.27) and CH-14 ($\delta_{C\text{-}14}$ 140.7, $\delta_{H\text{-}14}$ 5.86). The *Z* configuration of this double bond is deduced by the respective coupling constants in the range of 10 to 11 Hz.

The HRESI-MS signal of the myxenolone B ion $[M+H]^+$ at *m/z* 282.1851 (calc. 282.1853, Δ = 0.71 ppm) corresponds to the molecular sum formula $C_{19}H_{23}NO$ that has an unsaturation degree of 9 DBEs. It differs from **1** and **2** as it displays a 4-methyl-pentyl-residue instead of the pentyl-residue. This can be seen by COSY-correlations of the methine 18 ($\delta_{C\text{-}18}$ 27.7, $\delta_{H\text{-}18}$ 1.58) to two geminal methyl groups ($\delta_{C\text{-}19}$ 21.6, $\delta_{H\text{-}19}$ 0.91, $\delta_{C\text{-}20}$ 21.6, $\delta_{H\text{-}20}$ 0.91). Comparable to myxenolone A, myxenolone B was purified as a mixture of the isomers B1 (**3**) and B2 (**4**). Similar to **1**, both conjugated double bonds in **3** display the *E* configuration as the coupling constants between H-11, H-12 H-13 and H-14 are between 15 and 16 Hz. The *Z* configuration of the second double bond in **4**, similar to **2**, is evidenced by the coupling constants between H-13 and H-14.

Myxenolone C shows a HRESI-MS $[M+H]^+$ signal at *m/z* 302.1301 (calc. 302.1307, Δ = 1.99 ppm), corresponding to the molecular sum formula $C_{18}H_{20}ClNO$ with nine DBEs. The incorporation of chlorine was verified by the typical isotope pattern in the mass spectrum (Supporting information, Figure S 4.1). Compared to the respective spectra of **1** and **2**, the HSQC spectrum of myxenolone C lacks the signal of the deshielded olefinic methine CH-9. Instead, the ^{13}C spectrum displays a new olefinic signal at $\delta_{C\text{-}9}$ 115.6. The position of C-9 was verified by HMBC correlations from H-11 ($\delta_{H\text{-}11}$ 6.93) and H-12 ($\delta_{H\text{-}12}$ 7.33). These findings, and the fact that the rest of the signals and correlations showed close resemblence to **1**, indicate chlorine to be bound to C-9. Similar to the findings in the previously discussed derivatives, myxenolone C is a mixture of the isomers C1 (**5**) and C2 (**6**). As in **1** and **3**, both double bonds in **5** display an *E* configuration, evidenced by the coupling constants between H-11 and H-12 as well as H-13 and H-14 in the range of 15 Hz. In contrast to **2** and **4**, the *Z* configured double bond in **6** is the one next to the quinolone core, as displayed by coupling constants of ~11 Hz between H-11 and H-12 and of ~ 15 Hz between H-13 and H-14.

Evidenced by the HRESI-MS $[M+H]^+$ signal at *m/z* 316.1462 (calc. 316.1463, Δ = 0.32 ppm), myxenolone D1 (**7**) possesses a molecular sum formula of $C_{19}H_{22}ClNO$ and nine DBEs. As for myxenolone C, the typlical isotope pattern of chlorine was used to verify its presence in **7** (Figure S 4.1). Myxenolone D1 displays a 4-methyl-pentyl-residue bound

to the two conjugated double bonds, as shown for **3** and **4**. Two geminal methyl groups ($\delta_{C\text{-}19}$ 23.1, $\delta_{H\text{-}19}$ 0.92, $\delta_{C\text{-}20}$ 23.1, $\delta_{H\text{-}20}$ 0.92) are bound to a methine ($\delta_{C\text{-}18}$ 29.2, $\delta_{H\text{-}18}$ 1.59), as displayed by COSY correlations between H-18 with H-19 and H-20. Furthermore, similar to **5** and **6**, the ^{13}C spectrum of **7** displays an olefinic signal at $\delta_{C\text{-}9}$ 115.6. The lack of a deshielded olefinic methine in the HSQC spectrum as well as an HMBC correlation from H-11 ($\delta_{H\text{-}11}$ 6.93) to C-9 led to the conclusion that the chlorine in **7** is bound to C-9 as well. Differently to the other myxenolones, myxenolone D1 was isolated as only one conformer. As for **1**, **3** and **5**, both double bonds are *E* configured, as evidenced by coupling constants greater 15 Hz between H-11 and H-12 and between H-13 and H-14.

Altogether, myxenolones possess the 4-hydroxy-2-alkylquinoline scaffold, frequently observed in *Pseudomonas*, *Burkholderia* and further bacteria[36]. Nevertheless, within this scaffold they have several unique structural features. The two conjugated double bonds directly adjacent to the quinolone-moiety of all described myxenolone derivatives are unprecedented for 4-hydroxy-2-alkylquinolines. Furthermore, myxenolones C and D are the first described 4-hydroxy-2-alkylquinolines that are halogenated at position 3.

4.3.3 Purification and structure elucidation of novel thuggacin derivatives

The herein described thuggacin P derivatives add to the thuggacin scaffold, consisting of the thuggacin subclass, purified from *S. cellulosum* So ce895 and the thuggacin cmc subclass from *Chondromyces crocatus* Cm c5[33]. As displayed in figure 4.3 A, thuggacin A (**I**) and thuggacin cmc-A (**IV**) only differ in their hydroxylation pattern and in the alkyl-residue next to the carboxylic acid part of the macrolactone. Based on the structural similarities of both reported subclasses, a shared nomenclature was applied, following the size of the respective macrolactones. Consequently, as shown in figure 4.3 A for thuggacins A (**I**), B (**II**) and C (**III**), the suffix “A” is used for 16-membered macrolactones, while “B” and “C” describe their 17- or 18-membered congeners[33].

Due to the improved production, thuggacin P1-A, thuggacin P1-C, thuggacin P2-B and thuggacin P2-C were purified from axenic cultures of MSr12523 in RGSR medium. The production in co-cultures of MSr12523 with *T. pseudospumae*, and purification of oxo-thuggacin P1, hydroxyl-thuggacin P1 and oxo-thuggacin-P2 were performed and described by Markus Neuber[25].

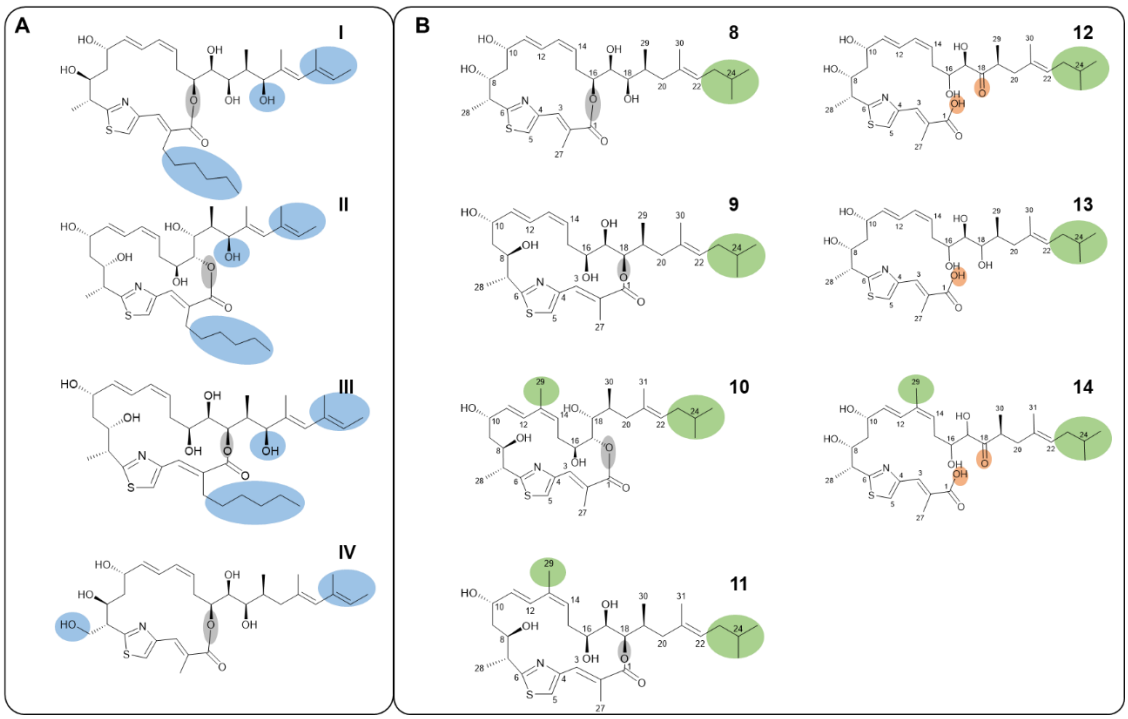

Figure 4.3: Chemical structures of previously reported and newly purified thuggacin derivatives. (**A**) Thuggacins A (**I**), B (**II**) and C (**III**), purified from *S. cellulosum* So ce895 and thuggacin cmc-A (IV), purified from *C. crocatus* Cm c5[33]. (**B**) Macrolactone thuggacins P1-A (**8**), P1-C (**9**), P2-B (**10**) and P2-C (**11**) and uncyclised oxo-thuggacin P1 (**12**), hydroxy-thuggacin P1 (**13**) and oxo-thuggacin P2 (**14**), all purified from MSr12523. Structural motifs, only observed in previously reported thuggacin derivatives, are highlighted in blue. The positions of the ester-bonds are marked in grey. They determine the size of the macrolactone and therefore identify if the natural product is a thuggacin A, B or C derivative. The 2-methylpropanyl residue observed in all thuggacin P derivatives as well as the additional methyl-residue, observed in the thuggacin P2 subclass, are highlighted in green. The free carboxylic acid of all uncyclised thuggacin P derivatives as well as the keto-group in both oxo-thuggacin P derivatives are highlighted in organge.

HRESI-MS of thuggacin P1-A (**8**) and thuggacin P1-C (**9**) show $[M+H]^+$ signals at *m/z* 548.3042 (calc. 548.3041, Δ = 0.18 ppm), respectively, that correspond to a molecular sum formula of $C_{30}H_{45}NO_6S$ with nine double bond equivalents (DBEs). Similar to reported thuggacin derivatives[33], **8** features a thiazole ($\delta_{C\text{-}4}$ 151.0, $\delta_{C\text{-}5}$ 120.5, $\delta_{H\text{-}5}$ 7.66, $\delta_{C\text{-}6}$ 171.7) connected to an acrylic acid moiety ($\delta_{C\text{-}1}$ 169.2, $\delta_{C\text{-}2}$ 128.0, $\delta_{C\text{-}3}$ 135.7, $\delta_{H\text{-}3}$ 8.08). As in thuggacin cmc-A (**IV**)[33], the acrylic acid moiety in thuggacin P1-A is methylated ($\delta_{C\text{-}27}$ 13.8, $\delta_{H\text{-}27}$ 2.03) at C-2. Evidenced by COSY and HMBC correlations, this structural part belongs to a macrolactone with the same structure as thuggacin A (**I**)[33]. Its ring size was determined by the HMBC correlation of H-16 ($\delta_{H\text{-}16}$ 5.03) to C-1 ($\delta_{C\text{-}1}$ 169.2). The structural part between the hydroxylated methine CH-17 ($\delta_{C\text{-}17}$ 74.4, $\delta_{H\text{-}17}$ 3.75) and the olefinic methine CH-22 ($\delta_{C\text{-}22}$ 126.9, $\delta_{H\text{-}22}$ 5.21) is equivalent to the one in **IV** [33]. In contrast to the reported thuggacins, **8** has a terminal iso-butyl residue, as shown by COSY correlations of a methine ($\delta_{C\text{-}24}$ 30.4, $\delta_{H\text{-}24}$ 1.57) with two geminal methyl groups ($\delta_{C\text{-}25}$ 23.1, $\delta_{H\text{-}25}$ 0.87, $\delta_{C\text{-}26}$ 23.0, $\delta_{H\text{-}26}$ 0.87) and a methylene ($\delta_{C\text{-}23}$ 38.5, $\delta_{H\text{-}23}$ 1.87). This

iso-butyl residue is bound to methine 22 as demonstrated by COSY correlations between H-22 ($\delta_{H\text{-}22}$ 5.21) and H-23 ($\delta_{H\text{-}23}$ 1.87). The configuration of the conjugated double bonds was assigned as *E* and *Z* based on the coupling constants of H-12 to H-11 of 15.0 Hz and of H-13 to H-14 of 11.0 Hz. The configuration of the remaining double bonds as well as the stereochemistry of positions 7, 8, 10, 16, 17, 18 and 19 were assigned based on *in silico* analysis of the thuggacin P biosynthetic gene cluster.

Thuggacin P1-C differs from **8** only in the size of the macrolactone. This is shown by a HMBC correlation of H-18 ($\delta_{H\text{-}18}$ 5.10) to C-1 ($\delta_{C\text{-}1}$ 169.5). Furthermore, in contrast to **8**, H-16 ($\delta_{H\text{-}16}$ 3.64) of **9** shows a shift that would be expected for a hydroxylated methine, while H-18 ($\delta_{H\text{-}18}$ 5.10) displays a typical shift of a hydroxylated methine that is part of an ester bond.

The HRESI-MS signal of the thuggacin P2-B (**10**) and thuggacin P2-C (**11**) ions $[M+H]^+$ at *m/z* 562.3194 (calc. 562.3198, Δ = 0.71 ppm) correspond to the molecular sum formula $C_{31}H_{47}NO_6S$ that has an unsaturation degree of 9 DBEs. Compared to **8** and **9**, thuggacin P2-B (**10**) displays a further methyl-group ($\delta_{C\text{-}29}$ 21.1, $\delta_{H\text{-}29}$ 1.82) which is bound to the olefinic C-13 ($\delta_{C\text{-}13}$ 135.0), as demonstrated by a HMBC correlation from H-29 and further reciprocal HMBC correlations of the new methyl group with both surrounding methines ($\delta_{C\text{-}12}$ 127.6, $\delta_{H\text{-}12}$ 6.42, $\delta_{C\text{-}14}$ 128.2, $\delta_{H\text{-}14}$ 5.39). Furthermore, **10** has a 17-membered macrolactone, as displayed by the HMBC correlation from H-17 ($\delta_{H\text{-}17}$ 5.05) to the acrylic acid carbon ($\delta_{C\text{-}1}$ 171.0).

Similar to thuggacin P2-B (**10**), the additional methyl-group ($\delta_{C\text{-}29}$ 20.7, $\delta_{H\text{-}29}$ 1.74) in **11** is connected to the olefinic C-13 ($\delta_{C\text{-}13}$ 133.1), also shown by HMBC correlations to the surrounding olefinic methines ($\delta_{C\text{-}12}$ 128.4, $\delta_{H\text{-}12}$ 6.59, $\delta_{C\text{-}14}$ 129.7, $\delta_{H\text{-}14}$ 5.51). HMBC correlations from the proton of the hydroxylated methine 18 ($\delta_{C\text{-}18}$ 76.8, $\delta_{H\text{-}18}$ 5.11) to the carbonyl ($\delta_{C\text{-}1}$ 169.5) as well as the characteristic proton shift within this group display the ring size for thuggacin P2-C (**11**).

Oxo-thuggacin P1 (**12**) shows a HRESI-MS $[M+H]^+$ signal at *m/z* 564.2990 (calc. 564.2990, Δ = 0.00 ppm), corresponding to the molecular sum formula $C_{30}H_{45}NO_7S$ with nine DBEs. Compared to the respective spectra of **8**, the HSQC spectrum of oxo-thuggacin P1 (**12**) only displays four instead of five hydroxylated methines. Instead, the ^{13}C spectrum shows a ketone carbon ($\delta_{C\text{-}18}$ 218.1). Its position can be deduced from HMBC correlations of H-16 ($\delta_{H\text{-}16}$ 3.98), H-17 ($\delta_{H\text{-}17}$ 4.10), H-19 ($\delta_{H\text{-}19}$ 3.23), H-20a ($\delta_{H\text{-}20a}$ 2.42) and H-20b ($\delta_{H\text{-}20b}$ 1.88) to the ketone. The additional oxygen of **12** compared to **8** as well as the lack of HMBC correlation of the remaining hydroxylated methines ($\delta_{C\text{-}16}$ 73.4, $\delta_{H\text{-}12}$ 3.98, $\delta_{C\text{-}17}$ 79.2, $\delta_{H\text{-}17}$ 4.10) to the carbonyl of the acryclic acid moiety ($\delta_{C\text{-}1}$ 172.7) led to the conclusion that oxo-thuggacin P1 (**12**) is not a macrolactone.

Evidenced by the HRESI-MS $[M+H]^+$ signal at *m/z* 566.3142 (calc. 566.3146, Δ = 0.71 ppm), hydroxy-thuggacin P1 (**13**) possesses a molecular sum formula of $C_{30}H_{47}NO_7S$ and eight DBEs. The loss of one DBE as well as the additional H_2O in the sum formula, compared to **8**, can be explained by an open-chain molecule instead of a macrolactone. Consequently, neither HMBC correlations nor shift values characteristic for a proton of hydroxylated methines (~ 5 ppm) can be observed, which would be responsible for ring closure in cyclised thuggacin derivatives.

The HRESI-MS signal of the oxo-thuggacin P2 (**14**) ion $[M+H]^+$ at *m/z* 578.3146 (calc. 578.3146, Δ = 0.00 ppm) corresponds to the molecular sum formula $C_{31}H_{47}NO_7S$ that has an unsaturation degree of 9 DBEs. Oxo-thuggacin P2 (**14**) shows the same methylation position, C-13 ($\delta_{C\text{-}13}$ 135.2), as **10** and **11**, evidenced by HMBC correlations to the neighbouring olefinic methines ($\delta_{C\text{-}12}$ 128.9, $\delta_{H\text{-}12}$ 6.71, $\delta_{C\text{-}14}$ 127.6, $\delta_{H\text{-}14}$ 5.46). Similar to **12**, the ^{13}C spectrum of **14** displays a ketone carbon ($\delta_{C\text{-}18}$ 218.3) with HMBC correlations from H-16 ($\delta_{H\text{-}16}$ 3.97), H-17 ($\delta_{H\text{-}17}$ 4.08), H-19 ($\delta_{H\text{-}19}$ 3.24), H-20a ($\delta_{H\text{-}20a}$ 2.42) and H-20b ($\delta_{H\text{-}20b}$ 1.88). As no DBE is unaccounted for and further reasons elaborated for **12** and **13** are also applicable, it is evident that oxo-thuggacin P2 is not cyclised as a macrolactone, either.

Structurally, especially the macrolactone part, the thuggacin P family seems to be a mixture of the previously reported thuggacin and thuggacin cmc compound families. They possess the methyl-group C-27 and the fully saturated methylene C-20 of the thuggacin cmc congeners as well as the unaltered methyl-group C-28 of the thuggacin compound family. Furthermore, the thuggacin P2 derivatives display an additional methylation at C-13, similar to the methylation of the previously described, but poorly produced methyl-thuggacin A[33]. However, the herein described thuggacin P derivatives display a 2-methylpropanyl residue bound to C-22 that, based on biosynthetic logic, has a different origin than the 1-methylprop-1-enyl residue in previously reported thuggacin derivatives.

Furthermore, all previously described thuggacin derivatives display a macrolactone between the acrylic acid moiety and one of the three neighbouring hydroxyl-groups at C-16 to C-18. None of the oxo- or hydroxyl-thuggacin P derivatives, purified from co-cultures of MSr12523 with *T. pseudospumae* have this macrolactone, setting them apart from all other thuggacin derivatives. Their putative genesis will be covered later within this chapter.

4.3.4 *In silico* anaylses of the myxenolone BGC and biosynthesis hypothesis

In order to find the biosynthetic origin of the myxenolone compound family, the antiSMASH[37] output for the genome of MSr12523 was screened for regions with genes potentially encoding halogenases. One hit included several clustered genes that seemed to resemble a region of clustered genes in several *Burkholderia* strains. Based on the capability of different *Burkholderia* strains to produce 4-hydroxy-3-methyl-2-alkylquinolines[38] and the 4-hydroxy-2-alkylquinoline scaffold of myxenolones, this region was established as putative *mxo* BGC *in silico*. This hypothesis was strengthened as most biosynthetic enzymes for the production of the pseudomonas quinolone signal (PQS)[39] in *Pseudomonas aeruginosa* PA01 and 4-hydroxy-3-methyl-2-heptenylquinoline (HMQ)[40] in *Burkholderia thailandensis* E264 display homology to several putative enzymes encoded within this region (Table S 4.17). The putative *mxo* BGC consists of nine genes and spans about 14.5 kb. A detailed analysis of the *mxo* BGC in MSr12523 was carried out (Table S 4.18). It encodes enzymes corresponding to HmqB (MxoC), HmqC (MxoG), HmqD (MxoD), HmqE (MxoA) and HmqF (MxoF) in *Burkholderia* strains as well as further enzymes putatively involved in the unsaturation of the alkenyl-moiety (MxoE, MxoH, MxoI) and the halogenation of myxenolones C and D (Figure 4.4 A).

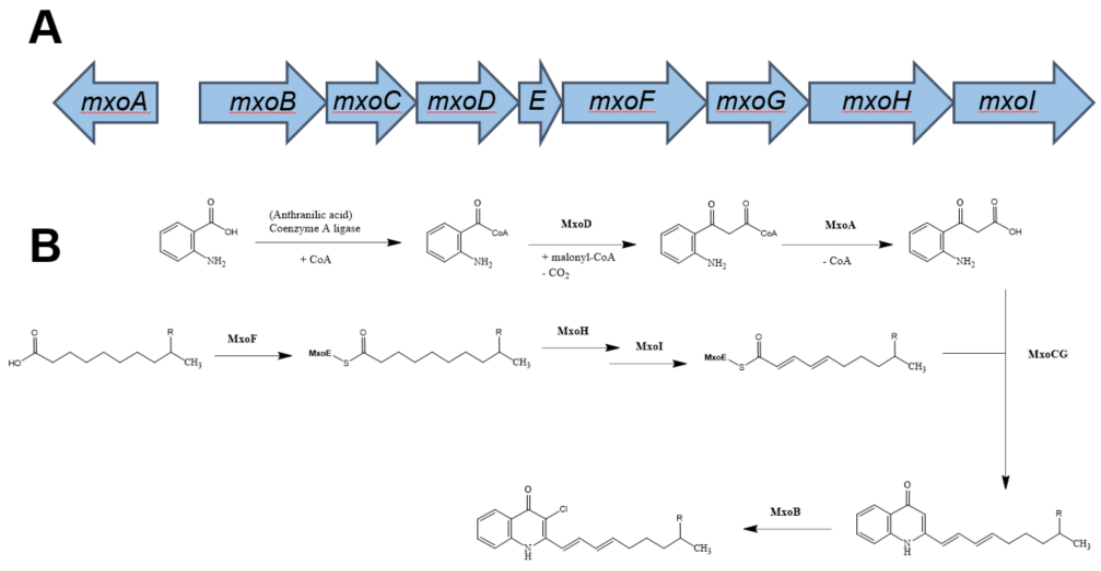

Figure 4.4: Putative myxenolone BGC and *in silico* biosynthesis. (**A**) Schematic display of the genes in the putative myxenolone BGC. (**B**) Model of the myxenolone biosynthesis.

Following the elucidated biosyntheses of 4-hydroxy-2-alkylquinolines in *Burkholderia* and *P. aeruginosa* strains[36,38,41], we developed a biosynthetic model of the production of the myxenolone compound family in MSr12523 (Figure 4.4 B). Unlike the BGCs of PQS and HMQ, the *mxo* BGC does not contain a gene coding for an anthraniloyl-CoA ligase. However, it seems likely that the biosynthesis of myxenolones also starts with anthranilic acid, possibly derived from primary metabolism, which is activated to anthraniloyl-CoA by an enzyme encoded in a different region in the genome of MSr12523. In the next step, MxoD forms 2-aminobenzoylacetatyl-CoA in a Claisen-condensation like reaction of anthraniloyl-CoA and malonyl-CoA. Similar to the biosynthesis of PQS and HMQ, the thioester of 2-aminobenzoylacetatyl-CoA is then hydrolysed by MxoA to release 2-aminobenzoylacetate.

One obvious difference between myxenolones and hitherto described 4-hydroxy-2-alkylquinolones are the two conjugated double bonds next to the quinolone-moiety. This structural feature might originate from the fatty acid that is incorporated into the molecule during the biosynthesis. Therefore, decanoic acid or 9-methyldecanoic acid, possibly derived from primary metabolism, could be tethered to the ACP-like MxoE by MxoF. The activated fatty acid could be then unsaturated at the α,β- and γ,δ-positions by the acyl-CoA dehydrogenase like enzymes MxoH and MxoI.

Comparable to the PQS and HMQ biosyntheses, 2-aminobenzoylacetate and the activated unsaturated fatty acid could be fused by the MxoCG-complex to form the quinolone moiety. The resulting myxenolones A and B are then halogenated by the halogenase MxoB to form the chlorinated derivatives C and D.

4.3.5 *In silico* anaylses of the thuggacin P BGC, biosynthesis hypothesis and stereochemistry prediction

The putative *thg* BGC in the genome MSr12523 was identified with antiSMASH[37], based on similarity to the *tga* BGC in *S. cellulosum* So ce895 and the *tgu* BGC in *C. croactus* Cm c5[42]. It consists at least of *thg*A, *thg*B and *thg*C, encoding the biosynthetic megaenzymes, *thg*D, coding for the putative hydroxylase similar TgaE and TugE in the two other producers of thuggacins[33,42]. Furthermore, it might be flanked by *thg*1-3 upstream and *thg*4-10 downstream the core BGC, coding for putative regulatory or transport-related enzymes (Table S 4.19). It is noteworthy that, similar to the *tga* BGC in *S. cellulosum* So ce895, the biosynthetic machinery of the *thg* BGC in MSr12523 is distributed over three genes, but they differ as *thg*B is equivalent to *tug*B and *tug*C in *C. croactus* Cm c5, while *tga*A covers *tug*A and *tug*B (Figure S 4.2). Altogether, the

biosynthetic machinery for the thuggacin P family consists of the loading module, nine polyketide synthase (PKS) modules and one nonribosomal peptide synthetase (NRPS) module. Its architecture is highly similar to the biosynthetic machinery encoded in the *tug* BGC in *C. croactus* Cm c5 with two exceptions. First, it lacks one PKS extender module, equivalent to module one or two in TugA. Second, it contains an additional dehydratase (DH) domain in module eight, which is, however, inactive. Similar to the acyl transferase (AT) domains in the thuggacin cmc biosynthesis, AT domains in modules 3, 4, 6 and 7 selectively incorporate malonyl-CoA, while AT domains in modules 1, 2, 8 and 10 are selective for methylmalonyl-CoA (Table S 4.20). According to *in silico* predictions by antiSMASH and typical fingerprints[43], the substrate specificity of the AT domain for the starter unit is much less clear and the observed starter unit is not among the best fits (Table S 4.21). However, the same was observed for the AT domains in the loading modules in the respective biosynthetic machineries in *S. cellulosum* So ce895 and *C. croactus* Cm c5 (Table S 4.21). Similarly, the predicted substrate specificity of the AT domain in module 5 does not comply with the incorporated extender units malonyl-CoA and methylmalonyl-CoA (Table S 4.20). Furthermore, this AT domain does not display the recognition site with its conserved motif HASH that was used to explain the incorporation of malonyl-CoA and methylmalonyl-CoA by the AT domain in module 3 of the epothilone biosynthesis[44]. Instead, it displays the recognition site motif YAGH (Figure S 4.2), that is very close to the methylmalonyl-CoA recognition site motif YASH[43]. However, it has been shown before that little changes in this recognition site can lead to a relaxed substrate specificity of the respective AT domains[45,46]. Interestingly, the equivalent AT domain in the *tga* BGC in *S. cellulosum* So ce895, displays the recognition site for the incorporation of methylmalonyl-CoA, but the resulting methyl-thuggacins are produced in much lower titers than their non-methylated counterparts[33,42]. Similar to the ones in the *tga* and *tgu* BGCs[42], the adenylation (A) domain of module 9 incorporates cysteine, according to antiSMASH 7.0 (Table S 4.20). Analysis of the ketoreductase (KR), DH and enoylreductase (ER) domains was done by antiSMASH and according to fingerprints[43,47,48]. With the exception of the DH domain in module 8, all domains of the reductive loops are active, which is in accordance with the observed structure. *In silico* stereochemistry predictions based on the KR[47] and ER[48] domains match the ones of the respective modules in the biosynthetic machinery of thuggacin-cmc family in *C. croactus* Cm c5 with one exception. While the KR domain in module 9 of the previously reported thuggacin biosyntheses belongs to the A1 type[42], the equivalent KR domain in module 8 of the thuggacin P biosynthesis in MSr12523 is a B1 type, therefore inversing the stereochemistry at C-8 compared to previously published thuggacins[42,49].

Based on the structures of the thuggacin P compound family, their biosynthesis is likely to begin with isovaleryl-CoA as starter unit, as depicted in the biosynthesis model of thuggacin P1-A (Figure 4.5). After incorporation of the starter unit, thuggacin P1-A undergoes eight PKS-derived elongation steps including the incorporation of five malonyl-CoA and three methylmalonyl-CoA extender units. As described for the *tug* and *tga* BGCs, the equivalent module 5 in the *thg* BGC does not contain a DH domain, which is not in line with the observed double bond between C-13 and C-14[42]. The hypothesis that the DH domain of the following module acts iteratively and forms the double bonds between C-11 and C-12 as well as C-13 and C-14[42] is therefore extended to thuggacin P biosynthesis. The production of the polyketide chain is followed by the incorporation of L-cysteine and subsequent heterocyclisation and oxidation, as previously described[42]. Afterwards, the biosynthesis is continued by the final PKS module that incorporates another methylmalonyl-CoA extender unit. The final step within the biosynthetic machinery is the formation of the macrolactone and subsequent release from the mega-enzyme, catalysed by the thioesterase (TE) domain in module 10. Post-assembly line, thuggacin P1-A is formed by the hydroxylation at C-17 by the putative hydroxylase ThgD, analogous to the post-assembly line modifications of thuggacin derivatives produced by So ce985 and Cm c5[42]. The additional methylation at C-13 in the thuggacin P2 subclass can be explained by the putatively relaxed substrate specificity of the AT domain in module 5.

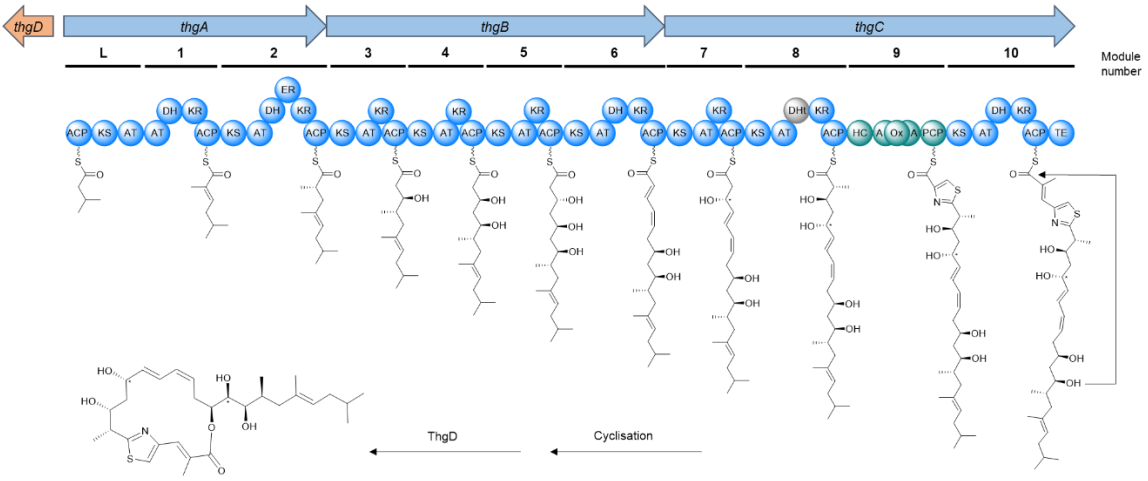

Figure 4.5: *In silico* biosynthesis of thuggacin P1-A. Scheme of the proposed thuggacin P BGC core and the thuggacin P1-A biosynthesis model by its megasynthase. Stereocenters are generally displayed based on the *in silico* predictions of the respective domains. The configuration of the two stereocenters marked with a * were assigned based on the reported stereochemistry of further thuggacin derivatives[49]. (A: adenlyation; ACP: acyl-carrier protein; DH: dehydratase; ER; enoylreductase; HC: heterocyclisation; KR: ketoreductase; KS: ketosynthase; Ox: oxidation; PCP: peptidyl-carrier protein, TE: thioesterase)

Similar to the previously reported biosynthetic models for thuggacin derivatives[42], the present biosynthetic model of the thuggacin P compound class could explain the formation of thuggacin P1-A, the observed, but so far unpurified thuggacin P2-A (Figure S 4.5), the formation of the respective C derivatives with the 18-membered macrolactone or a mixture of 16- and 18-membered macrolactones. However, storing thuggacin P1-A in methanol resulted in a partial transesterification into thuggacin P1-C and the presence of both derivatives within the sample. Therefore it seems likely that, similar to the reported rearrangements of thuggacin A into B and C in methanol[33], thuggacin P1-A and (so far unpurified) thuggacin P2-A undergo trans-esterification reactions to form the respective B and C derivatives in organic solvents. A formation of the oxo- and hydroxy-thuggacin derivatives was not observed and their probable origin will be explained and discussed later.

In silico predictions of the absolute stereochemistry of the respective thuggacin derivatives, based on KR, DH and ER domains in the *tga* BGC in *S. cellulosum* So ce895 and the *tgu* BGC in *C. crocatus* Cm c5 were in accordance with the experimentally determined stereochemistry[42,49–51]. Therefore, we assigned the stereochemistry of the thuggacin P compound family following the *in silico* predictions, based on the KR, DH and ER domains in the *thg* BGC in MSr12523. While the *in silico* stereochemistry predictions of all other KR and ER domains were shared by antiSMASH and their fingerprints[47,48], the KR domain of module 8 had an inconclusive fingerprint. However, the equivalent KR domains in the *tga* and *tug* BGCs also showed inconclusive fingerprints[49] and alignments between the three KR domains displayed highly similar motifs in the respective regions (Figure S 4.3). Therefore, the respective stereocenter at C-10 was determined as *S*, based on the reported stereochemistry of the thuggacin derivatives from So ce895 and Cm c5[49,50]. Furthermore, the stereochemistry of C-17 can not be determined by *in silico* predictions, as the hydroxyl-group is incorporated post-assembly line. Based on the high similarity of ThgD with TgaE and TugE (Table S 4.23), it seems likely that the hydroxylation reaction is performed accordingly, leading to a proposed stereochemistry of 17*S*[49,50].

4.3.6 **Bioactivities of both compound families**

As anticipated by the strong bioactivity against *M. tuberculosis* 7H37Ra, observed early in the extraction and purification process, several purified myxenolone and thuggacin P derivatives displayed antibiotic activity against mentioned pathogen (Table 4.1).

Especially myxenolones A (**1**/**2**) and C (**5**/**6**) proved to be highly active against *M. tuberculosis* 7H37Ra, with low one-digit minimum inhibitory concentrations (MICs). In

contrast to that, myxenolone D (**7**) only displayed a moderate activity against the test pathogen, while the B derivative (**3**/**4**) was inactive in all tested concentrations. Based on the various biological activities reported for different 4-hydroxy-2-alkylquinolones[36], all myxenolone derivatives with anti-mycobacterial activity were tested for their effect on a small panel of Gram positive and Gram negative pathogens as well as a cell line. Nevertheless, both tested derivatives did not exhibit activity against Gram negative bacteria and only myxenolone C (**5**/**6**) was moderately active (MIC: 32 µg/mL) against *S. aureus* Newman (Table S 4.24). Instead, the tested myxenolones displayed cytotoxic activities against the CHO-K1 cell line with IC_{50} values in the one digit µg/mL range (Table S 4.24). While the other observed bioactivities of the myxenolones are in line with previous findings[36,52], their strong activity against *M. tuberculosis* 7H37Ra stands out.

A possible explanation for this strong anti-mycobacterial activity could be the unusual motif of two conjugated double bonds directly next to the quinolone-moiety, as it presents the most obvious difference between myxenolones A (**1**/**2**) and C (**5**/**6**) compared to other 4-hydroxy-2-alkylquinolones. Within the myxenolone compound family, the terminal branch observed in derivatives B (**3**/**4**) and D (**7**) seems to have a (strong) negative effect on the biological activities, while the impact of the substituent at position 9 remains elusive. However, based on the limited set of only four derivatives, the effects of different structural motifs on observed bioactivities are highly speculative.

Table 4.1: Minimum inhibitory concentrations (MICs) of the myxenolone and thuggacin P compound families against *M. tuberculosis* 7H37Ra.

	MIC [µg/mL] ***M. tuberculosis* 7H37Ra**
Myxenolone A	0.5-1[a]
Myxenolone B	>64[a]
Myxenolone C	2-4[a]
Myxenolone D	32[a]
Thuggacin P1-A	16[a] -64[b]
Thuggacin P1-C	64[b]
Thuggacin P2-B	64[b]
Thuggacin P2-C	16[b]
Oxo-thuggacin P1	>64[a]
Hydroxy-thuggacin P1	>64[a]
Oxo-thuggacin P2	>64[a]
Thuggacin A[*]	32[b]

[a] Prepared as a 1 mg/mL DMSO stock.
[b] Prepared as a 1 mg/mL MeOH stock.
[*] Thuggacin A was tested alongside as comparison.

The thuggacin scaffold is particularly known for its moderate anti-mycobacterial activity[53] and consequently, all tested macrocyclic thuggacin P derivatives displayed moderate activities against the tested *M. tuberculosis* 7H37Ra. Neither of the non-cyclised thuggacin P derivatives inhibited growth of the test strain within the tested concentration range.

However, the MICs of macrocyclic thuggacin P derivatives are only preliminary. In a first assay, they were tested against *M. tuberculosis* 7H37Ra with thuggacin A (**I**) as comparison. This assay was performed with 1 mg/mL methanolic stock solutions of all tested compounds as the transesterification of thuggacin P derivatives was not known at that time. The second assay was performed with 10 mg/mL DMSO stock solutions and on this occasion the only tested macrocyclic derivative thuggacin P1-A (**8**) showed a four fold lower MIC. Given the known rearrangement of thuggacin A to the B (**II**) and C (**III**) derivatives in MeOH[33], it seems likely that the previous biological assays of thuggacin A and derivatives against *M. tuberculosis* 7H37Rv were performed with DMSO stock solutions[53,54]. The reported MIC of thuggacin A is fourfold lower than the 32 µg/mL present assay (in MeOH), raising the question, if this fourfold activity shift is due to the organic solvent of choice. In order to answer all remaining questions, bioactivity assays of all macrocyclic thuggacin P derivatives as well as thuggacin A should be repeated as DMSO stocks.

4.3.7 **Possible origin of non-cyclised thuggacins**

As oxo-thuggacin P1 (**12**), hydroxy-thuggacin P1 (**13**) and oxo-thuggacin P2 (**14**) were only observed in co-cultures of MSr12523 with *T. pseudospumae*, it seems likely that their presence is connected to this partner strain. A spontaneous formation originating from thuggacin derivatives bearing a macrolactone seems unlikely, as no similar observation was made in the past, and extracts of axenic cultures of MSr12523 did not contain those derivatives. It is noteworthy that the uncyclised thuggacin derivatives do not display antibiotic activity against *M. tuberculosis* 7H37Ra that, like *T. pseudospumae*, belongs to the phylogenetic order of *Mycobacteriaceae*. Therefore, a hydrolysis of the thuggacin macrolactone by *T. pseudospumae* as a potential detoxification or resistance mechanism was hypothesised (Figure 4.6 A). To test a possible hydrolysis of the thuggacin macrocylces by the alkaline milieu during cultivation, a mixture of macrocyclic thuggacin P1 derivatives **8** and **9** was incubated at a pH of 8.8 (Figure 4.6 B). As displayed in figure 4.6 B, both thuggacin P1 derivatives are fairly stable at this condition and for clarity, the intensities for both derivatives were combined. Furthermore, under this condition, concentration of macrocyclic thuggacin P1 (**8**&**9**) is slightly reduced over

time and low amounts of hydroxy-thuggacin P1 (**13**) can be observed. However, considering the high amounts of hydroxy-thuggacin P1 (**13**) and oxo-thuggacin P1 (**12**) in co-cultivations of MSr12523 with *T. pseudospumae*, it seems unlikely that this is the only source of non-cyclised thuggacin derivatives.

In order to test the ability of *T. pseudospumae* to hydrolyse the macrolactone, it was cultivated with 5, 10, and 25 µg/mL of a mixture of macrocyclic thuggacin P1 derivatives **8** and **9**. First, visual observations of the respective cultures after a cultivation time of 24 h showed a significant growth reduction of cultures with added thuggacins compared to the untreated control culture (Figure S 4.6), indicating an antibiotic effect of macrocyclic thuggacin P1 derivatives against *T. pseudospumae*.

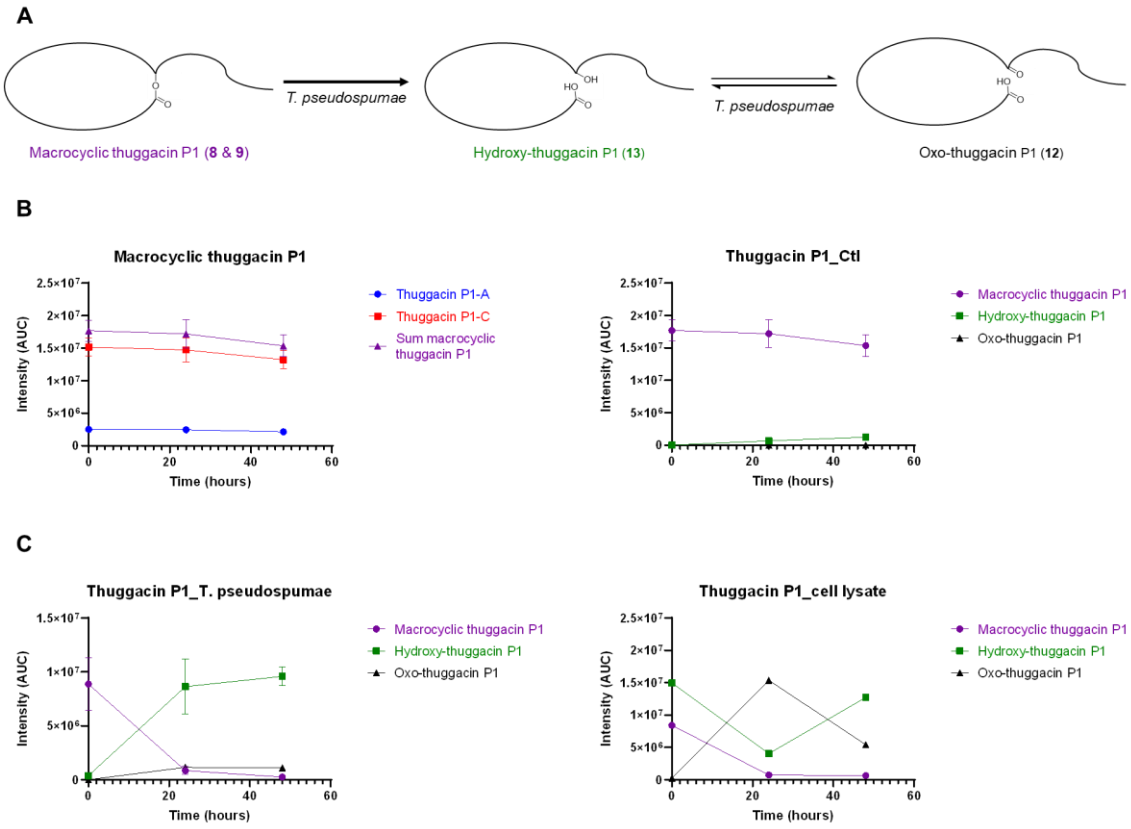

Figure 4.6: Possible resistance mechanism of *T. pseudospumae* against macrocyclic thuggacin P derivatives. (**A**) Schematic display of possible hydrolysis of macrocyclic thuggacin P1 derivatives **8** and **9** to hydroxy-thuggacin P1 (**13**) and subsequent partial conversion to oxo-thuggacin P1 (**12**) by *T. pseudospumae*. (**B**) Left hand side: Behaviour of 10 µg/mL thuggacin P1-A (**8**) and P1-C (**9**) in TSB medium at pH 8.8 over time. Right hand side: Conversion of 10 µg/mL macrocyclic thuggacin P1 derivatives **8** and **9** into hydroxy-thuggacin P1 (**13**) in TSB medium at pH 8.8 over time. (**C**) Conversion of 10 µg/mL macrocyclic thuggacin P1 derivatives **8** and **9** into hydroxy-thuggacin P1 (**13**) and oxo-thuggacin P1 (**12**) in a cultivation of *T. pseudospumae* (left hand side) and when added to a cell-free lysate of *T. pseudospumae* (right hand side) over time. (As cultivation assays were treated differently from *in vitro* assays and controls, the results differ in observed intensities. Thuggacin P1 conversion data with cell-free lysate only represents two replicates.)

Second, Metaboscape 2022b-assisted analysis of UHPLC-MS chromatograms of samples taken after 24 h and 48 h displayed a strong reduction of macrocyclic thuggacin P1 (**8**&**9**) and a strong increase of hydroxy-thuggacin P1 (**13**; 10 µg/mL: Figure 4.6 C; 5 and 25 µg/mL: Figure S 4.7). Furthermore, low amounts of hydroxy-thuggacin P1 (**13**) could already be observed in samples taken right after mixing macrocyclic thuggacin P1 (**8**&**9**) with *T. pseudospumae*, indicating a quick hydrolysation of the thuggacin lactone. In addition to that, low amounts of oxo-thuggacin P1 (**12**) were observed in samples taken after 24 h and 48 h of incubation, pointing towards an oxidation of hydroxy-thuggacin P1 (**13**) by *T. pseudospumae*.

To further study the origin of the observed resistance mechanism, 10 µg/mL of macrocyclic thuggacin P1 derivatives (**8**&**9**) were incubated with the culture supernatant as well as a cell-free lysate of *T. pseudospumae*. While incubation with the supernatant displayed results comparable to the negative control (Figure S 4.8), the cell-free lysate efficiently converted macroclyclic thuggacin P1 (**8**&**9**) to hydroxy-thuggacin P1 (**13**) and oxo-thuggacin P1 (**12**; Figure 4.6 C). In contrast to the observations made in the cultivation-based conversion of macrocyclic thuggacin P1 (**8**&**9**) by *T. pseudospumae*, the respective cell-free lysate already converted more than half of the substrate during the first mixing step (Figure 4.6 C), pointing towards a quick hydrolysis. However, the quicker initial conversion might be explained by the different concentrations of *T. pseudospumae* and its cell-free lysate in the different assays.

When incubated with the *T. pseudospumae* cell-free lysate, the concentration of hydroxy-thuggacin P1 (**13**) decreased between 0 h and 24 h, while the concentration of oxo-thuggacin P1 (**12**) strongly increased, pointing towards a conversion from **13** to **12** by *T. pseudospumae*. Interestingly, this trend was reversed between 24 h and 48 h (Figure 4.6 C). Whether this observed reduction of oxo-thuggacin P1 (**12**) to hydroxy-thuggacin P1 (**13**) is a spontaneous reaction in an aqueous solution or if it is enzyme-mediated, remains elusive.

Altogether, the conducted experiments display the hydrolysis and oxidation of macroclycic thuggacin P1 in *T. pseudospumae* by constitutively expressed enzymes that are not secreted into the medium. However, to further understand the resistance mechanism of *T. pseudospumae* against macrocyclic thuggacin P derivatives, further experiments, ideally with purified enzymes, are required.

Among well-studied resistance mechanisms of bacteria against antibiotics, the hydrolysis of β-lactam antibiotics by β-lactamases is the most prominent example of antibiotic degradation as detoxification strategy. Another example for this general resistance mechanism are so-called erythromycin esterases, used by various Gram

negative bacteria to hydrolyse macrolide antibiotics[55,56]. As the hydrolysis of the thuggacin P macrolactone is reminiscent of the effect of erythromycin esterases, it is conceivable that *T. pseudospumae* or further *Mycobacteriaceae* have the ability to produce appropriate enzymes. However, a search of the erythromycin esterase EreA (K06880) against the taxon *Tsukamurella* in the RefSeq non-redundant protein sequence database at NCBI with the blastp algorithm was unsuccessful, as no protein with significant similarity could be found. Nevertheless, representatives of the genus *Tsukamurella* produce enzymes that enatioselectively hydrolyse specific structural motifs like phenyl glycidyl ether or ethyl 2-(2-oxopyrrolidin-1-yl) butyrate[57,58], suggesting their ability to produce enzymes to hydrolyse sophisticated molecules.

4.4 **Conclusion**

Together with the data peviously presented in the doctoral thesis of Markus Neuber, this study reports MACB as potentially valuable partner strains for co-cultivation studies with myxobacteria[25]. Co-cultivation of MSr12523 with *T. pseudospumae* resulted in the upregulation and subsequent purification of two natural product classes with antibiotic activities against *M. tuberculosis*.

The myxenolones are the first myxobacterial representatives of the well-known 4-hydroxy-2-alkylquinoline scaffold. Possibly depending on the respective alkyl-residue, myxenolones A and C display a promising antibiotic activity against *M. tuberculosis* 7H37Ra. A further development of this compound class towards preclinical and clinical evaluation might be hindered by the strong cytotoxicity displayed by all tested myxenolone derivatives (Table S 4.24).

The herein described thuggacin P derivatives add to the previously reported thuggacin scaffold. Their structural differences compared to other thuggacin derivatives can be explained by the *in silico* biosynthetic model and the antibiotic activities of the macrolactone derivatives against *M. tuberculosis* 7H37Ra are similar to other representatives of this scaffold. However, the possible resistance mechanism of *T. pseudospumae* that leads to non-cyclised derivatives is a striking observation. Microorganisms have been reported to inactivate antibiotics through the enzymatic hydrolysis of lactams and lactones. However, to our knowledge, this is the first documented instance of a partner strain directly reacting to a compound produced by a producer strain.

4.5 References

1. World Health Orgaization (WHO). Global tuberculosis report 2022. *World Health Organization* (2022).
2. Dartois, V. A. & Rubin, E. J. Anti-tuberculosis treatment strategies and drug development: challenges and priorities. *Nat Rev Microbiol*; 10.1038/s41579-022-00731-y (2022).
3. Black, T. A. & Buchwald, U. K. The pipeline of new molecules and regimens against drug-resistant tuberculosis. *Journal of Clinical Tuberculosis and Other Mycobacterial Diseases* **25,** 100285; 10.1016/j.jctube.2021.100285 (2021).
4. Shetye, G. S., Franzblau, S. G. & Cho, S. New tuberculosis drug targets, their inhibitors, and potential therapeutic impact. *Translational research : the journal of laboratory and clinical medicine* **220,** 68–97; 10.1016/j.trsl.2020.03.007 (2020).
5. Newman, D. J. & Cragg, G. M. Natural Products as Sources of New Drugs over the Nearly Four Decades from 01/1981 to 09/2019. *Journal of natural products* **83,** 770–803; 10.1021/acs.jnatprod.9b01285 (2020).
6. Walesch, S. *et al.* Fighting antibiotic resistance-strategies and (pre)clinical developments to find new antibacterials. *EMBO reports,* e56033; 10.15252/embr.202256033 (2022).
7. Wright, G. D. Opportunities for natural products in 21st century antibiotic discovery. *Nat. Prod. Rep.* **34,** 694–701; 10.1039/c7np00019g (2017).
8. Wenzel, S. C. & Müller, R. Myxobacteria—'microbial factories' for the production of bioactive secondary metabolites. *Molecular bioSystems* **5,** 567–574; 10.1039/b901287g (2009).
9. Herrmann, J., Fayad, A. A. & Müller, R. Natural products from myxobacteria: novel metabolites and bioactivities. *Natural product reports* **34,** 135–160; 10.1039/c6np00106h (2017).
10. Bader, C. D., Panter, F. & Müller, R. In depth natural product discovery - Myxobacterial strains that provided multiple secondary metabolites. *Biotechnol. Adv.* **39,** 107480; 10.1016/j.biotechadv.2019.107480 (2020).
11. Wenzel, S. C. & Müller, R. The biosynthetic potential of myxobacteria and their impact on drug discovery. *Curr. Opin. Drug Discov. Devel.* **12,** 220–230 (2009).
12. Mohr, K. I. Diversity of Myxobacteria-We Only See the Tip of the Iceberg. *Microorganisms* **6**; 10.3390/microorganisms6030084 (2018).

13. Zaburannyi, N., Bunk, B., Maier, J., Overmann, J. & Müller, R. Genome analysis of the fruiting body forming myxobacterium *Chondromyces crocatus r*eveals high potential for natural product Biosynthesis. *Appl. Environ. Microbiol.* **82,** 1945–1957; 10.1128/AEM.03011-15 (2016).

14. Katz, L. & Baltz, R. H. Natural product discovery: past, present, and future. *J. Ind. Microbiol. Biotechnol.* **43,** 155–176; 10.1007/s10295-015-1723-5 (2016).

15. Covington, B. C., Xu, F. & Seyedsayamdost, M. R. A Natural Product Chemist's Guide to Unlocking Silent Biosynthetic Gene Clusters. *Annu. Rev. Biochem.* **90,** 763–788; 10.1146/annurev-biochem-081420-102432 (2021).

16. Bode, H. B., Bethe, B., Höfs, R. & Zeeck, A. Big effects from Small Changes: Possible Ways to Explore Nature's Chemical Diversity. *ChemBioChem* **3,** 619–627 (2002).

17. Bertrand, S. *et al.* Metabolite induction via microorganism co-culture: a potential way to enhance chemical diversity for drug discovery. *Biotechnol. Adv.* **32,** 1180–1204; 10.1016/j.biotechadv.2014.03.001 (2014).

18. Molloy, E. M. & Hertweck, C. Antimicrobial discovery inspired by ecological interactions. *Curr. Opin. Microbiol.* **39,** 121–127; 10.1016/j.mib.2017.09.006 (2017).

19. Jones, J. A. & Wang, X. Use of bacterial co-cultures for the efficient production of chemicals. *Curr. Opin. Biotechnol.* **53,** 33–38; 10.1016/j.copbio.2017.11.012 (2018).

20. Kurosawa, K. *et al.* Rhodostreptomycins, antibiotics biosynthesized following horizontal gene transfer from *Streptomyces padanus* to *Rhodococcus fascians*. *J. Am. Chem. Soc.* **130,** 1126–1127; 10.1021/ja077821p (2008).

21. Adnani, N. *et al.* Coculture of Marine Invertebrate-Associated Bacteria and Interdisciplinary Technologies Enable Biosynthesis and Discovery of a New Antibiotic, Keyicin. *ACS Chem. Biol.* **12,** 3093–3102; 10.1021/acschembio.7b00688 (2017).

22. Pishchany, G. *et al.* Amycomicin is a potent and specific antibiotic discovered with a targeted interaction screen. *Proceedings of the National Academy of Sciences of the United States of America* **115,** 10124–10129; 10.1073/pnas.1807613115 (2018).

23. Lee, N. *et al.* Iron competition triggers antibiotic biosynthesis in Streptomyces coelicolor during coculture with Myxococcus xanthus. *The ISME Journal* **14,** 1111–1124; 10.1038/s41396-020-0594-6 (2020).

24. Schäberle, T. F., Orland, A. & König, G. M. Enhanced production of undecylprodigiosin in Streptomyces coelicolor by co-cultivation with the corallopyronin A-producing myxobacterium, *Corallococcus coralloides*. *Biotechnol. Lett.* **36,** 641–648; 10.1007/s10529-013-1406-0 (2014).

25. Neuber, M. Alteration of the metabolite spectrum of myxobacteria through alternative cultivation and extraction techniques. Doctoral Thesis. Saarland University, 2022.

26. Marrakchi, H., Laneelle, M. A. & Daffe, M. Mycolic Acids: Structures, Biosynthesis, and Beyond. *Chem. Biol.* **21,** 67–85; 10.1016/j.chembiol.2013.11.011 (2014).

27. Onaka, H., Mori, Y., Igarashi, Y. & Furumai, T. Mycolic acid-containing bacteria induce natural-product biosynthesis in *Streptomyces* species. *Appl. Environ. Microbiol.* **77,** 400–406; 10.1128/AEM.01337-10 (2011).

28. Onaka, H. Novel antibiotic screening methods to awaken silent or cryptic secondary metabolic pathways in actinomycetes. *J Antibiot* **70,** 865–870; 10.1038/ja.2017.51 (2017).

29. Hoshino, S. *et al.* Niizalactams A-C, Multicyclic Macrolactams Isolated from Combined Culture of Streptomyces with Mycolic Acid-Containing Bacterium. *Journal of natural products* **78,** 3011–3017; 10.1021/acs.jnatprod.5b00804 (2015).

30. Hoshino, S. *et al.* Mirilactams C-E, Novel Polycyclic Macrolactams Isolated from Combined-Culture of *Actinosynnema mirum* NBRC 14064 and Mycolic Acid-Containing Bacterium. *Chem. Pharm. Bull.* **66,** 660–667; 10.1248/cpb.c18-00143 (2018).

31. Hoffmann, T. *et al.* Correlating chemical diversity with taxonomic distance for discovery of natural products in myxobacteria. *Nature communications* **9,** 803; 10.1038/s41467-018-03184-1 (2018).

32. Wang, M. *et al.* Sharing and community curation of mass spectrometry data with Global Natural Products Social Molecular Networking. *Nature biotechnology* **34,** 828–837; 10.1038/nbt.3597 (2016).

33. Steinmetz, H. *et al.* Thuggacins, macrolide antibiotics active against *Mycobacterium tuberculosis*: Isolation from myxobacteria, structure elucidation, conformation analysis and biosynthesis. *Chem. Eur. J.* **13,** 5822–5832; 10.1002/chem.200700269 (2007).

34. Bultel-Poncé, V., Berge, J. P., Debitus, C., Nicolas, J. L. & Guyot, M. Metabolites from the Sponge-Associated Bacterium Pseudomonas Species. *Marine Biotechnology* **1,** 384–390; 10.1007/PL00011792 (1999).

35. Kim, W. J. *et al.* Liquid Chromatography-Mass Spectrometry-Based Rapid Secondary-Metabolite Profiling of Marine Pseudoalteromonas sp. M2. *Marine drugs* **14,** 24; 10.3390/md14010024 (2016).

36. Saalim, M., Villegas-Moreno, J. & Clark, B. R. Bacterial Alkyl-4-quinolones: Discovery, Structural Diversity and Biological Properties. *Molecules (Basel, Switzerland)* **25**; 10.3390/molecules25235689 (2020).

37. Blin, K. *et al.* antiSMASH 6.0: improving cluster detection and comparison capabilities. *Nucleic Acids Res.* **49,** W29-W35; 10.1093/nar/gkab335 (2021).

38. Coulon, P. M. L., Groleau, M.-C. & Déziel, E. Potential of the *Burkholderia cepacia* Complex to Produce 4-Hydroxy-3-Methyl-2-Alkyquinolines. *Front. Cell. Infect. Microbiol.* **9,** 33; 10.3389/fcimb.2019.00033 (2019).

39. Gallagher, L. A., McKnight, S. L., Kuznetsova, M. S., Pesci, E. C. & Manoil, C. Functions required for extracellular quinolone signaling by Pseudomonas aeruginosa. *J. Bacteriol.* **184,** 6472–6480; 10.1128/JB.184.23.6472–6480.2002 (2002).

40. Vial, L. *et al. Burkholderia pseudomallei*, *B. thailandensis*, and *B. ambifaria* produce 4-hydroxy-2-alkylquinoline analogues with a methyl group at the 3 position that is required for quorum-sensing regulation. *J. Bacteriol.* **190,** 5339–5352; 10.1128/JB.00400-08 (2008).

41. Klaus, J. R. *et al.* Secondary metabolites from the *Burkholderia pseudomallei* complex: structure, ecology, and evolution. *J. Ind. Microbiol. Biotechnol.* **47,** 877–887; 10.1007/s10295-020-02317-0 (2020).

42. Buntin, K. *et al.* Biosynthesis of thuggacins in myxobacteria: comparative cluster analysis reveals basis for natural product structural diversity. *Chemistry & biology* **17,** 342–356; 10.1016/j.chembiol.2010.02.013 (2010).

43. Keatinge-Clay, A. T. The structures of type I polyketide synthases. *Nat. Prod. Rep.* **29,** 1050–1073; 10.1039/c2np20019h (2012).

44. Petkovic, H. *et al.* Substrate specificity of the acyl transferase domains of EpoC from the epothilone polyketide synthase. *Org. Biomol. Chem.* **6,** 500–506; 10.1039/b714804f (2008).

45. Del Vecchio, F. *et al.* Active-site residue, domain and module swaps in modular polyketide synthases. *J. Ind. Microbiol. Biotechnol.* **30,** 489–494; 10.1007/s10295-003-0062-0 (2003).

46. Zhang, F. *et al.* Structural Insights into the Substrate Specificity of Acyltransferases from Salinomycin Polyketide Synthase. *Biochemistry* **58,** 2978–2986; 10.1021/acs.biochem.9b00305 (2019).

47. Keatinge-Clay, A. T. A Tylosin Ketoreductase Reveals How Chirality is Determined in Polyketides. *Chem. Biol.* **14,** 898–908; 10.1016/j.chembiol.2007.07.009 (2007).

48. Kwan, D. H. *et al.* Prediction and manipulation of the stereochemistry of enoylreduction in modular polyketide synthases. *Chem. Biol.* **15,** 1231–1240; 10.1016/j.chembiol.2008.09.012 (2008).

49. Bock, M., Buntin, K., Müller, R. & Kirschning, A. Stereochemical determination of thuggacins A-C, highly active antibiotics from the myxobacterium Sorangium cellulosum. *Angewandte Chemie (International ed. in English)* **47,** 2308–2311; 10.1002/anie.200704897 (2008).

50. Tsutsumi, T. *et al.* Total Synthesis of Thuggacin cmc-A and Its Structure Determination. *Org. Lett.* **23,** 5208–5212; 10.1021/acs.orglett.1c01743 (2021).

51. Bock, M., Dehn, R. & Kirschning, A. Total synthesis of thuggacin B. *Angew. Chem. Int. Ed. Engl.* **47,** 9134–9137; 10.1002/anie.200803271 (2008).

52. Supong, K., Thawai, C., Supothina, S., Auncharoen, P. & Pittayakhajonwut, P. Antimicrobial and anti-oxidant activities of quinoline alkaloids from Pseudomonas aeruginosa BCC76810. *Phytochem. Lett.* **17,** 100–106; 10.1016/j.phytol.2016.07.007 (2016).

53. Irschik, H., Reichenbach, H., Höfle, G. & Jansen, R. The thuggacins, novel antibacterial macrolides from *Sorangium cellulosum* acting against selected Gram-positive bacteria. *J Antibiot.* **60,** 733–738; 10.1038/ja.2007.95 (2007).

54. Franke, J. *et al.* Total and semi-syntheses of antimicrobial thuggacin derivatives. *Chemistry (Weinheim an der Bergstrasse, Germany)* **21,** 4272–4284; 10.1002/chem.201405874 (2015).

55. Golkar, T., Zieliński, M. & Berghuis, A. M. Look and Outlook on Enzyme-Mediated Macrolide Resistance. *Front. Microbiol.* **9,** 1942; 10.3389/fmicb.2018.01942 (2018).

56. Zieliński, M., Park, J., Sleno, B. & Berghuis, A. M. Structural and functional insights into esterase-mediated macrolide resistance. *Nat Commun* **12,** 1732; 10.1038/s41467-021-22016-3 (2021).

57. Wu, K., Wang, H., Sun, H. & Wei, D. Efficient kinetic resolution of phenyl glycidyl ether by a novel epoxide hydrolase from Tsukamurella paurometabola. *Appl Microbiol Biotechnol* **99,** 9511–9521; 10.1007/s00253-015-6716-9 (2015).

58. He, J., Yuan, S., Wang, P. & Wang, N. Tsukamurella sp. E105 as a new biocatalyst for highly enantioselective hydrolysis of ethyl 2-(2-oxopyrrolidin-1-yl) butyrate. *Journal of Industrial Microbiology & Biotechnology* **39,** 1261–1268; 10.1007/s10295-012-1132-y (2012).

Supporting information

Co-cultivation of MSr12523 with *Tsukamurella* Strains Upregulates Production of Antitubercular Compound Families

Sebastian Walesch*, Markus Neuber*, Chantal D. Bader, Daniel Krug, Rolf Müller

Materials and methods

Bacterial strains and cultivation media

Table S 4.1: List of strains used in this study

Strain	Function	Source
MSr12523	Producer of myxenolone and thuggacin P	MINS-Lab
Tsukamurella pseudospumae DSM44118	Inductor strain in co-cultivation	DSMZ

Cultivation media

Each medium used in this study was prepared with deionised water. All media were sterilised by autoclaving at 121 °C, 2 bar for 20 min.

Tryptic soy broth- (TSB)-medium was used for cultivation of *T. speudospumae*, 2SWT and RGSR for myxobacteria.

Table S 4.2: List of culture medium recipes

TSB medium		
Amount	**Ingredient**	**Supplier**
30 g/L	Tryptic soy broth	Sigma Aldrich
PH adjusted to 7.3 with 1 N KOH.		
2SWT medium		
Amount	**Ingredient**	**Supplier**
1.0 g/L	Soytone	BD
2.0 g/L	Soluble starch	Roth
2.0 g/L	Glucose	Roth
1.0 g/L	Maltose monohydrate	Sigma Aldrich
2.0 g/L	Cellobiose	MP Biomedicals
0.5 g/L	$CaCl_2$ x 2 H_2O	Sigma Aldrich

1.0 g/L	$MgSO_4$ x 7 H_2O	Grüssing
2.38 g/L	HEPES	Roth
PH adjusted to 7.0 with 10 N KOH.		
RGSR medium		
Amount	**Ingredient**	**Supplier**
1.0 g/L	Soytone	BD
2.0 g/L	Casitone	BD
2.0 g/L	Glucose	Roth
1.0 g/L	Maltose monohydrate	Sigma Aldrich
2.0 g/L	Cellobiose	MP Biomedicals
2.5 g/L	Baker's yeast	Wonnemeyer
2.5 g/L	Potato starch	Roth
2.0 g/L	Soy flour	Hensel
1.0 g/L	Oatmeal	Holo
0.5 g/L	$MgSO_4$ x 7 H_2O	Grüssing
0.5 g/L	$CaCl_2$ x 2 H_2O	Sigma Aldrich
2.38 g/L	HEPES	Roth
PH adjusted to 7.0 with 10 N KOH.		

Microbiological methods

Fermentation of MSr12523 for analytical purposes

Cultures for analytical purposes were grown in 300 mL shaking flasks containing 100 mL of the respective fermentation medium inoculated with 2% (v/v) pre-culture. The medium was supplemented with 2% (v/v) of a sterile aqueous solution of XAD-16 adsorber resin (Sigma Aldrich) to bind secondary metabolites in the culture medium. After 7 d cultivation, the culture was pelleted in 50 mL falcon tubes in an Eppendorf centrifuge 5804R at 8288 x g and 4 °C for 10 min. The pellet was then stored at -20 °C until further use.

Large scale fermentation for compound purification

Pre-cultures of MSr12523 were cultivated in 300 mL shaking flasks containing 100 mL RGSR medium at 30 °C and 180 rpm for 5 d. These pre-cultures were used to inoculate (2% (v/v) inoculum) 6 x 1.67 L of the respective fermentation medium, supplemented with 2% (v/v) of a sterile aqueous solution of XAD-16 adsorber resin, in 5 L shaking flasks. Fermentation was performed at 30 °C and 170 rpm for 14 d. Afterwards the combined cultures were pelleted with an Avanti J-26 XP centrifuge, equipped with a JLA-8.1 rotor (Beckman Coulter) at 11978 x g and 4 °C for 15 min. The pellet was then frozen, freeze-dried and stored at -20 °C until further use.

Analytical methods

Crude extract generation for analytical purposes

Frozen or freeze-dried pellets from small scale cultivations were suspended in 80 mL acetone and stirred at 250 rpm at room temperature for 3 h. The supernatant was decanted into a round flask through a 125 micron folded filter. The solvent and potential residual water were removed on a rotary evaporator with a water bath temperature of 40 °C at appropriate pressures. The dried extract was dissolved/resuspended in 1100 µL MeOH. The crude extract was stored at -20 °C until further analysis. For the purpose of UHPLC-*hr*MS analysis, the crude extract was diluted 1:10 with methanol and centrifuged at 21500 x g and 4 °C (HIMAC CT15RE, Koki Holdings Co.) for 5 min to remove residual insolubilities such as salts, cell debris and XAD fragments.

Standardised UHPLC-MS conditions

UPLC-hrMS analysis was performed on a Dionex (Germering, Germany) Ultimate 3000 RSLC system using a Waters (Eschborn, Germany) BEH C18 column (50 x 2.1 mm, 1.7 µm) equipped with a Waters VanGuard BEH C18 1.7 µm guard column. Separation of 1 µL sample was achieved by a linear gradient from (A) H2O + 0.1 % formic acid (FA) to (B) ACN + 0.1 % FA at a flow rate of 600 µL/min and a column temperature of 45 °C. Gradient conditions for crude extract analysis were as follows: 0 – 0.5 min, 5% B; 0.5 – 18.5 min, 5 – 95% B; 18.5 – 20.5 min, 95% B; 20.5 – 21 min, 95 – 5% B; 21-22.5 min, 5% B. Following gradient conditions were applied to monitor angiolams during purification: 0 – 0.5 min, 5% B; 0.5 – 9.5 min, 5 – 95% B; 9.5 – 10.5 min, 95% B; 10.5 – 11 min, 95 – 5% B; 11-12.5 min, 5% B. UV spectra were recorded by a DAD in the range from 200 to 600 nm. The LC flow was split to 75 µL/min before entering the Bruker

Daltonics maXis 4G *hr*ToF mass spectrometer (Bremen, Germany) equipped with an Apollo II ESI source. Mass spectra were acquired in centroid mode ranging from 150 – 2500 m/z at a 2 Hz full scan rate. Mass spectrometry source parameters were set to 500 V as end plate offset; 4000 V as capillary voltage; nebuliser gas pressure 1 bar; dry gas flow of 5 L/min and a dry temperature of 200 °C. Ion transfer and quadrupole settings were set to funnel RF 350 Vpp.; multipole RF 400 Vpp as transfer settings and ion energy of 5 eV as well as a low mass cut of 300 m/z. Collision cell was set to 5.0 eV and pre-pulse storage time was set to 5 µs. Spectra acquisition rate was set to 2 Hz. Calibration was done automatically before every LC-MS run by injection of a sodium formate solution and calibration on the respective clusters formed in the ESI source. All MS analyses were acquired in the presence of the lock masses ($C_{12}H_{19}F_{12}N_3O_6P_3$, $C_{18}H_{19}O_6N_3P_3F_2$ and $C_{24}H_{19}F_{36}N_3O_6P_3$) which generate the [M+H]+ ions of 622.0289; 922.0098 and 1221.9906

Statistics based metabolome filtering

For statistical metabolomics analysis, both the myxobacterial culture and medium blanks were incubated and extracted in biological triplicates as described above. Each extract was measured as technical duplicate, giving a total number of six replicates each for the bacterial culture and medium blank extracts. T-ReX-3D molecular feature finder of MetaboScape 2021b (Bruker Daltonics, Billerica, MA, USA) was used to obtain molecular features. Detection parameters were set to intensity threshold 5×10^3 and minimum peak length of five spectra to ensure a precursor selection that has a sufficient intensity to generate tandem MS data. Identification of bacterial features was performed with the built-in ANOVA/t-test routine and filtered to appearance in all six bacterial extracts and in none of the medium blank extracts. The t-test table was used to create a scheduled precursor list (SPL) for tandem MS fragmentation[1].

Acquisition parameters for high-resolution tandem MS data

LC and MS conditions for SPL guided MS/MS data acquisitions were kept constant according to section standardised UHPLC-hrMS conditions. MS/MS data acquisition parameters were set to exclusively fragment scheduled precursor list entries. SPL tolerance parameters for precursor ion selection were set to 0.2 minutes and 0.05 m/z in the SPL MS/MS method. The method picked up to 2 precursors per cycle, applied smart exclusion after 5 spectra and performed CID and MS/MS spectra acquisition time ramping. CID Energy was ramped from 35 eV for 500 m/z to 45 eV for 1000 m/z and

60 eV for 2000 m/z. MS full scan acquisition rate was set to 2 Hz and MS/MS spectra acquisition rates were ramped from 1 to 4 Hz for precursor ion intensities of 10 kcts. to 1000 kcts..

Parameters for fragment based molecular networking

All supporting fragment based molecular networking data presented here was created based on the UHPLC-*hr*MS² chromatograms using the parameters specified in the previous section. The MS/MS chromatograms were exported containing all MS/MS data as an .mzML data file and uploaded to the GNPS server at University of California San Diego via FileZilla FTP upload to ftp:// ccms-ftp01.ucsd.edu and all acquired SPL MS/MS spectra were used for spectral network creation.[2] A molecular network was created using the online workflow at GNPS. The data was filtered by removing all MS/MS peaks within +/- 17 Da of the precursor m/z. MS/MS spectra were window filtered by choosing only the top 6 peaks in the +/- 50 Da window throughout the spectrum. The data was then clustered with a parent mass tolerance of 0.05 Da and a MS/MS fragment ion tolerance of 0.1 Da to create consensus spectra. No additional filtering of consensus spectra was conducted prior to the generation of the spectral network. Subsequently, a network was created where edges are filtered to have a cosine score above 0.65 and more than 4 matched peaks. Further edges between two nodes were kept in the network if and only if each of the nodes appeared in each other's respective top 10 most similar nodes.[2] The dataset was downloaded from the server and subsequently visualised using Cytoscape 3.9.1.

Compound purification and structure elucidation

Extraction and liquid/liquid partitioning

Extraction and liquid/liquid partitioning of cultures of MSr12523 in different RGSR medium was done with 100 mL of the respective solvents per 10 g freeze-dried pellet.

Freeze-dried pellets were extracted four times with a 1:1 mixture of methanol and acetone. For each extraction step, the suspension was stirred at 250 rpm for 30 min and decanted through glass wool and a 125 micron folded filter. The combined extracts were dried using a rotary evaporator at 40 °C water bath temperature and appropriate pressures. The dried extract was then dissolved/resuspended in a 95:5 mixture of methanol and water and defatted three times with hexane. Finally, the defatted extract was partitioned three times between water and dichloromethane (DCM). The thuggacin

P derivatives were retained in the DCM phase. The DCM phase was concentrated, moved to glass vials, dried and stored at -20 °C.

Size exclusion chromatography (SEC)

The DCM phase obtained by liquid-liquid partitioning was fractionated on a gravitation column (⌀ 3.5 cm, length 104 cm, packing height ~80 cm) using Sephadex LH 20 as stationary phase and analytical grade methanol as mobile phase. Therefore, 750-1000 µg of the dry phase was dissolved in 3-4 mL methanol and applied on the column. The drop rate was set to ~ 60 drops/ minute collecting for ~ 24 hours 600 drops per test tube via an auto sampler. 5 µL of fractions in batches of five were pooled to be analysed using UHPLC-MS. Fractions containing the same target masses were combined accordingly. Pooled fractions were dried at the rotary evaporator with appropriate pressure and a water bath temperature of 40 °C. They were transferred to 4 mL brown glass vials and stored dry at -20 °C.

Purification of macrocyclic thuggacin P1 and P2 derivatives

Purification of thuggacins P1-A, P1-C, P2-B and P2-C from the respective pooled SEC fractions was carried out on a Dionex (Germering, Germany) Ultimate 3000 SL system linked to a Bruker Daltonics HCT plus ion trap system (Bremen, Germany) with standard ESI ion source. Separation was carried out on a Waters xSelect Peptide CSH130 C18 5 µM, 250 x 10 mm column using H_2O +0.1% FA (A) and ACN + 0.1% FA (B) as mobile phase at a flow rate of 5 mL/min. Separation was started with 5% B for 2 min, followed by a ramp to 63% B over 0.5 min and an increase to 73% B over 15 min. The column was then flushed with a ramp to 95% B over 0.5 min, followed by a plateau at 95% B for 2 min brought back to 5% B within 1 min and was re-equilibrated at 5% for 2 min. Purified thuggacins P1-A, P1-C, P2-B and P2-C were dried with a rotary evaporator, moved to glass vials, dried and stored at -20 °C.

NMR-based structure elucidation

The chemical structures of all described myxenolone and thuggacin P derivatives were determined via multidimensional NMR analysis. 1D and 2D NMR spectra were recorded at 500 MHz (^{1}H) and 125 MHz (^{13}C) conduction using an Avance III (Ultrashield) 500 MHz spectrometer equipped with a cryogenically cooled triple resonance probe (Bruker Biospin Rheinstetten, Germany). All observed chemical shift values (δ) are given in in

ppm and coupling constant values (*J*) in Hz. Standard pulse programs were used for HMBC, HSQC, and gCOSY experiments. HMBC experiments were optimized for $^{2,3}J_{C\text{-}H}$ = 6 Hz. The spectra were recorded in methanol-d_3 and chemical shifts of the solvent signals at δ_H 3.31 ppm and δ_C 49.2 ppm were used as reference signals for spectra calibration. To increase sensitivity, the measurements were conducted in a 5 mm Shigemi tube (Shigemi Inc., Allison Park, PA 15101, USA). The NMR signals are grouped in the tables below and correspond to the numbering in the schemes corresponding to every table.

Biological assays

Antimicrobial assays

All microorganisms used in this study were obtained from the German Collection of Microorganisms and Cell Cultures (DSMZ), the Coli Genetic Stock Center (CGSC) or were part of our internal collection, and were handled according to standard sterile microbiological procedures and techniques.

Minimum inhibitory concentrations (MIC) of all myxenolone and thuggacin P derivatives against *Mycobacterium tuberculosis* 7H37Ra were determined by microbroth dilution assays. Methanolic or DMSO (dimethylsulfoxide) stocks (1 or 10 mg/mL) of all compounds were used to prepare serial dilutions (0.125 to 64 µg/mL) in sterile 96 well plates and the test strain was added to a final suspension of 1 x 10^5 colony forming units (CFU) CFU/mL. Afterwards the plates were incubated at 37 °C and 5% CO_2 for 7 d. The lowest concentration at which no growth was observed by visual observation was considered as the MIC.

Furthermore, MICs of myxenolones A, C and D against *Escherichia coli* BW25113, *E. coli* JW0451-2 (*acrB*-efflux pump deletion mutant of E. coli BW25113), *Staphylococcus aureus* Newman, *Pseudomonas aeruginosa* PA14 and *Acinetobacter baumannii* DSM 30008 were determined by microbroth dilution assays. Therefore, the respective overnight cultures were prepared from cryogenically preserved cultures and were diluted to achieve a final inoculum of 10^4–10^5 CFU/mL. 10 mg/mL DMSO stocks of the tested compounds were used to prepare serial dilutions as described above. The cell suspension was added and microorganisms were grown for 24 h at either 30 °C or 37 °C. Afterwards, the MIC was determined by visual observation.

Cytotoxicity assay

Cell lines were obtained from the German Collection of Microorganisms and Cell Cultures (Deutsche Sammlung für Mikroorganismen und Zellkulturen, DSMZ) or were part of our internal collection and were cultured under the conditions recommended by the depositor.

Cells were seeded at 6 x 10^3 cells per well of 96-well plates in 120 µl complete medium

and treated with purified compounds in serial dilution after 2 h of equilibration. Each compound was tested in duplicate as well as the internal solvent control. After 5 d incubation, 20 µL of 5 mg/mL MTT (thiazolyl blue tetrazolium bromide) in phosphate buffered saline (PBS) was added per well and it was further incubated for 2 h at 37°C. The medium was then discarded and before adding 100 µl 2-propanol/10 N HCl (250:1) in order to dissolve formazan granules. The absorbance at 570 nm was measured using a microplate reader (Tecan Infinite M200Pro), and cell viability was expressed as percentage relative to the respective methanol control. IC_{50} values were determined by sigmoidal curve fitting.

Thuggacin detoxification assay

Cultivation assays

100 mL shaking flasks containing 20 mL TSB medium were inoculated with 25 µL cryo stock of *Tsukamurella pseudospumae* DSM 44118 and incubated at 30 °C and 180 rpm for 2 days. Afterwards, 100 µL of that pre-culture was transferred into a reaction tube containing 5 mL of fresh TSB medium. A stock solution of cyclised thuggacin P1 derivatives was prepared with a concentration of 1 mg/mL in DMSO. The respective volume of the stock solution was used to obtain a final concentration of 5, 10 and 25 µg/mL. Only DMSO was added as a positive control. The negative control was adjusted to a pH of 8.8 to mimic the basic conditions during cultivation, but did not contain the bacteria. The assay was incubated for 48 hours at 30 °C and 180 rpm. All cultivations positive and negative controls were conducted in biological triplicates.

Samples of 500 µL were taken after 0, 24 and 48 h, frozen and subsequently freeze-dried. Freeze-dried pellets were extracted with 1000 µL MeOH in an ultrasonic bath for 15 min. The resulting extracts were concentrated to a volume of 50 µL MeOH and analysed by UHPLC-MS.

Assays with cell lysate and supernatant

300 mL shaking flasks containing 50 mL TSB medium were inoculated with 50 µL of *Tsukamurella pseudospumae* DSM 44118 from cryo stock and incubated at 30 °C and 180 rpm for 2 days. The whole culture was centrifuged (5.000 g, 10 min, 4°C) to obtain the supernatant. The resulting cell pellet was resuspended in 20 mL GF buffer (20 mM HEPES, 150 mM NaCl, 5 % [v/v] glycerol). Subsequently, the concentrated cell suspension was sonicated for 6 minutes (pulse: 15 sec on and 45 sec off, amplitude: 50%) and kept on ice. The treated cell suspension was centrifuged (15.000 g, 10 min, 4 °C) to obtain the cell lysate. For the assay, 1000 µL of untreated cell lysate or supernatant was mixed with 10 µL of the cyclised thuggacin P1 stock solution (1 mg/mL DMSO) and incubated for 48 hours at 30 °C and 180 rpm.

Samples of 300 µL were taken after 0, 24 and 48 h, frozen and subsequently freeze-dried. Freeze-dried pellets were extracted with 500 µL MeOH in an ultrasonic bath for 15 min. The resulting extracts were concentrated to a volume of 50 µL MeOH and analysed by UHPLC-MS.

Results

Isotope patterns of myxenolones C and D

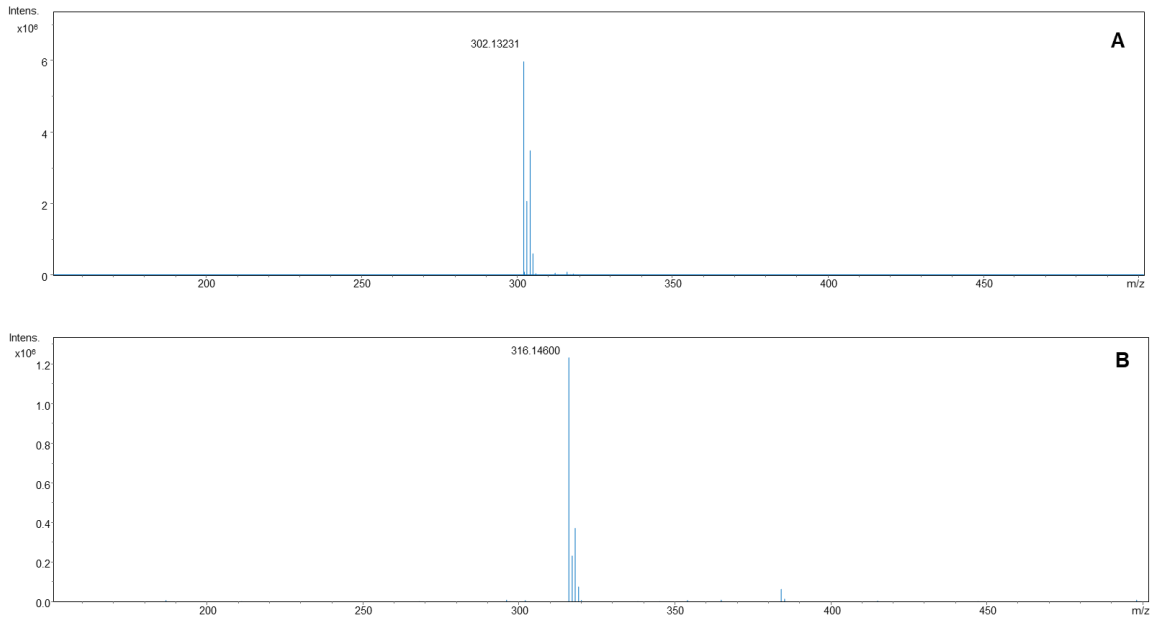

Figure S 4.1: Isotope patterns of myxenolone C (A) and D (B). *hr*MS spectra $[M+H]^+$ of myxenolones C and D acquired in positive ESI-mode display the characteristic isotope patterns of molecules with one chlorination.

NMR-based structure elucidation of the myxenolone compound family

The structures of all myxenolone derivatives were elucidated based on ^{1}H, ^{13}C, COSY, HSQC, and HMBC NMR spectra. COSY correlations used for the structure elucidation of myxenolones A1 and A2 are indicated in bold, relevant HMBC correlations as arrows. For all further myxenolone derivatives, only COSY and HMBC correlations indicating the differences from A1 and A2 are indicated as described.

Table S 4.3: NMR spectroscopic data for myxenolone A1 (1)

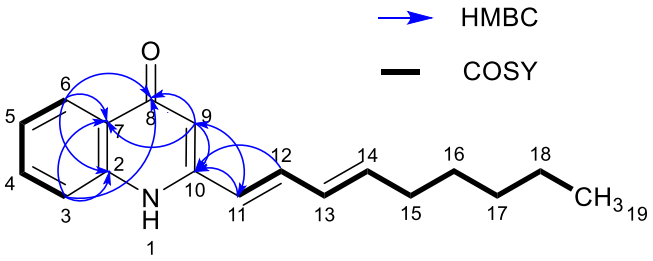

Position	δ_C[a] [ppm]	Type	δ_H[b] [ppm]	H Multiplicity (*J* [Hz])	COSY[c]	HMBC[d]
2	141.7	C				
3	119.4	CH	7.65	m	4, 5	2, 4, 5, 6, 7, 8
4	133.8	CH	7.69	m	3, 5, 6	2, 3, 5, 6
5	125.3	CH	7.39	m	3, 4, 6	2, 3, 4, 6
6	126.0	CH	8.19	dd (8.2, 1.2)	4, 5	2, 3, 4, 5, 7, 8
7	126.1	C				
8	180.5	C				
9	106.9	CH	6.45	S		7, 8, 10, 11
10	150.9	C				
11	123.2	CH	6.38	br d (15.6)	12	9, 10, 12, 13
12	139.3	CH	7.28	br dd (15.7, 10.5)	11, 13	10, 11, 13, 14
13	130.9	CH	6.34	M	12, 14, 15	11, 12, 14, 15, 16
14	143.8	CH	6.18	dt (15.0, 7.1, 7.1)	13, 15	12, 13, 15, 16
15	34.2	CH_2	2.23	q (7.0, 7.0, 7.0)	13, 14, 16	12, 13, 14, 16, 17
16	30.0	CH_2	1.48	m	15, 17	14, 15, 17, 18
17	32.8	CH_2	1.35	m	16, 18	15, 16, 18, 19
18	23.7	CH_2	1.37	m	17, 19	16, 17, 19
19	14.5	CH_3	0.93	m	18	17, 18

[a] Acquired in methanol-d_4 at 125 MHz and calibrated to solvent signal at 49.2 ppm.
[b] Acquired in methanol-d_4 at 500 MHz and calibrated to solvent signal at 3.31 ppm.
[c] Proton showing COSY correlations to indicated proton.
[d] Proton showing HMBC correlations to indicated carbon.

Table S 4.4: NMR spectroscopic data for myxenolone A2 (2)

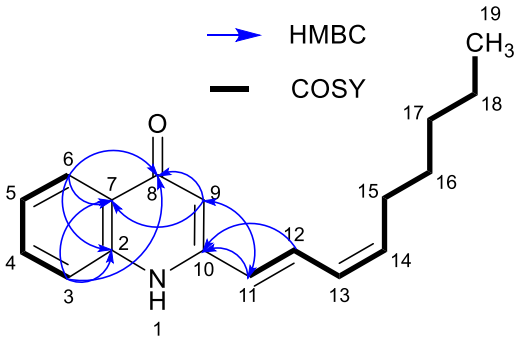

Position	δ_C[a] [ppm]	Type	δ_H[b] [ppm]	H Multiplicity (*J* [Hz])	COSY[c]	HMBC[d]
2	141.8	C				
3	119.4	CH	7.65	m	4, 5	2, 4, 5, 6, 7, 8
4	133.9	CH	7.70	m	3, 5, 6	2, 3, 5, 6
5	125.3	CH	7.39	m	3, 4, 6	2, 3, 6
6	126.1	CH	8.20	dd (8.2, 1.2)	4, 5	2, 3, 4, 5, 7, 8
7	126.1	C				
8	180.7	C				
9	107.6	CH	6.46	s		7, 8, 11
10	150.6	C				
11	125.5	CH	6.46	br d (15.6)	12	9, 10, 12, 13, 14
12	133.7	CH	7.67	m	11, 13, 14	10, 13, 14
13	129.0	CH	6.27	br t (10.9, 10.9)	12, 14, 15	11, 12, 15, 16
14	140.7	CH	5.86	dt (10.6, 7.9, 7.9)	12, 13, 15	12, 15, 16
15	29.4	CH_2	2.42	br q (7.5, 7.5, 7.5)	13, 14, 16	12, 13, 14, 16, 17
16	30.5	CH_2	1.49	m	15, 17	14, 15, 17, 18
17	32.8	CH_2	1.36	m	16, 18	15, 16, 18, 19
18	23.8	CH_2	1.37	m	17, 19	16, 17, 19
19	14.6	CH_3	0.93	m	18	17, 18

[a] Acquired in methanol-d_4 at 125 MHz and calibrated to solvent signal at 49.2 ppm.
[b] Acquired in methanol-d_4 at 500 MHz and calibrated to solvent signal at 3.31 ppm.
[c] Proton showing COSY correlations to indicated proton.
[d] Proton showing HMBC correlations to indicated carbon.

Table S 4.5: NMR spectroscopic data for myxenolone B1 (3)

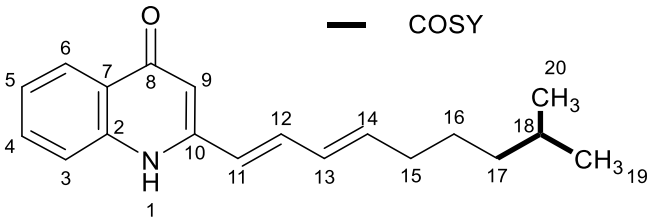

Position	δ_C[a] [ppm]	Type	δ_H[b] [ppm]	H Multiplicity (*J* [Hz])	COSY[c]	HMBC[d]
2	140.2	C				
3	117.9	CH	7.64	m	4, 5	4, 5, 6, 8, 10
4	132.2	CH	7.70	m	3, 5, 6	2, 3, 6
5	123.8	CH	7.39	m	3, 4, 6	3, 4, 6
6	124.5	CH	8.21	dd (8.2, 1.3)	4, 5	2, 3, 4, 5, 7, 8
7	124.5	C				
8	179.0	C				
9	105.3	CH	6.45	s		7, 8, 11
10	149.4	C				
11	121.7	CH	6.38	d (15.7)	12	8, 9, 10, 12, 13, 14
12	137.7	CH	7.28	dd (15.7, 10.5)	11, 13, 14	10, 11, 13, 14
13	129.4	CH	6.34	m	12, 14, 15	11, 12, 14, 15
14	142.3	CH	6.18	dt (15.0, 7.3, 7.3)	12, 13, 15	12, 13, 15, 16
15	32.9	CH_2	2.22	q (7.1, 7.1, 7.1)	13, 14, 16	12, 13, 14, 16, 17, 18
16	26.6	CH_2	1.49	m	15, 17	14, 15, 17, 18
17	38.3	CH_2	1.24	m	16, 18	15, 16, 18, 19, 20
18	27.7	CH	1.58	m	17, 19, 20	16, 17, 19, 20
19	21.6	CH_3	0.91	d (6.6)	18	17, 18, 20
20	21.6	CH_3	0.91	d (6.6)	18	17, 18, 19

[a] Acquired in methanol-d_4 at 125 MHz and calibrated to solvent signal at 49.2 ppm.
[b] Acquired in methanol-d_4 at 500 MHz and calibrated to solvent signal at 3.31 ppm.
[c] Proton showing COSY correlations to indicated proton.
[d] Proton showing HMBC correlations to indicated carbon.

Table S 4.6: NMR spectroscopic data for myxenolone B2 (4)

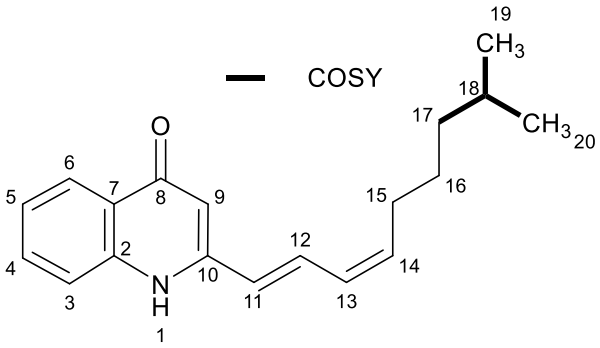

Position	δ_C[a] [ppm]	Type	δ_H[b] [ppm]	H Multiplicity (*J* [Hz])	COSY[c]	HMBC[d]
2	140.3	C				
3	117.9	CH	7.64	m	4, 5	4, 5, 6, 8, 10
4	132.3	CH	7.70	m	3, 5, 6	2, 3, 6
5	123.8	CH	7.39	m	3, 4, 6	3, 4, 6
6	124.5	CH	8.19	dd (8.2, 1.3)	4, 5	2, 3, 4, 5, 7, 8
7	124.6	C				
8	179.1	C				
9	106.1	CH	6.46	s		7, 8, 11
10	149.1	C				
11	124.0	CH	6.46	d (15.6)	12	8, 9, 10, 12, 13, 14
12	132.1	CH	7.66	m	11, 13, 14	10, 11, 13, 14
13	127.4	CH	6.27	t (10.9, 10.9)	12, 14, 15	11, 12, 14, 15
14	139.1	CH	5.86	dt (10.6, 7.9, 7.9)	12, 13, 15	12, 13, 15, 16
15	28.1	CH_2	2.41	qd (7.6, 7.6, 7.6, 1.3)	13, 14, 16	12, 13, 14, 16, 17, 18
16	27.1	CH_2	1.50	m	15, 17	14, 15, 17, 18
17	38.3	CH_2	1.29	m	16, 18	15, 16, 18, 19, 20
18	27.7	CH	1.58	m	17, 19, 20	16, 17, 19, 20
19	21.6	CH_3	0.91	br d (6.6)	18	17, 18, 20
20	21.6	CH_3	0.91	br d (6.6)	18	17, 18, 19

[a] Acquired in methanol-d_4 at 125 MHz and calibrated to solvent signal at 49.2 ppm.
[b] Acquired in methanol-d_4 at 500 MHz and calibrated to solvent signal at 3.31 ppm.
[c] Proton showing COSY correlations to indicated proton.
[d] Proton showing HMBC correlations to indicated carbon.

Table S 4.7: NMR spectroscopic data for myxenolone C1 (5)

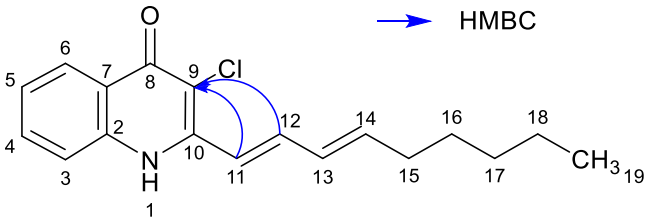

Position	δ_C[a] [ppm]	Type	δ_H[b] [ppm]	H Multiplicity (*J* [Hz])	COSY[c]	HMBC[d]
2	140.7	C				
3	119.5	CH	7.73	m	4, 5	2, 4, 7, 8
4	133.8	CH	7.70	m	3, 5, 6	2, 3, 5, 6
5	125.4	CH	7.40	ddd (8.2, 6.5, 1.6)	3, 4, 6	2, 3, 4, 6, 7
6	126.4	CH	8.24	m	4, 5	2, 3, 4, 7, 8
7	125.4	C				
8	174.6	C				
9	115.6	C				
10	147.0	C				
11	121.3	CH	6.93	d (15.9)	12, 13	9, 10, 13
12	140.3	CH	7.33	dd (15.8, 10.4)	11, 13, 14	9, 10, 11, 13, 14
13	131.2	CH	6.44	dd (14.7, 10.2)	11, 12, 14	11, 12, 15
14	144.6	CH	6.24	m	12, 13, 15	12, 13, 15, 16
15	34.2	CH_2	2.26	q (6.9, 6.9, 6.9)	13, 14, 16	12, 13, 14, 16, 17
16	29.9	CH_2	1.50	m	15, 17	14, 18
17	32.8	CH_2	1.37	m	16	15, 16, 18 ,19
18	23.7	CH_2	1.36	m	19	17, 19
19	14.5	CH_3	0.93	m	18	17, 18

[a] Acquired in methanol-d_4 at 125 MHz and calibrated to solvent signal at 49.2 ppm.
[b] Acquired in methanol-d_4 at 500 MHz and calibrated to solvent signal at 3.31 ppm.
[c] Proton showing COSY correlations to indicated proton.
[d] Proton showing HMBC correlations to indicated carbon.

Table S 4.8: NMR spectroscopic data for myxenolone C2 (6)

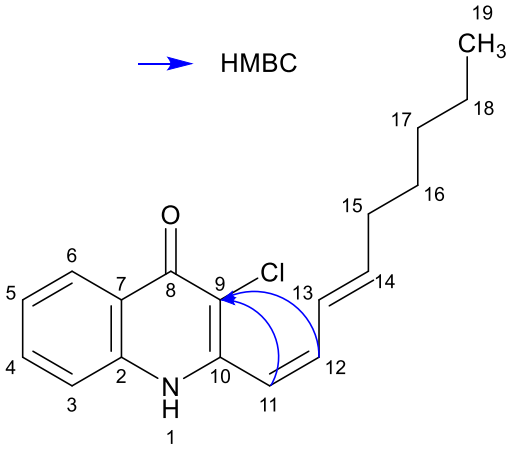

Position	δ_C[a] [ppm]	Type	δ_H[b] [ppm]	H Multiplicity (*J* [Hz])	COSY[c]	HMBC[d]
2	140.6	C				
3	119.7	CH	7.63	m	4, 5	4, 5, 6, 7, 8
4	133.6	CH	7.72	m	3, 5, 6	2, 3
5	125.7	CH	7.45	ddd (8.2, 7.0, 1.1)	3, 4, 6	2, 3, 4, 6, 7
6	126.5	CH	8.29	m	4, 5	2, 3, 4, 5, 8
7	125.2	C				
8	174.5	C				
9	115.6	C				
10	148.0	C				
11	119.5	CH	6.36	d (11.4)	12	9, 10, 12, 13
12	138.7	CH	6.66	t (11.3, 11.3)	11, 13	9, 10, 13, 14
13	127.1	CH	6.23	m	12, 14, 15	11, 12, 14, 15
14	143.9	CH	6.13	dt (15.0, 7.2, 7.2)	13, 15	12, 13, 15, 16
15	34.0	CH_2	2.14	q (7.3, 7.3, 7.3)	13, 14, 16	12, 13, 14, 16, 17
16	29.8	CH_2	1.42	m	15, 17	14, 15, 17, 18
17	32.7	CH_2	1.30	m	16	15, 16, 18, 19
18	23.7	CH_2	1.30	m	19	16, 17, 19
19	14.5	CH_3	0.88	m	18	17, 18

[a] Acquired in methanol-d_4 at 125 MHz and calibrated to solvent signal at 49.2 ppm.
[b] Acquired in methanol-d_4 at 500 MHz and calibrated to solvent signal at 3.31 ppm.
[c] Proton showing COSY correlations to indicated proton.
[d] Proton showing HMBC correlations to indicated carbon.

Table S 4.9: NMR spectroscopic data for myxenolone D1 (7)

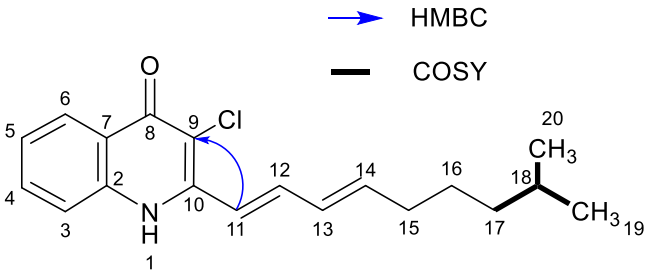

Position	δ_C[a] [ppm]	Type	δ_H[b] [ppm]	H Multiplicity (*J* [Hz])	COSY[c]	HMBC[d]
2	140.6	C				
3	119.4	CH	7.73	m	4, 5	2, 7
4	133.9	CH	7.71	m	3, 5, 6	2, 3, 5, 6
5	125.4	CH	7.41	ddd (8.2, 6.2, 1.9)	3, 4, 6	2, 3, 4, 7
6	126.4	CH	8.24	dd (7.9, 0.9)	4, 5	2, 3, 4, 8
7	124.9	C				
8	174.7	C				
9	115.6	C				
10	146.8	C				
11	121.2	CH	6.93	d (15.9)	12, 13, 14	9, 10, 12, 13
12	140.4	CH	7.33	dd (15.8, 10.4)	11, 13, 14	10, 11, 13, 14
13	131.2	CH	6.44	ddd (15.1, 10.4, 0.6)	11, 12, 14, 15	11, 12, 14, 15
14	144.7	CH	6.25	m	11, 12, 13, 15	12, 13, 15, 16
15	34.5	CH_2	2.25	q (7.1, 7.1, 7.1)	13, 14, 16	12, 13, 14, 16, 17
16	28.1	CH_2	1.51	m	15, 17	14, 15, 17, 18, 19, 20
17	39.9	CH_2	1.26	m	16, 18	15, 16, 18, 19, 20
18	29.2	CH	1.59	dt (13.4, 6.7, 6.7)	17, 19, 20	16, 17, 19, 20
19	23.1	CH_3	0.92	d (6.6)	18	17, 18, 20
20	23.1	CH_3	0.92	d (6.6)	18	17, 18, 19

[a] Acquired in methanol-d_4 at 125 MHz and calibrated to solvent signal at 49.2 ppm.
[b] Acquired in methanol-d_4 at 500 MHz and calibrated to solvent signal at 3.31 ppm.
[c] Proton showing COSY correlations to indicated proton.
[d] Proton showing HMBC correlations to indicated carbon.

NMR-based structure elucidation of the thuggacin P compound family

The structures of all thuggacin P derivatives were elucidated based on ^{1}H, ^{13}C, COSY, HSQC, and HMBC NMR spectra. COSY correlations used for the structure elucidation of thuggacin P1-A are indicated in bold, relevant HMBC correlations as arrows. For all further thuggacin P derivatives, only COSY and HMBC correlations indicating the differences from thuggacin P1-A are indicated as described.

Table S 4.10: NMR spectroscopic data for thuggacin P1-A (8)

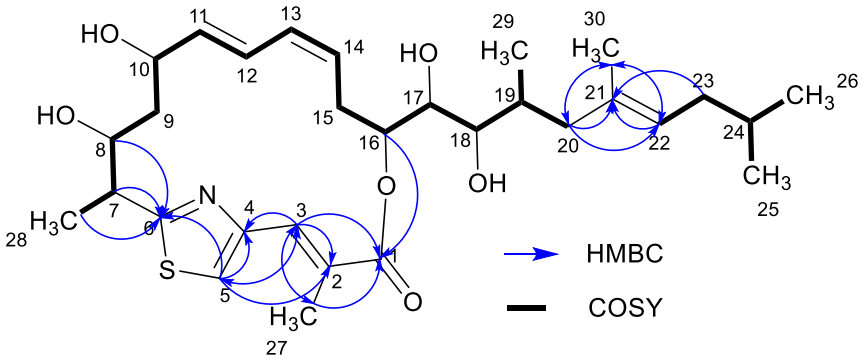

Position	δ_C[a] [ppm]	Type	δ_H[b] [ppm]	H Multiplicity (*J* [Hz])	COSY[c]	HMBC[d]
1	169.2	C				
2	128.0	C				
3	135.7	CH	8.08	m	5, 27	1, 2, 4, 5, 27
4	151.0	C				
5	120.5	CH	7.66	s	3, 7[e], 27[e]	2, 3, 4, 6
6	171.7	C				
7	42.8	CH	3.71	dd (7.3, 3.4)	5[e], 8, 28	6, 8, 28
8	71.6	CH	4.10	dt (11.0, 3.6, 3.6)	7, 9a, 9b	6, 9, 28
9a	44.7	CH_2	1.58	m	8, 9b, 10	7, 8, 10, 11
9b			0.57	br dd (13.5, 11.2)	8, 9a, 10	7, 8, 10, 11
10	70.8	CH	4.73	br t (9.8, 9.8)	9a, 9b, 11	8, 9, 11, 12
11	138.4	CH	5.40	m	10, 12	9, 10, 13
12	127.4	CH	6.65	dd (15.0, 11.3)	11, 13	9, 10, 13, 14
13	132.7	CH	5.92	br t (11.0, 11.0)	12, 14, 15a, 15b	11, 12, 15, 16
14	129.0	CH	5.35	m	13, 15a, 15b	12, 15, 16
15a	31.7	CH_2	2.99	dt (14.1, 11.4, 11.4)	13, 14, 15b, 16	13, 14, 16
15b			2.30	m	13, 14, 15a, 16	13, 14, 16
16	76.2	CH	5.03	dd (10.0, 3.8)	15a, 15b, 17	1, 14, 15, 18
17	74.4	CH	3.75	dd (6.0, 3.9)	16, 18	15, 16, 18, 19
18	74.5	CH	3.52	dd (6.0, 3.7)	17, 19	16, 17, 19, 20, 29
19	34.1	CH	2.05	m	18, 20a, 20b, 29	18, 20, 29
20a	46.0	CH_2	2.19	br dd (12.7, 6.1)	19, 20b, 22, 30	18, 19, 21, 22, 30
20b			1.85	m	19, 20a, 22, 30	18, 19, 21, 22, 29, 30
21	135.2	C				
22	126.9	CH	5.21	br t (6.9, 6.9)	20a, 20b, 23, 30	19, 20, 23, 24, 30
23	38.5	CH_2	1.87	m	22, 24	20, 21, 22, 24, 25, 26
24	30.4	CH	1.57	m	23, 25, 26	22, 23, 25, 26
25	23.1	CH_3	0.87	m	24	23, 24, 26
26	23.0	CH_3	0.87	m	24	23, 24, 25
27	13.8	CH_3	2.03	m	3, 5[e]	1, 2, 3, 4, 5
28	16.7	CH_3	1.51	d (7.3)	7	6, 7, 8
29	14.1	CH_3	0.86	m	19	18, 19, 20

30	16.4	CH_3	1.60	m	20a, 20b, 22	20, 21, 22

[a] Acquired in methanol-d_4 at 125 MHz and calibrated to solvent signal at 49.2 ppm.
[b] Acquired in methanol-d_4 at 500 MHz and calibrated to solvent signal at 3.31 ppm.
[c] Proton showing COSY correlations to indicated proton.
[d] Proton showing HMBC correlations to indicated carbon.
[e] Long range coupling.

Table S 4.11: NMR spectroscopic data for thuggacin P1-C (9)

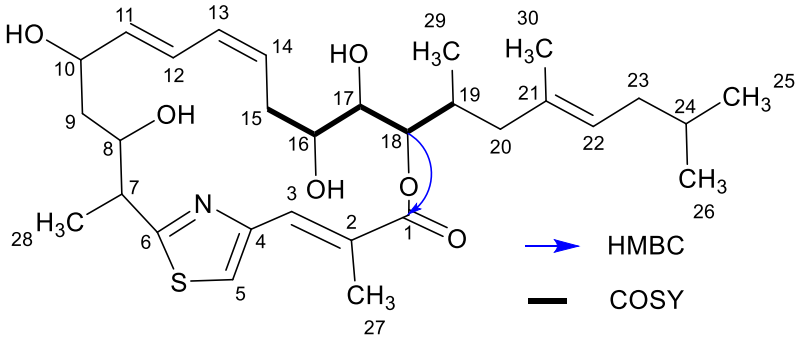

Position	δ_C[a] [ppm]	Type	δ_H[b] [ppm]	H Multiplicity (*J* [Hz])	COSY[c]	HMBC[d]
1	169.5	C				
2	129.9	C				
3	133.5	CH	7.98	m	5, 27	1, 2, 5, 27
4	151.4	C				
5	122.9	CH	7.76	s	3, 7[e], 27[e]	2, 3, 4, 6, 27
6	172.8	C				
7	42.5	CH	3.72	br dd (7.1, 2.6)	5[e], 8, 28	6, 28
8	71.3	CH	4.06	m	7, 9a, 9b	6, 7, 9, 28
9a	44.4	CH_2	1.67	br dd (4.0, 2.0)	8, 9b, 10	7, 8, 10, 11
9b			0.84	m	8, 9a, 10	7, 8, 10
10	71.2	CH	4.69	m	9a, 9b, 11, 12	8, 9, 11, 12
11	137.7	CH	5.52	dd (15.1, 8.2)	10, 12	9, 10, 13
12	126.9	CH	6.47	dd (15.1, 11.3)	10, 11, 13	9, 10, 11, 13, 14
13	129.6	CH	5.91	br t (11.0, 11.0)	12, 14, 15a, 15b	11, 12, 15
14	130.8	CH	5.58	td (10.3, 10.3, 3.2)	13, 15a, 15b	15, 16
15a	31.0	CH_2	3.03	br dd (16.0, 10.3)	13, 14, 15b, 16	12, 13, 14, 16
15b			1.63	m	13, 14, 15a, 16	13, 14
16	74.6	CH	3.64	m	15a, 15b, 17	14, 15, 17, 18
17	73.9	CH	3.84	br dd (5.7, 1.3)	16, 18	15, 16, 19
18	77.1	CH	5.10	dd (6.9, 1.4)	17, 19	1, 16, 19, 20, 29
19	33.9	CH	2.28	u	18, 20a, 20b, 29	17, 18, 20, 21, 29
20a	45.4	CH_2	2.39	m	19, 20b, 22, 30	18, 19, 21, 22, 29, 30
20b			1.88	m	19, 20a, 30	18, 19, 21, 22, 29, 30
21	135.0	C				
22	127.2	CH	5.22	m	20a, 23, 24, 30	20, 23, 24, 30
23	38.4	CH_2	1.91	m	22, 24	21, 22, 25, 26
24	30.4	CH	1.61	m	22, 23, 25, 26	21, 22, 23, 25, 26

25	23.0	CH_3	0.91	m	24	23, 24, 26
26	23.0	CH_3	0.91	m	24	23, 24, 25
27	15.1	CH_3	2.29	d (1.2)	3, 5[e]	1, 2, 3, 4, 5
28	18.7	CH_3	1.51	m	7	6, 7, 8
29	16.1	CH_3	0.89	m	19	18, 19, 20
30	16.2	CH_3	1.60	m	20a, 20b, 22	20, 21, 22, 23

[a] Acquired in methanol-d_4 at 125 MHz and calibrated to solvent signal at 49.2 ppm.
[b] Acquired in methanol-d_4 at 500 MHz and calibrated to solvent signal at 3.31 ppm.
[c] Proton showing COSY correlations to indicated proton.
[d] Proton showing HMBC correlations to indicated carbon.
[e] Long range coupling.

Table S 4.12: NMR spectroscopic data for thuggacin P2-B (10)

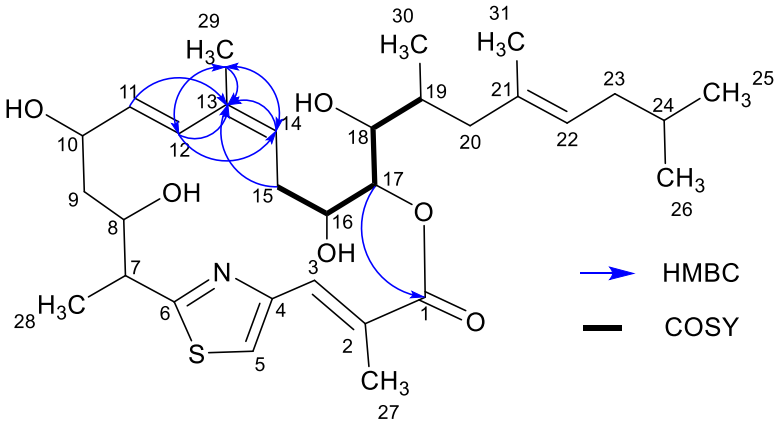

Position	δ_C[a] [ppm]	Type	δ_H[b] [ppm]	H Multiplicity (*J* [Hz])	COSY[c]	HMBC[d]
1	171.0	C				
2	131.0	C				
3	134.2	CH	8.03	dd (1.3, 0.7)	5, 27	1, 2, 5, 27
4	152.1	C				
5	120.9	CH	7.65	S	3, 27[e]	2, 3, 4, 6, 7, 27
6	172.8	C				
7	43.0	CH	3.60	dd (7.1, 3.0)	8, 28	6, 8, 9, 28
8	72.7	CH	4.10	m	7, 9a, 9b	6, 9, 10, 28
9a	42.6	CH_2	1.85	m	8, 9b, 10	7, 8, 10
9b			1.63	m	8, 9a, 10	7, 8, 10, 28
10	72.6	CH	4.14	m	9a, 9b, 11, 12	8, 9, 11, 12
11	135.3	CH	5.62	dd (15.6, 7.5)	10, 12	9, 10, 13, 14
12	127.6	CH	6.42	d (15.6)	10, 11, 14	9, 10, 13, 14, 29
13	135.0	C				
14	128.2	CH	5.39	m	12, 15a, 15b, 29	13, 15, 16, 29
15a	33.2	CH_2	2.68	m	14, 15b, 16	13, 14, 16, 17
15b			1.98	m	14, 15a, 16, 29	13
16	72.3	CH	3.92	m	15a, 15b, 17	14, 15, 17
17	80.3	CH	5.05	dd (7.6, 1.8)	16, 18	1, 15, 16, 18

18	74.5	CH	3.91	m	17, 19	17, 19, 20, 30
19	33.4	CH	2.05	m	18, 20a, 20b, 30	20
20a	46.1	CH_2	2.26	m	19, 20b, 22, 31	18, 19, 21, 22, 30, 31
20b			1.96	m	19, 20a, 22	18, 19, 21, 22, 30, 31
21	135.1	C				
22	127.0	CH	5.23	m	20a, 20b, 23, 31	20, 23, 24, 31
23a	38.5	CH_2	1.91	br d (5.0)	22, 24, 31	21, 22, 24, 25, 26
23b			1.49	m		22, 24
24	30.4	CH	1.60	m	23a, 25, 26	23, 25, 26
25	23.0	CH_3	0.90	m	24	23, 24, 26
26	23.1	CH_3	0.91	m	24	23, 24, 25
27	14.9	CH_3	2.21	d (1.3)	3, 5[e]	1, 2, 3, 4, 5
28	15.6	CH_3	1.51	m	7	6, 7, 8
29	21.1	CH_3	1.82	s	14, 15b	12, 13, 14
30	13.4	CH_3	0.92	m	19	18, 19, 20
31	16.3	CH_3	1.61	m	20a, 22, 23a	19, 20, 21, 22, 23, 24

[a] Acquired in methanol-d_4 at 125 MHz and calibrated to solvent signal at 49.2 ppm.
[b] Acquired in methanol-d_4 at 500 MHz and calibrated to solvent signal at 3.31 ppm.
[c] Proton showing COSY correlations to indicated proton.
[d] Proton showing HMBC correlations to indicated carbon.
[e] Long range coupling.

Table S 4.13: NMR spectroscopic data for thuggacin P2-C (11)

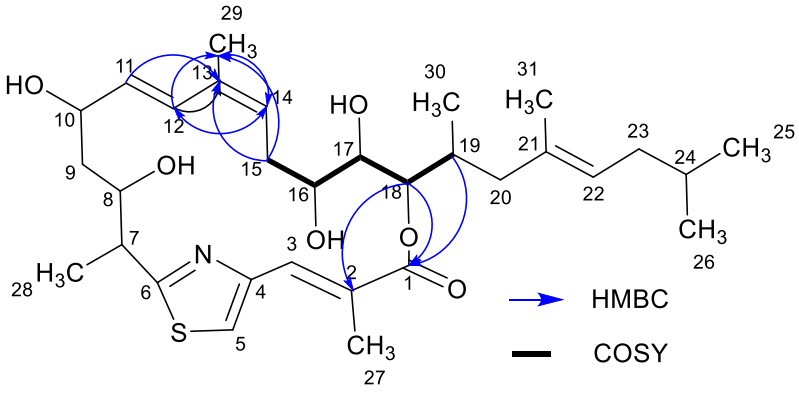

Position	δ_C[a] [ppm]	Type	δ_H[b] [ppm]	H Multiplicity (*J* [Hz])	COSY[c]	HMBC[d]
1	169.5	C				
2	129.9	C				
3	133.6	CH	8.01	d (0.9)	5, 27	1, 2, 5, 27
4	151.3	C				
5	122.8	CH	7.75	s	3, 7[e], 27[e]	2, 3, 4, 6, 7, 27
6	172.8	C				
7	42.6	CH	3.73	m	5[e], 8, 28	4, 6, 8, 9, 28
8	71.3	CH	4.08	m	7, 9a, 9b	6, 7, 9, 10, 28
9a	44.4	CH_2	1.70	q (2.0, 2.0, 2.0)	8, 9b, 10	7, 8, 11
9b			0.80	m	8, 9a, 10	7, 8

10	71.6	CH	4.72	m	9a, 9b, 11, 12	8, 9, 11, 12
11	134.1	CH	5.53	m	10, 12	9, 10, 12, 13, 14
12	128.4	CH	6.59	d (15.5)	10, 11	9, 10, 11, 13, 14, 29
13	133.1	C				
14	129.7	CH	5.51	m	15a, 15b, 29	12, 15, 16, 29
15a	30.3	CH_2	3.01	m	14, 15b, 16, 29	13, 14, 16, 17, 29
15b			1.61	m	14, 15a, 16, 29	29
16	74.9	CH	3.62	m	15a, 15b, 17	14, 15, 17, 18
17	73.7	CH	3.87	m	16, 18	1, 15, 16, 18, 19
18	76.8	CH	5.11	dd (7.1, 1.1)	17, 19	1, 2, 16, 17, 19, 20, 31
19	34.2	CH	2.28	m	18, 20a, 20b, 30	17, 18, 20, 21, 31
20a	45.3	CH_2	2.39	m	19, 20b, 22, 31	18, 19, 21, 22, 31
20b			1.88	m	19, 20a	18, 19, 21, 22, 31
21	135.1	C				
22	127.1	CH	5.22	t (7.3, 7.3)	20a, 23, 31	19, 20, 21, 23, 24, 29
23	38.4	CH_2	1.91	m	22, 24, 31	21, 22, 24, 25, 26
24	30.4	CH	1.61	m	23, 25, 26	22, 23, 25, 26
25	23.0	CH_3	0.90	m	24	23, 24, 26
26	23.0	CH_3	0.90	m	24	23, 24, 25
27	15.1	CH_3	2.27	d (1.1)	3, 5[e]	1, 2, 3, 4, 5
28	18.8	CH_3	1.51	m	7	6, 7, 8
29	20.7	CH_3	1.74	s	14, 15a, 15b	12, 13, 14, 15
30	16.1	CH_3	0.88	m	19	18, 19, 20
31	16.1	CH_3	1.59	s	20a, 22, 23	19, 20, 21, 22, 24

[a] Acquired in methanol-d_4 at 125 MHz and calibrated to solvent signal at 49.2 ppm.
[b] Acquired in methanol-d_4 at 500 MHz and calibrated to solvent signal at 3.31 ppm.
[c] Proton showing COSY correlations to indicated proton.
[d] Proton showing HMBC correlations to indicated carbon.
[e] Long range coupling.

Table S 4.14: NMR spectroscopic data for oxo-thuggacin P1 (12)

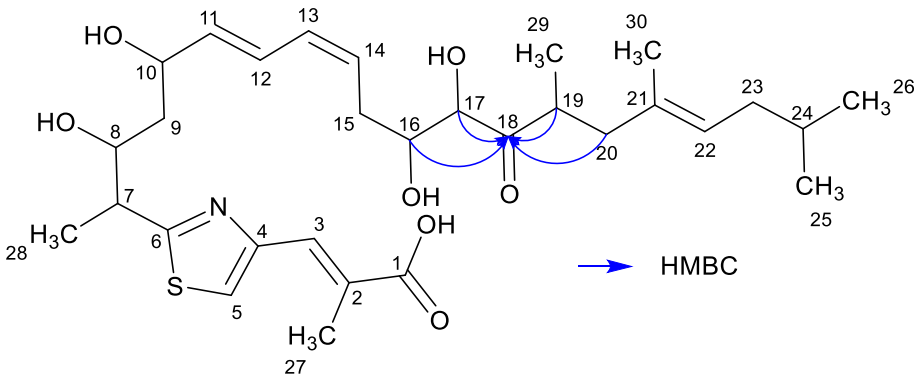

Position	δ_C[a] [ppm]	Type	δ_H[b] [ppm]	H Multiplicity (*J* [Hz])	COSY[c]	HMBC[d]
1	172.7	C				
2	130.7	C				
3	131.7	CH	7.64	d (0.9)	5, 27	1, 2, 4, 5, 27
4	152.6	C				
5	123.0	CH	7.62	m	3, 7[e]	3, 6, 7
6	174.4	C				
7	45.7	CH	3.37	dd (7.1, 4.3)	5[e], 8, 28	4, 6, 8, 9, 28
8	73.4	CH	3.97	m	7, 9	6, 7, 9, 10, 28
9	42.4	CH_2	1.63	m	8, 10	7, 8, 10, 11
10	71.9	CH	4.38	q (6.9, 6.9, 6.9)	9, 11, 12	8, 9, 11, 12, 13
11	137.4	CH	5.62	dd (15.1, 7.1)	10, 12, 13	9, 10, 12, 13, 14
12	127.4	CH	6.59	dd (15.1, 11.1)	10, 11, 13, 14	9, 10, 11, 13, 14, 15
13	131.7	CH	6.11	t (11.1, 11.1)	11, 12, 14, 15a, 15b	11, 12, 15, 16
14	128.8	CH	5.51	m	12, 13, 15a, 15b	12, 15, 16
15a	33.4	CH_2	2.58	m	13, 14, 15b, 16	13, 14, 16, 17
15b			2.43	m	13, 14, 15a, 16	13, 14, 16, 17
16	73.4	CH	3.98	m	15a, 15b, 17	14, 15, 17, 18
17	79.2	CH	4.10	d (2.1)	16	15, 16, 18
18	218.1	C				
19	40.5	CH	3.23	m	20a, 20b, 29	18, 20, 21, 29
20a	43.7	CH_2	2.42	m	19, 20b, 22, 29, 30	18, 19, 22, 30
20b			1.88	m	19, 20a, 22, 30	18, 19, 21, 22, 29
21	134.2	C				
22	127.7	CH	5.20	br t (7.3, 7.3)	20a, 20b, 23, 30	20, 23, 24, 30
23	38.4	CH_2	1.90	m	22, 24	21, 22, 24, 25, 26
24	30.3	CH	1.58	m	23, 25, 26	23, 25, 26
25	23.0	CH_3	0.89	d (6.6)	24	22, 23, 24, 26
26	22.9	CH_3	0.89	d (6.6)	24	22, 23, 24, 25
27	15.0	CH_3	2.28	d (1.3)	3	1, 2, 3, 4, 5
28	18.1	CH_3	1.43	d (7.1)	7	6, 7, 8
29	16.2	CH_3	0.98	d (6.9)	19, 20a	18, 19, 20
30	16.2	CH_3	1.61	m	20a, 20b, 22	20, 21, 22, 24

[a] Acquired in methanol-d_4 at 125 MHz and calibrated to solvent signal at 49.2 ppm.
[b] Acquired in methanol-d_4 at 500 MHz and calibrated to solvent signal at 3.31 ppm.
[c] Proton showing COSY correlations to indicated proton.
[d] Proton showing HMBC correlations to indicated carbon.
[e] Long range coupling.

Table S 4.15: NMR spectroscopic data for hydroxy-thuggacin P1 (13)

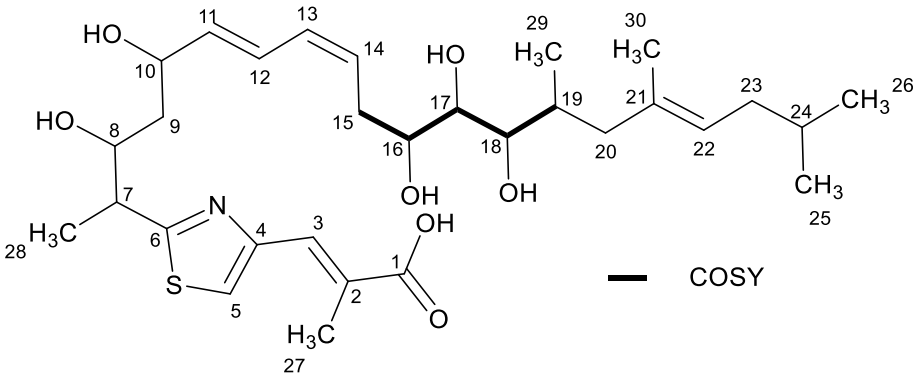

Position	δ_C[a] [ppm]	Type	δ_H[b] [ppm]	H Multiplicity (*J* [Hz])	COSY[c]	HMBC[d]
1	173.5	C				
2	131.7	C				
3	131.1	CH	7.60	d (1.0)	27	1, 2, 5, 27
4	152.8	C				
5	122.5	CH	7.59	br s	7[e]	3, 4, 6, 7
6	174.3	C				
7	45.7	CH	3.37	m	5[e], 8, 28	6, 8, 9, 28
8	73.4	CH	3.98	m	7, 9	6, 7, 9, 10, 28
9	42.4	CH_2	1.61	m	8, 10	8, 10, 11
10	71.9	CH	4.37	d (6.9)	9, 11, 12	8, 9, 11, 12, 13
11	137.2	CH	5.61	dd (15.1, 7.1)	10, 12, 13	9, 10, 13, 14
12	127.5	CH	6.58	dd (15.1, 11.1)	10, 11, 13, 14	9, 10, 11, 13, 14
13	131.3	CH	6.10	t (11.1, 11.1)	11, 12, 14, 15a, 15b	11, 12, 15, 16
14	129.3	CH	5.53	m	12, 13, 15a, 15b	12, 15, 16
15a	33.4	CH_2	2.53	m	13, 14, 15b 16	13, 14, 16, 17
15b			2.41	m	13, 14, 15a 16	13, 14, 16, 17
16	73.5	CH	3.66	m	15a, 15b, 17	14, 15
17	74.4	CH	3.45	m	16, 18	15, 18
18	76.6	CH	3.47	m	17, 19	16, 17, 19, 20, 29
19	34.2	CH	1.91	m	18, 20a, 20b, 29	18, 20, 29
20a	45.7	CH_2	2.18	br dd (12.8, 5.2)	19, 20b, 22, 30	18, 19, 21, 22, 29, 30
20b			1.82	m	19, 20a, 22	18, 19, 21, 22, 23, 29, 30
21	135.3	C				
22	126.8	CH	5.19	br t (7.0, 7.0)	20a, 20b, 23, 30	20, 23, 24, 30
23	38.4	CH_2	1.90	m	22, 24	21, 22, 24, 25, 26
24	30.4	CH	1.59	m	23, 25, 26	23, 25, 26
25	23.0	CH_3	0.90	d (6.6)	24	23, 24, 26
26	23.1	CH_3	0.89	d (6.6)	24	23, 24, 25
27	15.2	CH_3	2.28	d (1.2)	3	1, 2, 3, 4, 5
28	18.1	CH_3	1.42	d (7.1)	7	6, 7, 8
29	14.2	CH_3	0.82	d (6.7)	19	18, 19, 20
30	16.2	CH_3	1.58	m	20, 22	20, 21, 22, 24

[a] Acquired in methanol-d_4 at 125 MHz and calibrated to solvent signal at 49.2 ppm.
[b] Acquired in methanol-d_4 at 500 MHz and calibrated to solvent signal at 3.31 ppm.

[c] Proton showing COSY correlations to indicated proton.
[d] Proton showing HMBC correlations to indicated carbon.
[e] Long range coupling.

Table S 4.16: NMR spectroscopic data for oxo-thuggacin P2 (14)

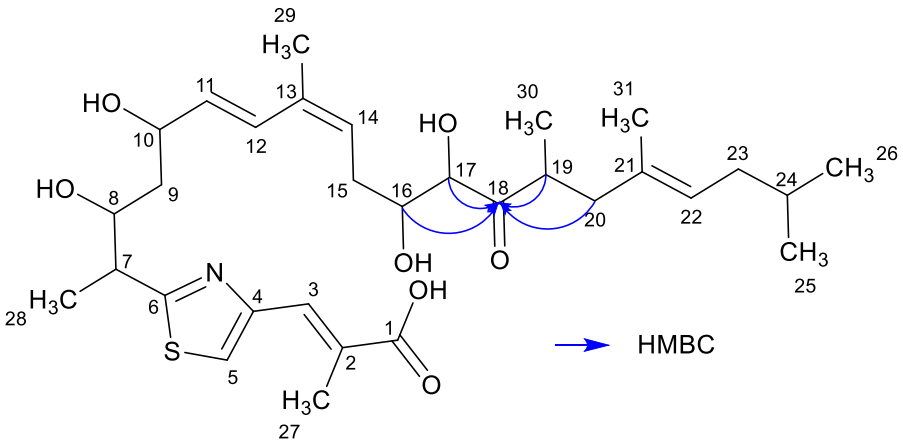

Position	δ_C[a] [ppm]	Type	δ_H[b] [ppm]	H Multiplicity (*J* [Hz])	COSY[c]	HMBC[d]
1	175.4	C				
2	134.5	C				
3	129.3	CH	7.51	m	27	1, 2, 4, 5, 27
4	153.3	C				
5	121.2	CH	7.51	m	7[e]	3, 6, 7
6	174.0	C				
7	45.6	CH	3.37	dd (7.1, 4.2)	5[e], 8, 28	6, 8, 28
8	73.5	CH	3.99	m	7, 9	6, 7, 9, 10, 28
9	42.5	CH_2	1.64	m	8, 10	7, 8, 10, 11
10	72.5	CH	4.40	q (6.9, 6.9, 6.9)	9, 11, 12	8, 9, 11, 12, 13
11	133.6	CH	5.63	dd (15.6, 7.1)	10, 12, 14	9, 10, 12, 13, 14
12	128.9	CH	6.71	d (15.6)	10, 11, 14, 29	9, 10, 11, 13, 14, 29
13	135.2	C				
14	127.6	CH	5.46	t (7.4, 7.4)	11, 12, 15a, 15b, 29	12, 13, 15, 16, 29
15a	33.1	CH_2	2.55	dt (14.4, 7.2, 7.2)	14, 15b, 16, 29	13, 14, 16, 17, 29
15b			2.42	m	14, 15a, 16, 29	13, 14, 16, 17, 29
16	73.7	CH	3.97	m	15a, 15b, 17	14, 15, 17, 18
17	79.3	CH	4.08	d (2.1)	16	15, 16, 18
18	218.3	C				
19	40.4	CH	3.24	td (4.7, 4.7, 2.1)	20a, 20b, 30	18, 20, 21, 30
20a	43.7	CH_2	2.42	m	19, 20b, 22, 31	18, 19, 21, 30
20b			1.88	m	19, 20a, 22, 31	18, 19, 21, 30
21	134.2	C				
22	127.7	CH	5.19	m	20a, 20b, 23, 31	20, 23, 24, 31
23	38.4	CH_2	1.89	m	22, 24	21, 22, 24, 25, 26
24	30.3	CH	1.59	m	23, 25, 26	23, 25, 26

25	22.9	CH_3	0.89	d (6.6)	24	22, 23, 24, 26
26	23.0	CH_3	0.89	d (6.6)	24	22, 23, 24, 25
27	15.7	CH_3	2.26	d (1.3)	3	1, 2, 3, 4, 5
28	17.9	CH_3	1.43	d (7.1)	7	6, 7, 8
29	21.1	CH_3	1.83	s	12, 14, 15a, 15b	12, 13, 14, 15, 16
30	16.1	CH_3	0.97	d (6.9)	19	18, 19, 20
31	16.2	CH_3	1.61	m	20a, 20b, 22	20, 21, 22, 24

[a] Acquired in methanol-d_4 at 125 MHz and calibrated to solvent signal at 49.2 ppm.
[b] Acquired in methanol-d_4 at 500 MHz and calibrated to solvent signal at 3.31 ppm.
[c] Proton showing COSY correlations to indicated proton.
[d] Proton showing HMBC correlations to indicated carbon.
[e] Long range coupling.

Analysis of the myxenolone biosynthetic gene cluster (BGC)

Genes encoding the biosyntheses of PQS[3] in *Pseudomonas aeruginosa* PA01 (BGC0000922) and HMAQ[4] in *Burkholderia thailandensis* E264 (GCF_000012365.1) were translated and used as templates for local BLAST searches against the genome of MSr12523 by Geneious prime 2022.2.2 to verify the putative *mxo* BGC (Table S 4.17). Based on observed homologies and the genetic architecture, the cluster borders of the putative *mxo* BGC were determined. The coding sequences of this putative BGC were extracted from the MSr12523 genome (ctg1_927-ctg1_935), translated and searched with the blastp algorithm against the RefSeq non-redundant protein sequence database at NCBI (Table S 4.18).

Table S 4.17: Comparison of PQS and HMAQ genes with the equivalent putative Mxo enzymes in MSr12523

	PQS homologue: identity [%] and query coverage[%]	**HMQ homologue: identity [%] and query coverage [%]**
MxoA	PqsE; 36.8; 92	HmqE; 40.3; 98
MxoB	-	-
MxoC	PqsB; 30.0; 90	HmqB; 40.8; 41
MxoD	PqsD; 53.2; 93	HmqD; 48.9; 93
MxoE	-	-
MxoF	-	HmqF; 34.2; 88
MxoG	PqsC; 39.7; 95	HmqC; 45,6; 96
MxoH	-	-
MxoI	-	-

Table S 4.18: Blastp results of the CDS regions in the mxo BGC

CDS Name	Length [AA]	Closest homologue [Organism of origin]	Identity [%] and query coverage [%]	Accession Nr.
MxoA	307	MBL fold metallo-hydrolase [Pseudoalteromonas citrea]	35.6; 97	WP_138596155.1
MxoB	484	tryptophan 7-halogenase [Chondromyces apiculatus]	56.5; 84	WP_044251132.1
MxoC	290	hypothetical protein [Arcicella aurantiaca]	37.0; 95	WP_109744980.1
MxoD	347	ketoacyl-ACP synthase III [Burkholderia sp. BDU5]	49.5; 93	WP_059471366.1
MxoE	76	acyl carrier protein [Alphaproteobacteria bacterium]	42.4; 84	MCB9681280.1
MxoF	584	AMP-binding protein [Myxococcales bacterium]	55.9; 92	MCA9541850.1
MxoG	356	3-oxoacyl-ACP synthase III family protein [Hymenobacter rubripertinctus]	48.8; 95	WP_119656068.1
MxoH	582	acyl-CoA dehydrogenase family protein [Streptomyces rimosus]	56.6; 98	WP_030640678.1
MxoI	563	acyl-CoA dehydrogenase [Streptomyces rimosus]	54.4; 99	WP_107066188.1

Analysis of the thuggacin P BGC

The putative *thg* BGC in the genome MSr12523 was identified with antiSMASH[5], based on similarity to the *tga* BGC in *Sorangium cellulosum* So Ce895 and the *tgu* BGC in *Chondromyces crocatus* Cm C5[6]. The coding sequences of the *thg* BGC were extracted from the MSr12523 genome (ctg1_2783-ctg1_2797), translated and searched with the blastp algorithm against the RefSeq non-redundant protein sequence database at NCBI (Table S 4.19).

Table S 4.19: Blastp results of the CDS regions in the thg BGC

CDS Name	Length [AA]	Closest homologue [Organism of origin]	Identity [%] and query coverage [%]	Accession Nr.
thg1	393	hypothetical protein [Actinomadura sp. HBU206391]	47.8; 97	WP_187236597.1
thg2	245	SDR family oxidoreductase [Mesorhizobium sp. M1E.F.Ca.ET.041.01.1.1]	83.2; 99	WP_127299490.1
thg3	403	L-2-hydroxyglutarate oxidase [Rhizobium lusitanum]	78.8; 99	WP_163988155.1

thgD	367	LLM class flavin-dependent oxidoreductase [Chondromyces crocatus]	78.1; 100	WP_063796353.1
thgA	4305	polyketide synthase [Sorangium cellulosum]	53.7; 99	CAL58681.1
thgB	6184	type I polyketide synthase [Streptomyces rhizosphaericus]	49.3; 99	WP_250853146.1
thgC	6365	TgaC [Sorangium cellulosum]	64.1; 98	ADH04641.1
thg4	742	alpha-N-acetylglucosaminidase C-terminal domain-containing protein [Amycolatopsis suaedae]	64.8; 94	WP_130474420.1
thg5	928	serine/threonine-protein kinase [Hyalangium sp. H56D21]	38.9; 96	WP_224368910.1
thg6	90	No significant similarity found	-	-
thg7	286	helix-turn-helix transcriptional regulator [Myxococcales bacterium]	59.9; 94	MBL9107384.1
thg8	170	DUF2938 domain-containing protein [Sulfidibacter corallicola]	68.8; 94	WP_237378590.1
thg9	527	DHA2 family efflux MFS transporter permease subunit [Deltaproteobacteria bacterium]	64.7; 99	TMA73505.1
thg10	411	HlyD family secretion protein [Polyangiaceae bacterium]	53.3; 92	MCL2450717.1

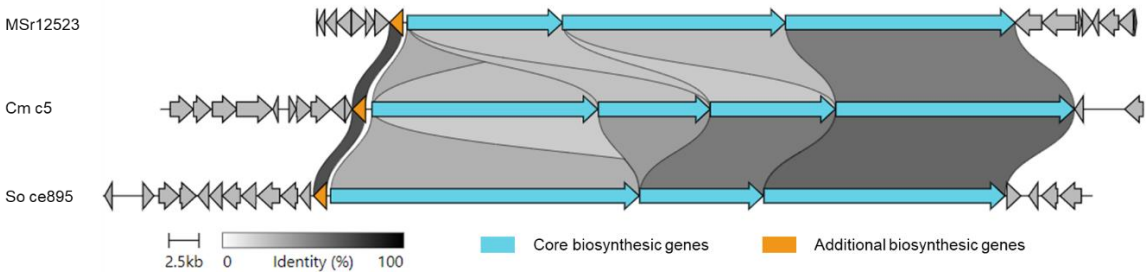

Figure S 4.2: Comparison of the genes in the different thuggacin BGCs in MSr12523, Cm c5 and So ce895. Alignment and graphic was done with the CAGECAT application[7].

Table S 4.20: Substrate specificities of thuggacin P BGC AT domains

	Substrate	antiSMASH	Fingerprint[8]
L	Isovaleryl-CoA	*	Unclear
M1	Methylmalonyl-CoA	Methylmalonyl-CoA	Methylmalonyl-CoA
M2	Methylmalonyl-CoA	Methylmalonyl-CoA	Methylmalonyl-CoA
M3	Malonyl-CoA	Malonyl-CoA	Malonyl-CoA
M4	Malonyl-CoA	Malonyl-CoA	Malonyl-CoA
M5	Methylmalonyl-CoA & Malonyl-CoA	Ethylmalonyl-CoA	Unclear
M6	Malonyl-CoA	Malonyl-CoA	Malonyl-CoA
M7	Malonyl-CoA	Malonyl-CoA	Malonyl-CoA
M8	Methylmalonyl-CoA	Methylmalonyl-CoA	Methylmalonyl-CoA
M9	Cysteine	Cysteine	-
M10	Methylmalonyl-CoA	Methylmalonyl-CoA	Methylmalonyl-CoA

* Substrate specificity predictions of the loading module AT domain can be found in table S 4.21.

Table S 4.21: Substrate specificity predictions by antiSMASH of the AT domains in the loading modules of the thg, tga and tgu BGCs

	***thg* AT-L (MSr12523)**	***tga* AT-L (So ce895)**	***tug* AT-L (Cm c5)**
AT signature	Ethylmalonyl-CoA: 70.8% Methylmalonyl-CoA: 70.8% Benzoyl-CoA: 70.8%	Benzoyl-CoA: 83.3% Methylmalonyl-CoA: 62.5% Ethylmalonyl-CoA: 58.3%	Methylmalonyl-CoA: 66.7% Benzoyl-CoA: 66.7% Ethylmalonyl-CoA: 58.3%
Minova	Benzoyl-CoA: 136.8 Methylmalonyl-CoA: 111.6 Ethylmalonyl-CoA: 104.7 Methoxymalonyl-CoA: 100.1 Isobutyryl-CoA: 83.6 2-Methylbutyryl-CoA: 70.7 trans-1,2-CPDA: 67.0 Propionyl-CoA: 58.4 Acetyl-CoA: 55.6 Malonyl-CoA: 49.3 CHC-CoA: 47.2 3-Methylbutyryl-CoA: 22.6 inactive: 19.9 fatty_acid: 18.5	Benzoyl-CoA: 200.5 Isobutyryl-CoA: 131.6 Methylmalonyl-CoA: 115.0 Methoxymalonyl-CoA: 94.7 Ethylmalonyl-CoA: 87.3 Acetyl-CoA: 64.9 trans-1,2-CPDA: 61.5 Malonyl-CoA: 61.0 Propionyl-CoA: 54.6 2-Methylbutyryl-CoA: 54.4 CHC-CoA: 50.5 3-Methylbutyryl-CoA: 49.4 fatty_acid: 27.1 inactive: 19.4	Benzoyl-CoA: 163.7 Methylmalonyl-CoA: 127.5 Isobutyryl-CoA: 123.9 Methoxymalonyl-CoA: 104.4 Ethylmalonyl-CoA: 100.2 Malonyl-CoA: 81.8 Propionyl-CoA: 74.9 2-Methylbutyryl-CoA: 71.9 trans-1,2-CPDA: 69.6 CHC-CoA: 55.5 Acetyl-CoA: 53.0 3-Methylbutyryl-CoA: 41.2 inactive: 32.0 fatty_acid: 30.5

Observed starter units of the respective biosyntheses are marked in green.

Table S 4.22: Reductive loops in thuggacin P BGC and in silico predictions of the stereochemistry of thuggacin P1-A

Module	Position	Final stereochemistry	Relative stereochemistry in module	AntiSMASH	KR type[9]	DH fingerprint[8]	ER fingerprint[10]
1	C22	double bond: *E*	double bond: *E*	D (KR)	B1: *R*	*E* (B1 KR)	No ER
	C21	double bond: *E*	double bond: *E*	-	B1: *R*	*E* (B1 KR	No ER
2	C20	-	-	D (KR)	B1: *R*	*E* (B1 KR)	-
	C19	*S*	*S*	*S* (ER)	B1: *R*	*E* (B1 KR)	*S*
3	C18	*R*	*R*/D	D (KR)	B1: *R*	No DH	No ER
	C17	*S*[a]	-	-	-	No DH	No ER
4	C16	*S*	*R*/D	D (KR)	B1: *R*[b]	No DH	No ER
	C15	-	-	-	-	No DH	No ER
5	C14	double bond: *Z*	*S*/L	L (KR)	A1: *S*	No DH[c]	No ER
	C13	double bond: *Z*	-	-	-	No DH[c]	No ER
6	C12	double bond: *E*	double bond: *E*	D (KR)	B1: *R*	*E* (B1 KR)	No ER
	C11	double bond: *E*	double bond: *E*	-	-	*E* (B1 KR)	No ER
7	C10	*S*[d]	*S*/L	L (KR)	Inconclusive	No DH	No ER
	C9	-	-	-	Inconclusive	No DH	No ER
8	C8	*R*	*R*/D	D (KR)	B1: *R*	Inactive[e]	No ER
	C7	*R*	*R*	-	B1: *R*	Inactive[e]	No ER
9	C4-C6	-	-	NRPS module	NRPS module	NRPS module	NRPS module
10	C3	double bond: *E*	double bond: *E*	D (KR)	B1: *R*	*E* (B1 KR)	No ER
	C2	double bond: *E*	double bond: *E*	-	B1: *R*	*E* (B1 KR)	No ER

In silico predictions of modules 1-10 and the positions the respective KR, DH and ER domains effect. Domains that determine the stereochemistry of the respective positions are marked in green.

[a] The hydroxyl group at C-17 is incorporated post-assembly line and the stereochemistry was assumed based on the observed stereochemistry of the respective thuggacin derivatives[6,11].

[b] The first L-aspartic acid in the LDD motif is interchanged by L-glutamic acid. Due to the similarity of both amino acids it was assumed that the KR domain in module 4 belongs to the B1 type.

[c] Based on the proposed biosyntheses of thuggacin derivatives in *S. cellulosum* So ce895 and *C. crocatus* Cm c5[6], it is assumed that the DH domain in module 6 acts iteratively and also performs the dehydrogenation reaction of the hydroxyl-group produced in module 5. Based on the A1 type KR domain in module 5, the resulting double bond has a *Z* configuration[8].

[d] The stereochemical orientation of C-10 was assigned to *S*, based on the antiSMASH predictions and based on similar motifs in the equivalent KR domains in the *tag* and *tug* BGCs (Figure S 4.4).

[e] The DH domain in module 8 does not possess the catalytic triad H, P, G.

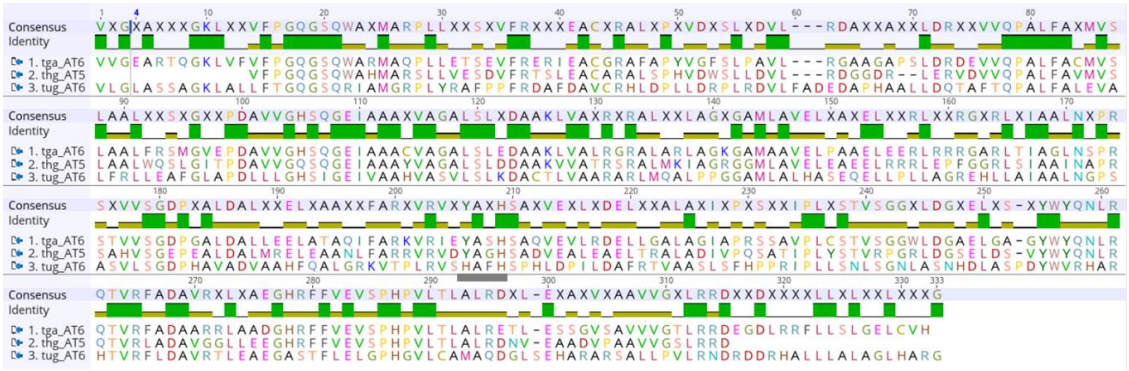

Figure S 4.3: Alignment of the AT domain in module 5 in the *thg* BGC with its equivalent AT domains in the *tga* and *tgu* BGCs. AT domains of module 6 in the *tga* BGC in *S. cellulosum* So ce895, of module 5 in the *thg* BGC in MSr12523 and of module 6 in the *tgu* BGC in *C. crocatus* Cm c5. The recognition motifs for different extender units are highlighted with a grey bar.

Figure S 4.4: Alignment of the KR domain in module 7 in the *thg* BGC with its equivalent AT domains in the *tga* and *tgu* BGCs. KR domains of module 7 in the *thg* BGC in MSr12523, of module 8 in the *tga* BGC in *S. cellulosum* So ce895 and of module 8 in the *tgu* BGC in *C. crocatus* Cm c5. As indicated by the short grey bar, neither KR domain possess the LDD fingerprint within the loop that is characteristic for type B KR domains. The long short grey bar indicates the catalytic region, that features a characteristic W residue 8 amino acids upstream the YAAAN motif in the case of type A KR domains[9]. As neither KR possesses this W residue, their fingerprint is inconclusive.

Figure S 4.5: Alignment of the KR domain in module 8 in the *thg* BGC with its equivalent AT domains in the *tga* and *tgu* BGCs. KR domains of module 8 in the *thg* BGC in MSr12523, of module 9 in the *tga* BGC in *S. cellulosum* So ce895 and of module 9 in the *tgu* BGC in *C. crocatus* Cm c5. As indicated by the short grey bar, the loop region of the KR domain in module 8 in the *thg* BGC displays the LDD motif and therefore belongs to the type B KR domains. In contrast to that, KR domains in modules 9 of the *tga* and *tug* BGCs possess the characteristic W residue eight amino acids upstream the YAAAN motif (long grey bar) and therefore belong to the type A KR domains[9].

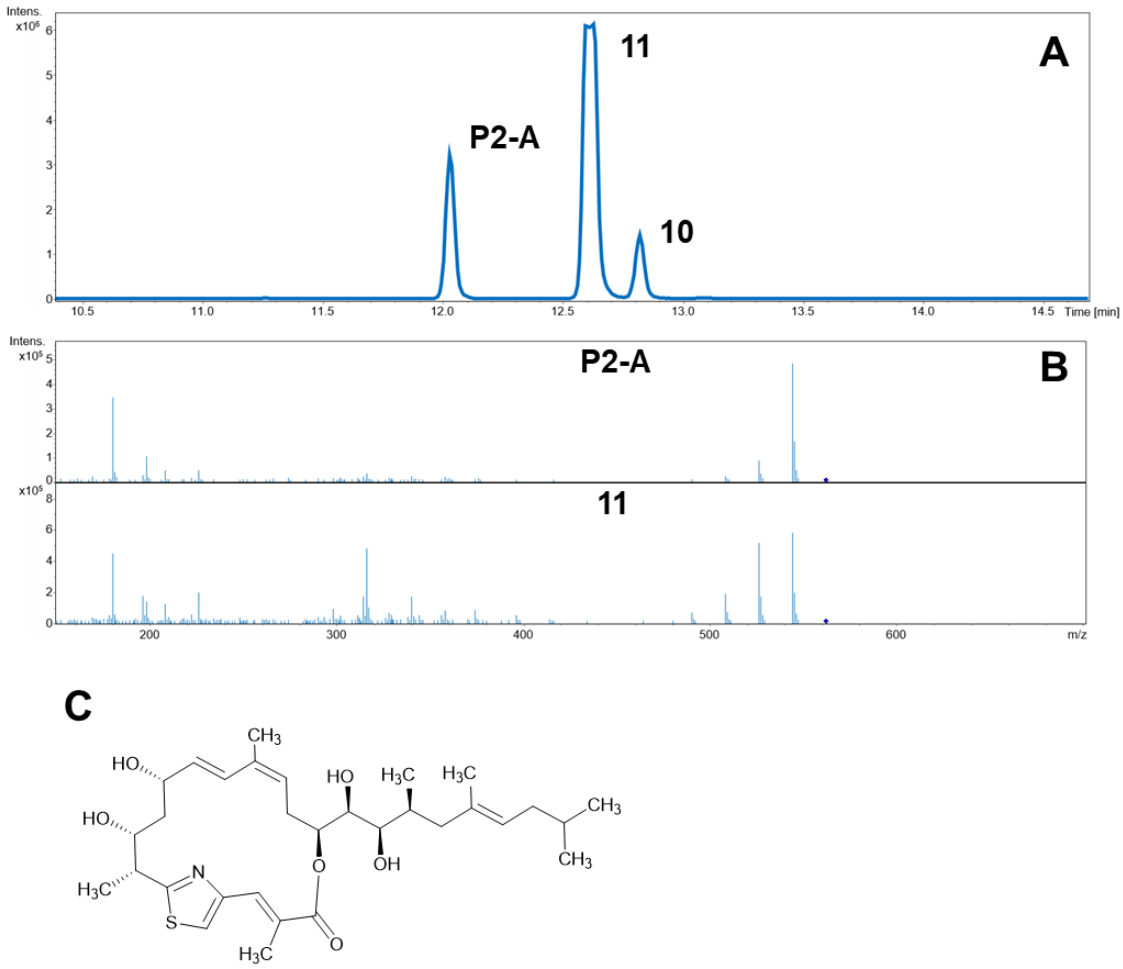

Figure S 4.6: LC-MS chromatogram, spectral data an putative structure of putative thuggacin P2-A: (**A**) Extracted ion chromatogram (EIC) of the thuggacin P2 subclass with *m/z* 562.32 in a crude extract of MSr12523 in RGSR medium, showing purified thuggacins P2-B (**10**) and P2-C (**11**) a third peak (putative thuggacin P2-A). (**B**) MS/MS spectra of putative thuggacin P2-A (P2-A) and purified thuggacin P2-C (**11**) display highly similar fragmentation patterns. (**C**) Structure of putative thuggacin P2-A, based on observed LC-MS chromatogram and MS/MS data as well as the underlying putative biosynthesis.

Table S 4.23: Identitiy [%] and query coverage [%] of ThgD, TgaE and TugE

	ThgD (MSr12523)	**TgaE (So ce895)**	**TugE (Cm c5)**
ThgD (MSr12523)		76.7; 97	78.0; 98
TgaE (So ce895)	76.7; 97		80,0; 98
TugE (Cm c5)	78.0; 98	80,0; 98	

Biological activities

Table S 4.24: Further MIC and IC_{50} values of myxenolones A, C and D

	MIC [µg/mL]					IC_{50} [µg/mL]
compound	*E.coli* WT (BW25113)	*E.coli* Δ*acrB* (JW0451-2)	*S.aureus* Newman	*A.baumannii* DSM3008	*P. aeruginosa* PA14	CHO-K1
Myxenolone A	>64	>64	>64	>64	>64	3.28 ± 0.59
Myxenolone C	>64	>64	>64	>128	>128	1.45 ± 0.13
Myxenolone D	>64	>64	>64	>64	>64	8.51 ± 5.21

Possible origin of non-cyclised thuggacin P derivatives

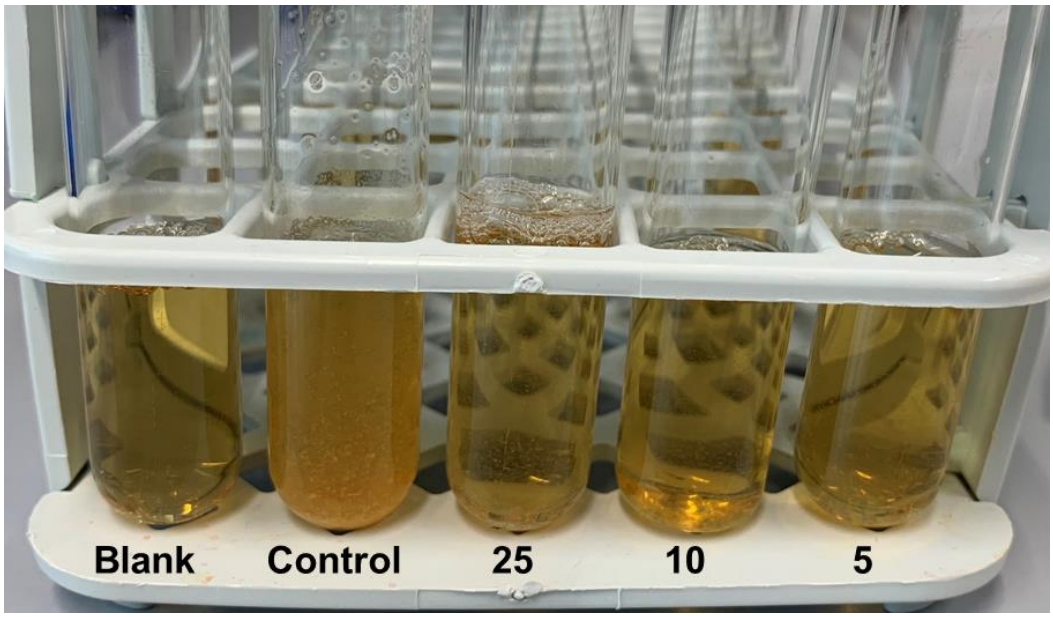

Figure S 4.7: Inhibitory effect of macrocyclic thuggacin P1 derivatives against *T. pseudopmuae* after 24 h cultivation. (Blank) TSB medium with 10 µg/mL macrocyclic thuggacin P derivatives. (Control) Untreated *T. pseudospumae* in TSB medium. (5, 10, 25) *T. pseudospumae* in TSB medium with 5, 10 and 25 µg/mL macrocyclic thuggacin P1 derivatives.

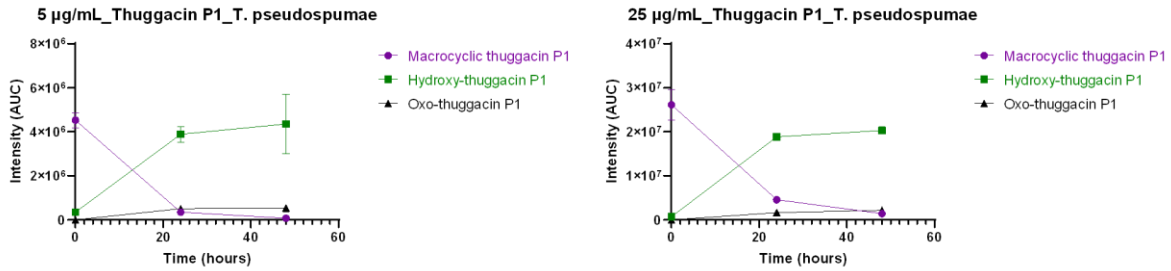

Figure S 4.8: Conversion of 5 µg/mL and 25 µg/mL macrocyclic thuggacin P1 derivatives into hydroxyl-thuggacin P1 and oxo-thuggacin P1 by *T. pseudospumae*.

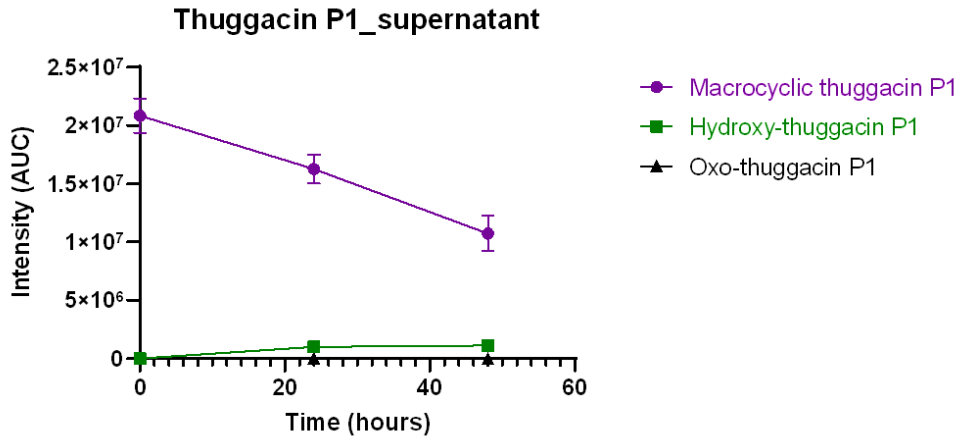

Figure S 4.9: Concentrations of different thuggacin P1 derivatives in *T. pseudospumae* supernatant.

NMR spectra employed in structure elucidation

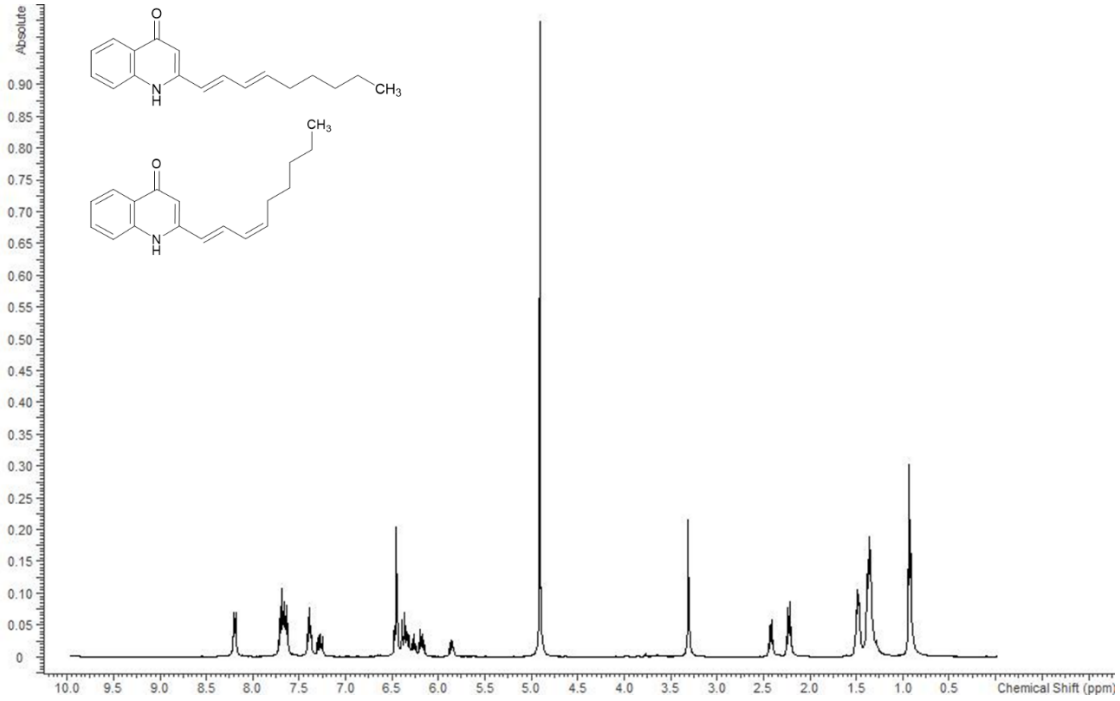

Figure S 4.10: ^{1}H spectrum of myxenolones A1 (1) and A2 (2) in methanol-d_4 at 500 MHz.

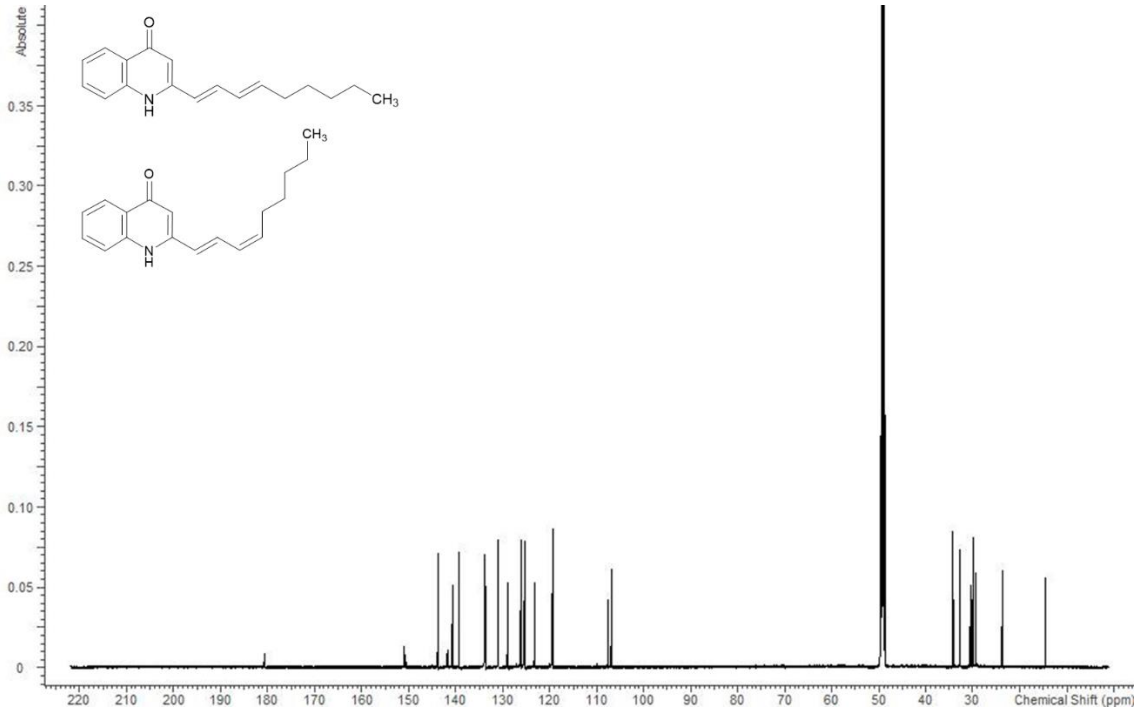

Figure S 4.11: ^{13}C spectrum of myxenolones A1 (1) and A2 (2) in methanol-d_4 at 125 MHz.

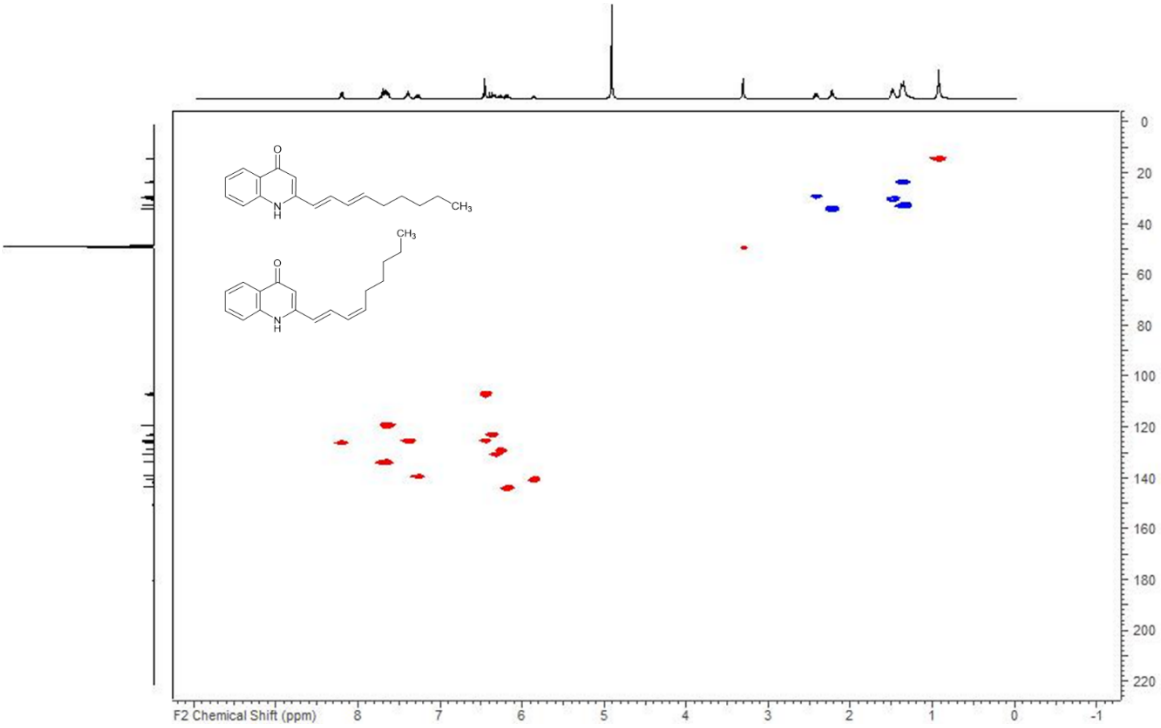

Figure S 4.12: HSQC spectrum of myxenolones A1 (1) and A2 (2) in methanol-d_4 at 125/500 (F1/F2) MHz.

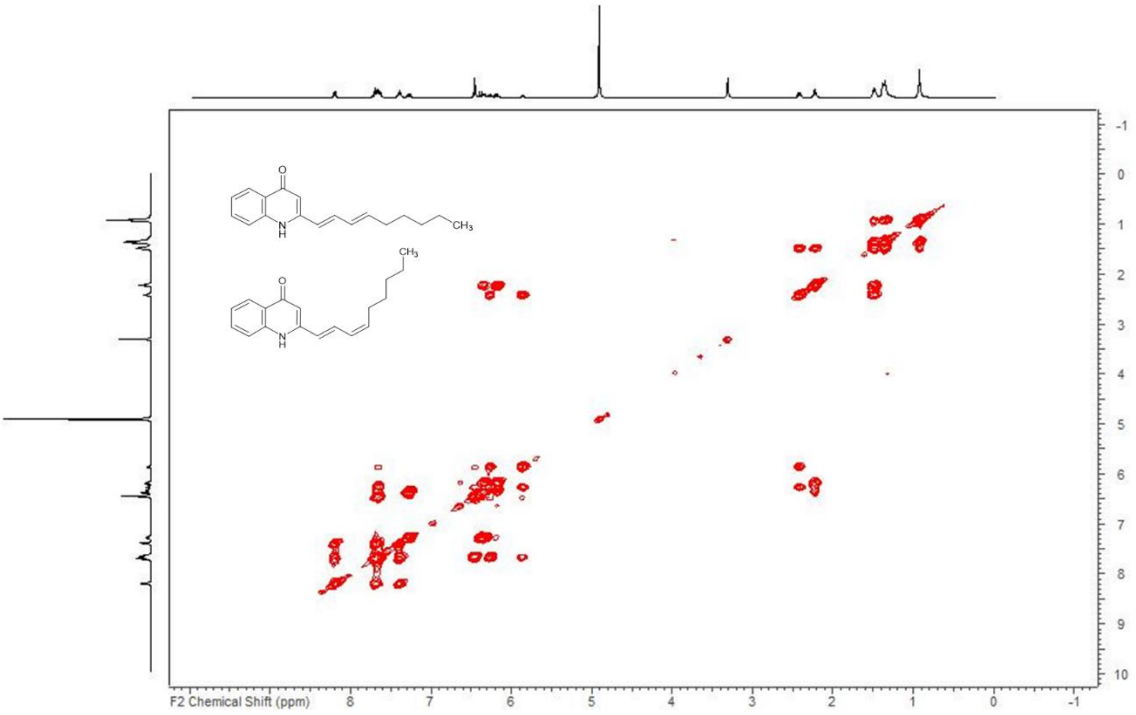

Figure S 4.13: COSY spectrum of myxenolones A1 (1) and A2 (2) in methanol-d_4 at 500 MHz.

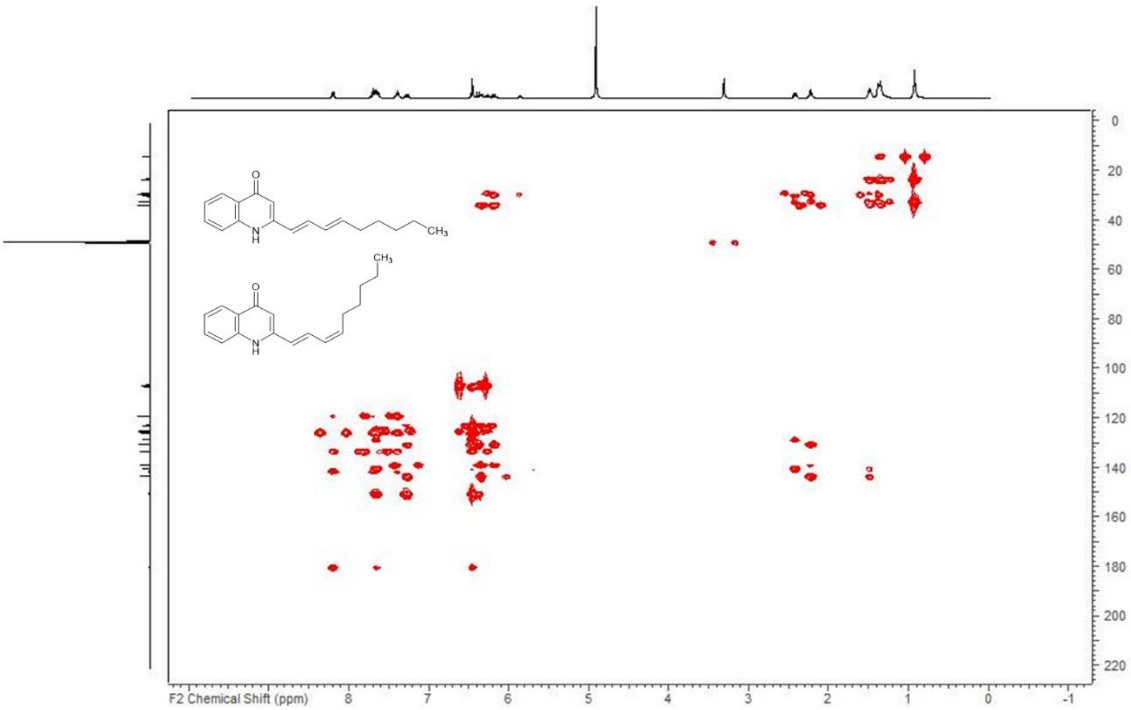

Figure S 4.14: HMBC spectrum of myxenolones A1 (1) and A2 (2) in methanol-d_4 at 125/500 (F1/F2) MHz.

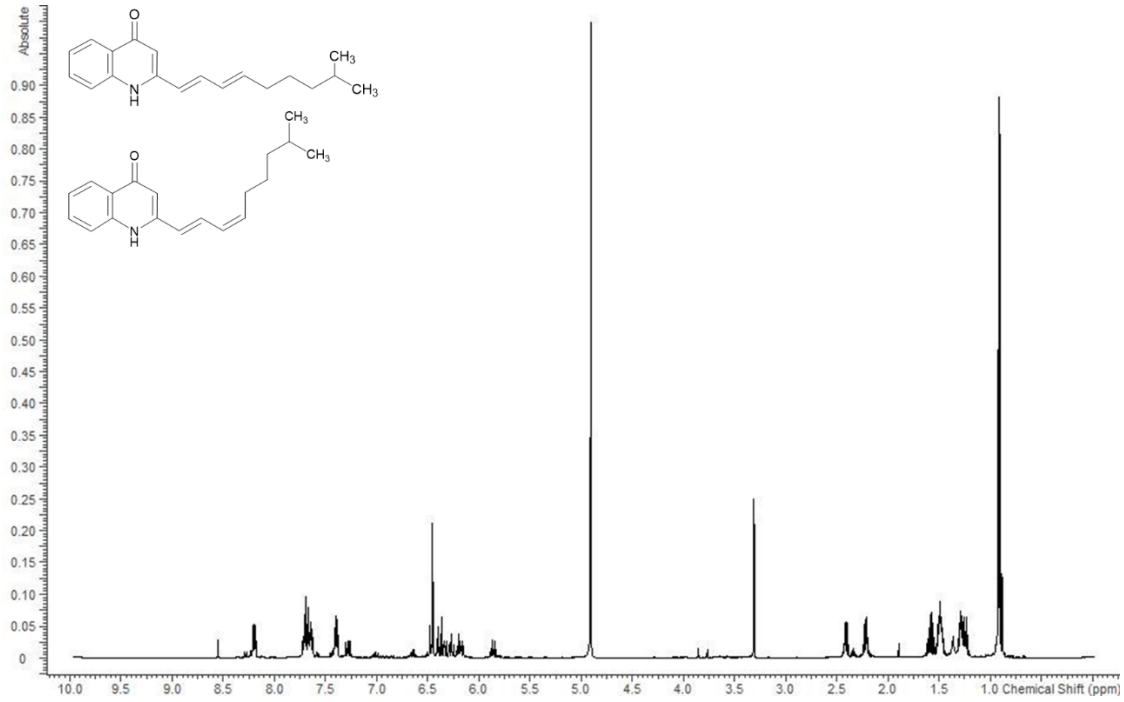

Figure S 4.15: ^{1}H spectrum of myxenolones B1 (3) and B2 (4) in methanol-d_4 at 500 MHz.

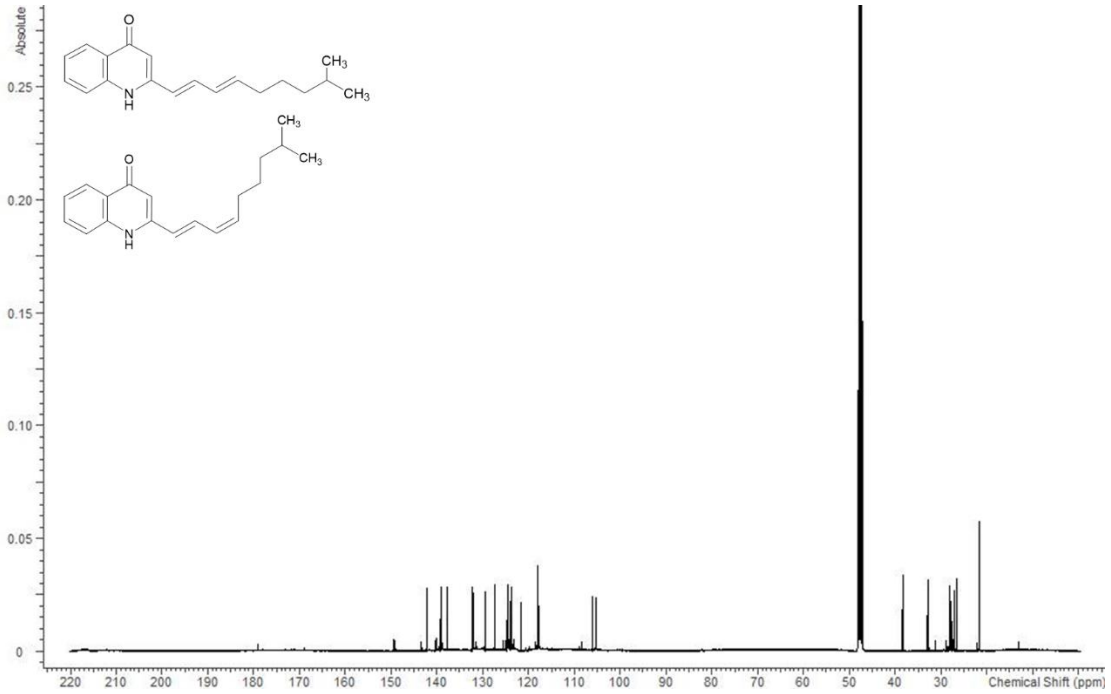

Figure S 4.16: ^{13}C spectrum of myxenolones B1 (3) and B2 (4) in methanol-d_4 at 125 MHz.

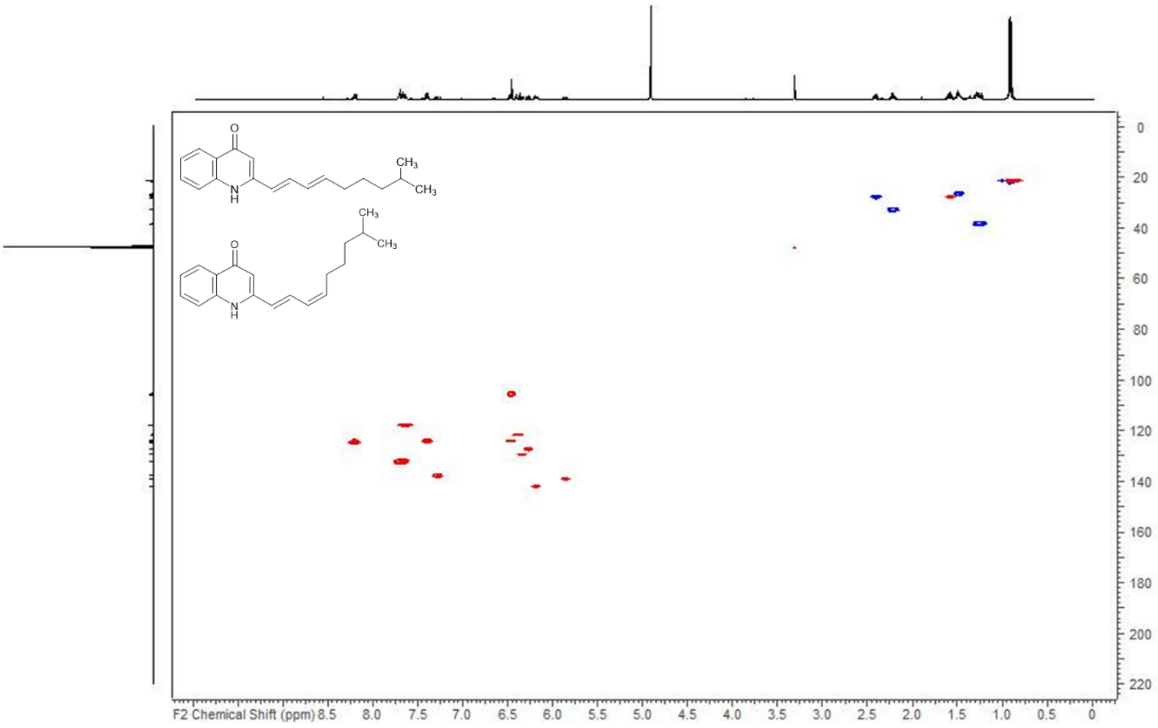

Figure S 4.17: HSQC spectrum of myxenolones B1 (3) and B2 (4) in methanol-d_4 at 125/500 (F1/F2) MHz.

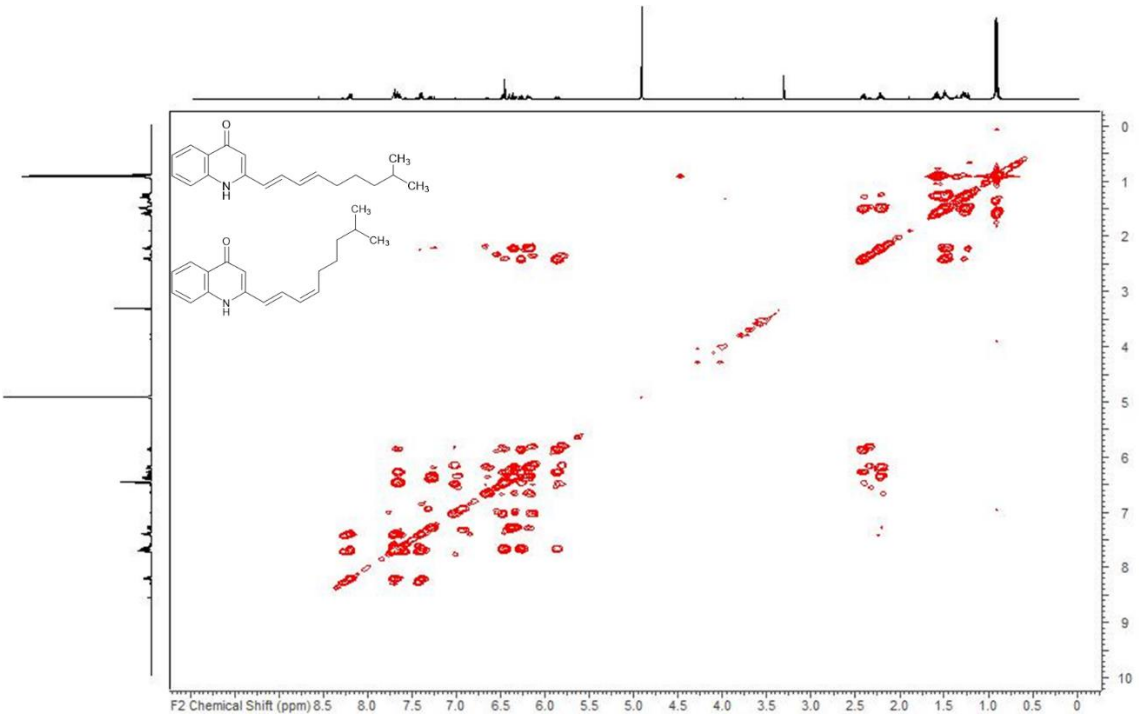

Figure S 4.18: COSY spectrum of myxenolones B1 (3) and B2 (4) in methanol-d_4 at 500 MHz.

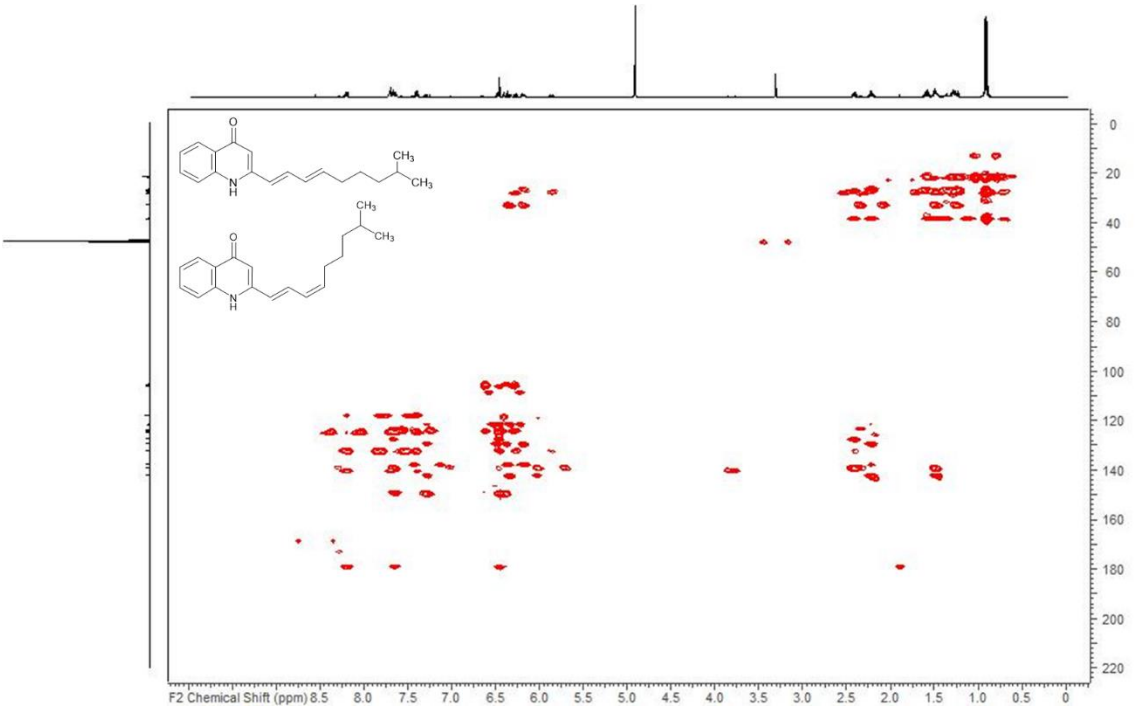

Figure S 4.19: HMBC spectrum of myxenolones B1 (3) and B2 (4) in methanol-d_4 at 125/500 (F1/F2) MHz.

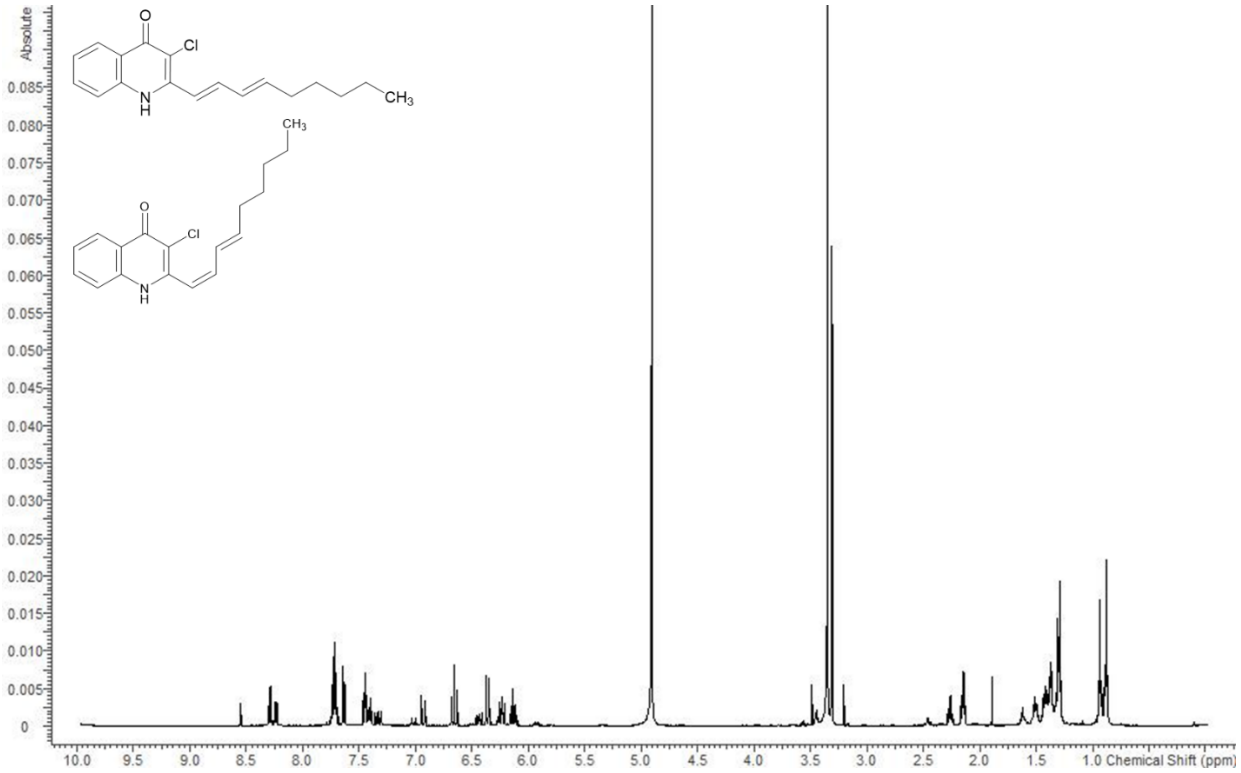

Figure S 4.20: ^{1}H spectrum of myxenolones C1 (5) and C2 (6) in methanol-d_4 at 500 MHz.

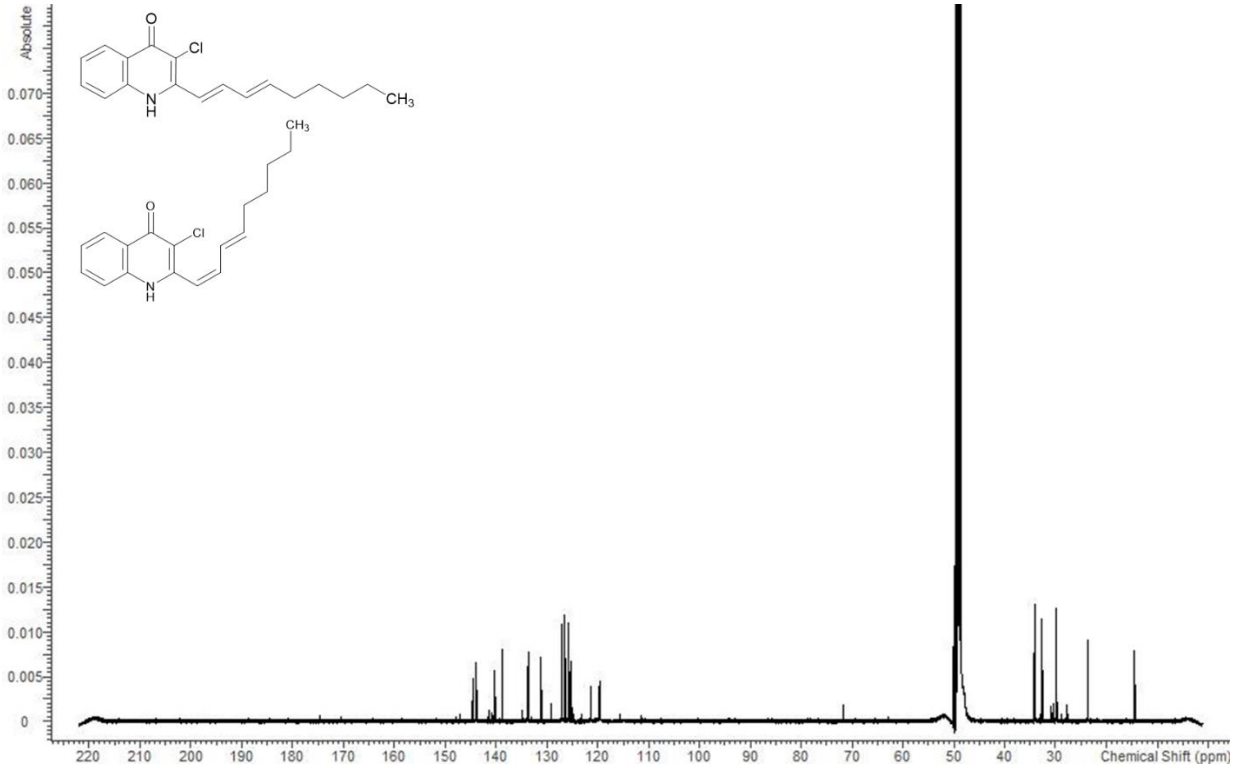

Figure S 4.21: ^{13}C spectrum of myxenolones C1 (5) and C2 (6) in methanol-d_4 at 125 MHz.

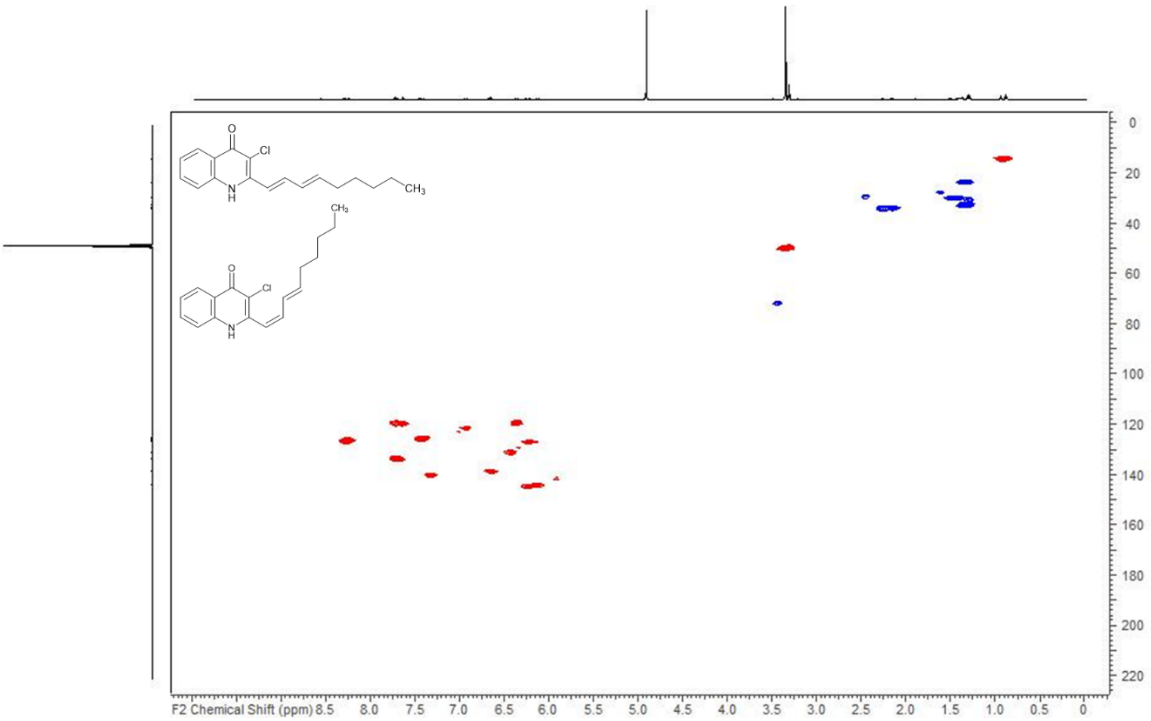

Figure S 4.22: HSQC spectrum of myxenolones C1 (5) and C2 (6) in methanol-d_4 at 125/500 (F1/F2) MHz.

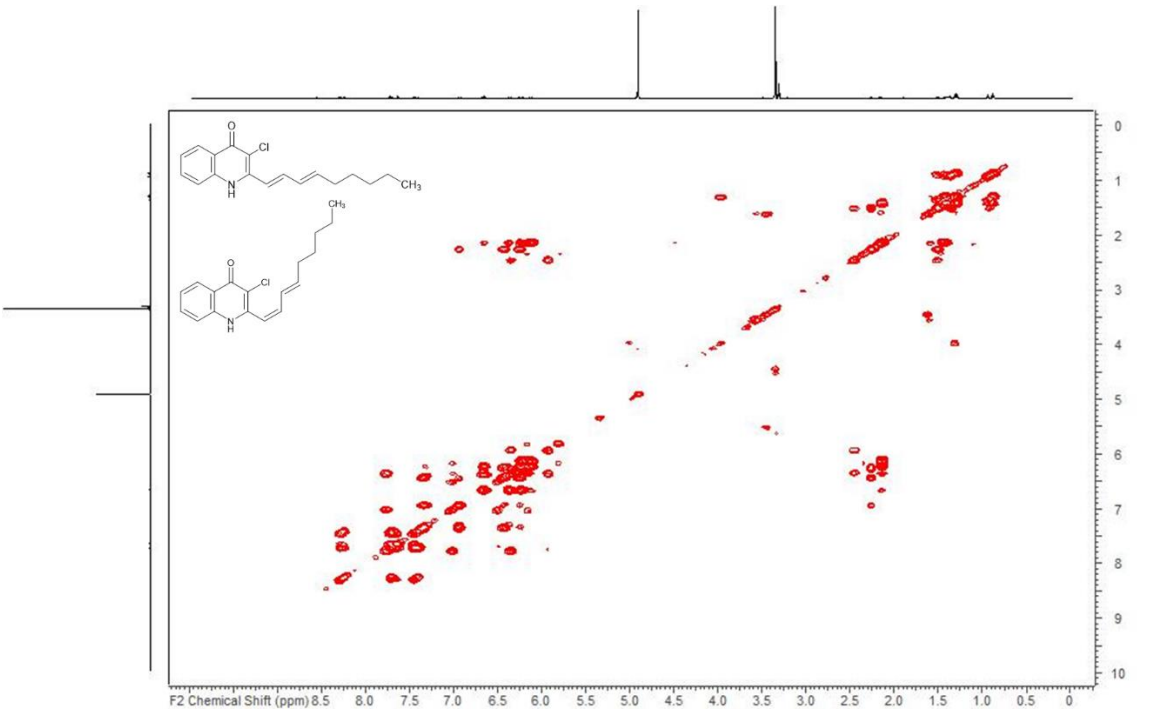

Figure S 4.23: COSY spectrum of myxenolones C1 (5) and C2 (6) in methanol-d_4 at 500 MHz.

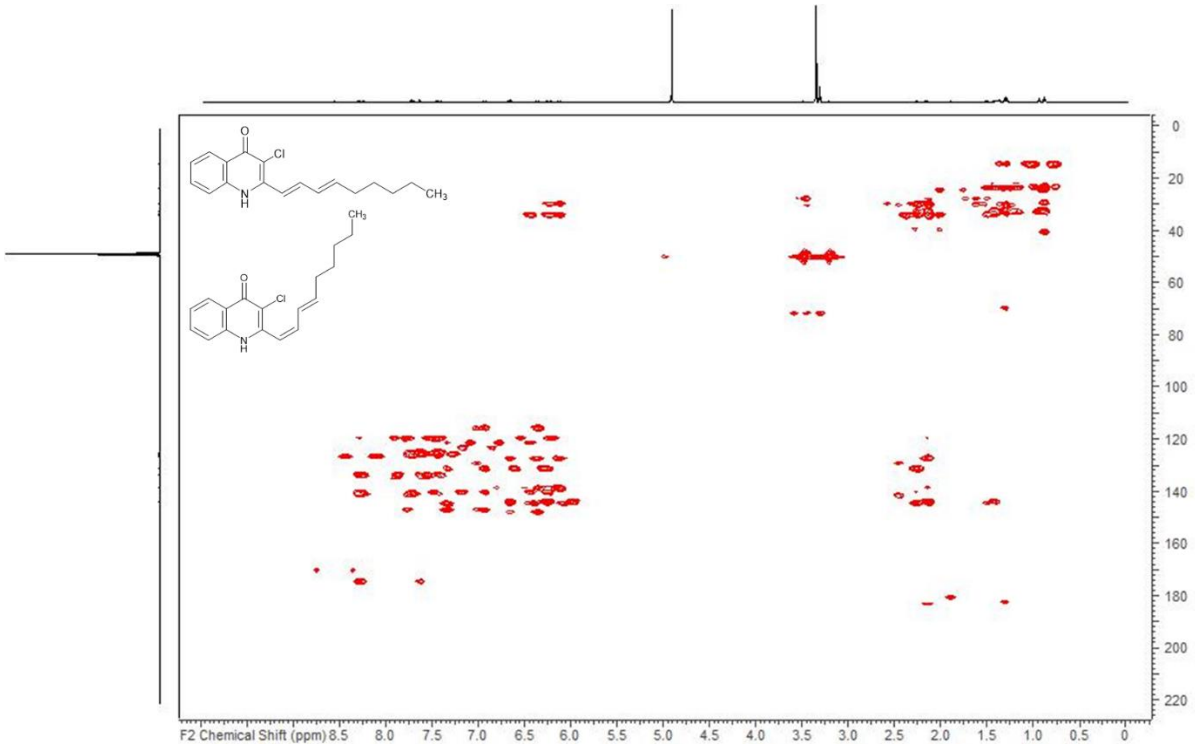

Figure S 4.24: HMBC spectrum of myxenolones C1 (5) and C2 (6) in methanol-d_4 at 125/500 (F1/F2) MHz.

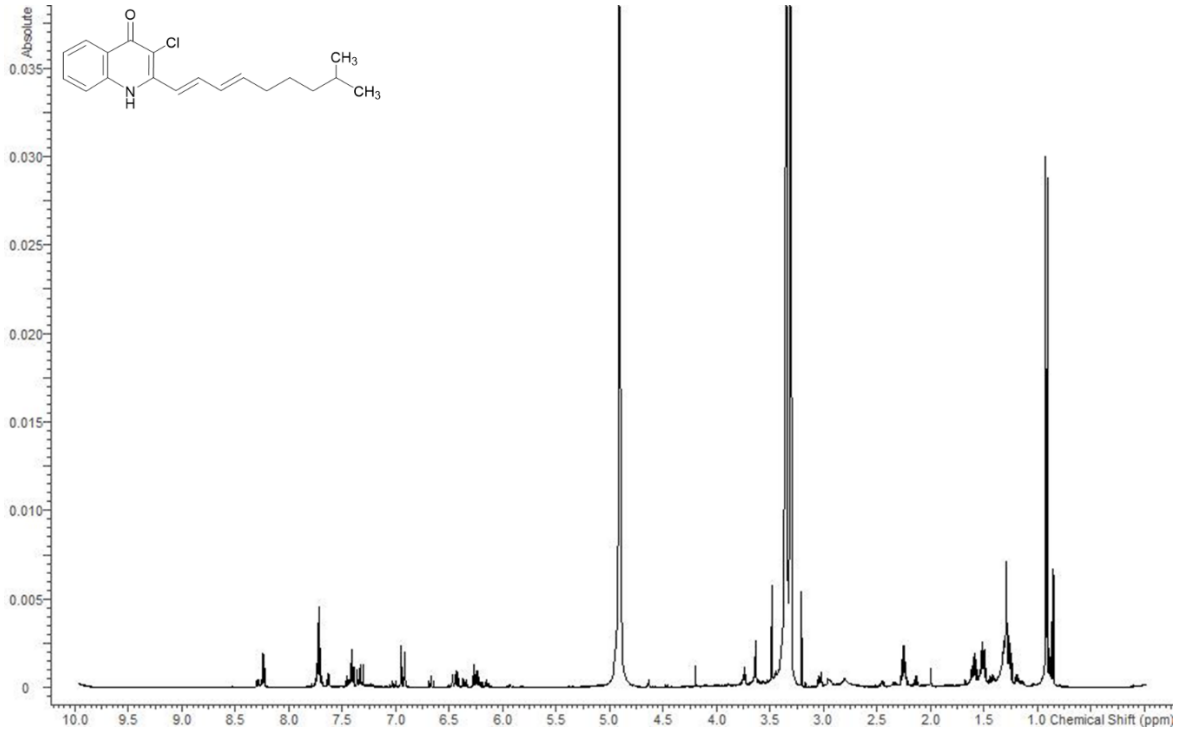

Figure S 4.25: ^{1}H spectrum of myxenolone D1 (7) in methanol-d_4 at 500 MHz.

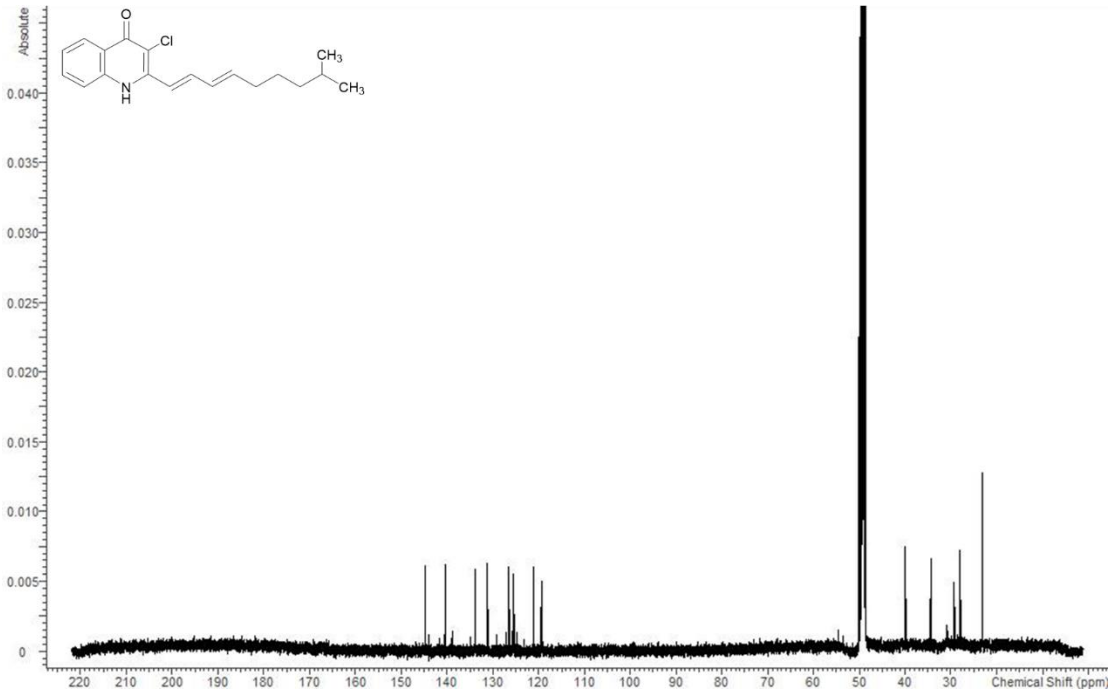

Figure S 4.26: ^{13}C spectrum of myxenolone D1 (7) in methanol-d_4 at 125 MHz.

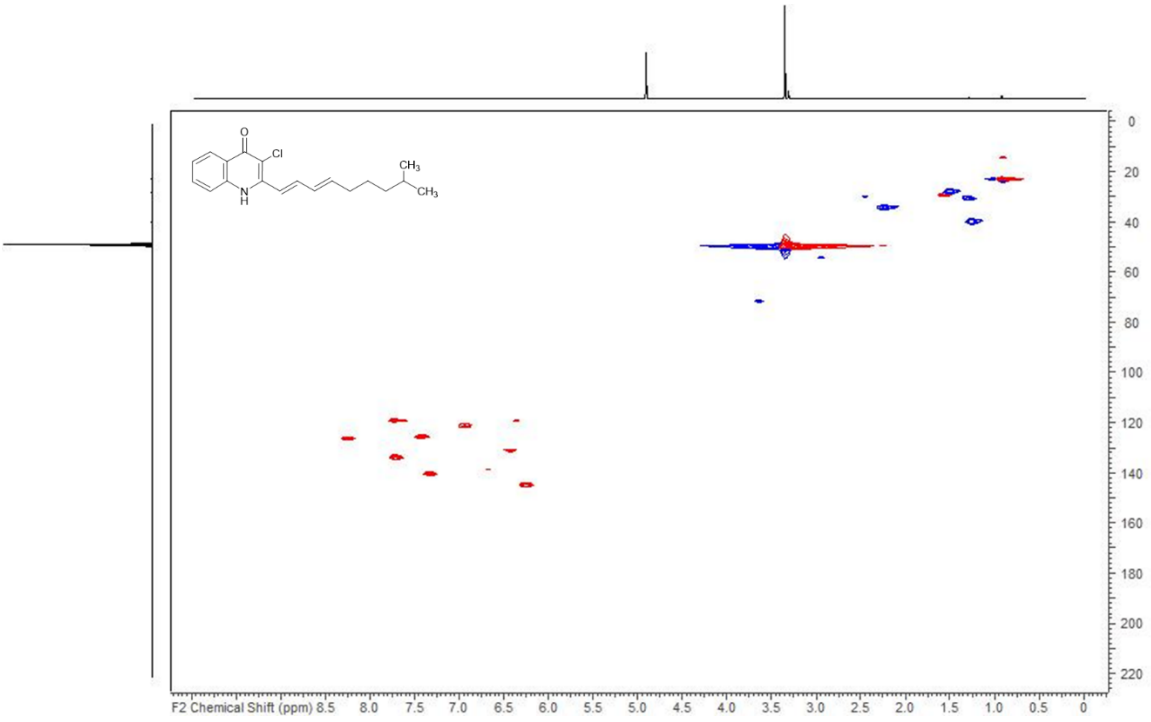

Figure S 4.27: HSQC spectrum of myxenolone D1 (7) in methanol-d_4 at 125/500 (F1/F2) MHz.

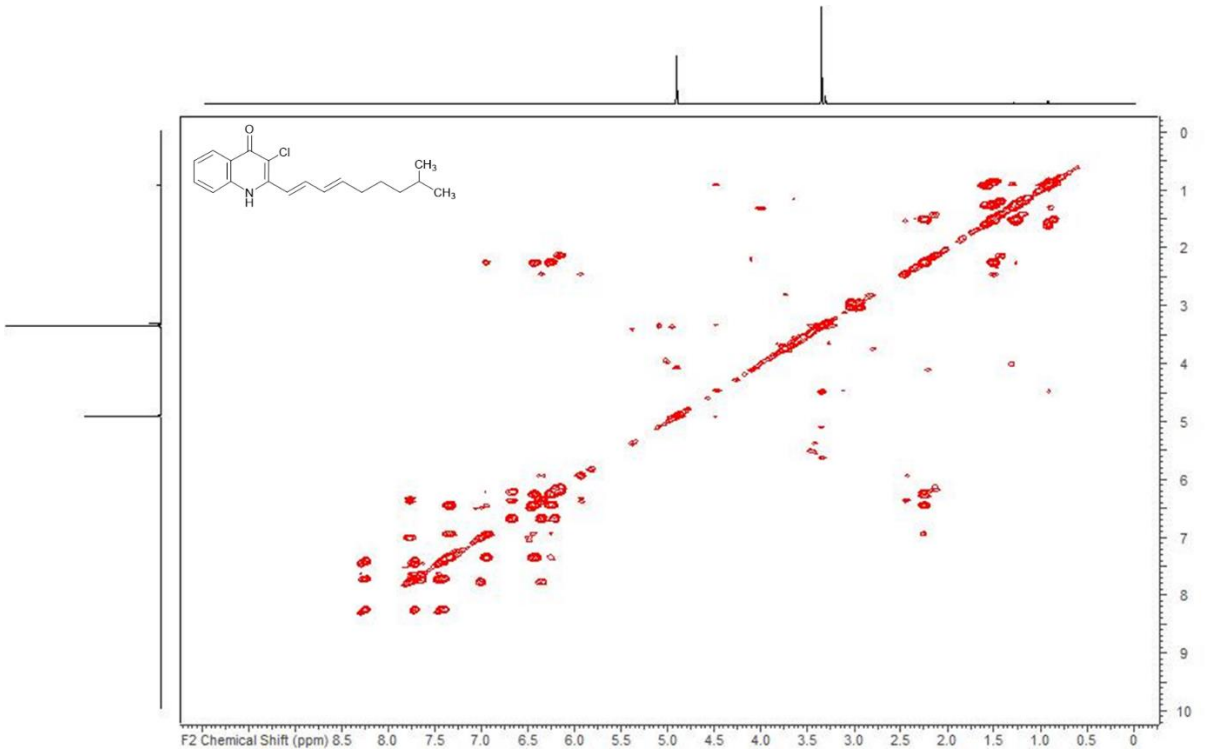

Figure S 4.28: COSY spectrum of myxenolone D1 (7) in methanol-d_4 at 500 MHz.

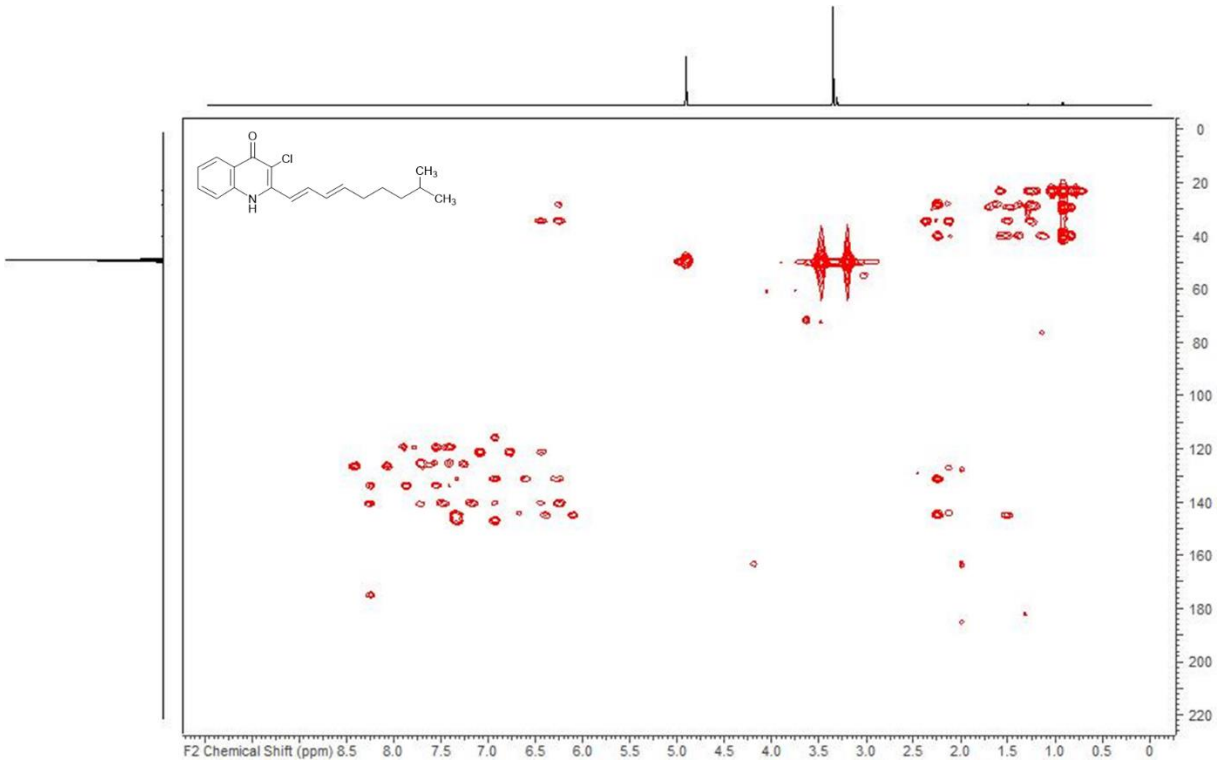

Figure S 4.29: HMBC spectrum of myxenolone D1 (7) in methanol-d_4 at 125/500 (F1/F2) MHz.

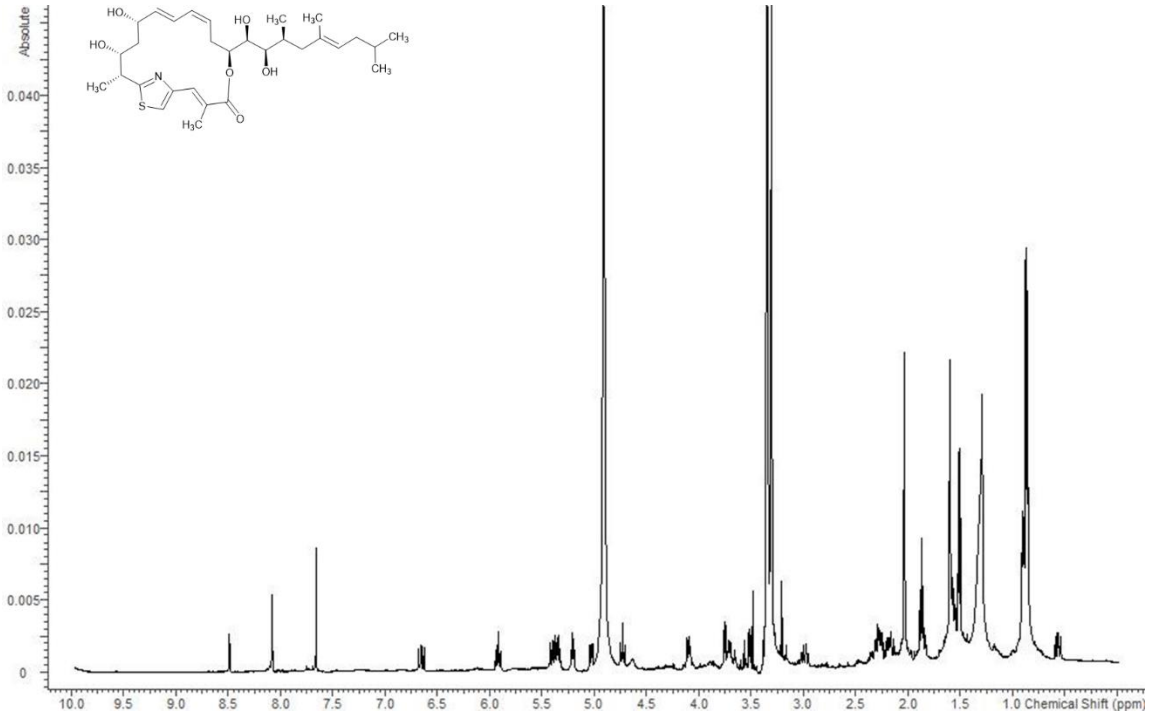

Figure S 4.30: ^{1}H spectrum of thuggacin P1-A (8) in methanol-d_4 at 500 MHz.

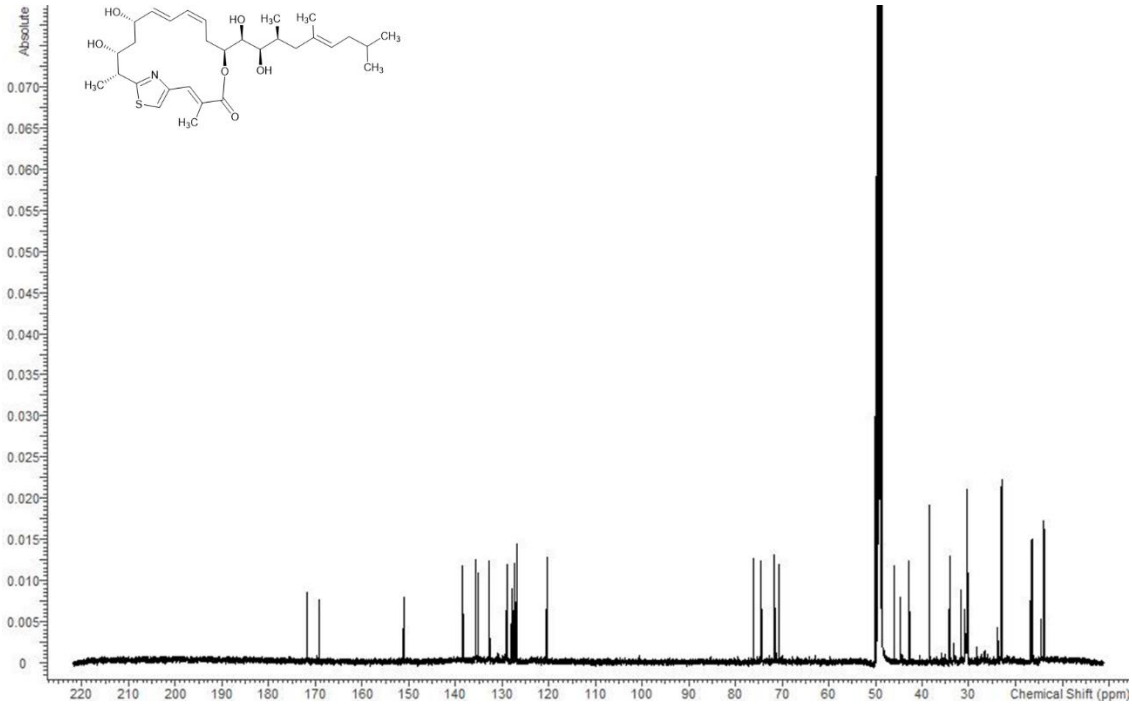

Figure S 4.31: ^{13}C spectrum of thuggacin P1-A (8) in methanol-d_4 at 125 MHz.

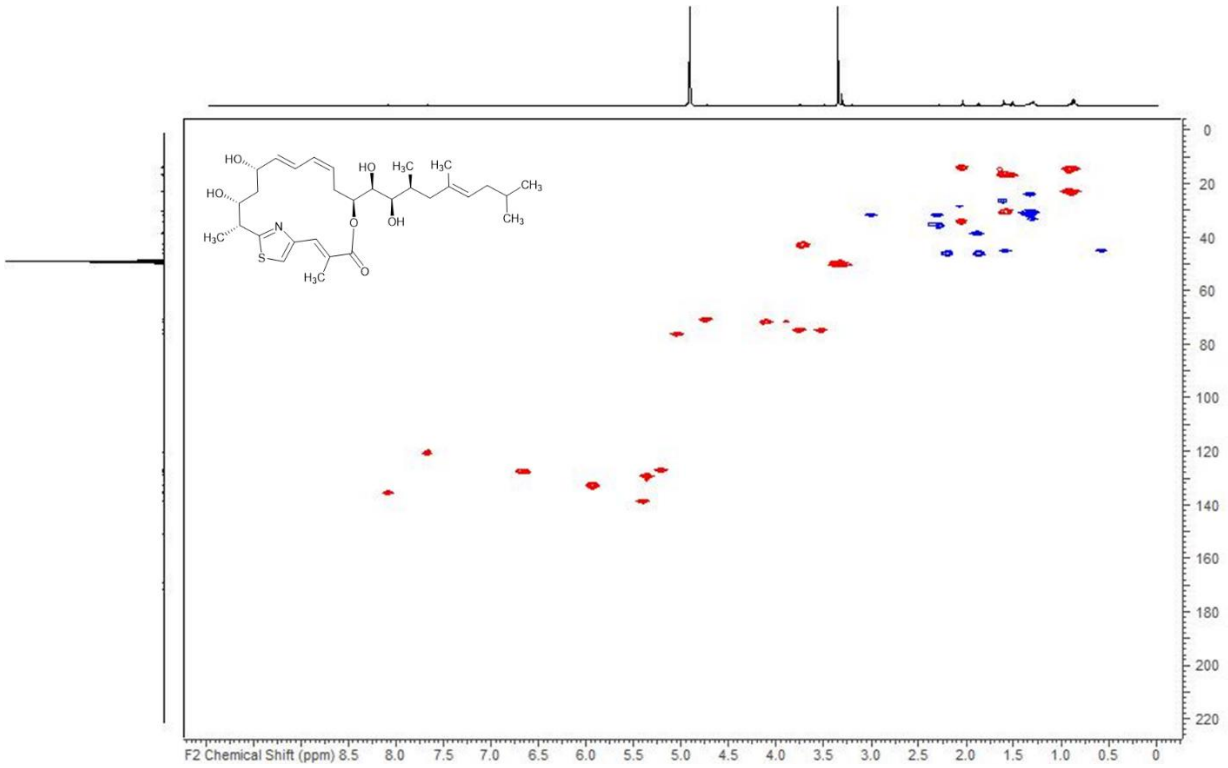

Figure S 4.32: HSQC spectrum of thuggacin P1-A (8) in methanol-d_4 at 125/500 (F1/F2) MHz.

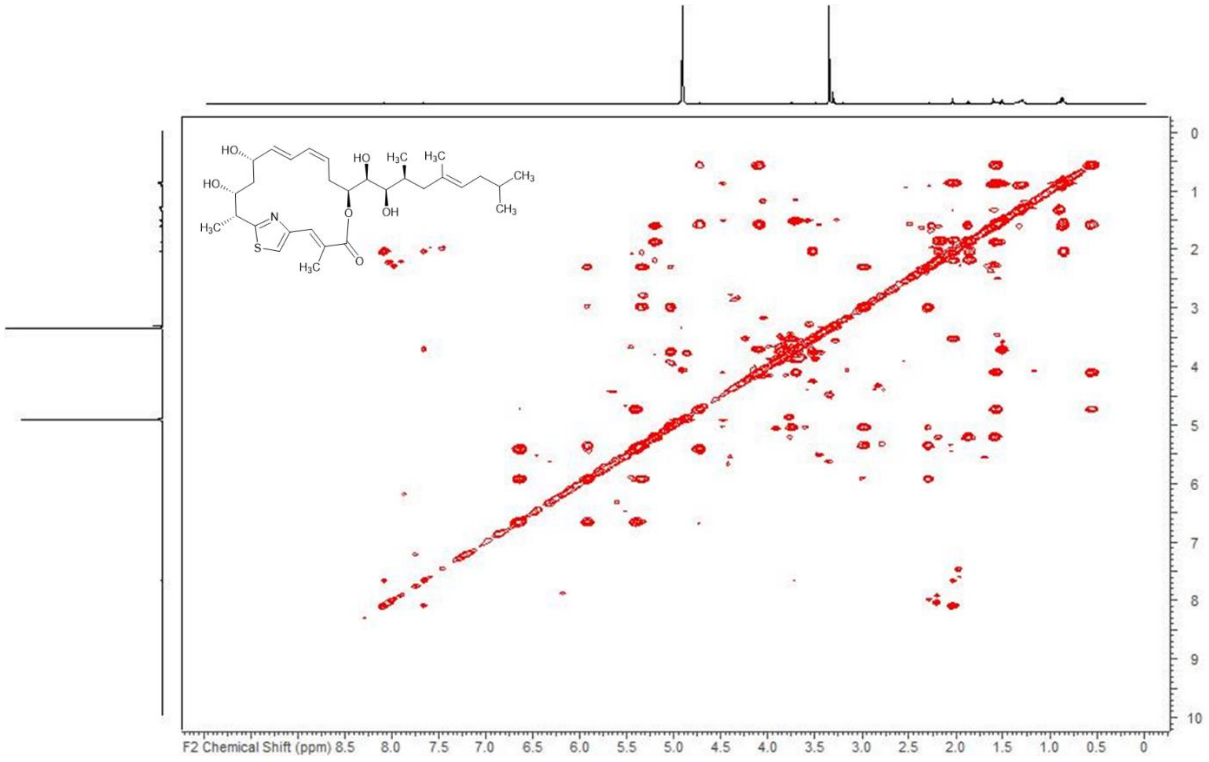

Figure S 4.33: COSY spectrum of thuggacin P1-A (8) in methanol-d_4 at 500 MHz.

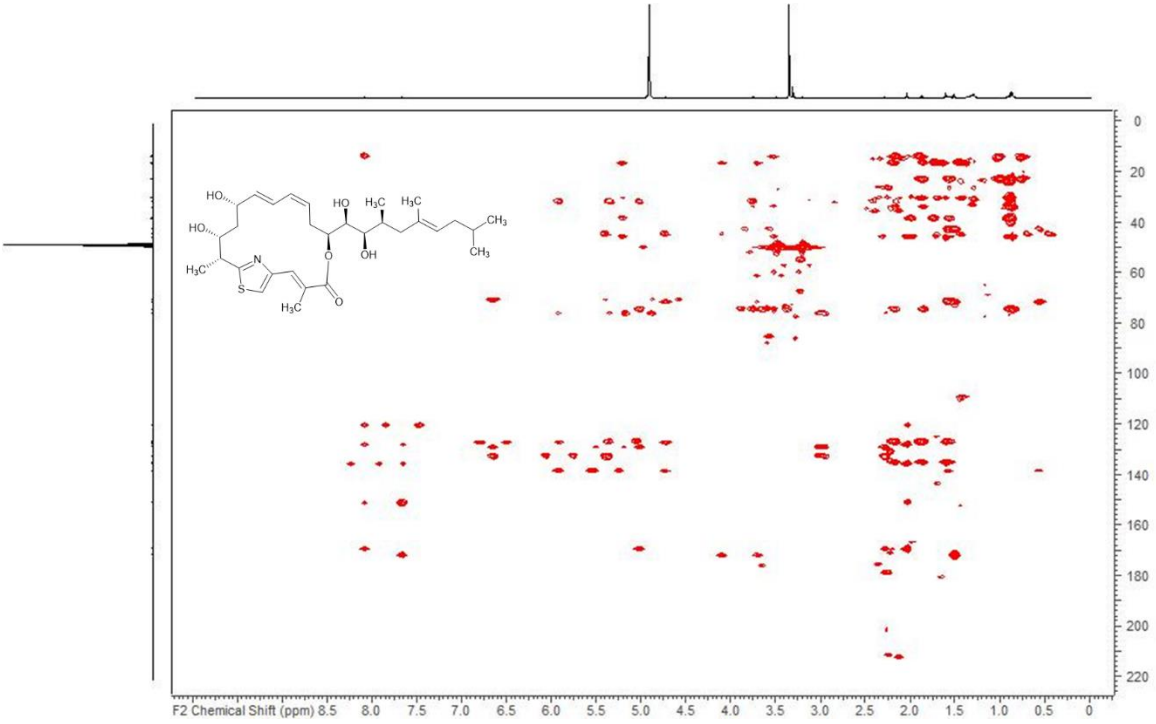

Figure S 4.34: HMBC spectrum of thuggacin P1-A (8) in methanol-d_4 at 125/500 (F1/F2) MHz.

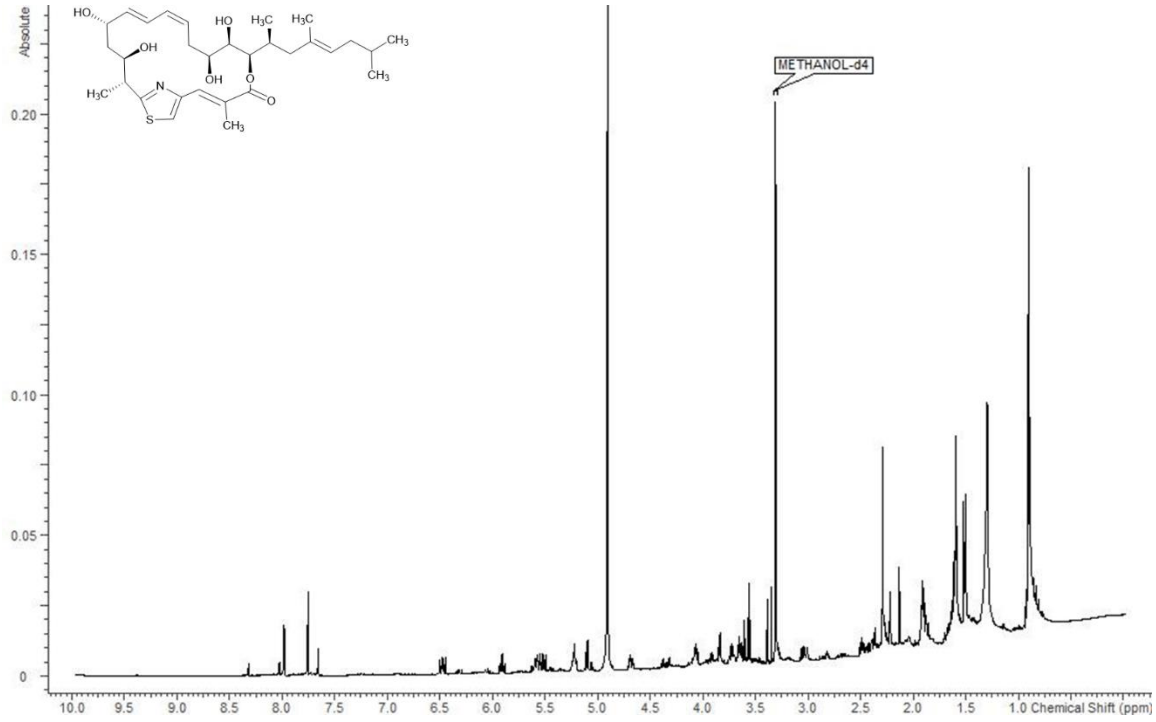

Figure S 4.35: ^{1}H spectrum of thuggacin P1-C (9) in methanol-d_4 at 500 MHz.

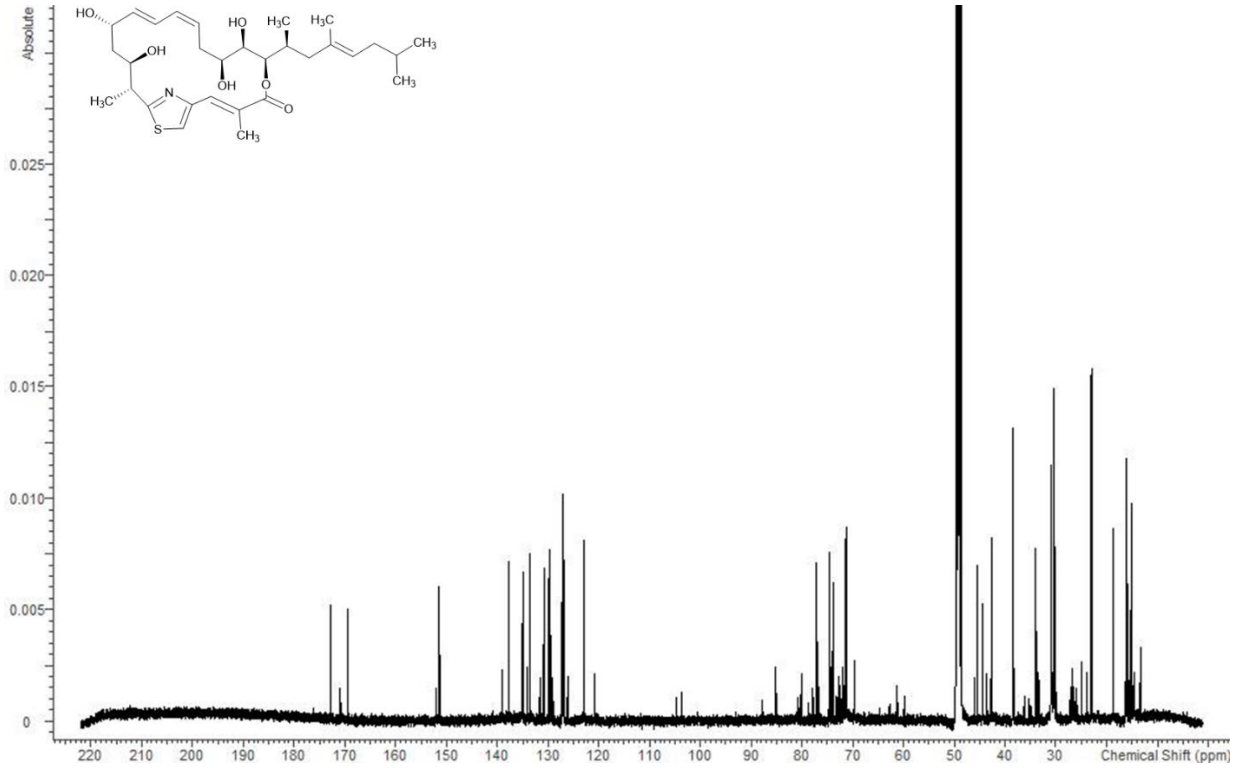

Figure S 4.36: ^{13}C spectrum of thuggacin P1-C (9) in methanol-d_4 at 125 MHz.

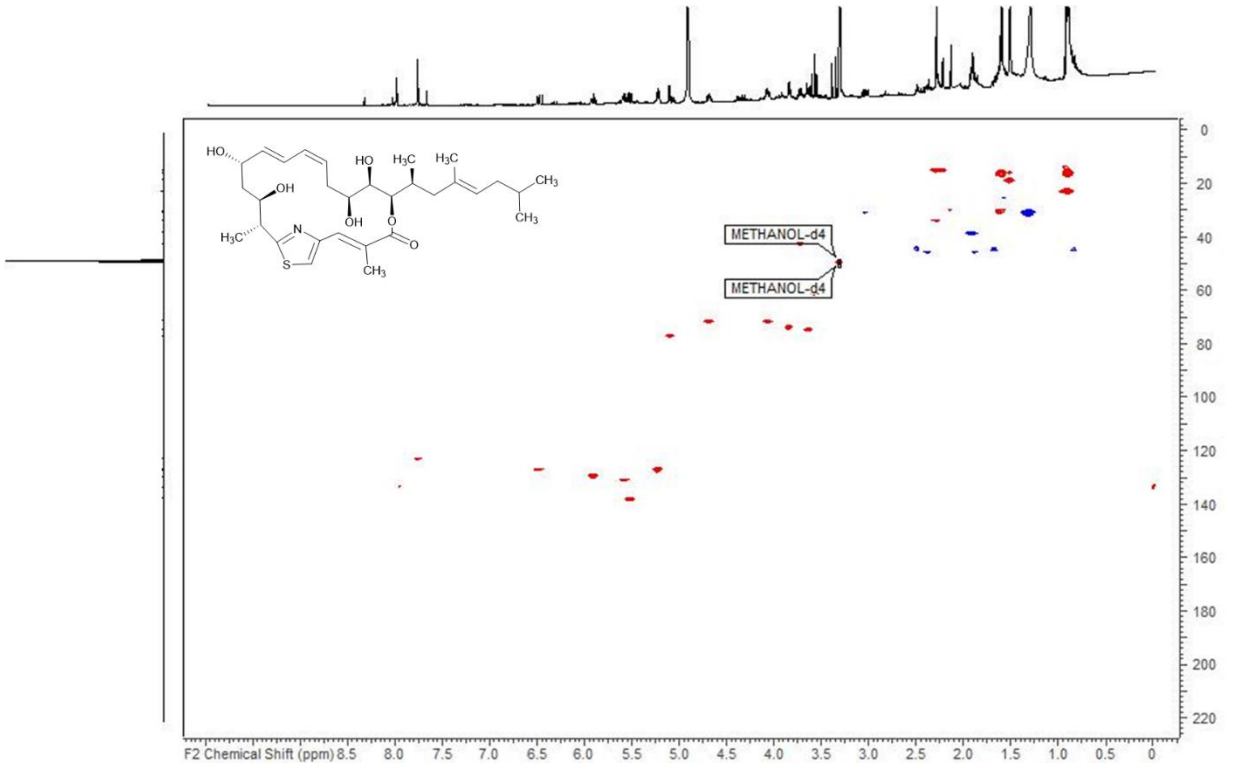

Figure S 4.37: HSQC spectrum of thuggacin P1-C (9) in methanol-d_4 at 125/500 (F1/F2) MHz.

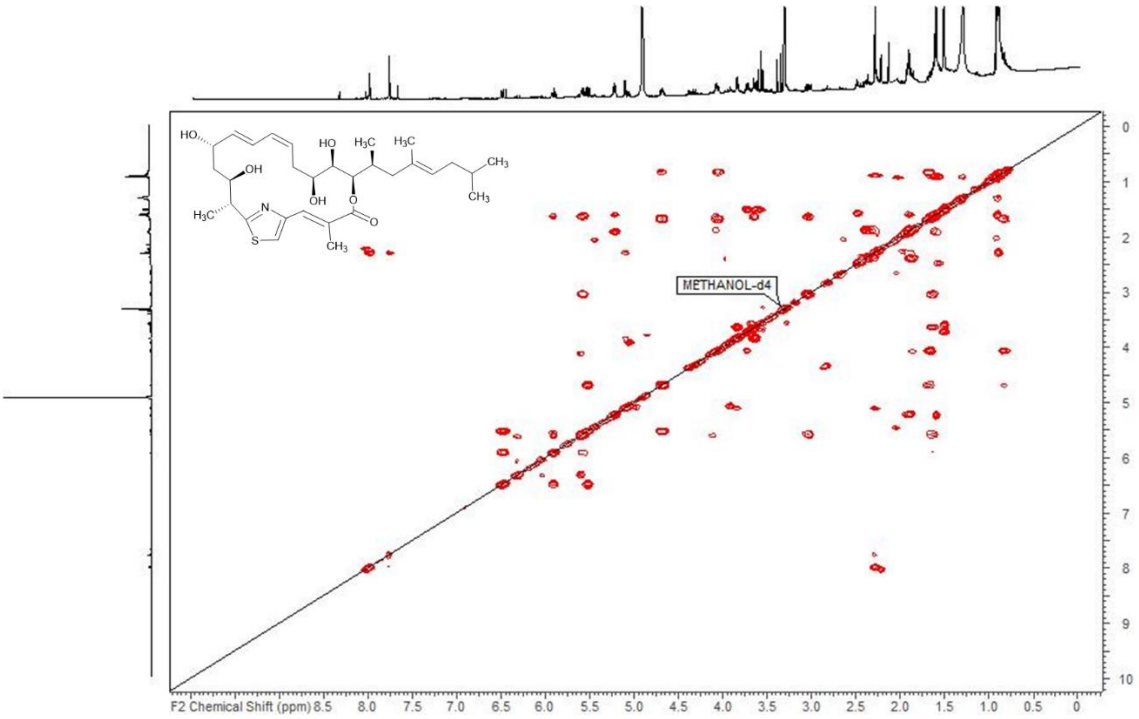

Figure S 4.38: COSY spectrum of thuggacin P1-C (9) in methanol-d_4 at 500 MHz.

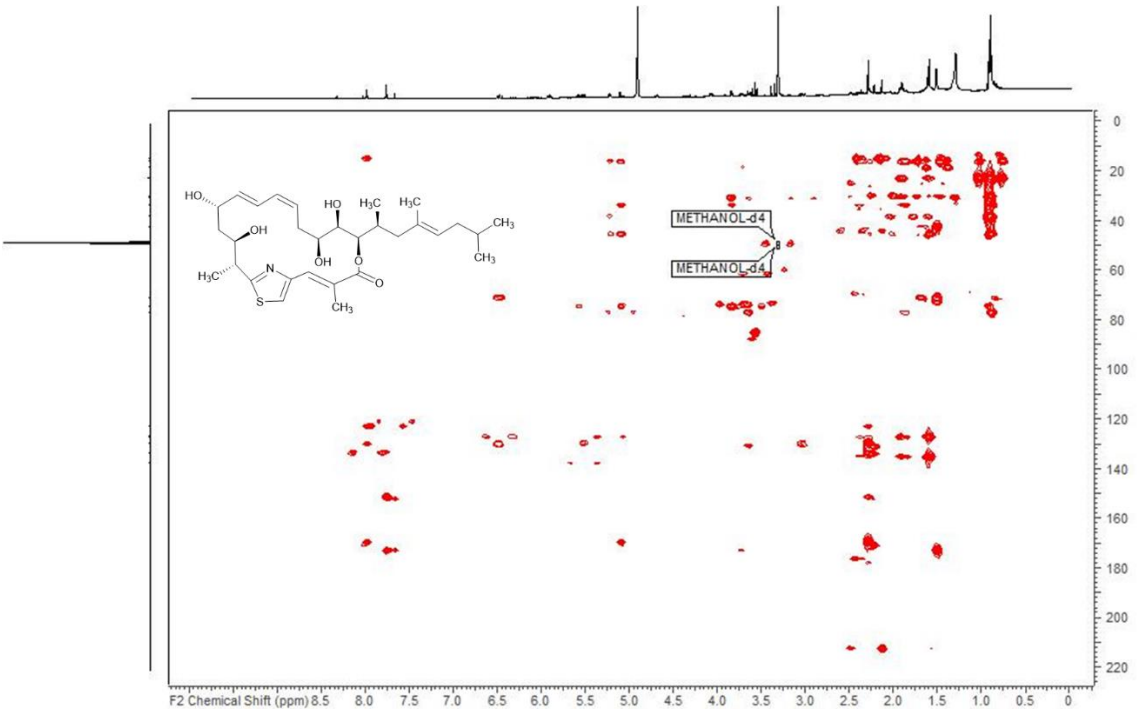

Figure S 4.39: HMBC spectrum of thuggacin P1-C (9) in methanol-d_4 at 125/500 (F1/F2) MHz.

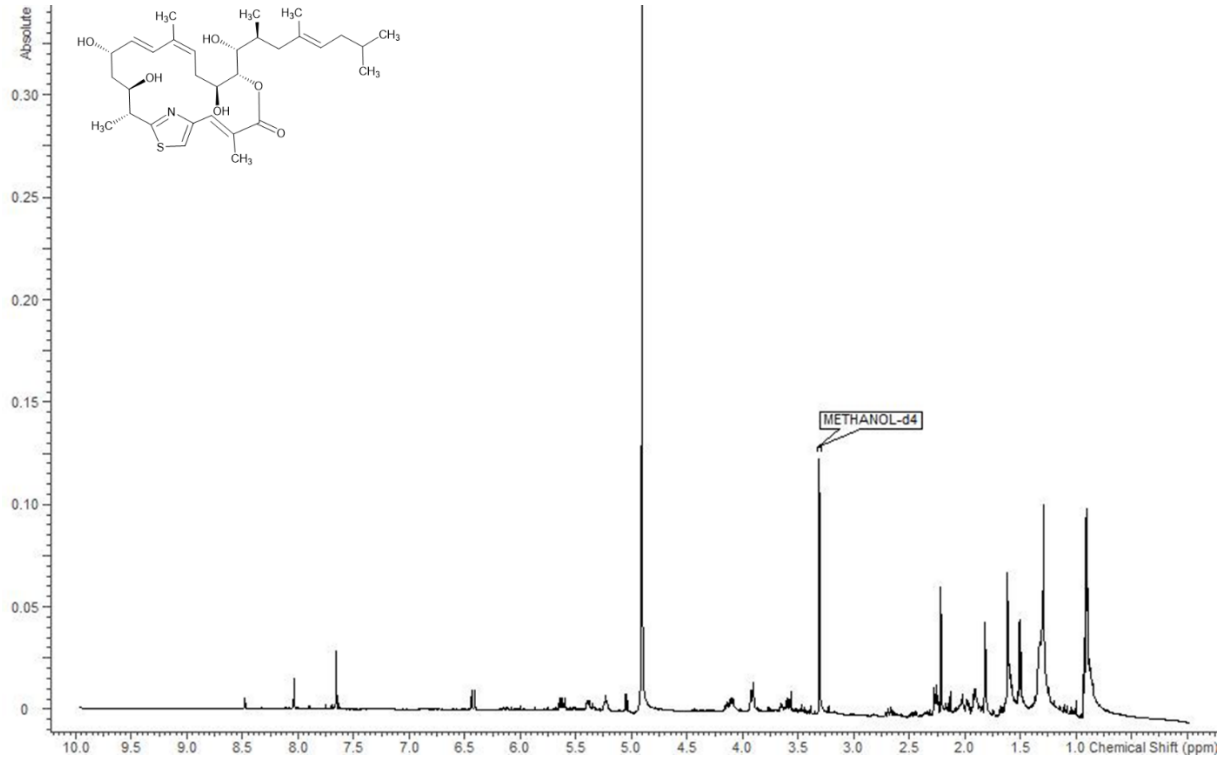

Figure S 4.40: ^{1}H spectrum of thuggacin P2-B (10) in methanol-d_4 at 500 MHz.

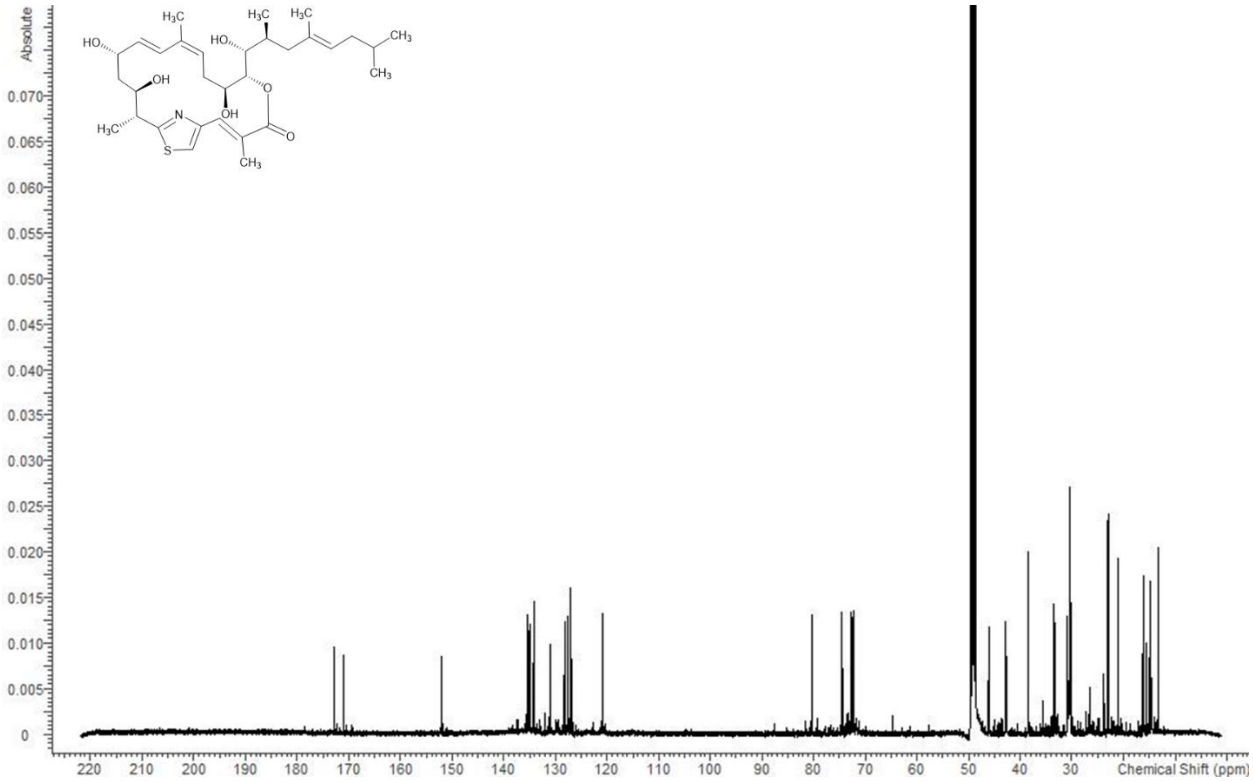

Figure S 4.41: ^{13}C spectrum of thuggacin P2-B (10) in methanol-d_4 at 125 MHz.

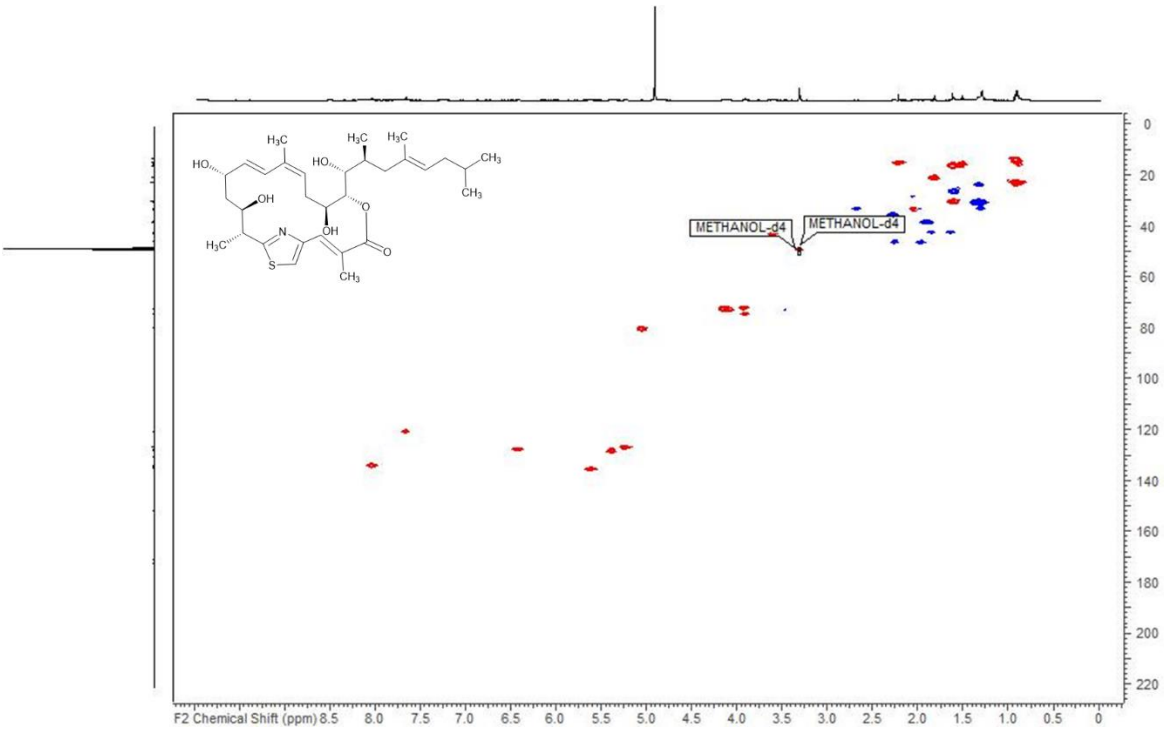

Figure S 4.42: HSQC spectrum of thuggacin P2-B (10) in methanol-d_4 at 125/500 (F1/F2) MHz.

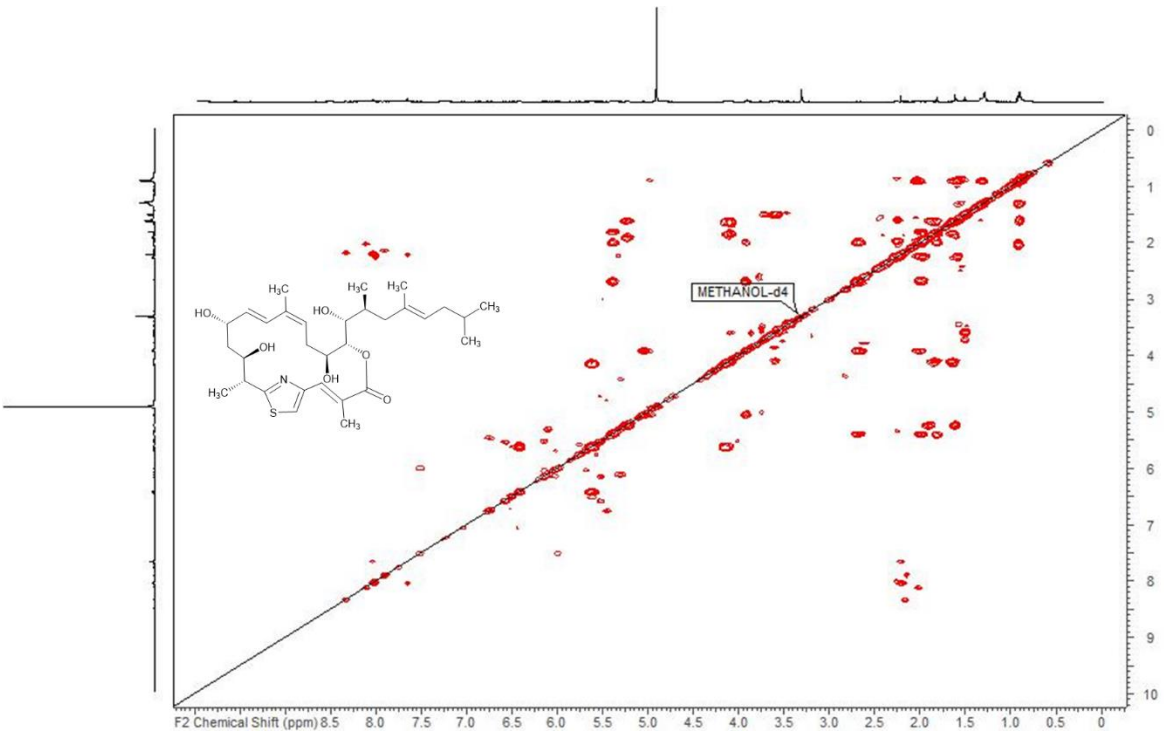

Figure S 4.43: COSY spectrum of thuggacin P2-B (10) in methanol-d_4 at 500 MHz.

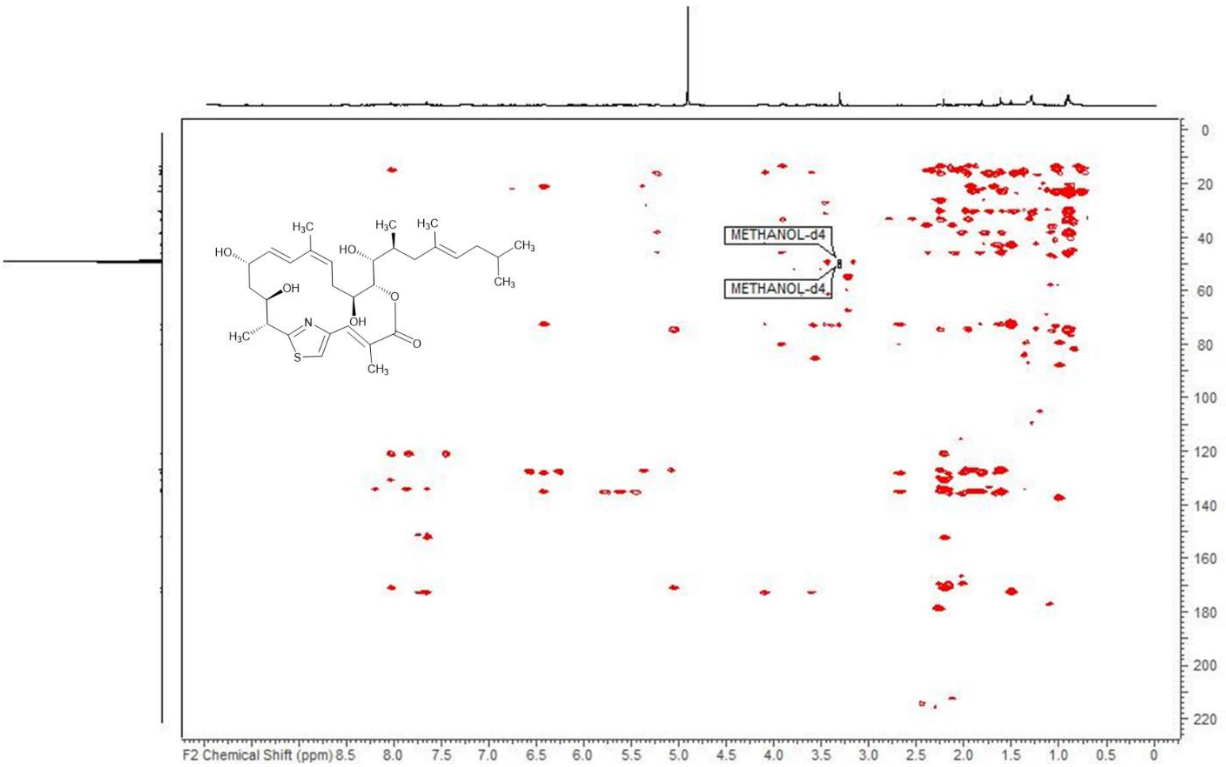

Figure S 4.44: HMBC spectrum of thuggacin P2-B (10) in methanol-d_4 at 125/500 (F1/F2) MHz.

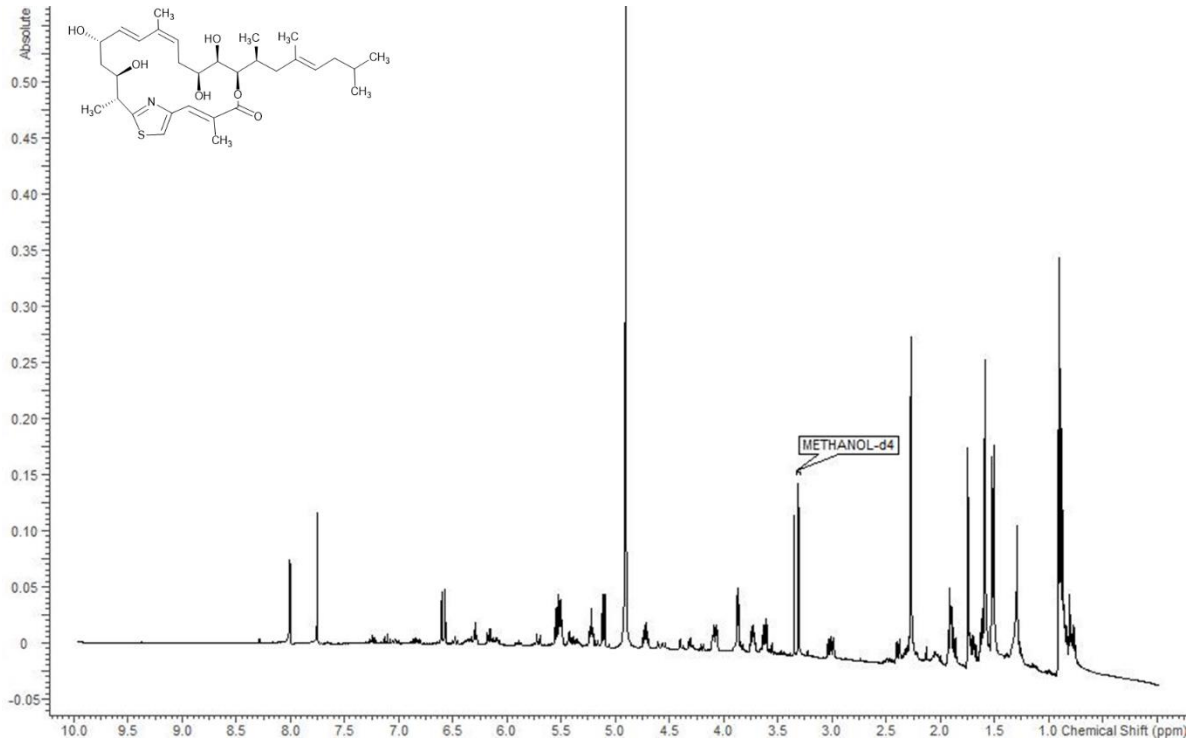

Figure S 4.45: ^{1}H spectrum of thuggacin P2-C (11) in methanol-d_4 at 500 MHz.

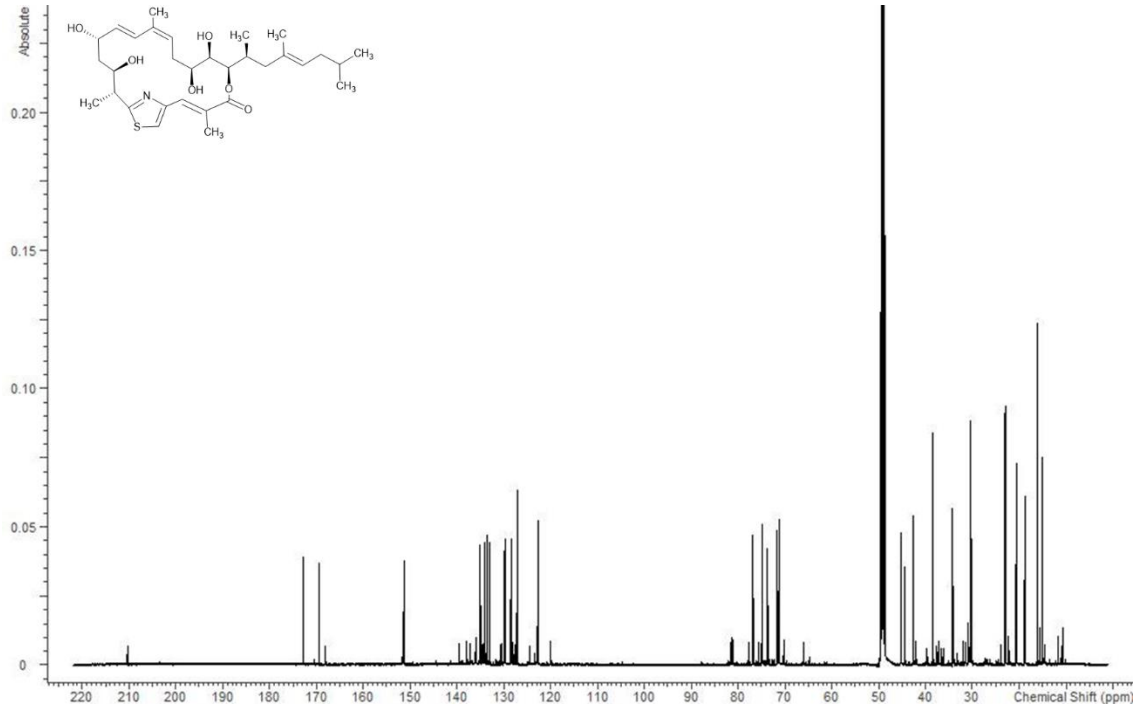

Figure S 4.46: ^{13}C spectrum of thuggacin P2-C (11) in methanol-d_4 at 125 MHz.

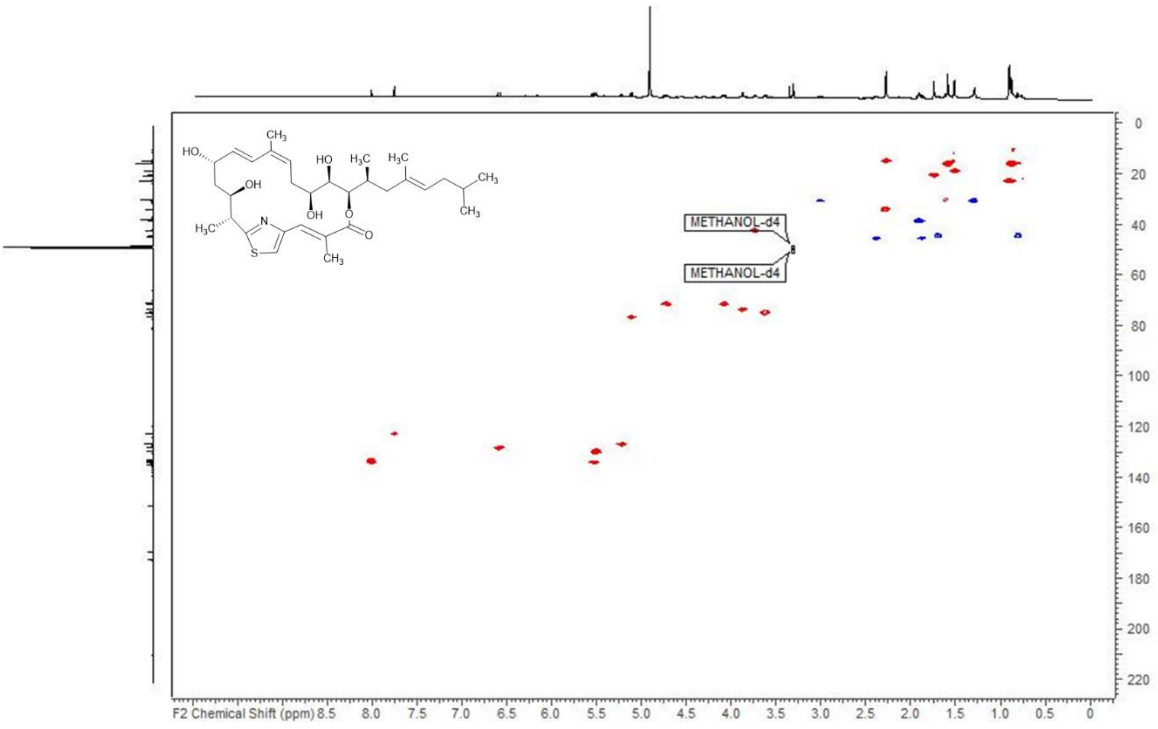

Figure S 4.47: HSQC spectrum of thuggacin P2-C (11) in methanol-d_4 at 125/500 (F1/F2) MHz.

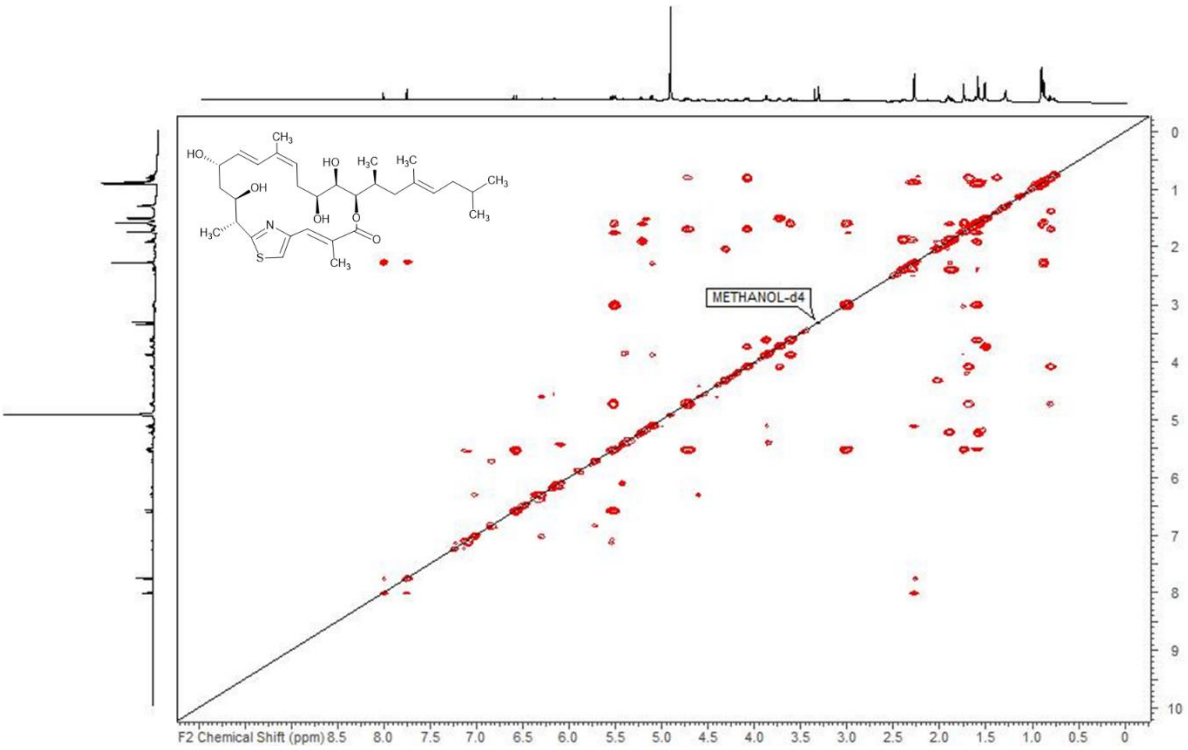

Figure S 4.48: COSY spectrum of thuggacin P2-C (11) in methanol-d_4 at 500 MHz.

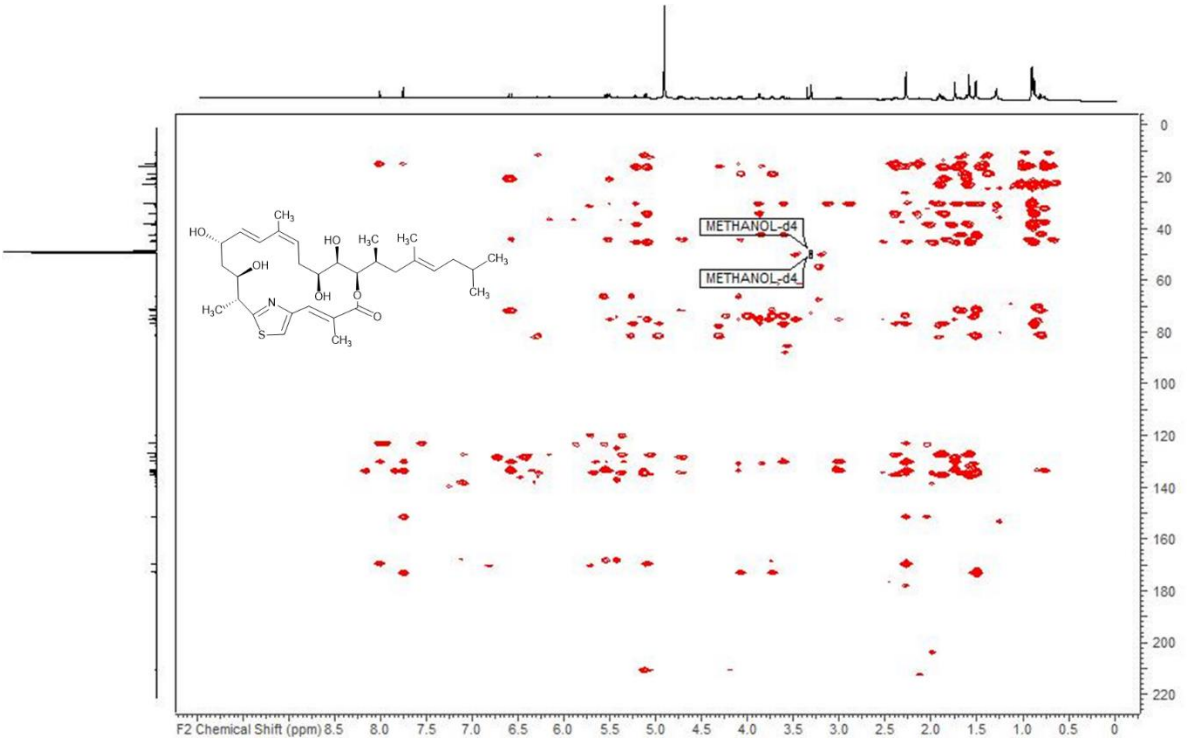

Figure S 4.49: HMBC spectrum of thuggacin P2-C (11) in methanol-d_4 at 125/500 (F1/F2) MHz.

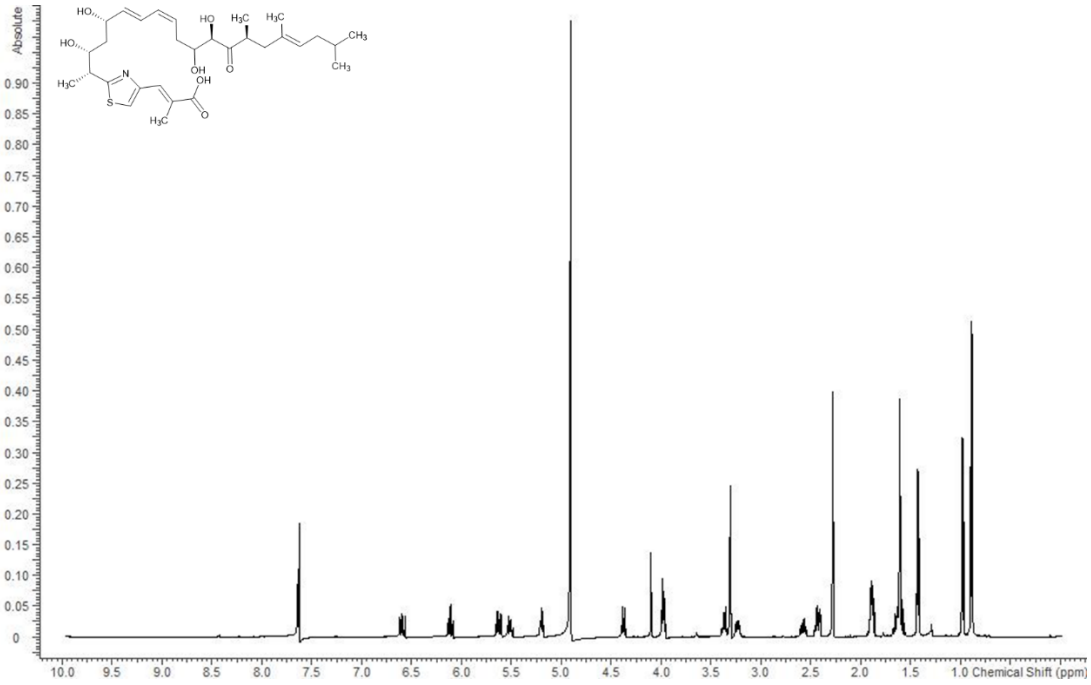

Figure S 4.50: ^{1}H spectrum of oxo-thuggacin P1 (12) in methanol-d_4 at 500 MHz.

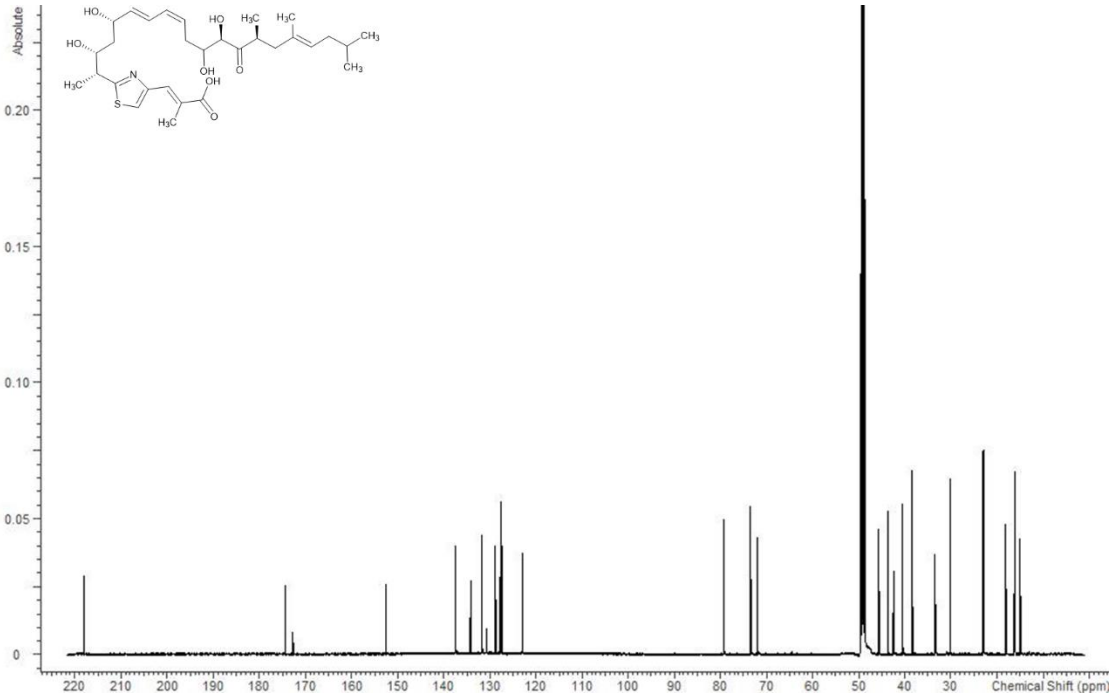

Figure S 4.51: ^{13}C spectrum of oxo-thuggacin P1 (12) in methanol-d_4 at 125 MHz.

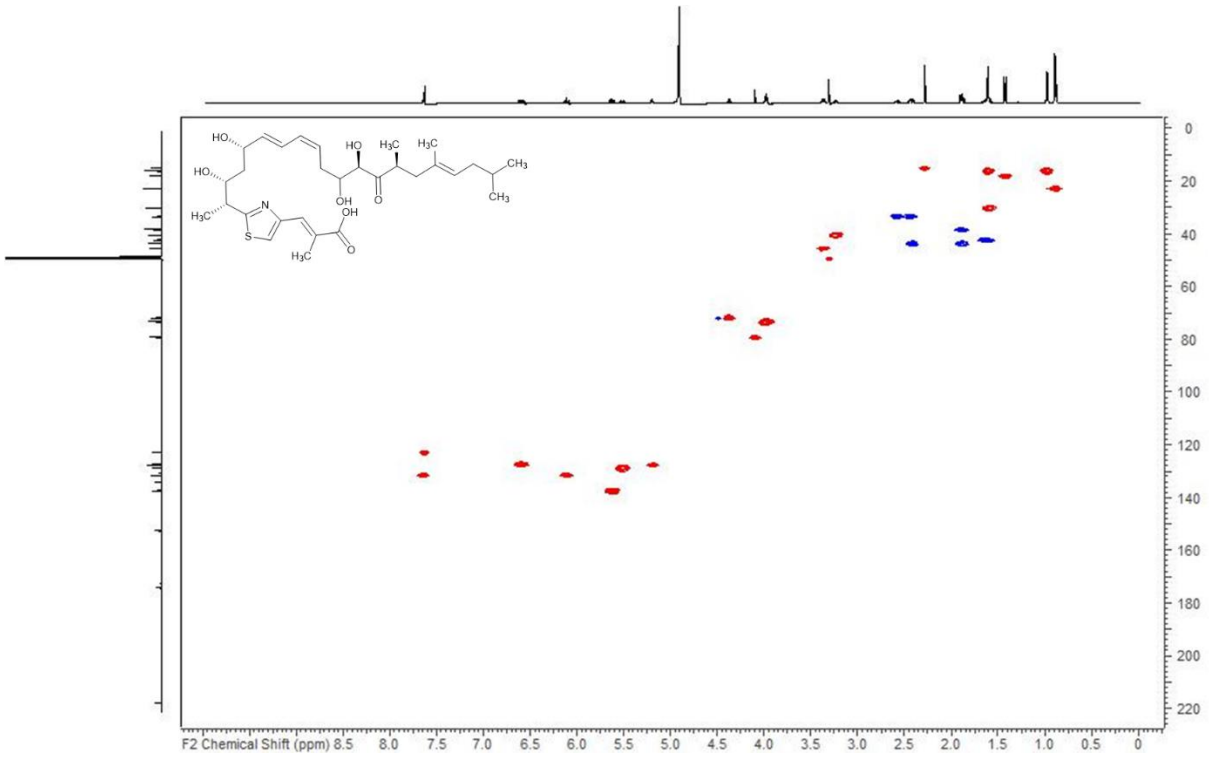

Figure S 4.52: HSQC spectrum of oxo-thuggacin P1 (12) in methanol-d_4 at 125/500 (F1/F2) MHz.

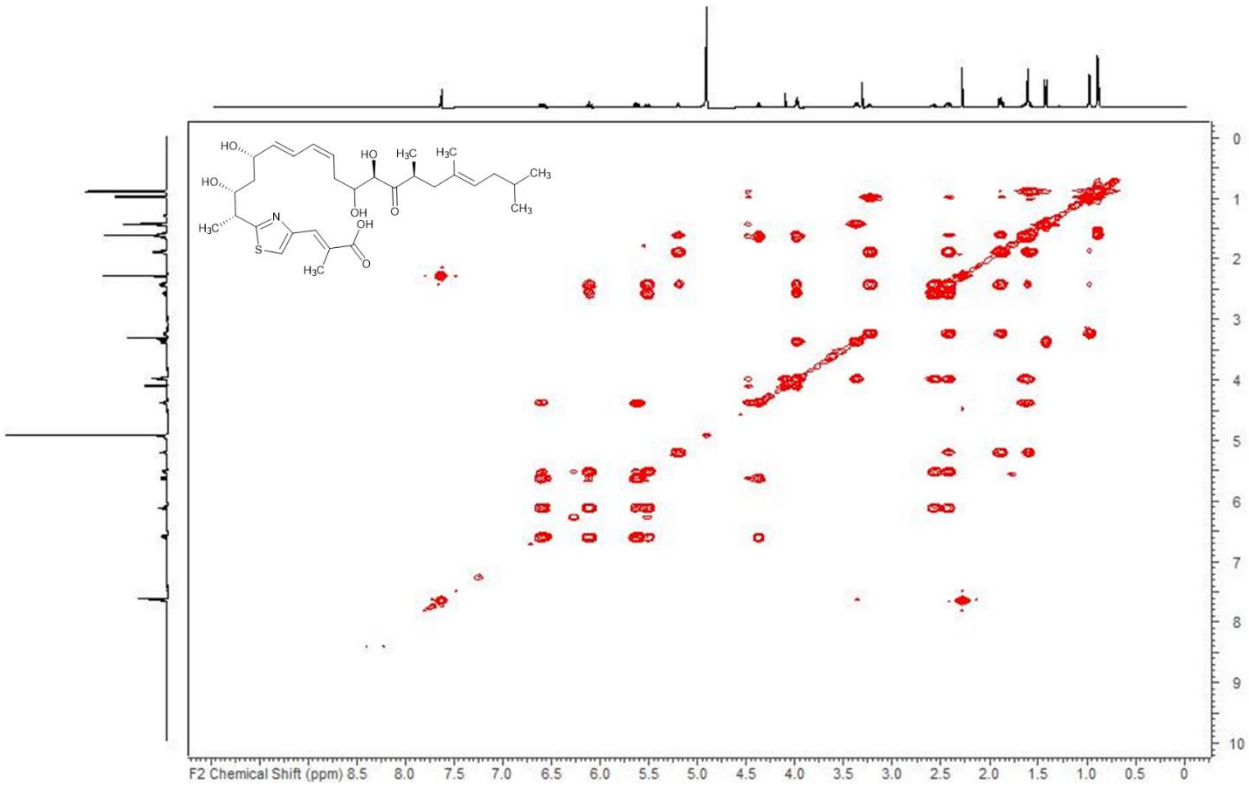

Figure S 4.53: COSY spectrum of oxo-thuggacin P1 (12) in methanol-d_4 at 500 MHz.

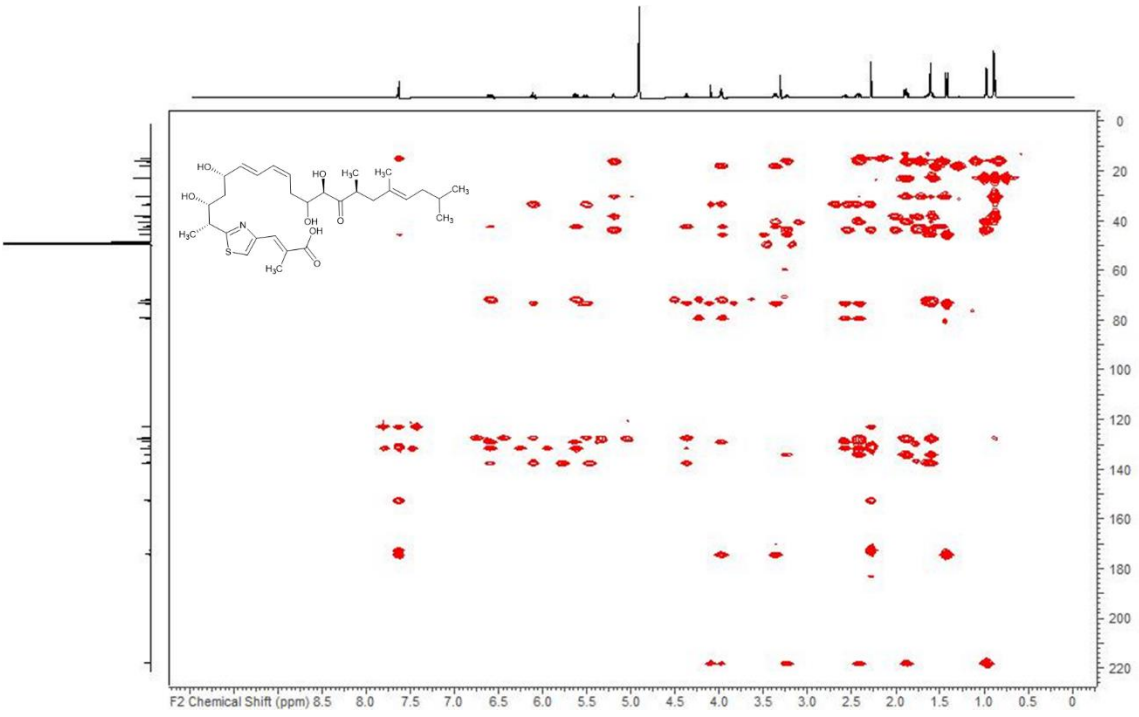

Figure S 4.54: HMBC spectrum of oxo-thuggacin P1 (12) in methanol-d_4 at 125/500 (F1/F2) MHz.

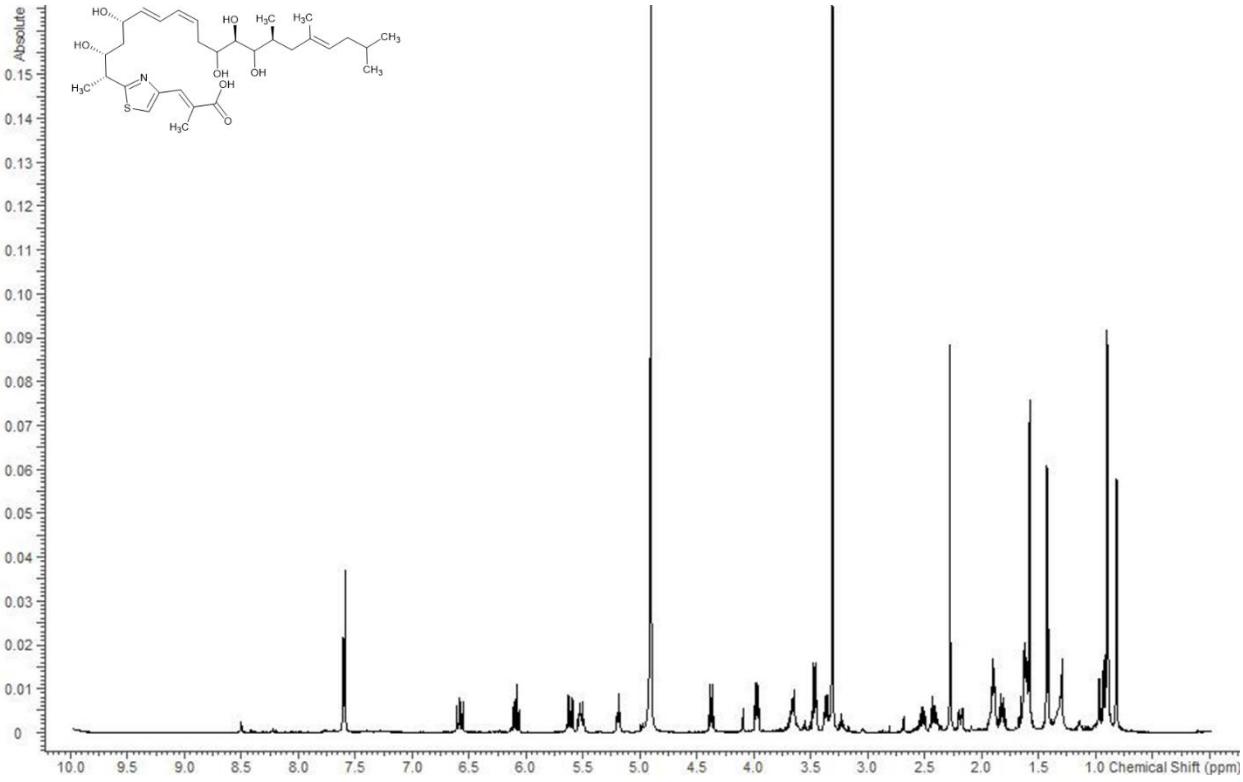

Figure S 4.55: ^{1}H spectrum of hydroxy-thuggacin P1 (13) in methanol-d_4 at 500 MHz.

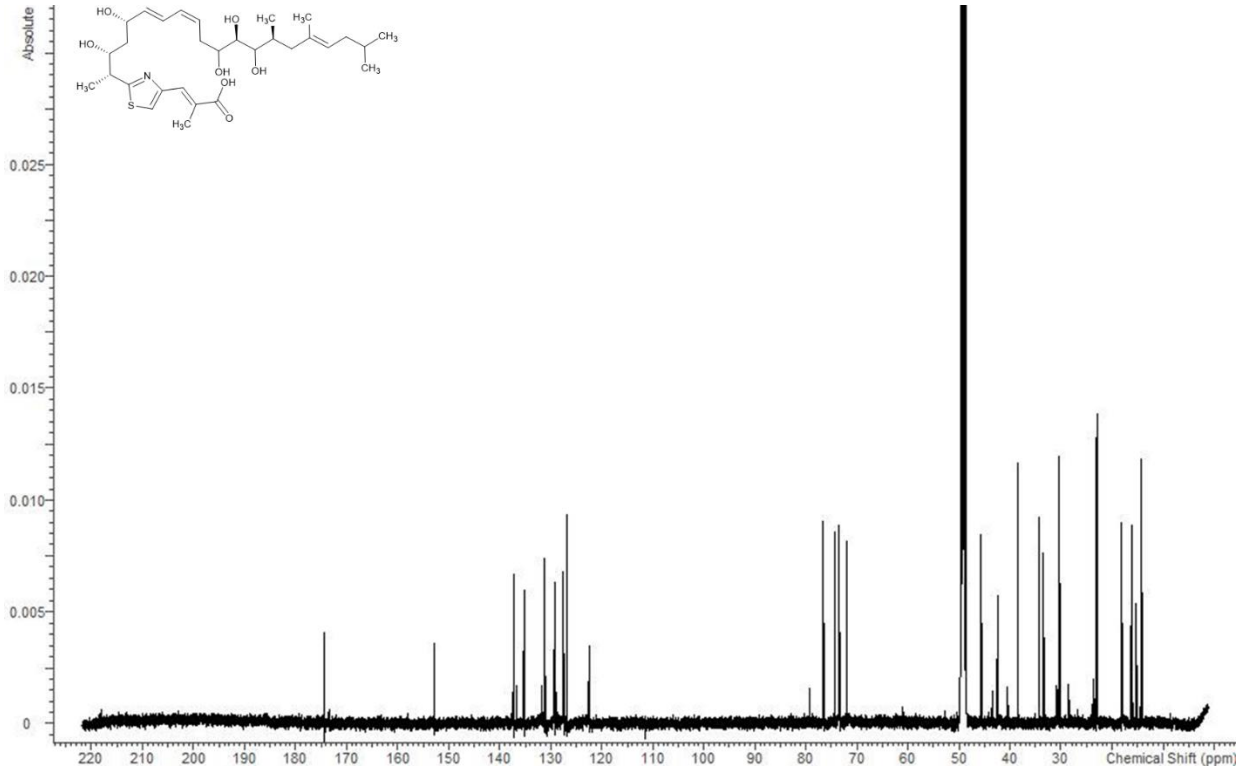

Figure S 4.56: ^{13}C spectrum of hydroxy-thuggacin P1 (13) in methanol-d_4 at 125 MHz.

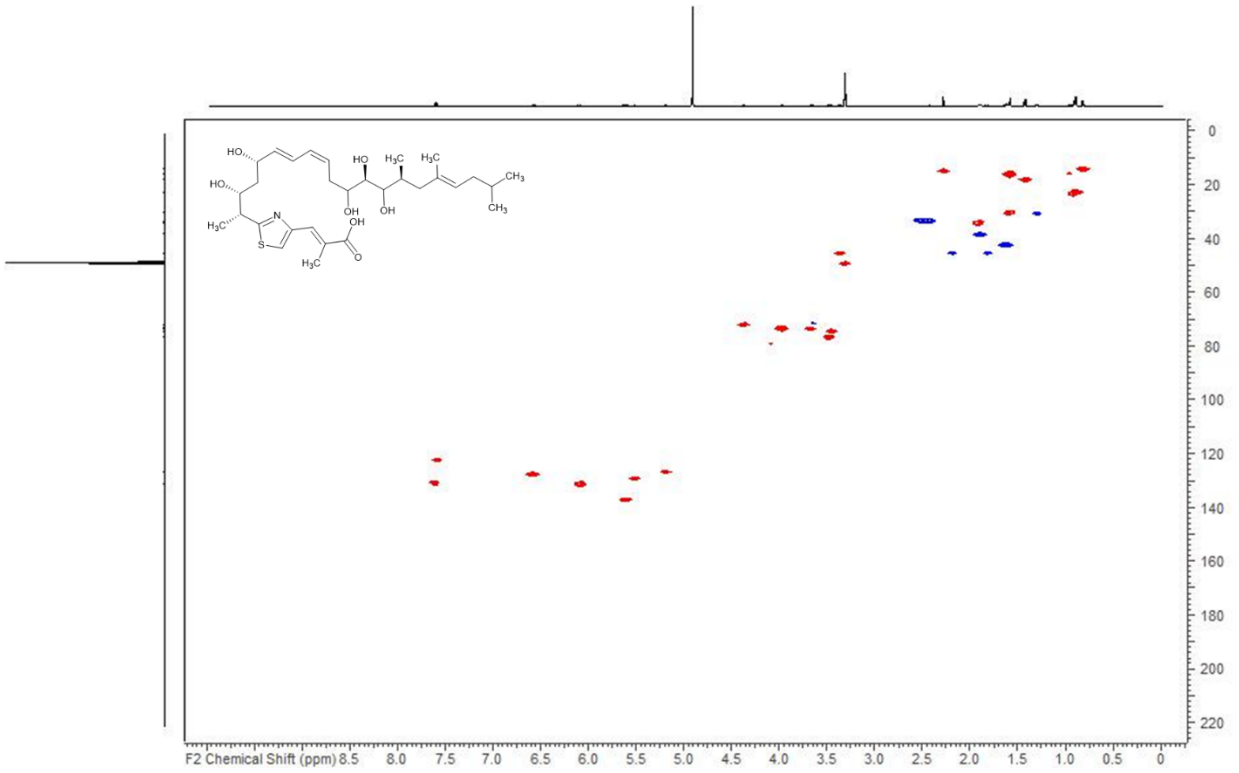

Figure S 4.57: HSQC spectrum of hydroxy-thuggacin P1 (13) in methanol-d_4 at 125/500 (F1/F2) MHz.

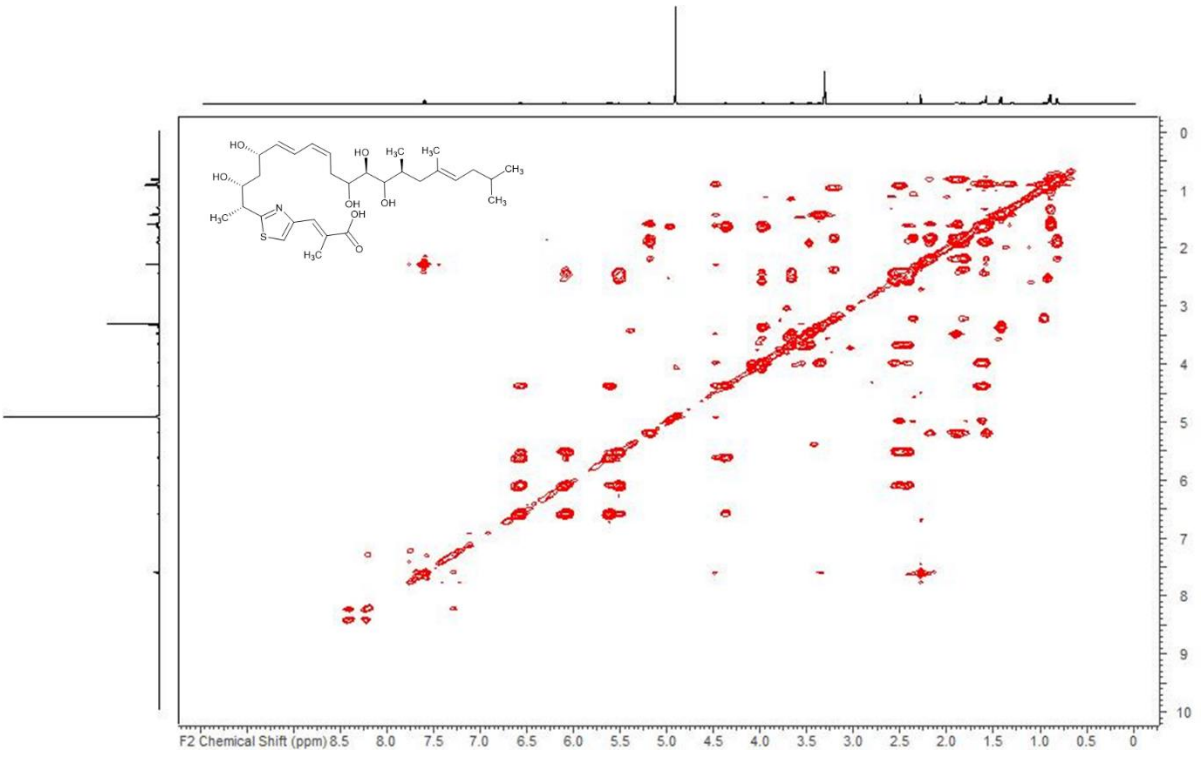

Figure S 4.58: COSY spectrum of hydroxy-thuggacin P1 (13) in methanol-d_4 at 500 MHz.

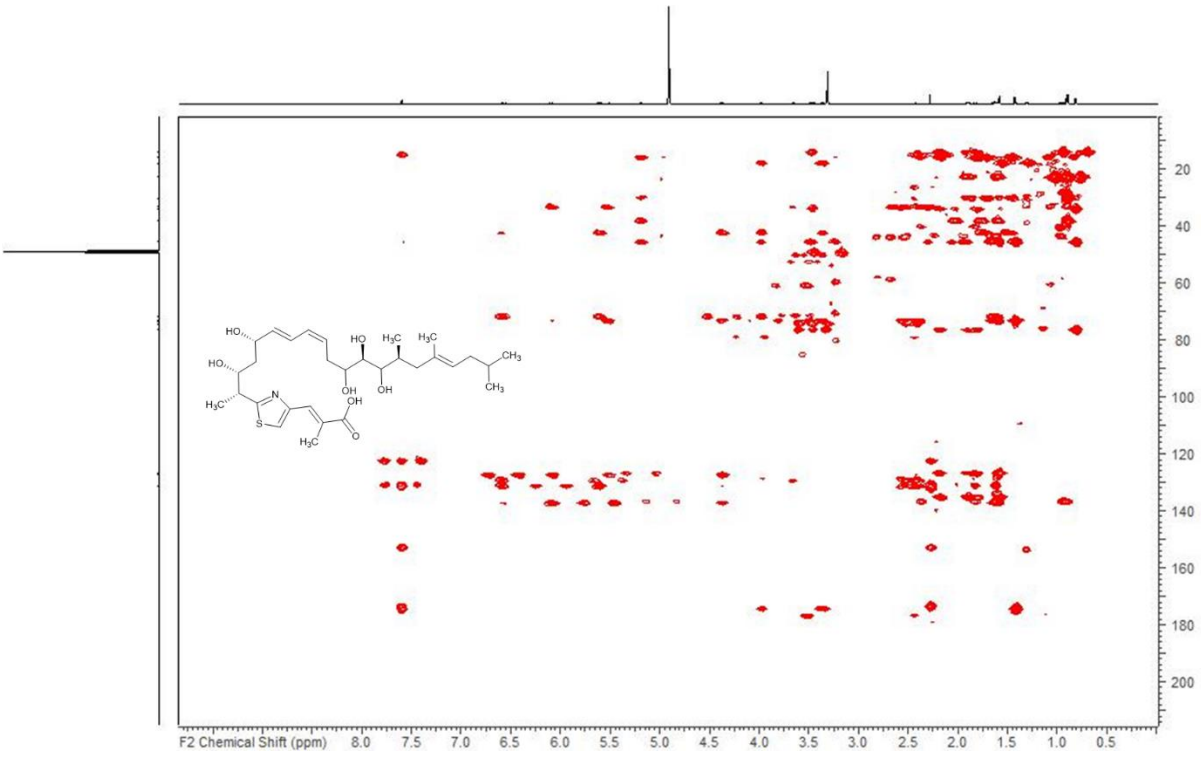

Figure S 4.59: HMBC spectrum of hydroxy-thuggacin P1 (13) in methanol-d_4 at 125/500 (F1/F2) MHz.

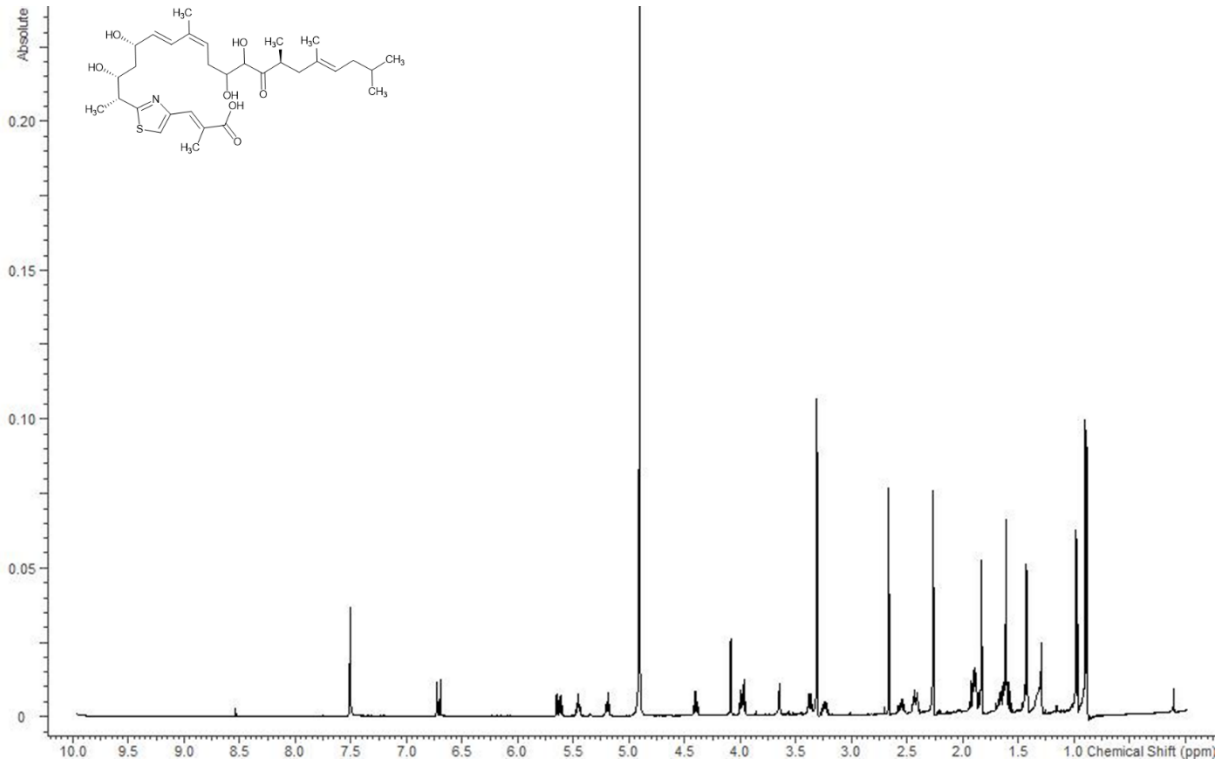

Figure S 4.60: ^{1}H spectrum of oxo-thuggacin P2 (14) in methanol-d_4 at 500 MHz.

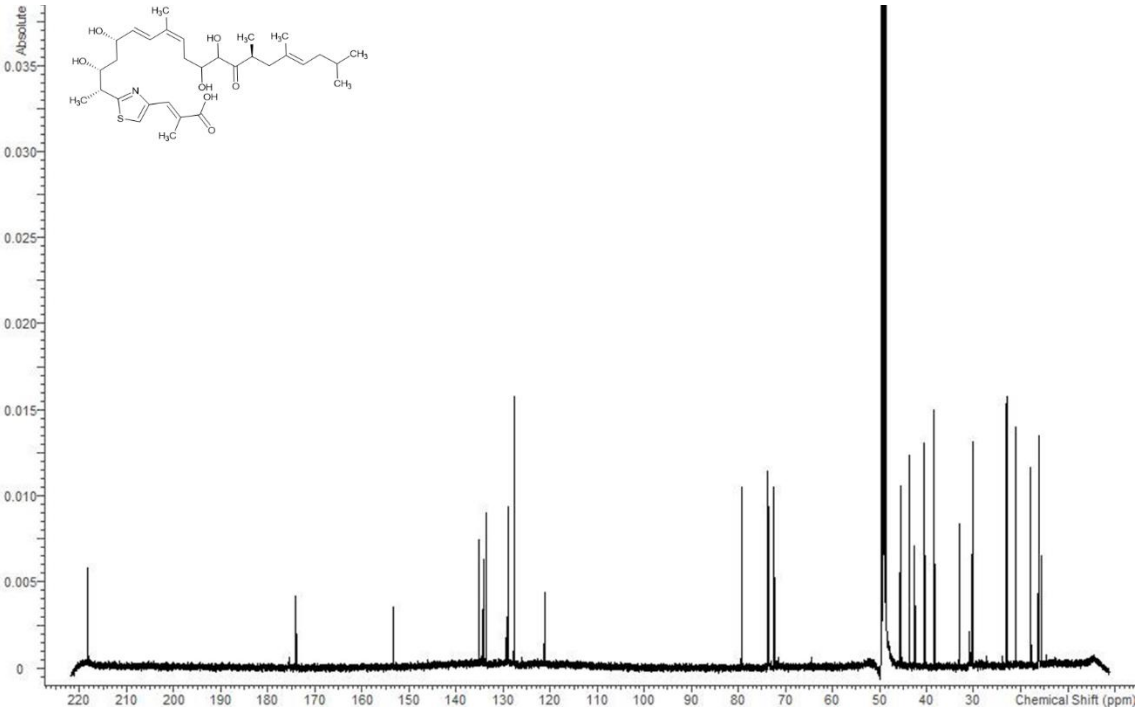

Figure S 4.61: ^{13}C spectrum of oxo-thuggacin P2 (14) in methanol-d_4 at 500 MHz.

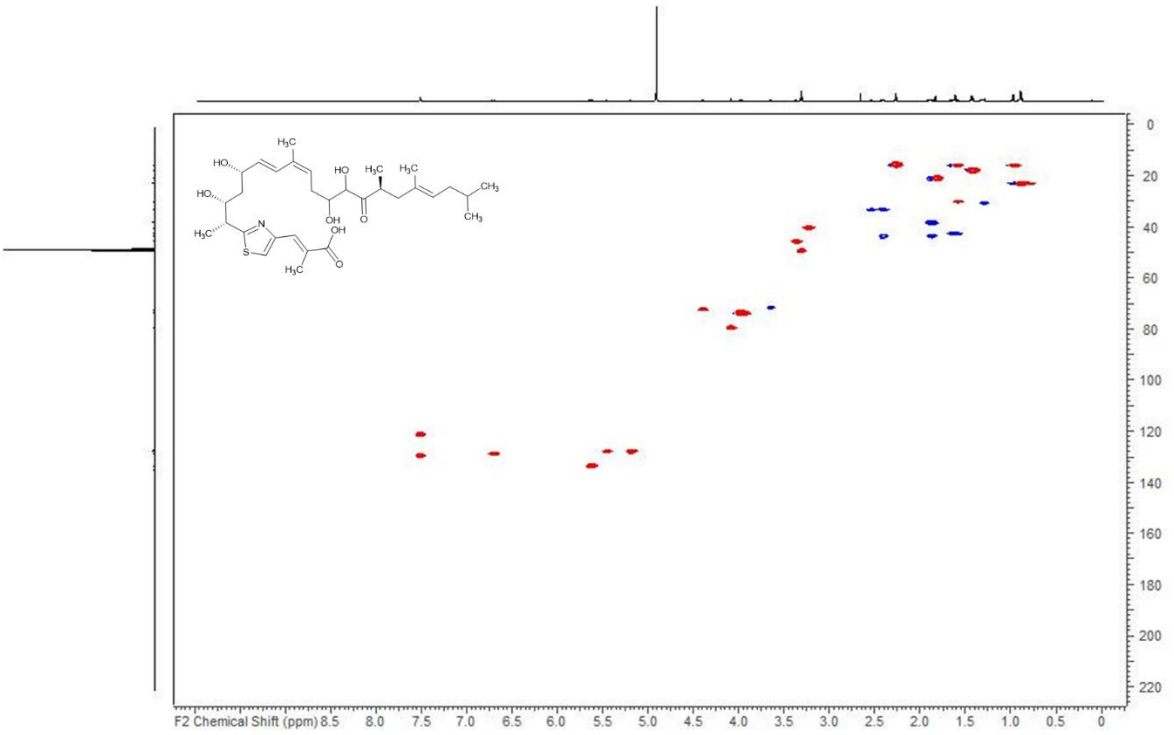

Figure S 4.62: HSQC spectrum of oxo-thuggacin P2 (14) in methanol-d_4 at 125/500 (F1/F2) MHz.

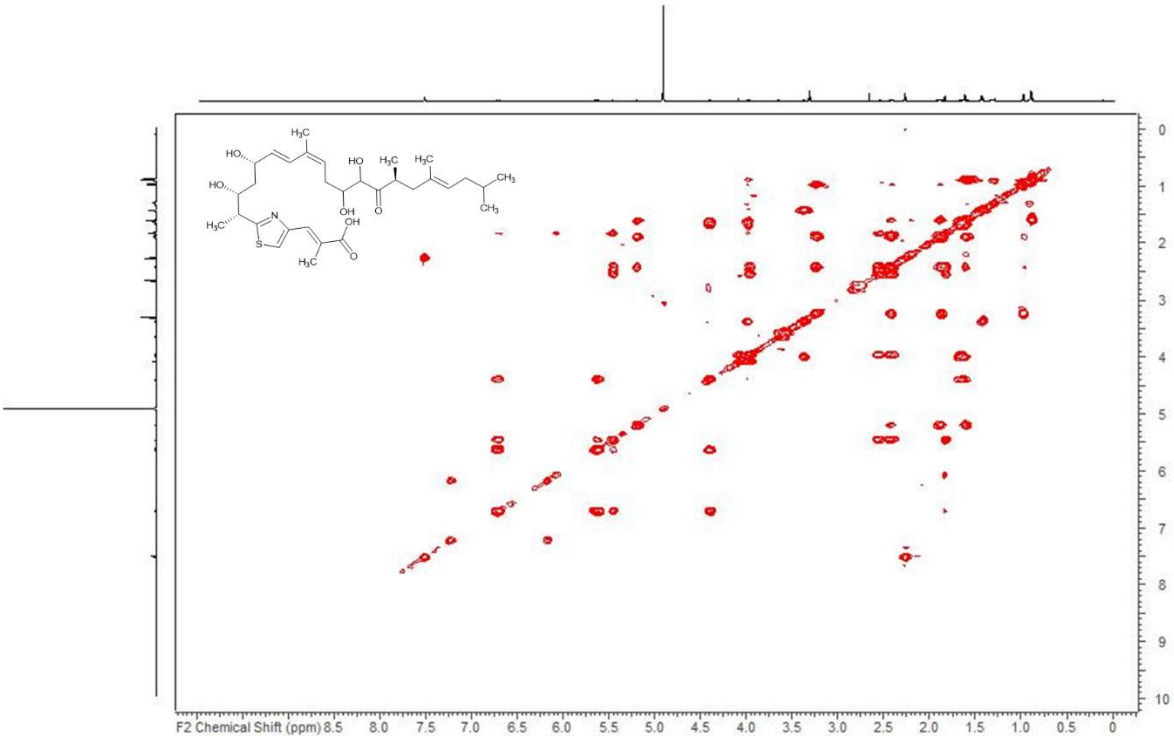

Figure S 4.63: COSY spectrum of oxo-thuggacin P2 (14) in methanol-d_4 at 500 MHz.

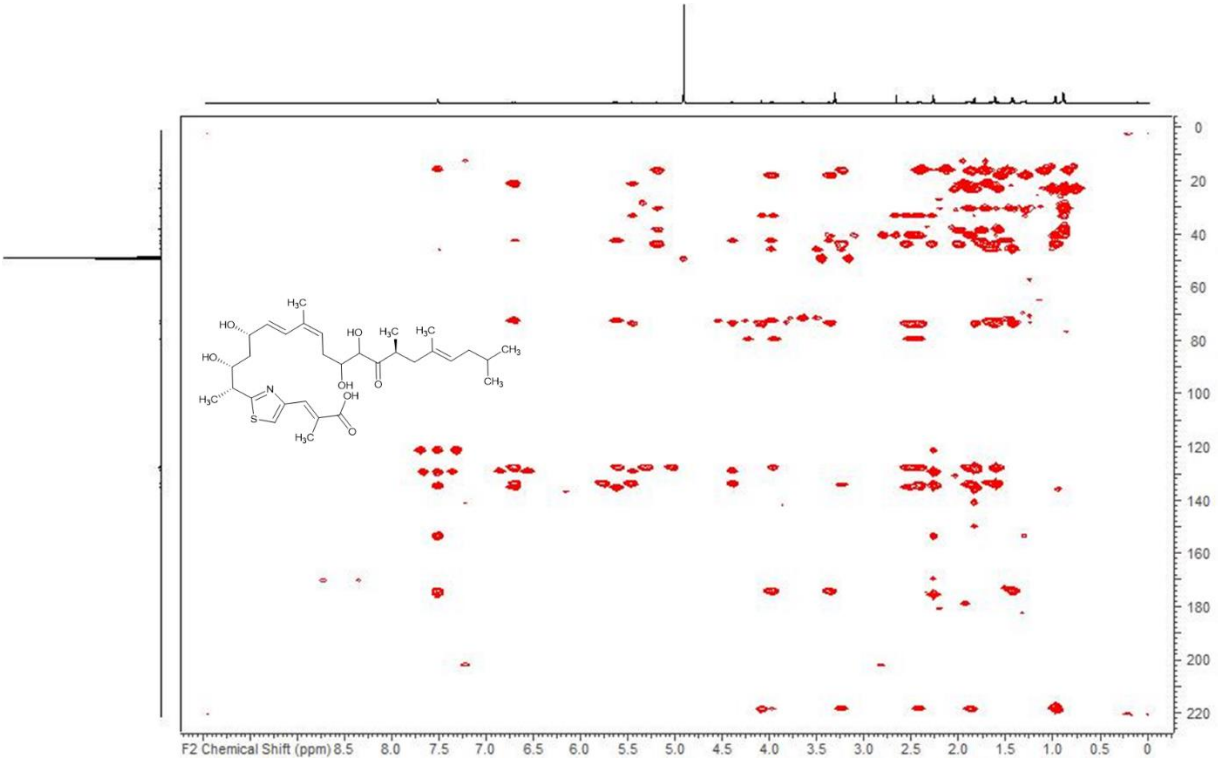

Figure S 4.64: HMBC spectrum of oxo-thuggacin P2 (14) in methanol-d_4 at 125/500 (F1/F2) MHz.

References

1. Hoffmann, T., Krug, D., Hüttel, S. & Müller, R. Improving natural products identification through targeted LC-MS/MS in an untargeted secondary metabolomics workflow. *Analytical chemistry* **86,** 10780–10788; 10.1021/ac502805w (2014).

2. Wang, M. *et al.* Sharing and community curation of mass spectrometry data with Global Natural Products Social Molecular Networking. *Nat. Biotechnol.* **34,** 828–837; 10.1038/nbt.3597 (2016).

3. Gallagher, L. A., McKnight, S. L., Kuznetsova, M. S., Pesci, E. C. & Manoil, C. Functions required for extracellular quinolone signaling by Pseudomonas aeruginosa. *J. Bacteriol.* **184,** 6472–6480; 10.1128/JB.184.23.6472–6480.2002 (2002).

4. Vial, L. *et al. Burkholderia pseudomallei*, *B. thailandensis*, and *B. ambifaria* produce 4-hydroxy-2-alkylquinoline analogues with a methyl group at the 3 position that is required for quorum-sensing regulation. *J. Bacteriol.* **190,** 5339–5352; 10.1128/JB.00400-08 (2008).

5. Blin, K. *et al.* antiSMASH 6.0: improving cluster detection and comparison capabilities. *Nucleic Acids Res.* **49,** W29-W35; 10.1093/nar/gkab335 (2021).
6. Buntin, K. *et al.* Biosynthesis of thuggacins in myxobacteria: comparative cluster analysis reveals basis for natural product structural diversity. *Chemistry & biology* **17,** 342–356; 10.1016/j.chembiol.2010.02.013 (2010).
7. van den Belt, M. *et al.* CAGECAT: The CompArative GEne Cluster Analysis Toolbox for rapid search and visualisation of homologous gene clusters. *Bmc Bioinform.* **24,** 181; 10.1186/s12859-023-05311-2 (2023).
8. Keatinge-Clay, A. T. The structures of type I polyketide synthases. *Nat. Prod. Rep.* **29,** 1050–1073; 10.1039/c2np20019h (2012).
9. Keatinge-Clay, A. T. A Tylosin Ketoreductase Reveals How Chirality is Determined in Polyketides. *Chem. Biol.* **14,** 898–908; 10.1016/j.chembiol.2007.07.009 (2007).
10. Kwan, D. H. *et al.* Prediction and manipulation of the stereochemistry of enoylreduction in modular polyketide synthases. *Chem. Biol.* **15,** 1231–1240; 10.1016/j.chembiol.2008.09.012 (2008).
11. Bock, M., Buntin, K., Müller, R. & Kirschning, A. Stereochemical determination of thuggacins A-C, highly active antibiotics from the myxobacterium Sorangium cellulosum. *Angewandte Chemie (International ed. in English)* **47,** 2308–2311; 10.1002/anie.200704897 (2008).

5 Chapter: Elicitor screening

Development of an Increased Throughput Elicitor Screening Platform for Myxobacteria

Sebastian Walesch, F. P. Jake Haeckl, Daniel Krug and Rolf Müller

Manuscript in preparation

Contributions to the presented work

Author's effort

The author contributed to the concept of this study, planned and executed experiments, evaluated and interpreted resulting data. He developed the higher-throughput elicitor screening platform, performed cultivations and analysed the resulting data. Moreover, the author contributed to the conception and writing of this manuscript.

Contributions by others

Jake Haeckl contributed to the concept of this study, performed UHPLC-*hr*MS/MS experiments and wrote the R script used for heatmap generation. Furthermore, he contributed in scientific discussions and with helpful ideas for data evaluation. Daniel Krug and Rolf Müller contributed by supervision of the project and conceiving, editing and proofreading of this manuscript. The authors thank Joy Birkelbach for scientific discussions and proof-reading of the manuscript.

5.1 **Abstract**

The exploration of microbial natural products has led to the discovery of thousands of metabolites with a variety of biological activities. However, these metabolites only account for a small fraction of the actual biosynthetic potential of microbes, as the majority of biosynthetic gene clusters cannot be linked to a natural product in standard laboratory cultivations. Over the past decade, different variations of a high-throughput elicitor screening approach have been used to exploit the hidden biosynthetic potential of microbes to produce novel natural products. In order to access the hidden biosynthetic potential of myxobacteria with the help of elicitors, a higher throughput elicitor screening platform in a 24 deep-well plate format was developed. The platform was used to pinpoint staurosporin and mitomycin C as promising elicitors for *Myxococcus xanthus* DK1622. In follow-up cultivations in conventional shaking flasks, these molecules displayed their ability to modify the metabolomes of the test strain and further myxobacteria and to elicit the production of (secondary) metabolites that were not observed in standard laboratory cultivation settings.

5.2 **Introduction**

Notwithstanding constant scientific advancements, nature remains among the most important contributors to treat human diseases[1]. Natural products are a mainstay of modern medicine, about one third of the small molecule drugs that were approved in the past four decades are natural products or derivatives thereof[2]. They are particularly important for the treatment of bacterial infections, as about two thirds of FDA-approved antibiotics are natural products or their congeners[3].

Among the microorganisms with a great capability to produce biologically active natural products are Gram-negative rod-shaped myxobacteria[4–6]. In the past decades, several hundred natural products with diverse chemical scaffolds and a variety of biological activities were isolated from this phylum[5,7]. Furthermore, recent reports about the discoveries of antiviral thiamyxins[8] and sandacrabins[9] or the antibiotic corramycin[10] raise the hope that myxobacteria will continue to be a prolific source of further biologically active chemical scaffolds.

The ongoing efforts to sequence genomes of various microorganisms has unveiled that the natural products produced by gifted producers like Actinomycetes[11], myxobacteria[6,12] or fungi[13] under standard laboratory cultivation conditions account for only a small fraction of their biosynthetic potential. Over the past two decades, natural product researchers have successfully applied a variety of cultivation- and molecular biology

based methods to access the products of these cryptic biosynthetic gene clusters (BGCs)[3,14,15]. Among these methods, the search for additives with the ability to alter the test strains' metabolome stands out as it can be implemented with a lower effort compared to other approaches to access the test strains cryptic biosynthetic potential[15]. Depending on the read-out method of a successful modification of the test strains (secondary) metabolome, screening for those so-called elicitors, can be done in a high-throughput manner. Consequently, high-throughput elicitor screening campaigns were performed for a variety of microorganisms with optical[16,17], bioactivity-dependent[18,19] or mass spectrometry-assisted[20–22] decision-making for effective elicitors.

This study describes the implementation and evaluation of a higher throughput elicitor screening platform in 24 deep-well plates for myxobacteria. Initial screening was conducted with ten different elicitors in three different concentrations with the myxobacterial model organism *Myxococcus xanthus* DK1622. Based on the results of the initial screen four elicitor conditions were selected for proof of concept flask cultivations with a comprehensive statistical evaluation of the strains' (secondary) metabolome with and without elicitor treatment. Two of the chosen elicitor conditions displayed promising capabilities to modify the (secondary) metabolome of *M. xanthus* DK1622 and further test strains, leading to the observation of so far undescribed metabolites. Furthermore, the validity of the screening platform was evaluated based on the data of screenings with *M. xanthus* DK1622 in two different media as well as five further myxobacteria. These findings were used to propose an improved elicitor screening workflow.

5.3 Results and discussion

Hitherto, the majority of successful activations of previously cryptic BGCs in myxobacteria was achieved by genetic manipulations of the respective microorganisms[6,23–25]. However, for many myxobacterial strains genetic manipulation is difficult to impossible to achieve, as displayed for several *Cystobacterineae*[26], *Sorangiineae*[26–28], and *Nannocysteineae*[29,30]. Although heterologous expression of BGCs of interest in the well-established host *M. xanthus* DK1622 is a successful strategy[31–33], this approach can be laborious for large BGCs[33] or impractical for "split-clusters" that do not harbour all genes for the entire biosynthesis within the BGC[27,30,34].

Recent studies have shown the effect of different cultivation media or additives on the metabolomes of several myxobacterial strains[28,35,36]. Nevertheless, the knowledge of the effect of small molecule elicitors on the metabolome of myxobacteria is scarce with only

two reported studies on this topic[28,37]. Therefore, a set of ten small molecule elicitors was chosen for this study based on their hypothetical or reported potential to elicit an alteration in the metabolome of myxobacteria. In addition to the RNA-polymerase inhibitor rifampicin, which affected the metabolome of *Sorangium* sp. MSr11367[28], and the DNA-cross linker mitomycin C that induced production of xanthacin in *M. xanthus* fb[37], the quorum sensing molecules N-butyryl-homoserine lactone (4C-HSL) and 2-heptyl-4-quinolone (HHQ) were selected because different homoserine lactones and HHQ have different effects on *M. xanthus*[38,39] and *Cystobacter ferrugineus*[39]. Furthermore, the cholerae autoinducer 1 (CAI-1) was added, as several representatives of the *Myxococcaceae* clade seem to possess genes coding for CAI-1 synthase homologues as well as the respective CqsS receptor[40], pointing to a possible response of myxobacteria to this molecule. The kinase inhibitor staurosporin was chosen for its effect on the development on *M. xanthus*[41], the HDAC inhibitor Na butyrate for its effects on the metabolism of several actinomycetes[42] and the naturally occurring siderophore nocardamine because iron deprivation in *Streptomyces coelicolor* resulted in an increased production of the antibiotic actinorhodin[43,44]. In order to account for natural product elicitors with no specific effect on myxobacteria, the fungicide cycloheximide and cytostatic daunorubicin were added.

High-throughput screening campaigns to evaluate the effects of elicitors, other additives or media constituents on the metabolome of myxobacteria, however, are hampered by the need for cultivation space and material, as well as the time-consuming processing of all prepared cultures.

Inspired by the success of the high-throughput elicitor screening (HiTES) approach[15,16] and taking into account reports about screening events of myxobacteria in 24 deep-well plates[36,45], a higher throughput cultivation of myxobacteria in 24 deep-well plates was realised. This approach allowed the evaluation of the effect of ten elicitors in three concentrations in two 24 deep-well plates (organisation of screening plates are in the Supporting Information, Figure S 5.1) with subsequent extraction and UHPLC-*hr*MS based analysis of the resulting extracts. The resulting metabolome data were evaluated and visualised using Metaboscape 2022b, Microsoft Excel, Tableau and Rstudio in order to detect effects of the different elicitors on the metabolism of several myxobacterial strains. Based on observed differences of elicitor-perturbed cultivations compared to control cultivations and medium blanks and, in case of the model organism *M. xanthus* DK1622, observed changes in the production levels of reported secondary metabolites, several elicitors were chosen for further investigation in appropriate concentrations (Figure 5.1).

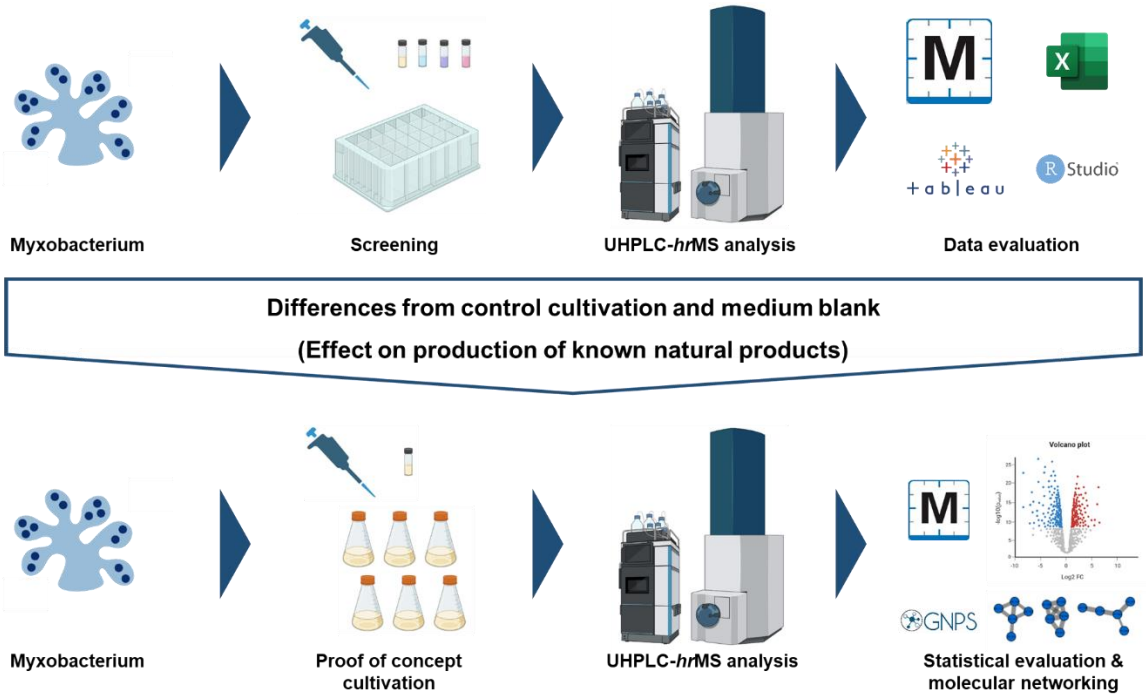

Figure 5.1: General workflow of the elicitor screening platform and the subsequent proof of concept cultivations to find upregulated secondary metabolites.

In order to verify and further study the effect of chosen elicitors on the metabolome of a chosen myxobacterium, the respective combinations were prepared in biological triplicates and technical duplicates and analysed by UHPLC-*hr*MS. Alterations in the metabolome were evaluated based on a comprehensive statistical analysis of UHPLC-*hr*MS data as well as feature-based molecular networking[46] of UHPLC-*hr*MS/MS data on the GNPS server[47] (Figure 5.1).

5.3.1 Evaluation and validation of a higher-throughput elicitor screening platform with *M. xanthus* DK1622

5.3.1.1 Elicitor screening in 24 deep-well plates with *M. xanthus* DK1622

Based on the comprehensive knowledge about the secondary metabolome of the model-strain *M. xanthus* DK1622[6], it was chosen to evaluate and potentially validate the higher-throughput elicitor screening workflow. Therefore, the effects of DMSO as vehicle control and of the ten different elicitors at different concentrations on the growth and secondary metabolome of *M. xanthus* DK1622 were investigated in the established CTT medium. In order to evaluate and compare the effects of the different elicitor and DMSO conditions on the metabolome of *M. xanthus* DK1622, the “feature difference value” of every

cultivation condition compared to the control cultivations and medium blanks was calculated based on the relative abundance of every LC-MS feature. For a better overview and comparability, these feature difference values were converted to relative feature difference values between 0 and 1 with 0 being the lowest and 1 the highest feature difference value observed. Furthermore, the relative production levels of known secondary metabolites of *M. xanthus* DK1622 compared to the control cultivations were used as a further indicator for assessing the effect of all elicitor and DMSO conditions on the myxobacterial metabolome.

Taking into account these readouts, as well as the appearance of the UHPLC-*hr*MS chromatograms of the crude extracts of different cultivation conditions and the medium blanks, the different elicitor conditions can be roughly divided into three groups (Figure 5.2 A). Group **1** (Figure 5.2 A and C) includes elicitor conditions with high relative feature difference values compared to the control cultivations and low relative feature difference values compared to the medium blanks. As displayed by the strongly reduced or omitted production of known secondary metabolites as well as the similarity of the UHPLC-*hr*MS chromatogram with the one of the medium blank (Figure 5.2 A), these elicitor conditions are toxic for *M. xanthus* DK1622 and reduce or inhibit its growth. This observation was made for more than two thirds of the chosen elicitors at a concentration of 50 µM as well as for the elicitors rifampicin and mitomycin C at a concentration of 5 µM (Figure 5.2 C).

In contrast to that, group **2** includes elicitor conditions with favourable characteristics. They display an average to high relative feature difference value compared to the control cultivations and an average to high relative feature difference value compared to the medium blanks (Figure 5.2 A and B). Within this group, the elicitor condition of 0.5 µM mitomycin C stood out by leading to improved production levels of (almost) all included known secondary metabolites produced by *M. xanthus* DK1622 (Figure 5.2 B). All other elicitor conditions within this group either displayed smaller effects on the production levels of known secondary metabolites, as exemplified by 0.5 µM sodium butyrate or (strongly) reduced the production of at least one class of secondary metabolites, as for instance 0.5 µM rifampicin or 5 µM staurosporin.

Finally, group **3** contains elicitor conditions that display low to moderate relative feature difference values compared to the control cultivations and give similar patterns to extracts of *M. xanthus* DK1622 cultivated with 0.01-1% DMSO as vehicle control (Figure 5.2 A and D). Many of these cultivation conditions entail low to moderate variations in the observed production levels of known secondary metabolites in *M. xanthus* DK1622, but without the obvious trends observed in the previous groups.

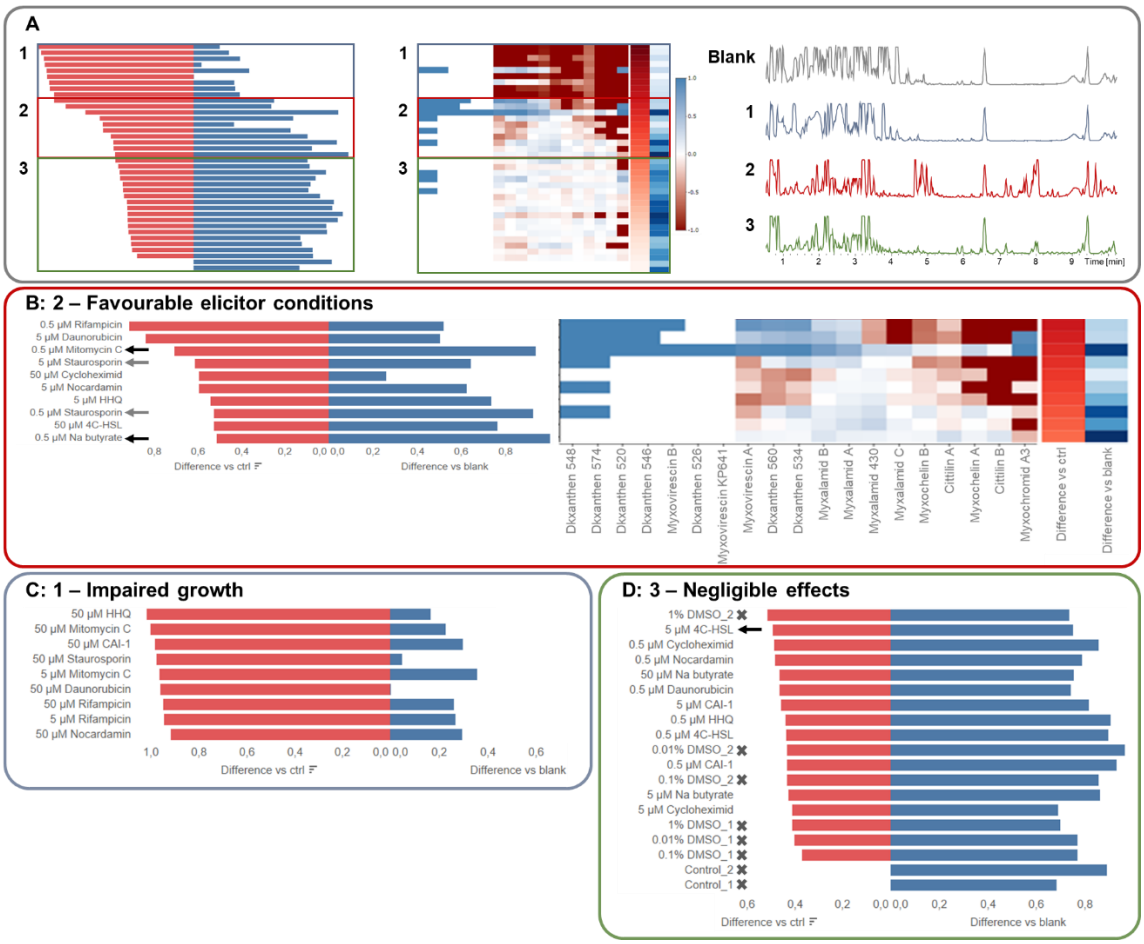

Figure 5.2: Grouping of elicitor conditions based on the effect on the (secondary) metabolome of *M. xanthus* DK1622. (**A**) Left: overview of the relative feature difference values compared to control cultivations and medium blanks. Middle: production of known secondary metabolites of *M. xanthus* DK1622 in the respective cultivation conditions. Elicitor conditions were divided into three groups. For a better understanding of the breakdown of the elicitor conditions into three groups, it was exemplarily visualised with Base Peak Chromatograms (BPCs) of a medium blank, an elicitor condition from groups 1, 2, and 3 on the right hand side. 1: Impaired growth; demonstrated by a high relative feature difference value compared to control cultivation, a low relative feature difference value compared to medium blanks and reduced to omitted production of known secondary metabolites. Those elicitor conditions are highlighted in panel (**C**). 2: Favourable elicitor conditions; demonstrated by an average to high relative feature difference value compared to control cultivation, a high relative feature difference value compared to medium blanks and (positive) effects on the production of known secondary metabolites. Those elicitor conditions and their effects on known secondary metabolites are highlighted in panel (**B**). 3: Negligible effects; demonstrated by lower relative feature difference values compared to control cultivation than the DMSO control, a high relative feature difference value compared to medium blanks and little effects on the production of known secondary metabolites. Those elicitor conditions are highlighted in panel (**D**). Colour coding: Bar plots: relative feature difference values compared to control cultivations (red, left) and to medium blanks (blue, right). Heatmaps: Production of secondary metabolite compared to control cultivation; decrease (red) and increase (blue). The intensities of the colours depend on the magnitude of the observed changes. Elicitor conditions that were chosen for proof of concept flask cultivations are marked an arrow, control and DMSO (vehicle control) cultivations are numbered based on the cultivation plate and marked with an x. Complete version of the bar plot and heatmap can be found in the Supporting Information (Figures S 5.2 and S 5.3).

In the applied set-up of the higher throughput cultivation approach, both screening plates contained a control cultivation of *M. xanthus* DK1622 as well as vehicle control cultivations with 0.01, 0.1 and 1% DMSO, respectively. As the 24 deep-well plate elicitor screening was performed in single cultivations, only these (vehicle) control cultivations were performed in duplicates and could therefore be used to assess the similarity and reproducibility of results and for observations within this cultivation setting. Displayed by the relative feature difference values compared to the medium blanks, the control cultivations of *M. xanthus* DK1622 in the two cultivation plates differed in their secondary metabolome (Figure 5.2 D). Furthermore, the relative feature difference values of the vehicle controls to the cultivation control in the respective cultivation plate showed different patterns. While the three vehicle control cultivations in the first cultivation plate displayed the lowest relative feature difference values compared to the control cultivation in this plate, the relative feature difference values of the vehicle controls of the second cultivation plate exceeded the ones of several elicitor conditions. Possible explanations for those observed differences might be variations in the (secondary) metabolome of *M. xanthus* DK1622 in this cultivation setting or could originate from flaws in the cultivation workflow, like an uneven distribution of bacterial cells in the cell-suspension that was used to fill the wells in the cultivation plate or inaccuracies during the manual filling of the wells. However, as the applied data evaluation workflow depends on concentration-based differences of every detected UHPLC-*hr*MS feature in a set of single cultivation datasets, it can only approximate the reproducibility of this cultivation approach. A more comprehensive evaluation can only be achieved by a cultivation with at least two biological replicates and a subsequent statistical evaluation of the bacterial metabolome.

5.3.1.2 Proof of concept cultivations in flasks with a number of elicitors in *M. xanthus* DK1622

Based on the results of the elicitor screening in the 24 deep-well cultivation setting, four elicitor conditions were selected for a proof of concept cultivation experiment in the standard shaking flask cultivation setting. In order to assess the predictability of the applied screening and evaluation workflow, those conditions were chosen due to different characteristics. From group **2** of favourable elicitor conditions, 0.5 µM mitomycin C was selected as it displayed improved production levels for most known secondary metabolites of *M. xanthus* DK1622, a medium concentration of 3 µM staurosporin as both 0.5 µM and 5 µM staurosporin showed effects in this, and 0.5 µM sodium butyrate as it displayed a very high relative feature difference value compared to the medium blank without having obvious effects on the known secondary metabolome of *M. xanthus*

DK1622 (Figure 5.2 B). Furthermore, 5 µM 4C-HSL was chosen as a representative of group **3**, hence an elicitor condition with a negligible effect on the secondary metabolome of *M. xanthus* DK1622 (Figure 5.2 D).

For a comprehensive evaluation of the effects of those four elicitor conditions on the metabolome of *M. xanthus* DK1622, they were cultivated and analysed alongside an untreated cultivation control and a vehicle control of 0.1% DMSO, corresponding to the highest amount of DMSO added in the tested elicitor conditions.

In order to assess the impact of the four chosen elicitors on the secondary metabolome of *M. xanthus* DK1622, their effect on the reported natural product families of cittilins, DKxanthes, myxalamids, myxochelins, myxochromids, and myxovirescins[6,48] was evaluated and visualised for the derivative with the highest observed production titre, respectively (Figure 5.3). Similar to the observations in the initial elicitor screening in the 24 deep-well plates (Figure 5.2 and Figure S 5.3), the production levels of the observed known metabolites in *M. xanthus* DK1622 were not strongly altered by the addition of Na butyrate and 4C-HSL. In contrast to that, addition of staurosporin and mitomycin C strongly affected the production levels of five out of six observed metabolites, respectively. Both elicitors reduced the detected amounts of cittilin A but improved the production of DKxanthen-534 and myxalamid A. Furthermore, addition of staurosporin to cultures of *M. xanthus* DK1622 resulted in a strongly increased production of myxochelin B, but reduced the production of myxovirescin A by approximately half. Finally, cultures of *M. xanthus* DK1622, supplemented with mitomycin C exhibited a strongly increased production of myxochromid A3. In all described natural product families, the changes in production levels of the main derivative were similarily observed for the other congeners.

As the biosynthetic potential of *M. xanthus* DK1622 is not restricted to those six natural products, the effect of the different additives on its (secondary) metabolome was investigated by statistical evaluation. Based on the t-test routine in Metaboscape 2022b, the number of (at least two fold) down-and upregulated, lost and additional UHPLC-*hr*MS features in every cultivation condition compared to the control cultivations was calculated (Figure 5.4). Furthermore, these data were used to determine the number of features that are only present in one condition and therefore unique to this cultivation condition.

Considering those calculations, the elicitors Na butyrate and 4C-HSL displayed similar or even inferior results compared to cultivations with the vehicle control, regarding the number of upregulated, new or unique features. Nevertheless, their impact on the metabolism of *M. xanthus* DK1622 was demonstrated by higher numbers of downregulated or lost features, in particular for cultivations with 4C-HSL (Figure 5.4).

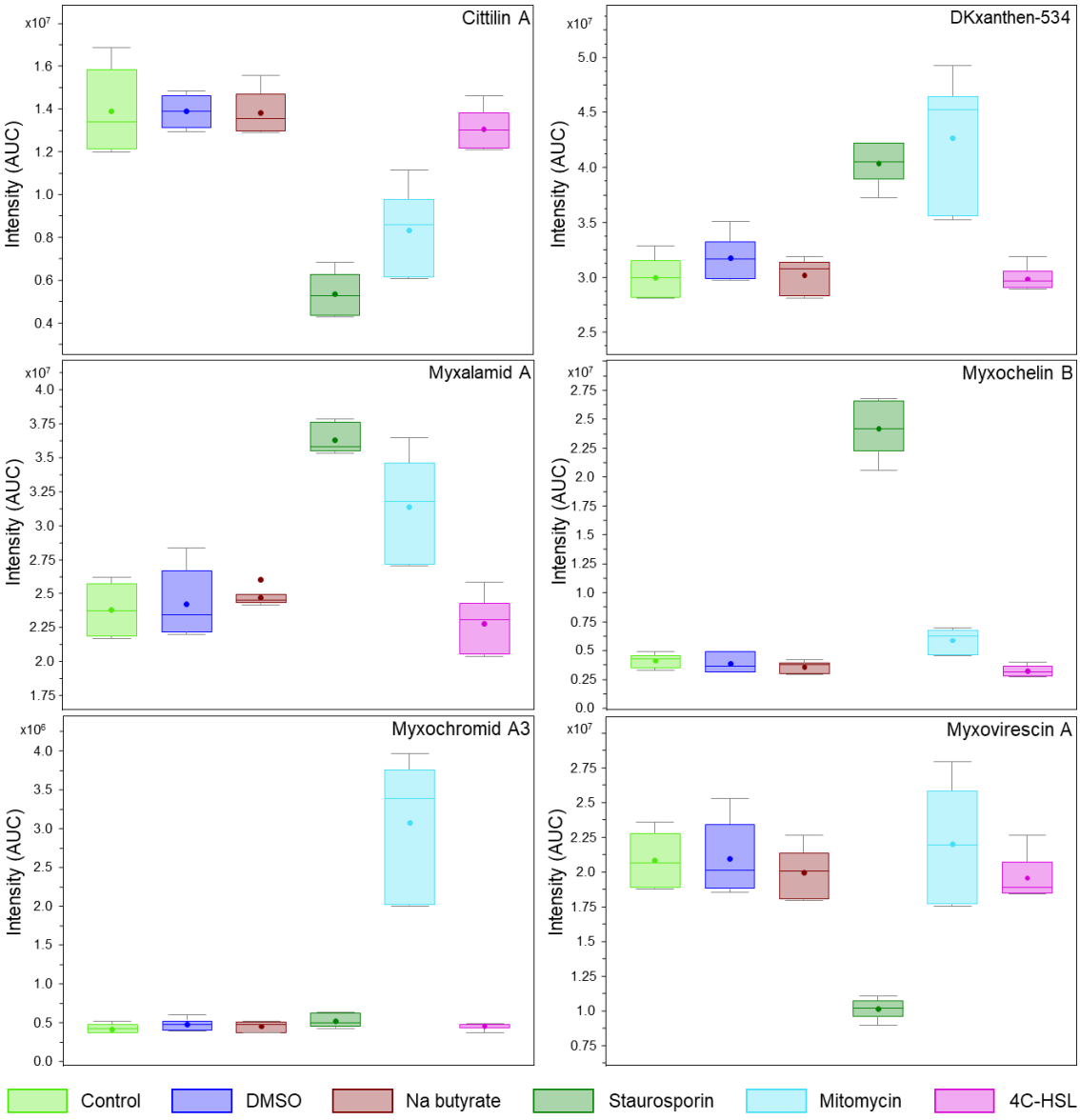

Figure 5.3: Influence of elicitors on relative production of selected natural products in *M. xanthus* DK1622.

As expected from their strong impact on more than one family of secondary metabolites, mitomycin C and staurosporin displayed a much greater effect on the metabolome of *M. xanthus* DK1622. Interestingly, both elicitors led to more upregulated features than downregulated features and the number of new features was at least twice as high as the number of lost features, compared to the control cultivation (Figure 5.4). Considering the outstanding effects of mitomycin C in the initial elicitor screening, it is noteworthy that staurosporin led to the upregulation and emergence of three to four fold more features compared to this elicitor. This trend is even more obvious for the number of unique features for a cultivation conditions, as the 552 unique features found in extracts of *M. xanthus* DK1622 with staurosporin is roughly ten times as high as the 56 features that can be exclusively found upon cultivation with mitomycin C.

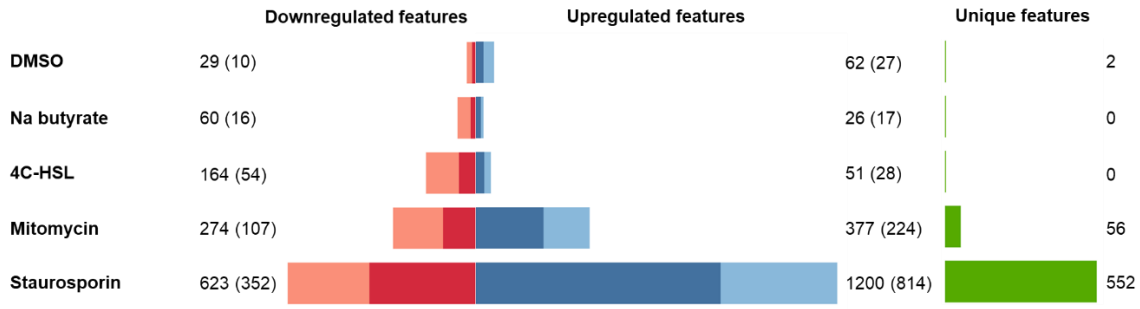

Figure 5.4: Production and regulation of features in cultivations of *M. xanthus* DK1622 with added DMSO and added elicitors in comparison to control cultivations. Total number of up- or downregulated features are indicated for each cultivation condition, the newly observed or lost features compared to the control cultivations are indicated in brackets, and in dark red or dark blue, respectively. Unique features are only observed in the respective cultivation condition.

Since the purification of any novel natural product hinges on its reliable production, the reproducibility of every detected feature was determined based on a statistical analysis of the biological triplicates and technical duplicates for all six investigated cultivation conditions.

In accordance with their relatively low variation regarding abundance and occurrence of features, untreated cultures of *M. xanthus* DK1622 and cultures with added DMSO and Na butyrate, displayed similar reproducibility patterns, as more than three quarters of the detected features could be found in all replicates. Furthermore, cultivations with staurosporin as elicitor yielded in a comparably high reproducibility (Figure 5.5). However, in cultivations with added 4C-HSL and mitomycin C, the reproducibility was reduced compared to the other cultivation settings with less than two thirds of all detected features being detected in all replicates, respectively. Considering the biological activity of mitomycin C as DNA cross-linker, the lower reproducibility might originate from an increased mutation rate in *M. xanthus* DK1622 upon treatment with this elicitor. Nevertheless, this explanation cannot be extrapolated to explain the lower reproducibility of cultivations with the quorum sensing molecule 4C-HSL. Altogether, the reason for the lower reproducibility between cultivations of *M. xanthus* DK1622 with added 4C-HSL and mitomycin C remains elusive.

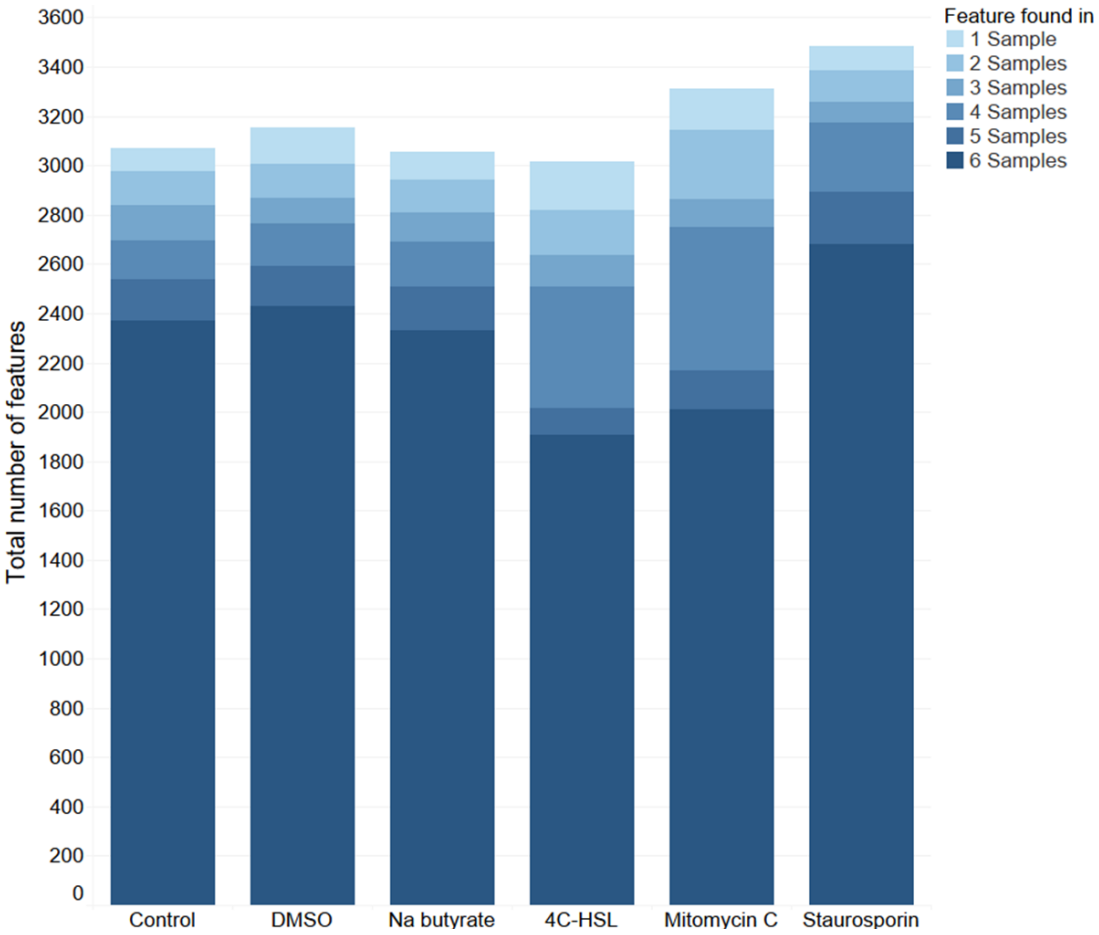

Figure 5.5: Feature reproducibility of cultivations of *M. xanthus* DK1622: control cultivations, with added DMSO and added elicitors. Occurrence of features in three biological and two technical replicates for each cultivation condition.

Although the comprehensive statistical evaluation of different cultivation conditions provides a depth of information on the capabilities of the tested elicitors to regulate the production of bacterial metabolites in a reproducible manner, it cannot provide any information on the origin of these metabolites or a possible connection with other metabolites. In order to evaluate possible relationships of novel features in cultivations of *M. xanthus* DK1622 with elicitors, UHPLC-*hr*-tandem MS data of all cultivation conditions as well as the medium blank was acquired and processed with Metaboscape 2022b. The resulting output files were used for feature-based molecular networking[46] on the GNPS-server[47]. After manual blank-removal and the removal of all singletons, the (secondary) metabolome of *M. xanthus* DK1622 was visualised in 203 nodes that are organised in 31 networks (Figure 5.6). While seven networks were identified as known metabolites from *M. xanthus* DK1622, the chemical scaffolds of the remaining 24 networks remain elusive.

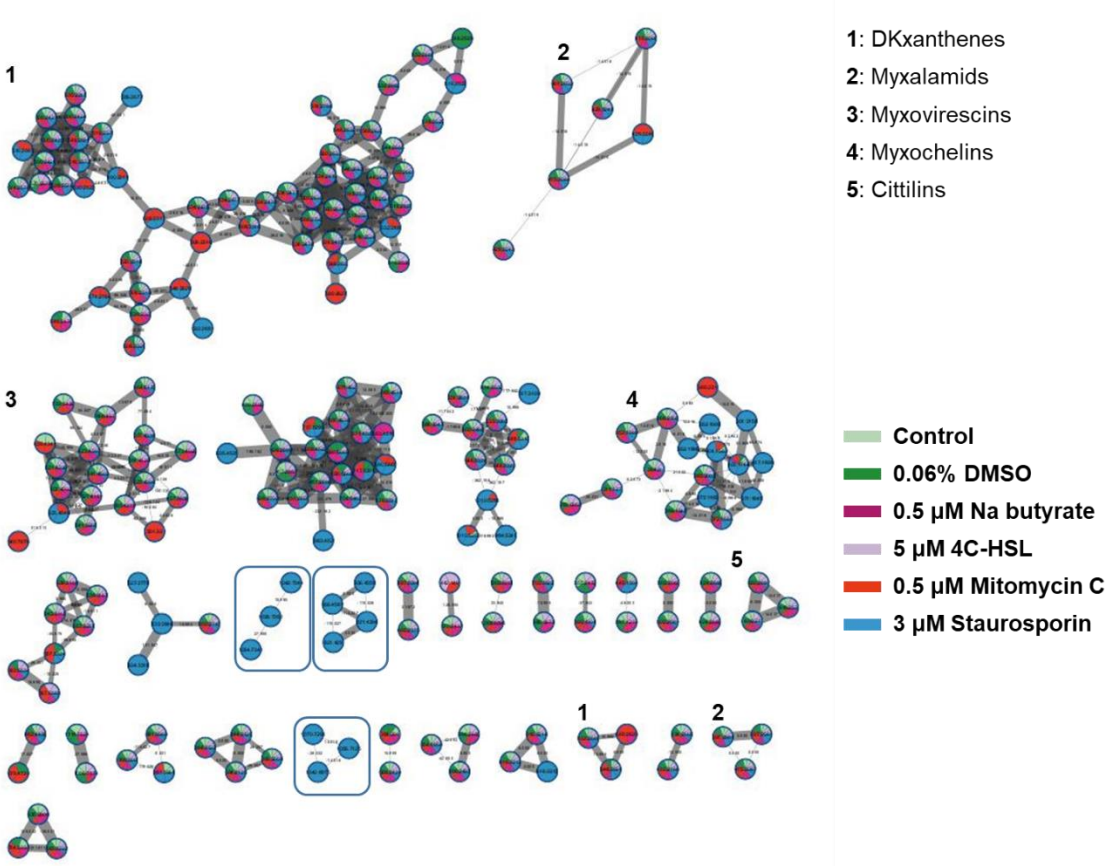

Figure 5.6: Feature-based molecular networks of the *M. xanthus* DK1622 metabolome with different elicitors, constructed with GNPS. Networks harbouring reported secondary metabolites are marked with numbers corresponding to the respective natural product families. Networks that are exclusively found in cultivations with added elicitors are highlighted with a frame. Network nodes are colour-coded in one colour or as pie-charts, based on their occurrence in one or more cultivation conditions. The thickness of the edges depend on the cosine score, which represents how closely related two congeners are. Singletons and molecular clusters that contained more than 20% medium blank were removed.

In agreement with the observed effects of mitomycin C and staurosporin on the production levels of selected derivatives (Figure 5.3), the molecular networks of myxalamids (**2**) and DKxanthens (**1**) harbour one or several features that are only present in cultivations with one or either elicitor (Figure 5.6). Furthermore, the molecular network of myxochelins (**4**) consists of several features that were only observed in cultivations with staurosporin. While the majority of molecular networks consisted of at least one feature that was produced in untreated or vehicle control cultivations, three molecular networks were only produced upon addition of staurosporin, highlighting the observed effects of this elicitor on the (secondary) metabolism of *M. xanthus* DK1622.

The results of the proof of concept flask cultivation of *M. xanthus* DK1622 with several chosen elicitor conditions demonstrate the ability of several small molecules to alter the myxobacterial metabolome and lead to the production of potentially unknown natural products. However, it also displays the limited predictability of the current elicitor

screening platform for promising elicitor conditions. Addition of 0.5 µM mitomycin C was one of the best elicitor conditions during the elicitor screening and displayed its capability to alter the metabolome of *M. xanthus* DK1622 in the flask cultivations. In contrast to that, staurosporin did not perform as well during the initial screening, but displayed even greater potential to modify the metabolome of *M. xanthus* DK1622. Finally, addition of 0.5 µM Na butyrate seemed to be a promising elicitor condition based on the high relative feature difference value compared to the medium blanks. However, in flask cultivations, its impact on the bacterial metabolism was comparable to the one of the vehicle control DMSO.

5.3.2 Further screening campaigns with the higher throughput elicitor screening platform

In order to further investigate the applicability of the described higher throughput elicitor screening platform for myxobacteria, further screening campaigns were performed in the 24 deep-well cultivation setting. These campaigns included a second round of elicitor screening in *M. xanthus* DK1622 in another cultivation medium, to explore the impact of the cultivation medium on the results of the tested elicitors. Furthermore, the elicitor screening was done with the strains *Cystobacter* sp. MCy12796 and MCy12977, *Sorangium* sp. NOSO3 and sp. MSr12523 and *Nannocystis exedens* Na e487, representing the three myxobacterial suborders *Cystobacterineae*, *Sorangiineae* and *Nannocystineae*, respectively. Those strains were selected based on their phylogenetically distinct positions and due to their high number of BGCs, which have not been linked to a secondary metabolite (data not shown).

5.3.2.1 Elicitor screening with *M. xanthus* DK1622, cultivated in a different medium

The choice of cultivation medium can greatly influence the (secondary) metabolism of myxobacteria[28,35,36]. Therefore, the elicitor screening in *M. xanthus* DK1622 was done in the 2SWT cultivation medium to find out, if the strains' response to the elicitor treatment is altered by the change of cultivation medium. The cultivation and subsequent data evaluation was performed analogously to the elicitor screening in *M. xanthus* DK1622 in CTT medium (Figure 5.7). Interestingly, cultivation of *M. xanthus* DK1622 in 2SWT medium increased the number of known and automatically annotated metabolites to 25, compared to 19 automatically annotated natural products in CTT medium.

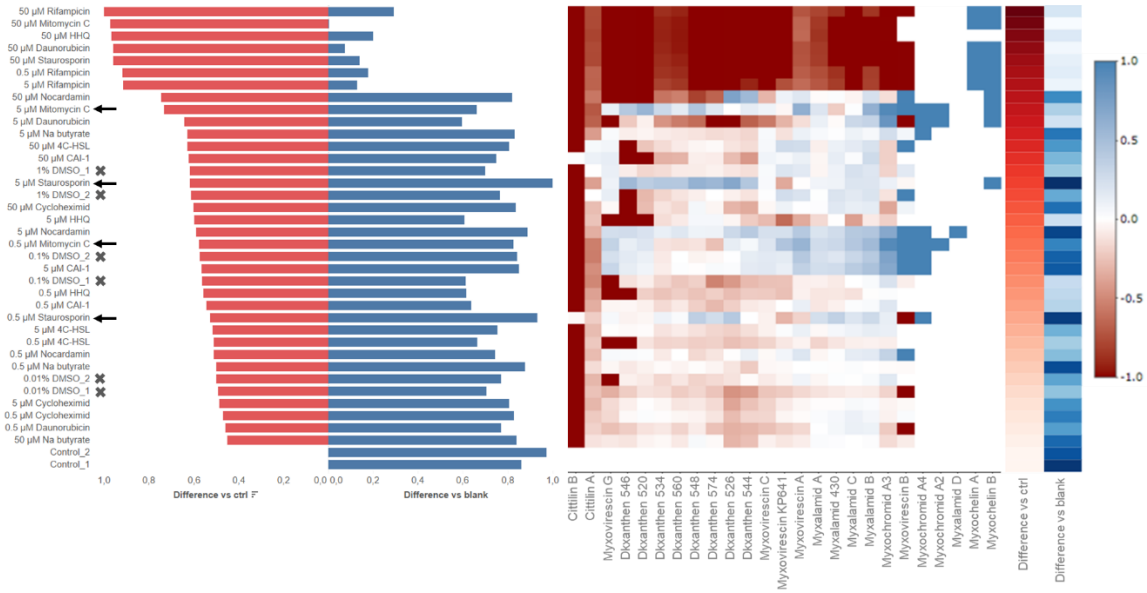

Figure 5.7: Impact of elicitors on the (secondary) metabolome of *M. xanthus* DK1622 in 2SWT medium. Left: Effects on the relative feature difference values compared to cultivation control and medium blanks. Right: impact on relative production levels of reported secondary metabolites of *M. xanthus* DK1622. Colour coding: Bar plots: relative feature difference values compared to control cultivations (red, left) and to medium blanks (blue, right). Heatmaps: Production of secondary metabolite compared to control cultivation; decrease (red) and increase (blue). The intensities of the colours depend on the magnitude of the observed changes. Elicitors with strong effect on the metabolome of *M. xanthus* DK1622 in CTT in the proof of concept flask cultivations in relevant concentrations are indicated with an arrow, vehicle control (DMSO) cultivations are marked with an x. (The bar plot and heatmap can be found in a larger scale in the supporting information as figures S 5.9 and S 5.10.)

Similar to the observations in the elicitor screening in CTT medium, a number of elicitor conditions reduced or inhibited growth of M. xanthus DK1622 in 2SWT medium, evidenced by high relative feature difference values compared to the cultivation control, low relative feature difference values compared to the medium blanks and strongly reduced or omitted production of (most) known metabolites. However, the change of medium seemed to alter the sensitivity of *M. xanthus* DK1622 to certain elicitors, displayed by an increased toxic effect of rifampicin or a better tolerability of high concentrations of nocardamin or CAI-1 in 2SWT medium compared to CTT medium (Figure 5.7).

Moreover, this trend can also be observed for mitomycin C and staurosporin, displaying a strong effect on the metabolome of *M. xanthus* DK1622 in CTT medium in both observed cultivation settings. Both elicitors exhibited a positive effect on the production levels of most known metabolites in 2SWT medium. While addition of staurosporin had this effect at concentrations of 0.5 and 5 µM in both media, mitomycin C was tolerated by *M. xanthus* DK1622 up to 5 µM in 2 SWT medium in contrast to only 0.5 µM in CTT medium (Figure 5.7).

Furthermore, the addition of 5 µM nocardamin, 5 µM CAI-1 and surprisingly also 0.1% DMSO on cultivation plate 2 resulted in increased production levels of several known compounds compared to the cultivation controls on the respective plates (Figure 5.5). Partly comparable with the observations in CTT medium, the vehicle control cultivations displayed a greater relative feature difference value compared to the respective control cultivations than several elicitor conditions. However, in contrast to the previous results, the relative feature difference values of the vehicle control cultivations compared to the respective control cultivations align with the added concentrations of 0.01, 0.1, and 1% DMSO. Furthermore, during the elicitor screening in 2SWT medium, the equivalent vehicle controls in both plates display similar relative feature difference values compared to the cultivation controls in their respective plates (Figure 5.7).

Taken together, the results of the elicitor screening campaigns with *M. xanthus* DK1622 in two different media point towards a medium-independent reaction of the strain towards the elicitor. However, depending on elicitor and medium, the effect might occur at a different concentration of the respective elicitor.

5.3.2.2 Elicitor screening with further strains of the *Cystobacterineae* suborder

In order to probe the applicability of the elicitor screening platform for further myxobacteria, it was first tested with further strains of the *Cystobacterineae* suborder. Therefore, elicitor screening campaigns were performed with the two strains *Cystobacter* MCy12796 and MCy12977.

As the secondary metabolomes of the tested strains are much less studied than the one of *M. xanthus* DK1622, evaluation of elicitor conditions could only be performed with the relative feature difference values compared to the cultivation controls and medium blanks. Similar to the observations of screening campaigns with *M. xanthus* DK1622 (Figures 5.2 and 5.7), potentially toxic elicitor conditions for *Cystobacter* MCy12796 and MCy12977 could be distinguished from other elicitor conditions by their high relative feature difference values compared to the cultivation controls and the low relative feature difference values compared to medium blanks (Figure 5.8). These toxic conditions included several elicitors at concentrations of 50 µM as well as rifampicin and mitomycin C at 5 µM for MCy12796 (Figure S 5.11) and rifampicin in all tested concentrations for MCy12977 (Figure S 5.12).

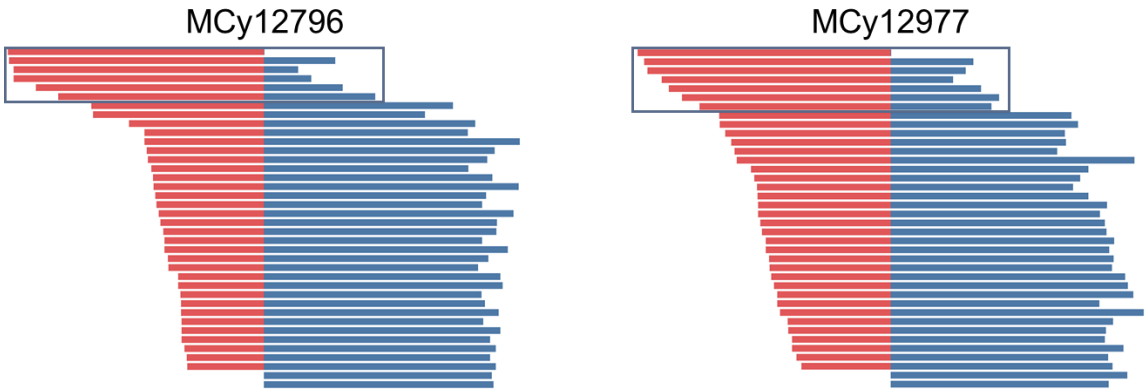

Figure 5.8: Impact of different elicitor conditions on the growth and metabolome of the *Cystobacterineae* MCy12796 and MCy12977. Potentially toxic conditions for MCy12796 and MCy12977 are highlighted with boxes. The complete bar plots for MCy12796 (Figure S 5.11) and MCy12977 (Figure S 5.12) can be found in the supporting information. Colour coding: relative feature difference values compared to control cultivations (red, left) and to medium blanks (blue, right).

Application of the elicitor screening platform to other representatives of the suborder *Cystobacterineae* was successful, as the patterns in the metabolome of both strains were similar to the ones observed in *M. xanthus* DK1622. Potentially toxic elicitor conditions were distinguished by a clear cut-off in the relative feature difference values compared to the medium blanks. Furthermore, the toxic conditions were similar to previous observations, with several elicitors being toxic at 50 µM and one or two elicitors being toxic at lower concentrations. However, considering the limited predictability of the current data evaluation workflow on the ability of an elicitor to modify the metabolome of the respective bacterium, no elicitor condition was chosen for subsequent proof of concept flask cultivations.

5.3.2.3 **Elicitor screening with strains of the other suborders**

Since the initial elicitor screening platform could be successfully adopted for further *Cystobacterineae* strains, its applicability for the suborders of *Sorangiineae* and *Nannocystineae* was tested with the *Sorangium* strains NOSO3 and MSr12523, and *Nannocystis exedens* Na e487.

Following the limited knowledge on the secondary metabolomes of the investigated strains, the impact of the different elicitor conditions was evaluated only based on the relative feature difference values of those conditions compared to cultivation controls and medium blanks. The effect of the elicitor conditions on the tested *Sorangiineae* strains resulted in different patterns depending on the strain (Figure 5.9 A). Similar to the observations for the tested *Cystobacterineae* strains (Figures 5.2, 5.7 and 5.8), putatively toxic elicitor conditions against NOSO3 were distinguished from other elicitor conditions

by their high relative feature difference values compared to the cultivation controls and the low relative feature difference values compared to medium blanks (Figure 5.9 A). In accordance with previous observations addition of several elicitors at a concentration of 50 µM, as well as the antibiotic rifampicin at 5 µM inhibited the growth of NOSO3 (Figure S 5.15). In case of the other *Sorangiineae* strain MSr12532, no clear threshold for the relative feature difference values compared to medium blanks was observed, which served as an indicator for the inhibition of bacterial growth in elicitor screening campaigns with other myxobacteria (Figures 5.9 A and S 5.13). One possible explanation is a high tolerance of MSr12523 against those molecules, which is supported by the observed tolerance of this strain against a wide range of antibiotics (Chapter 3). However, a comparison of UHPLC-*hr*MS chromatograms of MSr12523 cultivated in the 24 deep-well plate and a standard shaking flask, display a much lower number of detectable metabolites in the plate setting (Figure S 5.14). Therefore, the detected relative feature difference values between the different elicitor screening conditions compared to the medium blanks might be too small to detect clear trends.

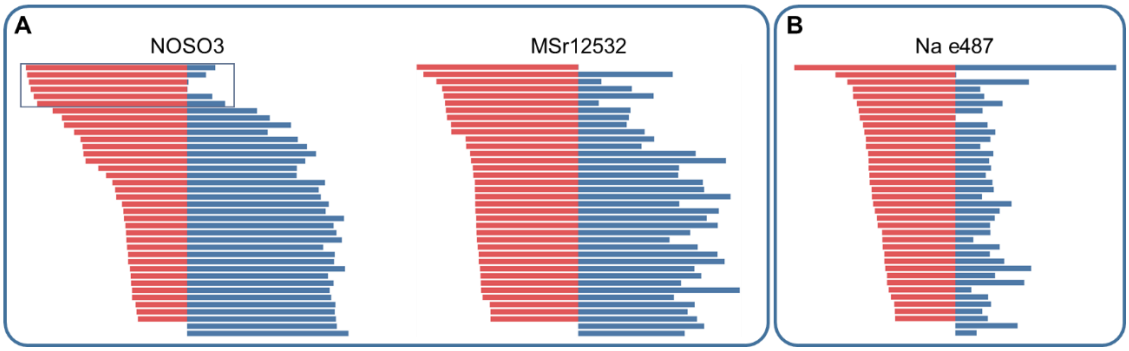

Figure 5.9: Impact of different elicitor conditions on the growth of chosen *Sorangiineae* (A) and *Nannocystineae* (B) strains. Potentially toxic conditions for NOSO3 are highlighted with a box. The complete bar plots for NOSO3 (Figure S 5.15), MSr12523 (Figure S 5.13), and Na e487 (Figure S 5.20) can be found in the supporting information. Colour coding: relative feature difference values compared to control cultivations (red, left) and to medium blanks (blue, right).

Evaluation of the effect of different elicitor conditions on the metabolome of *Nannocystis exedens* Na e487 was impossible with the current elicitor screening and data evaluation workflow. The observed variations in the relative feature difference values of the elicitor conditions compared to the cultivation controls and medium blanks could not be associated with high elicitor concentrations or elicitors that displayed toxic effects against other tested strains (Figure S 5.20). Unlike the findings for MSr12523, cultivation of Na e487 in the 24 deep-well setting did not have obvious negative effects on its metabolome. However, the concentrations of detected metabolites varied greatly between cultivations

(Figure S 5.21). This variation might be the result of the clump-like growth of Na e487, leading to high differences in the number of cells in the different wells during inoculation.

5.3.2.4 Proof of concept flask cultivations with strains of other suborders

In order to investigate the ability of elicitors to alter the metabolome of myxobacteria of all suborders, *Sorangium* sp. NOSO3 and *Nannocystis exedens* Na e487 were chosen for proof of concept cultivations in shaking flasks. Based on the weakness of the applied elicitor screening and data evaluation process to predict the most fruitful elicitor conditions, both strains were cultivated with one of the two elicitors displaying the most promising effect on the metabolome of *M. xanthus* DK1622, and an arbitrarily chosen elicitor condition, respectively.

Therefore, the effects of 5 µM mitomycin C and 50 µM cycloheximide on the metabolome of NOSO3 were studied compared to an untreated cultivation control and a vehicle control with 0.1% DMSO. Furthermore, the impact of 0.5 µM Na butyrate and 5 µM staurosporin on the metabolome of Na e487 were tested in a similar manner.

As the metabolome of NOSO3 did not contain any reported natural products and the only known secondary metabolites produced by Na e487 were siderophores, the effects of the tested elicitors were assessed based on a statistical evaluation of treated and untreated cultures of the respective organisms.

Cultivation of NOSO3 with 50 µM cycloheximide led to the occurrence of 75 new features compared to the control cultivation, whereas the majority of these features was only detected in this cultivation setting (Figure 5.10 A). However, based on the statistical evaluation, its effects on the upregulation, downregulation, and loss of features compared to the cultivation control were comparable with the ones of 0.1% DMSO. However, addition of 5 µM mitomycin C elicited significant changes in the metabolome of NOSO3 (Figure 5.10 A). Similar to the observations with *M. xanthus* DK1622, the number of newly detected metabolites was almost twice as high as the number of lost metabolites compared to the cultivation control. Furthermore, over 500 of these new features were only detected in cultivations with mitomycin C, emphasising the capability of this elicitor to enable the detection of potentially new chemistry. Consequently, the GNPS-built feature-based molecular networks[46,47] of all cultivation conditions with NOSO3 emphasised these findings, as most of the molecular networks displayed at least one feature that was only detected in cultivations with mitomycin C, whereas two molecular networks were only found in this cultivation condition (Figure 5.10 B).

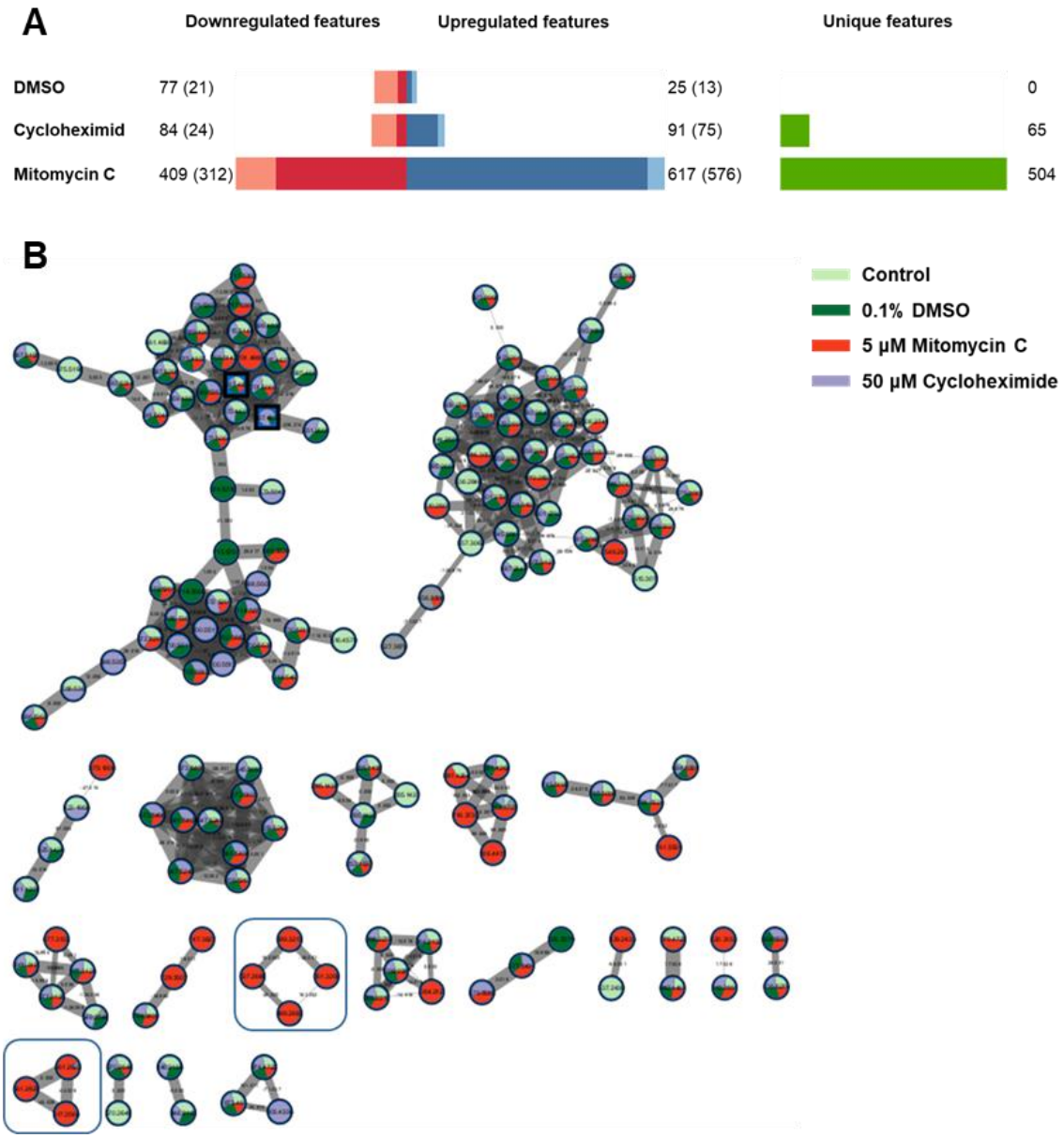

Figure 5.10: Impact of chosen elicitor conditions on the regulation and production of (secondary) metabolites of *Sorangium* sp. NOSO3. (**A**) Production and regulation of features in cultivations with added DMSO and added elicitors in comparison to control cultivations. Total number of up- or downregulated features are indicated for each cultivation condition, the newly observed or lost features compared to the control cultivations are indicated in brackets and in dark red and dark blue, respectively. Unique features are only observed in the respective cultivation condition. (**B**) Feature-based molecular networks of the NOSO3 metabolome with different elicitors, constructed with GNPS. Networks that are (almost) exclusively found in cultivations with added elicitors are highlighted with a frame. Network nodes are colour-coded in one colour or as pie-charts, based on their occurrence in one or more cultivation conditions. The thickness of the edges depend on the cosine score, which represents how closely related two congeners are. Singletons and molecular clusters that contained more than 20% medium blank were removed.

In line with the observations made for mitomycin C on the metabolome of NOSO3, addition of the “established” elicitor staurosporin greatly affected the metabolism of *Nannocystis exedens* Na e487 (Figure 5.11 A). Cultivation of Na e487 with 5 µM staurosporin led to the detection of 543 features that were not observed in the untreated cultivation control. Furthermore, 522 of these features were unique to this cultivation condition. However, this cultivation condition also had negative effects on parts of the metabolism of Na e487, as evidenced by the loss of 420 features compared to the detected metabolome of the untreated strain. Addition of 0.5 µM Na butyrate (in an aqueous solution) on the other hand displayed only minor changes on the metabolome of Na e487, the numbers of altered metabolites were even lower than the ones of the vehicle control cultivations (Figure 5.11 A).

GNPS-built feature-based molecular networking[46,47] of all cultivation conditions displayed the effects of staurosporin on the metabolome of Na e487 (Figure 5.11 B). The vanished production of (secondary) metabolites was more obvious here than for any other strain-elicitor combination, as several molecular networks did contain only few or no nodes found under these cultivation condition. On the other hand, the capability of staurosporin to elicit the production of potentially novel metabolites in Na e487 was highlighted as five molecular networks were mostly exclusive to these cultivations.

The cultivations of *Sorangium* sp. NOSO3 and *Nannocystis exedens* Na e487 with mitomycin C and staurosporin displayed the potential of these elicitors to alter the metabolomes of the respective strains. In both cases, the newly detected molecular networks under elicitor treatment could be evaluated whether they are promising targets for further studies and purification. Furthermore, the regulation of other unstudied molecular networks should be investigated under elicitor treatment, as an increased production may enable the purification of an otherwise inaccessible metabolite family. The high reproducibilities of all cultivation conditions of both strains (Figures S 5.19 and S 5.25) raise the possibility that metabolites of interest could be successfully purified.

Altogether, these results demonstrated convincing transferability of promising elicitors from one myxobacterial strain to representatives of other suborders. However, considering the limited number of elicitors and strains evaluated so far, more data should be gathered to validate the transferability of elicitor screening results between different strains or even suborders. As the investigation of the capability of chemical elicitors to increase or enable the production of novel chemical scaffolds is still in its infancy, it still awaits the isolation of a new scaffold as conclusive proof of concept.

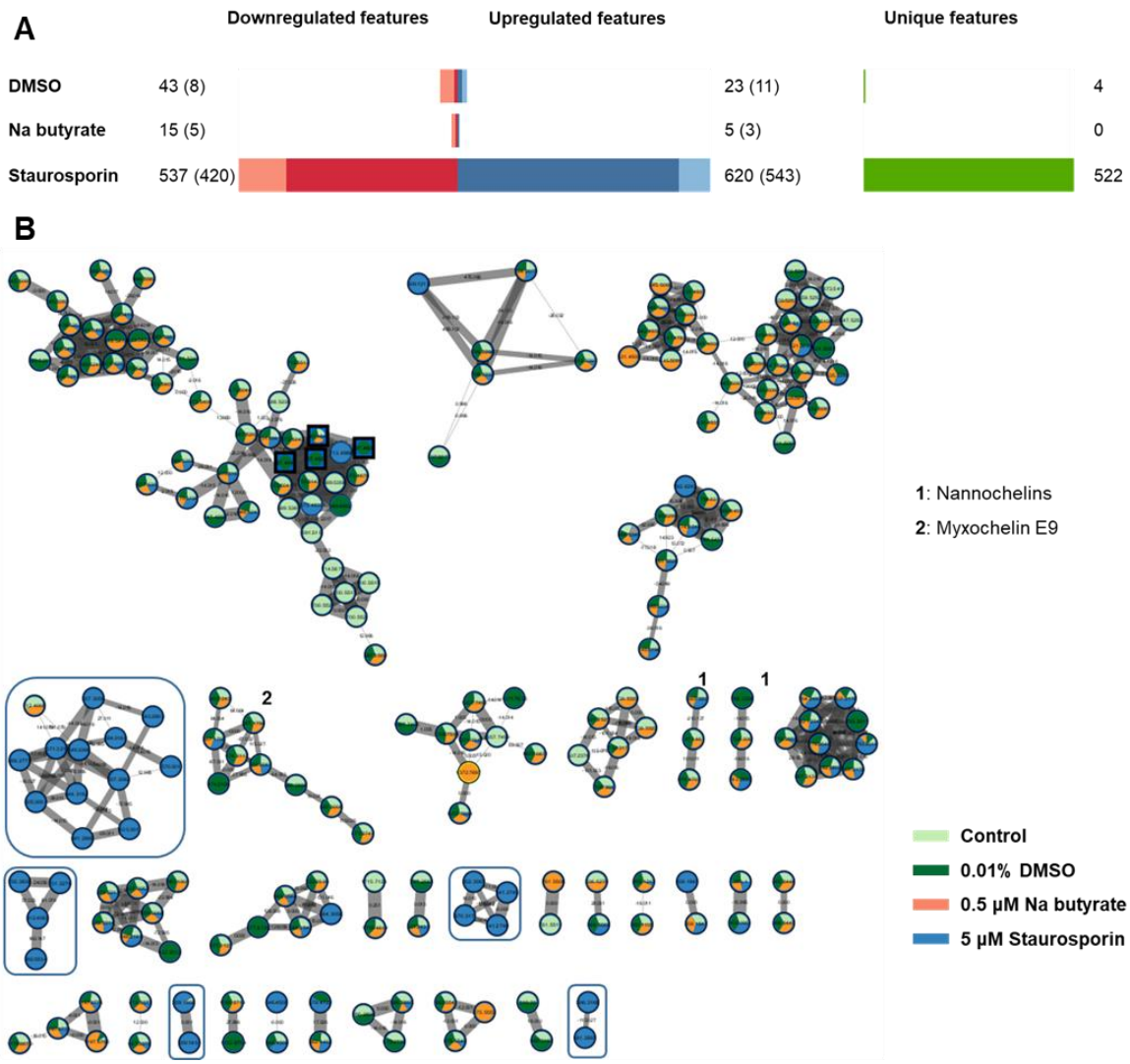

Figure 5.11: Impact of chosen elicitor conditions on the regulation and production of (secondary) metabolites of *Nannocystis exedens* Na e487. (**A**) Production and regulation of features in cultivations with added DMSO and added elicitors in comparison to control cultivations. Total number of up- or downregulated features are indicated for each cultivation condition, the newly observed or lost features compared to the control cultivations are indicated in brackets and in dark red and dark blue, respectively. Unique features are only observed in the respective cultivation condition. (**B**) Feature-based molecular networks, constructed with GNPS, of the NOSO3 metabolome with different elicitors. Networks harbouring reported secondary metabolites are marked with numbers corresponding to the respective natural product families. Networks that are (almost) exclusively found in cultivations with added elicitors are highlighted with a frame. Network nodes are colour-coded in one colour or as pie-charts, based on their occurrence in one or more cultivation conditions. The thickness of the edges depend on the cosine score, which represents how closely related two congeners are. Singletons and molecular clusters that contained more than 20% medium blank were removed.

5.3.3 Lessons learned from pilot study and future workflow for elicitor screening

The higher throughput elicitor screening platform and data evaluation method used in this study led to the identification of two promising elicitor conditions in *M. xanthus* DK1622. However, the ability to predict the possible effects of elicitors in follow-up flask cultivations was impaired. This can be associated with flaws in the workflow as well as in the design of the experiment and in the subsequent data evaluation.

First, the manual dispersion of bacterial cultures into the wells of the 24 deep-well plates could lead to variations in the amount of cells and cultivation volume between wells, which could generate variations in production levels of (secondary) metabolites and therefore reduce their significance of detection. Application of an (automated) microplate dispending system could be helpful to ensure an even distribution of cells in the single wells, as demonstrated for a variety of strains in elicitor screening campaigns[16,20,21].

Second, the current screening platform relies on the results of just one biological replicate per tested condition and therefore gives no information about the reproducibility of any observed modification of a strains metabolome. Furthermore, evaluation of the recorded data is restricted to comparing production levels of identified secondary metabolites as done for *M. xanthus* DK1622, to estimating the differences compared to cultivation controls and medium blanks, and to observing obvious changes in UHPLC-*hr*MS chromatograms. Performing the initial elicitor screening in at least two biological replicates could help to identify elicitors with reproducible effects on the (secondary) metabolome and enable a more comprehensive statistical evaluation of the recorded data.

Third, the current data evaluation workflow was useful to detect potentially toxic elicitor conditions, but struggled to reliably display the capability of an elicitor condition to modify the (secondary) metabolome of the tested organism. Application of a comprehensive statistical evaluation of up- and downregulated features as well as newly detected or lost features compared to control cultivations will be a more precise method to evaluate the effect of elicitor conditions on the metabolism of a test strain, as demonstrated in the proof of concept flask cultivations in this study.

Furthermore, the number of different concentrations could be reduced to one to enable a higher throughput. A screening concentration of 50 µM seems to be too high, as many elicitors displayed toxic effects on the test strains in this concentration. In addition to that, screening at just one elicitor concentration may be sufficient, as many elicitors displayed similar trends for screening events with 0.5 µM and 5 µM.

Taking those considerations into account, the following adjustments for improving the higher throughput elicitor screening platform should be made:

1. Ensuring a more equal distribution of cells and medium in every well.
2. Perform screening in at least two biological replicates to assess the reproducibility of any given elicitor condition, and to enable a comprehensive statistical evaluation of the impact of elicitor conditions on the metabolome of a test strain.
3. Perform elicitor screening at one concentration for all elicitors to enable a higher throughput of elicitors. Following the observations made with the current platform, a screening concentration of 3 µM seems promising.
4. The capability of an elicitor to modify the metabolome of the test strain should be assessed based on a comprehensive statistical evaluation and comparison of metabolomics data of the test strain cultivated with and without elicitor treatment.

5.4 **Conclusion**

The results of this study contribute a new chapter among the approaches to unlock the cryptic biosynthetic potential in myxobacteria, alongside the variation of cultivation media, co-cultivation with other microorganisms, cultivation with different additives and further OSMAC-style variations of cultivation conditions[28,35,36,49]. The application of the higher throughput elicitor screening platform led to the identification and subsequent validation of two promising elicitors and displayed the applicability of a 24 deep-well cultivation approach for a number of myxobacteria from all suborders. The promising elicitors in the present study, mitomycin C and staurosporin, have previously demonstrated their ability to enable the production of a bacteriocin[37] and alter the development[41] in *M. xanthus* strains, respectively.

During proof of concept flask cultivations with three different test strains spanning all three myxobacterial suborders, the elicitors mitomycin C and staurosporin displayed their ability to modify the (secondary) metabolome, resulting in the observation of potentially novel natural product families that await further investigation.

Taken together, this study highlights the capability of small molecule elicitors to alter the metabolome of several myxobacterial test strains in 24 deep-well plate and shaking flask cultivation settings, and advocates to screen for further additives with the ability to elicit the production of cryptic metabolites. Moreover, the data of the applied initial elicitor screening workflow with six different myxobacteria was used to critically evaluate this workflow and propose adjustments to improve the output of this platform.

5.5 References

1. Katz, L. & Baltz, R. H. Natural product discovery: past, present, and future. *J. Ind. Microbiol. Biotechnol.* **43,** 155–176; 10.1007/s10295-015-1723-5 (2016).
2. Newman, D. J. & Cragg, G. M. Natural Products as Sources of New Drugs over the Nearly Four Decades from 01/1981 to 09/2019. *Journal of natural products*; 10.1021/acs.jnatprod.9b01285 (2020).
3. Walesch, S. *et al.* Fighting antibiotic resistance-strategies and (pre)clinical developments to find new antibacterials. *EMBO Rep.,* e56033; 10.15252/embr.202256033 (2022).
4. Wright, G. D. Opportunities for natural products in 21st century antibiotic discovery. *Nat. Prod. Rep.* **34,** 694–701; 10.1039/c7np00019g (2017).
5. Mohr, K. I. Diversity of Myxobacteria-We Only See the Tip of the Iceberg. *Microorganisms* **6**; 10.3390/microorganisms6030084 (2018).
6. Bader, C. D., Panter, F. & Müller, R. In depth natural product discovery - Myxobacterial strains that provided multiple secondary metabolites. *Biotechnol. Adv.* **39,** 107480; 10.1016/j.biotechadv.2019.107480 (2020).
7. Herrmann, J., Fayad, A. A. & Müller, R. Natural products from myxobacteria: novel metabolites and bioactivities. *Nat. Prod. Rep.* **34,** 135–160; 10.1039/C6NP00106H (2017).
8. Haack, P. A. *et al.* Thiamyxins: Structure and Biosynthesis of Myxobacterial RNA-Virus Inhibitors. *Angew. Chem. Int. Ed.* **61,** e202212946; 10.1002/anie.202212946 (2022).
9. Bader, C. D. *et al.* Sandacrabins - Structurally Unique Antiviral RNA Polymerase Inhibitors from a Rare Myxobacterium. *Chemistry – A European Journal* **28,** e202104484; 10.1002/chem.202104484 (2022).
10. Couturier, C. *et al.* Structure Elucidation, Total Synthesis, Antibacterial In Vivo Efficacy and Biosynthesis Proposal of Myxobacterial Corramycin. *Angew. Chem., Int. Ed. Engl.,* 10.1002/anie.202210747; 10.1002/anie.202210747 (2022).
11. Nett, M., Ikeda, H. & Moore, B. S. Genomic basis for natural product biosynthetic diversity in the actinomycetes. *Nat. Prod. Rep.* **26,** 1362–1384; 10.1039/b817069j (2009).

12. Wenzel, S. C. & Müller, R. The biosynthetic potential of myxobacteria and their impact on drug discovery. *Curr. Opin. Drug Discov. Devel.* **12,** 220–230 (2009).

13. Lee, S. R. & Seyedsayamdost, M. R. Induction of Diverse Cryptic Fungal Metabolites by Steroids and Channel Blockers. *Angewandte Chemie (International ed. in English)* **61,** e202204519; 10.1002/anie.202204519 (2022).

14. Scherlach, K. & Hertweck, C. Triggering cryptic natural product biosynthesis in microorganisms. *Org. Biomol. Chem.* **7,** 1753–1760; 10.1039/b821578b (2009).

15. Covington, B. C., Xu, F. & Seyedsayamdost, M. R. A Natural Product Chemist's Guide to Unlocking Silent Biosynthetic Gene Clusters. *Annu. Rev. Biochem.* **90,** 763–788; 10.1146/annurev-biochem-081420-102432 (2021).

16. Seyedsayamdost, M. R. High-throughput platform for the discovery of elicitors of silent bacterial gene clusters. *Proc. Natl. Acad. Sci. USA* **111,** 7266–7271; 10.1073/pnas.1400019111 (2014).

17. Craney, A., Ozimok, C., Pimentel-Elardo, S. M., Capretta, A. & Nodwell, J. R. Chemical perturbation of secondary metabolism demonstrates important links to primary metabolism. *Chem. Biol.* **19,** 1020–1027; 10.1016/j.chembiol.2012.06.013 (2012).

18. Han, E. J., Lee, S. R., Hoshino, S. & Seyedsayamdost, M. R. Targeted Discovery of Cryptic Metabolites with Antiproliferative Activity. *ACS Chem. Biol.* **17,** 3121–3130; 10.1021/acschembio.2c00588 (2022).

19. Moon, K., Xu, F., Zhang, C. & Seyedsayamdost, M. R. Bioactivity-HiTES Unveils Cryptic Antibiotics Encoded in Actinomycete Bacteria. *ACS Chem. Biol.* **14,** 767–774; 10.1021/acschembio.9b00049 (2019).

20. Xu, F. *et al.* A genetics-free method for high-throughput discovery of cryptic microbial metabolites. *Nat. Chem. Biol.*; 10.1038/s41589-018-0193-2 (2019).

21. Zhang, C. & Seyedsayamdost, M. R. Discovery of a Cryptic Depsipeptide from Streptomyces ghanaensis via MALDI-MS-Guided High-Throughput Elicitor Screening. *Angewandte Chemie (International ed. in English)* **59,** 23005–23009; 10.1002/anie.202009611 (2020).

22. Covington, B. C. & Seyedsayamdost, M. R. MetEx, a Metabolomics Explorer Application for Natural Product Discovery. *ACS Chem. Biol.* **16,** 2825–2833; 10.1021/acschembio.1c00737 (2021).

23. Panter, F., Bader, C. D. & Müller, R. The Sandarazols are Cryptic and Structurally Unique Plasmid-Encoded Toxins from a Rare Myxobacterium*. *Angewandte*

Chemie (International ed. in English) **60,** 8081–8088; 10.1002/anie.202014671 (2021).

24. Panter, F., Krug, D., Baumann, S. & Müller, R. Self-resistance guided genome mining uncovers new topoisomerase inhibitors from myxobacteria. *Chem. Sci.* **9,** 4898–4908; 10.1039/C8SC01325J (2018).
25. Hug, J. J., Panter, F., Krug, D. & Müller, R. Genome mining reveals uncommon alkylpyrones as type III PKS products from myxobacteria. *Journal of Industrial Microbiology & Biotechnology* **46,** 319–334; 10.1007/s10295-018-2105-6 (2019).
26. Gemperlein, K., Rachid, S., Garcia, R. O., Wenzel, S. C. & Müller, R. Polyunsaturated fatty acid biosynthesis in myxobacteria. Different PUFA synthases and their product diversity. *Chem. Sci.* **5,** 1733–1741; 10.1039/C3SC53163E (2014).
27. Irschik, H. *et al.* Analysis of the sorangicin gene cluster reinforces the utility of a combined phylogenetic/retrobiosynthetic analysis for deciphering natural product assembly by trans-AT PKS. *Chembiochem : a European journal of chemical biology* **11,** 1840–1849; 10.1002/cbic.201000313 (2010).
28. Walt, C., Bader, C. D., Krug, D. & Müller, R. Aggravated Cultivation of Myxobacteria Stimulates Secondary Metabolism. *(Manuscript in preparation)*.
29. Hug, J. J., Kjaerulff, L., Garcia, R. & Müller, R. New Deoxyenhygrolides from Plesiocystis pacifica Provide Insights into Butenolide Core Biosynthesis. *Marine drugs* **20**; 10.3390/md20010072 (2022).
30. Akone, S. H., Hug, J. J., Kaur, A., Garcia, R. & Müller, R. Structure Elucidation and Biosynthesis of Nannosterols A and B, Myxobacterial Sterols from Nannocystis sp. MNa10993. *J. Nat. Prod.*; 10.1021/acs.jnatprod.2c01143 (2023).
31. Hug, J. J. *et al.* Genome-Guided Discovery of the First Myxobacterial Biarylitide Myxarylin Reveals Distinct C–N Biaryl Crosslinking in RiPP Biosynthesis. *Molecules* **26,** 7483; 10.3390/molecules26247483 (2021).
32. Gao, Y., Walt, C., Bader, C. D. & Müller, R. Genome Guided Discovery of the Myxobacterial Thiolactone-containing Sorangibactins **submitted** (2023).
33. Groß, S., Schnell, B., Haack, P. A., Auerbach, D. & Müller, R. In vivo and in vitro reconstitution of unique key steps in cystobactamid antibiotic biosynthesis. *Nat. Commun.* **12,** 1696; 10.1038/s41467-021-21848-3 (2021).

34. Wenzel, S. C. & Müller, R. Myxobacterial natural product assembly lines: fascinating examples of curious biochemistry. *Natural product reports* **24,** 1211–1224; 10.1039/b706416k (2007).

35. Schwarz, J., Hubmann, G., Rosenthal, K. & Lütz, S. Triaging of Culture Conditions for Enhanced Secondary Metabolite Diversity from Different Bacteria. *Biomolecules* **11**; 10.3390/biom11020193 (2021).

36. Jenny Schwarz, Georg Hubmann, Ayla Schwarz, Katrin Rosenthal & Stephan Lütz. Bivariate OSMAC Designs Expand the Secondary Metabolite Production Space in Corallococcus Coralloides; 10.20944/preprints202203.0118.v1 (2022).

37. Mccurdy, H. D. & MacRae, T. H. Xanthacin. A bacteriocin of Myxococcus xanthus fb. *Can. J. Microbiol.* **20,** 131–135; 10.1139/m74-021 (1974).

38. Lloyd, D. G. & Whitworth, D. E. The myxobacterium *Myxococcus xanthus c*an sense and respond to the quorum signals secreted by potential prey organisms. *Front. Microbiol.* **8,** 439; 10.3389/fmicb.2017.00439 (2017).

39. Akbar, S., Phillips, K. E., Misra, S. K., Sharp, J. S. & Stevens, D. C. Differential response to prey quorum signals indicates predatory specialization of myxobacteria and ability to predate Pseudomonas aeruginosa. *Environmental microbiology* **24,** 1263–1278; 10.1111/1462-2920.15812 (2022).

40. Whitworth, D. E. & Zwarycz, A. A Genomic Survey of Signalling in the Myxococcaceae. *Microorganisms* **8,** 1739; 10.3390/microorganisms8111739 (2020).

41. Jain, R. & Inouye, S. Inhibition of development of *Myxococcus xanthus* by eukaryotic protein kinase inhibitors. *J. Bacteriol.* **180,** 6544–6550 (1998).

42. Tomm, H. A., Ucciferri, L. & Ross, A. C. Advances in microbial culturing conditions to activate silent biosynthetic gene clusters for novel metabolite production. *Journal of Industrial Microbiology & Biotechnology* **46,** 1381–1400; 10.1007/s10295-019-02198-y (2019).

43. Coisne, S., Béchet, M. & Blondeau, R. Actinorhodin production by Streptomyces coelicolor A3(2) in iron-restricted media. *Lett. Appl. Microbiol.* **28,** 199–202; 10.1046/j.1365-2672.1999.00509.x (1999).

44. Lee, N. *et al.* Iron competition triggers antibiotic biosynthesis in Streptomyces coelicolor during coculture with Myxococcus xanthus. *The ISME Journal* **14,** 1111–1124; 10.1038/s41396-020-0594-6 (2020).

45. Koller, T. O. *et al.* The Myxobacterial Antibiotic Myxovalargin: Biosynthesis, Structural Revision, Total Synthesis, and Molecular Characterization of Ribosomal Inhibition. *J. Am. Chem. Soc.* **accepted**; 10.1021/jacs.2c08816 (2023).

46. Nothias, L.-F. *et al.* Feature-based molecular networking in the GNPS analysis environment. *Nat Methods* **17,** 905–908; 10.1038/s41592-020-0933-6 (2020).

47. Wang, M. *et al.* Sharing and community curation of mass spectrometry data with Global Natural Products Social Molecular Networking. *Nat. Biotechnol.* **34,** 828–837; 10.1038/nbt.3597 (2016).

48. Krug, D. *et al.* Discovering the hidden secondary metabolome of Myxococcus xanthus: a study of intraspecific diversity. *Applied and environmental microbiology* **74,** 3058–3068; 10.1128/AEM.02863-07 (2008).

49. Neuber, M. Alteration of the metabolite spectrum of myxobacteria through alternative cultivation and extraction techniques. Doctoral Thesis. Saarland University, 2022.

Supporting information

Development of an Increased Throughput Elicitor Screening Platform for Myxobacteria

Sebastian Walesch, F. P. Jake Haeckl, Daniel Krug and Rolf Müller

Materials and methods

Bacterial strains and cultivation media

Table S 5.1: List of strains used in this study

Strain	**Source**
Myxococcus xanthus DK1622	MINS-Lab
Cystobacter sp. MCy12796	MINS-Lab
Cystobacter sp. MCy12977	MINS-Lab
Sorangium sp. NOSO3 (DSM53667)	GBF
Sorangium sp. MSr12523	MINS-Lab
Nannocystis exedens Na e487 (BacDive ID 21720)	GBF

Cultivation media

Each medium used in this study was prepared with deionised water. All media were sterilised by autoclaving at 121 °C, 2 bar for 20 min.

Table S 5.2: List of culture medium recipes

CTT medium		
Amount	**Ingredient**	**Supplier**
10.0 g/L	Casitone	BD
1.21 g/L	TRIS	Sigma Aldrich
0.14 g/L	KH_2PO_4	Roth
1.97 g/L	$MgSO_4$ x 7 H_2O	Grüssing
PH adjusted to 7.3 with 1 N KOH.		
2SWT medium		
Amount	**Ingredient**	**Supplier**
1.0 g/L	Soytone	BD
2.0 g/L	Soluble starch	Roth
2.0 g/L	Glucose	Roth
1.0 g/L	Maltose monohydrate	Sigma Aldrich

2.0 g/L	Cellobiose	MP Biomedicals
0.5 g/L	$CaCl_2$ x 2 H_2O	Sigma Aldrich
1.0 g/L	$MgSO_4$ x 7 H_2O	Grüssing
2.38 g/L	HEPES	Roth
PH adjusted to 7.0 with 10 N KOH.		

Elicitors

All elicitors were prepared as 5 mM stock solutions in DMSO or, in case of Na butyrate, in MQ water.

Table S 5.3: List of elicitors

Elicitor	**Natural function**	**Supplier**
N-butyryl-homoserin lactone (4C-HSL)	Quorum signalling molecule	Sigma Aldrich
2-Heptyl-4-quinolone (HHQ)	Quorum signalling molecule	Sigma Aldrich
Cholerae autoinducer 1 (CAI-1)	Quorum signalling molecule	Hirsch lab[a]
Nocardamin	Siderophore	Luzhetskyy lab[b]
Rifampicin	RNA-polymerase inhibitor	Sigma Aldrich
Cycloheximide	Protein biosynthesis inhibitor	Roth
Daunorubicin	DNA intercalator	Hölzel diagnostica
Mitomycin C	DNA crosslinker	Bioaustralis
Na butyrate	HDAC inhibitor	Sigma Aldrich
Staurosporin	Kinase inhibitor	LC laboratories

[a] Kindly provided by Dr. Christian Schütz, Hirsch lab, HIPS, Saarbrücken
[b] Kindly provided by Dr. Marc Stierhof, Luzhetskyy lab, Saarland University, Saarbrücken

Microbiological methods

Screening in 24 deep-well plates

Cultivations for screenig purposes were performed in 24 deep-well plates on a Duetz System (Kuhner, Birsfelden, Switzerland). Each well was filled with 5 mL of the respective medium, inoculated with 5% (v/v) pre-culture or, in case of media controls, just the medium. Each well was supplemented with 0.5, 5 or 50 µL of 1 mM DMSO stocks

of the respective elicitors or with 0.5, 5 or 50 µL DMSO as vehicle control. The elicitor Na butyrate was added as a 1 mM aqueous stock. Afterwards the plates were incubated at 30 °C and 180 rpm for 7 d. After cultivation, the plates were frozen and subsequently dried with a RVC 2-33 CDplus rotary vacuum concentrator (Martin Christ Gefriertrocknungsanlagen, Osterode am Harz, Germany) and stored at – 20 °C until further use.

E1 (E6) 0.5 µM	**E2 (E7)** 0.5 µM	**E3 (E8)** 0.5 µM	**E4 (E9)** 0.5 µM	**E5 (E10)** 0.5 µM	0.5 µL DMSO
E1 (E6) 5 µM	**E2 (E7)** 5 µM	**E3 (E8)** 5 µM	**E4 (E9)** 5 µM	**E5 (E10)** 5 µM	5 µL DMSO
E1 (E6) 50 µM	**E2 (E7)** 50 µM	**E3 (E8)** 50 µM	**E4 (E9)** 50 µM	**E5 (E10)** 50 µM	50 µL DMSO
Medium blank 5 µM **E1 (E6)**	Medium blank 5 µM **E2 (E7)**	Medium blank 5 µM **E3 (E8)**	Medium blank 5 µM **E4 (E9)**	Medium blank 5 µM **E5 (E10)**	Untreated culture

E1: Na butyrate
E2: Staurosporin
E3: Cycloheximide
E4: Daunorubicin
E5: Rifampicin
E6: Mitomycin C
E7: Nocardamin
E8: 4C-HSL
E9: HHQ
E10: CAI-1

Figure S 5.1: Layout of elicitor screening experiments in 24 deep-well plates. All elicitors were screened in three concentrations with the respective amounts of DMSO as vehicle controls. Elicitors E1 to E5 were screened in plate one. Elicitors E6 to E10 (in brackets) were screened in plate two.

Proof of concept fermentation in shaking flasks

Proof of concept cultures were grown in 300 mL shaking flasks containing 50 mL of the respective fermentation medium inoculated with 5% (v/v) pre-culture and supplemented with with the respective elicitor or DMSO as vehicle control, when appropriate. After 6 d cultivation, 4% (v/v) of a sterile aqueous solution of XAD-16 adsorber resin (Sigma Aldrich) were added to the culture to bind secondary metabolites in the culture medium. After 7 d cultivation, the culture was pelleted in 50 mL falcon tubes in an Eppendorf centrifuge 5804R at 8288 x g and 4 °C for 10 min. The pellet was then freeze-dried and stored at room temperature until further use.

Analytical methods

Crude extract generation from deep-well plate cultivations

Dried extracts in 24 deep-well plates were extracted twice with 2 mL MeOH by sonication for 1 h. The respective extracts were moved to 96 deep-well plates, dried in a RVC 2-33 CDplus rotary vacuum concentrator (Martin Christ Gefriertrocknungsanlagen, Osterode am Harz, Germany), dissolved in 200 µL MeOH for the first round of extraction and 100

µL MeOH for the second round of extraction, and centrifuged at 4000 rpm for 10 min. Afterwards, 175 µL of the supernatant from the first round of extraction and 75 µL from the second round were pooled, and stored in 96 well plates at – 20 °C or submitted for UHPLC-*hr*MS analysis.

Crude extract generation from shaking flask cultivations

Freeze-dried pellets from shaking flask cultivations were suspended in 40 mL methanol and stirred at 250 rpm at room temperature for 2 h. The supernatant was decanted into a round bottom flask through a 125 micron folded filter. The solvent was removed on a rotary evaporator with a water bath temperature of 40 °C at an appropriate pressure. The dried extract was dissolved/resuspended in 1000 µL MeOH/100 mL cultivation volume. The crude extract was stored at -20 °C until further analysis. For the purpose of UHPLC-*hr*MS analysis, the crude extract was diluted 1:5 with methanol and centrifuged at 21500 x g and 4 °C (HIMAC CT15RE, Koki Holdings Co.) for 5 min to remove residual insolubilities such as salts, cell debris and XAD fragments.

Standardised UHPLC-MS conditions

UHPLC-*hr*MS analysis was performed on a Dionex (Germering, Germany) Ultimate 3000 RSLC system using a Waters (Eschborn, Germany) BEH C18 column (50 x 2.1 mm, 1.7 µm) equipped with a Waters VanGuard BEH C18 1.7 µm guard column. Separation of 1-3 µL sample was achieved by a linear gradient from (A) H2O + 0.1 % formic acid (FA) to (B) ACN + 0.1 % FA at a flow rate of 600 µL/min and a column temperature of 45 °C. Gradient conditions for crude extracts from screening cultivations were as follows: : 0 – 0.5 min, 5% B; 0.5 – 9.5 min, 5 – 95% B; 9.5 – 10.5 min, 95% B; 10.5 – 11 min, 95 – 5% B; 11-12.5 min, 5% B. Following gradient conditions were applied for crude extracts from shaking flask cultivations: 0 – 0.5 min, 5% B; 0.5 – 18.5 min, 5 – 95% B; 18.5 – 20.5 min, 95% B; 20.5 – 21 min, 95 – 5% B; 21-22.5 min, 5% B. UV spectra were recorded by a DAD in the range from 200 to 600 nm. The LC flow was split to 75 µL/min before entering the Bruker Daltonics maXis 4G *hr*ToF mass spectrometer (Bremen, Germany) equipped with an Apollo II ESI source. Mass spectra were acquired in centroid mode ranging from 150 – 2500 *m/z* at a 2 Hz full scan rate. Mass spectrometry source parameters were set to 500 V as end plate offset; 4000 V as capillary voltage; nebuliser gas pressure 1 bar; dry gas flow of 5 L/min and a dry temperature of 200 °C. Ion transfer and quadrupole settings were set to funnel RF 350 Vpp.; multipole RF 400 Vpp as transfer settings and ion energy of 5 eV as well as a low mass cut of 300 *m/z*. Collision cell was set to 5.0 eV

and pre-pulse storage time was set to 5 µs. Spectra acquisition rate was set to 2 Hz. Calibration was done automatically before every LC-MS run by injection of a sodium formate solution and calibration on the respective clusters formed in the ESI source. All MS analyses were acquired in the presence of the lock masses ($C_{12}H_{19}F_{12}N_3O_6P_3$, $C_{18}H_{19}O_6N_3P_3F_2$ and $C_{24}H_{19}F_{36}N_3O_6P_3$) which generate the [M+H]+ ions of 622.0289; 922.0098 and 1221.9906.

Acquisition of high-resolution tandem MS data

High-resolution tandem MS data was acquired on a Bruker Daltonics timsTOF flex mass spectrometer (Bremen, Germany) connected to an UHPLC system with the same specifications as described in 1.3.3 for crude extracts from shaking flask cultivations.The timsTOF fleX was operated in positive ESI mode, with 1.0 bar nebuliser pressure, 5.0 L/min dry gas, 200°C dry heater, 4000 V capillary voltage, 500 V end plate offset, 600 Vpp funnel 1 RF, 400 Vpp funnel 2 RF, 80 V deflection delta, 5 eV ion energy, 10 eV collision energy, 1500 Vpp collision RF, 10 µs pre pulse storage, 100 µs transfer time. TIMS delta values were set to -20 V (delta 1), -120 V (delta 2), 80 V (delta 3), 100 V (delta 4), 0 V (delta 5), and 100 V (delta 6). The 1/K0 (inverse reduced ion mobility) range was set from 0.55 Vs/cm2 to 1.9 Vs/cm2 , the mass range was *m/z* 100-2000. MS/MS spectra were acquired using the PASEF DDA mode with a collision energy of 30 eV. Ion charge control (ICC) was enabled and set to 7.5 mio counts. The samples were analysed with TIMS ramp times of 100 ms.The analysis accumulation and ramp time was set at 100 ms with a spectra rate of 9.43 Hz and a total cycle of 0.32 sec was also selected resulting in one full TIMS-MS scan and two PASEF MS/MS scans. TIMS dimension was calibrated linearly using 4 selected ions from ESI Low Concentration Tuning Mix (Agilent Technologies, USA) [*m/z*, $1/k_0$: (301.998139, 0.6678 Vs cm^{-2}), (601.979077, 0.8782 Vs cm−2)] in negative mode and [*m/z*, $1/k_0$: (322.048121, 0.7363 Vs cm^{-2}), (622.028960, 0.9915 Vs cm^{-2})] in positive mode. The mobility for mobility calibration was taken from the CCS compendium[1].

Evaluation of screening data

All extracts from primary screening were analysed with MetaboScape 2022b (Bruker Daltonics, Billerica, MA, USA). The T-ReX-3D molecular feature finder was used to obtain molecular features with detection parameters of an intensity threshold 2.5×10^4 and a minimum peak length of five spectra. Spectra were recalibrated on sodium formate cluster mix. Afterwards, the newly generated feature table was annotated with an analyte

list containing retention time and *hr*MS data of mostly myxobacterial natural products, based on the in-house database "Myxobase"[2].

A feature table containing data of all samples of a given screening campaign was exported as CSV-file and used for calculating the difference of every crude extract to the control cultivation as well as the medium blank in Microsoft Excel (Microsoft Corporation, Redmond, WA, USA). The "feature difference values" were calculated based on the log2 fold change of every detected feature relative to the control cultivation or the medium blank. The intensity count of 0 for every non-existent feature in any sample was exchanged by the artificial intensity count of 100 to enable these calculations. In order to estimate the overall change of a sample compared to the control cultivation and medium blank, the square root of the sum of the square of all log2 fold changes was calculated for every feature, as indicated in the formula below.

$$Feature\ difference\ value = \sqrt[2]{\sum (log2\ (\frac{Intensity(Feature\ x\ in\ sample)}{Intensity(Feature\ x\ in\ control)}))^2}$$

All treated cultures and the DMSO vehicle controls of one 24 deep-well plate were compared to the control culture of the respective plate. The feature difference values of all cultivations compared to the medium blanks were calculated against the mean intensities of all blank samples. For a better overview, all feature difference values were presented as relative feature difference values between 0 and 1 with 0 being the lowest difference and 1 being the highest difference. The relative feature difference values of all samples within a screening campaign were visualised with Tableau 2021.2 (Tableau Software, Seattle, WA, USA) and organised based on a decreasing relative feature difference values compared to the control culture.

For screening events in *M. xanthus* DK1622, the relative production levels of reported natural products were used as another parameter to assess the effect of added elicitors on the bacterial metabolism. All treated cultures and the DMSO vehicle controls of one 24 deep-well plate were compared to the control culture of the respective plate. The relative production of reported production was calculated as follows.

$$Relative\ production_{Compound\ X} = \frac{(Intensity\ Compound\ X_{Sample} - Intensity\ Compound\ X_{Control})}{(Intensity\ Compound\ X_{Sample} + Intensity\ Compound\ X_{Control})}$$

The relative production levels of reported natural products in *M. xanthus* DK1622 were visualised in RStudio (posit, Boston, MA, USA) using the heatmaply package[3].

Statistics-based analysis of proof of concept cultivation crude extracts

For statistical metabolomics analysis, all myxobacterial cultures as well as the medium blank were incubated and extracted in triplicates as described above. Each extract was measured as technical duplicate, giving a total number of six replicates each for each cultivation condition and medium blank extracts. T-ReX-3D molecular feature finder of MetaboScape 2022b (Bruker Daltonics, Billerica, MA, USA) was used to obtain molecular features. Detection parameters were set to an intensity threshold 2.5×10^4 and a minimum peak length of five spectra. Spectra were recalibrated on sodium formate cluster mix. Features were accepted when detected in 4/6 samples for each condition. Features detected in any blank extract were excluded from further analysis. Afterwards, the newly generated feature table was annotated with an analyte list containing retention time and *hr*MS data of mostly myxobacterial natural products, based on the in-house database "Myxobase"[2]. The built-in t-test/ANOVA routine was used to compare all cultivation conditions among each other to determine features that are unique to one cultivation condition and to compare all extracts with added elicitor or DMSO to the control cultivations in order to evaluate the number of up- or downregulated features. To ensure a clear distinction between the up- or downregulation of features and their addition or loss compared to the control cultivations, all missing values for the t-test/ANOVA routine were substituted with the arbitrarily chosen value of 100 counts. Any feature with a p-value smaller or equal to 0.05 and a log2 fold change greater 1 or smaller -1 was considered up- or downregulated, respectively. Further analysis was performed in Microsoft Excel (Microsoft Corporation, Redmond, WA, USA) and the respective results were visualised with Tableau 2021.2 (Tableau Software, Seattle, WA, USA).

Parameters for feature based molecular networking

All supporting feature based molecular networking data presented here was created based on the UHPLC-*hr*MS² chromatograms using the parameters specified above. All molecular features in the retention time window between 1 and 19 min were obtained by Metaboscape 2022b (Bruker Daltonics, Billerica, MA, USA), using the T-Rex 4D processing routine with the intensity threshold set to 1000 counts and the minimum 4D peak size to 100 counts. The resulting output files were exported with the built-in "Export for GNPS/Sirius" function and uploaded to the GNPS server[4] at University of California

San Diego via FileZilla FTP upload to ftp:// ccms-ftp01.ucsd.edu for feature-based network creation[5]. A feature-based molecular network was created using the online workflow at GNPS. The data was filtered by removing all MS/MS peaks within +/- 17 Da of the precursor *m/z*. MS/MS spectra were window filtered by choosing only the top 6 peaks in the +/- 50 Da window throughout the spectrum. The data was then clustered with a parent mass tolerance of 0.02 Da and a MS/MS fragment ion tolerance of 0.02 Da to create consensus spectra. No further filtering of consensus spectra was done before spectral network creation. A network was then created where edges are filtered to have a cosine score above 0.7 and more than 4 matched peaks. Further edges between two nodes were kept in the network if and only if each of the nodes appeared in each other's respective top 10 most similar nodes. Furthermore, library search parameters were set to a cosine of 0.7 and a minimum of 6 matched peaks. Library searches included analogues with mass differences up to 200 Da. The dataset was downloaded from the server and subsequently visualised using Cytoscape 3.9.1. Networks were excluded from analysis, when more than 20% of their nodes were present in the medium blanks. Furthermore, all singletons were removed from the analysis.

Results

Evaluation and validation of a higher-throughput screening platform with *M. xanthus* DK1622

Elicitor screening in 24 deep-well plates with *M. xanthus* DK1622

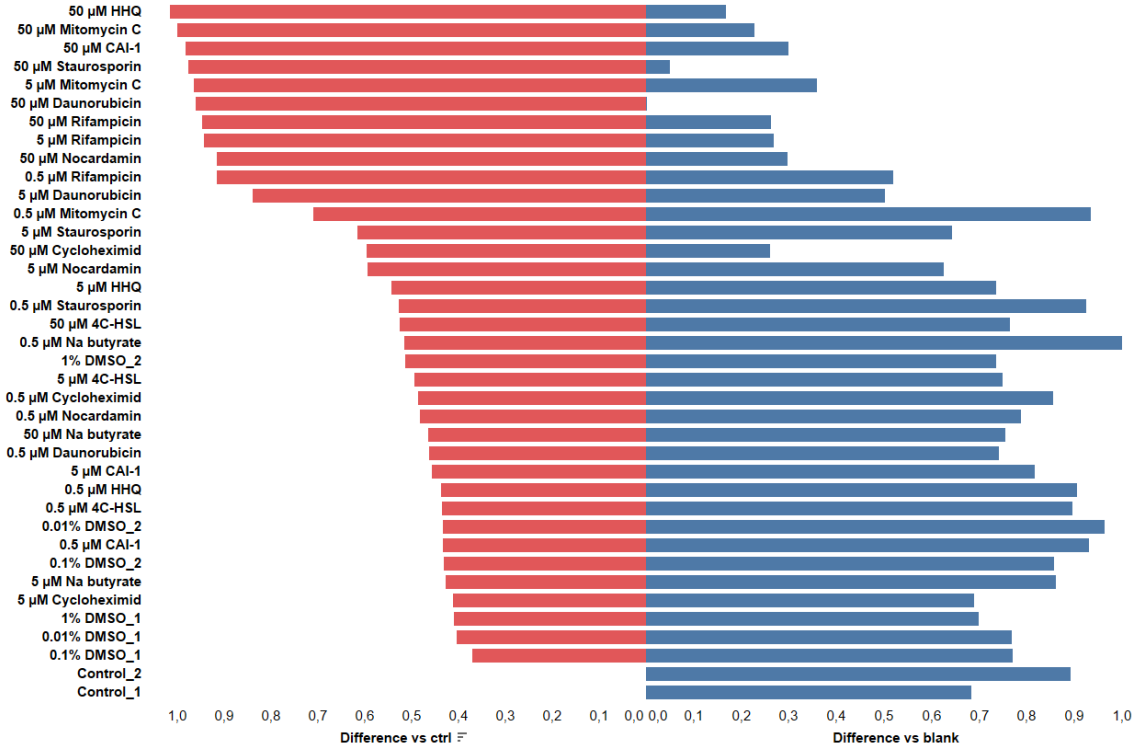

Figure S 5.2: Relative difference of extracts of *M. xanthus* DK1622 with added elicitors or DMSO compared to control cultivations and medium blanks.

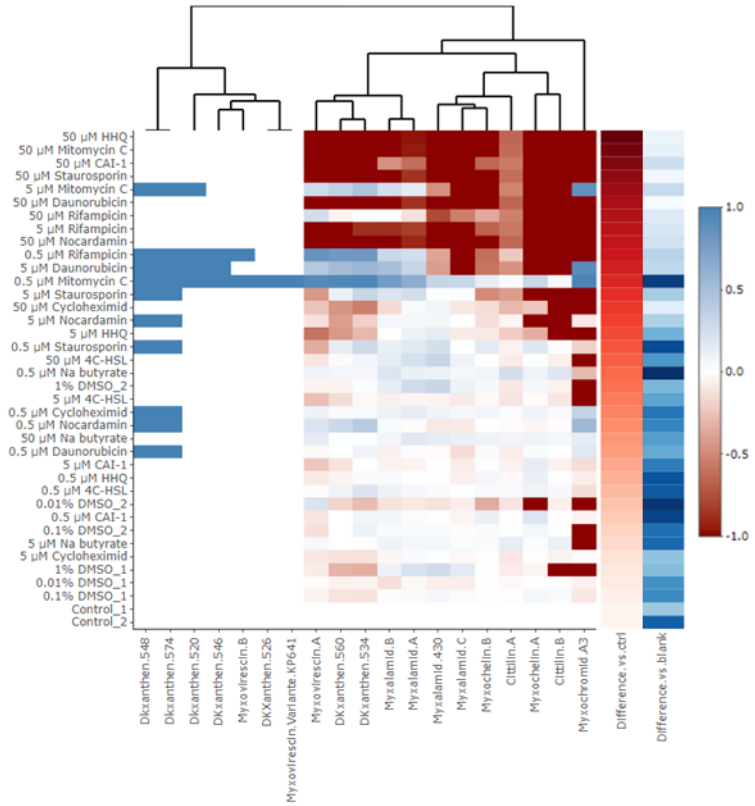

Figure S 5.3: Relative production levels of known secondary metabolites in cultivations of *M. xanthus* DK1622 with added elicitors or DMSO compared to control cultivations.

Regulation of features in proof of concept flask cultivations with *M. xanthus* DK1622

Using the t-test/ANOVA routine of Metaboscape 2022b, the regulation of all features in *M. xanthus* DK1622 cultivations with added elicitors or DMSO were compared to the control cultivation and visualised as volcano plots.

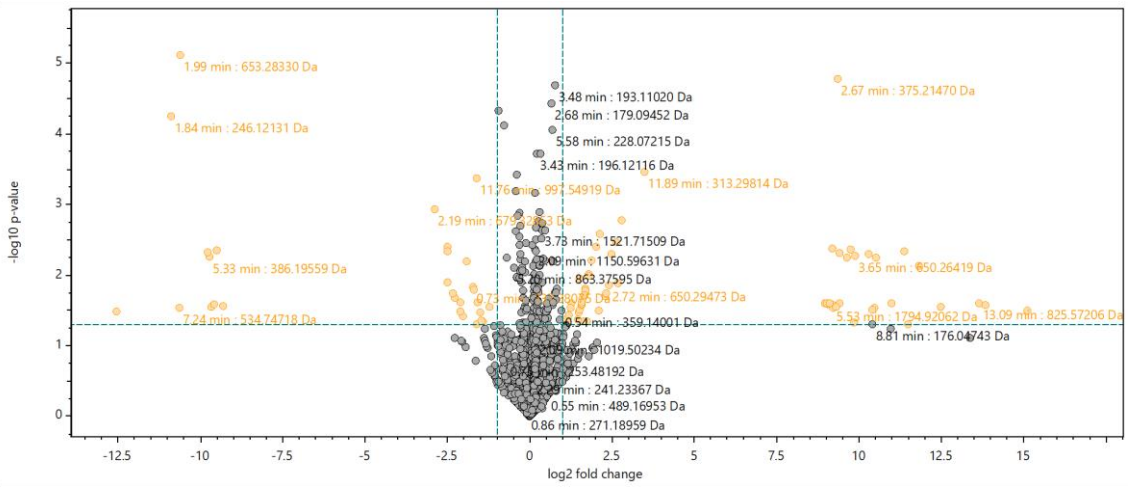

Figure S 5.4: Volcano plot of significance (-log10 p-value) versus fold change (log2 fold change) of *M. xanthus* DK1622, cultivated with 0.1% DMSO compared to a control cultivation. Data points appearing towards the top of the plot indicate high significance; data

points towards the left side of the plot indicate downregulation and towards the right side upregulation of features.

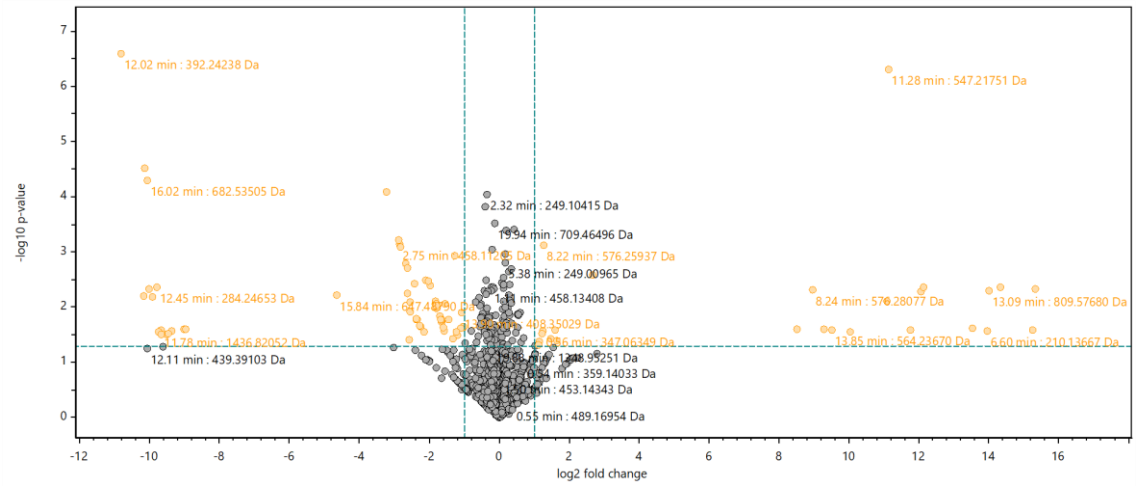

Figure S 5.5: Volcano plot of significance (-log10 p-value) versus fold change (log2 fold change) of *M. xanthus* DK1622, cultivated with 0.5 µM Na butyrate compared to a control cultivation. Data points appearing towards the top of the plot indicate high significance; data points towards the left side of the plot indicate downregulation and towards the right side upregulation of features.

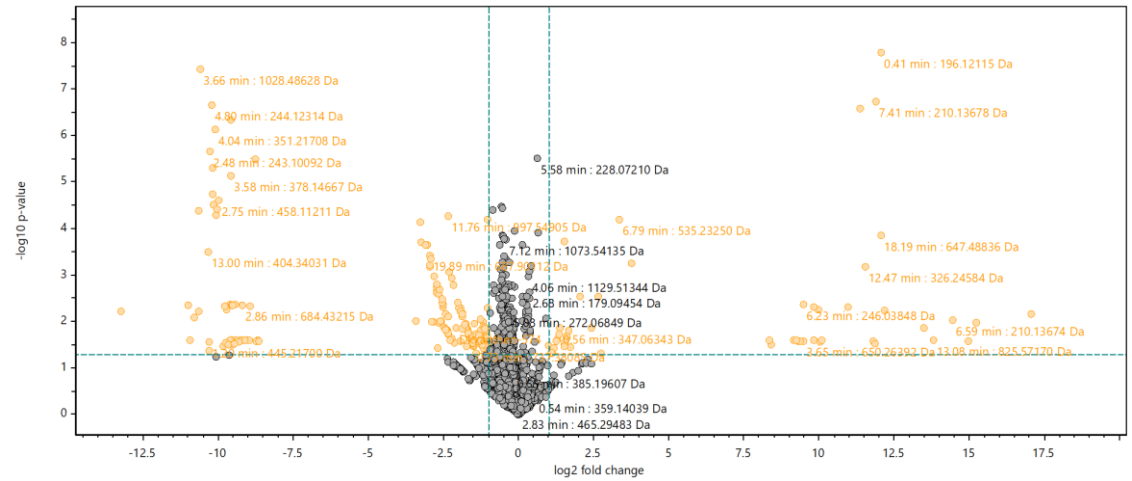

Figure S 5.6: Volcano plot of significance (-log10 p-value) versus fold change (log2 fold change) of *M. xanthus* DK1622, cultivated with 5 µM N-butyryl-homoserin lactone (4C-HSL) compared to a control cultivation. Data points appearing towards the top of the plot indicate high significance; data points towards the left side of the plot indicate downregulation and towards the right side upregulation of features.

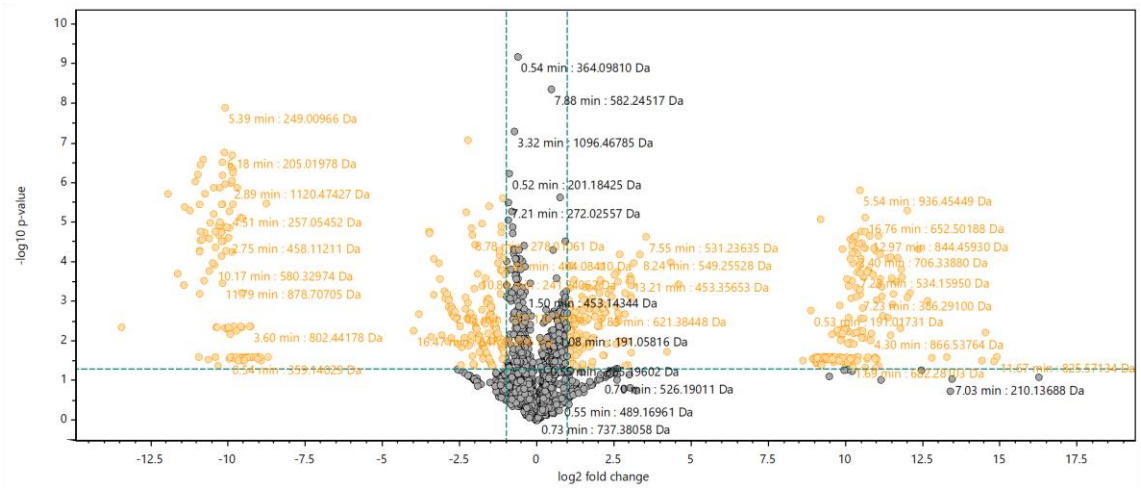

Figure S 5.7: Volcano plot of significance (-log10 p-value) versus fold change (log2 fold change) of *M. xanthus* DK1622, cultivated with 0.5 µM mitomycin C compared to a control cultivation. Data points appearing towards the top of the plot indicate high significance; data points towards the left side of the plot indicate downregulation and towards the right side upregulation of features.

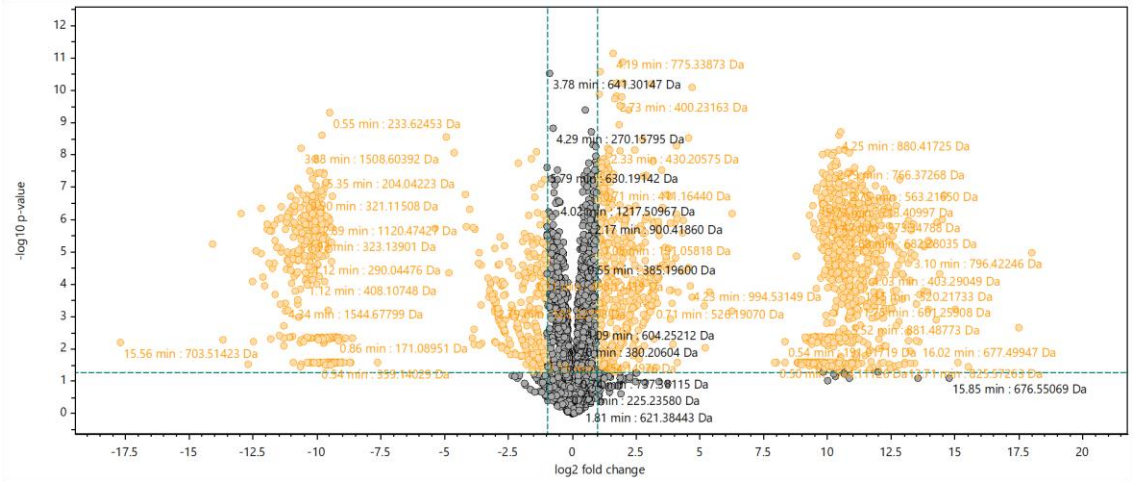

Figure S 5.8: Volcano plot of significance (-log10 p-value) versus fold change (log2 fold change) of *M. xanthus* DK1622, cultivated with 3 µM staurosporin compared to a control cultivation. Data points appearing towards the top of the plot indicate high significance; data points towards the left side of the plot indicate downregulation and towards the right side upregulation of features.

The regulation of all features in *M. xanthus* DK1622 cultivations with added elicitors or DMSO compared to the control cultivation was calculated based on the t-test/ANOVA results. The observation of unique features in any cultivation setting was determined by analysing a feature table of all samples within the *M. xanthus* DK1622 proof of concept cultivation experiment.

Table S 5.4: Number of up- and downregulated, newly observed and lost features per cultivation condition in *M.xanthus* DK1622 compared to cultivation control and number of unique features for every cultivation condition.

Elicitor	Lost features	Downregulated features	Upregulated features	New features	Unique features
DMSO	10	19	35	27	2
Na butyrate	16	44	9	17	0
Cycloheximide	54	110	23	28	0
Mitomycin C	107	167	153	224	56
Staurosporin	352	271	386	814	552

Reproducibility of features in proof of concept flask cultivations with *M. xanthus* DK1622

The reproducibilities of features in any cultivation setting was determined by analysing a feature table of all samples within the *M. xanthus* DK1622 proof of concept cultivation experiment.

Table S 5.5: Reproducibilities of features within a cultivation condition in *M. xanthus* DK1622 calculated as their presence in number of samples in three biological and two technical replicates.

Cultivation condition	In 6 samples	In 5 samples	In 4 samples	In 3 samples	In 2 samples	In 1 sample
Control	2368	172	153	144	137	96
DMSO	2428	166	172	101	140	148
Na butyrate	2330	178	183	116	137	111
Cycloheximide	1906	107	494	130	181	196
Mitomycin C	2012	157	580	116	280	168
Staurosporin	2682	209	281	87	127	100

Further screening campaigns with the higher throughput elicitor screening platform

M. xanthus DK1622 in 2SWT medium

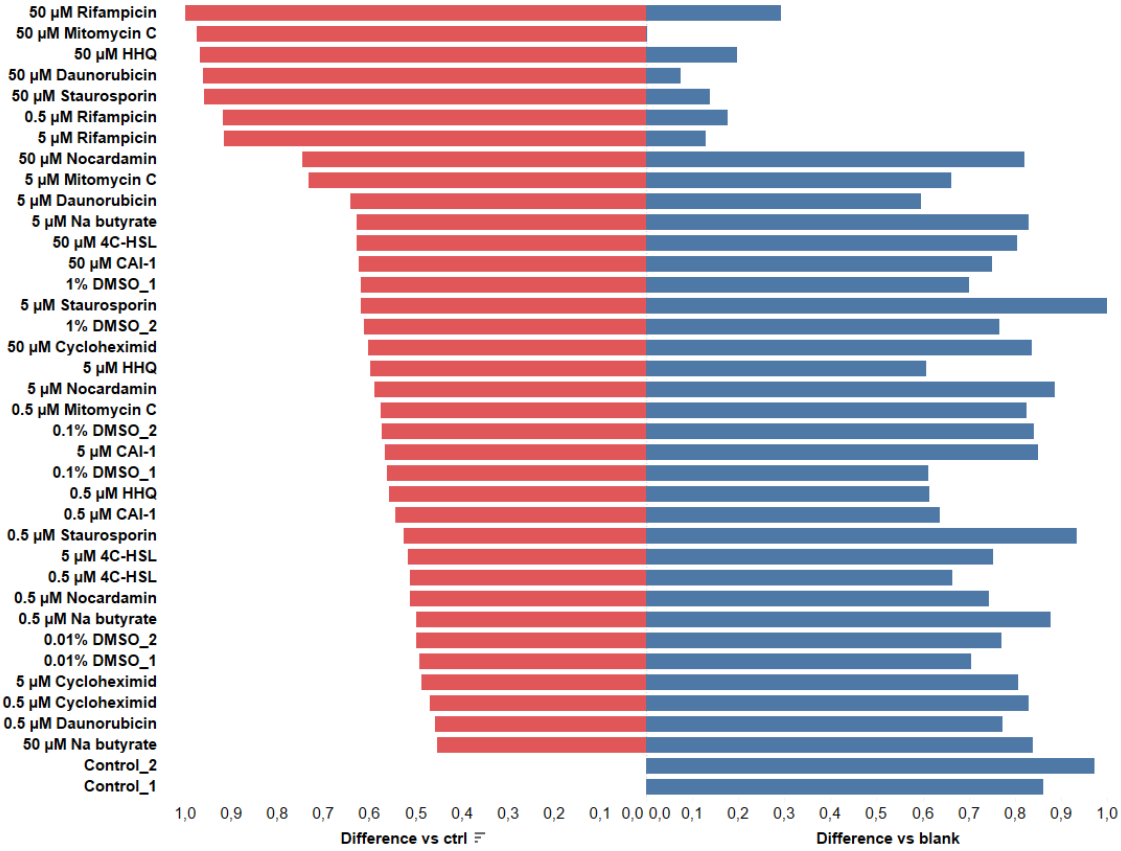

Figure S 5.9: Relative difference of extracts of *M. xanthus* DK1622 in 2SWT medium with added elicitors or DMSO compared to control cultivations and medium blanks.

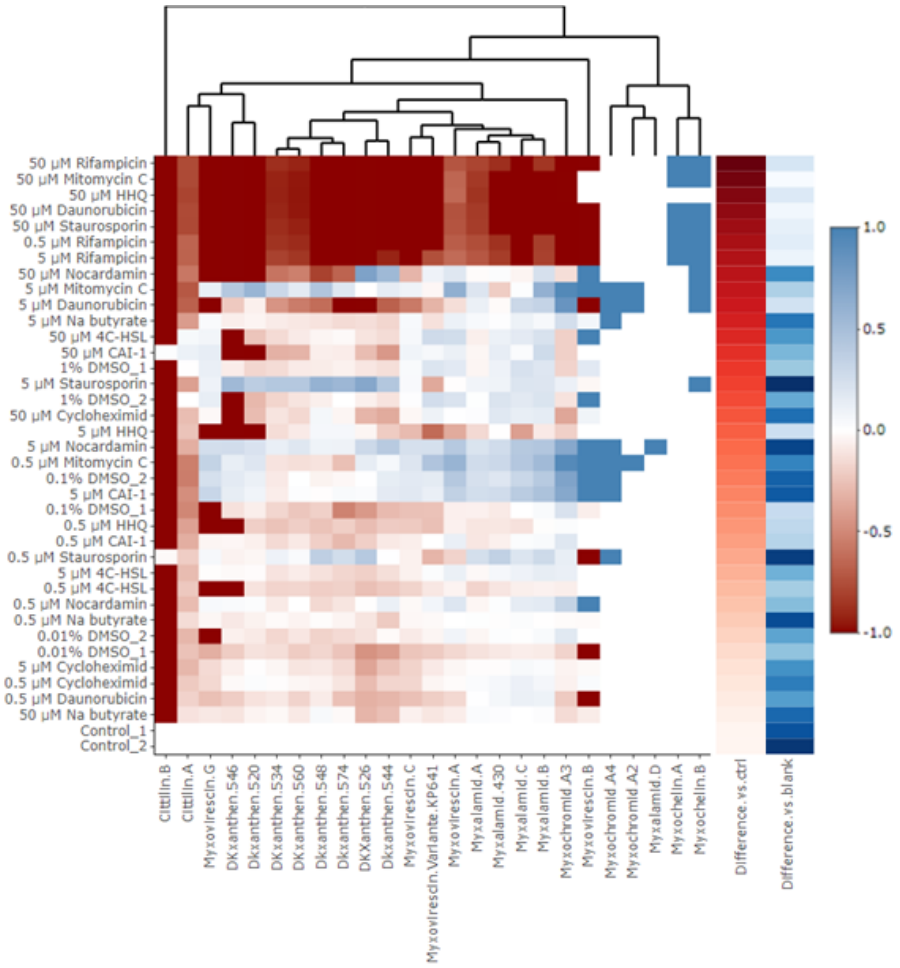

Figure S 5.10: Relative production levels of known secondary metabolites in cultivations of *M. xanthus* DK1622 with added elicitors or DMSO compared to control cultivations.

Cystobacter sp. MCy12796

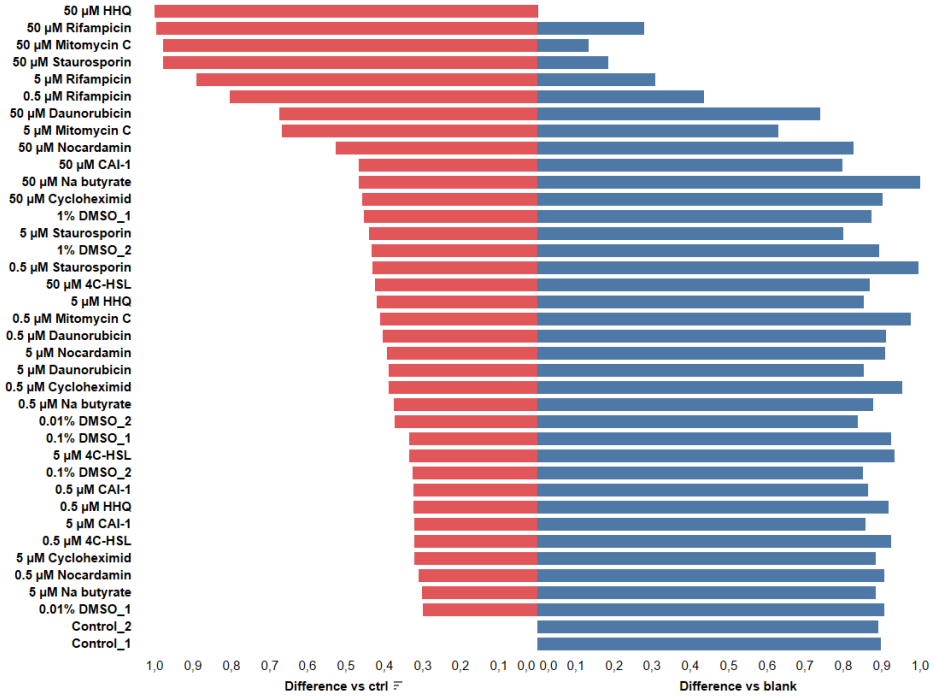

Figure S 5.11: Relative difference of extracts of *Cystobacter* sp. MCy12796 with added elicitors or DMSO compared to control cultivations and medium blanks.

Cystobacter sp. MCy12977

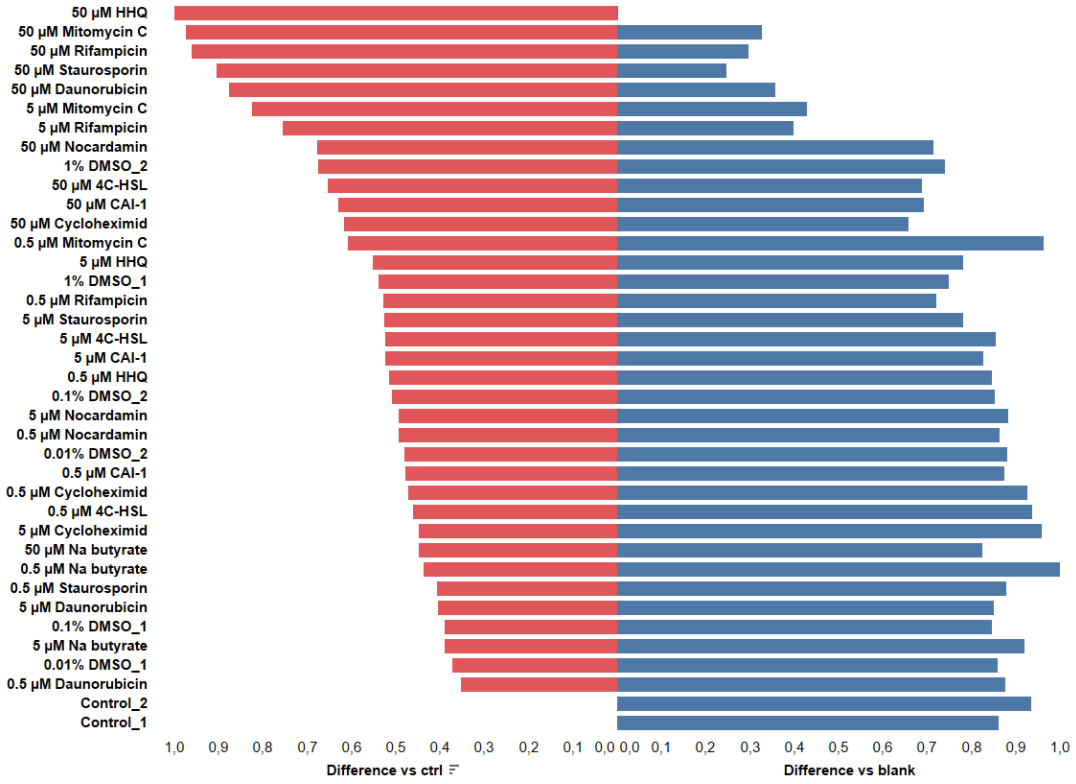

Figure S 5.12: Relative difference of extracts of *Cystobacter* sp. MCy12977 with added elicitors or DMSO compared to control cultivations and medium blanks.

Sorangium sp. MSr12523

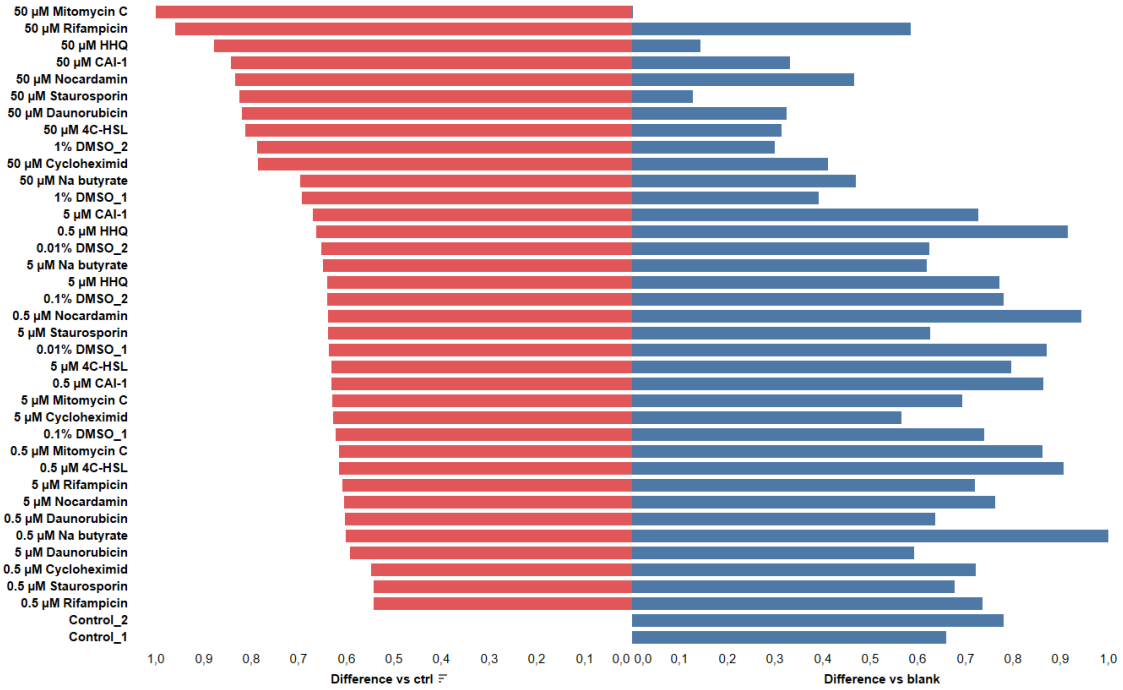

Figure S 5.13: Relative difference of extracts of *Sorangium* sp. MSr12523 with added elicitors or DMSO compared to control cultivations and medium blanks.

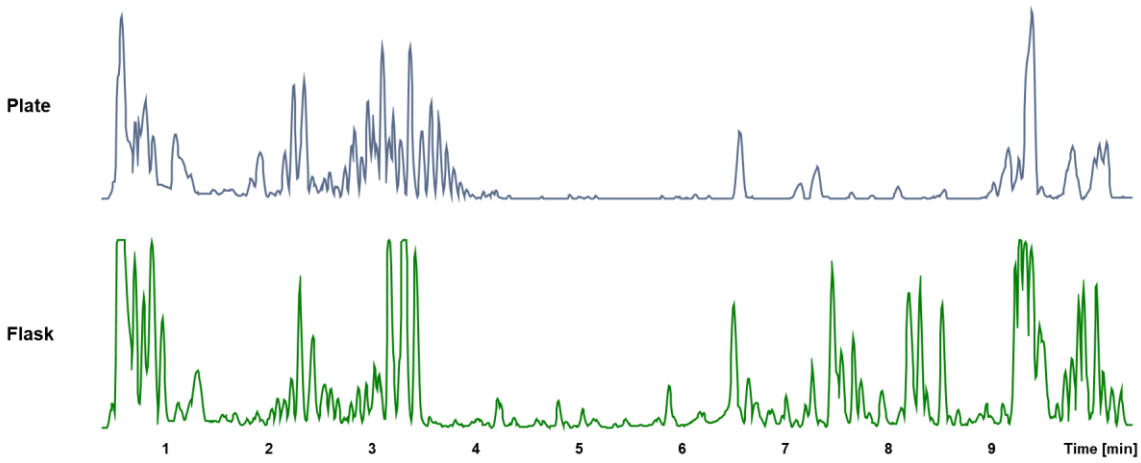

Figure S 5.14: Comparison of the metabolome of MSr12523 in 2SWT medium, cultivated in a 24 deep-well plate and in a shaking flask.

Sorangium sp. NOSO3

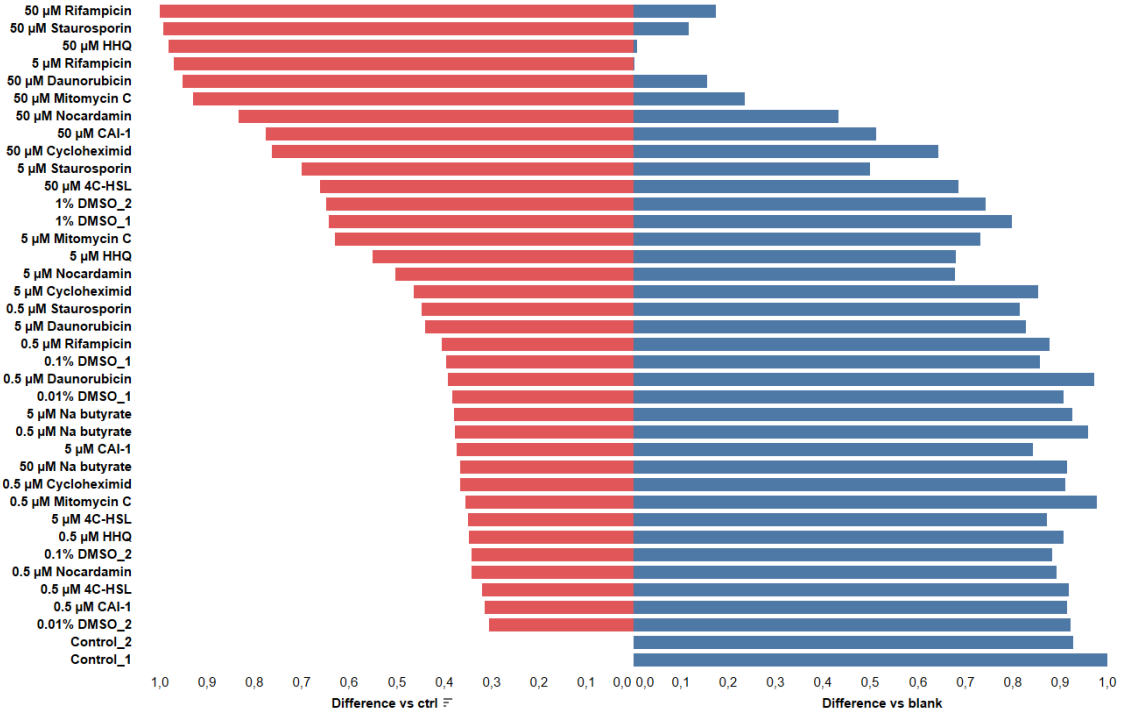

Figure S 5.15: Relative difference of extracts of *Sorangium* sp. NOSO3 with added elicitors or DMSO compared to control cultivations and medium blanks.

Using the t-test/ANOVA routine of Metaboscape 2022b, the regulation of all features in *Sorangium* sp. NOSO3 cultivations with added elicitors or DMSO were compared to the control cultivation and visualised as volcano plots.

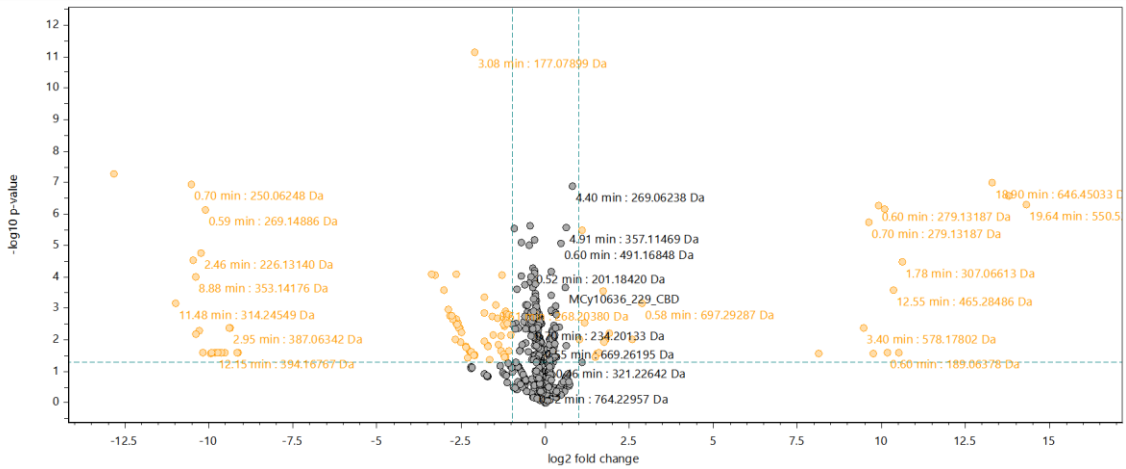

Figure S 5.16: Volcano plot of significance (-log10 p-value) versus fold change (log2 fold change) of *Sorangium* sp. NOSO3, cultivated with 0.5% DMSO compared to a control cultivation. Data points appearing towards the top of the plot indicate high significance; data points towards the left side of the plot indicate downregulation and towards the right side upregulation of features.

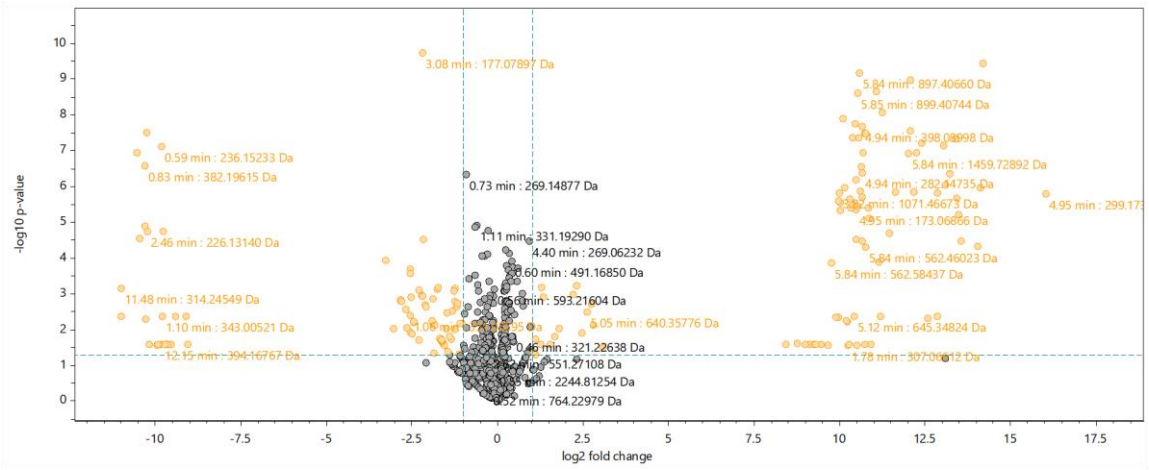

Figure S 5.17: Volcano plot of significance (-log10 p-value) versus fold change (log2 fold change) of *Sorangium* sp. NOSO3, cultivated with 50 µM cycloheximide compared to a control cultivation. Data points appearing towards the top of the plot indicate high significance; data points towards the left side of the plot indicate downregulation and towards the right side upregulation of features.

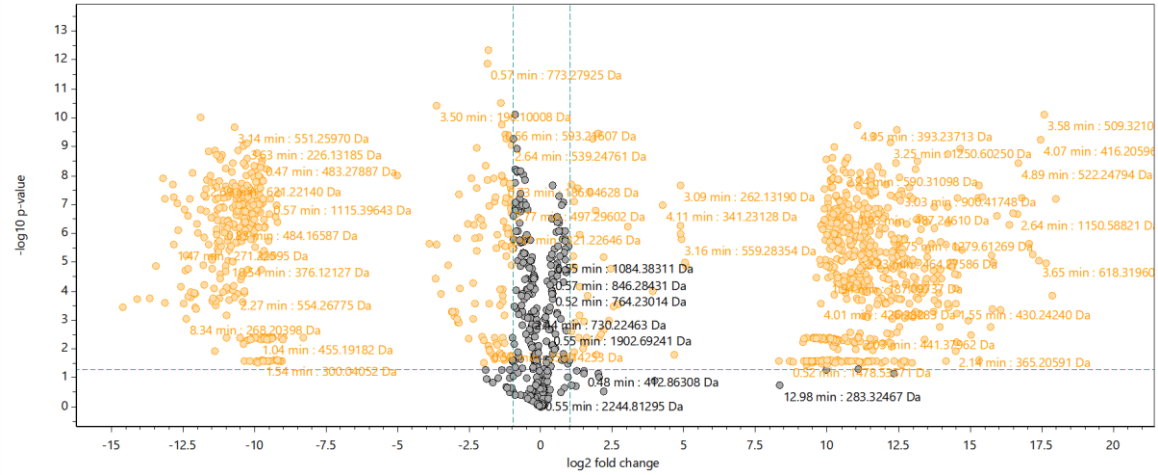

Figure S 5.18: Volcano plot of significance (-log10 p-value) versus fold change (log2 fold change) of *Sorangium* sp. NOSO3, cultivated with 5 µM mitomycin C compared to a control cultivation. Data points appearing towards the top of the plot indicate high significance; data points towards the left side of the plot indicate downregulation and towards the right side upregulation of features.

The regulation of all features in *Sorangium* sp. NOSO3 cultivations with added elicitors or DMSO compared to the control cultivation was calculated based on the t-test/ANOVA results. The observation of unique features in any cultivation setting was determined by analysing a feature table of all samples within the *Sorangium* sp. NOSO3 flask cultivation experiment.

Table S 5.6: Number of up- and downregulated, newly observed and lost features per cultivation condition *Sorangium* sp. NOSO3 compared to cultivation control and number of unique features for every cultivation condition.

Elicitor	Lost features	Downregulated features	Upregulated features	New features	Unique features
DMSO	21	56	12	13	0
Cycloheximide	24	60	16	75	65
Mitomycin C	312	97	41	576	504

The reproducibilities of features in any cultivation setting was determined by analysing a feature table of all samples within the *Sorangium* sp. NOSO3 flask cultivation experiment.

Table S 5.7: Reproducibilities of features within a cultivation condition in *Sorangium* sp. NOSO3 calculated as their presence in number of samples in three biological and two technical replicates.

Cultivation condition	In 6 samples	In 5 samples	In 4 samples	In 3 samples	In 2 samples	In 1 sample
Control	672	40	53	12	20	45
DMSO	633	29	40	27	24	69
Cycloheximide	640	56	53	43	68	29
Mitomycin C	825	84	98	15	18	24

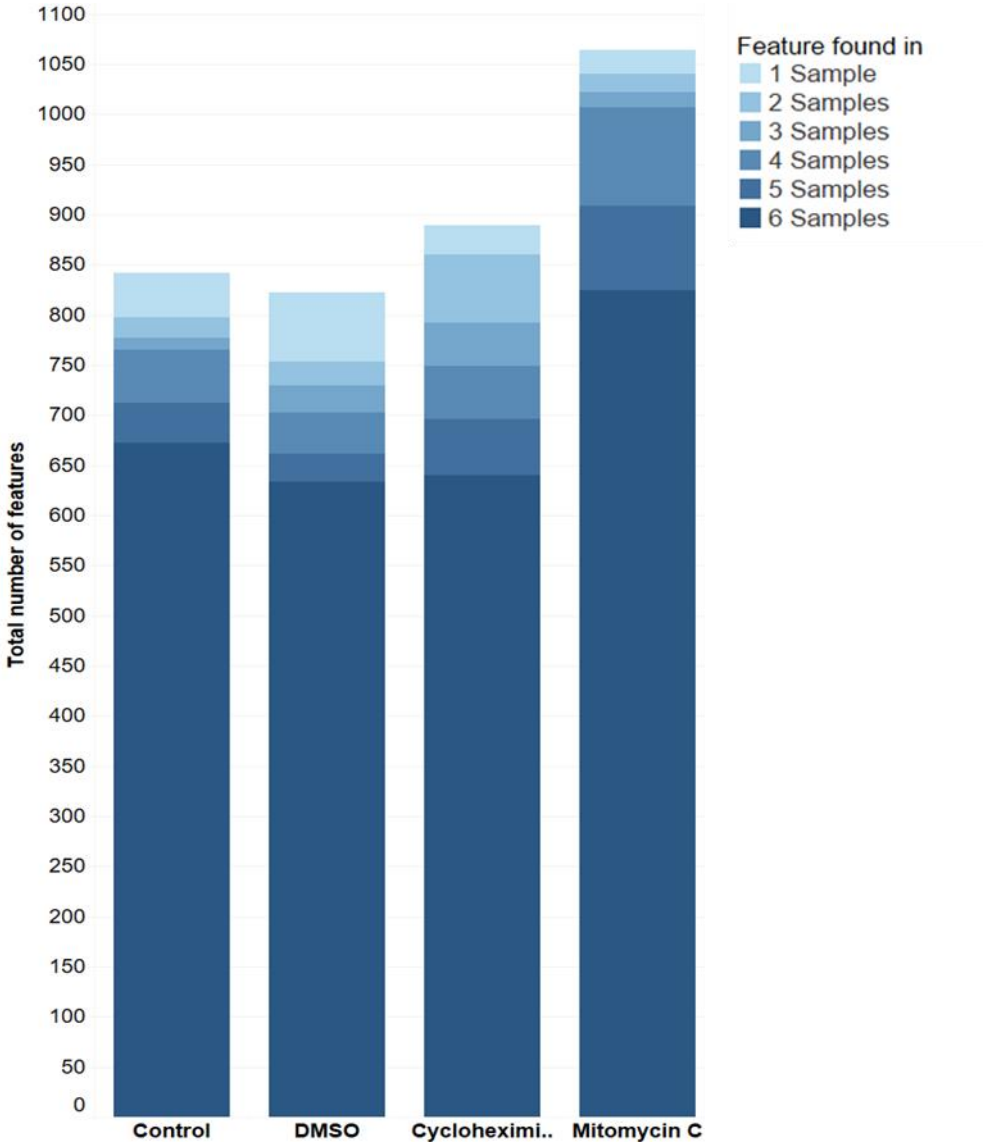

Figure S 5.19: Feature reproducibility of cultivations of *Sorangium* sp. NOSO3 control cultivations, with added DMSO and added elicitors. Occurrence of features in three biological and two technical replicates for each cultivation condition.

Nannocystis exedens Na e487

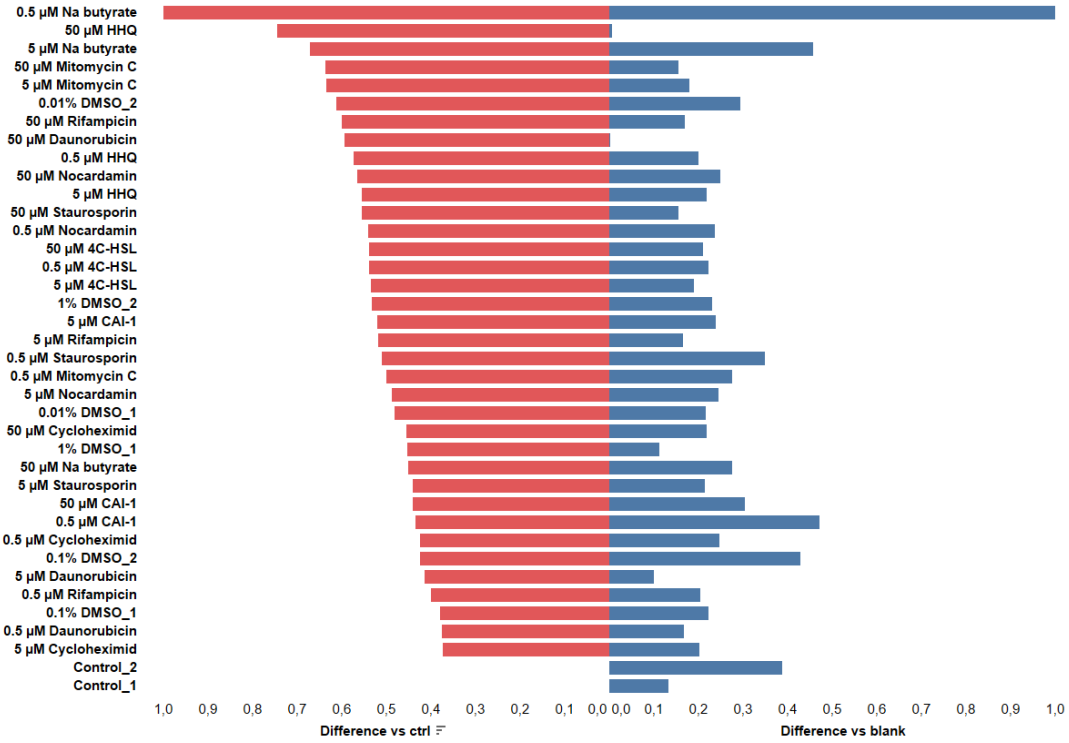

Figure S 5.20: Relative difference of extracts of *Nannocystis exedens* Na e487 with added elicitors or DMSO compared to control cultivations and medium blanks.

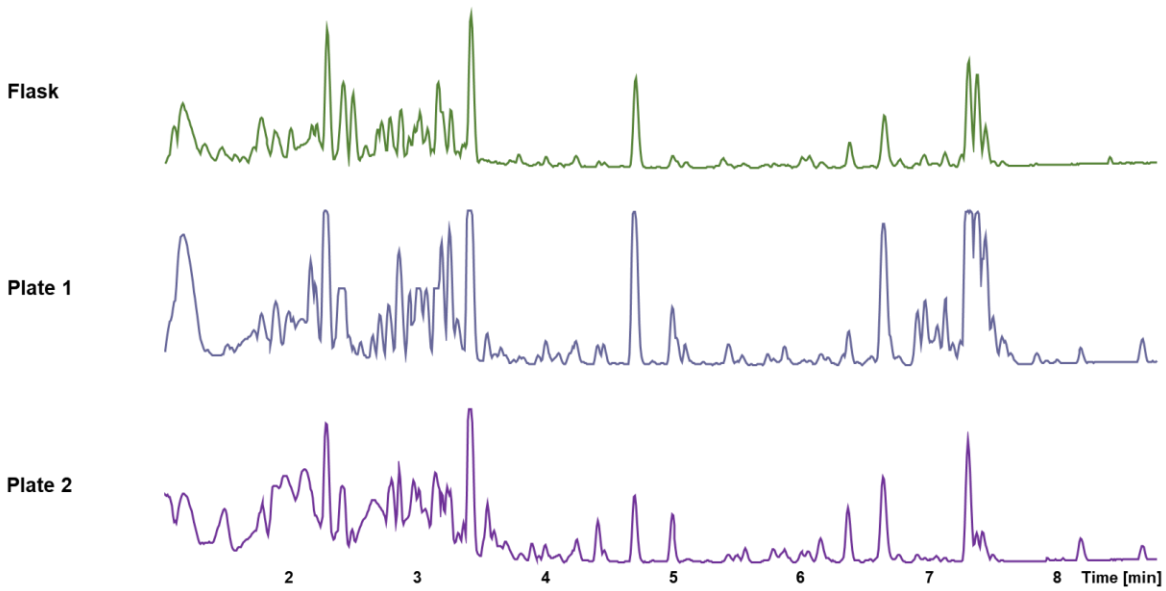

Figure S 5.21: Comparison of the metabolome of Na e487 in 2SWT medium, cultivated in a shaking flask and two individual 24 deep-well plates.

Using the t-test/ANOVA routine of Metaboscape 2022b, the regulation of all features in *Nannocystis exedens* Na e487 cultivations with added elicitors or DMSO were compared to the control cultivation and visualised as volcano plots.

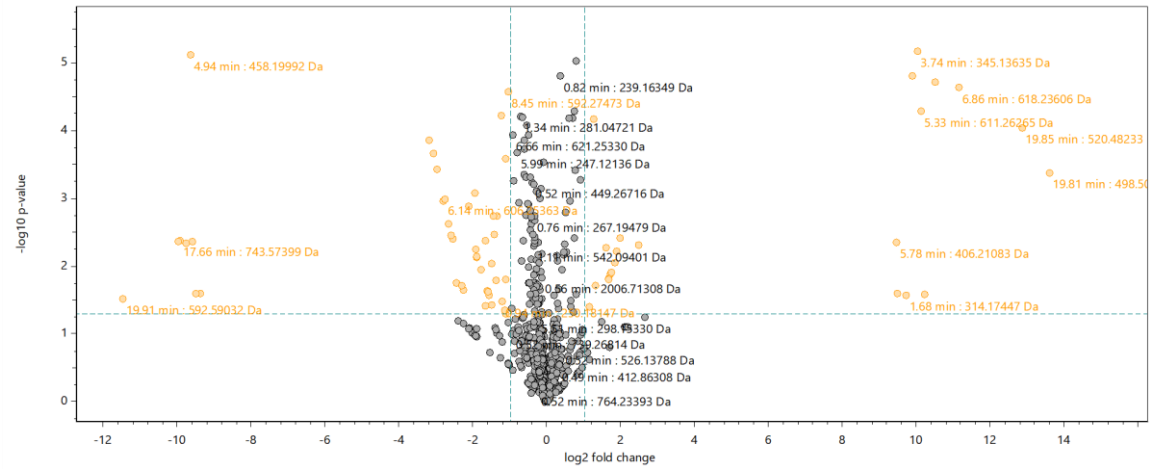

Figure S 5.22: Volcano plot of significance (-log10 p-value) versus fold change (log2 fold change) of *Nannocystis exedens* Na e487, cultivated with 0.5% DMSO compared to a control cultivation. Data points appearing towards the top of the plot indicate high significance; data points towards the left side of the plot indicate downregulation and towards the right side upregulation of features.

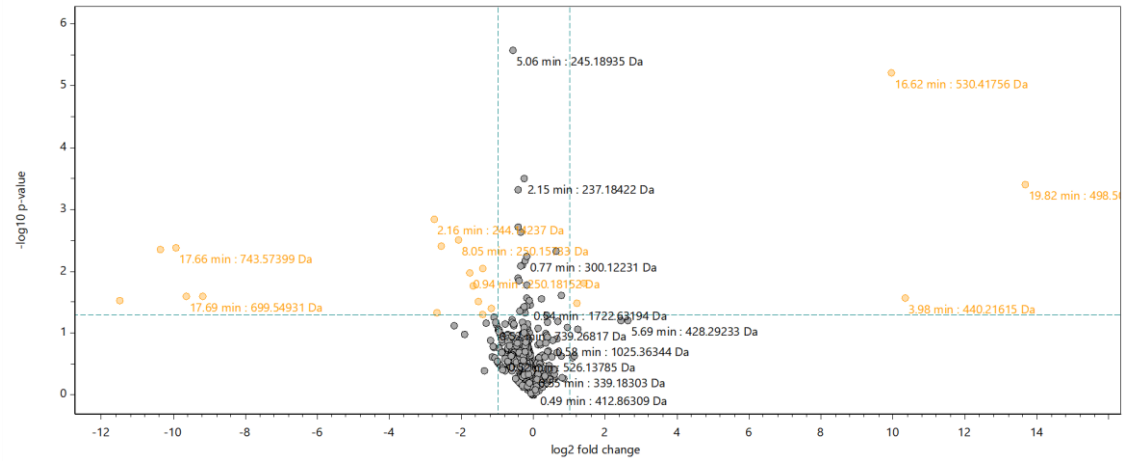

Figure S 5.23: Volcano plot of significance (-log10 p-value) versus fold change (log2 fold change) *of Nannocystis exedens* Na e487, cultivated with 5 µM Na butyrate compared to a control cultivation. Data points appearing towards the top of the plot indicate high significance; data points towards the left side of the plot indicate downregulation and towards the right side upregulation of features.

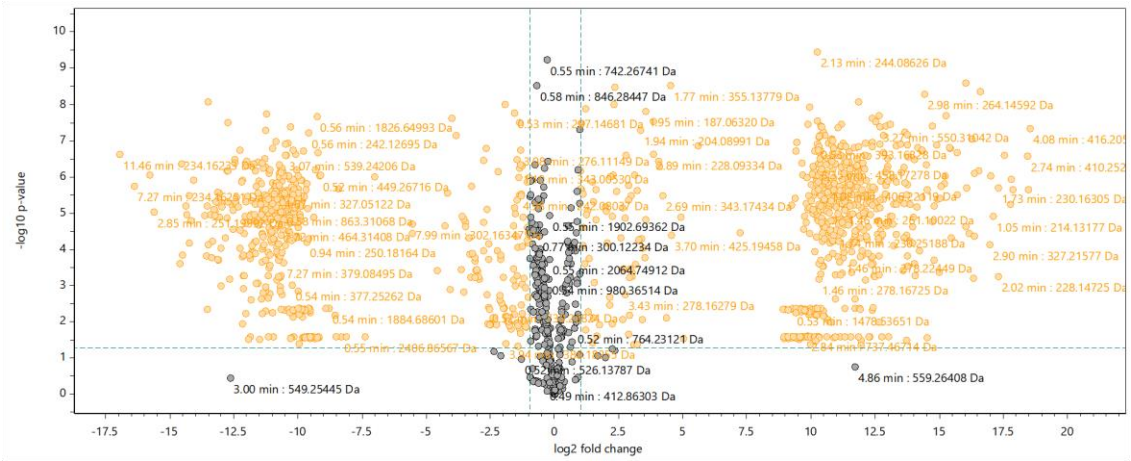

Figure S 5.24: Volcano plot of significance (-log10 p-value) versus fold change (log2 fold change) *of Nannocystis exedens* Na e487, cultivated with 5 µM staurosporin compared to a control cultivation. Data points appearing towards the top of the plot indicate high significance; data points towards the left side of the plot indicate downregulation and towards the right side upregulation of features.

The regulation of all features in *Nannocystis exedens* Na e487 cultivations with added elicitors or DMSO compared to the control cultivation was calculated based on the t-test/ANOVA results. The observation of unique features in any cultivation setting was determined by analysing a feature table of all samples within the *Nannocystis exedens* Na e487 flask cultivation experiment.

Table S 5.8: Number of up- and downregulated, newly observed and lost features per cultivation condition *Nannocystis exedens* Na e487 compared to cultivation control and number of unique features for every cultivation condition.

Elicitor	Lost features	Downregulated features	Upregulated features	New features	Unique features
DMSO	8	35	12	11	4
Na butyrate	5	10	2	3	0
Staurosporin	420	117	77	543	522

The reproducibilities of features in any cultivation setting was determined by analysing a feature table of all samples within the *Nannocystis exedens* Na e487 flask cultivation experiment.

Table S 5.9: Reproducibilities of features within a cultivation condition in *Nannocystis exedens* Na e487 calculated as their presence in number of samples in three biological and two technical replicates.

Cultivation condition	In 6 samples	In 5 samples	In 4 samples	In 3 samples	In 2 samples	In 1 sample
Control	765	61	52	23	25	31
DMSO	738	51	66	27	26	47
Na butyrate	671	79	75	59	42	18
Staurosporin	814	69	77	16	36	32

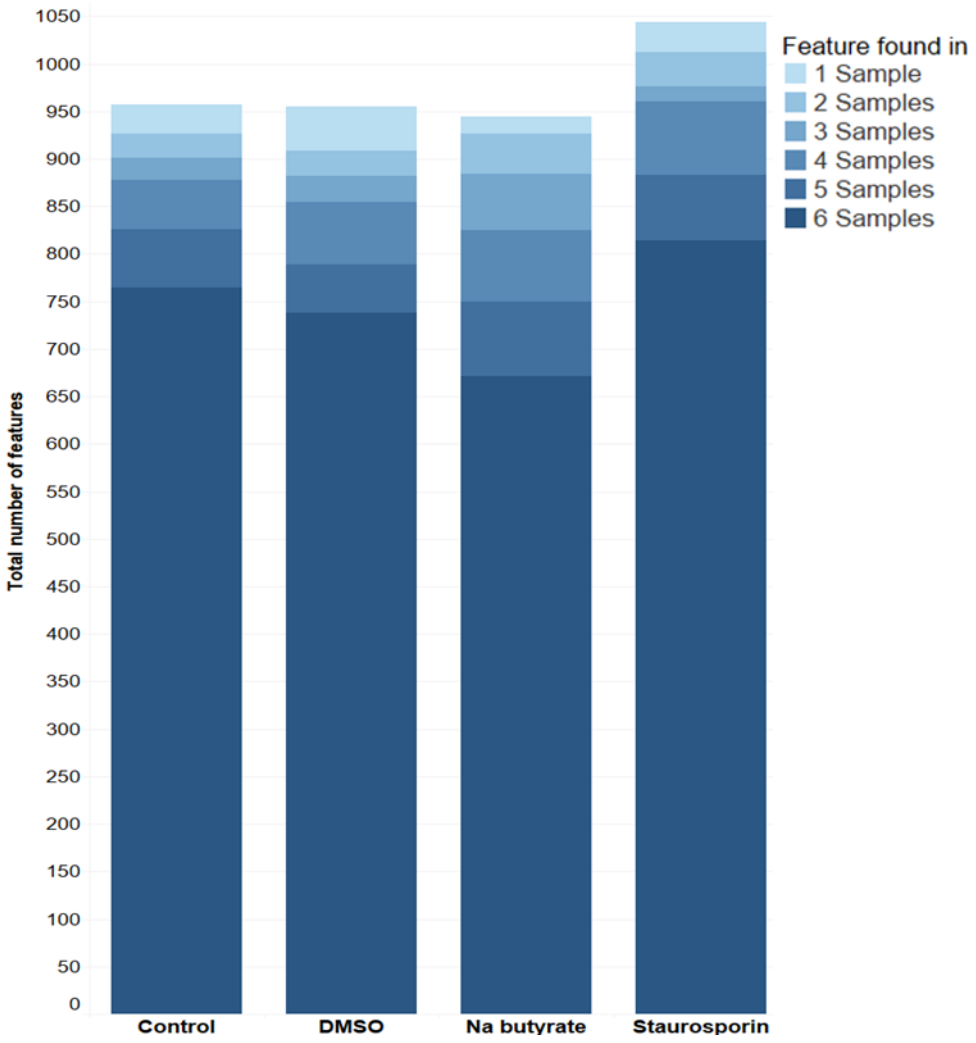

Figure S 5.25: Feature reproducibility of cultivations of *Nannocystis exedens* Na e487 control cultivations, with added DMSO and added elicitors. Occurrence of features in three biological and two technical replicates for each cultivation condition.

References

1. Picache, J. A. *et al.* Collision cross section compendium to annotate and predict multi-omic compound identities. *Chem. Sci.* **10,** 983–993; 10.1039/c8sc04396e (2019).
2. Hoffmann, T. *et al.* Correlating chemical diversity with taxonomic distance for discovery of natural products in myxobacteria. *Nat. Commun.* **9,** 803; 10.1038/s41467-018-03184-1 (2018).
3. Galili, T., O'Callaghan, A., Sidi, J. & Sievert, C. heatmaply: an R package for creating interactive cluster heatmaps for online publishing. *Bioinformatics (Oxford, England)* **34,** 1600–1602; 10.1093/bioinformatics/btx657 (2018).
4. Wang, M. *et al.* Sharing and community curation of mass spectrometry data with Global Natural Products Social Molecular Networking. *Nat. Biotechnol.* **34,** 828–837; 10.1038/nbt.3597 (2016).
5. Nothias, L.-F. *et al.* Feature-based molecular networking in the GNPS analysis environment. *Nat Methods* **17,** 905–908; 10.1038/s41592-020-0933-6 (2020).

6 Discussion and outlook

In the 21st century, the interest in microbial natural products as a promising source for novel drugs is on the rise again, as advancements in different scientific disciplines started to resolve the three major shortcomings of natural product discovery in the past century.

“First, most screening efforts were built around Actinomycetes, largely ignoring the biosynthetic and antibiotic potential of other microorganisms. Second, the hidden or cryptic biosynthetic potential of microorganisms (including Actinomycetes) was not known. This only changed when complete genome sequences of organisms became available. For example, the genome sequence of the well-studied bacterium *Streptomyces coelicolor* revealed that the number of biosynthetic gene clusters (BGCs) by far exceeded the number of natural products previously connected to the strain (Bentley et al, 2002). In routine cultivation settings, most microorganisms produce natural products that account only for fewer than 10% of their BGCs (Katz & Baltz, 2016). Third, with insufficient analytical methods and computational resources it was impossible to quickly de-replicate extracts of newly cultivated microorganisms for known natural products. Without this knowledge, it was difficult to directly de-prioritise extracts featuring known antibiotics or to estimate whether those extracts contained additional antibiotics.”[1]

With their capability to produce chemically diverse natural products with fascinating biological activities and their immense biosynthetic potential, myxobacteria are among the promising sources for natural product-based drug research[2–4]. Furthermore, the phylogenetic and biosynthetic potential of myxobacteria is far from exhausted with the currently known taxa and purified natural products[5,6]. Based on the myxobacteria that were cultivated and strategies that were applied in this thesis, I will discuss approaches to find novel and bioactive natural products from myxobacteria in section 6.1.

Furthermore, the previously unknown anti-protozoal bioactivities of the angiolam scaffold (chapter 2) and the potent antibiotic activities of several myxenolone derivatives against *Mycobacterium tuberculosis* demonstrate the opportunity of discovering unknown bioactivities in known and deprioritised natural product scaffolds. Therefore, the opportunities of revisiting old and known natural product scaffolds will be discussed in section 6.2.

6.1 Strategies to find novel and bioactive natural products in myxobacteria

In the course of this thesis, the metabolomes of different myxobacteria, ranging from the model organism *Myxococcus xanthus* DK1622 to the recently isolated and phylogenetically distinct *Pendulispora* sp. MSr12523 were evaluated for (novel) natural products, preferably with unknown biological activities. Based on the observed discrepancy between the numbers of BGCs encoded in the genomes of these myxobacteria and the number of observed compound families in standard cultivation crude extracts, different strategies to trigger or enhance the production of cryptic or poorly expressed BGCs were applied in chapters 3 to 5. Comprehensive screening campaigns for variations in the detected metabolome of myxobacteria usually require a lot of space for strain cultivation, manual work for extract preparation and measurement time to analyse the resulting extracts. In order to address these limiting factors, the higher throughput elicitor screening platform was developed and evaluated for its capability to reliably identify elicitors or cultivation conditions worthy of closer investigation.

Considering the findings presented in this thesis and the current literature, the following three sections will cover, evaluate and propose strategies that might increase the chances to find novel and bioactive natural products from myxobacteria

6.1.1 Increasing the phylogenetic diversity to find novel chemistry

As of 2018, the reported phylogeny of cultivated myxobacteria comprised 58 species, distributed over 29 genera[5]. Considering a report about the collection of myxobacteria at the Helmholtz-Centre for Infection Research (HZI), the majority of cultivated myxobacteria belong to the frequently isolated genera *Corallococcus*, *Myxococcus*, *Nannocystis* and *Sorangium*[2]. The capability of myxobacteria to produce a wide array of natural products is demonstrated by multiple compound families that were purified from - or observed in - cultures of different genera belonging to all three of the myxobacterial suborders[6]. Investigating further representatives of well-studied species can still lead to the discovery of novel natural products as displayed by the observation of strain specific compounds and strong variations in the detected metabolites in a study of intraspecific diversity of 98 *M. xanthus* strains[7].

However, a comprehensive analysis with about 2300 strains displayed a clear correlation between the taxonomic distance and chemical diversity in myxobacteria[8]. Therefore, it is

evidently more fruitful to invest more effort into the investigation of novel or understudied myxobacterial taxa. Good examples for the promise of finding novel chemical scaffolds in understudied myxobacterial taxa are the myxenolones and other natural products discovered by investigating several representatives of the family *Pendulisporaceae*[9,10], and metabolites recently reported from *Sandaracinus defensii*[11,12].

The observed phylogenetic diversity in samples from different geographic locations is much greater than the number of subsequently isolated myxobacteria[13,14]. Although the number of cultivated myxobacterial taxa at HIPS is far greater than the published ones (R. Garcia and R. Müller, unpublished), many more taxa have evaded isolation so far. In an attempt to increase the chances to isolate further myxobacterial taxa, a metagenomics-based workflow is currently developed in our lab to prioritise soil samples, based on the observation of unknown or understudied myxobacteria (D. Krug, personal communication).

In a recent metagenomics study on the small subunit rRNA-inferred abundance of preying microorganisms in different soils, *Myxococcaceae*, the family of the frequently isolated genera *Corallococcus* and *Myxococcus*, presented only a very small fraction of the observed myxobacteria. Instead, the rarely isolated *Haliangiaceae* presented the biggest fraction of detected myxobacteria in all tested soil samples and also further rarely isolated families like *Sandarinaceae* or *Phaselicystidaceae* made up a surprisingly big share of detected myxobacteria in some soil samples[15]. The often applied workflow to isolate myxobacteria uses dried soil samples and nutrient-poor agar plates with microorganism or cellulose as a bait to favour spore-forming and swarming myxobacteria over other, competing soil-dwelling microbes[2,5,16] (Figure 6.1A). While this strategy strongly reduces the growth of undesirable microorganisms, it is rather unsuitable for isolating myxobacteria that either are not present as spores at that time or require more nutrients to grow[5].

Many factors like the used bait, the isolation agar and its pH, illumination or temperature can influence the isolation of myxobacterial taxa out of an environmental sample. Moreover, isolation plates must be investigated regularly for myxobacterial swarms or fruiting bodies, because it can take several weeks to a few months until slow-growing representatives of the suborders *Sorangiineae* and *Nannocystineae* might be detected. In addition to this labour-intensive and time-consuming workflow, researchers who want to isolate myxobacteria need to be familiar with their morphology and taxonomy to recognise myxobacterial swarms or fruiting bodies[16].

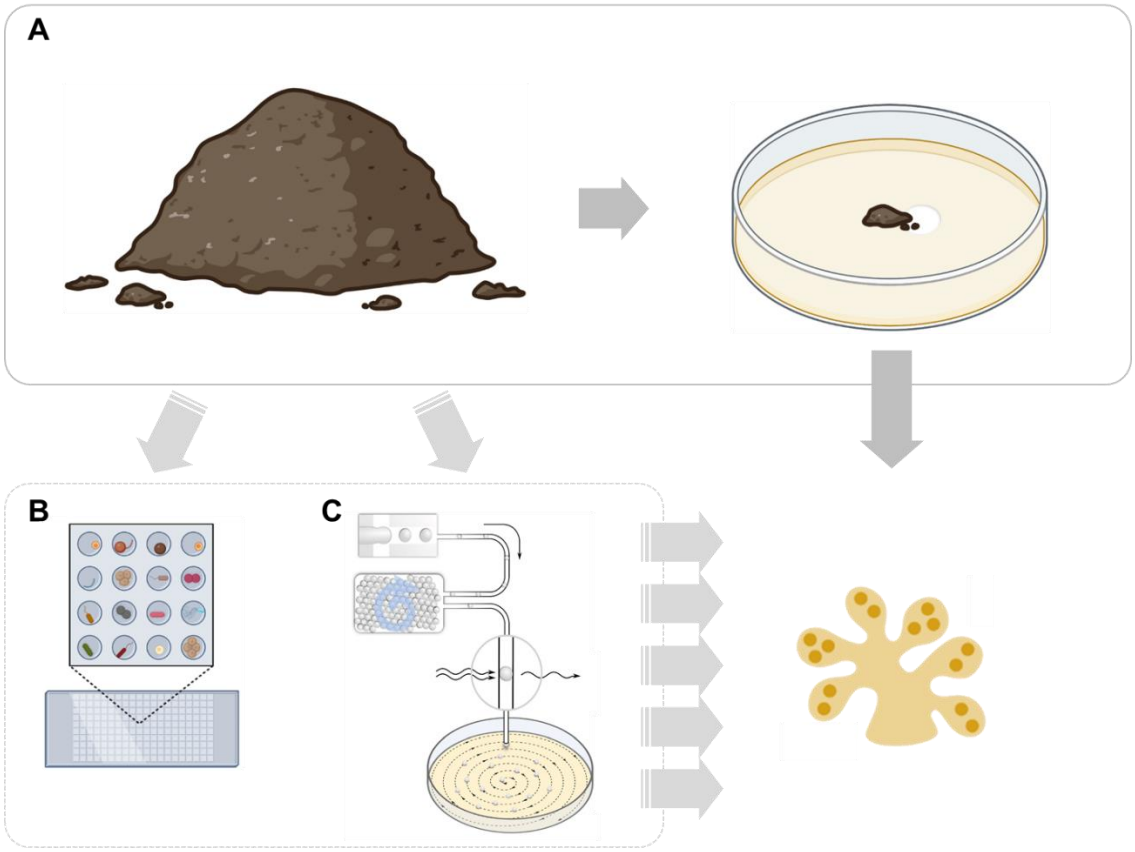

Figure 6.1: Isolation of myxobacteria from soil samples. (**A**) Conventional isolation workflow on agar plates. Adaption of the ichip (**B**) and microdroplet (**C**) isolation methods could increase the throughput of strain isolation. The microdroplet isolation workflow was taken from Mahler *et al.*[17]

In the past decade, the isolation chip (ichip) and microdroplet cultivation were introduced as miniaturised high-throughput platforms for the improved isolation of a diverse set of bacteria[17,18]. So far, these methods have not led to reports about the isolation of myxobacteria. This may be attributed to the fact that many myxobacterial taxa display a very long lag phase when cultivations are started with a low cell density. However, with adapted sample preparations and the use of cultivation conditions that favour their growth at low initial density, these methods might display an opportunity to facilitate the isolation of myxobacteria (Figure 6.1B and 6.1C). Considering the high amounts of isolated microorganisms such high-throughput workflows could produce, software-assisted workflows to prioritise potential myxobacterial isolates need to be developed for an efficient analysis. The recently reported MALDI-TOF MS-based IDBac workflow might be a possible way to efficiently identify myxobacteria and other interesting bacterial taxa[19]. A non-destructive possibility to identify myxobacteria within the isolates might be an adaptation of the microscopy-based bacterial cytological profiling workflow that was used to identify cellular pathways targeted by antibiotics[20]. Given the recent advances in bioinformatics and machine learning, an automated prioritisation of isolates with

myxobacteria-like behaviours like swarming or fruiting body formation should be achievable.

6.1.2 Improving the chemical output of myxobacteria by harnessing their cryptic biosynthetic potential

In addition to their remarkable social behaviour and their large genomes with many BGCs, many myxobacteria produce more than one family of natural products in standard cultivation settings[6,21]. Some well-studied myxobacteria like *M. xanthus* DK1622, *Chondromyces crocatus* Cm c5 or *Stigmatella aurantiaca* Sg a15 are known to produce eight or nine different reported compound families, respectively[6]. However, even in these extensively investigated organisms, about two thirds of the observed BGCs could not be linked to natural products yet[22].

As the observation that the majority of the observed BGCs cannot be linked to the production of natural products repeats for many microorganisms[23–25], a plethora of methods and strategies have been developed to enable or increase the production of such cryptic metabolites [26]. Interestingly, many of the methods, which can be used to find cryptic metabolites have been used in different myxobacteria to increase the production of known metabolites or to find or verify their biosynthesis.

Although the work described in this thesis only covers a subset of these methods, some of the previously evaluated and most promising cultivation-based and molecular-biological strategies to unlock the cryptic biosynthetic potential in myxobacteria will be discussed in the following sections (Figure 6.2).

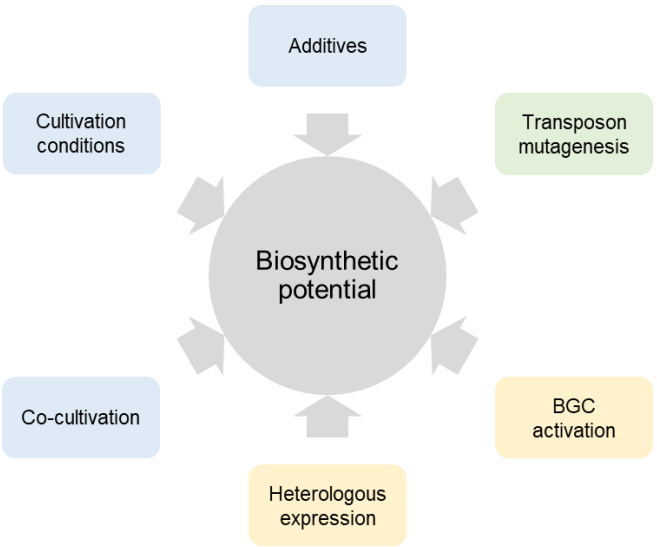

Figure 6.2: Different strategies to exploit the biosynthetic potential of myxobacteria.

6.1.2.1 **Cultivation-based strategies**

Based on the chapters 3 to 5 of this thesis and the applicability for myxobacteria, the cultivation-based strategies are here divided into the classical OSMAC-style methods such as changing cultivation media and physical parameters, the co-cultivation with other microorganisms and the addition of small-molecule elicitors or other cues.

The undoubtedly simplest approach to affect the metabolome of a microorganisms is to change the cultivation medium or ingredients of the medium. Consequently, evaluation of the effect of different cultivation media on the production of the angiolam scaffold identified RG5 as a good production medium for these compounds in chapter 2. Similarly, production levels of myxovalargins were strongly influenced by the choice of cultivation media[27], and the heterologous expression of the myxobacterial antibiotics corallopyronin and myxopyronin displayed much higher yields in optimised production media[28]. Moreover, the addition of biosynthetic precursors or co-factors for enzymes can shift the biosynthesis towards the production of one or few derivatives, as displayed for angiolams D and F or several argyrin congeners[29].

Additionally, the cultivation in different media can lead to the production of new and bioactive natural products as displayed by the discovery of the sorangicin P subclass in chapter 3. Interestingly, there are only very few reports about the observation of novel natural products through a change of the cultivation media in myxobacteria and they have to date not resulted in the purification of one of these compounds[30,31]. In other microorganisms like Actinomycetes, marine bacteria or fungi changes in cultivation media and their composition have reportedly led to the discovery of many novel metabolites[32–34].

In addition to the reported effects on the production of different natural products, the importance of the cultivation medium for myxobacterial natural product discovery is demonstrated by the fact that 14 different cultivation media were used for the purification of 17 compound families that were reported between 2018 and 2022[10]. Therefore, a more comprehensive investigation of the effects of a range of cultivation media on the metabolomes of different myxobacterial taxa might be a promising endeavour to increase the chemical output from myxobacteria.

Next to the type and composition of cultivation medium, the variation of physical parameters like cultivation vessel, illumination, temperature and aeration are easily accessible[32]. Although the effects of physical parameters on the metabolome of myxobacteria were not investigated in the course of this thesis, the metabolome of MSr12523 was strongly effected by several cultivation vessels as observed and reported in chapters 3 and 5. The strongly reduced production of the sorangicin P subclass during

upscaling to 5 L shaking flasks is a recurring observation in myxobacteria. In some occasions novel natural products can only be purified from cultivations in standard 300 mL shaking flasks as exemplified by the macyranones[35] and myxofacyclines[36]. On the other hand, the good production of sorangicin P in 2 L fermenters in chapter 3, and observed variations of the metabolomes of MSr12523 (own unpublished observation, data not shown) after cultivating in standard, Fernbach and Ultra Yield flasks, demonstrate the effects of cultivation vessels and their aeration efficiency on the production of natural products in myxobacteria.

So far, the knowledge about the effect of further physical parameters on the production of natural products in myxobacteria is very limited. However, a recent study has demonstrated the impact of cultivation on the detected metabolome of one myxobacterial strain at different temperatures, under constant illumination or with limited oxygen supply[10]. Considering these findings alongside the published effects of small temperature changes on the production levels of validamycin A[37], or a short heat shock on the production of jadomycin B[38], the comprehensive investigation of the effects of physical parameters on the metabolomes of myxobacteria should be pursued further to potentially develop the approach into a useful tool for the discovery of novel natural products.

Taking into account the complex social behaviour of many myxobacteria, such as swarming and fruiting-body formation when cultivated on solid media[39], it seems plausible that the observed metabolome of myxobacteria in this setting differs from the one in standard cultivation in liquid media. This consideration is verified by the observation that, depending on the investigated myxobacterial strain, 68-91% of LC-MS features from solid cultivation extracts cannot be found in liquid cultivation extracts of the same strain[40]. However, the purification of natural products from solid cultivation settings is very cumbersome and so far, only one compound family, the homospermidine lipids, has been purified from myxobacteria in this cultivation setting[41]. In an attempt to facilitate the investigation and purification of myxobacterial natural products unique to solid media cultivation settings, the solid-liquid cultivation platform “Flow plate” is currently developed in our laboratory[42]. The “Flow plate” aims to concentrate such metabolites in a reservoir of liquid medium that is constantly pumped underneath the solid cultivation layer. Further evaluation of this platform will show if it can become a default method for the purification of natural products that are only observed in cultivations on solid media.

As microorganisms have to share their natural habitat with other microbes, the co-cultivation of two or more microbial strains is probably the most natural approach to trigger the production of cryptic metabolites in laboratory cultivation settings. However, one of the biggest problem in microbial co-cultivation is to find a successful combination

of microbes for the reproducible production of natural products[43]. The purification of antibiotic myxenolones from co-cultivation extracts of *Pendulispora* sp. MSr12523 with *Tsukamurella pseudospumae*, described in the thesis of Markus Neuber[42] and in chapter 4 of this thesis, is the first co-cultivation study leading to the isolation of novel bioactive natural products in myxobacteria. The positive effects of co-cultivation on the production of bioactive compounds in myxobacteria was already demonstrated by increased levels of epothilones in intra-species co-cultivations of *S. cellulosum* strains[44]. Furthermore, cultivations of *M. xanthus* DK1622 with *Streptomyces coelicolor* increased the production of the siderophore myxochelin[45], and in a co-cultivation of *M. xanthus* DK1622 with *Escherichia coli* on agar plates the abundance of some myxobacterial natural products was highest in the predation zone between both strains[46]. Looking at the effects of *T. pseudospumae* and other mycolic acid containing bacteria (MACB) on the metabolomes of MSr12523 and related myxobacteria[42], they should be evaluated for their potential effects on further myxobacterial taxa. The success rates of MACB to alter the metabolomes of *Streptomyces* strains[47] and the reports of successful co-cultivations with other Actinomycetes[48] might indicate that these bacteria have a great capability to effect the production of natural products in other microbes.

However, the combined cultivation of two or more microorganisms is often hard to control[26,43]. As every co-cultivation set-up needs optimisation, higher throughput screening efforts for novel bioactive natural products might proof difficult. In some Actinobacteria, the positive effects of co-cultivation on the metabolome could be traced back to single molecules[49–51]. Co-cultivations with myxobacteria are much less studied, but the addition of autoclaved pellets or filtered supernatants of other microbes resulted in some changes in several myxobacterial strains[30,31,42]. Therefore, it might be interesting to further investigate the possibility to use the culture supernatants or inactivated cells of partner strains for the activation of cryptic BGCs in myxobacteria.

Although the report about mitomycin C triggering the production of the bacteriocin xanthacin in *M. xanthus* fb dates back almost 50 years[52], the effects of (small molecule) additives on the metabolome of myxobacteria have been researched very sparsely. The development and evaluation of a higher-throughput elicitor screening platform described in chapter 5 was a first attempt to implement a platform to screen for additives, which trigger the production of cryptic metabolites in myxobacteria. While the initial screening step in 24 deep-well plates should be optimised for a better reproducibility and analysability, it still pointed towards two potent elicitors of the secondary metabolism in *M. xanthus* DK1622. The capability of staurosporin and mitomycin C to effect the detected metabolome of *M. xanthus* DK1622 and other myxobacteria was verified in flask cultivations and led to the observation of several molecular networks that could not be

observed in untreated cultivation conditions. Interestingly, similar to the findings in elicitor screening campaigns with *Streptomyces*[53] or *Burkholderia*[54], these molecules were toxic for myxobacteria in high concentrations but elicited changes in the metabolomes in low concentrations. In addition to small molecules, other additives like organic solvents, rare earth elements or soil extract have been shown to lead to the production of novel natural products in myxobacteria[10,30,31]. The capability of small molecules and other additives with known and unknown effects on the tested microbes to enable the production of cryptic metabolites are also established for other microorganisms[26,33,34].

One big advantage of employing additives to elicit the expression of cryptic BGCs is the simplicity of the approach, as observed variations in the metabolome are related to the respective additive. This simplicity enables high-throughput screens for metabolome-altering additives, using simple readouts in order to prioritise the most promising elicitors. Building on the observations and results of the higher throughput elicitor screening platform in chapter 5, a high throughput screening platform for promising additives in myxobacteria could be developed.

6.1.2.2 **Molecular-biological strategies**

Different molecular-biological methods have been used in myxobacteria to improve the production of natural products of interest, to find and manipulate their biosynthetic pathways, and to discover novel compounds. The majority of these strategies target the activation or heterologous expression of chosen BGCs. Nevertheless, untargeted transposon-based manipulations have been successfully applied to find the biosynthetic pathways of several myxobacterial natural products.

Activation of the respective BGCs with constitutive or inducible promoters in myxobacteria led to the discovery and description of the pyxidicyclines in *Pyxidicoccus fallax* An d48[55], the sandarazols in *Sandaracinus defensii* MSr10575[12] and the alkylpyrones in *M. xanthus* DK1622[56]. Moreover, the same strategy was applied to improve the production of myxobacterial natural products to facilitate their purification, such as the myxofacyclines[36] or the myxoprincomides[57]. Although the activation of BGCs in their native host has the advantage that all needed precursors and cofactors are available[26], it cannot be realised in some myxobacterial taxa due to the lack of functioning genetic tools[58,59].

Interesting BGCs, which are found in the genomes of genetically intractable, difficult to cultivate or slowly growing myxobacteria can be heterologously expressed in genetically amenable and fast growing myxobacteria like *M. xanthus* DK1622[60]. The heterologous

expression of unknown myxobacterial BGCs led to the discovery of the sorangibactins[61] and alkylpyrones[56]. Furthermore, heterologous expression was used to increase the yields, study and manipulate or verify the biosynthesis of a variety of myxobacterial natural products. Successful examples of heterologously produced and studied natural products from myxobacteria include the antibiotics cystobactamid[62] and corallopyronin[63], the cytotoxic epothilones[64] and disorazols[65] or biosynthetically or structurally rare scaffolds like myxarylin[66] and the myxofacyclines[36]. Notwithstanding the many instances of successful heterologous expression of BGCs from myxobacteria, it can be difficult to achieve for large BGCs and may involve reorganisation and gene synthesis as shown for the heterologous expressions of cystobactamid[62] and myxovalargin[67]. Moreover, some biosynthetic pathways in myxobacteria seem to be organised in “split-clusters”, where one or more genes that are needed for distinct biosynthetic steps are located somewhere else in the genome instead of being part of the BGC[68,69]. These observations may help to explain the low success rates to heterologously express unknown myxobacterial BGCs in *M. xanthus* DK1622 in a recent study[70] or the lack of a heterologous expression system for the well-studied antibiotic sorangicin A[69].

The biggest advantage of these methods to activate or heterologously express BGCs of interest is the focus on potentially promising natural products, for instance based on the observation of putative self-resistance genes or interest in the underlying biosynthetic pathway[71]. This targeted approach allows researchers to dedicate their efforts to natural products that are more likely to possess biological activities or belong to a certain group of compounds. However, in particular the heterologous expression requires a comprehensive analysis of the BGC and the development of tailored cloning strategies that are often unique to the respective BGC[71,72]. The time-consuming planning and preparation work that has to be done before a novel natural product might be produced restricts the throughput of targeted molecular-biological strategies to discover novel natural products[72].

In the past years, transposon-guided mutagenesis has been established as an untargeted molecular-biological strategy to unlock cryptic BGCs in *Streptomyces* and *Burkholderia*.[73–76]. Interestingly, transposon-based mutagenesis was used to find the biosynthetic machineries of some myxobacterial natural products like tubulysin[77], disorazol[78] and sorangicin[69]. With improved analytical systems and chemoinformatic resources to analyse the resulting data, the transposon-guided mutagenesis seems a fruitful approach to unlock cryptic BGCs in genetically tractable myxobacteria. Furthermore, mutant strains with unusual chemical phenotypes could be evaluated for their mutation sites[77] in order to find BGC specific or pleiotropic regulators of secondary metabolism. Using this strategy, pathway-specific regulators could be discovered in

Sorangium cellulosum So ce56[79] and *Cystobacter fuscus* Cb f17.1[80], respectively. Similarly, in a comprehensive transposition mutagenesis of *Streptomyces coelicolor* more than 250 genes were identified that influence the production of the toxic pigment undecylprodigiosin[81].

6.1.2.3 Prioritising strategies to exploit the myxobacterial biosynthetic potential

With the arsenal of methods that could be used to better exploit the biosynthetic potential of myxobacteria, it is important to consider the strengths and limitations of the different strategies and to prioritise them based on the aim of the respective study. Pathway specific strategies, such as the activation of BGCs in their natural host or their heterologous expression, give researchers control about the biosynthetic pathways they intend to activate, and therefore allow estimates about the structure and potential biological activity of the resulting natural products[72]. Therefore these approaches are useful for the targeted activation of BGCs that were prioritised based on observations like self-resistance genes against antibiotic metabolites or the similarity to biosynthetic pathways that have led to the production of biologically active scaffolds[55,71,82]. Depending on the growth, manageability and genetic amenability of the natural host of the BGC, it could be activated in said host or heterologously expressed in a selected expression system like *M. xanthus* DK1622. However, targeted strategies are biased towards natural products with known resistance mechanisms or biosynthetic machineries, as the prioritisation of BGCs is based on the similarity to already described resistance mechanisms or promising chemical scaffolds[71]. Moreover, established targeted molecular-biological methods typically focus on a single BGC, which places all expectations on a single output in terms of compound production and anticipated biological activities and thus creates an inconvenient “make or break” scenario.

Untargeted or pleiotropic approaches on the other hand are a good strategy to exploit the biosynthetic potential of myxobacteria with many unknown BGCs. As it is difficult to predict the potential effect of such approaches on the metabolism of a given myxobacterium and whether an effect will lead to the production of novel and bioactive natural products[72], it is important to consider their applicability in high-throughput screenings, which increases the chance to discover metabolites with the desired properties. Although OSMAC style variations in medium composition or cultivation parameters are easily accessible and are likely to result in some changes of the observed metabolomes in many myxobacteria as shown in this thesis and other studies[10,30,31,42], their applicability in high-throughput screenings is limited. Screening campaigns in many

different media might be complicated by variations in growth rates of the strain and by the comparative evaluation of datasets with different matrices. Similarly, variations in physical parameters like temperature, illumination or aeration cannot be realised in a high throughput manner. Therefore, OSMAC-style experiments might be a good strategy to find cultivation conditions that are favourable for subsequent high-throughput screenings, such as a good growth in suspension or a high number of molecular features as an indicator of metabolic activity. Furthermore, OSMAC-style experiments could be used to increase the production levels of promising metabolites that were triggered in screening events.

Due to their demonstrated effects on the metabolomes of several *Pendulispora*[42] and many *Streptomyces* strains[47], co-cultivation with MACBs should be investigated as a possible strategy to access the biosynthetic potential of further myxobacterial taxa. Moreover, other microbes should be investigated for their capability to alter the myxobacterial metabolism in co-cultivation. However, as co-cultivations can be difficult to control, might have reproducibility issues and may lead to complex extracts with new metabolites produced by either partner strain, finding suitable partner strains for the co-cultivation with myxobacteria is hardly feasible in a high throughput manner. Instead, the supernatants or inactivated cells of a wide variety of microorganisms could be evaluated for their potential to alter the myxobacterial metabolism in high throughput screens.

With the simplicity in implementation and evaluation, the investigation of the effects of small-molecule elicitors, organic solvents or rare earth elements on the secondary metabolism of myxobacteria is superior for high throughput screening campaigns. As these experiments are usually performed in one cultivation medium, every observed change in the metabolome has to be caused by the tested additive. Furthermore, with reported effects on the metabolite production in myxobacteria, more complex additives like soil extract[10], or supernatants and inactivated cells of other microorganisms[30,31,42] could be investigated in a high throughput manner. Nevertheless, with these complex additives, the downstream comparative data evaluation procedure is prone to becoming much more sophisticated.

Similarly, a transposon-mutant library could be cultivated and screened for changes in the metabolome or biological activity in a high throughput manner.

As mentioned for the OSMAC-style cultivation experiments, the observed effects of all cultivation-based strategies to exploit the myxobacterial biosynthetic potential should be investigated for trends that could indicate a transferability of results from one strain to similar strains or even to strains from different myxobacterial taxa. In doing so, a set of cultivation conditions with encouraging success rates to alter the myxobacterial

secondary metabolism might be found or developed. Applying such promising conditions to many myxobacteria – provided they display a good growth and metabolite production in a multi-well plate setting – could provide an opportunity to greatly expand the known chemical space of this phylum. Furthermore, the molecular biolgical investigation of transposon-mutants with obvious changes in the secondary metabolome might lead to the discovery of regulators of the secondary metabolism in myxobacteria. Subsequently, the targeted manipulation of identified regulators in further myxobacteria might be another fruitful addition of the armoury of approaches to exploit the myxobacterial biosynthetic potential.

6.1.3 Considerations to implement a high-throughput screening platform into natural product discovery in myxobacteria

As discussed in the last section, several strategies to better exploit the biosynthetic potential of myxobacteria could be performed as high throughput screening. Based on the observations and findings in chapter 5 of this thesis, as well as examples of myxobacteria and other microorganisms in the literature, considerations for strain selection, cultivation setting, data collection and data evaluation are discussed in this section to implement a successful high-throughput screening platform.

In principle, any myxobacterial strain could be used for untargeted screenings to exploit their biosynthetic potential, since even in the best studied myxobacteria the products of the majority of BGCs are unknown[6,22]. However, the chances to find novel chemistry can be increased by focusing screening events on novel or understudied myxobacterial families or genera[8]. Furthermore, the number and potential novelty of BGCs could be evaluated with bioinformatic tools and databases like antiSMASH[83], BiG-SCAPE/CORASON[84] and MIBiG[85] to prioritise sequenced myxobacteria with a high number of unknown BGCs to increase the chances of finding novel natural products.

A basic prerequisite for the success of a high throughput screening campaign is that the corresponding strains can be cultivated in multi-deep-well plates and deliver reproducible productions of natural products in that setting. The successful cultivation of several myxobacteria in 24 deep-well plates, presented in chapter 5 of this thesis and further studies[27,31], displays the opportunity of high-throughput screening campaigns in a multi-well plate scale. The diminished production of natural products by *Pendulispora* sp. MSr12523 and low reproducibility in between cultivations with *Nannocystis exedens* Na e487, when cultivated in 24 deep-well plates display the importance of evaluating the behaviour of every strain in a multi-well scale prior to a screening event. Cultivation of

myxobacteria could be further miniaturised as demonstrated by recent successful cultivation experiments in our laboratory with 96 deep-well plates (Alexander Voltz, personal communication).

With the possibility to simultaneously produce hundreds of samples in high-throughput cultivations, a rapid prioritisation of potentially interesting additives or transposon mutants is needed (Figure 6.3). When aiming to find novel compounds with a certain biological activity, the prioritisation can be done based on the activity of samples against certain test organisms as displayed for high-throughput elicitor screening campaigns with *Streptomyces clavuligerus*[86] and further Actinomycetes[87]. However, some of the tested additives itself might display activities against the test organism, therefore lead to false positives or mask the activity of a newly produced natural product[88]. In the transposon-mutagenesis based discovery of the BGCs of disorazol or sorangicin in *S. cellulosum* So ce12, transposon mutants without the ability to produce the natural product of interest were determined by bioactivity assays[69,78]. In a similar way, this approach could be utilised for the discovery of bioactive natural products, connecting transposon mutants with newly produced natural products and bioactivities. However, bioactivity-based prioritisation is always biased towards novel natural products with a certain biological activity. Furthermore, a high-throughput prioritisation based on biological activity favours myxobacteria that do not produce natural products with this particular activity in a standard cultivation setting. Thus, for a more holistic prioritisation of transposon mutants or additives, a high throughput MS-based method to quickly identify the samples with obvious changes in the observed metabolome might be more preferable. Such data-based prioritisations have been previously reported based on LAESI-IMS[89], MALDI-MS[90] and (short) LC-MS[76] data collection and subsequent data evaluation by comparative metabolomics[91] and the use of tools like “MetEx”[92].

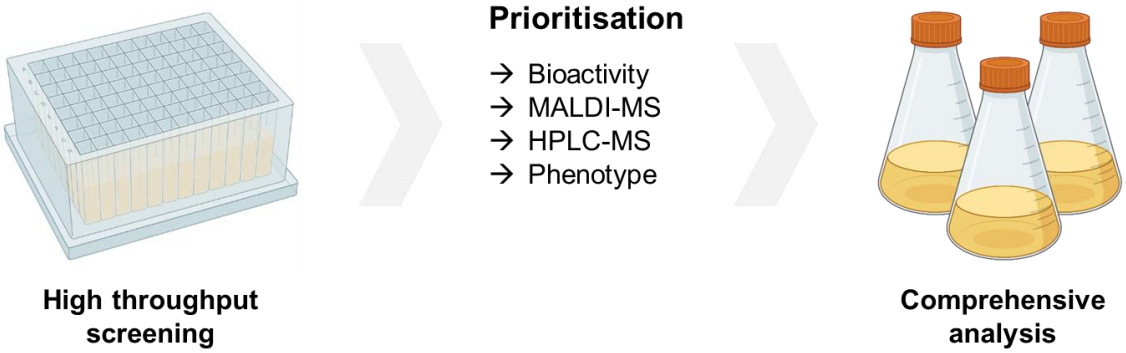

Figure 6.3: High throughput screen with subsequent prioritisation.

Cultivation of prioritised transposon mutants or with the prioritised additives should be subsequently repeated in standard shaking flasks for a comprehensive evaluation of the observed changes in this setting. Changes in the metabolome can be evaluated with the current HPLC-MS and HPLC-MS/MS-based workflow[8,93], with a subsequent dereplication of newly observed metabolites against databases, like the MINS in-house "Myxobase"[8] and the Natural Product Atlas[94], and by feature-based molecular networking[95] on the GNPS server[96]. However, the molecular fragment-based dereplication to detect derivatives of known compounds can be limited by the availability of fragmentation spectra of published natural products in the respective databases or potential changes in the fragmentation pattern as displayed for the sorangicin P and thuggacin P derivatives in chapters 3 and 4. Next to the ongoing efforts in our laboratory to record and deposit MS/MS spectra to the respective repositories (Jake Haeckl, personal communication), the evaluation of MS/MS spectra with additional tools like the currently developed VarMet[97] might become a promising strategy to improve the dereplication of myxobacterial natural products.

6.2 Revisiting old and known natural product scaffolds as opportunity for drug discovery

As discussed in the previous section and in chapters 3 and 4, the applied dereplication workflow has failed to identify the subsequently purified sorangicin P and thuggacin P derivatives as part of previously reported respective scaffolds[98,99]. The neglected antibiotic angiolam A[100] on the other hand was directly identified in the extracts of the new producer strains and prioritised based on the observation of yet unknown biological activities and the very limited knowledge about this natural product scaffold (Chapter 2). Although the myxenolones are a new natural product class in myxobacteria, they share many structural features of the 4-hydroxy-2-alkylquinoline scaffold, which is wide-spread in *Pseudomonas* and *Burkholderia* strains[101]. The characterisation of the different natural products, their biological activities, biosynthesis and further parameters in chapters 2 to 4 demonstrate the value of revisiting known natural product scaffolds for drug discovery (Figure 6.4).

The observation of a previously unknown biological activity or the discovery and development of novel derivatives with improved activities can reinvigorate the interest in old natural product scaffolds as exemplified by the potent activity of myxovalargin A against *Mycobacterium tuberculosis*[27] and the report of novel griselimycin derivatives[102]. Based on the observed anti-protozoal bioactivities (chapter 2) and the antibiotic activity

against the *acrB*-deficient *E.coli* JW0451-2[103], the metabolome of novel myxobacterium MCy12716 was investigated, identifying it as a novel producer of the weak antibiotic angiolam A. Angiolam A and some of the subsequently purified novel angiolam derivatives displayed moderate to good biological activities against several protozoa (chapter 2) and *E. coli* JW0451-2 and *E.coli ΔtolC*[103]. With these biological activities against different organisms, the angiolam scaffold adds to the myxobacterial scaffolds that display more than one promising activity, such as chlorotonils[104,105] and argyrins[106,107]. The small structural differences between different natural angiolam derivatives resulted in strong changes in their activity profiles in protozoa (chapter 2) and bacteria (own unpublished data). This information and further mode of action studies could lead to the development of novel angiolam derivatives with improved biological activities (Figure 6.4).

In order to facilitate the production of new angiolam derivatives, chemical synthesis or biotechnological methods could be applied (Figure 6.4). An organic synthesis has been developed for angiolam A[108], but displayed rather low yields. On the other hand, analysis of the sequenced genomes of new angiolam producers MCy12716 and MCy12733 resulted in the discovery of the angiolam BGC, which was subsequently verified by single-crossover gene disruption in the genetically amenable producer *Pyxidicoccus fallax* An d48 (chapter 2). In case of a further analysis of the angiolam scaffold for its anti-bacterial or anti-protozoal potential, the heterologous expression of the angiolam BGC in an appropriate host might be a good strategy to increase the production levels and to alter the biosynthetic pathway to develop novel derivatives. Prominent examples of this approach in myxobacteria are the heterologous expressions of corallopyronin[63], argyrin[29] and cystobactamid[62].

In contrast to the observation of angiolam A and its derivatives in different strains, the producer of the sorangicin P and thuggacin P subclasses does not produce the previously described representatives of these scaffolds. However, small changes in the biosynthetic pathways can lead to changes in the chemical structure and spectrum of biological activities. This effect has also been shown by the antifungal properties of ajudazol derivatives isolated from *C. crocatus* Cm c5[109] and the cytotoxic properties of the ajudazol congeners that were isolated from *Cystobacter* sp. SBCb004[110].

The new sorangicin P-796 derivative from *Pendulipora* sp. MSr12523 displays comparable antibacterial activities to the reported ones of sorangicin A[111] and also shares the cross-resistance with the RNA-polymerase inhibitor rifampicin (chapter 3). However, it is possible that the characterisation of the sorangicin P subscaffold and its BGC might be helpful to decipher the complete biosynthesis of sorangicin A. Similar to

the *sor* BGC in *S. cellulosum* So ce12[69], the *sra* BGC in *Pendulispora* sp. MSr12523 (chapter 3) does not include a cytochrome P450 monooxygenase-encoding gene that is putatively needed for the biosynthesis of the different sorangicin congeners. Therefore, a comparison of such genes in the genomes of both sorangicin producers might be helpful to identify candidate genes that could be involved in the biosynthesis of the sorangicin scaffold. This information could be used to realise the heterologous expression of sorangicin A (Figure 6.4). Given the recently reported antibiotic activities of sorangicin A against *M. abscessus* complex[112] and *Chlamydia*[113] as well as its potential to inhibit the activity of rifampicin-resistant RNA-polymerases from *M. tuberculosis*[114], a heterologous expression system for sorangicin A might be helpful to increase production and enable molecular-biological engineering of the biosynthesis.

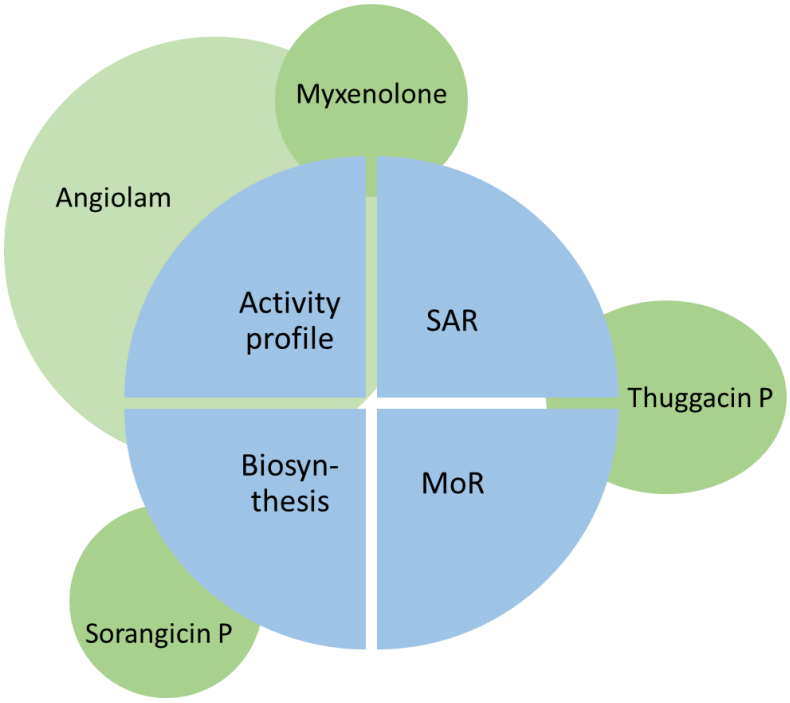

Figure 6.4: Natural product classes investigated in this thesis and gained information valuable for drug discovery.

Due to early reports about the activity of thuggacin A against *M. tuberculosis*[98,115], the thuggacin scaffold gained attention. This led to the organic synthesis of several natural thuggacin derivatives[116,117], and the semi-synthetic and fully synthetic generation of further unnatural thuggacins[118]. Interestingly, the antibiotic activity against *M. tuberculosis* was only reported for thuggacin A[115] and one semisynthetic derivative[118], while the antibiotic activity of several other thuggacin derivatives was reported to be comparable to the one of thuggacin A against other Gram-positive bacteria[98,115,118]. Upon a preliminary evaluation, the thuggacin P subclass seems to display an antibiotic activity

against *M. tuberculosis*, which is comparable to the one of thuggacin A (chapter 4). Contrary to previous reports of antibiotic activities of the thuggacin derivatives from *S. cellulosum* So ce895 against other bacteria[115], thuggacin P2-C seems to display an increased antibiotic activity against *M. tuberculosis* compared to its congeners with smaller macrocycles (chapter4). Therefore, the isolation of the thuggacin P subclass might be a good opportunity to assess and compare the antibiotic activities of the different thuggacin congeners against *M. tuberculosis* (Figure 6.4).

Interestingly, the hydroxy- and oxo-thuggacin P derivatives in co-cultivations of MSr12523 with *T. pseudospumae* do not display antibiotic activity against *M. tuberculosis*. Furthermore, the hydrolysis of the thuggacin macrolactone by cultures and cell-free lysates of *T. pseudospumae* is reminiscent of antibiotic-deactivating enzymes like β-lactamases[119,120] or erythromycin-esterases[121,122]. The ability of pathogenic bacteria to hydrolyse the thuggacin antibiotics as a potential resistance mechanism could be tested analogously to the protocol applied with *T. pseudospumae*. If the enzymatic hydrolysis as a resistance mechanism against the thuggacin antibiotics can be confirmed in pathogenic bacteria, (semi-)synthetic generation of thuggacin derivatives could overcome this mechanism (Figure 6.4). The possibly simplest way to increase the stability of the thuggacin macrocycle might be a conversion from a macrolactone to a macrolactam. By way of example, converting the macrolactone of cytotoxic epothilone B into a macrolactam yielded the (subsequently FDA-approved) semi-synthetic ixabepilone with improved metabolic stability and pharmacokinetics[123].

Mostly found in genera *Pseudomonas* and *Burkholderia*, representatives of the 4-hydroxy-2-alkylquinoline have displayed a wide array of biological activities[101]. The potent antibiotic activity of several myxenolone derivatives against *M. tuberculosis* expanded the spectrum of known biological activities of this scaffold. Considering the strong cytotoxicity of all myxenolone derivatives, a preclinical or clinical development of this compound family as an antibiotic seems unlikely (chapter 4). Nevertheless, the simplicity of the chemical scaffold and the high number of biologically active 4-hydroxy-2-alkylquinoline derivatives[101] could enable a straight-forward implementation of structure-activity relationship studies with a set of synthetic 4-hydroxy-2-alkylquinoline congeners (Figure 6.4).

6.3 **Concluding remarks**

For the past century, microorganisms have proven themselves as a prolific source of biologically active natural products. Among the lesser studied but biosynthetically gifted

microbes are Gram-negative myxobacteria. Although several hundred natural products with diverse biological activities and a variety of chemical scaffolds have been purified from this phylum so far, the phylogenetic and biosynthetic potential of myxobacteria is far from exhausted. The work in this thesis demonstrates the capability of different cultivation-based approaches to modify the secondary metabolism in myxobacteria. Furthermore, it provides a first version of a higher throughput screening workflow, which could be used to quickly assess and prioritise promising cultivation conditions to alter the observed metabolome of myxobacteria. Finally, this thesis displays the opportunity of new discoveries in known scaffolds, i.e. regarding biological activities, biosynthesis and potential resistance mechanisms.

Considering the high numbers of orphan BGCs in myxobacterial genomes, exploiting the biosynthetic potential of myxobacteria could be a promising strategy to discover novel and biologically active natural products. To increase the output of such compounds, it is a good idea to prioritise strains based on their phylogeny and biosynthetic potential and to improve the throughput of screening campaigns to exploit this potential. As discussed above, this could be achieved by automating and miniaturising the isolation of novel myxobacteria, their cultivation and subsequent processing. With the technological and computational possibilities of the 21st century, the phylogeny- and genome-informed drug discovery could reinforce natural products as a promising source for novel drugs.

6.4 References

1. Walesch, S. *et al.* Fighting antibiotic resistance-strategies and (pre)clinical developments to find new antibacterials. *EMBO Rep.,* e56033; 10.15252/embr.202256033 (2022).
2. Landwehr, W., Wolf, C. & Wink, J. Actinobacteria and Myxobacteria-Two of the Most Important Bacterial Resources for Novel Antibiotics. *Curr. Top. Microbiol. Immunol.*; 10.1007/82_2016_503 (2016).
3. Herrmann, J., Fayad, A. A. & Müller, R. Natural products from myxobacteria: novel metabolites and bioactivities. *Nat. Prod. Rep.* **34,** 135–160; 10.1039/C6NP00106H (2017).
4. Wenzel, S. C. & Müller, R. The biosynthetic potential of myxobacteria and their impact on drug discovery. *Curr. Opin. Drug Discov. Devel.* **12,** 220–230 (2009).
5. Mohr, K. I. Diversity of Myxobacteria-We Only See the Tip of the Iceberg. *Microorganisms* **6**; 10.3390/microorganisms6030084 (2018).

6. Bader, C. D., Panter, F. & Müller, R. In depth natural product discovery - Myxobacterial strains that provided multiple secondary metabolites. *Biotechnol. Adv.* **39,** 107480; 10.1016/j.biotechadv.2019.107480 (2020).

7. Krug, D. *et al.* Discovering the Hidden Secondary Metabolome of *Myxococcus xanthus*: a Study of Intraspecific Diversity. *Appl. Environ. Microbiol.* **74,** 3058–3068; 10.1128/AEM.02863-07 (2008).

8. Hoffmann, T. *et al.* Correlating chemical diversity with taxonomic distance for discovery of natural products in myxobacteria. *Nat. Commun.* **9,** 803; 10.1038/s41467-018-03184-1 (2018).

9. Garcia, R. *et al.* Pendulisporaceae – a unique myxobacterial family with distinct sporulation behaviour and high potential for natural product discovery **Manuscript in preparation** (2023).

10. Walt, C., Bader, C. D., Krug, D. & Müller, R. Aggravated Cultivation of Myxobacteria Stimulates Secondary Metabolism. *(Manuscript in preparation)*.

11. Bader, C. D. *et al.* Sandacrabins - Structurally Unique Antiviral RNA Polymerase Inhibitors from a Rare Myxobacterium. *Chemistry – A European Journal* **28,** e202104484; 10.1002/chem.202104484 (2022).

12. Panter, F., Bader, C. D. & Müller, R. The Sandarazols are Cryptic and Structurally Unique Plasmid-Encoded Toxins from a Rare Myxobacterium*. *Angewandte Chemie (International ed. in English)* **60,** 8081–8088; 10.1002/anie.202014671 (2021).

13. Mohr, K. I., Stechling, M., Wink, J., Wilharm, E. & Stadler, M. Comparison of myxobacterial diversity and evaluation of isolation success in two niches: Kiritimati Island and German compost. *MicrobiologyOpen* **5,** 268–278; 10.1002/mbo3.325 (2016).

14. Mohr, K. I., Zindler, T., Wink, J., Wilharm, E. & Stadler, M. Myxobacteria in high moor and fen: An astonishing diversity in a neglected extreme habitat. *MicrobiologyOpen* **6,** e00464; 10.1002/mbo3.464 (2017).

15. Petters, S. *et al.* The soil microbial food web revisited: Predatory myxobacteria as keystone taxa? *ISME J.*; 10.1038/s41396-021-00958-2 (2021).

16. Garcia, R., Krug, D. & Müller, R. Discovering natural products from myxobacteria with emphasis on rare producer strains in combination with improved analytical methods. In *Methods in Enzymology. Complex Enzymes in Microbial Natural*

Product Biosynthesis. Part A: Overview Articles and Peptides, edited by David A. Hopwood (2009), Vol. 458, pp. 59–91.

17. Mahler, L. *et al.* Highly parallelized droplet cultivation and prioritization on antibiotic producers from natural microbial communities. *eLife* **10**; 10.7554/eLife.64774 (2021).

18. Nichols, D. *et al.* Use of Ichip for High-Throughput *In Situ* Cultivation of "Uncultivable" Microbial Species. *Appl. Environ. Microbiol.* **76,** 2445–2450; 10.1128/AEM.01754-09 (2010).

19. Costa, M. S., Clark, C. M., Ómarsdóttir, S., Sanchez, L. M. & Murphy, B. T. Minimizing Taxonomic and Natural Product Redundancy in Microbial Libraries Using MALDI-TOF MS and the Bioinformatics Pipeline IDBac. *J. Nat. Prod.* **82,** 2167–2173; 10.1021/acs.jnatprod.9b00168 (2019).

20. Nonejuie, P., Burkart, M., Pogliano, K. & Pogliano, J. Bacterial cytological profiling rapidly identifies the cellular pathways targeted by antibacterial molecules. *Proc. Natl. Acad. Sci. USA* **110,** 16169–16174; 10.1073/pnas.1311066110 (2013).

21. Wenzel, S. C. & Müller, R. Myxobacteria—''microbial factories' for the production of bioactive secondary metabolites. *Mol. Biosyst.* **5,** 567–574; 10.1039/b901287g (2009).

22. Zaburannyi, N., Bunk, B., Maier, J., Overmann, J. & Müller, R. Genome analysis of the fruiting body forming myxobacterium *Chondromyces crocatus r*eveals high potential for natural product Biosynthesis. *Appl. Environ. Microbiol.* **82,** 1945–1957; 10.1128/AEM.03011-15 (2016).

23. Nett, M., Ikeda, H. & Moore, B. S. Genomic basis for natural product biosynthetic diversity in the actinomycetes. *Nat. Prod. Rep.* **26,** 1362–1384; 10.1039/b817069j (2009).

24. Robey, M. T., Caesar, L. K., Drott, M. T., Keller, N. P. & Kelleher, N. L. An interpreted atlas of biosynthetic gene clusters from 1,000 fungal genomes. *Proceedings of the National Academy of Sciences of the United States of America* **118,** 1–9; 10.1073/pnas.2020230118 (2021).

25. Weissman, K. J. & Müller, R. Myxobacterial secondary metabolites: bioactivities and modes-of-action. *Nat. Prod. Rep.* **27,** 1276–1295; 10.1039/c001260m (2010).

26. Covington, B. C., Xu, F. & Seyedsayamdost, M. R. A Natural Product Chemist's Guide to Unlocking Silent Biosynthetic Gene Clusters. *Annu. Rev. Biochem.* **90,** 763–788; 10.1146/annurev-biochem-081420-102432 (2021).

27. Koller, T. O. *et al.* The Myxobacterial Antibiotic Myxovalargin: Biosynthesis, Structural Revision, Total Synthesis, and Molecular Characterization of Ribosomal Inhibition. *J. Am. Chem. Soc.* **accepted**; 10.1021/jacs.2c08816 (2023).

28. Sucipto, H., Pogorevc, D., Luxenburger, E., Wenzel, S. C. & Müller, R. Heterologous production of myxobacterial α-pyrone antibiotics in *Myxococcus xanthus*. *Metab. Eng.* **44,** 160–170; 10.1016/j.ymben.2017.10.004 (2017).

29. Pogorevc, D. & Müller, R. Biotechnological production optimization of argyrins – a potent immunomodulatory natural product class. *Microb. Biotechnol.*; 10.1111/1751-7915.13959 (2021).

30. Schwarz, J., Hubmann, G., Rosenthal, K. & Lütz, S. Triaging of Culture Conditions for Enhanced Secondary Metabolite Diversity from Different Bacteria. *Biomolecules* **11**; 10.3390/biom11020193 (2021).

31. Jenny Schwarz, Georg Hubmann, Ayla Schwarz, Katrin Rosenthal & Stephan Lütz. Bivariate OSMAC Designs Expand the Secondary Metabolite Production Space in Corallococcus Coralloides; 10.20944/preprints202203.0118.v1 (2022).

32. Bode, H. B., Bethe, B., Höfs, R. & Zeeck, A. Big effects from Small Changes: Possible Ways to Explore Nature's Chemical Diversity. *ChemBioChem* **3,** 619–627 (2002).

33. Pan, R., Bai, X., Chen, J., Zhang, H. & Wang, H. Exploring Structural Diversity of Microbe Secondary Metabolites Using OSMAC Strategy: A Literature Review. *Front. Microbiol.* **10,** 294; 10.3389/fmicb.2019.00294 (2019).

34. Romano, S., Jackson, S. A., Patry, S. & Dobson, A. D. W. Extending the "One Strain Many Compounds" (OSMAC) Principle to Marine Microorganisms. *Mar. Drugs* **16**; 10.3390/md16070244 (2018).

35. Keller, L. *et al.* Macyranones: Structure, Biosynthesis, and Binding Mode of an Unprecedented Epoxyketone that Targets the 20S Proteasome. *J. Am. Chem. Soc.* **137,** 8121–8130; 10.1021/jacs.5b03833 (2015).

36. Popoff, A. *et al.* Structure and Biosynthesis of Myxofacyclines: Unique Myxobacterial Polyketides Featuring Varing and Rare Heterocycles *. *Chemistry (Weinheim an der Bergstrasse, Germany)* **27,** 16654–16661; 10.1002/chem.202103095 (2021).

37. Liao, Y., Wei, Z.-H., Bai, L., Deng, Z. & Zhong, J.-J. Effect of fermentation temperature on validamycin A production by Streptomyces hygroscopicus 5008. *J. Biotechnol.* **142,** 271–274; 10.1016/j.jbiotec.2009.04.015 (2009).

38. Doull, J. L., Singh, A. K., Hoare, M. & Ayer, S. W. Conditions for the production of jadomycin B by Streptomyces venezuelae ISP5230: effects of heat shock, ethanol treatment and phage infection. *J. Ind. Microbiol.* **13,** 120–125; 10.1007/BF01584109 (1994).

39. Munoz-Dorado, J., Marcos-Torres, F. J., Garcia-Bravo, E., Moraleda-Munoz, A. & Perez, J. Myxobacteria: Moving, Killing, Feeding, and Surviving Together. *Front. Microbiol.* **7,** 781; 10.3389/fmicb.2016.00781 (2016).

40. Bader, C. D., Haack, P. A., Panter, F., Krug, D. & Müller, R. Expanding the Scope of Detectable Microbial Natural Products by Complementary Analytical Methods and Cultivation Systems. *J. Nat. Prod.*; 10.1021/acs.jnatprod.0c00942 (2021).

41. Hoffmann, M. *et al.* Homospermidine Lipids: A compound class specifically formed during fruiting body formation of *Myxococcus xanthus* DK1622. *ACS Chem. Biol.* **13,** 273–280; 10.1021/acschembio.7b00816 (2018).

42. Neuber, M. Alteration of the metabolite spectrum of myxobacteria through alternative cultivation and extraction techniques. Doctoral Thesis. Saarland University, 2022.

43. Bertrand, S. *et al.* Metabolite induction via microorganism co-culture: a potential way to enhance chemical diversity for drug discovery. *Biotechnol. Adv.* **32,** 1180–1204; 10.1016/j.biotechadv.2014.03.001 (2014).

44. Li, P. F. *et al.* Co-cultivation of *Sorangium cellulosum* strains affects cellular growth and biosynthesis of secondary metabolite epothilones. *FEMS Microbiol. Ecol.* **85,** 358–368; 10.1111/1574-6941.12125 (2013).

45. Lee, N. *et al.* Iron competition triggers antibiotic biosynthesis in Streptomyces coelicolor during coculture with Myxococcus xanthus. *The ISME Journal* **14,** 1111–1124; 10.1038/s41396-020-0594-6 (2020).

46. Ellis, B. M., Fischer, C. N., Martin, L. B., Bachmann, B. O. & McLean, J. A. Spatiochemically Profiling Microbial Interactions with Membrane Scaffolded Desorption Electrospray Ionization-Ion Mobility- Imaging Mass Spectrometry and Unsupervised Segmentation. *Anal. Chem.*; 10.1021/acs.analchem.9b02992 (2019).

47. Onaka, H., Mori, Y., Igarashi, Y. & Furumai, T. Mycolic acid-containing bacteria induce natural-product biosynthesis in *Streptomyces* species. *Appl. Environ. Microbiol.* **77,** 400–406; 10.1128/AEM.01337-10 (2011).

48. Hoshino, S., Onaka, H. & Abe, I. Activation of silent biosynthetic pathways and discovery of novel secondary metabolites in actinomycetes by co-culture with

mycolic acid-containing bacteria. *Journal of Industrial Microbiology & Biotechnology* **46,** 363–374; 10.1007/s10295-018-2100-y (2019).

49. Yamanaka, K. *et al.* Desferrioxamine E produced by *Streptomyces griseus* stimulates growth and development of *Streptomyces tanashiensis*. *Microbiology* **151,** 2899–2905; 10.1099/mic.0.28139-0 (2005).

50. Onaka, H., TABATA, H., Igarashi, Y., SATO, Y. & Furumai, T. Goadsporin, a Chemical Substance which Promotes Secondary Metabolism and Morphogenesis in Streptomycetes. I. Purification and Characterization. *J. Antibiot.* **54,** 1036–1044; 10.7164/antibiotics.54.1036 (2001).

51. Sho-ichi Amano *et al.* Promomycin, a polyether promoting antibiotic production in Streptomyces spp. *J Antibiot* **63,** 486–491; 10.1038/ja.2010.68 (2010).

52. Mccurdy, H. D. & MacRae, T. H. Xanthacin. A bacteriocin of Myxococcus xanthus fb. *Can. J. Microbiol.* **20,** 131–135; 10.1139/m74-021 (1974).

53. Craney, A., Ozimok, C., Pimentel-Elardo, S. M., Capretta, A. & Nodwell, J. R. Chemical perturbation of secondary metabolism demonstrates important links to primary metabolism. *Chem. Biol.* **19,** 1020–1027; 10.1016/j.chembiol.2012.06.013 (2012).

54. Seyedsayamdost, M. R. High-throughput platform for the discovery of elicitors of silent bacterial gene clusters. *Proc. Natl. Acad. Sci. USA* **111,** 7266–7271; 10.1073/pnas.1400019111 (2014).

55. Panter, F., Krug, D., Baumann, S. & Müller, R. Self-resistance guided genome mining uncovers new topoisomerase inhibitors from myxobacteria. *Chem. Sci.* **9,** 4898–4908; 10.1039/C8SC01325J (2018).

56. Hug, J. J., Panter, F., Krug, D. & Müller, R. Genome mining reveals uncommon alkylpyrones as type III PKS products from myxobacteria. *J. Ind. Microbiol. Biotechnol.* **46,** 319–334; 10.1007/s10295-018-2105-6 (2019).

57. Cortina, N. S., Krug, D., Plaza, A., Revermann, O. & Müller, R. Myxoprincomide: a natural product from *Myxococcus xanthus* discovered by comprehensive analysis of the secondary metabolome. *Angew. Chem. Int. Ed. Engl.* **51,** 811–816; 10.1002/anie.201106305 (2012).

58. Gemperlein, K., Rachid, S., Garcia, R. O., Wenzel, S. C. & Müller, R. Polyunsaturated fatty acid biosynthesis in myxobacteria. Different PUFA synthases and their product diversity. *Chem. Sci.* **5,** 1733–1741; 10.1039/C3SC53163E (2014).

59. Akone, S. H., Hug, J. J., Kaur, A., Garcia, R. & Müller, R. Structure Elucidation and Biosynthesis of Nannosterols A and B, Myxobacterial Sterols from Nannocystis sp. MNa10993. *J. Nat. Prod.*; 10.1021/acs.jnatprod.2c01143 (2023).

60. Hug, J. J. & Müller, R. Host Development for Heterologous Expression and Biosynthetic Studies of Myxobacterial Natural Products. 6.09. In *Comprehensive Natural Products III,* edited by H.-W. (. Liu & T. P. Begley (Elsevier, Oxford, 2020), Vol. 6, pp. 149–216.

61. Gao, Y., Walt, C., Bader, C. D. & Müller, R. Genome-Guided Discovery of the Myxobacterial Thiolactone-Containing Sorangibactins. *ACS Chem. Biol.* **18,** 924–932; 10.1021/acschembio.3c00063 (2023).

62. Groß, S., Schnell, B., Haack, P. A., Auerbach, D. & Müller, R. In vivo and in vitro reconstitution of unique key steps in cystobactamid antibiotic biosynthesis. *Nat. Commun.* **12,** 1696; 10.1038/s41467-021-21848-3 (2021).

63. Pogorevc, D. *et al.* Production optimization and biosynthesis revision of corallopyronin A, a potent anti-filarial antibiotic. *Metab. Eng.* **55,** 201–211; 10.1016/j.ymben.2019.07.010 (2019).

64. Julien, B. & Shah, S. Heterologous expression of epothilone biosynthetic genes in *Myxococcus xanthus*. *Antimicrob. Agents Chemother.* **46,** 2772–2778; 10.1128/AAC.46.9.2772–2778.2002 (2002).

65. Tu, Q. *et al.* Genetic engineering and heterologous expression of the disorazol biosynthetic gene cluster via Red/ET recombineering. *Sci. Rep.* **6,** 21066; 10.1038/srep21066 (2016).

66. Hug, J. J. *et al.* Genome-Guided Discovery of the First Myxobacterial Biarylitide Myxarylin Reveals Distinct C–N Biaryl Crosslinking in RiPP Biosynthesis. *Molecules* **26,** 7483; 10.3390/molecules26247483 (2021).

67. Schlemmer, J. Developing heterologous expression platforms for biosynthetic pathways of myxobacterial natural products. Doctoral Thesis. Saarland University, 2022.

68. Wenzel, S. C. & Müller, R. Myxobacterial natural product assembly lines: fascinating examples of curious biochemistry. *Nat. Prod. Rep.* **24,** 1211–1224; 10.1039/b706416k (2007).

69. Irschik, H. *et al.* Analysis of the sorangicin gene cluster reinforces the utility of a combined phylogenetic/retrobiosynthetic analysis for deciphering natural product

assembly by trans-AT PKS. *ChemBioChem* **11,** 1840–1849; 10.1002/cbic.201000313 (2010).

70. Gao, Y. Heterologous Expression for the Discovery and Biosynthesis Studies of Myxobacterial Natural Products. Dissertation. Universität des Saarlandes, 2023.

71. Panter, F., Bader, C. D. & Müller, R. Synergizing the potential of bacterial genomics and metabolomics to find novel antibiotics. *Chem. Sci.,* 5994–6010; 10.1039/D0SC06919A (2021).

72. Rutledge, P. J. & Challis, G. L. Discovery of microbial natural products by activation of silent biosynthetic gene clusters. *Nat. Rev. Microbiol.* **13,** 509–523; 10.1038/nrmicro3496 (2015).

73. Ahmed, Y., Rebets, Y., Tokovenko, B., Brötz, E. & Luzhetskyy, A. Identification of butenolide regulatory system controlling secondary metabolism in Streptomyces albus J1074. *Sci Rep* **7,** 9784; 10.1038/s41598-017-10316-y (2017).

74. Park, J.-D. *et al.* Thailandenes, Cryptic Polyene Natural Products Isolated from Burkholderia thailandensis Using Phenotype-Guided Transposon Mutagenesis. *ACS Chem. Biol.* **15,** 1195–1203; 10.1021/acschembio.9b00883 (2020).

75. Mao, D., Yoshimura, A., Wang, R. & Seyedsayamdost, M. R. Reporter-Guided Transposon Mutant Selection for Activation of Silent Gene Clusters in Burkholderia thailandensis. *ChemBioChem*; 10.1002/cbic.201900748 (2020).

76. Yoshimura, A. *et al.* Unlocking Cryptic Metabolites with Mass Spectrometry-Guided Transposon Mutant Selection. *ACS Chem. Biol.* **15,** 2766–2774; 10.1021/acschembio.0c00558 (2020).

77. Sandmann, A., Sasse, F. & Müller, R. Identification and analysis of the core biosynthetic machinery of tubulysin, a potent cytotoxin with potential anticancer activity. *Chem. Biol.* **11,** 1071–1079; 10.1016/j.chembiol.2004.05.014 (2004).

78. Kopp, M., Irschik, H., Pradella, S. & Müller, R. Production of the tubulin destabilizer disorazol in *Sorangium cellulosum*: biosynthetic machinery and regulatory genes. *ChemBioChem* **6,** 1277–1286; 10.1002/cbic.200400459 (2005).

79. Rachid, S., Gerth, K., Kochems, I. & Müller, R. Deciphering regulatory mechanisms for secondary metabolite production in the myxobacterium *Sorangium cellulosum* So ce56. *Mol. Microbiol.* **63,** 1783–1796; 10.1111/j.1365-2958.2007.05627.x (2007).

80. Rachid, S., Sasse, F., Beyer, S. & Müller, R. Identification of StiR, the first regulator of secondary metabolite formation in the myxobacterium *Cystobacter fuscus* Cb f17.1. *J. Biotechnol.* **121,** 429–441; 10.1016/j.jbiotec.2005.08.014 (2006).

81. Xu, Z. *et al.* Large-Scale Transposition Mutagenesis of Streptomyces coelicolor Identifies Hundreds of Genes Influencing Antibiotic Biosynthesis. *Applied and environmental microbiology* **83**; 10.1128/AEM.02889-16 (2017).

82. Shen, B. *et al.* Enediynes: Exploration of microbial genomics to discover new anticancer drug leads. *Bioorganic & Medicinal Chemistry Letters* **25,** 9–15; 10.1016/j.bmcl.2014.11.019 (2015).

83. Blin, K. *et al.* antiSMASH 7.0: new and improved predictions for detection, regulation, chemical structures and visualisation. *Nucleic Acids Res.*; 10.1093/nar/gkad344 (2023).

84. Navarro-Muñoz, J. C. *et al.* A computational framework to explore large-scale biosynthetic diversity. *Nat. Chem. Biol.* **16,** 60–68; 10.1038/s41589-019-0400-9 (2020).

85. Terlouw, B. R. *et al.* MIBiG 3.0: a community-driven effort to annotate experimentally validated biosynthetic gene clusters. *Nucleic Acids Res.* **51,** D603-D610; 10.1093/nar/gkac1049 (2023).

86. Han, E. J., Lee, S. R., Hoshino, S. & Seyedsayamdost, M. R. Targeted Discovery of Cryptic Metabolites with Antiproliferative Activity. *ACS Chem. Biol.* **17,** 3121–3130; 10.1021/acschembio.2c00588 (2022).

87. Moon, K., Xu, F., Zhang, C. & Seyedsayamdost, M. R. Bioactivity-HiTES Unveils Cryptic Antibiotics Encoded in Actinomycete Bacteria. *ACS Chem. Biol.* **14,** 767–774; 10.1021/acschembio.9b00049 (2019).

88. Walt, C. Discovery and Characterization of Myxobacterial and Actinobacterial Natural Products by Metabolome and Genome Mining Approaches. Saarland University, 2023.

89. Xu, F. *et al.* A genetics-free method for high-throughput discovery of cryptic microbial metabolites. *Nat. Chem. Biol.*; 10.1038/s41589-018-0193-2 (2019).

90. Zhang, C. & Seyedsayamdost, M. R. Discovery of a Cryptic Depsipeptide from Streptomyces ghanaensis via MALDI-MS-Guided High-Throughput Elicitor Screening. *Angewandte Chemie (International ed. in English)* **59,** 23005–23009; 10.1002/anie.202009611 (2020).

91. Covington, B. C., McLean, J. A. & Bachmann, B. O. Comparative mass spectrometry-based metabolomics strategies for the investigation of microbial secondary metabolites. *Nat. Prod. Rep.* **34,** 6–24; 10.1039/c6np00048g (2017).

92. Covington, B. C. & Seyedsayamdost, M. R. MetEx, a Metabolomics Explorer Application for Natural Product Discovery. *ACS Chem. Biol.* **16,** 2825–2833; 10.1021/acschembio.1c00737 (2021).

93. Hoffmann, T., Krug, D., Hüttel, S. & Müller, R. Improving natural products identification through targeted LC-MS/MS in an untargeted secondary metabolomics workflow. *Anal. Chem.* **86,** 10780–10788; 10.1021/ac502805w (2014).

94. van Santen, J. A. *et al.* The Natural Products Atlas 2.0: a database of microbially-derived natural products. *Nucleic Acids Res.* **50,** D1317-D1323; 10.1093/nar/gkab941 (2022).

95. Nothias, L.-F. *et al.* Feature-based molecular networking in the GNPS analysis environment. *Nat Methods* **17,** 905–908; 10.1038/s41592-020-0933-6 (2020).

96. Wang, M. *et al.* Sharing and community curation of mass spectrometry data with Global Natural Products Social Molecular Networking. *Nat. Biotechnol.* **34,** 828–837; 10.1038/nbt.3597 (2016).

97. Tagirdzhanov, A., Mohimani, H. & Gurevich, A. (eds.). *VarMet: high-throughput annotation of small molecule mass spectra via the modification-tolerant search of chemical databases. HIPS Symposium 2023* (2023).

98. Steinmetz, H. *et al.* Thuggacins, macrolide antibiotics active against *Mycobacterium tuberculosis*: Isolation from myxobacteria, structure elucidation, conformation analysis and biosynthesis. *Chem. Eur. J.* **13,** 5822–5832; 10.1002/chem.200700269 (2007).

99. Jansen, R. *et al.* Antibiotika aus Gleitenden Bakterien, XXXVII. Sorangicin A, ein hochwirksames Antibiotikum mit neuartiger Makrolid-Polyether-Struktur aus *Sorangium cellulosum*, So ce12: Spektroskopische Strukturaufklärung, Kristall- und Lösungsstruktur. *Liebigs Ann. Chem.* **1989,** 111–119; 10.1002/jlac.198919890124 (1989).

100. Werner Kohl, Barbara Witte, Brigitte Kunze, Victor Wray, Dietmar Schomburg, Hans Reichenbach und Gerhard Höfle. Angiolam A - ein neues Antibiotikum aus Angiococcus. *Liebigs Ann. Chem.,* 2088–2097 (1985).

101. Saalim, M., Villegas-Moreno, J. & Clark, B. R. Bacterial Alkyl-4-quinolones: Discovery, Structural Diversity and Biological Properties. *Molecules (Basel, Switzerland)* **25**; 10.3390/molecules25235689 (2020).

102. Kling, A. *et al.* Targeting DnaN for tuberculosis therapy using novel griselimycins. *Science* **348,** 1106–1112; 10.1126/science.aaa4690 (2015).

103. Hönig, S. Isolation and characterisation of novel myxobacteria from regional samples. Masterthesis. Saarland University, 2020.

104. Gerth, K., Steinmetz, H., Höfle, G. & Jansen, R. Chlorotonil A, a macrolide with a unique gem-dichloro-1,3-dione functionality from *Sorangium cellulosum*, So ce1525. *Angew. Chem. Int. Ed. Engl.* **47,** 600–602; 10.1002/anie.200703993 (2008).

105. Jungmann, K. *et al.* Two of a kind-The biosynthetic pathways of chlorotonil and anthracimycin. *ACS Chem. Biol.* **10,** 2480–2490; 10.1021/acschembio.5b00523 (2015).

106. Sasse, F. *et al.* Argyrins, immunosuppressive cyclic peptides from myxobacteria. I. Production, isolation, physico-chemical and biological properties. *J. Antibiot.* **55,** 543–551 (2002).

107. Vollbrecht, L. *et al.* Argyrins, immunosuppressive cyclic peptides from myxobacteria. II. Structure elucidation and stereochemistry. *J. Antibiot.* **55,** 715–721; 10.7164/antibiotics.55.715 (2002).

108. Gieseler, M. T. & Kalesse, M. Synthesis of Angiolam A. *Org. Lett.* **16,** 548–551; 10.1021/ol403423r (2014).

109. Kunze, B., Jansen, R., Hofle, G. & Reichenbach, H. Ajudazols, new inhibitors of the mitochondrial electron transport from Chondromyces crocatus. Production, antimicrobial activity and mechanism of action. *J. Antibiot.* **57,** 151–155 (2004).

110. Zeng, H. *et al.* Expanding the Ajudazol Cytotoxin Scaffold: Insights from Genome Mining, Biosynthetic Investigations, and Novel Derivatives. *Journal of natural products*; 10.1021/acs.jnatprod.2c00637 (2022).

111. Irschik, H., Jansen, R., Gerth, K., Hofle, G. & Reichenbach, H. The sorangicins, novel and powerful inhibitors of eubacterial RNA polymerase isolated from myxobacteria. *J. Antibiot.* **40,** 7–13 (1987).

112. Sullivan, J. R. *et al.* Natural Products Lysobactin and Sorangicin A Show In Vitro Activity against Mycobacterium abscessus Complex. *Microbiology Spectrum,* e0267222; 10.1128/spectrum.02672-22 (2022).

113. Graspeuntner, S. *et al.* Sorangicin A Is Active against Chlamydia in Cell Culture, Explanted Fallopian Tubes, and Topical In Vivo Treatment. *Antibiotics* **12,** 795; 10.3390/antibiotics12050795 (2023).

114. Lilic, M. *et al.* The antibiotic sorangicin A inhibits promoter DNA unwinding in a *Mycobacterium tuberculosis* rifampicin-resistant RNA polymerase. *Proc. Natl. Acad. Sci. U.S.A.*; 10.1073/pnas.2013706117 (2020).

115. Irschik, H., Reichenbach, H., Höfle, G. & Jansen, R. The thuggacins, novel antibacterial macrolides from *Sorangium cellulosum* acting against selected Gram-positive bacteria. *J Antibiot.* **60,** 733–738; 10.1038/ja.2007.95 (2007).

116. Bock, M., Dehn, R. & Kirschning, A. Total synthesis of thuggacin B. *Angew. Chem. Int. Ed. Engl.* **47,** 9134–9137; 10.1002/anie.200803271 (2008).

117. Tsutsumi, T. *et al.* Total Synthesis of Thuggacin cmc-A and Its Structure Determination. *Org. Lett.* **23,** 5208–5212; 10.1021/acs.orglett.1c01743 (2021).

118. Franke, J. *et al.* Total and semi-syntheses of antimicrobial thuggacin derivatives // Total and Semi-Syntheses of Antimicrobial Thuggacin Derivatives. *Chem. Eur. J.* **21,** 4272–4284; 10.1002/chem.201405874 (2015).

119. Abraham, E. P. & Chain, E. An Enzyme from Bacteria able to Destroy Penicillin. *Nature* **146,** 837; 10.1038/146837a0 (1940).

120. Ambler, R. P. The structure of beta-lactamases. *Philos.Trans.R.Soc.Lond B Biol.Sci.* **289,** 321–331; 10.1098/rstb.1980.0049 (1980).

121. Golkar, T., Zieliński, M. & Berghuis, A. M. Look and Outlook on Enzyme-Mediated Macrolide Resistance. *Front. Microbiol.* **9,** 1942; 10.3389/fmicb.2018.01942 (2018).

122. Zieliński, M., Park, J., Sleno, B. & Berghuis, A. M. Structural and functional insights into esterase-mediated macrolide resistance. *Nat Commun* **12,** 1732; 10.1038/s41467-021-22016-3 (2021).

123. Conlin, A., Fornier, M., Hudis, C., Kar, S. & Kirkpatrick, P. Ixabepilone. *Nat Rev Drug Discov* **6,** 953–954; 10.1038/nrd2469 (2007).